

Geophysical, climatological and anthropogenic hazards and disaster: Vulnerability, risk assessment, and sustainability

Edited by

Shankar Karuppannan, Sandipan Das and Suresh Kumar

Coordinated by

Uday Chatterjee

Published in

Frontiers in Environmental Science

Frontiers in Earth Science



FRONTIERS EBOOK COPYRIGHT STATEMENT

The copyright in the text of individual articles in this ebook is the property of their respective authors or their respective institutions or funders. The copyright in graphics and images within each article may be subject to copyright of other parties. In both cases this is subject to a license granted to Frontiers.

The compilation of articles constituting this ebook is the property of Frontiers.

Each article within this ebook, and the ebook itself, are published under the most recent version of the Creative Commons CC-BY licence. The version current at the date of publication of this ebook is CC-BY 4.0. If the CC-BY licence is updated, the licence granted by Frontiers is automatically updated to the new version.

When exercising any right under the CC-BY licence, Frontiers must be attributed as the original publisher of the article or ebook, as applicable.

Authors have the responsibility of ensuring that any graphics or other materials which are the property of others may be included in the CC-BY licence, but this should be checked before relying on the CC-BY licence to reproduce those materials. Any copyright notices relating to those materials must be complied with.

Copyright and source acknowledgement notices may not be removed and must be displayed in any copy, derivative work or partial copy which includes the elements in question.

All copyright, and all rights therein, are protected by national and international copyright laws. The above represents a summary only. For further information please read Frontiers' Conditions for Website Use and Copyright Statement, and the applicable CC-BY licence.

ISSN 1664-8714
ISBN 978-2-8325-4464-8
DOI 10.3389/978-2-8325-4464-8

About Frontiers

Frontiers is more than just an open access publisher of scholarly articles: it is a pioneering approach to the world of academia, radically improving the way scholarly research is managed. The grand vision of Frontiers is a world where all people have an equal opportunity to seek, share and generate knowledge. Frontiers provides immediate and permanent online open access to all its publications, but this alone is not enough to realize our grand goals.

Frontiers journal series

The Frontiers journal series is a multi-tier and interdisciplinary set of open-access, online journals, promising a paradigm shift from the current review, selection and dissemination processes in academic publishing. All Frontiers journals are driven by researchers for researchers; therefore, they constitute a service to the scholarly community. At the same time, the *Frontiers journal series* operates on a revolutionary invention, the tiered publishing system, initially addressing specific communities of scholars, and gradually climbing up to broader public understanding, thus serving the interests of the lay society, too.

Dedication to quality

Each Frontiers article is a landmark of the highest quality, thanks to genuinely collaborative interactions between authors and review editors, who include some of the world's best academicians. Research must be certified by peers before entering a stream of knowledge that may eventually reach the public - and shape society; therefore, Frontiers only applies the most rigorous and unbiased reviews. Frontiers revolutionizes research publishing by freely delivering the most outstanding research, evaluated with no bias from both the academic and social point of view. By applying the most advanced information technologies, Frontiers is catapulting scholarly publishing into a new generation.

What are Frontiers Research Topics?

Frontiers Research Topics are very popular trademarks of the *Frontiers journals series*: they are collections of at least ten articles, all centered on a particular subject. With their unique mix of varied contributions from Original Research to Review Articles, Frontiers Research Topics unify the most influential researchers, the latest key findings and historical advances in a hot research area.

Find out more on how to host your own Frontiers Research Topic or contribute to one as an author by contacting the Frontiers editorial office: frontiersin.org/about/contact

Geophysical, climatological and anthropogenic hazards and disaster: Vulnerability, risk assessment, and sustainability

Topic editors

Shankar Karuppannan — Adama Science and Technology University, Ethiopia
Sandipan Das — Symbiosis International University, India
Suresh Kumar — Indian Institute of Remote Sensing, India

Topic coordinator

Uday Chatterjee — Bhatler College, Dantan, India

Citation

Karuppannan, S., Das, S., Kumar, S., Chatterjee, U., eds. (2024). *Geophysical, climatological and anthropogenic hazards and disaster: Vulnerability, risk assessment, and sustainability*. Lausanne: Frontiers Media SA.
doi: 10.3389/978-2-8325-4464-8

Table of contents

- 05 **Editorial: Geophysical, climatological and anthropogenic hazards and disaster: vulnerability, risk assessment, and sustainability**
Uday Chatterjee, Suresh Kumar, Shankar Karuppannan and Sandipan Das
- 07 **The research on spatial-temporal evolution and influence factors of urban resilience: A case study in the Guangzhou metropolitan area**
Bo Tang and Zechuang Tan
- 31 **Hazard assessment of potential debris flow: A case study of Shaling Gully, Lingshou County, Hebei Province, China**
Zhong Fu Wang, Xu Sheng Zhang, Xu Zhu Zhang, Ming Tang Wu and Bo Wu
- 41 **Risk assessment of deep excavation construction based on combined weighting and nonlinear FAHP**
Shihao Liu, Zhanping Song, Yong Zhang, Desai Guo, Yinhao Sun, Tao Zeng and Jiangsheng Xie
- 54 **GIS-based modeling of landslide susceptibility zonation by integrating the frequency ratio and objective–subjective weighting approach: a case study in a tropical monsoon climate region**
Pham Viet Hoa, Nguyen Quang Tuan, Pham Viet Hong, Giang Thi Phuong Thao and Nguyen An Binh
- 74 **GIS-based flood susceptibility mapping using bivariate statistical model in Swat River Basin, Eastern Hindukush region, Pakistan**
Zahid Ur Rahman, Waheed Ullah, Shibiao Bai, Safi Ullah, Mushtaq Ahmad Jan, Mohsin Khan and Muhammad Tayyab
- 91 **A Modified Mercalli Intensity map of Bangladesh: a proposal for zoning of earthquake hazard**
Edris Alam
- 113 **Machine learning for high-resolution landslide susceptibility mapping: case study in Inje County, South Korea**
Xuan-Hien Le, Song Eu, Chanul Choi, Duc Hai Nguyen, Minh Yeon and Giha Lee
- 127 **Vulnerability and risk assessment mapping of Bhitarkanika national park, Odisha, India using machine-based embedded decision support system**
Shantakar Mohanty, Sk. Mustak, Dharmaveer Singh, Thanh Van Hoang, Manishree Mondal and Chun-Tse Wang

146 Seribu islands in the megacities of Jakarta on the frontlines of the climate crisis

Martiwi Diah Setiawati, Uday Chatterjee, Yudha Setiawan Djamil, La Ode Alifatri, Muhammad Rizki Nandika, Herlambang Aulia Rachman, Indarto Happy Supriyadi, Nuraini Rahma Hanifa, Aidy M. Muslim, Tsuyoshi Eguchi, Bayu Prayudha, Aulia Oktaviani, Novi Susetyo Adi, Jeverson Renyaan, Siti Sulha, Sam Wouthuyzen, Subodh Chandra Pal, Abu Reza Md. Towfiqul Islam, Edris Alam and Md Kamrul Islam

163 Geotechnical factors influencing earth retaining wall deformation during excavations

Seunghwan Seo, Jongjeon Park, Younghun Ko, Gunwoong Kim and Moonkyung Chung



OPEN ACCESS

EDITED AND REVIEWED BY
Alexander Kokhanovsky,
German Research Centre for Geosciences,
Germany

*CORRESPONDENCE
Uday Chatterjee,
✉ raj.chatterjee459@gmail.com

RECEIVED 15 January 2024
ACCEPTED 18 January 2024
PUBLISHED 01 February 2024

CITATION
Chatterjee U, Kumar S, Karuppannan S and
Das S (2024), Editorial: Geophysical,
climatological and anthropogenic hazards and
disaster: vulnerability, risk assessment,
and sustainability.
Front. Environ. Sci. 12:1370984.
doi: 10.3389/fenvs.2024.1370984

COPYRIGHT
© 2024 Chatterjee, Kumar, Karuppannan and
Das. This is an open-access article distributed
under the terms of the [Creative Commons
Attribution License \(CC BY\)](#). The use,
distribution or reproduction in other forums is
permitted, provided the original author(s) and
the copyright owner(s) are credited and that the
original publication in this journal is cited, in
accordance with accepted academic practice.
No use, distribution or reproduction is
permitted which does not comply with these
terms.

Editorial: Geophysical, climatological and anthropogenic hazards and disaster: vulnerability, risk assessment, and sustainability

Uday Chatterjee ^{1*}, Suresh Kumar ²,
Shankar Karuppannan ³ and Sandipan Das ⁴

¹Department of Geography, Bhatler College, Kharagpur, West Bengal, India, ²Agriculture, Forestry & Ecology Group, Indian Institute of Remote Sensing (IIRS), Indian Space Research Organization (ISRO), Department of Space, Government of India, Dehradun, Uttarakhand, India, ³Department of Applied Geology, School of Applied Natural Sciences (SoANS), Adama Science and Technology, Adama, Ethiopia, ⁴Symbiosis Institute of Geoinformatics, Symbiosis International (Deemed University), Pune, India

KEYWORDS

natural disaster, remote sensing, hazard assessment, environmental management, disaster risk reduction

Editorial on the Research Topic

Geophysical, climatological and anthropogenic hazards and disaster: vulnerability, risk assessment, and sustainability

In the contemporary era, the global community grapples with frequent natural and human-induced threats, spanning from droughts and floods to deforestation, placing a substantial population at risk of catastrophic destruction and loss of life. Recognizing the inevitability of natural hazards, the quantification of these events and the development of reliable forecasts emerge as crucial tools to mitigate their adverse impacts, contributing to the establishment of a more resilient and secure society. This Research Topic aims to consolidate existing knowledge on multiple hazards, emphasizing monitoring and management, with the objective of bridging the gap between scientific understanding, policy formulation, and community engagement. It focusses on applications of remote sensing, GIS and precision methodologies for precise and reliable evaluation of various natural and environmental hazards. Additionally, the studies underscore the implementation of eco-friendly and sustainable management approaches to foster resilient societies. The rich contents, both thematic and regional perspectives, sheds light on the dynamic nature of climate crisis, natural resources, landscapes, agricultural ecosystems and water systems, across various spatial and temporal scales. It covers both theoretical and applied aspects, serving as a comprehensive guide for future research endeavours. The research primarily focussed on exploring various aspects of hazards and disasters associated with natural resources covering groundwater depletion, occurrence of drought and floods, land use/land cover change, soil erosion, landslides, water scarcity and the investigation of SINDEI framework. The primary objective is to enhance comprehension of Geospatial Technologies, scrutinizing their interplay with

hazards, landscapes, land use, water scarcity, forestry, spatial modeling, artificial intelligence, and the environment to actively contribute to the sustainable development.

In summary, this Research Topic provides a comprehensive understanding of both conventional and cutting-edge geospatial technologies applied in atmospheric, lithospheric, hydrospheric, biospheric, and socio-economic contexts. Addressing hazards, disasters, and sustainable development and management, the compilation proves invaluable for researchers, scientists, non-governmental organizations (NGOs), academic professionals, policymakers, and university communities involved in hazard and disaster resilience, climate change, environmental sciences, geomorphology, remote sensing, natural resources management, GIS, hydrology, and soil sciences.

Tang et al. assessed the metropolitan area which plays a crucial role in shaping city agglomerations in China and is vital for achieving integrated development within the region. Specifically, the Guangzhou metropolitan area holds significant importance in Guangdong Province's economic development plan. This research investigates the multi-dimensional perspective of city resilience within the metropolitan area, focusing on the spatial-temporal pattern and the factors that influence it. The findings aim to offer valuable insights and serve as a reference for fostering the coordinated development of metropolitan areas.

Wang et al. evaluated the risk of debris flow in Shaling Gully through FLO-2D model and systematic approach. In this paper hazard zonation at different rainstorm frequencies was determined using ARCGIS 10.8 software and also highlighted the numerical simulation was employed to evaluate the efficacy of a retaining dam in mitigating debris flow, providing technical insights to improve the safety of downstream structures.

Hoa et al. highlighted a unique perspective to the discourse by combining knowledge-driven consultation with precise statistical analysis of geospatial data. This integration considers essential explanatory factors, leading to a dependable delineation of landslide-prone areas across both spatial and temporal dimensions in the tropical monsoon areas.

Liu et al. focused on delineating landslide susceptibility in a coastal mountainous area of Vietnam through the integration of the subjective Analytic Hierarchy Process (AHP) and the objective Shannon Entropy (SE). By combining these methods, the study provided a substantial advancement in the geographical information system (GIS)-based zoning of landslide susceptibility in Vietnam. This advancement enhances the capacity for early warning and mitigation of catastrophic hazards. Notably, the approach not only draws on expert knowledge but also incorporates reliable statistical evidence, offering resilience against potential uncertainties associated with future climate changes.

Rahman et al. assessed the flood susceptibility map for the SRB in the eastern Hindu Kush region of Pakistan, utilizing a GIS-based FR model. Additionally, the research explores how various factors contributing to floods impact the increased vulnerability to flooding in the area. The paper assesses the effectiveness of the FR bivariate

statistical model in delineating flood susceptibility in the SRB. The insights gained from this research offer valuable perspectives for stakeholders, aiding in the implementation of efficient flood risk management strategies and promoting sustainable development.

Alam prepared an innovative Modified Mercalli Intensity (MMI) map, crafted by analyzing the cumulative impact of 80 earthquakes in Bangladesh spanning from BC 810–2015, covering both Bangladesh and its neighboring regions. The paper commences with an exploration of earthquake hazard zoning and preparedness initiatives.

Le et al. evaluated the effectiveness of six machine learning (ML) algorithms in land surface mapping (LSM) specifically in Inje County, South Korea. This research serves as a valuable initial step for exploring the application of ML techniques in LSM not only in South Korea but also in other geographical areas around the world as well.

Mohanty et al. made a comparison of traditional decision support models like AHP and machine learning algorithms in the evaluation of flood vulnerability and risk within Bhitarkanika National Park, Odisha, India.

Setiawati et al. explores local climate trends, evaluates their potential consequences, and analyzes policy interventions in the Seribu Islands, Indonesia.

Seo et al. comprehensively examines the factors affecting the behavior of retaining walls in response to ground excavations in urban areas. The results of this study suggest that the lateral movement of the wall caused by excavation is closely tied to both the unit weight and shear strength of the soil.

Author contributions

UC: Conceptualization, Writing—original draft, Writing—review and editing. SuK: Conceptualization, Writing—review and editing. SaK: Supervision, Writing—review and editing. SD: Conceptualization, Formal Analysis, Supervision, Writing—review and editing.

Conflict of interest

The authors declare that the research was conducted in the absence of any commercial or financial relationships that could be construed as a potential conflict of interest.

Publisher's note

All claims expressed in this article are solely those of the authors and do not necessarily represent those of their affiliated organizations, or those of the publisher, the editors and the reviewers. Any product that may be evaluated in this article, or claim that may be made by its manufacturer, is not guaranteed or endorsed by the publisher.



OPEN ACCESS

EDITED BY

Sandipan Das,
Symbiosis International University, India

REVIEWED BY

Voltaire Alvarado Peterson,
University of Concepcion, Chile
Maxim A. Dulebenets,
Florida Agricultural and Mechanical
University, United States

*CORRESPONDENCE

Bo Tang,
tballen196@163.com

SPECIALTY SECTION

This article was submitted to
Environmental Informatics and Remote
Sensing,
a section of the journal
Frontiers in Environmental Science

RECEIVED 24 September 2022

ACCEPTED 27 October 2022

PUBLISHED 10 November 2022

CITATION

Tang B and Tan Z (2022), The research
on spatial-temporal evolution and
influence factors of urban resilience: A
case study in the Guangzhou
metropolitan area.

Front. Environ. Sci. 10:1052930.

doi: 10.3389/fenvs.2022.1052930

COPYRIGHT

© 2022 Tang and Tan. This is an open-
access article distributed under the
terms of the [Creative Commons
Attribution License \(CC BY\)](#). The use,
distribution or reproduction in other
forums is permitted, provided the
original author(s) and the copyright
owner(s) are credited and that the
original publication in this journal is
cited, in accordance with accepted
academic practice. No use, distribution
or reproduction is permitted which does
not comply with these terms.

The research on spatial-temporal evolution and influence factors of urban resilience: A case study in the Guangzhou metropolitan area

Bo Tang^{1*} and Zechuang Tan^{1,2}

¹School of Resources and Planning, Guangzhou Xinhua University, Guangzhou, China, ²College of Resources and Environment, Fujian Agriculture and Forestry University, Fuzhou, China

Resilience city, a new concept of city sustainable development, becomes one of the important subjects of high-quality development research. Compared to the traditional urban disaster mitigation approach, resilient cities focus more on the organizational capacity and coordination within the urban systems. Taking Guangzhou metropolitan area as an instance, which is featured a highly developed economy and society and frequently happened hazards and disturbances, the paper constructs an evaluation index system from four city subsystems, including economy, society, ecology, and engineering. Meanwhile, by applying the methods of global entropy weight, variation coefficient, geographic information system, and obstacle degree model, the paper explores the time changes, space evolution, and obstacle degree factors of city resilience in the Guangzhou metropolitan area from 2010 to 2020. The research results show that: (1) There is a significant change in the time difference of city comprehensive resilience of the Guangzhou metropolitan area. The resilience of each city's resilience subsystem has grown steadily, of which the development level of economic resilience, social resilience, and engineering resilience has been steadily improved, and ecology resilience level shows a slight decline among a steadily increasing. (2) The overall city resilience of the Guangzhou metropolitan area shows a radial pattern taking Guangzhou as the core, of which the city economy, society, and engineering resilience grades mainly show a medium and low resilience level, the ecology resilience mainly shows a medium and high resilience level, and the general performance of resilience space distribution level is high in the southeast and low in the northwest. (3) Social resilience and ecological resilience are the main driving subsystems in the early and late stages of city resilience development in Guangzhou metropolitan area during the research period, and engineering resilience is the main constraint subsystem. (4) Water and soil loss control area and population density are the main obstacle factors in the early and late stages of city resilience in the Guangzhou metropolitan area. The density of the city drainage pipeline and the total import and export volume are the basic resilience barrier factors. The paper analyzes the spatial-temporal pattern and influencing factors of city resilience in the metropolitan area from a multi-dimensional perspective, provides a new thinking and analysis

framework for the management and sustainability of city resilience in the metropolitan area, and provides a reference for the coordinated development of the metropolitan area.

KEYWORDS

urban resilience, spatial-temporal evolution, global entropy weight method, obstacle degree, Guangzhou metropolitan area

1 Introduction

As the main place for human activities and the energy flow cycle space carrier, the city is constantly challenged by its systems and external environment. Meanwhile, the city is a comprehensive society-economy-ecology system with certain “Resilience” and is capable of resisting external interference and reducing disaster losses with its capabilities to make the system realize a new balance status through adaptation or recovery (Zhao, et al., 2020). City resilience, an emerging concept in the field of ecology and environment, mainly focuses on the relationships between the structural complexity and functional diversity of the city and nature, economy, and society (Xu et al., 2018). The research on resilience theory and resilience city launched early and developed rapidly in foreign countries. Through exploring the potential problems and risks of the city system and improving the city’s reaction capability to uncertain disturbances and shocks, the concept of city resilience has increasingly been cared for worldwide under the support of international organizations, government agencies, and private foundations. The concept analysis, index construction, and research methods of resilience city in foreign countries are relatively perfect, and many research achievements have been obtained in the fields of natural science, engineering technology, and society economy (Herrera et al., 2016; Lorenz, 2013; Meerow et al., 2016). Based on this, the paper proposes and plans, and builds “Resilient City” (Turner et al., 2003) and “Resilient Community” (Colclough et al., 2021) in a targeted manner, and actively promotes interdisciplinary research and cross-field cooperation. The concept of city resilience was proposed at the American Ecological Academic Year Meeting in 2002. There is still no broad consensus on its scientific definition, which is mainly because the composition and characteristics of the city system are highly different on the global, regional, and even local scales, and the city system is subject to the disturbance factors of the external environment with diversity and dynamics (Müller, 2010), including various natural disasters, public health, and public safety events. Meanwhile, with global climate change, cities have begun to vigorously promote carbon peaking and carbon neutrality, deepen ecological civilization and promote green and low-carbon lifestyles to improve their ability to cope with weather and climate extremes and adapt to the adverse effects of climate change (Osman, 2021). Scholars focus on global environmental issues caused by different sectors (e.g., production, construction, shipping, manufacturing, etc.)

(Zhang et al., 2021; Dulebenets, 2018), actively explore the mechanisms of energy consumption structure, industrial development degree, technical equipment, energy efficiency and other factors on urban ecological environment, and deepen the study of the resilience of urban ecosystem (Grzegorz et al., 2021; Liang et al., 2021). In terms of research content, there are different levels and dimensions involved. For instance, the City Resilience Index (CRI) published by the Rockefeller Foundation is a city resilience evaluation system with a relative influencing power at present (Marjolein and Bas, 2017). There are four dimensions in CRI: health and well-being, economy and society, infrastructure construction and environment, and leadership and strategy, which combines qualitative and quantitative methods to evaluate and has a relatively comprehensive index system. Desouza and Flanery (2013) thought that the deficiencies of the city could be understood through resilience evaluation. Through three intervention activities of planning, designing, and managing, the dynamics and physical factors inside a resilient city could be influenced. From four perspectives of infrastructure resilience, policy resilience, economic resilience, and social resilience, Jabareen (2013) studied multidisciplinary and complex city resilience. In terms of research methods, attention was paid to the improvement of the conceptual framework, the index system, and data analysis (Paulo and Luís, 2019). For instance, the “Global 100 Resilient Cities” plan puts emphasizes the complexity and diversity of the system and constructed a general framework with seven characteristics, including reflection, resource availability, inclusiveness, integrity, robustness, surplus, and plasticity, reflecting resilience city to manage with sudden disturbances and slow pressure (Amirzadeh et al., 2022). Through establishing an index system to evaluate community resilience, Simon et al applied the interview to determine the index level to evaluate the infrastructure status of slum communities. This method can be applied to quickly evaluate community resilience, making the evaluation results more general and comprehensive (Simon et al., 2016). During the study of community anti-seismic resilience, Michel et al (2012) innovatively established a functional model of infrastructure resilience probability and resilience recovery time to obtain city infrastructure resilience through quantitative calculation and analysis. With the continuous accumulation of city big data and the continuous progress of cloud computing technology, it is promising that the quantitative evaluation mode, urban systems abstraction hierarchy (USAH), and

simulation dynamic analysis method and technology of resilience city can be realized (McClymont et al., 2022).

The theoretical research on resilient cities in China launched relatively late. In recent years, with the national attention on public safety, many achievements have been accumulated on the research ideas, research objects, and research methods of resilient cities based on different perspectives (Li, 2017). However, it is still in the initial exploration stage, lacking systematizations and standardization, and the relevant theoretical framework needs improvement. In terms of theoretical research, the construction of a domestic city resilience evaluation index system is mainly based on the three perspectives of city basic elements, city resilience characteristics, and the staging process of resilience development (Ni and Li, 2021). Xu and Shao (2015) made a comprehensive analysis of the connotation of a resilient city, what characteristics a resilient city shall have, and how to shape a city's resilience, which provides a new idea for managing crisis. Standing at the perspective of the social ecology system, Sun et al. (2017) analyzed and obtained the city resilience status and space differentiation characteristics of each region in the Yangtze River Delta region from four levels, including economy, society, ecology, and municipal facilities. Wu and Chen (2018) divided the recovery capacity of resilient cities into four stages, including resilience recovery, recovery capacity loss, recovery capacity enhancement, and recovery capacity loss, to reveal its evolution mechanism and summarize the social significance of the recovery capacity of the resilient city. In terms of case studies, taking provinces and city agglomerations as research objects, scholars mainly evaluated city resilience characteristics and influencing factors from different research perspectives. Bai et al. (2019) constructed a comprehensive city resilience measurement index system from four systems, including economy, society, ecology, and infrastructure to quantitatively evaluate cities' resilience above the prefecture level in China. In terms of research methods, there are prevailing methods, including the analytic hierarchy process, TOPSIS entropy weight, cloud model risk matrix, and neural network. The construction of city resilience reflects the risk awareness and bottom-line thinking of city development and is the basic guarantee for constructing a new development pattern and promoting high-quality city development (Liu, 2021). In recent years, with the progressive impact of natural disasters and public health events on cities, research on resilience regulation and management has been gradually gaining the attention of scholars. The research objects of city resilience governance in China mainly focus on city risks, the construction of a resilience governance system around the evaluation system, and the resilience governance path centered on sustainable development (He et al., 2022). The rapid development of urbanization in China urgently needs to improve city resilience through city and rural planning. City resilience can be improved by standing at four dimensions of nature, function, space, and governance, and combining material

aspects of planning technology and construction standards and social aspects of social regulation and public participation (Fei et al., 2014). These resilience management measures have played an important role in the city's response to natural disasters and public health emergencies (Yang et al., 2019).

Standing at the perspective of the city system, foreign scholars analyze the composition and combination of city resilience under different scales, pay close attention to the influence of natural disasters on the city system, and focus on the study of community resilience of city human settlements. Domestic scholars pay more attention to resilience evaluation based on the basic elements of cities. Based on quantitative statistical analysis methods, they study city resilience development under different spatial scales and propose relevant city resilience planning concepts. In conclusion, there are numerous efforts and work have been performed on city resilience for concept connotation, theoretical framework, and evaluation methods at home and abroad, which have obtained numerous inspirations. The research scale on city resilience is gradually diversified. In terms of the index system, multi-disciplinary crossover and integration are conducted to break through the constraints of "Internal Risks", and gradually expand to external factors, including nature, society, economy, and ecology. However, there is difficulty in reaching a consensus on the theoretical framework of city resilience, and the rapid changes and uncertainties of constituent factors, functional linkage structure, and regional and internal and external environments of the city have increased the complexity of the city resilience evaluation systems and evaluation process (Ni and Li, 2021). Currently, there is still room for improvement in specific research as follows, including insufficient analysis of the development process and changing characteristics of city resilience; the research scales are mostly concentrated at the macro level (country, province) and micro level (community), and there are few research on the city resilience of metropolitan areas in the middle scale field; there are few analysis on the restrictive factors restricting the comprehensive resilience of cities, and insufficient attention paid to the regulation and management of resilience.

With the rapid urbanization process, lagging construction of supporting facilities, and lack of urban emergency and response systems and social governance mechanisms, urban vulnerability is very obvious. Secondly, since the types of risks faced by cities in different regions vary greatly, a uniform risk management mechanism cannot effectively mitigate crises. Therefore, it has become a pressing issue to study how cities can cope with "uncertainty disturbances" and enhance urban resilience. The Metropolitan area, an important node in the construction of city agglomerations in China, is important in realizing area-integrated and regional coordinated development. The Guangzhou metropolitan area is a key area in the economic development plan of Guangdong Province. Evaluating its city resilience and grasping the development path of city resilience

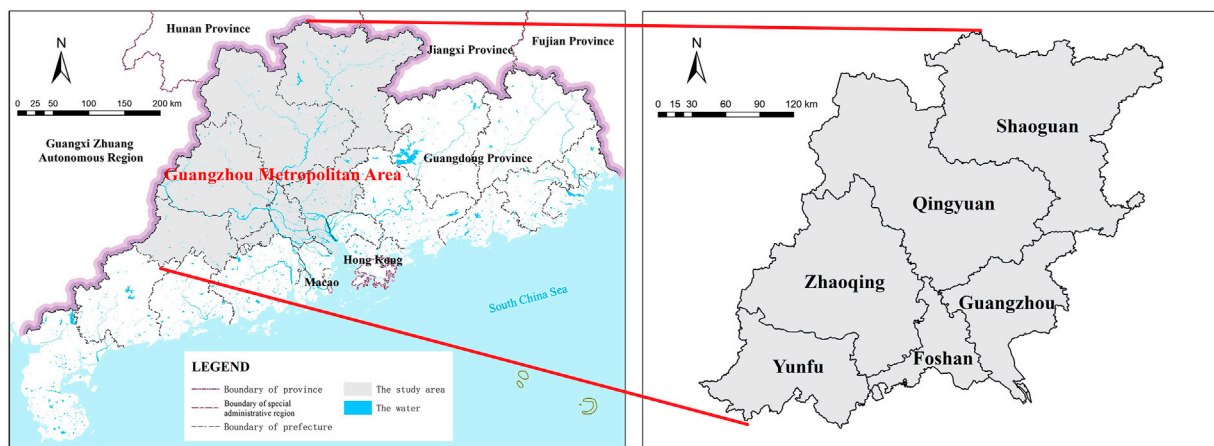


FIGURE 1
Study area.

can effectively prevent serious losses caused by city public safety issues. Therefore, adopting the global entropy weight method, taking time sections of 2010, 2012, 2014, 2016, 2018, and 2020, and starting from the basic factors of the four resilient dimensions, including economy, society, ecology, and engineering, the paper conducts a dynamic spatial-temporal evolution. Meanwhile, combining with system factor and the obstacle degree factor of city resilience development in the Guangzhou metropolitan area, the paper analyzes its influence mechanism, aiming at providing a reference for the general development and planning of cities in the Guangzhou metropolitan area in the future and achieving the optimization of resource allocation to promote the resilient development of Guangzhou metropolitan area. Furthermore, the paper can offer experience and suggestions for the development of city resilience in other metropolitan areas in Guangdong Province, as well as a reference for the high-quality development of cities in Guangdong Province.

2 Study area and data sources

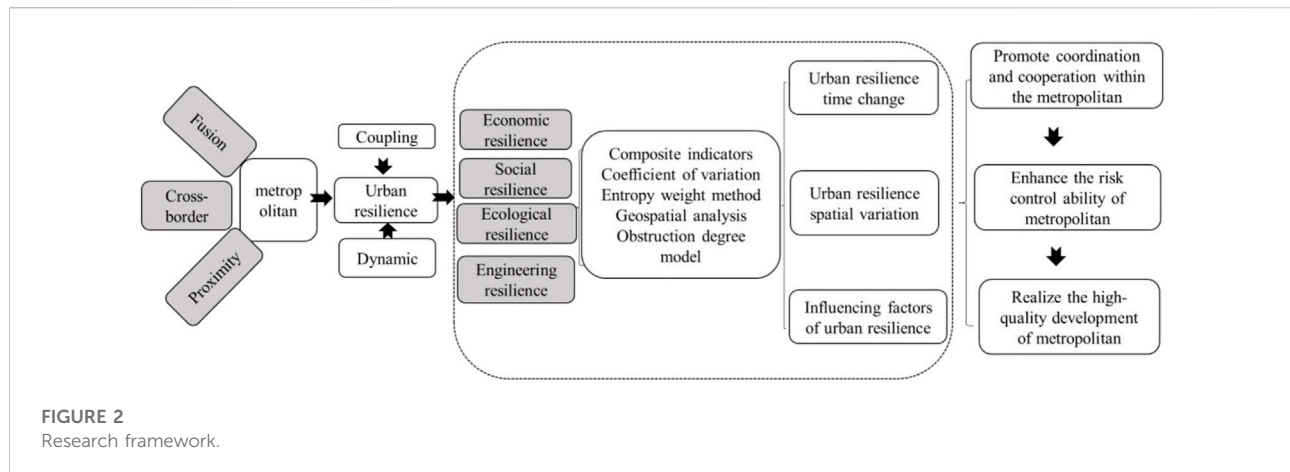
2.1 Study area

Figure 1 shows the study area. The Guangzhou metropolitan is the largest one of the five major metropolitan areas in Guangdong Province. It includes six cities, Guangzhou, Foshan, Zhaoqing, Qingyuan, Yunfu, and Shaoguan, with a total area of 71,171 km², accounting for 39.6% of Guangdong Province. By the end of 2020, the resident population of the Guangzhou metropolitan area was 41.59 million, and the total Gross Domestic Product (GDP) was 422,805 billion, accounting for 32.94% and

38.17% respectively of Guangdong Province. The development within the Guangzhou metropolitan area is fast, but the economic growth, ecological environment, social conditions, and infrastructure development are unbalanced and insufficient. The Guangzhou metropolitan area will become a core area for developing advanced manufacturing industries, and strategic emerging industries and their supporting industries, it is the main area for Guangdong to move towards high-quality and regional coordinated development.

2.2 Data sources

The indicator statistics of this study mainly involve six cities within the Guangzhou metropolitan area and apply the content of 28 indicator evaluation factors for 6 years in 2010, 2012, 2014, 2016, 2018, and 2020. The specific indicator data were obtained from 2011, 2013, 2015, 2017, 2019, and 2021 Guangdong Statistical Yearbook, Guangdong Rural Statistical Yearbook, China Urban Statistical Yearbook, and each city's statistical yearbook national economic and social development statistical bulletin. The ecological environment condition index is obtained from the environmental quality and monitoring bulletin of the department of ecology and environment of Guangdong province (<http://gdee.gd.gov.cn/sthjzs/index.html>). The number of Internet broadband access users has been obtained from the China urban statistical yearbook and China entrepreneur Investment Club (CEIC) statistical database (<https://www.ceicdata.com/en>). In the case of missing data from individual indicators, the mean value method is applied to make up the data according to the adjacent years.



3 Methods

3.1 Theoretical framework

Initially applied in the field of mechanical engineering, resilience was later introduced into ecological research. Defined as the capability of a system to return to its original equilibrium state after being subjected to external perturbations, resilience is used as a term to describe the characteristics of an ecosystem in its stable form (Li, 2017). At present, the theory of resilience has evolved from the engineering resilience of single homeostasis to the ecological resilience of multiple equilibria, and then to the continuous evolutionary resilience of complex fitness systems. It encompasses three theories of perturbation, systemic and adaptive capacity (Yang et al., 2021). The concept of a resilient city represents the integration of resilience theory with urban planning and management theory. In definition, an urban system can resist change, recover stability, and even reach a new equilibrium state through learning and adaptation, thus maintaining fundamental structures, critical functions, and significant features in response to internal disturbances and external shocks. Through an in-depth study of the theory and connotation of a resilient city, it is found that it is characterized mainly by redundancy, dynamic balance, diversity, adaptability, and others. Redundancy means that when damage is caused to the essential facilities of the urban system, there are backup facilities in place to ensure the normal operation of the urban system under exceptional circumstances. Dynamic equilibrium means the improvement and disturbance involved in the process of urban design. As for the overall balance and stability, they mean that the urban system consists of multiple subsystems that can withstand different risks. Adaptability is referred to as the capability of the urban system to deal with various threats through learning and improvement (Xu et al., 2019). To sum up, these elements provide general guidance on building the evaluation index system. At the same time, urban resilience

evaluation plays a role in connecting theory with practice, the implication of which is two-fold. On the one hand, it is necessary to focus on the impact of uncertainty perturbations and the limited capacity of a city; on the other hand, it is essential to ensure the integrity of urban patterns and the continuity of functional operation. Urban resilience is inseparable from the support of the natural system, human system, and environmental system, including ecological, economic, social, institutional, facility and disaster dimensions (Zhang and Wang, 2019). As a territorial spatial organization of fusion, cross-border, and proximity, the urban resilience of the metropolitan area is coupled and dynamic. The analysis of the spatial and temporal evolution of urban resilience and the influencing factors can help coordination and cooperation within the metropolitan area, enhance the risk regulation ability of the metropolitan area, and realize the high-quality development of the metropolitan area. Figure 2 shows the theoretical basis for the research method in this study.

3.2 Index system

Urban resilience is a new idea of integrated regional risk response and governance, focusing on improving the ability of urban cluster systems to organize themselves, coordinate their functions, and adapt to uncertainty (Abid, 2016), emphasizing the plasticity, responsiveness, and evolution of changes in natural elements and human factors. The current urban resilience evaluation mainly focuses on three different scales: community, city, and region, and the evaluation focus of different scales are different, which leads to differences in the evaluation system (Shao and Xu 2015; Fang and Wang, 2015). Based on the concept of the resilient city, concerning summarizing the current literature research results (Turner et al., 2003; Marjolein and Bas 2017; Yang et al., 2019), and combined with the development characteristics of the

TABLE 1 Urban resilience evaluation index system in the Guangzhou metropolitan area.

Target layer	Criterion layer	Factor Layer (unit)	Indicator properties
Urban Resilience in Guangzhou Metropolitan Area	Economic Resilience	E1: DP per capita (yuan)	+
		E2: Per capita disposable income (yuan)	+
		E3: The tertiary industry's share of GDP (%)	+
		E4: Annual growth rate of fixed asset investment (%)	+
		E5: Total import and export (hundred million dollars)	+
		E6: Public budget expenditure (hundred million yuan)	+
		E7: Savings deposit balance per capita (yuan)	+
	Social Resilience	E8: Population density (people/km ²)	+
		E9: Urban registered unemployment rate (%)	–
		E10: The proportion of urban and rural essential medical insurance participants in the permanent population (%)	+
		E11: Unemployment insurance as a percentage of employment (%)	+
		E12: Number of licensed (assistant) physicians per 10,000 people (people)	+
		E13: Number of hospital beds per 10,000 people(a)	+
		E14: The fatality rate of production safety accidents in each city's GDP per 100 million yuan (%)	–
	Ecological Resilience	E15: Per capita park green space (m ²)	+
		E16: Green coverage in built-up areas (%)	+
		E17: Urban sewage treatment rate (%)	+
		E18: The rate of harmless treatment of municipal solid waste (%)	+
		E19: Soil erosion control area (kkm ²)	+
		E20: Growth rate of energy consumption per unit of GDP (%)	–
		E21: Ecological environment condition index	+
	Engineering Resilience	E22: Highway mileage per square kilometer (km/km ²)	+
		E23: Urban Drainage Pipe Density (km/km ²)	+
		E24: Electricity consumption per capita (kW·h)	+
		E25: Total gas supply per capita (people/m ³)	+
		E26: Number of mobile phone users (million households)	+
		E27: Number of Internet Broadband Access Users (million households)	+
		E28: Standard operation number of urban public transport vehicles(a)	+

Guangzhou metropolitan area and urban elements, the city resilience evaluation system is constructed from four criteria layers of economic, social, ecological, and engineering. Table 1 is the urban resilience evaluation index system in this study.

By identifying and analyzing the factors of each urban resilience domain, the effect of each element on the development of urban resilience is explored below:

(1) Economic factors: The economic level of a city is the vane of its development and determines the development speed of its emergency system. High economic resilience systems often support cities with high comprehensive resilience to guarantee the coordination and adaptability among subsystems within the town. The economic indicators represented by GDP per capita can reflect the level of development of the city society, the degree of action, and the comprehensive macroeconomic operation; in addition,

the per capita disposable income and the per capita savings balance can indicate the high standard of living of the residents and their property reserves, respectively. The public budget expenditure level reflects the investment in public utilities. The proportion of tertiary industry to GDP reflects the layout of the modern service industry in the city, and the expanding market scale of the tertiary sector can be the leading force in driving economic growth and absorbing employment. As the southern gate of China, Guangdong Province is the frontline of China's reform and opening up and an essential window for attracting investment. Its inner cities, such as Guangzhou, Shenzhen, and Foshan, are famous for their robust commercial and financial environment.

(2) Social factors: social stability is the cornerstone of the long-term stability of the country and the city, and maintaining urban security and social stability is the top priority for

development. Since 2019, the sudden health event represented by the new crown pneumonia epidemic has been the primary problem common to all countries worldwide. The fight against the epidemic has become a massive test of the world's governance capacity, in which the number of licensed (assistant) physicians and the number of hospital beds directly affect the city's relief for the infected population and the stability of the economic and social side of the city. The urban registered unemployment rate is the percentage of the registered unemployed population in a region, which reflects the unemployment status of urban residents. The ratio of the number of people insured by unemployment insurance to the number of employed people and the balance of the number of people insured by urban and rural basic medical insurance to the resident population can effectively reflect the ability of urban residents to effectively manage risk through insurance as a contractual economic relationship when experiencing unemployment and suffering from illness. Population density reflects the basic situation of the number of people per unit area in a region. The mortality rate of production and safety accidents with a gross domestic product of 100 million yuan can effectively reflect the level of investment and attention to safety production in cities, curbing the occurrence of safety accidents and maintaining social stability. It is worth noting that studies have shown that population mobility between cities, and between rural and urban areas are gradually becoming an important cause of regional land use, resource development, environmental change, and public health, and these are among the important drivers for studying urban resilience (Morrow, 1999). At the same time, population mobility also involves the issue of efficient transfer and sharing of public services, such as the employment market, housing market, medical and education system, infrastructure, and security management (Wang et al., 2012). Therefore, it is necessary to strengthen the scientific research and analysis of the mobile population at a later stage and to track and analyze the important outflow and inflow areas to better improve urban resilience (Betty et al., 2017).

- (3) Ecological environment factors: The ecological environment is the material basis for human survival and the basic premise of development. Its ability to resist disasters and the quality of the green product directly affect the level of human survival and growth. The per capita park green area and the greening coverage rate of the built-up regions can reflect the level of urban residents living environment and quality of life. The rate of urban sewage treatment and the rate of harmless treatment of urban domestic waste can indicate the city's ability to treat sewage and solid waste, which can help reduce urban pollutants in the ecological environment, improve the ecological resilience of the city and establish an environmentally sustainable city. Guangdong region is

TABLE 2 The results of the weights.

Criterion layer	Factor layer	Total factor weights
Economic Resilience	E1(0.1167)	0.0292
	E2 (0.1010)	0.0253
	E3 (0.1004)	0.0251
	E4 (0.0196)	0.0049
	E5 (0.3211)	0.0803
	E6 (0.2196)	0.0549
	E7 (0.1215)	0.0303
Social Resilience	E8 (0.4298)	0.1075
	E9 (0.0242)	0.0060
	E10 (0.0745)	0.0186
	E11 (0.2238)	0.0560
	E12 (0.0842)	0.0210
	E13 (0.1181)	0.0295
	E14 (0.0454)	0.0114
Ecological Resilience	E15 (0.1621)	0.0405
	E16 (0.0820)	0.0205
	E17 (0.0433)	0.0108
	E18 (0.0711)	0.0178
	E19 (0.4559)	0.1140
	E20 (0.0357)	0.0089
	E21 (0.1499)	0.0375
Engineering Resilience	E22 (0.0481)	0.0120
	E23 (0.2908)	0.0727
	E24 (0.0352)	0.0088
	E25 (0.1338)	0.0334
	E26 (0.1647)	0.0412
	E27 (0.1147)	0.0287
	E28 (0.2127)	0.0532

hot and rainy all year round, and soil erosion is joint on mountain slopes. The area of soil erosion control can indicate the city's ability to reduce regional soil erosion and guarantee the stability of the regional ecological environment. The growth rate of energy consumption per unit of GDP reflects the change in energy consumption by regional living and production, concentrates on the sustainable development ability of the region, and is an essential indicator of comprehensive energy utilization efficiency. The ecological condition index reflects the multi-level complete ecological level of urban vegetation cover, biodiversity, and ecosystem stability, and the size of its index value is positively correlated with ecological resilience.

- (4) Engineering facilities factor: Municipal infrastructure is the fundamental guarantee for the daily life of urban residents and is the indispensable material foundation for the survival

and development of the city. Guangdong is prone to rain and floods in summer and the higher the density of urban drainage pipes, the stronger the city's resilience to floods. Information and communication technology and development is an essential metric for urban resilience evaluation, which can enhance the ability of urban basic service facility system and community to cope with external disturbances (Song, 2020), and the number of cell phone users and Internet broadband access users better reflect the level of residents' condition on essential information communication and exchange. The total gas supply and electricity consumption per capita reflect the city's energy demand. Road mileage per square kilometer, the number of urban public transport vehicles standard operation demonstrates the level of function of urban road traffic and public transport; it's within a specific limit, the more road mileage, the more public transport operations, the higher the operational efficiency of urban transportation, the higher the engineering resilience.

3.3 Global entropy weighting method

The global entropy weighting method is based on the traditional one, adding the time dimension for longitudinal comparison to determine the index weights. For the analysis of the original data, the greater the indicator dispersion, the greater the practical information of the indicator, the greater the entropy value, the higher the weight value, and *vice versa* smaller (Fang and Wang, 2015); the weighting results are shown in Table 2. The specific steps are as follows:

- (1) Building the original matrix

$$X = \{x_{tij}\}_{p \times m \times n} \quad (1 \leq t \leq p, 1 \leq i \leq m, 1 \leq j \leq n) \quad (1)$$

where X_{tij} indicates the j th index of the i th city in the t year.

- (2) Standardizing the data

Assuming that the evaluation index x_{tij} is a positive index or negative index, the following can be derived

$$\text{Positive indicators: } a_{tij} = \frac{x_{tij} - \min(x_{tij})}{\max(x_{tij}) - \min(x_{tij})} \quad (2)$$

$$\text{Negative indicator: } a_{tij} = \frac{\max(x_{tij}) - x_{tij}}{\max(x_{tij}) - \min(x_{tij})}$$

- (3) Calculate the ratio q_{tij} of the i th city/year to the j th index

$$q_{tij} = \frac{X_{ij}^*}{\sum_{i=1}^n X_{ij}^*} \quad (3)$$

- (4) Calculate the entropy value e_j of the j th index

$$e_j = -k \sum_{i=1}^m \sum_{j=1}^p (q_{tij} \times \ln q_{tij}), \quad k = \frac{1}{lpm}, \quad 0 \leq e \leq 1 \quad (4)$$

- (5) Calculate the weight w_j of the j th index

$$w_j = (1 - e_j) / \sum_{j=1}^n (1 - e_j) \quad (5)$$

3.4 Coefficient of variation method

$$CV = \sigma / AVG \quad (6)$$

CV represents the coefficient of variation for the city's resilience each year during the study period. The higher the average value of the variable, the more significant the relative difference, and *vice versa*. σ indicates the standard deviation of urban resilience each year during the study period, which can reflect the degree of dispersion of the data set, and the larger the value, the more significant the difference between the original value and the average value; Conversely, the smaller the value, the smaller the absolute difference (Zhou et al., 2017). AVG indicates the average urban resilience each year.

3.5 Obstacle degree analysis

The obstacle degree analyzes the diagnosis of regional urban resilience development disorders by three indicators: factor contribution, index deviation, and obstacle degree (Ma et al., 2014).

- (1) Calculating factor contribution

$$U_j = w_j \quad (7)$$

U_j representing the contribution of the factor, refers to the degree of influence of a single element on the overall goal, w_j is the weight of the single element on the entire plan.

- (2) Calculating the indicator deviation

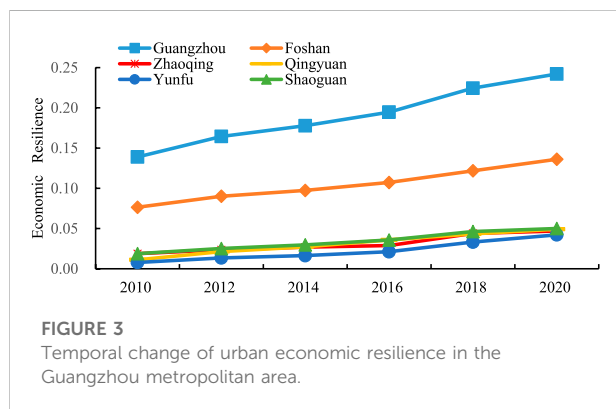
$$V_{tj} = \sum_{i=1}^n (1 - a_{tij}) \quad (8)$$

V_{tj} indicates the degree of variation of the indicator, which refers to the gap between the individual indicators in a particular year and the overall urban resilience goal of the region.

- (3) Calculating the degree of obstacle

TABLE 3 Standard deviation and coefficient of variation of economic resilience in the Guangzhou metropolitan area from 2010 to 2020.

	Economic resilience	Standard deviation	Coefficient of variation
2010	0.0453	0.0478	1.0550
2012	0.0564	0.0547	0.9696
2014	0.0625	0.0581	0.9283
2016	0.0706	0.0624	0.8833
2018	0.0855	0.0688	0.8047
2020	0.0944	0.0737	0.7801



$$M_{ij} = (U_j \times V_{ij}) / \sum_{j=1}^n (U_j \times V_{ij}) \times 100\% \quad (9)$$

M_{ij} is the degree of an obstacle is indicated, which refers to the influence value of a single index on the level of resilience development of regional cities in a particular year.

4 Analysis of the results

4.1 Temporal evolution

4.1.1 Economic resilience

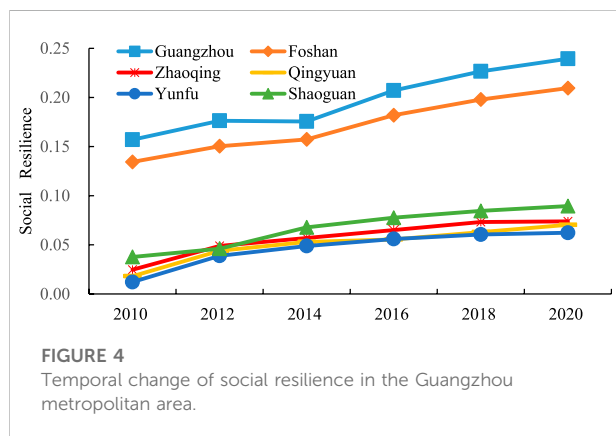
The results of the temporal evolution of the economic resilience degree of the Guangzhou metropolitan area are shown in Table 3. The standard deviation value of economic resilience of the Guangzhou metropolitan area also increases from 0.0478 to 0.0737 from 2010 to 2020, indicating that the absolute difference in economic resilience of the Guangzhou metropolitan area gradually expands. The coefficient of variation of economic resilience of the Guangzhou metropolitan area shows a decreasing trend year by year during the study period, with a decrease of nearly 26.06% in 2020 compared with 2010, indicating that the gap between the economic resilience of cities within Guangzhou metropolitan area gradually decreases, but the relative difference is still significant.

Figure 3 shows the temporal changes in economic resilience in the Guangzhou metropolitan area. Each city's overall economic resilience degree shows an upward trend, but the increase rate of economic resilience degree is more variable. The cities represented by Guangzhou and Foshan have a significant increment of economic resilience during the study period. The overall annual growth rate is around 10%, with a more stable change. The cities represented by Zhaoqing show fluctuating changes in their economic resilience growth rates, with economic resilience growth slowing down during 2014–2016 to a rapid increase in urban economic resilience during 2016–2018, after which the economic resilience growth rates slow down to normal levels. Yunfu, Qingyuan, and Shaoguan have relatively small increments of economic resilience during the study period. Still, their underlying economic resilience is low, with an overall annual growth rate of about 20%, which is a more significant growth rate.

Guangzhou and Foshan, as one of the most developed regions in the country in terms of the private economy and foreign trade, are ranked among the top in the Pearl River Delta region in terms of trade strength and openness intensity. The enormous total import and export volume can make the area enter the international market through exporting goods, which can also create foreign exchange income while making full use of production capacity and also ease the economic use of some of the strained resources through imported goods and develop city economy, to drive the city's economic resilience to improve. Shaoguan and Qingyuan, in recent years, relying on the existing natural environment and humanities and history, and other tourism resources, vigorously develop the tourism service economy; the economy has introduced several measures to promote the development of high-end service industry clusters, boosting the growth of economic resilience of measures. In 2012, Zhaoqing New District began construction through a series of investments, actively strengthening the industrial chain aggregation and upgrading; Zhaoqing elevated its gross regional product and tertiary industry development and became the main driving force of economic resilience development. The main economic resilience degrees in Yunfu city during 2010–2014 benefited from the annual growth rate of fixed asset investment. The per capita savings deposit balance

TABLE 4 Standard deviation and coefficient of variation of social resilience in the Guangzhou metropolitan area.

	Social resilience	Standard deviation	Coefficient of variation
2010	0.0640	0.0587	0.9167
2012	0.0841	0.0566	0.6734
2014	0.0933	0.0523	0.5611
2016	0.1072	0.0626	0.5842
2018	0.1176	0.0679	0.5769
2020	0.1242	0.0719	0.5791



and the share of tertiary industry in GDP grow faster in the later period, reflecting that the focus of economic development in Yunfu city gradually moves to the tertiary sector as a new economic resilience growth point.

4.1.2 Social resilience

As depicted in Table 4, social resilience has a higher index in all years. The social resilience of the Guangzhou metropolitan area shows a shift from rapid increase to steady improvement during the study period, rising from 0.0640 in 2010 to 0.1243 in 2020, which is 1.94 times that in 2010. Among them, the highest average annual growth rate of 31.42% was recorded from 2010 to 2012, and the lowest average growth rate of only 5.56% was recorded from 2018 to 2020. The standard deviation of social resilience of the Guangzhou metropolitan area shows a “V” shape change, decreasing from 0.0587 to 0.0719 from 2010 to 2014 and then increasing to reach 0.0719 in 2020 gradually, indicating the absolute difference in social resilience of the Guangzhou metropolitan area decreases first and then increases. At the same time, the coefficient of variation of social resilience in the Guangzhou metropolitan area shows a fluctuating downward trend, and the coefficient of variation of social resilience reached the lowest value of 0.5611 in 2014, indicating that the relative difference in social resilience of Guangzhou metropolitan area cities fluctuates and changes significantly.

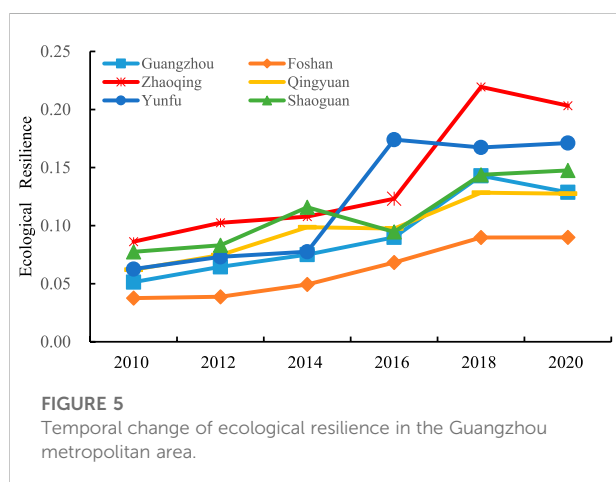
Figure 4 is the temporal change of social resilience. As depicted in Figure 4, the overall social resilience of each city showed a steady trend of improvement, but the rate of increase in social resilience varied widely among cities. As represented by Zhaoqing, Qingyuan, and Yunfu, the increase rate of social resilience in these cities showed an explosive increase in the early period, and the change rate tended to slow down in the middle and late periods. The annual growth rates of social resilience in Guangzhou and Foshan are the same during the study period, both showing a steady increase in the early period, a constant change in the middle period, and a gradual rise in the late period; the increment of social resilience in both cities is significant, but their social resilience base is extensive, with an overall annual growth rate around 10%. Social resilience of Shaoguan developed in an “S” curve, with a relatively small general increment. However, its base social resilience was lower, with an overall annual growth rate of 10% or less, and the growth rate was more significant. Each city is influenced by its social development foundation, and the main contributing factors of social resilience are different, but the overall change from pursuing a quantity to quality improvement. For example, Shaoguan increased focus on health care and primary health insurance has expanded its social resilience capacity. Guangzhou and Foshan focus on population density, recognizing that urban social resilience spirals from concern for groups to individuals to groups, protecting the safety and health of workers and ensuring the stable development of social fundamentals. On the other hand, Qingyuan, Yunfu, and Zhaoqing avoid economic losses due to disease risks by implementing urban and rural basic medical insurance coverage and preventing sick members of society from becoming “sick and poor.”

4.1.3 Ecological resilience

Table 5 is the standard deviation and coefficient of variation of ecological resilience. As shown in Table 5, the overall trend of ecological resilience is gradually increasing. From 0.0629 in 2010 to 0.1486 in 2018 and then declined to 0.1447 in 2020, the overall improvement is 0.0818, which is 2.30 times of 2010, with the highest average annual growth rate of 37.70% in 2016–2018 and the lowest average annual growth rate of –2.65% in 2018–2020. The standard deviation value shows

TABLE 5 Standard deviation and coefficient of variation of ecological resilience in the Guangzhou metropolitan area.

	Ecological resilience	Standard deviation	Coefficient of variation
2010	0.0629	0.0160	0.2538
2012	0.0728	0.0192	0.2643
2014	0.0874	0.0225	0.2579
2016	0.1079	0.0336	0.3117
2018	0.1486	0.0394	0.2648
2020	0.1447	0.0358	0.2475



a steady increasing trend, from 0.0160 in 2010 to 0.58 in 2020, with a significant increase, indicating that the absolute difference in ecological resilience of the Guangzhou metropolitan area gradually expands. The coefficient of variation of ecological resilience in the Guangzhou metropolitan area shows a fluctuating trend, indicating that the relative differences between the ecological resilience degrees of cities within the Guangzhou metropolitan area fluctuate significantly.

Figure 5 is the temporal change of ecological resilience. As shown in Figure 5, the overall ecological resilience of each city generally showed a trend of stepwise jumping improvement. The ecological resilience degree of Yunfu city increased more during 2014–2016, and after that, its ecological resilience degree changed more steadily; the ecological resilience degrees of Guangzhou, Foshan, Zhaoqing, Qingyuan, and Shaoguan increased faster during 2016–2018, and after that, the ecological resilience degrees of their cities increased and decreased to different degrees, but the overall changes were not significant. The increased rate of ecological resilience degree varies widely among cities. In Qingyuan and Shaoguan, ecological resilience increased steadily in the first period, decreased to different degrees in the middle period due to disturbances, and increased significantly and remained relatively stable later. The annual growth rates of ecological resilience in Guangzhou and

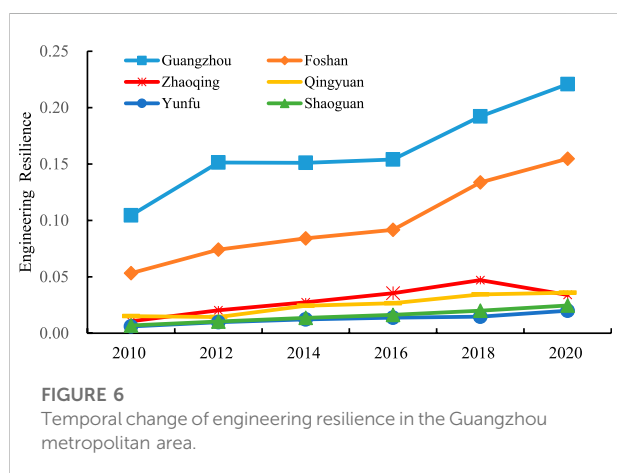
Zhaoqing were the same, showing a steady increase in the early stage, a jump in the middle and late stages, and a slight decline in the late stage, with an average annual growth rate of 22%. The ecological resilience of Foshan City showed an “S” curve development, with minor changes in the early and late stages, a steady increase in the middle stage, and a relatively small increase overall. Still, its ecological resilience is low, and the annual average ecological resilience growth rate is around 20%. During the study period, influenced by the natural primary environmental conditions, the cities’ green, environmental protection, and sustainability requirements increased. Qingyuan, Yunfu, and Shaoguan have a more significant increase in the ecological and environmental condition index on the ecological resilience level of the cities, focusing on soil erosion management. Guangzhou and Foshan are mainly influenced by the ecological resilience degree from the harmless treatment rate of urban domestic waste and urban sewage treatment to the area of green park space per capita, reflecting the shift of Guangzhou’s concern for ecological resilience from the macro level of environmental protection and sustainability to the micro level of human living environment. Zhaoqing’s ecological resilience degree, on the other hand, focuses on green park space per capita to the ecological environment and ecological management construction of soil erosion, which also reflects China’s inevitable requirements and development goals for environmental and resource protection and ecological cities.

4.1.4 Engineering resilience

As shown in Table 6, the evolution of engineering resilience is in a stepwise development. The engineering resilience degree increases year by year during 2010–2020, from 0.0327 in 2010 to 0.0817 in 2020, an increase of 0.049, which is 2.49 times that in 2010, and there are two times when the city has a significant increase in engineering resilience degree, which are the average annual growth rate of 42.77% from 2010 to 2012 and the average annual growth rate of 2016–2018 growth rate of 30.88%. Same to the time-domain changes of the metropolitan area engineering resilience, the standard deviation values show a stepwise increase, with more significant gains in 2010–2012 and 2016–2018, indicating the absolute difference of the Guangzhou

TABLE 6 Standard deviation and coefficient of variation of engineering resilience in the Guangzhou metropolitan area.

	Engineering resilience	Standard deviation	Coefficient of variation
2010	0.0327	0.0360	1.0992
2012	0.0467	0.0519	1.1101
2014	0.0521	0.0505	0.9679
2016	0.0563	0.0509	0.9042
2018	0.0737	0.0662	0.8984
2020	0.0817	0.0776	0.9504



metropolitan area engineering resilience has experienced “expanding-stabilizing-expanding” dynamic change. The coefficient of variation of engineering resilience in the Guangzhou metropolitan area shows a trend of small fluctuation changes, indicating that the relative differences between the engineering resilience degrees of cities in the Guangzhou metropolitan area fluctuate significantly, and the changes in the evolution pattern of time-domain differences are not noticeable.

Figure 6 is the temporal change of engineering resilience level. As shown in Figure 6, each city’s engineering resilience growth pattern shows two patterns of stepped growth and stable improvement. Guangzhou and Foshan have a stepped growth pattern, and their annual growth rate of engineering resilience is significant during 2010–2012, reaching about 40%; the change in yearly growth rate tends to stabilize in the middle term and then ushers in a substantial increase in the annual growth rate of engineering resilience during 2016–2020. Except for Qingyuan in 2010–2012 and Zhaoqing in 2018–2020, where the engineering toughness declined, the cities represented by Zhaoqing, Qingyuan, Yunfu and Shaoguan showed a steady increase in the annual rate of growth in engineering toughness during the study period, reflecting the increase in the demand for infrastructure by regional residents and the strengthening of

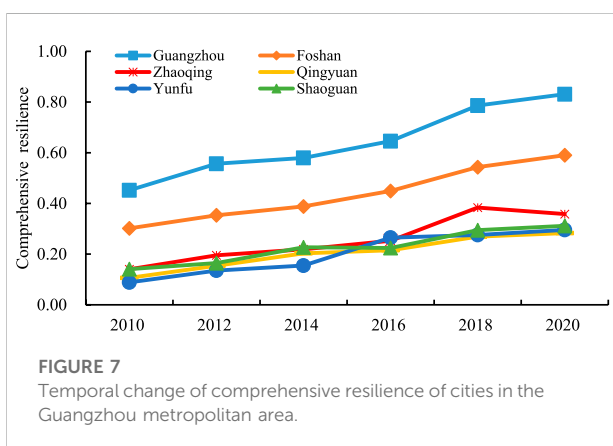
the local government’s investment in and maintenance of public facilities. The main contributing factors of engineering resilience vary among cities with different infrastructure coverage and perfection during the study period. As an important industrial city in Guangdong, the degree of supply and security of Shaoguan for industrial and domestic electricity can considerably bring considerable industrial infrastructure advantages and contribute to the city’s engineering resilience. As an important node city in the Pearl River-Xijiang River Economic Belt, the scale of its road construction and development and the density of its transportation network plays a vital role in the circulation of its urban resource elements and economic development. The engineering toughness of Guangdong and Florida cities is mainly concerned with the operation of urban public transportation and the construction of urban drainage pipes at a later stage to improve the overall structure of urban flood resistance and prevention after solving the flow of urban population elements. The engineering resilience of Qingyuan and Zhaoqing cities shows concern for infrastructure projects, such as road mileage, the number of Internet groups, and the supply management of primary energy for residents and enterprises.

4.1.5 Comprehensive resilience

As shown in Table 7, the comprehensive resilience shows a balanced growth during the study period, rising from 0.2049 in 2010 to 0.4449 in 2020, 2.17 times that of 2010, with the highest average growth rate of 28.69% from 2010 to 2012 and lowest average growth rate of only 4.46% from 2018 to 2020. The value of the standard deviation of the comprehensive resilience of the Guangzhou metropolitan area shows an overall increasing trend year by year except for a decline in 2014, reaching 0.2017 in 2020, indicating the absolute difference of the comprehensive resilience shows an overall increasing development. The coefficient of variation of social resilience in the Guangzhou metropolitan area offers a “V-shaped” rebound trend during the study period, with the coefficient of variation decreasing year by year from 2010 to 2018, reaching a minimum value of 0.4947 in 2014 and increasing in 2020 after that, indicating that the relative differences between the comprehensive resilience of cities within Guangzhou metropolitan area

TABLE 7 Standard deviation and coefficient of variation of comprehensive resilience in the Guangzhou metropolitan area.

	Comprehensive resilience	Standard deviation	Coefficient of variation
2010	0.2049	0.1303	0.6360
2012	0.2599	0.1510	0.5807
2014	0.2953	0.1461	0.4947
2016	0.3420	0.1569	0.4586
2018	0.4254	0.1870	0.4396
2020	0.4449	0.2017	0.4533



experience a process of The coefficient of variation decreases year by year from 2010 to 2018, reaching the lowest value of 0.4947 in 2014, and then increases in 2020, indicating that the relative differences among cities within Guangzhou metropolitan area experience a process of decreasing and then increasing.

Figure 7 is the temporal change of the comprehensive resilience level of cities in the Guangzhou Metropolitan Area.

As can be seen from Figure 7, the overall comprehensive resilience of each city shows a balanced growth trend, but the increased rate of complete annual resilience varies widely among cities. Guangzhou and Foshan experienced two rapid and two stable increases in the growth rate of integrated resilience during the study period, and the average value of their annual growth rate of integrated resilience was about 13%. Qingyuan, Yunfu, Zhaoqing, and Shaoguan, whose overall increase in comprehensive resilience is relatively tiny, but their essential comprehensive resilience is lower, with an overall annual growth rate of 20% or less, the growth rate is more significant.

Figure 8 is the trend of urban comprehensive resilience in the Guangzhou Metropolitan Area from 2010 to 2020. As shown in Figure 8, the primary driving subsystem of urban resilience development is social resilience in the early stage, and ecological resilience is the primary driving subsystem of resilience development in the later stage. Under the guidance of people-oriented and people-centered development ideology, the people's growing need for a better life has changed from the pursuit of a quantity to quality, and maintaining the stability of social fundamentals has dramatically improved the development level of urban resilience, which is manifested in the significant improvement of the city's public health care, residents'

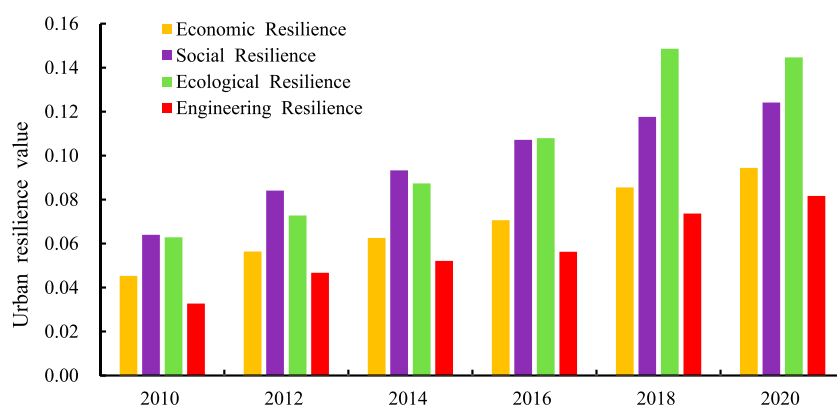


TABLE 8 Classification of urban resilience in the Guangzhou metropolitan area.

Type	Lower resilience	Low resilience	Moderate resilience	High resilience	Higher resilience
Economic Resilience	(0,0.0214)	(0.0214,0.0358)	(0.0358,0.0765)	(0.0765,0.1390)	>0.1390
Social Resilience	(0,0.0388)	(0.0388,0.0650)	(0.0650,0.0895)	(0.0895,0.1819)	>0.1819
Ecological Resilience	(0,0.0514)	(0.0514,0.0775)	(0.0775,0.1078)	(0.1078,0.1475)	>0.1475
Engineering Resilience	(0,0.0162)	(0.0162,0.0274)	(0.0274,0.0532)	(0.0532,0.1046)	>0.1046
Comprehensive Resilience	(0,0.1648)	(0.1648,0.2270)	(0.2270,0.3534)	(0.3534,0.4519)	>0.4519

employment work security services and other capabilities, prompting the people's sense of national identity and happiness of life. This has led to a significant increase in the people's sense of national identity and well-being, which has led to the development of urban social resilience. In the late stage of the study period, thanks to the correct assertion that "mountains, water, forests, fields, lakes, grasses, and sand are a community of life," the scientific concept that "Lucid waters and lush mountains are invaluable assets" and the "river chief system, lake chief system". Since the 18th Party Congress, the Guangzhou metropolitan area has improved significantly in terms of urban green space system level and ecological environment condition, and became the primary driving subsystem of the Guangzhou metropolitan area in 2016, surpassing the social resilience level. However, engineering resilience is the primary constraining subsystem for developing urban resilience. As the lifeline of the urban system, the completeness of the facilities of urban infrastructure directly affects the resilience level of the urban system. With the improvement of urban residents' living standards, residents have put forward higher requirements for urban infrastructures such as transportation, energy, communication, water supply, and drainage, which are essential for living and production activities. These contradictions can affect other urban resilience areas in a chain and thus restrict the development of urban resilience.

4.2 Spatial pattern

According to the changes in economic, social, ecological, engineering, and comprehensive resilience levels of the Guangzhou metropolitan area during 2010–2020, the natural break point method was applied to classify the resilience levels into five types: low resilience, lower resilience, moderate resilience, high resilience, and higher resilience, as shown in Table 8.

4.2.1 Economic resilience

Figure 9 is the spatial evolution of economic resilience. As can be seen from Figure 9, the economic resilience of cities in the Guangzhou metropolitan area from 2010 to 2016 is dominated by lower resilience and low resilience; the economic toughness

level from 2018 to 2020 is dominated by moderate resilience. The economic resilience level in the region is dominated by lower and moderate resilience, showing a spatial distribution pattern of high in the southeast and low in the northwest. From the geographical location of the cities, the economic resilience development of Zhaoqing, Qingyuan, and Shaoguan in the northern region is highly synchronized, mainly due to the unique geographical advantage of the three cities adjacent to the highly developed economy of Guangzhou and Foshan, forming a series of economic cooperation such as the Guangzhou-Foshan-Zhaoqing economic circle, Guangzhou-Shaoguan strategic collaboration, and Guangzhou-Qingyuan special price cooperation zone, which substantially promotes the related economic development and improve the level of economic resilience. Guangzhou, as the core city of the Guangzhou metropolitan area, is far ahead of the surrounding cities in terms of its level of urban economic resilience development, which has a radiation-driven effect on the economic resilience development of the surrounding cities. In addition, under the background of regional integration construction, Guangzhou and Foshan break through the administrative barriers between the two cities through economic interaction and promote the synergistic development of Guangzhou and Foshan using industrial complementation, resource sharing, and shared culture; therefore, there is also a synchronous effect on the economic resilience development of the two cities.

4.2.2 Social resilience

Figure 10 is the spatial evolution of social resilience in the Guangzhou Metropolitan Area from 2010 to 2020. As seen in Figure 10, the social resilience of cities has steadily improved, among which the social resilience of Zhaoqing, Qingyuan, and Shaoguan in the north has improved the most, from lower social resilience in 2010 to moderate social resilience in 2020. The spatial distribution of social resilience evolved from high southeast and low northwest in 2010, to a high east and familiar west layout in 2014–2016, and then presented a spatial pattern of high southeast and low northwest in 2020, with the distribution of the northwest-southeast axis of Guangzhou-Foshan. Guangzhou and Foshan's social resilience level changes synchronized, which is mainly influenced by the

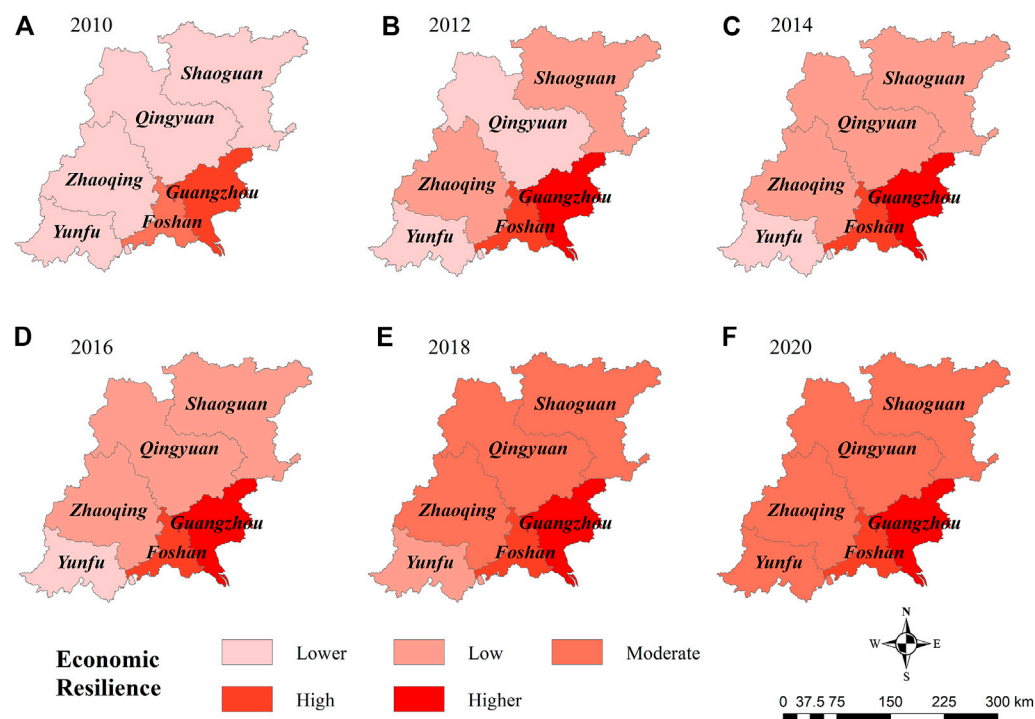


FIGURE 9
Spatial evolution of economic resilience in the Guangzhou metropolitan area in (A) 2010, (B) 2012, (C) 2014, (D) 2016, (E) 2018 and (F) 2020.

role of the Guangzhou-Foshan co-city, the two cities in the medical insurance, and social security information are gradually achieving mutual recognition due to the existence of knowledge-intensive industries in Guangzhou and labor-intensive industries in Foshan complementary role, prompting the construction of modern enterprises in Guangzhou and Foshan to accelerate, providing more jobs for city residents and stabilizing people's livelihood. Shaoguan has had a high level of social resilience development since 2014. It has implemented primary medical insurance for urban and rural residents, which has expanded the population covered by significant diseases and improved medical security.

4.2.3 Ecological resilience

Figure 11 is the Spatial evolution of ecological resilience, as shown from Figure 11, the spatial pattern of ecological resilience varies greatly. It differs significantly from the spatial distribution of urban economic and social resilience. From 2010 to 2012, the ecological resilience was high in the northwest and low in the southeast, developed into a north-high-south-low trend in 2014, and finally evolved into a west-high-east-low distribution pattern from 2016 to 2020. From the analysis of each city's ecological resilience evolution, Guangzhou and Foshan have lower urban ecological resilience grades, mainly because the two cities belong to large cities with high population concentration and high

industrial concentration. The metropolitan built-up area increases year by year, which significantly damages the natural ecosystem environment, especially Foshan, as the manufacturing capital and building materials capital in China, its processing and production activities also cause certain damage to the environment and weaken the overall ecological resilience. During the study period, the general urban ecological resilience level of Shaoguan in the northeastern part of the metropolitan area gradually increased. Still, its ecological resilience level decreased from higher to moderate from 2014 to 2016, due to the decrease in ecological construction treatments for soil erosion. Zhaoqing maintains a high level of ecological resilience especially since 2010 because Zhaoqing has established the River Chief System, Lake Chief System, and Forest Chief System to force industrial transformation through environmental protection and realize the harmonious coexistence of humans and nature.

4.2.4 Engineering resilience

As shown in Figure 12, the urban engineering resilience level of the Guangzhou metropolitan area mainly showed a spatial distribution of high in the southeast and low in the northwest. During 2012–2016, the southeast-northwest engineering resilience development axis was mainly formed, radiating the engineering resilience level of Zhaoqing and Qingyuan in the

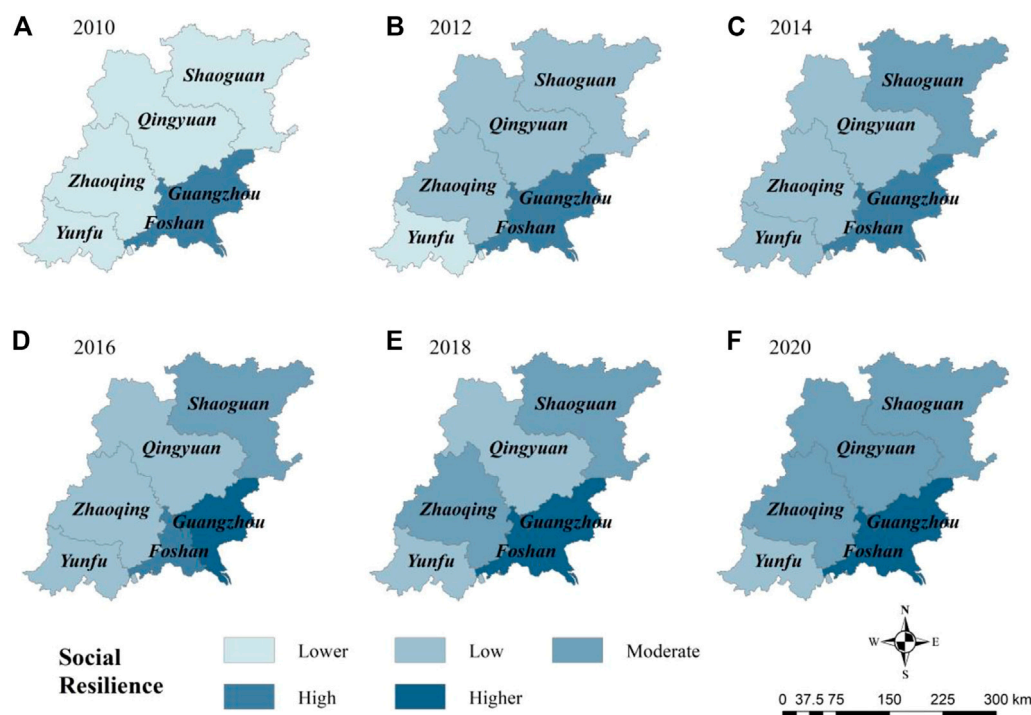


FIGURE 10
Spatial evolution of social resilience in the Guangzhou metropolitan area in (A) 2010, (B) 2012, (C) 2014, (D) 2016, (E) 2018 and (F) 2020.

vicinity of Guangzhou-Foshan; in 2018–2020, a symmetrical distribution of urban engineering resilience level was finally formed with southeast to the northwest as the axis, and the distribution pattern of decreasing urban resilience level from inside to outside along the axis direction was presented. Zhaoqing and Qingyuan are influenced by the “Guang-Fo-Zhao economic circle” and Guangzhou-Qingyuan integration construction, which introduced advanced industries and built integrated infrastructure (eg: the Guang-Fo-Zhao intercity railroad and Guangzhou-Qingyuan intercity railroad) to improve regional transportation operation capacity and communication technology level, prompting the restricted resource endowment to be fully utilized and improving the overall engineering resilience level. The construction of the Guangzhou-Foshan co-city influences Guangzhou and Foshan, and the two cities are integrated into the transportation road network planning and construction. The infrastructure construction resources are shared, forming a peaceful development of complementary industrial development advantages, further making the synchronization development of urban engineering resilience.

4.2.5 Comprehensive resilience

Figure 13 is the spatial evolution of comprehensive resilience from 2010 to 2020. As can be seen from Figure 13, the

comprehensive resilience of the cities in the Guangzhou metropolitan area has increased year by year. 2010–2014, the comprehensive resilience was mainly lower and low resilience, with an overall distribution pattern of high in the southeast and low in the northwest; after that, comprehensive resilience was mainly moderate and high resilience in 2016, with an overall spatial layout of high in the south and low in the north; in 2018–2020, which had a temporary increase in 2018 except Zhaoqing; the comprehensive resilience level in the range was mainly medium and higher, and generally reverted to the spatial distribution of high southeast and low northwest. During the early 2010–2014 period, Zhaoqing, Qingyuan, and Shaoguan had better development of comprehensive urban resilience, which was mainly due to the integrated development of economic, social, ecological, and engineering; Zhaoqing had an outstanding performance in economic resilience and ecological resilience, Shaoguan had higher levels of social resilience and ecological resilience, Qingyuan had high engineering resilience. In late 2016–2020, Yunfu practiced the concept of ecological civilization development and made full use of ecological advantages, to improve the city’s comprehensive resilience level. Zhaoqing was affected by the new crown pneumonia epidemic in 2020, and its infrastructure development rate decreased, which decreased the city’s comprehensive resilience level. As the leading cities in the Guangzhou metropolitan area,

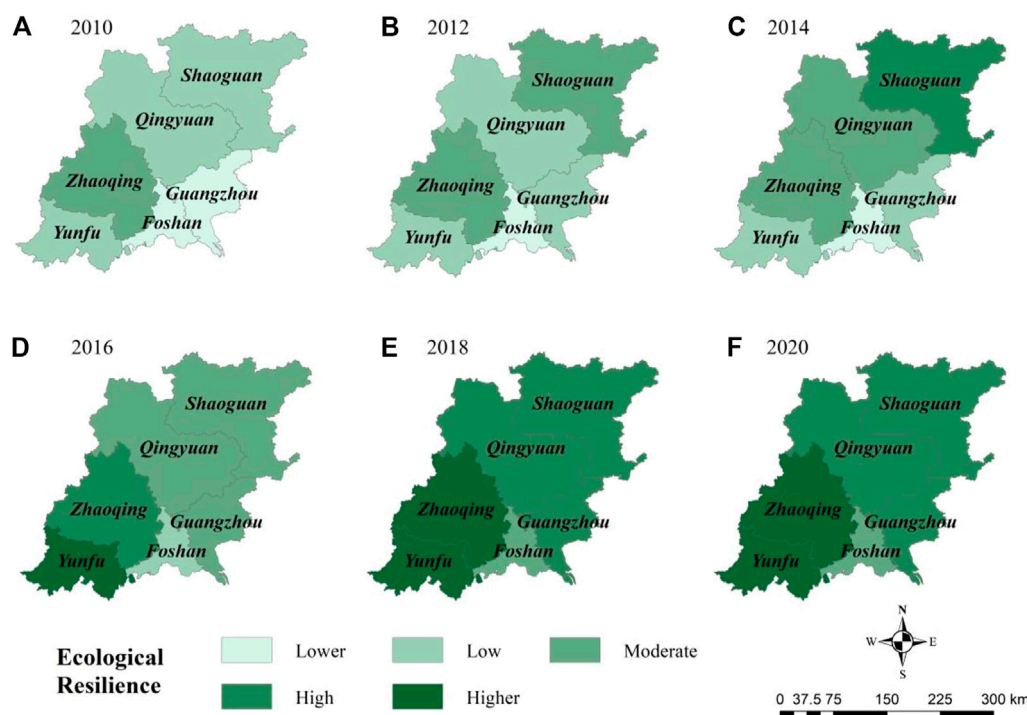


FIGURE 11

Spatial evolution of ecological resilience in the Guangzhou metropolitan area in (A) 2010, (B) 2012, (C) 2014, (D) 2016, (E) 2018 and (F) 2020.

Guangzhou and Foshan have a high resilience capacity, which radiates the simultaneous resilience development of the surrounding cities and the coordinated development of the region was enhanced.

4.3 Obstacle degree analysis

4.3.1 Obstacle of subsystems

Table 9 is the resilience obstacle of urban subsystems in the Guangzhou Metropolitan Area from 2010 to 2020. As can be seen from Table 9, the engineering factor hinders the development of urban resilience the most, followed by the economic sector, while the social and ecological habitat impedes the development of urban resilience to a relatively small extent.

(1) The economic subsystem obstacle has a slight overall increase in the barrier degree during 2010–2020, and the average value of the barrier degree in all years is 27.07%. Since the international financial crisis in 2008, countries worldwide have fallen into an economic downturn. The fundamentals of China's economy have also undergone substantial changes, entering a new normal stage of China's economic development since 2010. In this context, the total imports and export in the urban

economic field of the Guangzhou metropolitan area are affected by the downward pressure of the external economy, and the growth rate of senses and export slows down year by year, which has a holding effect on the economic resilience development of Guangzhou, Foshan and other large commercial cities.

- (2) The social subsystem obstacle shows an overall fluctuating decline in the degree of barriers during the study period, except for a significant increase in 2016–2018, with an average value of 22.58% for the degree of barriers in all years. The fundamental reason is that influenced by the transformation of the leading social contradictions in China since the 19th Party Congress, people's demands for medical and employment security, urban living environment, etc. Have been increasing, from the original order for quantity to qualitative improvement, and their contradictions have experienced the spiral of "generation-solution-again." Therefore, the hindering effect of social factors on the development of urban resilience has been maintained at a high level.
- (3) The ecological subsystem obstacle showed a significant decrease in the barrier degree during the study period, with a mean value of 21.46% for the barrier degree in all years. There was polarization in the barrier degree of the factors in their domains, with the erosion control area factor

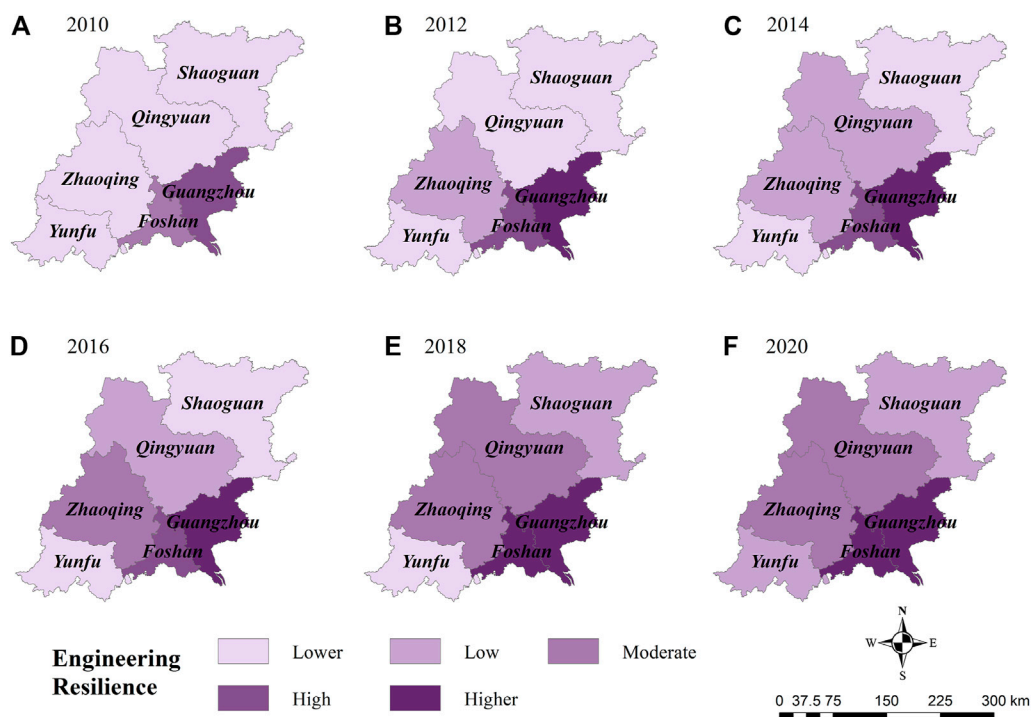


FIGURE 12
Spatial evolution of engineering resilience in the Guangzhou metropolitan area in (A) 2010, (B) 2012, (C) 2014, (D) 2016, (E) 2018 and (F) 2020.

having a more significant constraint on the development of urban resilience and the rest having a minor restriction. Since the implementation of the amendment to the Environmental Protection Law of China, which was called the most stringent in history in 2015, Guangzhou metropolitan area cities have performed outstandingly in the factors of soil erosion control, per capita park green space construction, sewage treatment rate and household waste recycling and harmless treatment, which led to a significant decrease in the degree of ecological domain factor barriers within the region and reached the lowest value of 17.64% in 2018, after 2020, the degree of ecological domain barriers in the metropolitan area increases due to insufficient investment in the comprehensive environmental management of soil erosion.

- (4) The engineering subsystem obstacle degree increases steadily during the study period, and the average value of the barrier degree in all years is 28.87%, which has the most restrictive effect on the development of urban resilience in the metropolitan area. Influenced by the density of urban drainage pipes, public transportation operation, and mobile communication, the infrastructure of cities in the Guangzhou metropolitan area fail to meet the daily needs of citizens, especially in the low density of urban drainage pipes in the metropolitan area and the failure to realize rainwater

and sewage diversion measures, which leads to the inability of cities to maximize the role of flood drainage and flood removal when suffering from heavy rainfall and flooding and causes particular water pollution in the region. Environmental pollution problems play a restrictive part in improving urban engineering resilience.

4.3.2 Obstacle of factors

Table 10 is the major obstacle factors and levels of urban resilience in the Guangzhou Metropolitan Area from 2010 to 2020. Table 10 shows that the primary obstacle of factors is *E19* (erosion control area) in the early stage and *E8* (population density) in the later stage. However, with the increase of local government's unprecedented investment in the last period, the constraining effect on the development of urban resilience gradually diminishes. *E8* (population density) fluctuates and strengthens over time as an obstacle to the development of urban resilience, increasing from 10.08% obstacle degree in 2010 to 12.45% in 2020, an increase of 2.37%. The reason for this phenomenon is mainly due to the influence of the interaction of the development of cities within the Guangzhou metropolitan area, for Zhaoqing, Qingyuan, Yunfu and Shaoguan, their *E8* (population density) growth is slow due to the siphon effect of the neighboring mega such as Guangzhou-Foshan, which shows a severe phenomenon of population loss, making the gap in

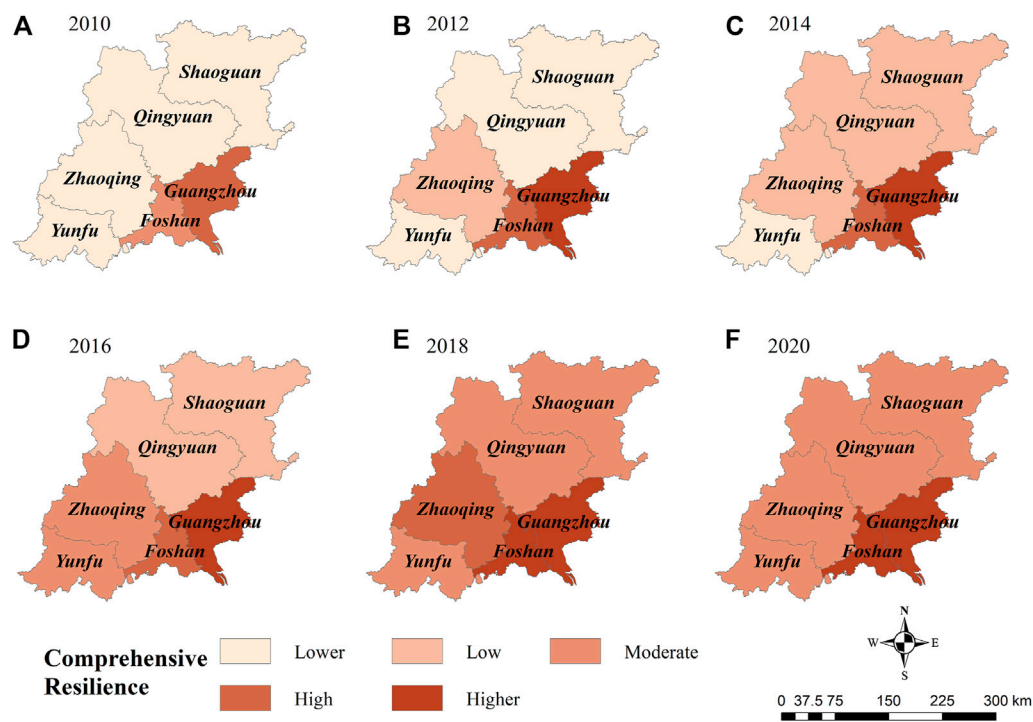


FIGURE 13 Spatial evolution of comprehensive resilience in the Guangzhou metropolitan area in (A) 2010, (B) 2012, (C) 2014, (D) 2016, (E) 2018 and (F) 2020.

TABLE 9 Resilience obstacle of urban subsystems in the Guangzhou metropolitan area from 2010 to 2020.

Type	2010 (%)	2012 (%)	2014 (%)	2016 (%)	2018 (%)	2020 (%)
Economic subsystem obstacle	25.74	26.16	26.60	27.26	28.63	28.03
Social subsystem obstacle	23.40	22.42	22.24	21.71	23.04	22.67
Ecological subsystem obstacle	23.53	23.95	23.08	21.59	17.64	18.97
Engineering subsystem obstacle	27.33	27.47	28.08	29.44	30.69	30.33

TABLE 10 The top 6 major obstacle factors and levels of urban resilience in the Guangzhou Metropolitan Area from 2010 to 2020.

Year	The first obstacle factor	The second obstacle factor	The third obstacle factor	The fourth obstacle factor	The fifth obstacle factor	The sixth obstacle factor
2010	E19 (13.99%)	E8 (10.08%)	E23 (8.59%)	E5 (8.20%)	E6 (6.30%)	E28 (5.76%)
2012	E19 (14.89%)	E8 (10.74%)	E23 (9.19%)	E5 (8.50%)	E6 (6.51%)	E28 (5.52%)
2014	E19 (14.35%)	E8 (11.21%)	E23 (9.53%)	E5 (8.63%)	E6 (6.67%)	E28 (5.87%)
2016	E19 (13.38%)	E8 (11.04%)	E23 (10.16%)	E5 (9.36%)	E6 (6.73%)	E28 (6.18%)
2018	E8 (12.25%)	E5 (10.29%)	E19 (9.95%)	E23 (9.90%)	E6 (7.21%)	E28 (6.86%)
2020	E8 (12.45%)	E19 (12.35%)	E5 (10.76%)	E23 (9.17%)	E28 (7.08%)	E6 (6.95%)

economic development between them and the Guangzhou-Foshan region further widen, which is not conducive to coordinated action within the metropolitan area (Wu and Sun, 2017), and secondly, for Guangzhou and Foshan, their co-location construction makes their economic volume and industrial structure more rationalized, which attracts a large inflow of foreign population and significantly increases *E8* (population density), but their ability to optimize the allocation of urban resources does not fully meet the needs of unfamiliar people, which leads to a series of urban diseases such as traffic congestion and housing tension, and restricts the resilient development of the cities. *E23* (density of urban drainage pipes) and *E5* (total import and export) are the essential resilience obstacle factors of Guangzhou metropolitan area, which fluctuate and change during the study period, but generally remain in the top 4 obstacle factors. *E5* (total import and export): With the large proportion of the export-oriented economy in the Guangzhou metropolitan area, the growth rate of import and export is slowing down year by year due to the downward pressure of the external economy, which has a restraining effect on the economic resilience development of Guangzhou, Foshan and other large commercial cities.

The critical limiting factors of urban resilience development in the Guangzhou metropolitan area during 2010–2020 are *E6* (public finance budget expenditure) and *E28* (standard number of urban public vehicles operating). The growth of public finance budget expenditures in cities in the Guangzhou metropolitan area is relatively stable. Still, the ability to respond to new social changes in the actual implementation process is low, affecting the improvement of urban resilience's adaptive capacity. For the cities of Yunfu, Zhaoqing, Qingyuan, and Shaoguan in northern Guangdong, which were previously in the stage of a rapid transition to urbanization, there is still a lack of urban public transportation planning and construction and information and communication penetration, leading to a series of underutilized resources and information in the process of urban development. For Guangzhou and Foshan, with the promotion of Guangzhou-Foshan co-city construction, the economic and industrial exchanges between the two cities are active, and the population frequently flows, the original public transportation operation system cannot fully meet the needs of the citizens' daily production activities and plays a restraining role in the improvement of urban resilience.

During the study period, the sum of the top 6 significant barriers to urban resilience in the Guangzhou metropolitan area has been steadily increasing yearly. The sum of the obstacles has increased from 52.92% in 2010 to 58.76% in 2020, with an increase of 5.85% before and after, which fully indicates that with the development of urban resilience level in the Guangzhou metropolitan area, the significant barriers of urban resilience. The regional government should focus on the first six significant barriers, analyze the impact of specific resilience barriers, prevent

potential problems and external threats, and improve the city's overall resilience.

5 Discussions

As the hinterland of human activities and the spatial carrier of energy circulation, cities have been constantly faced with threats from hidden dangers and the external environment. Given the insufficient and unbalanced development of resilience in Chinese cities, the concept of a “resilient city” is adopted in this paper to evaluate urban resilience, which provides a theoretical reference for disaster prevention and control, urban governance, and the sustainable development of cities by establishing a scientific index system and conducting a thorough analysis of the resilience characteristics and components of cities. According to the relevant literature on urban resilience evaluation, the influencing factors for economic, social, ecological, and engineering resilience of the Guangzhou metropolitan area are identified. On this basis, an urban resilience assessment model is constructed to explore the spatial and temporal changes in urban resilience in the Guangzhou metropolitan area. Besides, an analysis is conducted regarding the barriers to the development of urban resilience in the Guangzhou metropolitan area, which contributes a new perspective to the research on urban resilience evaluation and sustainable development in those metropolitan cities. In addition, it also enriches the connotation of urban resilience research while promoting the multidisciplinary and cross-disciplinary analyses of resilience research. However, urban resilience evaluation involves a comprehensive and complex research process, this paper has the following shortcomings: Firstly, due to the limited availability of data, there are some flaws in the resilience evaluation index system, the impact of indicators such as population mobility, cultural governance, policies, and institutions on urban resilience can be analyzed in depth. Secondly, the formation mechanism and management of resilience are not deeply studied. The research on the theoretical framework, research methods, and management of urban resilience can be further supplemented and deepened at a later stage to enhance the applicability of urban resilience. In future research, attention will be paid to micro-scale resilience studies (e.g., communities). Efforts will be made to explore research content such as identifying vulnerable populations, constructing healthy community environmental systems, and quantitative evaluation of community resilience. At the same time, in face of the impact and challenges of the Covid-19 pandemic, there is a concern about how to further improve the resilience system of Chinese metropolitan cities and realize the restructuring and functional optimization of cities under multiple risk scenarios to enhance the response capacity of cities to cope with public risk emergencies and public health events.

6 Conclusion and recommendations

6.1 Conclusion

- (1) The resilience of each subsystem in an individual city has improved steadily, and the comprehensive resilience has been enhanced significantly.

During the study period, the resilience of the Guangzhou metropolitan area improved steadily in different ways. To be specific, economic resilience showed a steady improvement, social resilience improved substantially, ecological resilience was enhanced at a varying pace, and engineering resilience improved progressively. The comprehensive urban resilience of the Guangzhou metropolitan area improved significantly from 0.2049 in 2010 to 0.4449 in 2020, with the annual growth rate reaching 17.05% on average. As a measure of the absolute difference in urban resilience development, the standard deviation increases by 54.75% from 0.1303 in 2010 to 0.2017 in 2020. The coefficient of variation is used to characterize the relative difference in the urban resilience level, whose value shows a “V-shaped” change. From 2010 to 2018, the coefficient of variation decreased year on year, reaching a minimum of 0.4396 in 2014. Then, it recovered in 2020, indicating a steady increase in the absolute difference in comprehensive resilience between the cities within the Guangzhou metropolitan area. The relative difference showed a decreasing trend and then an increasing trend.

- (2) The urban resilience in the Guangzhou metropolitan area shows a spatial pattern of radioactive development with Guangzhou as the core, with the spatial distribution of resilience level being typically high in the southeast and low in the northwest.

Economic, social, engineering, and comprehensive resilience support the radial improvement of resilience with Guangzhou as the core. In terms of urban ecological resilience, Guangzhou and Foshan perform less well. At the same time, Yunfu, Zhaoqing, and Shaoguan attach more significance to preserving the ecological environment, reducing soil erosion, strengthening ecosystem construction, and promoting the spontaneous resistance and self-healing ability of the local ecosystem for improved urban ecological resilience. In addition, the level of urban engineering resilience is low in Yunfu, Zhaoqing, Qingyuan, and Shaoguan, and the overall improvement of urban engineering and infrastructure resilience has not yet been brought into play. There is a disconnect between their urban engineering resilience levels and those of Guangzhou and Foshan. Yunfu shows limited growth in terms of per capita GDP, per capita disposable income, and public budget expenditure, which constrains the enhancement of its urban economic resilience, thus leading to a city with limited economic

resilience. In addition, except for ecological resilience, the spatial distribution of urban subsystem resilience and comprehensive resilience in the Guangzhou metropolitan area is high in the southeast and low in the northwest. Among them, the level of urban economic, social, and engineering resilience is mainly affected by medium resilience, and ecological resilience is primarily in the order from medium to high.

- (3) Social resilience and ecological resilience as the main driving subsystems in the early and late stages of urban resilience improvement, engineering resilience is the primary constraining subsystem during the study period.

Social resilience, as the primary driving subsystem in the early stage of urban resilience improvement in the Guangzhou metropolitan area, is reflected in the shift of people's growing need for a better life from the pursuit of a quantity to that quality under the guidance of people-centered development ideology. This is manifested in the significant improvement of public health care, employment, and job security services in the city, which has played a crucial role in substantially enhancing the sense of national identity and happiness among people in their life. As a result, social resilience improves considerably in the city. In the late stage of the study period, given the advanced assertion that “mountain, water, forest, lake, grass, and sand are a community of life,” the scientific ideology that “Lucid waters and lush mountains are invaluable assets” and the effective initiatives such as the “river chief system and lake chief system” launched since the 18th Party Congress, the Guangzhou metropolitan area has witnessed a significant improvement in terms of urban green space system and ecological environment. Becoming the primary driving subsystem in 2016, it surpassed the social resilience level. Engineering resilience is the primary constraint on the improvement of urban resilience. Currently, residents have stronger demands for such urban infrastructures as transportation, energy, communication, water supply, and drainage, all of which are essential for living and production activities. This evidences the development of resilience.

- (4) Soil erosion control area and population density are the primary obstacles in the early and late stages, respectively, the essential resilience factors include urban drainage pipe density and total import and export.

Due to the limited capacity of erosion control construction in the early stage in the Guangzhou metropolitan area, soil erosion caused by human activities and natural disasters occurs on some hills and slopes, thus resulting in casualties and property losses. In the later period, the “siphon effect” manifested in the big cities imposes certain constraints on the inflow and outflow of the population. The above resilience factors have improved over time, and the adverse effect on the development of urban resilience has become more significant. In addition, the

6 most significant barriers to urban resilience in the Guangzhou metropolitan area have been steadily increasing over time, which indicates that the significant barriers to urban resilience gradually concentrate with the rise of urban resilience level. Furthermore, among the urban resilience subsystems, the engineering domain factor is the most significant constraint on urban resilience improvement, followed by the economic domain. In contrast, the social and ecological environments are relatively less obstructive to improving urban resilience. The overall urban subsystem domain obstacle degree shows a trapezoidal distribution from top to bottom.

6.2 Recommendations

- (1) Strengthen the overall development of urban system resilience, highlight the story of resilience in critical areas, and make up for the shortcomings of resilience. The current thinking of urban subsystems in coping with risks and disturbances has changed from a model that focuses on short-term disaster prevention and mitigation to a concept that focuses on long-term safety and security. The embodiment of urban resilience capacity is the result of the organic action of each urban subsystem coordinating and cooperating, so the development of urban resilience should adhere to the idea of highlighting the key areas and making up the short boards, taking the outstanding areas of resilience as the breakthrough of urban resilience development and the temporary board areas of resilience as the focus of urban resilience development. Taking Yunfu, Zhaoqing, and Shaoguan as examples, the ecological resilience of the cities is high during the study period. The comprehensive resilience of the town fully proves the scientific assertion that green water and green mountains are the silver mountains of gold. As the core city of the Guangzhou metropolitan area, Guangzhou is significantly ahead of the surrounding cities in economic, social, and engineering resilience, but its urban ecological resilience is poor.
- (2) Pay attention to the top-level design of resilient city planning and construction in the Guangzhou metropolitan area, and promote the flow of resources and information within the metropolitan area. In the context of the new development pattern of the post-epidemic era, with the domestic circulation as the main body and the domestic and international double circulation promoting each other, the resilient urban development of the Guangzhou metropolitan area should be based on the domestic and foreign perspectives, taking into account the effect of urban economy, society, ecology, engineering and other fields from the policy level, improving institutions and policies to guarantee the high-quality development of resilient cities

(Jiang and Meng, 2021). Guangzhou, as the core city in the metropolitan area, should take the initiative to break its spillover barriers, enhance the flow of resources and information exchange with neighboring cities, realize the development of diffusion from point to point, and then make the organic joint resistance to risks and disturbances among cities in Guangzhou metropolitan area improve (Zhu and Sun, 2020). At the same time, urban resilience planning and construction should focus on how to improve the resistance of the urban system to disasters and risks; rather than reducing the economic and property losses caused by a particular disaster, we cannot just pursue zero risk, we must clearly understand that risk control is required to be integrated. Power is needed when the risk exceeds the acceptable level.

- (3) To build a scientific and reasonable urban resilience evaluation system according to local conditions to guide the planning and construction of resilient cities. Currently, the urban resilience evaluation index system structure is similar at all levels in each region, failing to highlight the characteristics of regional resilience factor development. As different urban areas face different types of disasters and other urban resilience background conditions, the comprehensive resilience capacity of their cities is additional. Therefore, it is necessary to scientifically construct the urban resilience index system and reasonably determine the index weights according to the actual situation of the evaluation object. In addition, as a new urban development concept, the ultimate destination of the resilient city should be in practice and abandon the original pursuit of large city scale, complex urban functions, and a high concentration of resources unreasonable phenomenon. Through rational analysis and evaluation of the current situation of urban resilience development, digging out the shortcomings and deficiencies of urban resilience development, taking into account the effect of each urban subsystem, actively practicing and exploring urban resilience planning and construction, striving to avoid, contain and eliminate risks from the root, and helping to promote the high-quality development of urban resilience (Zhai et al., 2022).

Data availability statement

The raw data supporting the conclusions of this article will be made available by the authors, without undue reservation.

Author contributions

Conceptualization, BT and ZT; methodology, ZT; data curation, ZT; writing—original draft preparation, BT and ZT;

writing—review and editing, BT and ZT; funding acquisition, BT. All authors have read and agreed to the published version of the manuscript.

Funding

This research was funded by project of the 14th five-year plan for the development of Philosophy and Social Sciences in Guangzhou in 2021 (Grant No. 2021GZYB22); Project of Special Innovation Classes for Regular Universities in Guangdong Province (Grant No. 2020WTSCX136); College students' innovative entrepreneurial training program (Grant No. 202213902008); Guangzhou Xinhua University's Educational Reform Project (Grant No. 2022J002).

References

- Abid, M. (2016). Of resilient places: Planning for urban resilience. *Eur. Plan. Stud.* 24 (2), 407–419. doi:10.1080/09654313.2015.1082980
- Amirzadeh, M., Sobhaninia, S., and Sharifi, A. (2022). Urban resilience: A vague or an evolutionary concept? *Sustain. Cities Soc.* 81, 103853. doi:10.1016/J.SCS.2022.103853
- Bai, L. M., Xiu, C. L., Feng, X. H., Mei, D. W., and Wei, Y. (2019). Comprehensive assessment of city resilience in China and its spatial and temporal differentiation characteristics. *World Reg. Stud.* 28 (6), 77–87. doi:10.3969/j.issn.1004-9479.2019.06.2018403
- Betty, P., Richard, L. V., and Rose, L. P. (2017). A conceptual framework to enhance community resilience using social capital. *Clin. Soc. Work J.* 45 (2), 102–110. doi:10.1007/s10615-015-0556-z
- Colclough, G., Gonzalez-Gomez, A., Velasco, M., Stevens, J., Goodey, P., Henderson, R., et al. (2021). Governance of city resilience. *Int. J. Urban Plan. Smart Cities* 2 (2), 70–93. doi:10.4018/ijupsc.2021070105
- Desouza, K. C., and Flanery, T. H. (2013). Designing, planning, and managing resilient cities: A conceptual framework. *Cities* 35 (4), 89–99. doi:10.1016/j.cities.2013.06.003
- Dulebenets, M. A. (2018). A comprehensive multi-objective optimization model for the vessel scheduling problem in liner shipping. *Int. J. Prod. Econ.* 196, 293–318. doi:10.1016/j.ijpe.2017.10.027
- Fang, C. L., and Wang, Y. (2015). A comprehensive assessment of urban vulnerability and its spatial differentiation in China. *Acta Geogr. Sin.* 70 (2), 234–247. doi:10.11821/dlxb201502005
- Fei, X., Wen, J. H., Du, S. Q., and Xu, H. (2014). Advances in natural disaster resilience research. *J. Nat. Hazards* (6), 19–31. doi:10.13577/j.jnd.2014.0603
- Grzegorz, I., Katarzyna, M., Dawid, S., Konstantinos, M., Anna, W. K., and Katarzyna, C. (2021). Potential environmental pollution from copper metallurgy and methods of management. *Environ. Res.* 197, 111050. doi:10.1016/J.ENVRES.2021.111050
- He, J. X., Meng, Y. H., and Zheng, P. Q. (2022). Research progress and trends of urban resilience governance in China(2000-2021)—visual analysis based on CiteSpaceV. *J. Catastrophology* 37 (3), 148–154.
- Herrera, M., Abraham, E., and Stoianov, I. (2016). A graph-theoretic framework for assessing the resilience of sectorised water distribution networks. *Water Resour. Manage.* 30 (5), 1685–1699. doi:10.1007/s11269-016-1245-6
- Jabareen, Y. (2013). Planning the resilient city: Concepts and strategies for coping with climate change and environmental risk. *Cities* 31 (2), 220–229. doi:10.1016/j.cities.2012.05.004
- Jiang, X., and Meng, L. J. (2021). Mainly inner circulation, outer circulation empowerment and higher level double circulation: International experience and Chinese practice. *Manag. World* 37 (1), 1–19. doi:10.3969/j.issn.1002-5502.2021.01.001
- Li, T. Y. (2017). New progress in study on resilient cities. *Int. Urban Plan.* 32 (5), 15–25. doi:10.22217/upi.2015.284
- Liang, X. D., Lin, S. F., Bi, X. Y., Lu, E. F., and Li, Z. (2021). Chinese construction industry energy efficiency analysis with undesirable carbon emissions and construction waste outputs. *Environ. Sci. Pollut. Res.* 28 (13), 15838–15852. doi:10.1007/s11356-020-11632-z
- Liu, Y. P. (2021). Urban resilience system development measurement: based on an empirical study of 288 Chinese cities. *Urban Dev. Stud.* 28 (6), 93–100. doi:10.3969/j.issn.1006-3862.2021.06.020
- Lorenz, D. F. (2013). The diversity of resilience: Contributions from a social science perspective. *Nat. Hazards (Dordr.)* 67 (1), 7–24. doi:10.1007/s11069-010-9654-y
- Ma, X. D., Shen, Z. P., and Song, X. J. (2014). Analysis of urban and rural public service development gap and its obstacle factors in Jiangsu Province. *Hum. Geogr.* 29 (1), 89–93. doi:10.13959/j.issn.1003-2398.2014.01.016
- Marjolein, S., and Bas, W. (2017). Building up resilience in cities worldwide—Rotterdam as participant in the 100 resilient cities programme. *Cities* 61, 109–116. doi:10.1016/j.cities.2016.05.011
- Mcclymont, K., Bedinger, M., Beevers, L., Visser-Quinn, A., and Walker, G. H. (2022). Understanding urban resilience with the urban systems abstraction hierarchy (USAH). *Sustain. Cities Soc.* 80, 103729. doi:10.1016/J.SCS.2022.103729
- Meerow, S., Newell, J. P., and Stults, M. (2016). Defining urban resilience: A review. *Landsc. Urban Plan.* 147, 38–49. doi:10.1016/j.landurbplan.2015.11.011
- Michel, B., Stephanie, E. C., Ronald, T. E., George, C. L., Thomas, D. O., Andrei, M. R., et al. (2012). A framework to quantitatively assess and enhance the seismic resilience of communities. *Earthq. Spectra* 19 (4), 733–752. doi:10.1193/1.1623497
- Morrow, B. H. (1999). Identifying and mapping community vulnerability. *Disasters* 23 (1), 1–18. doi:10.1111/1467-7717.00102
- Müller, B. (2011). “Urban and regional resilience – a new catchword or a consistent concept for research and practice?,” in *German annual of spatial research and policy 2010. German annual of spatial research and policy*. Editor B. Müller (Berlin, Heidelberg: Springer). doi:10.1007/978-3-642-12785-4_1
- Ni, X. L., and Li, X. Q. (2021). Three types of resilient city evaluation systems and their new development directions. *Int. City Plan.* 36 (3), 76–82. doi:10.19830/j.upi.2019.07
- Osman, T. (2021). A framework for cities and environmental resilience assessment of local governments. *Cities* 118, 103372. doi:10.1016/J.CITIES.2021.103372
- Paulo, J., and Luis, A. (2019). Urban resilience: A conceptual framework. *Sustain. Cities Soc.* 50, 101625. doi:10.1016/j.scs.2019.101625
- Shao, Y. W., and Xu, J. (2015). Urban resilience: A conceptual analysis based on an international literature review. *Int. City Plan.* 30 (2), 48–54.
- Simon, W., John, T., Priti, P., Anna, K., and Tarek, C. (2016). Towards measurable resilience: A novel framework tool for the assessment of resilience levels in slums. *Int. J. Disaster Risk Reduct.* 19, 280–302. doi:10.1016/j.ijdrr.2016.08.003
- Song, L. (2020). Is intelligence compatible with resilience?—the resilience evaluation of smart city construction. *J. Soc. Sci.* 3, 21–32. doi:10.13644/j.cnki.cn31-1112.2020.03.004
- Sun, Y., Zhang, J. C., and Yao, S. M. (2017). Resilience evaluation of prefecture-level cities in the Yangtze River Delta based on the perspective of social ecosystem. *China Popul. Resour. Environ.* 27 (8), 151–158. doi:10.12062/cpre.20170465

Conflict of interest

The authors declare that the research was conducted in the absence of any commercial or financial relationships that could be construed as a potential conflict of interest.

Publisher's note

All claims expressed in this article are solely those of the authors and do not necessarily represent those of their affiliated organizations, or those of the publisher, the editors and the reviewers. Any product that may be evaluated in this article, or claim that may be made by its manufacturer, is not guaranteed or endorsed by the publisher.

- Turner, B. L., Kasperson, R. E., Matson, P. A., Mccarty, J. J., Corell, R. W., Christensen, L., et al. (2003). A framework for vulnerability analysis in sustainability science. *Proc. Natl. Acad. Sci. U. S. A.* 100 (14), 8074–8079. doi:10.1073/pnas.1231335100
- Wang, M. Z., Amati, M., and Thomalla, F. (2012). Understanding the vulnerability of migrants in Shanghai to typhoons. *Nat. Hazards (Dordr)*. 60, 1189–1210. doi:10.1007/s11069-011-9902-9
- Wu, B. H., and Chen, A. (2018). Construction of resilient city resilience evaluation model. *Sci. Technol. Rev.* 36 (16), 94–99.
- Wu, K., and Sun, D. Q. (2017). Progress in urban shrinkage research. *Econ. Geogr.* 37 (11), 59–67. doi:10.15957/j.cnki.jjdl.2017.11.008
- Xu, J., and Shao, Y. W. (2015). Resilient city: New ideas for coping with city crisis. *Int. City Plan.* 30 (2), 1–3.
- Xu, Y. Y., Li, G., Cui, S., Xu, Y. P., Pan, J., Tong, N., et al. (2018). Review and perspective on resilience science: From ecological theory to urban practice. *Acta eco. Sin.* 38 (15), 5297–5304. doi:10.5846/stxb201709081620
- Xu, Z. F., Tian, J. F., and Zhang, J. (2019). Evaluation system and optimization strategy of urban resilience from the perspective of disaster prevention. *China Saf. Sci. J.* 29 (3), 1–7. doi:10.16265/j.cnki.issn1003-3033.2019.03.001
- Yang, X. P., Wang, L. K., Li, Y. B., Hou, Y. J., and Niu, J. (2021). Review and prospects of resilient city theory. *Geogr. Geo-Information Sci.* 37 (6), 78–84. doi:10.16619/j.cnki.rmltxsqy.2022.1112.004
- Yang, Y., Lin, L., Zhong, Z. P., Ou, Y. Y., Xu, Q., Meng, M. Y., et al. (2019). Comprehensive evaluation and spatial differentiation of community resilience in Guangzhou based on response of the city to public health hazards. *Acta Geogr. Sin.* 74 (2), 266–284. doi:10.11821/dlxb201902005
- Zang, X. Y., and Wang, Z. (2019). The evolution of the urban resilience concept, and its research contents and development trend. *Sci. Technol. Rev.* 37 (22), 94–104.
- Zhai, G. F., Huang, H., Leng, H., Luo, X., Ma, D. H., W, J., et al. (2022). Scientific planning, improving resilience. *Urban Plan.* 46 (3), 29–36. doi:10.11819/cpr20220304s
- Zhang, X., Jiao, K., Zhang, J., and Guo, Z. (2021). A review on low carbon emissions projects of steel industry in the world. *J. Clean. Prod.* 306, 127259. doi:10.1016/j.jclepro.2021.127259
- Zhao, R. D., Fang, C. L., and Liu, H. M. (2020). Progress and prospect of urban resilience research. *Progresses Geogr. Sci.* 39 (10), 1717–1731. doi:10.18306/dlkxjz.2020.10.011
- Zhou, C. S., Luo, L. J., Shi, C. Y., and Wang, Y. H. (2017). Spatio-temporal evolution characteristics of economic development in the Guangdong-Hong Kong-Macao Greater Bay Area and its influencing factors. *Trop. Geogr.* 37 (6), 802–813. doi:10.13284/j.cnki.rddl.003011
- Zhu, J. H., and Sun, H. X. (2020). Research on spatial-temporal evolution and influencing factors of urban resilience of China's three metropolitan agglomerations. *Soft Sci.* 34 (2), 72–79. doi:10.13956/j.ss.1001-8409.2020.02.12



OPEN ACCESS

EDITED BY
Sandipan Das,
Symbiosis International University, India

REVIEWED BY
Kana Nakatani,
Kyoto University, Japan
Suvana Tikle,
Max Planck Society, Germany

*CORRESPONDENCE
Zhong Fu Wang,
✉ xjftwzf@163.com

[†]These authors have contributed equally to this work and share first authorship

SPECIALTY SECTION

This article was submitted to Geohazards and Georisks, a section of the journal Frontiers in Earth Science

RECEIVED 04 November 2022

ACCEPTED 27 January 2023

PUBLISHED 16 February 2023

CITATION

Wang ZF, Zhang XS, Zhang XZ, Wu MT and Wu B (2023), Hazard assessment of potential debris flow: A case study of Shaling Gully, Lingshou County, Hebei Province, China.
Front. Earth Sci. 11:1089510.
doi: 10.3389/feart.2023.1089510

COPYRIGHT

© 2023 Wang, Zhang, Zhang, Wu and Wu. This is an open-access article distributed under the terms of the [Creative Commons Attribution License \(CC BY\)](#). The use, distribution or reproduction in other forums is permitted, provided the original author(s) and the copyright owner(s) are credited and that the original publication in this journal is cited, in accordance with accepted academic practice. No use, distribution or reproduction is permitted which does not comply with these terms.

Hazard assessment of potential debris flow: A case study of Shaling Gully, Lingshou County, Hebei Province, China

Zhong Fu Wang^{1*†}, Xu Sheng Zhang^{1†}, Xu Zhu Zhang²,
Ming Tang Wu³ and Bo Wu¹

¹North China University of Water Resources and Electric Power, Zhengzhou, China, ²Beijing Engineering Corporation Limited, Beijing, China, ³Huadong Engineering Corporation Limited, Hangzhou, China

The debris flows in the Taihang Mountain region in North China are basically triggered by rainstorms. Firstly, the debris flow susceptibility of the Shaling Gully, Lingshou County, Hebei Province, China was analyzed in this paper to evaluate its hazard and effect on the downstream proposed structures. Secondly, the maximum flow depth and velocity of the potential debris flow in Shaling Gully were numerically simulated based on the FLO-2D model, and the simulation results indicate that the flow depths under the 50-year and 100-year rainstorms will have some effect on the downstream proposed structures. With debris flow intensity classification, the hazard of potential debris flow in Shaling Gully was classified. According to the flow depths and velocities simulated by FLO-2D model, the ARCGIS10.8 software was adopted to optimize the hazard zones, and therefore the hazard zonation map was established. With consideration of simulation results under natural conditions and other factors such as gully feature, a 4 m high and 40 m wide retaining dam was designed. The numerical simulation results show that the retaining dam may decrease the debris flow hazard to a negligible level, which offers some beneficial reference to the subsequent engineering design for Shaling Gully.

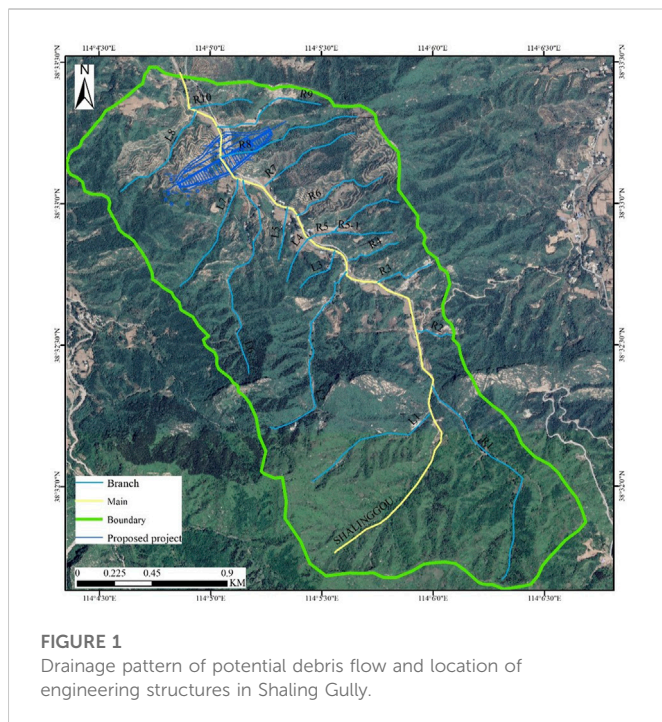
KEYWORDS

hazard of potential debris flow, FLO-2D, ArcGIS, retaining dam, numerical simulation

1 Introduction

Debris flows are considered to be very dangerous mass movement in the world (Lee and Widjaja, 2013). In China, the debris flows basically occur in the Loess Plateau region and northern and southwestern mountains, and those in the northern mountains generally result from rainstorm. Therefore, the research in the debris flow hazard is important to the hazard mitigation and prevention due to the wide distribution and severe damage of debris flow.

Researchers in different countries have established various numerical models to interpret, simulate and predict the debris flow events (Zegers et al., 2020). FLO-2D model based on the non-Newtonian fluid and central finite difference (O'Brien et al., 1993), and this model was proven to be effective in terms of Omega parameter (Chang et al., 2017). FLO-2D model as used to numerically simulate the discharges of debris flow in Huaxi Gully under operational and dam-failure conditions, respectively (Fang et al., 2019). FLO-2D model was also applied to precisely simulate the movement and deposition processes (Stancanelli et al., 2017) and estimate the maximum depth of moving debris flow on the base of NAM model (Wei et al., 2017). FLO-2D model is also used to simulate terrain changes caused by debris flow caused by rainstorm during typhoon period (Chen and Wang, 2017). The FLO-2D PRO model is used to analyze the

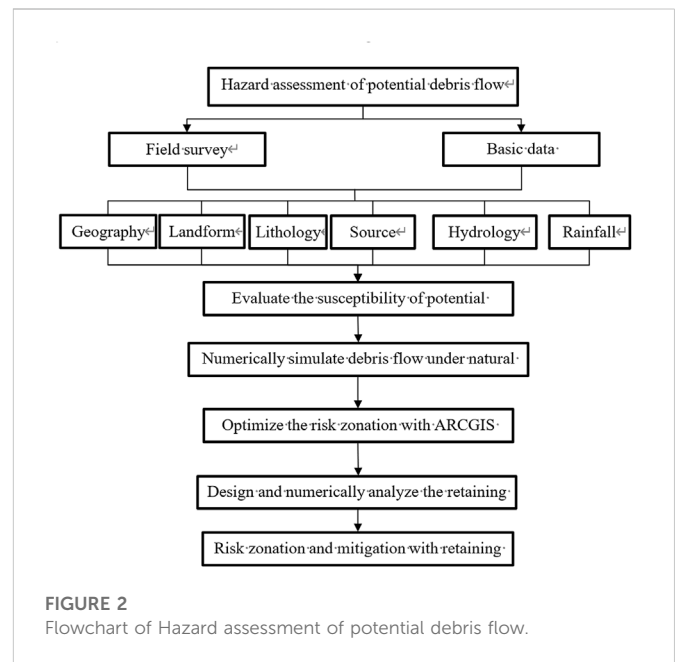


sedimentation, velocity, impact force and influence area of debris flow based on SCS-CN method (Zhang et al., 2014). In addition, the sediment yield of debris flow in Sulin Town, Hualian County, China was estimated with the FLO-2D model (Hsu et al., 2012). Many scholars also evaluated the debris flow hazard by the FLO-2D model. For example, the numerical simulation on the Chengbei Gully in Shanxi Province, China was carried out with FLO-2D model, and then the hazard zonation was conducted (Tang et al., 2022). Numerically estimated the depth and scope of debris flow of Boshui Gully with FLO-2D model under the 100-year and 50-year rainfall conditions, and provided a method to assess the debris flow hazard with consideration of solid source and water (Zhang et al., 2022). Estimated the debris flow hazard with FLO-2D model, and then classified the debris flow hazard in Anzhou City, Sichuan Province, China (Deng et al., 2021). The FLO-2D model was also applied to simulate the movement process of debris flow of Hou Gully in Shimian County, Yaan City, China under different cycles, and then the intensity classification of slag debris flow was established (Deng et al., 2021). Additionally, the FLO-2D model was used to determine the intensity of Zhouqu debris flow (Zhang et al., 2018) and obtain the hazard zonation map of debris flow in Songhe Stream region (Lin et al., 2011).

The hazard of debris flow in Shaling Gully was assessed in this paper. Firstly, the susceptibility of debris flow was analyzed according to the field survey data. Secondly, the debris flow was numerically simulated with FLO-2D model. Thirdly, the hazard zonation at various rainstorm frequencies was determined by ARCGIS10.8 software. Finally, the retaining dam for debris flow mitigation was evaluated by numerical simulation, which provided technical support for the safety of downstream structures.

2 Study area

The Shaling Gully is located in Lingshou County, Shijiazhuang City, Hebei Province, China, with 18 dendritic branch gullies on two



banks. The main gully is 3.876 km long, and the catchment area is approximately 4.91 km². Abundant alluvial, colluvial and man-made deposits are found in these gullies, and a little residual deposit in some gullies. Some structures of the lower reservoir of Lingshou pumped-storage station are just located in the study area, as shown in Figure 1.

The study area is situated in the Taihang Mountain uplift zone, and 25 pre-Quaternary faults are found within 25 km of the study area. These faults mostly have NE- and NW-strike, partly with NS and EW strike.

The lithology in the study area consists mainly of the Archean biotite plagioclase-feldspar gneiss of Fangli Formation (Fgn), plagioclase-feldspar amphibolite of Chejiangou Formation (Ca), and Archean granite gneiss of Gangnan Formation (Ggn). The Quaternary strata consist basically of the 1 m–2 m thick residual (Q₄^{edl}) gravel soil on the mountain peak and slope, 1 m–3 m thick alluvial (Q₄^{pal}) sandy gravel on the gully bottom, 1 m–5 m thick diluvial (Q₄^{pl}) 0.2 m–0.5 m-diameter gravel soil on the gully banks, and 1 m–3 m thick (partially about 5 m thick) man-made (Q₄^{ml}) gravel soil on the upper terrace and gully bottom. The well developed gneissoid structures are widely found on the gully banks, generally with attitude of NE60°–80°, SE∠60°–80°.

The warm continental monsoon dominates the study area, with distinct wet and dry seasons. The average annual precipitation is 497 mm, 64% of which occurs during the period from June to August, and the average annual evaporation is 1,685.3 mm.

The human activities in the study area involve the abandoned open mining and artificial deposit on the gully bottom. The mining activities result in not only some colluvium due to rock cracking but also abundant slag. The terraces, which are generally located in the midstream and downstream Shaling Gully, have large scale and loose structure, providing abundant source for triggering the debris flow during flood season.

3 Methodology

Firstly, the susceptibility of debris flow was analyzed according to the field survey data and remote sensing interpretation. Secondly, the FLO-2D model was applied to evaluate the maximum flow depths and

velocities at various rainstorm frequencies. Thirdly, the hazard zonation at various rainstorm frequencies was determined based on the debris flow intensity classification, and the effect of debris flow on the downstream proposed structures was estimated. Finally, the retaining dam for debris flow mitigation was designed, and the operational effect of the dam was numerically simulated with FLO-2D model. The flowchart of hazard assessment is shown in Figure 2.

3.1 Data acquisition

The sophisticated UAV oblique photography is frequently applied to obtain the data about contour line (Li et al., 2021b, 2021c; Almalki and Angelides, 2022; Trepekli et al., 2022; Zan et al., 2022). High definition photos about the region concerned can be taken by high resolution cameras attached to the UAV, and then the real terrain and landform about the study area will be achieved by image processing and information extraction. The UAV behaves better in field survey due to its high definition, wide survey range, easy operation, few site limitations and good suitability. In this paper, the 1:5,000 contour lines obtained by UAV was imported into ARCGIS10.8 to create and process the DEM data. The distribution and volume of debris flow source in Shaling Gully were determined by field survey and UAV technique.

3.2 Susceptibility evaluation

The susceptibility of debris flow is commonly referred to as the occurrence probability of a debris flow. Currently, the susceptibility is basically evaluated by the direct index evaluation method, which is a subjective judgement, or indirect index evaluation method, which is widely used by most scholars (Li et al., 2020; Sujatha, 2020; Mehmood et al., 2021; Jingbo et al., 2021). In this paper, the indirect index evaluation method was selected to estimate the susceptibility of debris flow in Shaling Gully.

3.3 FLO-2D simulation

FLO-2D, evolved from the diffusive hydrodynamic model, is a two-dimensional finite difference model that numerically simulates flood and debris flow (O'Brien et al., 1993). The model discretizes the surface topography into uniform square-grid elements in terms of central finite difference routing scheme, and the each grid has corresponding elevation and Manning's coefficient. The continuity equation and motion equations govern the conservation of mass and momentum, which are expressed as

$$\frac{\partial h}{\partial t} + \frac{\partial h V_x}{\partial x} + \frac{\partial h V_y}{\partial y} = i \quad (1)$$

$$S_{fx} = S_{ox} - \frac{\partial h}{\partial t} - \frac{V_x}{g} \left(\frac{\partial V_x}{\partial x} \right) - \frac{V_y}{g} \left(\frac{\partial V_x}{\partial y} \right) - \frac{1}{g} \left(\frac{\partial V_x}{\partial t} \right) \quad (2)$$

$$S_{fy} = S_{oy} - \frac{\partial h}{\partial t} - \frac{V_y}{g} \left(\frac{\partial V_y}{\partial y} \right) - \frac{V_x}{g} \left(\frac{\partial V_y}{\partial x} \right) - \frac{1}{g} \left(\frac{\partial V_y}{\partial t} \right) \quad (3)$$

where h is the flow depth, i is the rainfall duration, t is fluid movement time, V_x is the average velocity along x coordinate, V_y is the average velocity along y coordinate, g is the gravity acceleration, S_{fx} is the

friction slope component along x coordinate, S_{fy} is the friction slope component along y coordinate, S_{ox} is the bed slope along x coordinate, and S_{oy} is the bed slope along y coordinate.

Besides, the solid particles in the debris flow may collide against each other during movement, increasing the inertial stresses, and therefore the effect of particle collision on debris flow movement should be considered by the following equation:

$$S_f = S_y + S_v + S_{td} = \frac{\tau_y}{\gamma_m h} + \frac{K \eta v}{8 \gamma_m h^2} + \frac{n^2 v^2}{h^{\frac{4}{3}}} \quad (4)$$

where S_f is the friction slope, S_y is the yield slope, S_v is the viscous slope, S_{td} is the turbulent-dispersive slope, τ_y is the yield stress, η is the viscosity coefficient, γ_m is the specific gravity of fluid, K is the resistance parameter for laminar flow, v is the flow velocity, and n is the equivalent Manning's coefficient.

4 Susceptibility assessment of potential debris flow in Shaling Gully

The indirect index evaluation method always selects the terrain, source and rainfall as evaluation factors, and then the selected factors are normalized and weighted (Jun et al., 2017; Li et al., 2021a). In this paper, the AHP (Analytic Hierarchy Process) method was used to evaluate these factors (Mehmood et al., 2021).

4.1 Selection of evaluation factors

The occurrence of debris flow are greatly affected by the terrain, source and rainfall, and the selected factors should be representative and easily quantified. According to the gully characteristics in the study area and other scholars' achievements (Lin et al., 2012; Niu et al., 2015; Cao et al., 2017; Xiao et al., 2020; Gu et al., 2021), the susceptibility of debris flow in Shaling Gully was evaluated by eight factors, namely, catchment area S1, main gully length S2, maximum elevation difference S3, ravine density S4, average longitudinal slope ratio S5, loose material length supply ratio S6, loose material volume S7, and maximum daily (24 h) rainfall S8.

4.2 AHP model

The AHP model for susceptibility assessment of potential debris flow in Shaling Gully is shown in Figure 3.

The weight of each factor was determine by the importance to its parent layer, with S1 = 0.0145, S2 = 0.0258, S3 = 0.0487, S4 = 0.0258, S5 = 0.0487, S6 = 0.3597, S7 = 0.1799, and S8 = 0.3070.

5 Hazard assessment of debris flow under natural conditions

5.1 Parameter determination

The contour lines measured in the field were converted into DEM format and then into ASCII format with ARCGIS10.8. The ASCII format data were imported into FLO-2D, and then the simulation

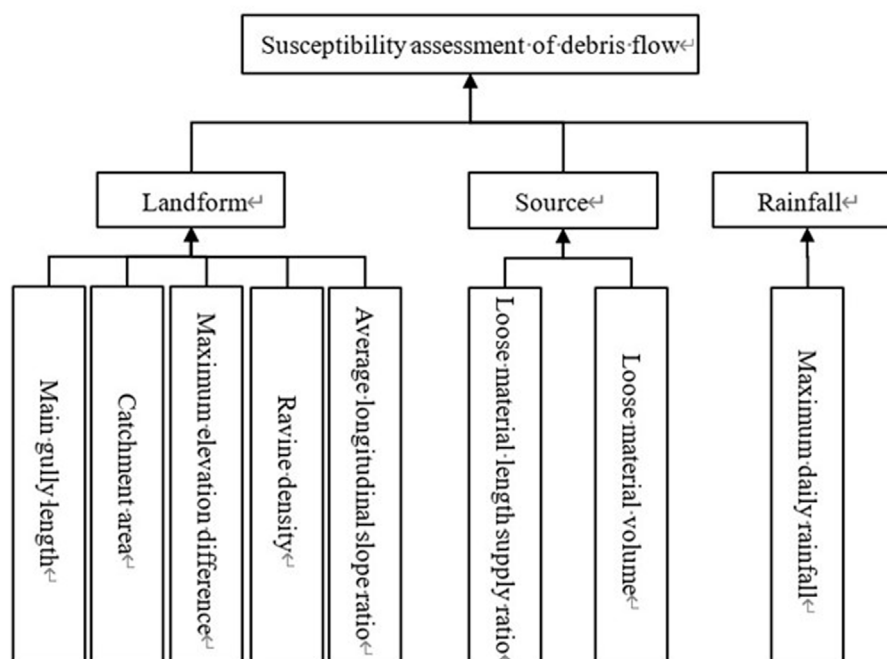


FIGURE 3

AHP model for susceptibility assessment of potential debris flow in Shaling Gully.

domain and grid sizes were appropriately determined. In this paper, the grid size is 20 m × 20 m, and the calculation region was subsequently determined and assigned with elevation values.

5.1.1 Resistance parameter for laminar flow and Manning's coefficient

The Manning's coefficient was applied to represent the effect of ground roughness on debris flow in FLO-2D, and this coefficient is greatly influenced by the terrain and vegetation. The Manning's coefficient was determined jointly by the field survey results, Eq. 5 proposed by Wang Yuyi et al., and some research achievements (Chen et al., 2021; Deng et al., 2021; Zhang et al., 2022). Finally, the Manning's coefficient is 0.1 and the resistance parameter for laminar flow is 2,285.

$$n_c = 0.033R_{ns}^{-0.51} \exp(0.34R_{ns}^{0.17}) \ln h \quad (5)$$

5.1.2 Volumetric sediment concentration

The volumetric sediment concentration was calculated with Eq. 6.

$$C_V = \frac{\gamma_C - \gamma_W}{\gamma_S - \gamma_W} \quad (6)$$

where C_V is the volumetric sediment concentration, γ_C is the unit weight of debris flow (g/cm^3), γ_S is the unit weight of solid particles of debris flow (g/cm^3), and γ_W is the unit weight of water (g/cm^3).

Here the calculated C_V is 0.35.

5.1.3 Viscosity coefficient

In terms of $\eta = \alpha_1 e^{\beta_1 C_V}$ and $\tau_y = \alpha_2 e^{\beta_2 C_V}$, if α_1 , β_1 , α_2 , and β_2 are determined, the viscosity coefficient and yield stress T_y will be achieved. According to field survey results and empirical relations

TABLE 1 Parameters for FLO-2D.

Parameter	n	α_1	β_1	α_2	β_2	K
Value	0.1	0.00025	15.48	0.03	14.42	2,280

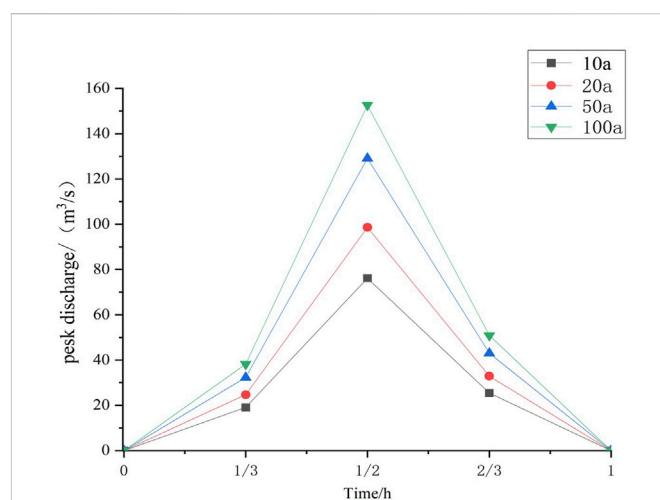


FIGURE 4

Variations of peak discharge of debris flow with time in Shaling Gully.

(Wang et al., 2007; Zhang et al., 2014; Stancanelli et al., 2017; Wei et al., 2017), these parameters were determined, as listed in Table 1.

$$BF = \frac{1}{1 - C_v} \quad (7)$$

5.3 Simulation results

For the method of using FLO-2D to assess the hazard of debris flow, many scholars have verified and achieved good results (Zhang et al., 2018; Chang et al., 2020; Tang et al., 2022). As this paper is a potential debris flow, the numerical simulation results are mainly based on the field investigation, combined with the gully terrain and material source conditions, through the comparison of theoretical calculation and numerical simulation results, to determine the numerical simulation model.

The debris flow is numerically simulated immediately after the related parameters were input into FLO-2D. The simulation results are shown in Figure 5, indicating that the maximum flow depths and velocities have positive correlation to the rainfall. Under the 10-year and 20-year rainfall conditions, the velocities and flow depths are generally small, which has minor effect on downstream structures, and more than 90% of flow depths are less than 1 m, with velocities of 0.5 m/s–1 m/s. Under the 50-year and 100-year rainfall conditions, the velocities and flow depths increase, and 18.4% of 50-year flow depths and 26.7% of 100-year flow depths are greater than 1 m, with most velocities larger than 1 m/s.

5.4 Hazard assessment of debris flow in Shaling Gully under natural conditions

The hazard of potential debris flow was assessed according to the maximum flow depths and maximum velocities simulated by FLO-2D, and then the effect of debris flow on the downstream structures is estimated. The classification standard of debris flow intensity in terms of maximum flow depth and maximum velocity has good suitability (Lin et al., 2011; Chang et al., 2017; Zhang et al., 2018; Chang et al., 2020). Table 2 lists the classification standard of debris flow intensity in Shaling Gully according to the influence on downstream proposed structures, site terrain and engineering design data.

The hazard of potential debris flow and its effect on the downstream proposed structures were evaluated in terms of rainstorm frequencies. For quantitative analysis, the V_h value of each grid was calculated by the Spatial Join tool of ARCGIS, and the zones whose parameters are not listed in Table 2 were marked by special signs. If the hazard zones by ARCGIS were not identical to those by Hazard plug-in of FLO-2D, those zones were reasonably evaluated in a qualitative way according to site conditions, empirical methods and rainfall frequency. The final hazard zonation map of debris flow in Shaling Gully at vario is obtained. According to the intensity classification of debris flow and the qualitative and quantitative classification standards, the hazard zoning of debris flow under different rainfall frequencies is obtained. The maximum flow depth in high-hazard zones is more than 2.5 m. Low hazard zones are all with velocities less than 0.5 m/s or maximum flow depth less than 0.5 m. The H_v value of the medium hazard zones are between 0.5 m/s² and 2.5 m/s².

The simulation results indicate that, under 10-year rainfall condition, the high, medium and low hazard zones account for

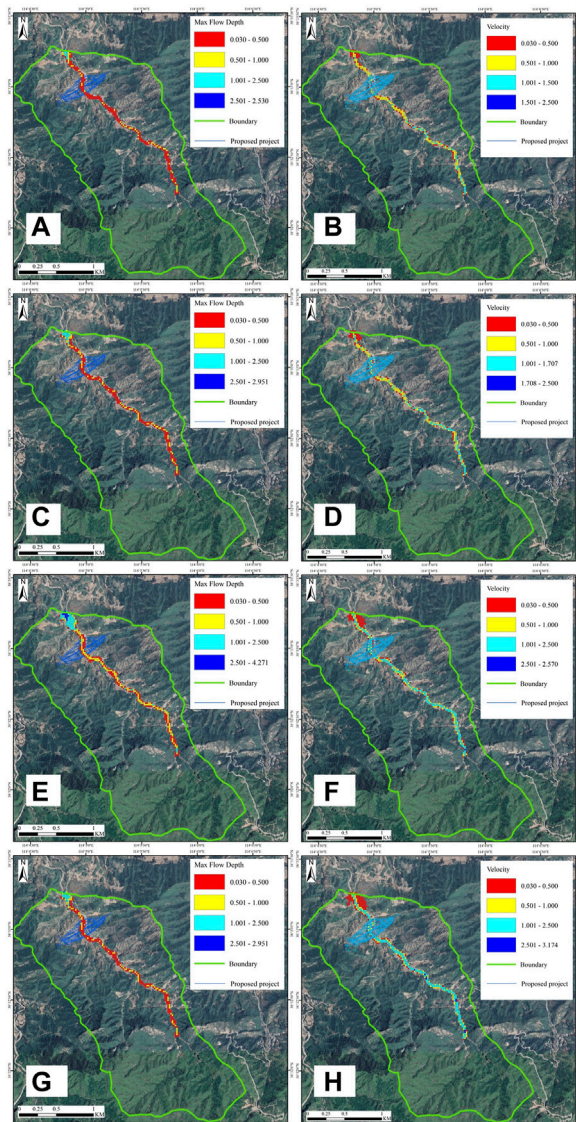


FIGURE 5

Maximum flow depths and velocities at various rainfall frequencies.

(A)(a) Distribution of 10-year maximum flow depth (m) (B)(b) Distribution of 10-year velocity (m/s), (C)(c) Distribution of 20-year maximum flow depth (m), (D)(d) Distribution of 20-year velocity (m/s), (E)(e) Distribution of 50-year maximum flow depth (m), (F)(f) Distribution of 50-year velocity (m/s), (G)(g) Distribution of 100-year maximum flow depth (m), (H)(h) Distribution of 100-year velocity (m/s).

5.2 Inflow node and peak discharge

It is very important to select appropriate inflow nodes for FLO-2D simulation (Genevois et al., 2022). The zone with abundant loose deposit was defined as the inflow node according to the field survey and rainfall data. Because the capturing and erosion of debris flow was not considered in the FLO-2D simulation, the bulking factor (BF) was introduced for compensation (Elci et al., 2017). BF is frequently calculated with Eq. 7. Before numerical simulation, the peak discharge - time curves at various rainstorm frequencies were optimized according to peak discharges, BF and generalized pentagon method, as shown in Figure 4.

TABLE 2 Classification standard of debris flow.

Intensity	Maximum flow depth	Relation	Product of maximum flow depth and velocity
High	$h > 2.5\text{ m}$	OR	$Vh > 2.5\text{ m/s}$
Medium	$0.5\text{ m} < h < 2.5\text{ m}$	AND	$0.5\text{ m/s} < Vh < 2.5\text{ m/s}$
Low	$h < 0.5\text{ m}$	AND	$Vh < 0.5\text{ m/s}$

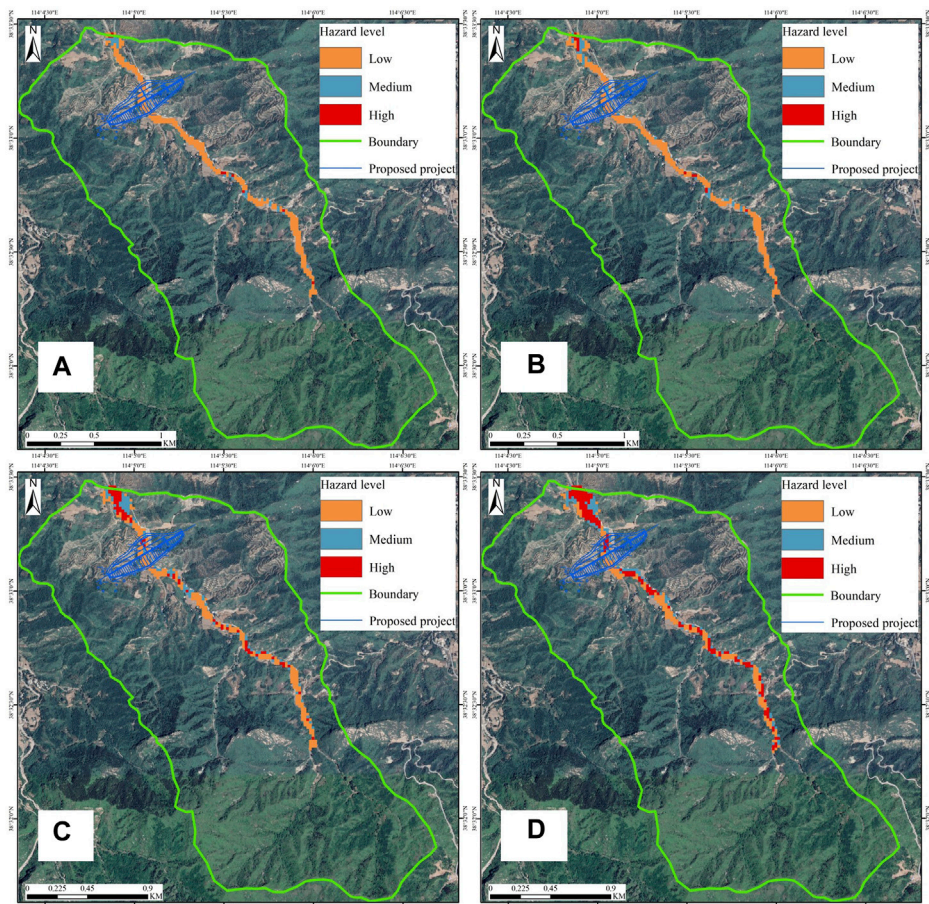


FIGURE 6 Hazard zonation of debris flow at various rainfall frequencies. (A)(a)Hazard zonation under 10-year rainfall, (B)(b)Hazard zonation under 20-year rainfall, (C)(c)Hazard zonation under 50-year rainfall, (D)(d)Hazard zonation under 100-year rainfall.

2.9%, 9.4%, and 87.7%, respectively. All the engineering structures are in the low hazard zones, and thus are safety.

Under 20-year rainfall condition, the high, medium and low hazard zones account for 4.9%, 12.9%, and 82.8%, respectively. Most engineering structures are in the low hazard zones, but few in medium hazard zones. According to qualitative analysis, the medium hazard zones have relatively larger deposition depth and small velocity, and therefore have generally low hazard to the structures.

Under 50-year rainfall condition, the high, medium and low hazard zones account for 18.9%, 21.2%, and 59.9%, respectively. Most engineering structures are in the low hazard zones, partially in medium hazard zones, and few in high hazard zones. According to

qualitative analysis, the maximum flow depths increase, and therefore have some hazard to the structures.

Under 100-year rainfall condition, the high, medium and low hazard zones account for 26.2%, 22.1%, and 51.7%, respectively. A few engineering structures in gully outlet are in high hazard zones, and may be highly threatened by potential debris flow according to qualitative analysis. Under 100-year rainfall condition, the high, medium and low hazard zones account for 26.2%, 22.1%, and 51.7%, respectively. A few engineering structures in gully outlet are in high hazard zones, and may be highly threatened by potential debris flow according to qualitative analysis.

Generally, the proposed structures may be generally subject to low hazard under 10-, 20- and 50-year rainfall conditions, but to high

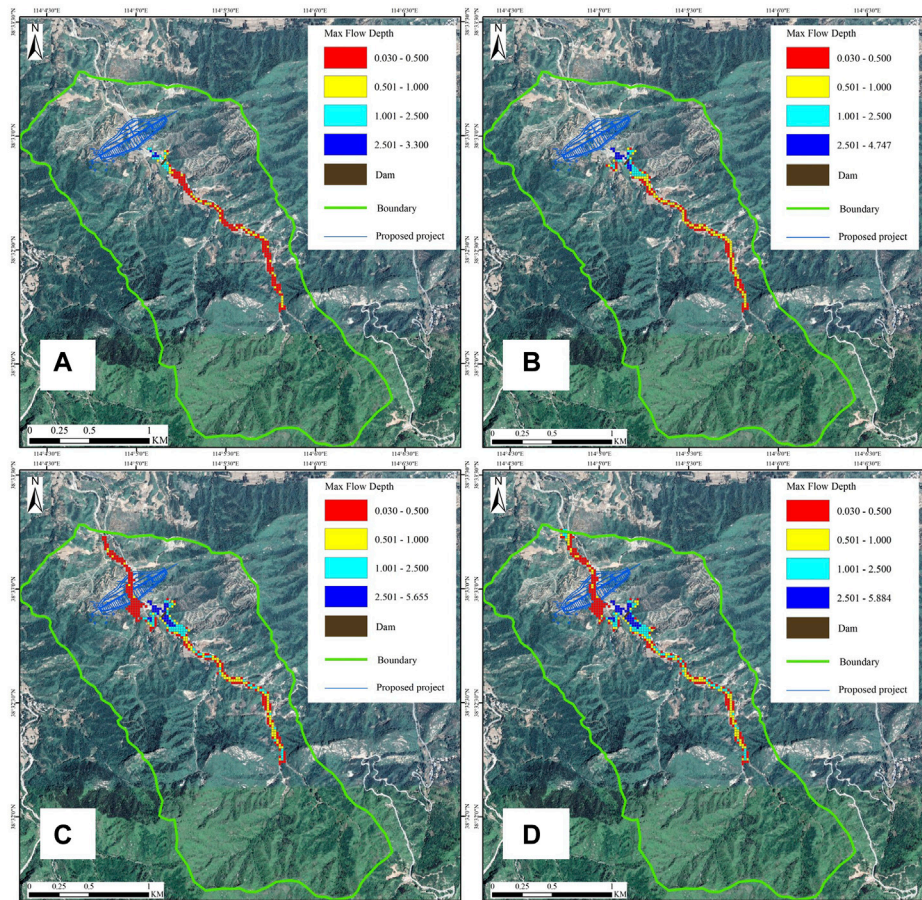


FIGURE 7

Distribution of maximum flow depths (m) with retaining dam at various rainfall frequencies (A)Hazard zonation with dam under 10-year rainfall, (B)Hazard zonation with dam under 20-year rainfall, (C)Hazard zonation with dam under 50-year rainfall, (D)Hazard zonation with dam under 100-year rainfall.

hazard under 100-year rainfall condition. Therefore, some retaining measures should be taken under 100-year rainfall condition. As frequencies is shown in Figure 6.

6 Design of retaining structures

6.1 Type and location

The research on the prevention and mitigation of debris flow is conducted many year ago. In China, the integrated technique is frequently applied for hazard mitigation by combinations of prevention, treatment, engineering measures, biological structures, and resource utilization (Gao and Tian, 2020; Zhang et al., 2020), and the retaining structures are predominately used to control the debris flow in mountains (Lee et al., 2014; Zhang et al., 2021).

The retaining dam scheme was taken to control the debris flow in Shaling Gully in terms of construction feasibility and cost by deeply analyzing the its profile, activity and effect according to on-site survey and simulation results. The retaining dam is located in the straight gully section with a rural road, which is suitable for construction. Furthermore, it can prevent the downstream structures from debris flow because most unstable soil source is in the midstream and

upstream gully. The retaining dam was designed to be 4 m high and 50 m wide because the effective sediment retaining volume depends greatly on the dam height, width and upstream terrain.

6.2 Numerical simulation under retaining structures conditions

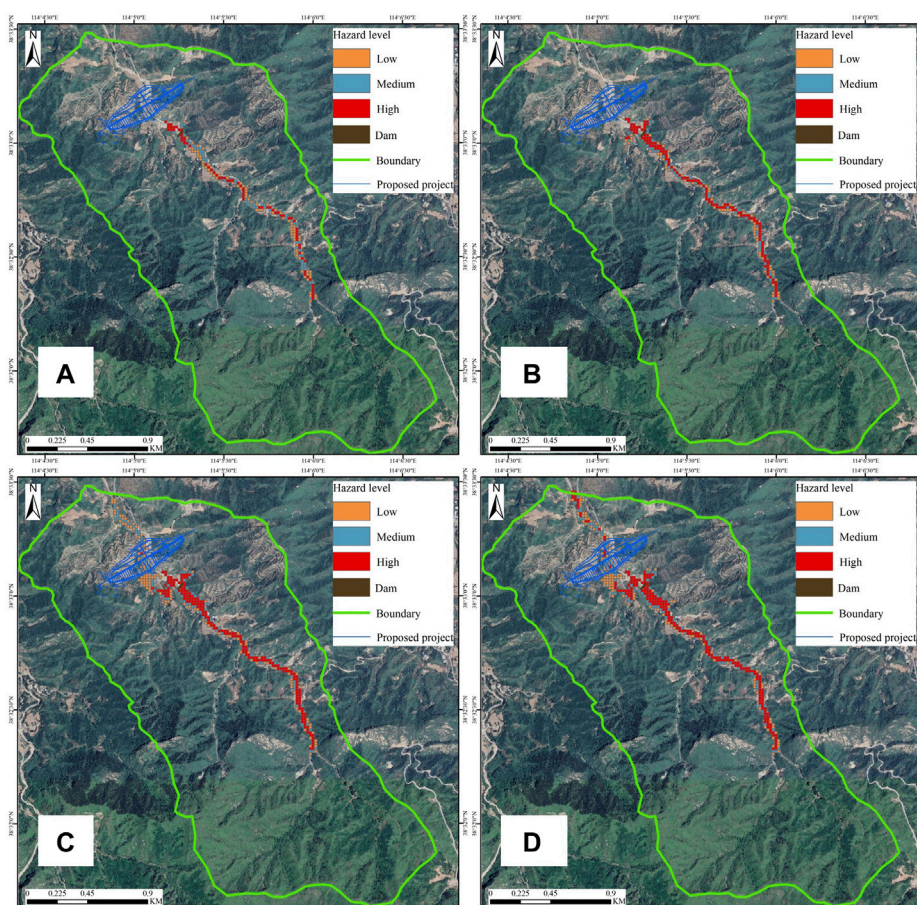
Firstly, the dam location was determined and imported into FLO-2D. Secondly, the dam model was established with Levee module (Wang, 2019). Thirdly, the maximum flow depths were calculated by appropriately setting relative parameters, as shown in Figure 7.

The simulation results show that almost 100% potential debris flow is blocked by the retaining dam under 10-year and 20-year rainfall conditions, but small amount of debris flow discharges under 50-year and 100-year rainfall conditions, posing a little threat to downstream structures. Due to the dam blockage and riverbed silting, the flow depths and ranges increase in the upstream of dam and obviously decrease in the downstream of dam.

Table 3 indicates that the percents of flow depths greater than 1 m increase remarkably at the back of dam due to riverbed silting. The dam completely blocks the debris flow under 10-year and 20-year frequencies and no debris flow occurs at the front of the dam, which

TABLE 3 Percent of flow depth before and after retaining dam.

Return period/year	Condition	< 0.5 m (%)	0.5 m–1 m (%)	1 m–2.5 m (%)	> 2.5 m (%)
10	Natural	77.1	17.9	4.0	0.0
	Remedial	67.9	21.7	8.0	2.4
20	Natural	67.8	24.9	7.0	0.3
	Remedial	42.6	37.6	11.6	8.2
50	Natural	42.4	37.2	16.4	4.0
	Remedial	50.4	23.1	17.2	9.3
100	Natural	32.5	34.7	18.6	9.9
	Remedial	45.1	26.4	20.8	12.0

**FIGURE 8**

Hazard zonations with retaining dam at various rainfall frequencies. (A)(a)Hazard zonation with dam under 10-year rainfall, (B)(b)Hazard zonation with dam under 20-year rainfall, (C)(c)Hazard zonation with dam under 50-year rainfall, (D)(d)Hazard zonation with dam under 100-year rainfall.

has no threat to the downstream structures. In addition, the percents of flow depths less than 0.5 m increase obviously. Furthermore, the flow depths are almost less than 1 m at the front of the dam, indicating that the dam can effectively block the debris flow. Due to the existence of retaining dam, the debris flow has little hazard to the downstream structures. The hazard zonations with retaining dam at various rainfall frequencies are shown in Figure 8.

7 Discussion

Based on FLO-2D model, the hazard zoning of potential debris flow is obtained by simulating the maximum flow depth and velocity of potential debris flow. In recent years, as a two-dimensional dynamic simulation model, FLO-2D has been widely used in the hazard quantification of debris flow disasters, and has shown satisfactory

results (Deng et al., 2021; Tang et al., 2022). In the study of regional debris flow hazard, FLO-2D simulation program can determine the temporal and spatial distribution of debris flow fluid depth and velocity. However, in the study of potential debris flow, although the reasonable velocity and flow depth can be simulated, there is no debris flow, so the simulation of potential debris flow cannot be verified in reality. For FLO-2D numerical simulation, ARCGIS10.8 can be used for correction in hazard zoning. But in the simulation of FLO-2D, the following assumptions needs to be done.

- (1) Assume that the water pressure distribution is hydrostatic;
- (2) The debris flow is stable in the time interval of difference calculation;
- (3) The debris flow satisfies the steady flow retardation equation;
- (4) Assume that each grid point has a unique elevation value and Manning coefficient;
- (5) It is assumed that the roughness of debris flow movement surface in the grid is an average value.

Therefore, grid selection is also very important in FLO-2D simulation. Based on the existing computer tools and considering the accuracy requirements of this paper, choose 20 m × 20 m grid size. If the computer conditions permit, you can also choose a finer grid size of 20 m. In addition, the erosion and entrainment of debris flow cannot be considered due to the assumption problem, which is worth further studying.

8 Conclusion

The debris flow may be triggered in Shaling Gully under rainstorm due to abundant loose sediment, and its hazard was assessed in this paper. The maximum flow depths and velocities under 10-year, 20-year, 50-year, and 100-year rainfall conditions were numerically simulated, and then the hazard zonations at various rainfall frequencies were determined according to the intensity classification standard. Some conclusions are as follows:

- (1) Abundant residual, alluvial and diluvial gravel soil as well as artificial deposit of mining slag and terraces, which provides solid material source for triggering debris flow.
- (2) The susceptibility of debris flow was estimated to be medium by direct and indirect methods. Additionally, the maximum flow depths and velocities were numerically simulated with FLO-2D.
- (3) The hazard of debris flow at various rainfall frequencies were assessed according to the intensity classification standard of debris flow. Furthermore, the hazard zonation maps at various rainfall frequencies were completed by ARCGIS and Hazard module of FLO-2D, which is beneficial for the design and construction of downstream structures.

References

Almalki, F. A., and Angelides, M. C. (2022). Autonomous flying IoT: A synergy of machine learning, digital elevation, and 3D structure change detection. *Comput. Commun.* 190 (1), 154–165. doi:10.1016/j.comcom.2022.03.022

- (4) The retaining dam was designed to be 4 m high and 40 m wide according to the simulation results under natural conditions and gully features. The numerical simulation by FLO-2D indicates that the potential debris flow may pose little hazard to downstream structures under the existence of retaining dam.

Data availability statement

The original contributions presented in the study are included in the article/Supplementary Material, further inquiries can be directed to the corresponding author.

Author contributions

All authors contributed to the study conception and design. Material preparation, data collection and analysis were performed by ZW, SZ, and ZZ. The pictures and tables were performed by MW and BW. The first draft of the manuscript was written by SZ and ZW and all authors commented on previous versions of the manuscript. All authors read and approved the final manuscript.

Funding

The authors would like to acknowledge the National Key Research and Development Program (Grant No. 2019YFC1509704), National Natural Science Foundation of China (Grant No. U1704243), High-level Talent Project of North China University of Water Resource and Electric Power (Grant No. 201518), and Levee Safety and Disaster Prevention Engineering Research Center of Ministry of Water Resources.

Conflict of interest

XZZ was employed by Beijing Engineering Corporation Limited. MW was employed by Huadong Engineering Corporation Limited.

The remaining authors declare that the research was conducted in the absence of any commercial or financial relationships that could be construed as a potential conflict of interest.

Publisher's note

All claims expressed in this article are solely those of the authors and do not necessarily represent those of their affiliated organizations, or those of the publisher, the editors and the reviewers. Any product that may be evaluated in this article, or claim that may be made by its manufacturer, is not guaranteed or endorsed by the publisher.

Cao, C., Xu, P., Chen, J., Zheng, L., and Niu, C. (2017). Hazard assessment of debris-flow along the baicha river in heshigten banner, inner Mongolia, China. *Int. J. Env. Res. Pub He* 14, 30. doi:10.3390/ijerph14010030

- Chang, M., Liu, Y., Zhou, C., and Che, H. X. (2020). Hazard assessment of a catastrophic mine waste debris flow of Hou Gully, Shimian, China. *Eng. Geol.* 275, 105733. doi:10.1016/j.enggeo.2020.105733
- Chang, M., Tang, C., Van Asch, T., and Cai, F. (2017). Hazard assessment of debris flows in the Wenchuan earthquake-stricken area, South West China. *Landslides* 14 (17), 1783–1792. doi:10.1007/s10346-017-0824-9
- Chen, C. Y., and Wang, Q. (2017). Debris flow-induced topographic changes: Effects of recurrent debris flow initiation. *Environ. Monit. Assess.* 189 (9), 449–511. doi:10.1007/s10661-017-6169-y
- Chen, M., Tang, C. A., Zhang, X. Z., Xiong, J., Chang, M., Shi, Q. Y., et al. (2021). Quantitative assessment of physical fragility of buildings to the debris flow on 20 August 2019 in the Cutou gully, Wenchuan, southwestern China. *Eng. Geol.* 293, 106319. doi:10.1016/j.enggeo.2021.106319
- Deng, Z. F., Liu, J. F., Guo, L. L., Li, J. Y., Li, J. M., and Jia, Y. R. (2021). Pure risk premium rating of debris flows based on a dynamic run-out model: A case study in Anzhou, China. *Nat. Hazards* 106 (23), 235–253. doi:10.1007/s11069-020-04459-x
- Elci, S., Tayfur, G., Haltas, I., and Kocaman, B. (2017). Numerical modeling of two dimensional flood wave propagation in residential areas after the dambreak. *Tek. Dergi* 28 (79), 55–75. doi:10.18400/tekderg.307456
- Fang, Q. S., Tang, C., Chen, Z. H., Wang, S. Y., and Yang, T. (2019). A calculation method for predicting the runoff volume of dam-break and non-dam-break debris flows in the Wenchuan earthquake area. *Geomorphology* 327 (20), 201–214. doi:10.1016/j.geomorph.2018.10.023
- Gao, F., and Tian, W. (2020). Dynamic response analysis of blocks-combined dam under impact load. *J. Mt. Sci.* 17 (11), 2827–2839. doi:10.1007/s11629-019-5619-0
- Genevois, R., Tecca, P. R., and Genevois, C. (2022). Mitigation measures of debris flow and landslide risk carried out in two mountain areas of North-Eastern Italy. *J. Mt. Sci-Engl* 19 (18), 1808–1822. doi:10.1007/s11629-021-7212-6
- Gu, X. B., Wu, S. T., Ji, X. J., and Zhu, Y. H. (2021). The risk assessment of debris flow hazards in banshanmen gully based on the entropy weight-normal cloud method. *Adv. Civ. Eng.* 20 (21), 1–11. doi:10.1155/2021/8841310
- Hsu, S. M., Wen, H. Y., Chen, N. C., Hsu, S. Y., and Chi, S. Y. (2012). Using an integrated method to estimate watershed sediment yield during heavy rain period: A case study in hualien county, taiwan. *Nat. Hazard Earth Sys* 12 (19), 1949–1960. doi:10.5194/nhess-12-1949-2012
- Jingbo, S., Shengwu, Q., Shuangshuang, Q., Yang, C., Gang, S., Qiushi, C., et al. (2021). Exploring the impact of introducing a physical model into statistical methods on the evaluation of regional scale debris flow susceptibility. *Nat. Hazards* 106 (1), 881–912. doi:10.1007/s11069-020-04498-4
- Jun, X., Xianfeng, C., Qianrui, H., Yu, C., Wufu, Q., Jia, Y., et al. (2017). Susceptibility evaluation of debris flow based on experience weight method combined with “3S” technology: A case study from dongchuan in yunnan Province, China. *IOP Conf. Ser. Earth Environ. Sci.* 95, 022051. doi:10.1088/1755-1315/95/2/022051
- Lee, K., Kim, S. W., and Kim, J. M. (2014). *Simulation of inundation zone triggered by dam failure using FLO-2D*. America: (American Geophysical Union) AGU Fall Meeting Abstracts.
- Lee, S., and Widjaja, B. (2013). Phase concept for mudflow based on the influence of viscosity. *Soils Found.* 53, 77–90. doi:10.1016/j.sandf.2012.12.005
- Li, B. Y., Hou, J. M., Li, D. L., Yang, D., Han, H., Bi, X., et al. (2021c). Application of LiDAR UAV for high-resolution flood modelling. *Water Resour. Manag.* 35, 1433–1447. doi:10.1007/s11269-021-02783-w
- Li, Y., Chen, J., Tan, C., Gu, F., and Zhang, Y. (2021b). Application of the borderline-SMOTE method in susceptibility assessments of debris flows in Pinggu District, Beijing, China. *Nat. Hazards* 105 (3), 2499–2522. doi:10.1007/s11069-020-04409-7
- Li, Y., Chen, J., Zhang, Y., Song, S., Han, X., and Ammar, M. (2020). Debris flow susceptibility assessment and runoff prediction: A case study in shiyang gully, beijing, China. *Int. J. Environ. Res.* 14 (3), 365–383. doi:10.1007/s41742-020-00263-4
- Li, Z., Chen, J., Tan, C., Zhou, X., Li, Y., and Han, M. (2021a). Debris flow susceptibility assessment based on topo-hydrological factors at different unit scales: A case study of mentougou district, beijing. *Environ. Earth Sci.* 80 (9), 365–419. doi:10.1007/s12665-021-09665-9
- Lin, J. W., Chen, C. W., and Peng, C. Y. (2012). Potential hazard analysis and risk assessment of debris flow by fuzzy modeling. *Nat. Hazards* 64 (2), 273–282. doi:10.1007/s11069-012-0236-z
- Lin, J. Y., Yang, M. D., Lin, B. R., and Lin, P. S. (2011). Risk assessment of debris flows in Songhe Stream, taiwan. *Eng. Geol.* 123 (1), 100–112. doi:10.1016/j.enggeo.2011.07.003
- Mehmood, Q., Qing, W., Chen, J., Yan, J., Ammar, M., Rahman, G., et al. (2021). Susceptibility assessment of single gully debris flow based on AHP and extension method. *Civ. Eng. JOURNAL-TEHRAN* 7, 953–973. doi:10.28991/cej-2021-03091702
- Niu, C. C., Wang, Q., Chen, J. P., Zhang, W., Xu, L. M., and Wang, K. (2015). Hazard assessment of debris flows in the reservoir region of wudongde hydropower station in China. *Sustainability-Basel* 7, 15099–15118. doi:10.3390/su71115099
- O'Brien, J. S., Julien, P. Y., and Fullerton, W. T. (1993). Two-dimensional water flood and mudflow simulation. *J. hydraulic Eng. (New York, N.Y.)* 119, 244–261. doi:10.1061/(asce)0733-9429(1993)119:2(244)
- Stancanelli, L. M., Peres, D. J., Cancelliere, A., and Foti, E. (2017). A combined triggering-propagation modeling approach for the assessment of rainfall induced debris flow susceptibility. *J. Hydrol.* 550, 130–143. doi:10.1016/j.jhydrol.2017.04.038
- Sujatha, E. R. (2020). A spatial model for the assessment of debris flow susceptibility along the Kodaikkal-Palani traffic corridor. *Front. Earth Sci.* 14 (2), 326–343. doi:10.1007/s11707-019-0775-7
- Tang, Y. M., Guo, Z. Z., Wu, L., Hong, B., Feng, W., Su, X. H., et al. (2022). Assessing debris flow risk at a catchment scale for an economic decision based on the LiDAR DEM and numerical simulation. *Front. EARTH Sci.* 10, 821735. doi:10.3389/feart.2022.821735
- Trepekli, K., Balstrom, T., Friborg, T., Fog, B., Allotey, A. N., Kofie, R. Y., et al. (2022). UAV-Borne, LiDAR-based elevation modelling: A method for improving local-scale urban flood risk assessment. *Nat. Hazards* 23 51, 423–451. doi:10.1007/s11069-022-05308-9
- Wang, Y. (2019). Analysis of engineering treatment effect of debris flow based on numerical simulation. Master's thesis (China: Lanzhou University).
- Wang, Y. Y., Hu, K. H., Wei, F. Q., and Chen, J. (2007). Relationship between rheology/erosion-deposit properties of debris flow and its hazard degree. *J. Nat. disasters* 119, 17–22. doi:10.3969/j.issn.1004-4574.2007.01.004
- Wei, Z. L., Shang, Y. Q., Lu, Q., Yu, Z., and Pan, P. (2017). Application and design of an efficient siphon dewatering system for debris flow mitigation: A case study of a small catchment in zhejiang Province, China. *Eng. Geol.* 226, 146–160. doi:10.1016/j.enggeo.2017.06.004
- Xiao, H., Tang, X., and Zhang, H. (2020). Risk assessment of debris flow in longchi area of dujiangyan based on GIS and AHP. *IOP Conf. Ser. Earth Environ. Sci.* 474, 042010. doi:10.1088/1755-1315/474/4/042010
- Zan, W. B., Zhang, W. J., Wang, N., Zhao, C. C., Yang, Q., and Li, H. (2022). Stability analysis of complex terrain slope based on multi-source point cloud fusion. *J. Mt. Sci-Engl.* 19, 2703–2714. doi:10.1007/s11629-022-7307-8
- Zegers, G., Mendoza, P. A., Garces, A., and Montserrat, S. (2020). Sensitivity and identifiability of rheological parameters in debris flow modeling. *Nat. Hazard Earth Sys* 20, 1919–1930. doi:10.5194/nhess-20-1919-2020
- Zhang, P., Ma, J., Shu, H., Han, T., and Zhang, Y. (2014). Simulating debris flow deposition using a two-dimensional finite model and Soil Conservation Service-curve number approach for Hanlin gully of southern Gansu (China). *Environ. Earth Sci.* 73 (10), 6417–6426. doi:10.1007/s12665-014-3865-6
- Zhang, S., Sun, P., Zhang, Y. L., Ren, J., and Wang, H. J. (2022). Hazard zonation and risk assessment of a debris flow under different rainfall condition in wudu district, gansu Province, northwest China. *Water-Sui* 14, 2680. doi:10.3390/w14172680
- Zhang, S., Zhang, L. M., Li, X. Y., and Xu, Q. (2018). Physical vulnerability models for assessing building damage by debris flows. *Eng. Geol.* 247, 145–158. doi:10.1016/j.enggeo.2018.10.017
- Zhang, W. T., Liu, J. F., You, Y., Sun, H., Yang, H. Q., and Lu, M. (2021). Analysis and evaluation of the treatment effect of the geotechnical engineering of debris flow: Case of xingfu gully in wolong. *J. Catastrophology* 36 (3), 208–214. doi:10.3969/j.issn.1000-811X.2021.03.036
- Zhang, Y., Chen, J., Yue, W., and Liu, D. (2020). “Development characteristics and prevention measures of debris flow disaster in bajiao Town, Shifang City, Sichuan Province,” in *Conference proceedings of the 8th international symposium on Project managemnt* (China, Beijing: Aussino Academic Publishing House), 667–676.



OPEN ACCESS

EDITED BY

Sandipan Das,
Symbiosis International University, India

REVIEWED BY

Rabin Chakraborty,
University of Burdwan, India
Subodh Chandra Pal,
University of Burdwan, India

*CORRESPONDENCE

Zhanping Song,
✉ songzhp@xauat.edu.cn

RECEIVED 12 April 2023

ACCEPTED 16 May 2023

PUBLISHED 30 May 2023

CITATION

Liu S, Song Z, Zhang Y, Guo D, Sun Y,
Zeng T and Xie J (2023), Risk assessment
of deep excavation construction based
on combined weighting and
nonlinear FAHP.
Front. Earth Sci. 11:1204721.
doi: 10.3389/feart.2023.1204721

COPYRIGHT

© 2023 Liu, Song, Zhang, Guo, Sun, Zeng
and Xie. This is an open-access article
distributed under the terms of the
[Creative Commons Attribution License
\(CC BY\)](https://creativecommons.org/licenses/by/4.0/). The use, distribution or
reproduction in other forums is
permitted, provided the original author(s)
and the copyright owner(s) are credited
and that the original publication in this
journal is cited, in accordance with
accepted academic practice. No use,
distribution or reproduction is permitted
which does not comply with these terms.

Risk assessment of deep excavation construction based on combined weighting and nonlinear FAHP

Shihao Liu¹, Zhanping Song^{1,2*}, Yong Zhang², Desai Guo³,
Yinhao Sun⁴, Tao Zeng^{1,2} and Jiangsheng Xie⁴

¹School of Civil Engineering, Xi'an University of Architecture and Technology, Xi'an, China, ²Key Laboratory of Geotechnical and Underground Space Engineering, Xi'an University of Architecture and Technology, Xi'an, China, ³School of Civil Engineering, Hunan University, Changsha, Hunan, China, ⁴China Railway 20th Bureau Group Limited, Xi'an, China

Deep excavation construction safety has become a challenging and crucial aspect of modern infrastructure engineering, and its risk assessment is frequently carried out using the Fuzzy Analytic Hierarchy Process (FAHP). However, when using FAHP to evaluate the risks of deep excavation construction, the results of the weightings obtained through subjective weighting are heavily influenced by the subjective factors of the evaluators. In addition, using linear operators to calculate the risk level can easily cause a weakening effect on the influence of prominent risk factors, resulting in poor rationality of the evaluation results. To address these problems, this paper constructs a deep excavation construction risk evaluation model based on combined weighting and nonlinear FAHP. The WBS-RBS method is used to guide the construction of the risk evaluation index system for deep excavation construction. The combined weighting values of subjective and objective weightings are calculated through the game theory combined weighting method. The fuzzy relation matrix is constructed using the membership degree vector obtained from the expert evaluation method. Nonlinear operators are introduced for comprehensive calculation. According to the maximum membership degree principle, the final risk level of the excavation construction is obtained. The newly constructed model is applied to the risk analysis of the deep excavation construction of the Rongmin Science and Innovation Park project in Xi'an. The evaluation result for the excavation construction risk is $N = [0.3125, 0.3229, 0.1939, 0.0854, 0.0854]$, and according to the maximum membership degree principle, the risk level of the excavation is classified as Level 2, which is a relatively low risk. Based on the deep excavation construction of the Rongmin Science and Innovation Park project, this paper discusses the differences between the new model and the traditional FAHP evaluation method, further verifies the reliability of the new model, optimizes the construction plan based on the evaluation results, avoids risks, and determines its guiding significance.

KEYWORDS

deep excavation, nonlinearity, risk assessment, FAHP, game theory method, WBS-RBS

1 Introduction

With the continuous increase of high-rise buildings, the vigorous development of municipal construction and the utilization of space, a large number of deep excavations have been created, and their construction safety issues have become a hotspot and difficulty in current foundation engineering (Fan et al., 2021). The demand for deep excavations in engineering is developing towards greater excavation depth, wider excavation area, and higher technical level. In relatively narrow urban spaces, improper operation during excavation of deep excavations can have serious effects on surrounding structures. The construction phase of deep excavation engineering is of utmost importance in engineering management, and risk assessment of deep excavation construction is even more critical.

Currently, some domestic and foreign experts and scholars have conducted related research and made certain achievements. WANG (2005) and Huchzermeier (2001) proposed to establish risk analysis-based management for excavation engineering. Zhou Hongbo et al. (2022) coupled the evaluation indicators of excavations using the WBS-RBS method, and analyzed the excavation of subway excavations using fault tree analysis. Feng et al. (2021) proposed an innovative method that combines analytic hierarchy process (AHP) with finite element method (FEM) to assess the potential impact risk of uncertain factors on the surrounding environment of the bridge excavation. Issa et al. (2022) introduced and applied an approach to support decision makers in construction projects by distinguishing among different deep excavation supporting systems. Meng et al. (2020) analyzed risk from two aspects—severity of consequences and probability of occurrence. They divided the severity of consequences into five indexes, calculated risk using AHP, and established expert weight index to obtain an objective calculation result from subjective expert scoring. Zhang G. H. et al. (2020) proposed a comprehensive methodology for dynamic risk analysis of foundation pit collapse during construction based on fuzzy Bayesian network (FBN) and fuzzy analytical hierarchy process (FAHP).

In conclusion, scholars and experts commonly use the Fuzzy Analytic Hierarchy Process (FAHP) for evaluating the risks of deep excavation construction, which effectively addresses the fuzziness and randomness of the evaluation. FAHP often employs the AHP method for weighting, and there have been abundant research advancements on AHP in recent years. For instance, Rabin et al. (2018) modeled and mapped groundwater potential zones using AHP and GIS technology. Sadhan et al. (2018) utilized AHP, Knowledge Driven, Fuzzy Logic, and Logistic Regression Four models to predict flood-prone areas. Xu et al. (2020) proposed a cloud model-based FAHP for risk assessment of tunnels. Moreover, Alireza et al. (2021), Shahab et al. (2020), Indrajit et al. (2020), Guo et al. (2022), Zhao et al. (2021), Song et al. (2021) and other researchers combined methods such as machine learning, Numerical simulation, and the N-K model with FAHP approach to broaden its application scope.

However, there are various problems with existing risk evaluation models for deep excavations, so it is necessary to establish a scientific and reasonable risk evaluation model for deep excavations. AHP is subject to subjective weighting, and the weighting results are heavily influenced by the evaluators' subjective factors. To address the limitations of using a single weighting method to calculate

indicator weights, this paper employs the Analytic Hierarchy Process (AHP) and Entropy Weight Method to calculate the subjective and objective weights of the risk evaluation indicators for deep excavation construction. The combination weights of the evaluation indicators are obtained by using the Game Theory method to combine the subjective and objective weights. In order to establish a scientific and rational risk evaluation indicator system for deep excavation construction, the Work Breakdown Structure- Risk Breakdown Structure (WBS-RBS) method is adopted to identify and construct the risk evaluation indicator system. However, the Fuzzy Analytic Hierarchy Process (FAHP) using the linear operator to calculate risk levels cannot address the non-linear problems in deep excavation construction risk evaluation, which reduces the accuracy of the final risk evaluation results. To address this issue, this paper introduces a non-linear operator into the traditional FAHP for risk evaluation of deep excavation construction. Finally, the newly developed risk evaluation model based on the combination weighting and non-linear FAHP is applied to the deep excavation construction of the Rongmin Science and Technology Innovation Park project on Gaoxin Second Road in Xi'an City to verify the scientific and accurate nature of the new model.

2 Construction of risk assessment indicators for deep excavation construction based on the WBS-RBS method

The construction of a reasonable and effective risk assessment indicator system is the first step in analyzing the risk of deep excavation construction. The Work Breakdown Structure (WBS) refers to the overall hierarchical structure of the deep excavation construction project. The Risk Breakdown Structure (RBS) refers to the decomposition of possible risk sources into smaller risk factors, until the risk factors can be ignored (Yang, 2006). Hillson et al. (2006) were the first to combine WBS and RBS methods by coupling them to establish an engineering project WBS-RBS risk identification coupling matrix, highlighting risk factors and establishing a risk assessment indicator system.

2.1 Developing a work breakdown structure for the construction of deep excavations

To ensure that the risk assessment indicators for deep excavation construction are appropriately detailed, expert opinions were consulted and the construction work was decomposed into a two-level structure. Based on the construction process of deep excavations, the first level is divided into five stages, including preparation for deep excavation construction (W_1), enclosure engineering (W_2), drainage engineering (W_3), excavation engineering (W_4), and monitoring engineering (W_5).

Through an analysis of the characteristics of each stage of deep excavation construction work, some work procedures that are not significant enough have been combined and eliminated, resulting in a breakdown of the first-level structure. The second-level structure has 15 units. Figure 1 shows the constructed work breakdown structure for deep excavation construction.

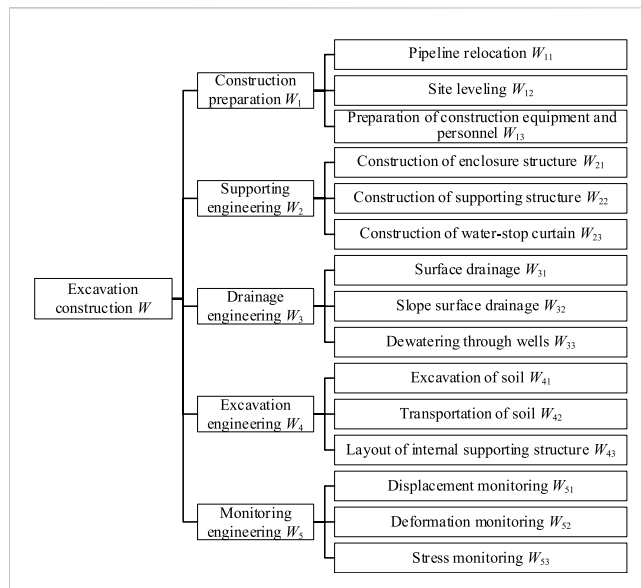


FIGURE 1
Deep excavation construction work decomposition structure diagram.

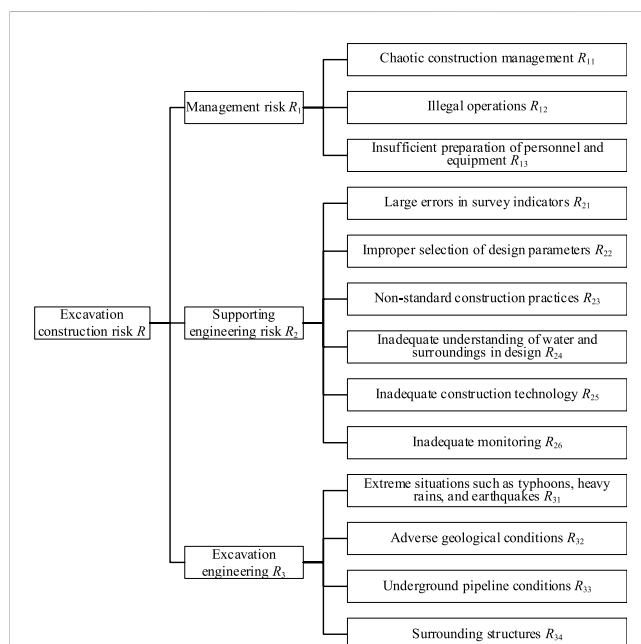


FIGURE 2
Decomposition structure of deep excavation construction risk sources.

2.2 Developing a structure for the breakdown of risk sources in the construction of deep excavations

The risk sources were also broken down into a two-level structure, with the first level of risk breakdown including

management risks (R_1), technical risks (R_2), and surrounding environmental and geological risks (R_3). Based on this, factors such as extreme weather and personnel safety were considered, and the first-level structure was further decomposed to establish a second-level risk factor structure, with 13 units. Figure 2 shows the constructed risk breakdown structure for deep excavation construction.

2.3 Developing a risk identification coupling matrix for the construction of deep excavations

Based on the work breakdown structure and risk breakdown structure of deep excavation construction, the second-level units of both structures were coupled to obtain a coupling matrix for identifying risks in deep excavation construction (Huang et al., 2004). The coupling matrix for risk identification in deep excavation construction is shown in Table 1, where “1” indicates a risk resulting from the coupling of the two structures, and “0” indicates no risk. The risks identified in the coupling matrix for risk identification in deep excavation construction are as follows.

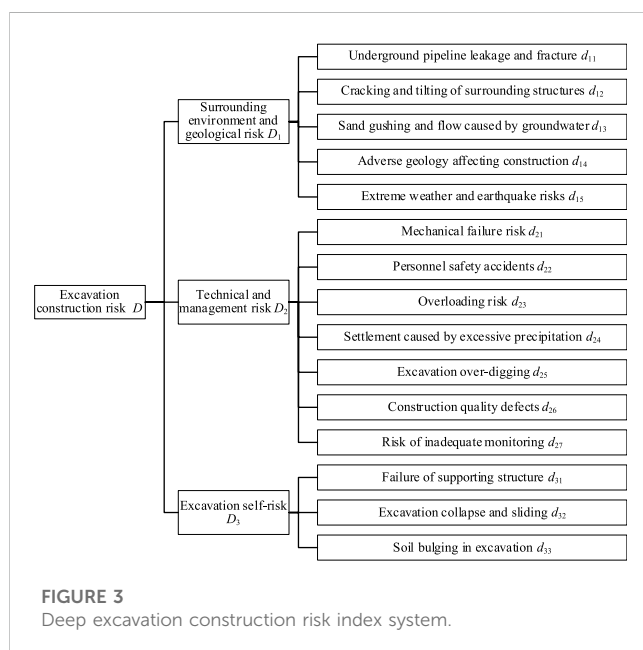
1) The risk of $W_{11}R_{11}$, $W_{11}R_{21}$, $W_{11}R_{25}$, $W_{11}R_{31}$, $W_{11}R_{33}$ is the leakage or fracture of underground pipelines; 2) The risk of $W_{11}R_{13}$, $W_{12}R_{13}$, $W_{21}R_{13}$, $W_{22}R_{13}$, $W_{23}R_{13}$, $W_{31}R_{13}$, $W_{33}R_{13}$, $W_{41}R_{13}$, $W_{42}R_{13}$, $W_{43}R_{13}$ is personnel safety accidents; 3) The risk of $W_{12}R_{25}$, $W_{21}R_{25}$, $W_{22}R_{25}$, $W_{23}R_{25}$, $W_{31}R_{25}$, $W_{32}R_{25}$, $W_{33}R_{25}$ is construction quality defects; 4) The risk of $W_{13}R_{11}$, $W_{13}R_{13}$, $W_{13}R_{23}$ is construction machinery failure; 5) The risk of $W_{21}R_{21}$, $W_{21}R_{22}$, $W_{21}R_{23}$, $W_{21}R_{24}$, $W_{21}R_{31}$ is failure of retaining structure; 6) The risk of $W_{23}R_{24}$ is water seepage in excavation; 7) The risk of $W_{33}R_{21}$, $W_{33}R_{22}$, $W_{33}R_{24}$ is blowout sand flow caused by excessive or inadequate precipitation-induced dewatering; 8) The risk of $W_{22}R_{34}$, $W_{33}R_{34}$, $W_{41}R_{24}$, $W_{41}R_{34}$, $W_{43}R_{34}$ is cracking and tilting of surrounding buildings; 9) The risk of $W_{41}R_{12}$, $W_{41}R_{21}$, $W_{41}R_{25}$, $W_{41}R_{31}$ is collapse and sliding of deep excavation; 10) The risk of $W_{41}R_{22}$ is upheaval of soil in deep excavation; 11) The risk of $W_{41}R_{23}$ is over-excavation of deep excavation; 12) The risk of $W_{42}R_{11}$, $W_{42}R_{12}$, $W_{42}R_{23}$ is excessive foundation load; 13) The risk of $W_{22}R_{21}$, $W_{22}R_{22}$, $W_{22}R_{23}$, $W_{22}R_{24}$, $W_{22}R_{31}$, $W_{43}R_{12}$, $W_{43}R_{22}$, $W_{43}R_{23}$, $W_{43}R_{25}$ is failure of support structure; 14) The risk of $W_{51}R_{11}$, $W_{51}R_{13}$, $W_{51}R_{26}$, $W_{52}R_{11}$, $W_{52}R_{13}$, $W_{52}R_{26}$, $W_{53}R_{11}$, $W_{53}R_{13}$, $W_{53}R_{26}$ is Inadequate monitoring leading to failure to handle accidents in a timely manner; 15) The risk of $W_{21}R_{32}$, $W_{22}R_{32}$, $W_{41}R_{32}$ is geological difficulties hindering construction.

2.4 Developing a system of risk evaluation indicators for the construction of deep excavations

Based on the opinions of technical personnel and experts at the construction site, referring to the coupling matrix for risk identification in deep excavation construction, an evaluation index system for the risks in deep excavation construction was established as shown in Figure 3.

TABLE 1 Coupling matrix of deep excavation construction risk identification.

Primary indicator	Secondary indicator	W_1			W_2			W_3			W_4			W_5		
		W_{11}	W_{12}	W_{13}	W_{21}	W_{22}	W_{23}	W_{31}	W_{32}	W_{33}	W_{41}	W_{42}	W_{43}	W_{51}	W_{52}	W_{53}
R_1	R_{11}	1	0	1	0	0	0	0	0	0	0	1	0	1	1	1
	R_{12}	0	0	0	0	0	0	0	0	0	1	1	1	0	0	0
	R_{13}	1	1	1	1	1	1	1	1	1	1	1	1	1	1	1
R_2	R_{21}	1	0	0	1	1	0	0	0	1	1	0	0	0	0	0
	R_{22}	0	0	0	1	1	0	0	0	1	1	0	1	0	0	0
	R_{23}	0	0	1	1	1	0	0	0	0	1	1	1	0	0	0
	R_{24}	0	0	0	1	1	1	0	0	1	1	0	0	0	0	0
	R_{25}	1	1	0	1	1	1	1	1	1	1	0	1	0	0	0
	R_{26}	0	0	0	0	0	0	0	0	0	0	0	0	1	1	1
R_3	R_{31}	1	0	0	1	1	0	0	0	0	1	0	0	0	0	0
	R_{32}	0	0	0	1	1	0	0	0	0	1	0	0	0	0	0
	R_{33}	1	0	0	0	0	0	0	0	0	0	0	0	0	0	0
	R_{34}	0	0	0	0	1	0	0	0	1	1	0	1	0	0	0

FIGURE 3
Deep excavation construction risk index system.

3 Risk assessment for the construction of deep excavations

3.1 Developing a fuzzy relation matrix

3.1.1 Developing a set of risk factors

The risk factor set of the deep excavation construction risk assessment index system established through the WBS-RBS method includes two levels. The first-level indicator layer risk factor set is $D = \{D_1, D_2, D_3\}$, and the second-level factor layer risk factor set

includes $D_1 = \{d_{11}, d_{12}, d_{13}, d_{14}, d_{15}\}$, $D_2 = \{d_{21}, d_{22}, d_{23}, d_{24}, d_{25}, d_{26}, d_{27}\}$, and $D_3 = \{d_{31}, d_{32}, d_{33}\}$.

3.1.2 Developing a set of risk assessment comments

The risk evaluation comment set for deep excavation construction is established based on the “The code of construction project management” (GB/T 50326-2006). The risk evaluation comment set for deep excavation construction is divided into five levels from low to high: $V = \{v_1, v_2, v_3, v_4, v_5\} = \{\text{low risk, relatively low risk, moderate risk, relatively high risk, high risk}\}$.

3.1.3 Building a fuzzy relation matrix using membership degree vectors

A membership degree vector is constructed for risk assessment in deep excavation construction using the expert evaluation method (Xie et al., 2005). A group of experts form an evaluation team and score each evaluation index in the risk factor set based on the five levels in the risk evaluation comment set. The membership degree vector is then organized. The fuzzy relationship matrix S between the risk evaluation comment set and the risk factor set is constructed using this vector.

$$S = \begin{bmatrix} s_{11} & \cdots & s_{1j} & \cdots & s_{1m} \\ \vdots & \ddots & \vdots & \ddots & \vdots \\ s_{i1} & \cdots & s_{ij} & \cdots & s_{im} \\ \vdots & \ddots & \vdots & \ddots & \vdots \\ s_{n1} & \cdots & s_{nj} & \cdots & s_{nm} \end{bmatrix} \quad (1)$$

In the equation, S is the fuzzy relationship matrix between the risk evaluation comment set and the risk factor set, where $0 \leq s_{ij} \leq 1$, and s_{ij} represents the membership degree of the i th deep excavation construction risk factor to the j th level risk rating.

3.2 Determination of weight vectors

There are mainly two methods for determining index weights: subjective weighting and objective weighting. Subjective weighting relies on the subjective experience of decision-makers or experts to determine the weight of risk evaluation indicators. However, this method can be influenced by various factors such as the decision-maker's knowledge structure, work experience, and preferences, which may not fully reflect the importance of risk evaluation indicators.

Objective weighting determines the weight of risk evaluation indicators based on the amount of discerning information provided by the indicators and the relationships between them. However, this method may ignore the rich experience of experts and scholars, and the results may not always match the actual situation, with a strong dependence on the samples.

Compared to subjective and objective weighting, combination weighting can comprehensively integrate the subjective and objective weights of each evaluation indicator and reflect the objective information of the indicators and the subjective judgment of the evaluators, so it can correctly reflect the actual weight of each indicator. This paper uses the Analytic Hierarchy Process (AHP) and entropy method to calculate the subjective and objective weights of deep excavation construction risk evaluation indicators respectively. Then, using game theory, the subjective and objective weights are combined to obtain the composite weights of deep excavation construction risk evaluation indicators, which can incorporate the theoretical and empirical knowledge of experienced experts and judge the importance of each indicator while avoiding the shortcomings of these two methods (Shan et al., 2012).

3.2.1 Calculation of subjective weight using analytic hierarchy process

AHP weighting is a method of determining the relative importance of different factors by comparing them. AHP provides pair-wise comparison matrix, through which the criteria are structured according to their hierarchical order (Das et al., 2020).

Step 1. Constructing the judgment matrix:

$\ln(9e/9) \sim \ln(17e/1)$ was chosen as the scale for constructing the judgment matrix of risk evaluation indicators for deep excavation construction due to its improved stability, rationality, and effectiveness. This method involves comparing each indicator with all other indicators at the same level, including itself, to convert abstract subjective understanding into quantitative data. The specific evaluation criteria for $\ln(9e/9) \sim \ln(17e/1)$ as the scale of the judgment matrix are listed in Table 2.

Based on a constructed judgment matrix, the maximum eigenvalue and corresponding eigenvector can be determined by solving for the matrix's eigenvectors and eigenvalues. This provides the maximum eigenvalue λ_{\max} and the eigenvector associated with it.

Step 2. Consistency check.

To check the consistency of the constructed judgment matrix, a consistency ratio (CR) test is performed. If $CR < 0.10$, it indicates that the constructed judgment matrix has good consistency.

$$CR = \frac{\lambda_{\max} - n}{(n - 1)RI} \quad (2)$$

In the equation, n represents the order of the judgment matrix, and RI is the average random consistency index (Wang et al., 1990), with specific values shown in Table 3.

Step 3. Calculation of weight vector.

The eigenvector associated with the maximum eigenvalue λ_{\max} is normalized to obtain the subjective weight vector U_{k1} passing the consistency test of the judgment matrix.

3.2.2 Calculation of objective weight using Entropy Weight Method

Entropy was proposed by R Xlausis as a measure of the uniformity of the distribution of an ability in space. The entropy method can be used to calculate the objective weights of various indicators, providing a basis for multi-index comprehensive evaluation (Zhang et al., 2017). Compared with subjective weighting methods, the entropy method has higher accuracy and stronger objectivity, which can better explain the results obtained (Zhu et al., 2015). The steps are as follows:

Step 1. Constructing the entropy method judgment matrix:

The original data matrix $X = (x_{ij})_{n \times m}$ is formed based on n evaluation indicators and m samples. In this matrix, $i \leq n$, $j \leq m$, x_{ij} represents the value of the i th evaluation indicator.

Step 2. Standardization:

Extreme value entropy method was used for normalization. First, the extreme value method was applied to transform the original data into dimensionless values, which then underwent standardization to obtain the judgment matrix R :

$$r_{ij} = \frac{x_{ij} - \min\{x_{ij}\}}{\max\{x_{ij}\} - \min\{x_{ij}\}} \quad (3)$$

In the formula, r_{ij} represents an element of the standardized judgment matrix R , and $\min\{x_{ij}\}$ and $\max\{x_{ij}\}$, represent the minimum and maximum values, respectively.

Step 3. Handling of zeros in the matrix.

To ensure meaningful logarithmic operations, the standardized matrix is processed to eliminate zeros by shifting all elements to the right by a constant value, usually 0.001. The resulting matrix is $R = (r_{ij})_{n \times m}$, then normalized to obtain matrix $B = (b_{ij})_{n \times m}$.

Step 4. Determination of entropy value

$$e_j = -\frac{1}{\ln n} \sum_{i=1}^n (p_{ij} \ln p_{ij}) \quad (4)$$

In the formula, $p_{ij} = b_{ij} / \sum_{i=1}^n b_{ij}$, p_{ij} represents the probability of the i th factor being in the j th level of risk, and b_{ij} represents an element of the normalized matrix B .

Step 5. Calculation of entropy weighting W_j

$$W_j = \frac{1 - e_j}{\sum_{j=1}^n g_j} \quad (5)$$

After obtaining the entropy weights W_j , they are assembled into an entropy weight vector U_{k2} .

TABLE 2 Weight scale judging criteria.

Subjective interpretation	Quantitative scale
i is equally important as j	$\ln(\frac{9}{5}e)$, (1.000)
i is slightly more important than j	$\ln(\frac{11}{7}e)$, (1.452)
i is noticeably more important than j	$\ln(\frac{13}{5}e)$, (1.956)
i is significantly more important than j	$\ln(\frac{15}{3}e)$, (2.609)
i is extremely more important than j	$\ln(\frac{17}{1}e)$, (3.833)
i is importance falls somewhere in between the above comparisons with j	1.223,1.693,2.253,3.079

TABLE 3 RI comparison table.

n	1	2	3	4	5	6	7	8	9
RI	0	0	0.52	0.89	1.12	1.24	1.36	1.41	1.46

3.2.3 Calculation of combined weight using game theory method

The combined weighting vector for risk evaluation indicators in deep excavation construction is obtained by integrating subjective and objective weights using the game theory method. The game theory approach takes into account inherent information among various risk evaluation indicators, which ensures consistency and harmony among subjective, objective, and combined weights, minimizes deviations between different weights, and reduces the impact of subjectivity on risk evaluation results. The process for determining the combined weight using the game theory method is as follows (Zhou et al., 2022):

Step 1. Construct the set of basic weight vectors $U_k = \{U_{k1}, U_{k2}, \dots, U_{kn}\}$ ($k = 1, 2, \dots, L$), where U_k is the set of basic weight vectors, $U_{k1}, U_{k2}, \dots, U_{kn}$ are the basic weight vectors that need to be combined, L is the number of weighting methods used. Any linear combination of these vectors can be represented as:

$$U = \sum_{k=1}^L (\alpha_k U_k^T) \quad (6)$$

In the formula, U represents the combined weight vector; α_k is the linear combination coefficient, $\alpha_k > 0$, $\sum_{k=1}^L \alpha_k = 1$, and U_k is the set of basic weight vectors.

Step 2. Optimize the weight coefficients α_k to minimize the deviation between the combined weight vector U and the basic weight vectors U_k , that is:

$$\min \left\| \sum_{k=1}^L \alpha_k U_k^T - U_k \right\|_2 \quad (k = 1, 2, \dots, L) \quad (7)$$

In the formula, U_k is the set of basic weight vectors, and U_k^T is the transpose matrix of the basic weight vector set U_k .

Step 3. Normalize the weight coefficients $(\alpha_1, \alpha_2, \dots, \alpha_L)$ obtained from Eq. 7 using Eq. 8:

$$\alpha_k^* = \frac{|\alpha_k|}{\sum_{k=1}^L |\alpha_k|} \quad (8)$$

Step 4. The final weight vector M for the combination of various evaluation indicators is obtained as follows:

$$M = \sum_{k=1}^L (\alpha_k^* \cdot U_k^T) \quad (9)$$

The symbol M represents the final combination weight vector obtained after weighting and combining, where $M = [m_1, m_2, \dots, m_n]$

3.3 Nonlinear fuzzy comprehensive evaluation

FAHP method is employed for multi-criteria decision problems (Das et al., 2019). Traditional AHP method was modified by Van Laarhoven in 1983 to develop the hierarchical analysis more accurately by employing fuzzy ratios in place of exact ratios (Van et al., 1983).

However, the traditional AHP method employs a linear operator to calculate risk levels, which may weaken the importance of certain indicators. Moreover, the construction process of deep excavations is full of ambiguity and uncertainty due to various factors, and extreme situations are inevitable. Linear operators cannot reflect the actual situation on site. Therefore, a nonlinear fuzzy comprehensive evaluation method is adopted. The nonlinear fuzzy matrix synthesis operator used for risk assessment is (Zhang et al., 2005):

$$f(m_1, m_2, \dots, m_n; s_1, s_2, \dots, s_n; \Lambda) = (m_1 s_1^{\lambda_1} + m_2 s_2^{\lambda_2} + \dots + m_n s_n^{\lambda_n})^{\frac{1}{\lambda}} \quad (10)$$

The symbols used in the equation are: m_1, m_2, \dots, m_n represents the weight of the risk indicators in the combination weight vector M , where $m \geq 0$ and $\sum_{i=1}^n m_i = 1$; s_1, s_2, \dots, s_n are a certain column in the membership fuzzy evaluation matrix S ; Λ represents the coefficient vector of the degree of salient influence of the indicators; $\Lambda = [\lambda_1, \lambda_2, \dots, \lambda_n]$ and $\lambda_i \geq 1, i = 1, 2, \dots, n$; $\lambda = \max(\lambda_1, \lambda_2, \dots, \lambda_n)$.

The criteria for the values of salient influence coefficients are shown in Table 4.

After obtaining the salient influence coefficients at each level, the fuzzy judgment matrix is processed to meet the requirements for using nonlinear operators to synthesize fuzzy matrices. Since $s_i \geq 1$ in the nonlinear fuzzy evaluation matrix, but the membership degree values are between $[0, 1]$, it is necessary to convert the original fuzzy judgment matrix. The conversion is shown below:

TABLE 4 Criteria for taking outstanding impact coefficient.

Scale	Meaning
1	No significant impact of the indicator factor
1.5	Almost no significant impact of the indicator factor
2.5	Slightly prominent impact of the indicator factor
3.5	Noticeably prominent impact of the indicator factor
4.5	Strongly prominent impact of the indicator factor
5.5	Extremely prominent impact of the indicator factor
2.0,3.0,4.0,5.0	The median between adjacent scales, indicating the scale at times when it falls somewhere in between two adjacent scales

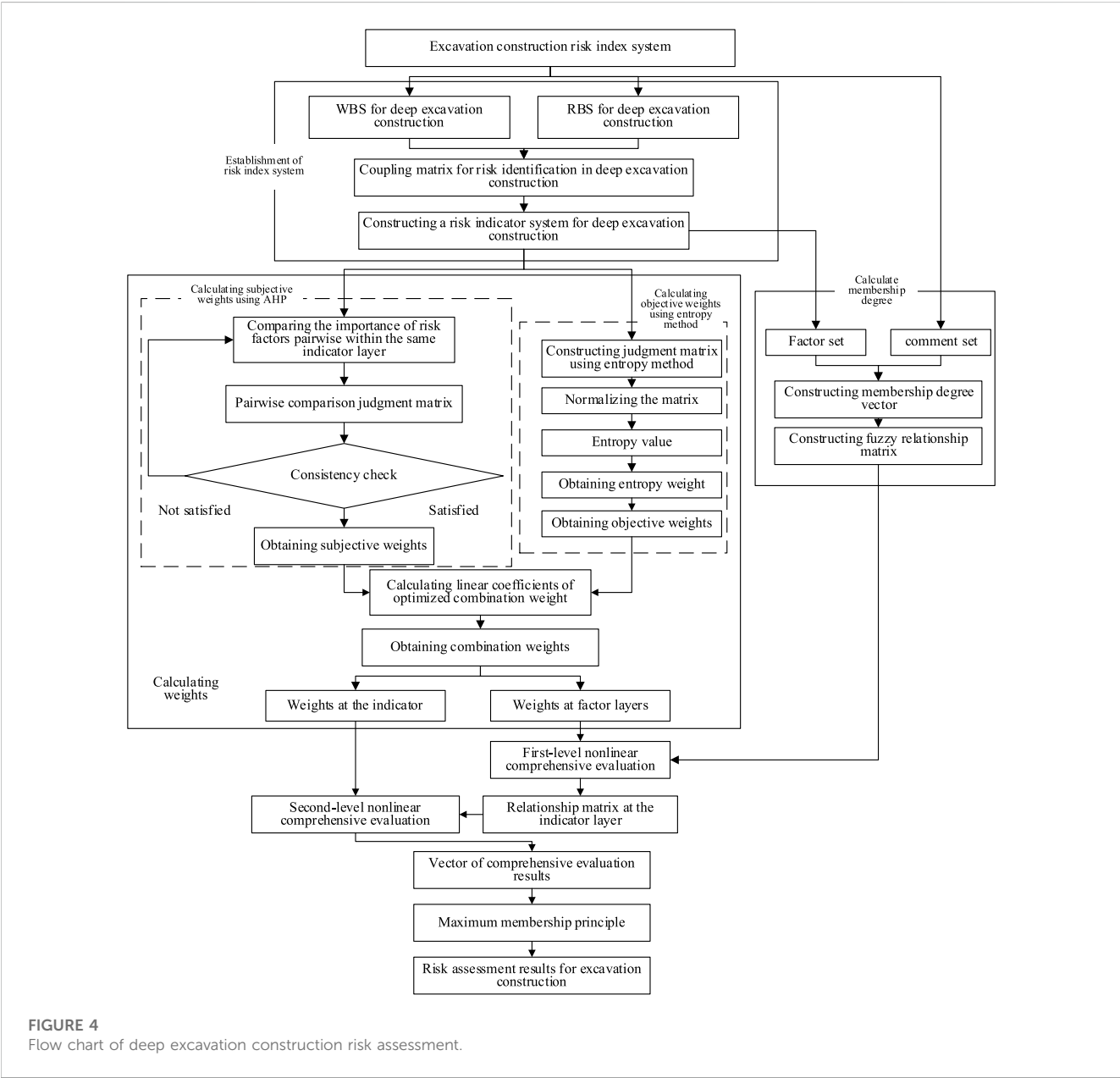


FIGURE 4 Flow chart of deep excavation construction risk assessment.

$$s_{ij}' = 10 \times s_{ij} \quad (11)$$

The symbol s_{ij}' represents the value of the transformed nonlinear fuzzy evaluation matrix, whereas the symbol s_{ij} represents the value of the original fuzzy judgment matrix.

3.4 A new model for risk assessment in the construction of deep excavations

The deep excavation construction risk evaluation model based on combination weighting and nonlinear FAHP is established through the above steps. The specific evaluation process is shown in Figure 4.

4 Case study analysis

4.1 Overview of the case project

The construction risk assessment model for deep excavations based on the combined weighting-nonlinear FAHP method was applied to verify the deep excavation construction of the Rongmin Science and Technology Innovation Park project on High-tech Second Road in the High-tech Zone of Xi'an City. The strata involved in the project are divided into 14 layers, including fill soil, loess-like fine-grained clay, loess, ancient soil, and 10 different types of fine-grained clay from top to bottom. The construction site belongs to Category II, and liquefaction of sandy soil can be disregarded based on geological data. The safety level of the excavation wall is Level I, the support safety level is Level I, and the safety level of the deep excavation is also Level I. The excavation depth is between 7.30 and 12.97 m, which is considered a deep excavation.

4.2 Weight calculation

4.2.1 Calculation of subjective weight

The subjective weight is determined by using the scale of $\ln(9e/9) \sim \ln(17e/1)$ as the judgment matrix. The importance of the judgment criteria is compared through expert evaluation to construct the judgment matrix. Taking the weight of the index layer as an example, the specific calculation process is as follows:

Step 1. Construct the judgment matrix A for establishing the evaluation indicators of deep excavation construction risk

$$A = \begin{bmatrix} 1 & 1/\ln\left(\frac{13}{5}e\right) & 1/\ln\left(\frac{10}{8}e\right) \\ \ln\left(\frac{13}{5}e\right) & 1 & \ln\left(\frac{11}{7}e\right) \\ \ln\left(\frac{10}{8}e\right) & 1/\ln\left(\frac{11}{7}e\right) & 1 \end{bmatrix} \quad (12)$$

Calculate the maximum eigenvalue $\lambda_{\max A}$ of 3.0012, and its corresponding eigenvector: $U_{k1A} = [0.4022, 0.7617, 0.5080]$

Step 2. Perform consistency check, and the matrix A passes the test.

Step 3. Normalize the eigenvector to obtain the subjective weight of the index layer. $U_{k1A}' = [0.2406, 0.4556, 0.3038]$.

Similarly, the subjective weight corresponding to each indicator in the deep excavation construction risk evaluation project is obtained. The specific subjective weights are shown in Table 5.

4.2.2 Calculation of objective weight

The entropy weight data matrix was obtained from a questionnaire survey of 11 experts and referred to the research of Chowdhuri et al. (2019). The 15 factor-level indicators and 3 criterion-level indicators were scored using a percentage-based scale. Taking objective weighting calculation at the criterion level as an example:

Step 1. After standardization, the entropy judgment matrix B with zeros processed values is:

$$B = \begin{bmatrix} 0.5863 & 0.4001 & 0.3549 \\ 0.5863 & 0.2001 & 0.7098 \\ 0.9311 & 0.4001 & 0.4517 \\ 1.0001 & 0.4001 & 0.7098 \\ 1.0001 & 0.0001 & 1.0001 \\ 0.0001 & 0.6001 & 0.7420 \\ 0.5863 & 0.6001 & 0.7098 \\ 0.8967 & 0.2001 & 0.7098 \\ 1.0001 & 0.4001 & 0.3549 \\ 0.2760 & 1.0001 & 0.0001 \\ 0.5863 & 0.8001 & 0.7098 \end{bmatrix} \quad (13)$$

Step 2. Calculate the determined entropy value e_j according to Eq. 4:

$$\left. \begin{aligned} e_{jD_1} &= 0.9367 \\ e_{jD_2} &= 0.9133 \\ e_{jD_3} &= 0.9413 \end{aligned} \right\} \quad (14)$$

Step 5. Calculate the entropy weight corresponding to each determined entropy value, and organize them into an entropy weight vector $U_{k2B} = [0.3033, 0.4154, 0.2813]$

Similarly, the entropy weight vector for other indicators can be obtained and is shown in Table 5.

4.2.3 Calculation of combination weight using game theory

Calculating the combination weight using game theory first requires determining the basic weight vector. Taking the combination of index layer weights as an example, the calculation process is as follows:

Step 1. Determine the basic weight vectors that need to be combined:

$$\begin{aligned} U_{k1A}' &= [0.2406, 0.4556, 0.3038] \\ U_{k2B} &= [0.3033, 0.4154, 0.2813] \end{aligned} \quad (15)$$

Step 2. Optimize the linear coefficients of the combination weight using Eq. 8 to obtain:

$$\alpha_{kA} = 1.6685 \quad \alpha_{kB} = 0.6879 \quad (16)$$

After normalization, the result is:

$$\alpha_{kA}^* = 0.7081 \quad \alpha_{kB}^* = 0.2919 \quad (17)$$

TABLE 5 Index weights for risk assessment of deep excavation construction.

Index layer	Subjective weight	Objective weight	Combined weight	Factor layer	Subjective weight	Objective weight	Combined weight
D_1	0.2406	0.3033	0.2589	d_{11}	0.1296	0.1344	0.1311
				d_{12}	0.3504	0.2750	0.3255
				d_{13}	0.1795	0.2291	0.1959
				d_{14}	0.0919	0.1270	0.1035
				d_{15}	0.2487	0.2345	0.2440
D_2	0.4556	0.4154	0.4438	d_{21}	0.0595	0.0956	0.0697
				d_{22}	0.2690	0.1772	0.2432
				d_{23}	0.1627	0.1584	0.1615
				d_{24}	0.1263	0.1459	0.1318
				d_{25}	0.0759	0.1257	0.0899
				d_{26}	0.2102	0.1699	0.1989
				d_{27}	0.0963	0.1273	0.1050
D_3	0.3038	0.2813	0.2973	d_{31}	0.3001	0.3072	0.3027
				d_{32}	0.5603	0.4512	0.5197
				d_{33}	0.1396	0.2416	0.1776

Step 3. Calculate the combination weight M of the index layer for deep excavation construction risk evaluation by using Eq. 9 to combine the linear coefficients with subjective and objective weights. The combination weights obtained based on game theory are shown in Table 5.

The overall weight vector is:

$$M = [0.2589, 0.4438, 0.2973] \quad (18)$$

Similarly, the weight vector for the factor layer can be obtained:

$$\left. \begin{aligned} M_1 &= [0.1311, 0.3255, 0.1959, 0.1035, 0.2440] \\ M_2 &= [0.0697, 0.2432, 0.1615, 0.1318, 0.0899, 0.1989, 0.105] \\ M_3 &= [0.3027, 0.5197, 0.1776] \end{aligned} \right\} \quad (19)$$

Based on the calculated weights, it can be seen that technical and management risks are the biggest risks in the construction of deep excavations for this project. This is because the geological conditions of the project are relatively good, and if the construction technology and management level are in place, risks can be avoided.

4.3 Membership degree calculation

Based on the actual construction situation of the deep excavation of the Rongmin Science and Technology Innovation Park project on High-tech Second Road in the High-tech Zone of Xi'an City, the fuzzy judgment matrix for the risk assessment of the deep excavation construction was obtained using the expert evaluation method. Experts rated the secondary risk projects established in the risk assessment indicator system through a questionnaire survey. The

membership degree values were obtained after processing the questionnaire data, as shown in Table 6.

The given text describes the construction of a single-factor evaluation matrix for the risk factors associated with the deep excavation construction of the Rongmin Science and Technology Innovation Park project on High-tech Second Road, according to Table 6. To perform nonlinear fuzzy comprehensive evaluation, the matrix is processed using Eq. 11 to obtain evaluation matrices $S_1 \sim S_3$ that can be used for nonlinear fuzzy comprehensive calculation.

$$S_1 = \begin{bmatrix} 7 & 2 & 1 & 0 & 0 \\ 0 & 6 & 2 & 1 & 1 \\ 7 & 2 & 1 & 0 & 0 \\ 9 & 1 & 0 & 0 & 0 \\ 3 & 3 & 2 & 1 & 1 \end{bmatrix} \quad (20)$$

$$S_2 = \begin{bmatrix} 9 & 1 & 0 & 0 & 0 \\ 4 & 3 & 2 & 1 & 1 \\ 6 & 3 & 2 & 0 & 0 \\ 5 & 5 & 0 & 0 & 0 \\ 8 & 2 & 0 & 0 & 0 \\ 5 & 3 & 2 & 0 & 0 \\ 7 & 2 & 1 & 0 & 0 \end{bmatrix} \quad (21)$$

$$S_3 = \begin{bmatrix} 4 & 3 & 3 & 0 & 0 \\ 0 & 5 & 3 & 1 & 1 \\ 6 & 3 & 1 & 0 & 0 \end{bmatrix} \quad (22)$$

4.4 Determination of prominent impact factors for risk indicators

According to Table 4 and expert opinions, combined with the actual situation of the deep excavation construction of Rongmin

TABLE 6 Membership degree of risk factors.

Risk level	d_{11}	d_{12}	d_{13}	d_{14}	d_{15}	d_{21}	d_{22}	d_{23}	d_{24}	d_{25}	d_{26}	d_{27}	d_{31}	d_{32}	d_{33}
Level 1	0.7	0	0.7	0.9	0.3	0.9	0.4	0.6	0.5	0.8	0.5	0.7	0.4	0	0.6
Level 2	0.2	0.6	0.2	0.1	0.3	0.1	0.3	0.3	0.5	0.2	0.3	0.2	0.3	0.5	0.3
Level 3	0.1	0.2	0.1	0	0.2	0	0.2	0.2	0	0	0.2	0.1	0.3	0.3	0.1
Level 4	0	0.1	0	0	0.1	0	0.1	0	0	0	0	0	0	0.1	0
Level 5	0	0.1	0	0	0.1	0	0.1	0	0	0	0	0	0	0.1	0

TABLE 7 Prominent influence coefficients of risk factors.

Primary indicator	D_1					D_2					D_3				
λ	4.5					5.5					5				
Secondary Indicator	d_{11}	d_{12}	d_{13}	d_{14}	d_{15}	d_{21}	d_{22}	d_{23}	d_{24}	d_{25}	d_{26}	d_{27}	d_{31}	d_{32}	d_{33}
λ	1.5	5.5	2.5	1.5	4.5	1.5	5.5	3.5	3	2.5	4.5	3.5	4.5	5.5	4

Science and Technology Innovation Park on High-tech Second Road, the prominent impact coefficients of the first-level risk factors and second-level risk factors are obtained, as shown in Table 7.

The prominent impact coefficient vectors corresponding to $S_1 \sim S_3$ can be obtained from Table 7 as follows:

$$\left. \begin{aligned} \Lambda_1 &= [1.5, 5.5, 2.5, 1.5, 4.5] \\ \Lambda_2 &= [1.5, 5.5, 3.5, 3, 2.5, 4.5, 3.5] \\ \Lambda_3 &= [4.5, 5.5, 4] \end{aligned} \right\} \quad (23)$$

And the prominent impact coefficient vectors of the indicator layer

$$\Lambda = [4.5, 5.5, 5] \quad (24)$$

4.5 First-level nonlinear fuzzy comprehensive evaluation

The factor layer weight vector $M_1 \sim M_3$, the nonlinear fuzzy evaluation judgment matrices $S_1 \sim S_3$, and the level-2 risk factor salient influence coefficient vectors $\Lambda_1 \sim \Lambda_3$ are inputted into Eq. 10 for nonlinear fuzzy comprehensive evaluation to obtain the evaluation results $N_1 \sim N_3$ for level-2 risk factors. Taking N_1 as an example, the calculation process is as follows:

$$N_1 = f(M_1, S_1, \Lambda_1) = [2.1352, 4.8976, 1.7330, 0.9027, 0.9027] \quad (25)$$

The calculated N_1 is normalized to obtain the result vector of first-level nonlinear fuzzy comprehensive evaluation for the construction risk assessment of deep excavations in the Rongmin Science and Innovation Park project on High-tech Second Road, as follows:

$$N_1 = [0.2020, 0.4633, 0.1639, 0.0854, 0.0854] \quad (26)$$

Similarly, the evaluation results for the other level-2 risk factors in the construction risk assessment of deep excavations in the Rongmin Science and Innovation Park project on High-tech Second Road are as follows:

$$\left. \begin{aligned} N_2 &= [0.3550, 0.2818, 0.1892, 0.0870, 0.0870] \\ N_3 &= [0.2474, 0.3731, 0.2306, 0.0744, 0.0744] \end{aligned} \right\} \quad (27)$$

4.6 Second-level nonlinear fuzzy comprehensive evaluation

The $N_1 \sim N_3$ are used as new factors to construct a second-level nonlinear fuzzy comprehensive evaluation matrix $S_N = [N_1 \ N_2 \ N_3]^T$, and the judgment matrix S_N is transformed into a second-level nonlinear fuzzy comprehensive evaluation matrix S_N' that can be used for nonlinear fuzzy evaluation calculation, as shown below:

$$S_N' = \begin{bmatrix} 2.0198 & 4.6330 & 1.6394 & 0.8539 & 0.8539 \\ 3.5498 & 2.8182 & 1.8920 & 0.8700 & 0.8700 \\ 2.4744 & 3.7313 & 2.3060 & 0.7442 & 0.7442 \end{bmatrix} \quad (28)$$

From Table 7, it can be obtained that the salient influence coefficient vector $\Lambda = [4.5, 5.5, 5]$ corresponds to level-1 risk factors in the construction risk assessment of deep excavations in the Rongmin Science and Innovation Park project on High-tech Second Road, and the weight vector $M = [0.2589, 0.4438, 0.2973]$ corresponds to level-1 risk factors.

By substituting the above results into Eq. 10 for nonlinear fuzzy comprehensive evaluation, the determined second-level nonlinear fuzzy comprehensive evaluation result vector N is obtained:

$$N = f(M, S_N', \Lambda) = [3.1011, 3.2038, 1.9241, 0.8471, 0.8471] \quad (29)$$

The result vector N is normalized to obtain the second-level nonlinear fuzzy comprehensive evaluation result vector for the

construction risk assessment of deep excavations in the Rongmin Science and Innovation Park project on High-tech Second Road:

$$N = [0.3125, 0.3229, 0.1939, 0.0854, 0.0854] \quad (30)$$

This vector is the comprehensive evaluation vector of total risk. Using the maximum membership principle, an overall evaluation of the construction risk of deep excavations in the Rongmin Science and Innovation Park project on High-tech Second Road in Xi'an High-tech Zone is conducted. According to the fuzzy comprehensive evaluation vector, the risk level of this project is level-2, with a comment of low risk. The overall risk of deep excavation construction is relatively small, as long as the construction quality is qualified and the site management is orderly, the construction risk of deep excavations for this project can be controlled. The evaluation result is consistent with the actual situation, indicating the accuracy of the model.

5 Discussion

To verify the effect of the non-linear operator in the risk evaluation process of the new model, a traditional FAHP is used to conduct a risk assessment of the deep excavation construction of the case project, with reference to [Zhang G. et al. \(2020\)](#). The values of the prominent influence coefficients are all 1, that is, $\lambda_i = 1$. The comprehensive evaluation result vector " N' " based on linear FAHP using the combination weighting method is as follows:

$$N' = [0.4040, 0.3392, 0.1748, 0.0410, 0.0410] \quad (31)$$

Using the linear FAHP method based on the combination weighting method for comprehensive evaluation, the risk level of the deep excavation construction is level 1, which is considered low risk. The introduction of the nonlinear fuzzy comprehensive evaluation method results in a risk assessment level of level 2, indicating a lower risk. The comparison between the result vector N' and N shows that the risk values of level 1 and level 2 are close. However, considering the actual engineering situation, the new model is more accurate because it incorporates prominent influence factors and considers the impact of technical management risks on construction safety during the construction process. Therefore, the new model evaluates the risk level higher.

In response to the risk assessment results, the following improvements will be made.

- (1) The design usage time for deep excavation support will be extended to 12 months, and the design value for the top load of the deep excavation will be increased to 20 kPa.
- (2) The deep excavation support system will be enhanced with the use of pumped piles, prestressed anchor cables, and soil nails.
- (3) Construction personnel will undergo additional technical training to enhance their skills.
- (4) Construction management will be strengthened to ensure construction quality and eliminate safety and quality hazards during the construction process.
- (5) Drainage ditches will be constructed outside the pit, and drainage ditches and sump pumps will be installed inside the pit to facilitate timely pumping.
- (6) Regular monitoring will be carried out, and monitoring information will be communicated to all units, with appropriate measures taken as necessary.

After making the improvements to the plan, there were no accidents during the construction of the deep excavation in Rongmin Science and Technology Innovation Park on High-tech Second Road in Xi'an High-tech Zone. This indicates that the improvements made based on the risk assessment model using a combination weighting method and nonlinear FAHP were effective, further demonstrating the rationality and effectiveness of the model.

Currently, this paper has made an innovative attempt to establish a risk evaluation model for deep excavation construction based on the combination weighting and non-linear FAHP. The main limitations of this study are that expert judgments and on-site data are required for a relatively accurate risk assessment, and the calculation process is relatively complex and has not yet been developed into an executable program. In constructing the judgment matrix, subjective evaluations are required from experts, which may introduce subjectivity and errors. Looking ahead, this risk evaluation model can be further expanded by integrating with Geographical Information System and machine learning to broaden its application scope [Hong-bo et al., 2009; Malik et al., 2020](#).

6 Conclusion

- (1) The WBS-RBS method is used to identify and construct an evaluation index system for the construction risks of deep excavations to ensure that no important factors are overlooked during the risk identification process and to obtain a scientifically reasonable risk evaluation index system.
- (2) A combination of subjective weights calculated by fuzzy analytic hierarchy process (AHP) and objective weights calculated by entropy method using game theory is used to obtain more reasonable combined weights, avoiding the limitations of both subjective and objective weighting methods.
- (3) Nonlinear operators are used to avoid weakening the influence of prominent risk factors in the calculation of risk levels using linear operators in fuzzy AHP, which can lead to reduced accuracy of the final evaluation results. This helps to make the results more reasonable.
- (4) The new model is applied to the risk assessment of deep excavation construction in the Rongmin Science and Innovation Park project on High-tech Second Road in Xi'an. Based on the evaluation results, the construction plan for the excavation is optimized. After improving the plan, no accidents occurred during the construction process of deep excavations for this project, further demonstrating the instructiveness of the new model in risk analysis for actual construction of deep excavations.
- (5) A novel risk evaluation model for deep excavation construction based on the combination weighting and non-linear FAHP has been established, and its feasibility has been verified through engineering examples. This model can provide reference and guidance for safety management of deep excavation construction in other countries around the world.

Data availability statement

The raw data supporting the conclusion of this article will be made available by the authors, without undue reservation.

Author contributions

Under the guidance of ZS, DG, and SL wrote this article. During the writing process, YZ, TZ, JX, and YS provided practical engineering information and assisted SL in conducting the questionnaire survey. All authors contributed to the article and approved the submitted version.

Funding

Shaanxi Province Hanjiang-to weihe river valley water diversion Joint Fund (2021JLM-52), Science and Technology Innovation Team of Shaanxi Innovation Capability Support Plan (No. 2020TD005), The Provincial Natural Science Foundation of Shaanxi (No. 2021JM-373).

References

- Arabameri, A., Pal, S. C., Rezaie, F., Chakraborty, R., Ngo, P., Blaschke, T., et al. (2021). Comparison of multi-criteria and artificial intelligence models for land-subsidence susceptibility zonation. *J. Environ. Manag.* 284 (2), 112067. doi:10.1016/j.jenvman.2021.112067
- Band, S. S., Janizadeh, S., Pal, S. C., Saha, A., Mosavi, A., Melesse, A. M., et al. (2020). Flash flood susceptibility modeling using new approaches of hybrid and ensemble tree-based machine learning algorithms. *Remote Sens.* 12 (3568), 3568. doi:10.3390/rs12213568
- Chowdhuri, I., Pal, S. C., Arabameri, A., Ngo, P. T. T., Roy, P., Malik, S., et al. (2020). Ensemble approach to develop landslide susceptibility map in landslide dominated Sikkim Himalayan region, India. *Environ. Earth Sci.* 79 (20), 476. doi:10.1007/s12665-020-09227-5
- Chowdhuri, I., Pal, S. C., and Chakraborty, R. (2019). Flood susceptibility mapping by ensemble evidential belief function and binomial logistic regression model on river basin of eastern India. *Adv. Space Res.* 65 (5), 1466–1489. doi:10.1016/j.asr.2019.12.003
- Das, B., and Pal, S. C. (2020). Assessment of groundwater vulnerability to over-exploitation using mcda, ahp, fuzzy logic and novel ensemble models: A case study of goghat-i and ii blocks of West Bengal, India. *Environ. Earth Sci.* 79 (5), 104. doi:10.1007/s12665-020-8843-6
- Das, B., and Pal, S. C. (2019). Combination of gis and fuzzy-ahp for delineating groundwater recharge potential zones in the critical goghat-ii block of West Bengal, India. *HydroResearch* 2, 21–30. doi:10.1016/j.hydres.2019.10.001
- Fan, S., Song, Z., Xu, T., Wang, K., and Zhang, Y. (2021). Tunnel deformation and stress response under the bilateral foundation pit construction: A case study. *Archives Civ. Mech. Eng.* 21, 109. doi:10.1007/s43452-021-00259-7
- Feng, S. X., Lei, H. Y., Wan, Y. F., Jin, H. Y., and Han, J. (2021). Influencing factors and control measures of excavation on adjacent bridge foundation based on analytic hierarchy process and finite element method. *Front. Struct. Civ. Eng.* 15 (2), 461–477. doi:10.1007/s11709-021-0705-0
- Gb/T 50326-2006 (2006). Construction project management specification. *GCBZ Eng. Stand. Netw.*
- Guo, D. S., Song, Z. P., Xu, T., Zhang, Y. W., and Ding, L. B. (2022). Coupling analysis of tunnel construction risk in complex geology and construction factors. *J. Constr. Eng. Manag.* 148 (9), 13. doi:10.1061/(asce)co.1943-7862.0002360
- Hillson, D., Grimaldi, S., and Rafele, C. (2006). Managing project risks using a cross risk breakdown matrix. *Risk Manag.* 8 (1), 61–76. doi:10.1057/palgrave.rm.8250004
- Hong-bo, Z. H. O. U., Gao, W.-J., Cai, L.-B., and Zhang, H. (2009). Risk identification and analysis of subway foundation pit by using fault tree analysis method based on WBS-RBS. *Rock Soil Mech.* (09), 2703–2707+2726. doi:10.16285/j.rsm.2009.09.012
- Huang, Y., and Jianxin, H. (2004). Risk pre-diagnosis in urban rail transit engineering using the WBS-RBS method. *Urban rapid transit. Urban Express Rail Transit* 13 (04), 9–12. doi:10.3390/su132011507
- Huchzermeier, A., and Loch, C. H. (2001). Project management under risk: Using the real options approach to evaluate flexibility in R.D. *Manag. Sci.* 47 (1), 85–101. doi:10.1287/mnsc.47.1.85.10661
- Issa, U., Saeed, F., Miky, Y., Alqurashi, M., and Osman, E. (2022). Hybrid AHP-fuzzy TOPSIS approach for selecting deep excavation support system. *Buildings* 12 (3), 295. doi:10.3390/buildings12030295
- Laarhoven, P. M. J. V., and Pedrycz, W. (1983). A fuzzy extension of saaty's priority theory. *Fuzzy Sets Syst.* 11 (13), 199–227. doi:10.1016/S0165-0114(83)80082-7
- Malik, S., Pal, S. C., Chowdhuri, I., Chakraborty, R., and Das, B. (2020). Prediction of highly flood prone areas by gis based heuristic and statistical model in a monsoon dominated region of bengal basin. *Remote Sens. Appl. Soc. Environ.* 19, 100343. doi:10.1016/j.rsase.2020.100343
- Meng, G. W., Huang, J. S., Wu, B., Zhu, Y. P., Xu, S. X., and Hao, J. H. (2020). Risk assessment of deep foundation pit construction based on analytic hierarchy process and fuzzy mathematics. *Adv. Civ. Eng.* 2020, 1–12. doi:10.1155/2020/8840043
- Rabin, C., Chandra, P. S., Sadhan, M., and Biswajit, D. (2018). Modeling and mapping of groundwater potentiality zones using ahp and gis technique: A case study of raniganj block, paschim bardhaman, West Bengal. *Model. Earth Syst. Environ.* 4, 1–26. doi:10.1007/s40808-018-0471-8
- Shan, C., Dong, Z., Fan, K., Yang, J., Chen, L. J. U., and Fang, Q. 1 (2012). Application of combined weighting method in the calculation of river health evaluation weights. *J. River Sea Univ. Nat. Sci. Ed.* (06), 622–628. doi:10.3876/j.issn.1000-1980.2012.06.005
- Song, Z., Su, W., Tian, X., Zhang, Y., and Zhou, G. (2021). Risk analysis of tunnel construction scheme change based on field monitoring and numerical analysis. *Adv. Civ. Eng.* 2021, 1–15. doi:10.1155/2021/8888886
- Wang, J., Hou, W., Wang, X., and Riqing, X. U. (2005). "Analysis of accident and risk sources factors for deep foundation pit," in Paper presented at the Asia Pacific Symposium on Safety; 20051102-04; Shaoxing(CN), Shaoxing, China, November 2005.
- Wang, L.F., and Xu, S. (1990). *Introduction to hierarchical analysis*. Beijing, China: People's University of China Press.
- Xie, J., and Liu, C. (2005). *Fuzzy mathematical methods and their applications*. Huazhong, China: Huazhong University of Technology Press.
- Xu, T., Song, Z., Guo, D., and Song, Y. (2020). A cloud model-based risk assessment methodology for tunneling-induced damage to existing tunnel. *Adv. Civ. Eng.* 2020 (14), 1–11. doi:10.1155/2020/8898362

Acknowledgments

The authors would like to express their sincere gratitude for the contribution of Hanjing-to weihe river valley water diversion project construction Co., Ltd.

Conflict of interest

YS and JX were employed by China Railway 20th Bureau Group Limited.

The remaining authors declare that the research was conducted in the absence of any commercial or financial relationships that could be construed as a potential conflict of interest.

Publisher's note

All claims expressed in this article are solely those of the authors and do not necessarily represent those of their affiliated organizations, or those of the publisher, the editors and the reviewers. Any product that may be evaluated in this article, or claim that may be made by its manufacturer, is not guaranteed or endorsed by the publisher.

- Yang, Y. (2006). "Work breakdown structures of construction project and its applications in engineering." Doctoral dissertation (Tianjin, China: Tianjin University).
- Zhang, A.-L., Zhang, X.-Y., Xu, Y.-J., and yang, C. (2017). Study on modified AHP-entropy method-based fuzzy comprehensive evaluation of urban utility tunnel construction schedule risk. *Archit. Technol.* (09), 922–926. doi:10.13731/j.issn.1000-4726.2017.09.006
- Zhang, G. H., Wang, C. T., Jiao, Y. Y., Wang, H., Qin, W. M., Chen, W., et al. (2020a). Collapse risk analysis of deep foundation pits in metro stations using a fuzzy bayesian network and a fuzzy AHP. *Math. Problems Eng.* 2020, 1–18. doi:10.1155/2020/4214379
- Zhang, G., Wang, C., Jiao, Y., Wang, H., Qin, W., Chen, W., et al. (2020b). *Collapse risk analysis of deep foundation pits in metro stations using a fuzzy bayesian network and a fuzzy ahp*. London, United Kingdom: Hindawi Limited.
- Zhang, X., and Feng, Y. (2005). A nonlinear fuzzy comprehensive assessment model. *J. Syst. Eng. Electron.* (10), 54–59. doi:10.1007/978-3-642-14880-4_53
- Zhao, M., Cheng, Y., Song, Z., Wang, T., Zhang, Y., Gong, Y., et al. (2021). Stability analysis of TBM tunnel undercrossing existing high-speed railway tunnel: A case study from yangtaishan tunnel of shenzhen metro line 6. *Adv. Civ. Eng.* 2021, 1–18. doi:10.1155/2021/6674862
- Zhou, Y., Wang, W., Lu, X., and Wang, K. (2022). Combination weighting prediction model and application of rock burst disaster based on game theory. *China Saf. Sci. J.* (07), 105–112. doi:10.16265/j.cnki.issn1003-3033.2022.07.0620
- Zhu, X., and Guodong, W. (2015). Exploration of the criteria of goodness of dimensionless method in entropy method. *Statistics Decis.* (02), 12–15. doi:10.13546/j.cnki.tjyjc.2015.02.003



OPEN ACCESS

EDITED BY

Sandipan Das,
Symbiosis International University, India

REVIEWED BY

Rabin Chakraborty,
University of Burdwan, India
Ionut Cristi Nicu,
Norwegian Institute for Cultural Heritage
Research, Norway
Subodh Chandra Pal,
University of Burdwan, India

*CORRESPONDENCE

Nguyen An Binh,
✉ nabinh@hcmig.vast.vn

RECEIVED 27 February 2023

ACCEPTED 11 May 2023

PUBLISHED 30 May 2023

CITATION

Hoa PV, Tuan NQ, Hong PV, Thao GTP
and Binh NA (2023), GIS-based modeling
of landslide susceptibility zonation by
integrating the frequency ratio and
objective–subjective weighting
approach: a case study in a tropical
monsoon climate region.
Front. Environ. Sci. 11:1175567.
doi: 10.3389/fenvs.2023.1175567

COPYRIGHT

© 2023 Hoa, Tuan, Hong, Thao and Binh.
This is an open-access article distributed
under the terms of the [Creative
Commons Attribution License \(CC BY\)](#).
The use, distribution or reproduction in
other forums is permitted, provided the
original author(s) and the copyright
owner(s) are credited and that the original
publication in this journal is cited, in
accordance with accepted academic
practice. No use, distribution or
reproduction is permitted which does not
comply with these terms.

GIS-based modeling of landslide susceptibility zonation by integrating the frequency ratio and objective–subjective weighting approach: a case study in a tropical monsoon climate region

Pham Viet Hoa¹, Nguyen Quang Tuan², Pham Viet Hong³,
Giang Thi Phuong Thao¹ and Nguyen An Binh^{1*}

¹Ho Chi Minh City Institute of Resources Geography, Vietnam Academy of Science and Technology, Hanoi, Vietnam, ²University of Sciences, Hue University, Hanoi, Vietnam, ³Institute of Marine Geology and Geophysics, Vietnam Academy of Science and Technology, Hanoi, Vietnam

Accurate detection of landslide spatial patterns is vital in susceptibility, hazard, and risk disaster mapping. Geographic Information System (GIS)-based quantitative approaches provide a rigorous procedure for gaining deep insight into natural and anthropogenic landslides from different scales. This study aims to implement a comprehensive solution for retrieving the landslide susceptibility index. For that purpose, a landslide inventory was performed in a tropical monsoon climate region, with a magnitude of elevation spanning from –65 m to 1,900 m above the sea, considering 15 fundamental causative factors belonging to the groups of topography, hydrology, geology, land cover conditions and anthropogenic activities, and weather. The frequency ratio (FR) was implemented to rank subclasses in each causative factor. For factor weight estimation, different approaches were applied, including the subjective-based analytic hierarchy process (AHP), objective-based Shannon entropy (SE), and a synergy of both methods (AHP–SE), built on these two approaches. Out of the 271 identified landslide locations, 70% (196 points) were used for training and the remaining 30% (71 points) were applied for validation. The results showed that the integrated AHP–SE outperformed the two individual approaches, with the area under the receiver operating characteristic curve (AUC) reaching 0.876, following SE (AUC = 0.848) and AHP (AUC = 0.818). In the synergy approach, the climate pattern under tropical monsoons was confirmed as the most crucial landslide-predisposing factor. The research contributes to a novel discussion by integrating knowledge-based consultation and statistical data analysis of accurate geospatial data, incorporating significant explanatory factors toward a reliable landslide-prone zonation over space and time dimensions.

KEYWORDS

landslide susceptibility, analytic hierarchy process, Shannon entropy, subjective and objective weighting, tropical monsoon climate

1 Introduction

Landslides, caused by the rapid movement of rock and soil, represent one of the most hazardous geological phenomena, with significant impacts on both natural systems and human societies (Highland and Bobrowsky, 2008). In natural environments, landslides can alter the landscape, disrupt ecosystems, and affect wildlife habitats. Furthermore, they can trigger other natural disasters, such as flash floods, and increase soil erosion and sediment deposits in rivers and streams (Lombardo et al., 2020). In populated areas, landslides can cause damage to infrastructure, resulting in significant financial losses and loss of life. The number of people killed by landslides has increased significantly in the 20th century due to the growing population density and accompanying economic activities in areas with a high risk of landslides, and this trend appears to be continuing in the 21st century (Froude and Petley, 2018). Moreover, most landslides normally occur in high mountain areas, and the destruction of landmass has more negative impacts on sustainable livelihood in rural communities (Mirdda et al., 2022).

The study of landslide probability has become a mature science, with various approaches applied at regional (Guo et al., 2023), continental (Van Den Eeckhaut and Hervás, 2012), and global scales (Stanley et al., 2021), while also considering the diverse landscapes of homogeneity (Sbroglia et al., 2018) or heterogeneity (Wang et al., 2020) in specific areas. The research topic has contributed to a broader scientific understanding of the Earth's surface processes, providing a basis for future research and innovation. Along with landslide inventories and hazard mapping, landslide susceptibility zonation indicates the probability or likelihood of a landslide occurring in a specific area based on different conditioning factors such as geology, topography, climate, land use, and human activities (Guzzetti et al., 2006). The fundamental science of landslide sensitivity has a long heritage since the pioneering research conducted in the late 1960s (Yong et al., 2022). Since the 19th century, geologists and engineers started to recognize the relationship between geology, topography, and the likelihood of landslides and then began using quantitative assessments for landslide probability zonation based on past landslide event observations (Reichenbach et al., 2018). The capabilities of the Geographic Information System (GIS) provided a promising opportunity to determine explicitly landslide-prone areas, while considering spatial relationships between both intrinsic and extrinsic factors (Nicu, 2017). Furthermore, the remote sensing data available in recent years resulted in big geospatial sources in order to construct a landslide-related geodatabase, a key point to form different GIS-based approaches for landslide-prone mapping (Scaioni et al., 2014).

Broadly speaking, predictive models of landslide predisposition can be distinguished by 1) qualitative, 2) quantitative, 3) hybrid or semi-qualitative approaches. Generally, quantitative strategies include a certain degree of objectivity compared to qualitative strategies. For quantification, there was a broad spectrum of data-driven methods, including statistics and machine learning techniques. In statistical analysis, numerous methods were applied to landslide susceptibility, mostly by frequency ratio (FR) (Nicu and Asăndulesei, 2018), Weight of Evidence (WoE) (Razavizadeh et al., 2017), Shannon entropy (SE) (Roodposhti

et al., 2016), and logistic regression (LR) (Budimir et al., 2015). The technological era of artificial intelligence has witnessed a variety of machine learning-based methods, such as the traditional algorithms support vector machine (SVM), random forest (RF), and recent innovations in deep learning models (Zhang et al., 2022; Ma et al., 2023). On the other hand, semi-qualitative approaches, such as the analytic hierarchy process (AHP) (Kayastha et al., 2013), fuzzy logic (Bui et al., 2015), and weighted linear combination (WLC) (Li et al., 2022), were also recognized for their significant applications in landslide probability zonation (Tyagi et al., 2022).

As mentioned previously, for the state-of-the-art machine and deep learning models, these advanced computational intelligence methods seem to outperform conventional models. Nevertheless, there is no standard benchmark for the best modeling due to the dominant uncertainty in landslide disasters. Updated studies continued to compare the performance of different landslide sensitivity models, for instance, knowledge-based versus data-driven methods (Zhu et al., 2018), multi-criteria decision analysis (MCDA) against machine learning (Khalil et al., 2022), statistical analysis and machine learning (Ling et al., 2022), traditional machine learning and deep learning (Zhang et al., 2022), and machine learning combined with optimization algorithms (Wang et al., 2022). Apart from that, the evaluation and selection of landslide-controlling factors was also an engaging subject. Unfortunately, there was no widespread guideline for the selection of landslide conditioning factors. The challenge is each factor also contributes to landslide risk and different natural conditions in a specific area, leading to the choice of appropriate factors to comprehensively describe the study area. In general, these factors are divided into two main groups: conditioning and triggering factors (Pourghasemi et al., 2018). Taking the comparison help to identify the most informative landslide explanatory factors as well as improve the accuracy landslide susceptibility model (Gaidzik and Ramírez-Herrera, 2021; Liao et al., 2022).

One of the major challenges in the procedure of landslide probability is assigning weights to conditioning factors and subclasses inside these factors. Weighting is a process used in landslide susceptibility mapping to determine the relative importance of different components that contribute to landslide occurrence (Hodasová and Bednarik, 2021). The two main approaches for weighting are subjective and objective. Subjective weighting is mainly based on expert judgment. The approach relies on the experience and knowledge of consultants to attach weights to different factors based on their perceived importance. Objective weighting, on the other hand, is followed by mathematical calculation. Statistical models are used to determine the weights of causative factors based on their correlation with landslide occurrences. Objective estimations are generally considered more reliable than subjective approaches due to their reliance on scientific evidence while avoiding personal biases. Despite that, it is common to use a combination of both subjective and objective methods to ensure the best results (Wang et al., 2012; Zhou et al., 2016).

Located in southeast Asia, Vietnam is a region with a high frequency of landslides (Shahabi and Hashim, 2015). As a coastal country, Vietnam is directly affected by annual devastating hurricanes originating from the Pacific Ocean. Landslides are often triggered by heavy rainfall, which is primarily influenced by

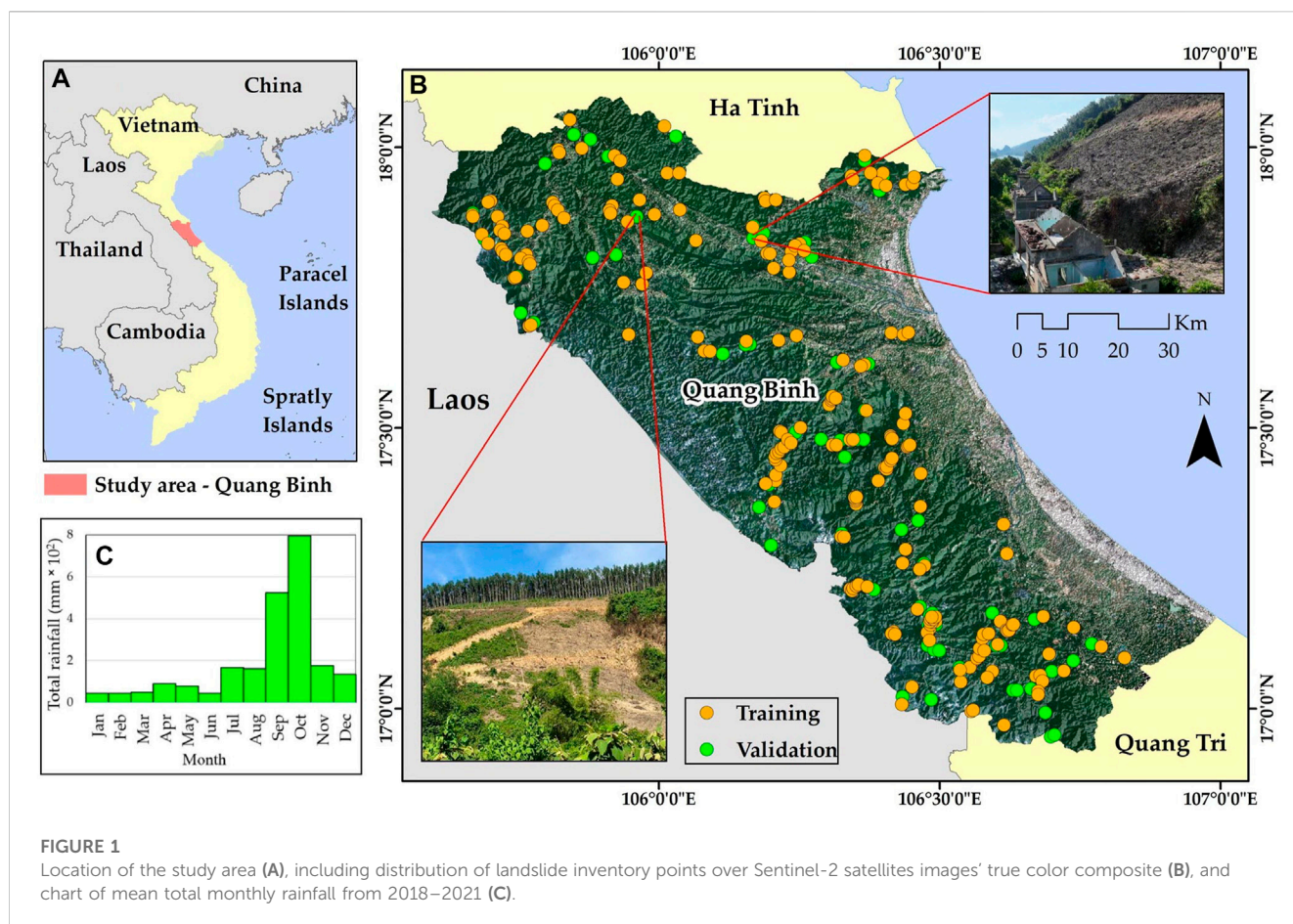


FIGURE 1

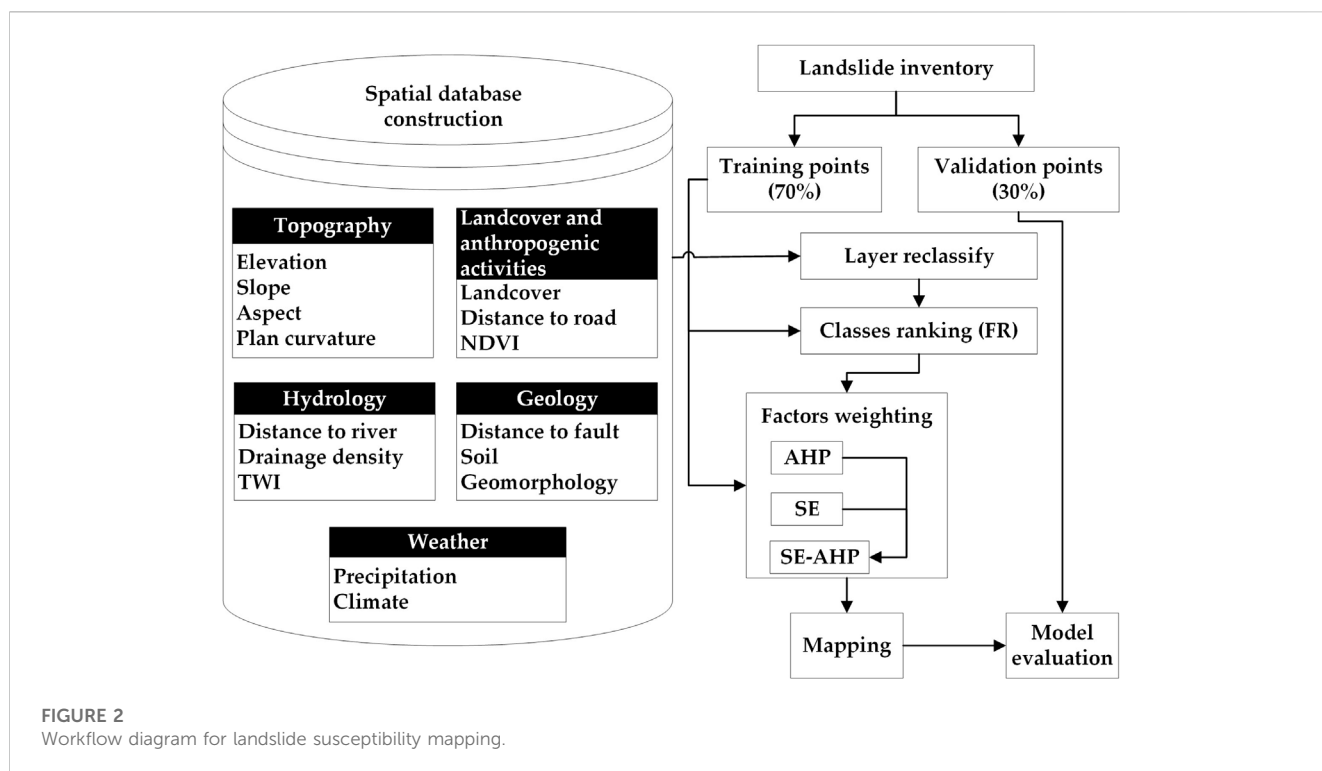
Location of the study area (A), including distribution of landslide inventory points over Sentinel-2 satellites images' true color composite (B), and chart of mean total monthly rainfall from 2018–2021 (C).

the tropical monsoon climate. This meteorological conditions is characterized by high temperatures and humidity throughout the year, with heavy seasonal rainfall occurring mostly from May to November, transitioning to the dry season from December to April with a high evaporation rate. With the continuous increasing trend of climate change, the frequency and magnitude of typhoons have significantly increased, leading to epic destruction caused by landslides (Gariano and Guzzetti, 2016). Therefore, landslide susceptibility zonation is one of the most crucial tasks to reduce damage to human life and property, while also supporting decision-making for future planning. Moreover, as a developing country with a remarkable increase in human population and urbanization in recent years, Vietnam faces an exacerbation of the risk of landslides and their consequences.

The literature on landslide susceptibility in Vietnam has explored various methods, including statistical techniques (Bui et al., 2015; Kieu and Ngo, 2022; Thanh et al., 2022), machine learning (Phong et al., 2021), and deep learning (Bui et al., 2020; Dao et al., 2020; Nhu et al., 2020), which have mostly been applied in the mountainous regions of the country. Unusual weather patterns have caused an increase in natural hazards that not only occur more frequently but also have greater magnitude and are expanding into coastal mountainous areas. Due to its unique geography, the Vietnamese Central region's mainland is usually the first area affected by tropical cyclones originating in the Pacific Ocean. Among coastal provinces in Central Vietnam, Quang Nam

(Pham et al., 2022), Quang Ngai (Cong et al., 2020; Long et al., 2022), and Hue (Long and De Smedt, 2018) were recently in focus for landslide-prone occurrences. Quang Binh has recently emerged as a region characterized by significant occurrence of landslides and flash floods, attributed to heavy precipitation during the rainy season, complex topography, and unstable geological features. Despite the frequency of these natural disasters, no systematic scientific investigation has yet been conducted to elucidate their underlying causes.

Based on the aforementioned perspectives, we utilized different techniques to generate landslide susceptibility maps in the coastal mountainous province Quang Binh, Vietnam. Compared to prior research, our methodology involved the integration of both the AHP and SE to reveal the better performance of the predictive model, emphasizing an underexplored approach by the synergy of both subjective and objective approaches in the landslide probability research domain. Formed by comprehensive data collections of topography, hydrology, geology, land cover conditions and anthropogenic activities, and weather, 15 independent landslide causative factors were adopted with a focus on the climate-specific spatial layer. This implies a significant impact of tropical monsoon climate on landslide events. From the exemplary area, we identified and analyzed the most influential factors, along with their respective subcategories. Our study results have significant scientific and practical implications, serving as a basis for scientific discourse and development of hazard



prevention and mitigation plans focused on complex coastal mountainous regions.

2 Study area

Quang Binh is a coastal mountainous province located in North Central Vietnam, covering an area of approximately 8,000 km² (Figure 1). Its geographic coordinates lie between 17°05′02″N to 18°05′12″N latitude and 105°03′55″E to 106°05′37″E longitude. The topography of Quang Binh is characterized by a narrow, west-to-east sloping landform, with hills and mountains accounting for 85% of the total natural area. The province experiences an annual rainfall of approximately 2,300 mm, with specific monthly precipitation patterns that mark seasonal transitions between dry and rainy periods. During the dry season (normally from April to August), rainfall is typically low, with the lowest value of around 44 mm in June. Conversely, in the rainy season (normally from September to March), the total amount of precipitation increases markedly, peaking at nearly 800 mm in October. Notably, based on our experience, the excessive intensity of precipitation during September and October may be a primary condition for triggering flash floods and landslides.

The evolution of landscapes and geological characteristics in Quang Binh through thousands of centuries resulted in the largest cave in the world, Son Doong (Limbert et al., 2016). Moreover, the national park Phong Nha-Ke Bang was recognized by UNESCO as a World Natural Heritage site for geology and geomorphology, ecology, and biodiversity (<https://whc.unesco.org/en/list/951/>). Under the major land cover of tropical forests, the diversity of geological features and prevalent escarpments are also recognized as the main motivation leading to incredible landform-related hazards.

3 Materials and methods

An overview of the landslide susceptibility mapping procedure is depicted in Figure 2. The mainly practiced steps are 1) landslide inventory; 2) spatial database construction of landslide conditioning factors; 3) layer reclassification and ranking the subclasses of corresponding factors using the FR method; 4) factor weighting by AHP, SE, and AHP-SE; 5) preparing landslide susceptibility mapping; and 6) model evaluation. The details of each step are further described in the following sections.

3.1 Landslide inventory

The landslide inventory is an essential commission for GIS-based landslide susceptibility modeling (Titti et al., 2021). The quality and quantity of landslide locations have an impact on the outcome and accuracy assessment of the predictive model. Satellite images are valuable sources that support the landslide inventory, especially in mountainous regions that are difficult to access. However, dense tropical forests may present challenges and uncertainty in detecting landslide occurrences based on these remotely sensed data. Hence, taking advantage of satellite images for landslide remote detection and ground true validation is essential for enhancing the truthfulness of the landslide inventory database. In the present study, we identified 271 landslide points over the examined area, including historical destructive geological events and field investigation. The points were first sampled based on numerous geospatial resources, including high-resolution Earth Engine images, optical satellite images from Sentinel-2, and thematic maps, which were then verified in field campaigns during the rainstorm season in

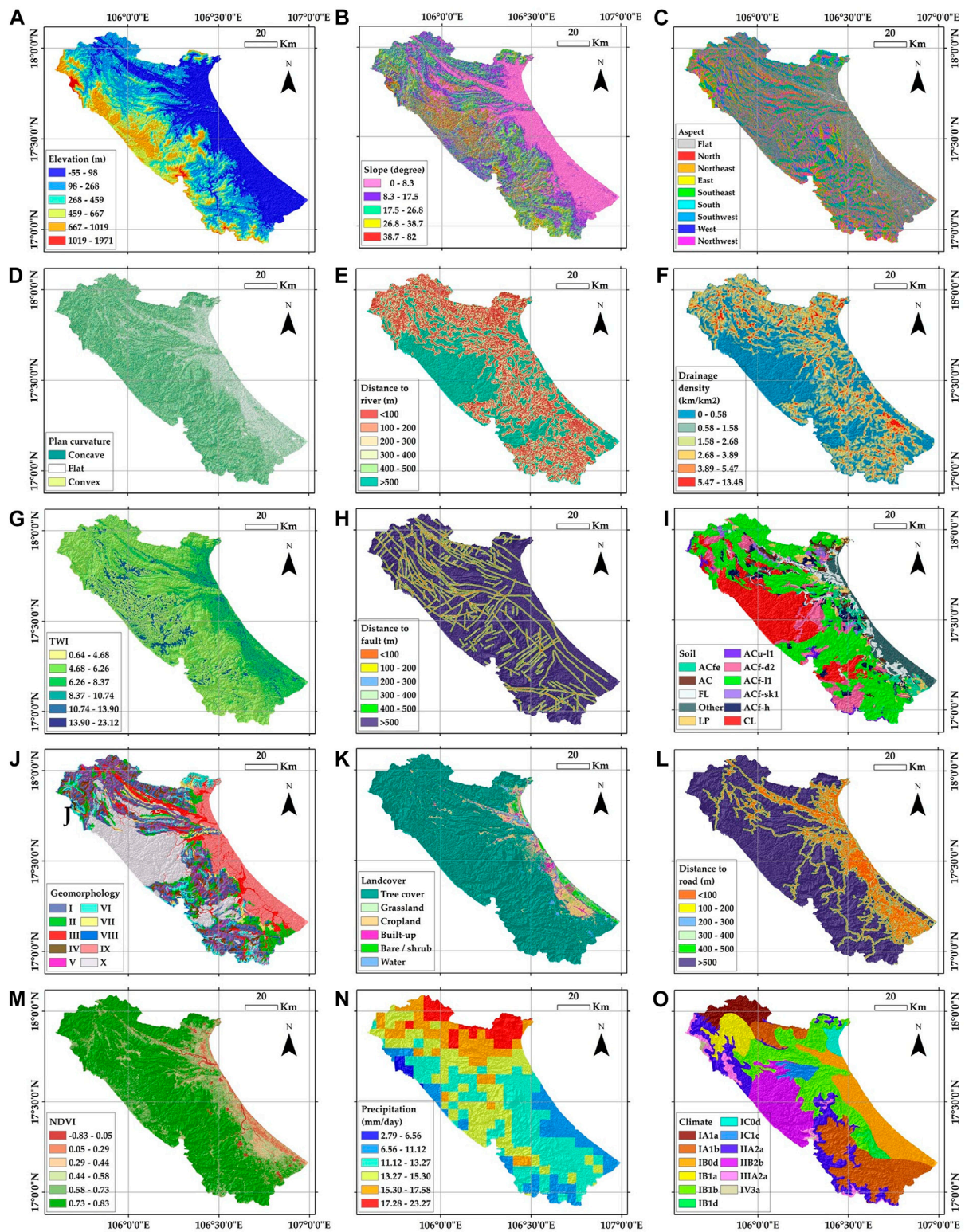


FIGURE 3

Maps of conditioning factors considered in landslide susceptibility models including (A) elevation, (B) slope, (C) aspect, (D) plan curvature, (E) distance to river, (F) drainage density, (G) TWI, (H) distance to fault, (I) soil, (J) geomorphology, (K) land cover, (L) distance to road, (M) NDVI, (N) precipitation, and (O) climate.

2022. As illustrated in Figure 1, the dataset was split into 70% (196 points) for the training phase and 30% for validation (71 points).

3.2 Spatial database construction of landslide causative factors

In the domain of GIS-based landslide susceptibility, preparing conditioning factors in a consistent spatial database required outstanding knowledge of not only geographic accuracy but also of the various types of features to fully reflect the interest domain. To date, to select landslide-related model variables, it should be noted that there are no standard guidelines or regulations for choosing optimal factors, as these are well-defined based on the specific case and research areas. Among a plethora of causative factors relating to landslide susceptibility, we recognized 15 significant factors through state-of-the-art literature reviews (Pourghasemi et al., 2018; Reichenbach et al., 2018; Yong et al., 2022). We categorized all factors into five fundamental groups, 1) topography, 2) hydrology, 3) geology, 4) land cover conditions and anthropogenic activities, and 5) weather, as an effort to exhaustively consider the contribution of related datasets to the disaster. Continuous data layers were reclassified using Jenks natural breaks optimization, while discrete data layers were stored in unique values for further analyses. For the post-processing, the final raster layers were geometrically corrected according to the World Geodetic System (WGS), 1984, and the UTM (Universal Transverse Mercator) Zone 48°N (North), which then transformed into a 10-m resolution. Figure 3 displays the maps of all 15 factors after standardization, as mentioned previously. Detailed descriptions of each group-based conditioning factor are provided in the following sections.

3.2.1 Group of topography

Topography-based components are one of the most decided characteristics related to landslide susceptibility. In this respect, we selected four remarkable factors to describe the terrain of the research area, i.e., 1) elevation, 2) slope, 3) aspect, and 4) plan curvature. To generate these topography-based factors, a digital elevation model (DEM) with an original resolution of 12.5 m was downloaded from <https://asf.alaska.edu/>. The DEM was generated based on products of Phased Array type L-band Synthetic Aperture Radar (PALSAR) instruments onboard the Advanced Land Observing Satellite (ALOS).

The distribution of elevation across the considered area offers an encompassing illustration of the terrain shape. Over the research area, height values extracted from the DEM ranged from −55 m under the sea level to 1,971 m above sea level due to the geographical location of the coastal mountainous region. The Jenks natural breaks optimization was applied to classify the elevation into five types. The result strongly indicates that the area is predominantly hilly, and the very high-altitude domain (>1000 m) only appears in the southeast (Figure 3A).

Slope is a crucial factor that relates to landslide triggering. Literature reviews have shown that slope is the most commonly used parameter in the field of landslide sensitivity spatial modeling

(Pourghasemi et al., 2018). Although a slope of over 30° has been identified as leading to instability and an increased risk of landslides, different slope domains also require comprehensive consideration due to the unique characteristics of the specific region (Moragues et al., 2021). In the present study, spatial analysis functions were applied with input from the DEM to derive the slope. Based on the thematic map shown in Figure 3B, the slope is complex in the west and becomes flatter while transitioning to the east. It should be noted that steep slope features (>38°) only cover a small percentage (4.77%) of the total area.

We also considered the aspect of slope, which indicates the direction of each slope form. The slope aspect affects solar radiation, wind exposure, and moisture availability, resulting in different vegetation growth, soil characteristics, and local microclimates (Cellek, 2021). Understanding the slope aspect in landslide susceptibility measurements provides professional knowledge for tackling natural disasters and further planning. The visual representation of the slope aspect with a continuous range of values from 0° to 360° was divided into 10 unique classes, including north, northeast, east, southeast, south, southwest, west, northwest, and flat direction (Figure 3C).

The function of the curvature is utilized to showcase the shape of the slope, where a segment of a surface can exhibit either concavity or convexity. There are two distinct types of curvature, i.e., planform and profile. In general, the planform curvature focuses on the lateral movement of fluid flow, while the profile curvature pertains to the vertical changes in fluid flow. Here, we only focus on planform curvature as this was used more than profile curvature in detecting the probability of landslide occurrences (Pourghasemi et al., 2018). The range of values obtained by planform curvature analysis is divided into classes of concave (<−0.05), convex (>0.05), or flat (−0.05–0.05) across the surface of the study area (Figure 3D).

3.2.2 Group of hydrology

Hydrology plays a required role in landslide susceptibility prediction. Hydrological elements can influence the stability of the terrain and trigger landslides. Understanding the interaction between these hydrological factors and environmental characteristics can provide valuable information for landslide hazard management. By incorporating hydrological data into the landslide model and considering the dynamic nature of these factors, researchers can improve the accuracy and reliability of landslide predictive models. Therefore, different variables related to hydrology are considered in this present research, including 1) distance to river, 2) drainage density, and 3) Topographic Wetness Index (TWI).

Distance to river can affect the water content in the soil and accumulation flow. Landslide occurrences are more likely to happen in areas located near rivers, especially in mountainous regions (Pal et al., 2022). Here, Euclidean distance was applied to the river network geospatial layer and buffered into five different zones from below 100 m to more than 500 m (Figure 3E).

Apart from distance to river, drainage density refers to the amount of water draining from a certain area, and a high drainage density can indicate areas that are prone to landslides. Hydrologists recognized the vital role of drainage density in relation to a range of factors, including flash flood severity, sediment load, water concentration, and overall water balance, within a specific drainage basin (Chapter VIII Stream

and Drainage Densities, 1985). Consequently, drainage density also contributed to the landslide process as one of the most significant variables representing the hydrological group setting. Figure 3F showed the distribution of six subcategories of drainage density built on the hydrological network.

Topographic wetness index, also known as the compound topographic index (CTI), was first introduced by Beven and Kirkby (1979). The index implies the effects of the spatial topographic scale on hydrological processes with the assumption of uniform soil properties. A summary of the application of the TWI was described in Sørensen et al. (2006); Pal et al. (2022) as proof of its vital role in hydrological applications. The TWI is often used to identify areas that are susceptible to landslides due to saturation-induced soil instability. To obtain the index, we applied the following equation:

$$TWI = \ln(\alpha / \tan \beta), \quad (1)$$

where α is the scaled flow accumulation and β is the local slope transfer to the radian unit. Figure 3G showed the distribution of the TWI values generated based on the DEM, with a range of continuous values converted to six discrete classes.

3.2.3 Group of geology

Not paying attention to geological-related components would be a significant limitation in the systematic assessment of landslide hazards. Given the thematic layer analysis conducted over the study area, three appropriate conditioning factors were adopted, i.e., 1) distance to fault, 2) soil, and 3) geomorphology.

Geological lineaments are characterized as one of the main driving forces leading to land movements, such as active faults, earthquakes, and geomorphological formation. Particularly in landslide hazards, the presence of faults can create deformation in the surrounding rock, which can weaken the material and increase the likelihood of failure. Additionally, faults can also create pathways for water to infiltrate the rock, which can further degrade the material and increase its susceptibility to landslides (Ramli et al., 2010). Thus, we extracted the geological lineament distribution and performed Euclidean distance functions with grades of 100-m intervals. The result was then reclassified into six classes of thematic layers, as represented in Figure 3H.

The soil affects the stability of geological characteristics and, thus, unequivocally relates to landslide sensitivity. We first prepared the soil map according to the FAO/UNESCO classification. Moreover, our national database provided the map representing the details of each soil class in Acrisols due to the predominance of this group in the considered area. The final soil map includes eleven units: Epi Lithi Humic Acrisols (ACu-I1), Calcisols (CLs), Epi Lithi Ferralic Acrisols (ACf-I1), Leptosols (LPs), Endolithe Ferralic Acrisols (ACf-d2), Hapli Ferralic Acrisols (ACf-h), Ferric Acrisols (ACfe), other Acrisols (Arenic, Albic, and Plinthic) (ACs), Fluvisols (FLs), Epi Skeletic Ferralic (ACf-sk1), and other soil types (Figure 3I).

Geomorphology is also an indisputable factor influencing landslide susceptibility. The geomorphological map with ten unique characteristics was obtained from the national geodatabase. Figure 3J showed the distribution of geomorphological units including slow gravity slope (I), wash slope (II), landform with origin of stream flow (III), corroded slope (IV), the remaining surface of pediment basin (V), quick gravity slope (VI), deluvi–coluvi agglomerating slope

(VII), the remaining surface of peneplain (VIII), others (IX), and karst landform (X).

3.2.4 Group of land cover conditions and anthropogenic activities

For selecting candidates related to landslides, the contribution of the landcover environment and built-up infrastructures should be emphasized. Accordingly, we adopted three sensitivity factors belonging to the group of land cover conditions and anthropogenic activities, namely, 1) land cover; 2) distance to road; and 3) Normalized Difference Vegetation Index (NDVI).

A land cover map was obtained using the product of ESA WorldCover version 2.0. The classification procedure was based on both Synthetic Aperture Radar Sentinel-1 data and Sentinel-2 optical images with a resolution of 10 m globally (Zanaga et al., 2022). In our examined area, six unique classes were identified with the largest land cover class, the tree cover (84.63%), following cropland (6.22%), grassland (3.54%), water bodies (1.95%), built-up land (1.83%), and bare soil and sparse vegetation (1.83%). Figure 3K showed the distribution of land cover as mainly forest cover in hilly and mountainous areas.

Anthropogenic activities, i.e., road construction, can indeed have a significant impact on the geological structure of a large basin. With the spatial modeling of landslide sensitivity, it is necessary to consider the distribution of road networks as one of the most man-made influenced factors. Compared to plain regions with stable slopes, the pressure from concrete road constructions can be particularly intense in mountainous regions. Moreover, the presence of roadways can also imply other human activities, leading to further impact on the surrounding landscape (Pal et al., 2022). Therefore, we applied Euclidean distance estimation with an interval of 100 m. The resulting map is shown in Figure 3L.

The NDVI is also one of the indicators used to assess the density of vegetation in tropical climates. Here, we calculated the index based on the MultiSpectral Instrument (MSI) onboard Sentinel-2, as shown in Figure 3M. It should be noted that the sensor includes 12 spectral bands with resolutions ranging from 10 m to 60 m. The red and near-infrared bands (10 m) were used to obtain the NDVI using the following equation:

$$NDVI = \frac{NIR - RED}{NIR + RED} = \frac{B8 - B4}{B8 + B4} \quad (2)$$

3.2.5 Group of weather

Two spatial layers of weather datasets related to landslide probability are 1) precipitation and 2) climate. Related to the previously mentioned factor, triggering of landslides in the tropical monsoon climate zone is often due to heavy rainfall (Funk et al., 2015). Therefore, remote sensing products of precipitation were processed through the cloud spatial computing platform Google Earth Engine using the catalog of Climate Hazards Group InfraRed Precipitation with Station Data (CHIRPS). These datasets provide daily gridded rainfall with a resolution of 0.05°. In order to focus on landslide susceptibility in rainy season, a monthly rainfall map was generated with the mean of all images collected in September 2022, the rainiest period over the research area (Figure 3N).

Climate is a long-term pattern of weather in a specific region. Furthermore, climate patterns are the main controlling parameters for

TABLE 1 Description of the climate components.

No.	Climate components	Description
1	Temperature	I: 22–24°
		II: 20–22°
		III: 18–20°
		IV: 15–18°
2	Rainfall	A: 2,500–2,800 mm
		B: 2,000–2,500 mm
		C: 1,500–2,000 mm
3	Cold time	0: non winter time
		1: 1–3 winter months
		2: 4–5 winter months
		3: 6–7 winter months
4	Drought condition	a: dry season during December to April with slight drought
		b: dry season during December to April with moderate drought
		c: dry season during January to July with moderate drought
		d: dry season during January to July with drought

the amount of precipitation. Aiming to understand the relationship between typical climates and landslides, we provided a thematic map to present the main climate patterns in detail. A description of specific climate patterns is provided in Table 1, and the map is shown in Figure 3O.

3.3 Frequency ratio

The bivariate statistical FR method was applied to estimate the landslide densities in all subclasses in each factor. The goal of this method is to compute the percentage of landslide pixels located in subcategories of all factors, correcting the associated raters to the propensity of landslide occurrences (Lee and Talib, 2005). To perform the estimation, the landslide inventory training dataset and factor maps were used for obtaining the following equations:

$$FR_{ij} = \frac{LS_{ij} / \sum LS_{ij}}{N_{ij} / \sum N_{ij}}, \quad (3)$$

$$RF_{ij} = \frac{FR_{ij}}{\sum FR_{ij}} \times 100, \quad (4)$$

where i is the subclass of the considered factor j ; LS_{ij} is the number of landslide pixels in each class; N_{ij} is the number of class pixels; FR_{ij} is the frequency ratio; RF_{ij} is the relative frequency (%).

3.4 Analytic hierarchy process

The subjective approach, AHP, was first introduced in Saaty, 1977 (1980), known as a widely used multi-criteria decision analysis that allows decision-makers to prioritize and evaluate alternative options

based on multiple criteria. In the field of critical landslide area assessment, this method provides a robust, yet simple to handle, complex decision-making problems. It is based on the principle of pairwise comparison, where the relative importance of a criterion is assessed in relation to others. Here, the AHP was implemented by a subjective hierarchical structure that contains 15 landslide causative factors. Based on judgments of multidisciplinary experts who collaborated with local officers, pairwise comparisons are then made to determine their relative importance. These comparisons are repeated at each level of the hierarchy until an acceptance consistency ratio is obtained, indicating that the criteria are consistent with others. The final step involves combining the pairwise comparisons to calculate the overall weight of individual factors. The metrics in the process, including Consistency Index (CI) and Consistency Ratio (CR), were estimated according to the following equation:

$$CI = \frac{\lambda_{\max} - n}{n - 1}, \quad (5)$$

$$CR = \frac{CI}{RI}, \quad (6)$$

where λ_{\max} is the maximum eigenvalue of the matrix, n is the number of considered criteria ($n = 15$); the random consistency index (RI) is 1.59, which was used for 15 criteria (Saaty, 1980). The obtained CR less than 0.1 implies the consistency and acceptance of the decision-makers' pairwise comparison matrix.

3.5 Shannon entropy

Initially proposed by Shannon (1948), SE is a well-established information theory-based method. The basic idea is to give more weight to events that have higher entropy, as they contain more

uncertainty and information, and less weight to events with lower entropy. Mainly based on ready-to-use data, the SE formula measures the average amount of information contained in a dataset, and the weights are derived from these entropy values. In risk assessment, the entropy of a hazard event can be used to determine its likelihood and potential impact. Events with higher entropy carry more uncertainty and, therefore, have a higher risk associated with them. Here, we computed the entropy of landslide susceptibility based on the distribution of detected landslides in the training dataset to the contributing factors. SE weighting was estimated using the following equations (Roodposhti et al., 2016; Agrawal and Dixit, 2022):

$$P_{ij} = FR_{ij} \div \sum_{i=1}^m FR_{ij}, \quad (7)$$

$$E_j = \left(\frac{-1}{\log_2(m_j)} \right) \times \sum_{i=1}^m P_{ij} \log_2 P_{ij}, \quad (8)$$

$$W_{SE}^j = (1 - E_j) \sum_{j=1}^n (1 - E_j), \quad (9)$$

where i is the subclass of the considered factor j , m is the number of subclasses in each conditioning factor, n is the number of conditioning factors ($n = 15$), P_{ij} is the probability density, FR_{ij} is the frequency ratio, E_j is the entropy value, and W_{SE}^j is the entropy weight.

3.6 The synergy of subjective and objective weighting approaches

The synergy of both objective and subjective approaches may enhance the performance of the model and mitigate issues related to the ill-posedness. Therefore, the data-driven method SE and knowledge-based method AHP were integrated to derive the combined weights for each of 15 conditioning factors, as seen in the following equation (Wang and Zhang, 2018):

$$W_{SE-AHP}^j = \frac{W_{SE}^j \times W_{AHP}^j}{\sum_{j=1}^n (W_{SE}^j \times W_{AHP}^j)} \quad (10)$$

where W_{SE}^j and W_{AHP}^j are derived from the objective-based SE and the subjective-based AHP, respectively; j is the considered factor; n is the total number of conditioning factors of the landslide susceptibility model ($n = 15$).

3.7 Landslide susceptibility mapping

To retrieve the landslide susceptibility index, a summation of the product of rating subclasses and respective weights of each conditioning factor is given by the following equation:

$$LSI = \sum_{j=1}^n W_j \times R_j^{FR}, \quad (11)$$

where n is the number of landslide conditioning factors ($n = 15$); W_j is the factor weight obtained by the corresponding methods of AHP, SE, and AHP-SE; and R_j is the two-dimensional matrix of factor j that has been reassigned to the RF. The continuous range value of the landslide susceptibility index is divided into five

probability categories, namely, very low, low, moderate, high, and very high, using the natural breaks Jenks function.

3.8 Model evaluation

The performance of various models was evaluated using the receiver operating characteristic (ROC) curve. The primary statistical metrics employed to measure the model accuracy are true positive rate (TPR), false positive rate (FPR), and AUC. The TPR, also referred to as sensitivity, reflects the proportion of correctly classified positive cases among all positive cases, while the FPR, also known as specificity, measures the likelihood of a true negative case being classified as negative. The AUC spans from 0 to 1. A retrieval value of the AUC closer to 1 results in the better performance of the model:

$$TPR = \frac{TP}{TP + FN} = \frac{TP}{P}, \quad (12)$$

$$FPR = \frac{TN}{TN + FP} = \frac{TN}{N}, \quad (13)$$

$$AUC = \frac{\sum TP + \sum TN}{P + N}, \quad (14)$$

where true positive (TP) and true negative (TN) are the values of correct landslide and non-landslide pixels, respectively; true negative and false positive (FP) are the values of incorrect landslide and non-landslide pixels, respectively; P and N are the corresponding total number of landslide and non-landslide pixels.

We also estimate the relative landslide density index to evaluate the performance of different models in each landslide-sensitive zone, using the following equation:

$$R = \left(\frac{n_i}{N_i} \right) / \sum \left(\frac{n_i}{N_i} \right) \times 100, \quad (15)$$

where n_i and N_i are the numbers of landslide pixels and total pixels in each susceptibility class, respectively.

4 Results

4.1 Weighting of subclasses and corresponding conditioning factors

Table 2 showed the FR and RF calculated for subclasses in landslide-controlling factors. By considering the quantity relationship between training points (196 points) that appeared in each subcategory (total of 79,865,948 pixels), higher FR values indicate higher sensitivity of a class to landslide occurrence compared to the remaining classes within a predisposing factor. It should be noted that even if a particular subclass has a small number of landslide inventory points, the FR value may still be high. This can occur when the percentage of pixels in the subclass is low relative to the total number of pixels in the thematic layer. The calculated RF (%) values were then assigned to reclassify thematic maps of all 15 causative factors as input for the landslide susceptibility model.

Regarding topographical groups, the highest elevation ranging from 1,019 m to 1,971 m, slope degree of 17.5–26.8°, east slope aspect, and convex plan curvature (>0.05) were determined as the

TABLE 2 Results of the frequency ratio for subclass weighting for the 15 causative factors used in the model.

No.	Factor	Class	Pixel (%)	Landslide pixel (%)	FR	RF
1	Elevation (m)	–55–98	33.84	19.39	0.57	7
		98–268	25.13	30.61	1.22	15
		268–459	17.51	27.04	1.54	19
		459–667	13.59	16.33	1.20	15
		667–1,019	9.29	4.59	0.49	6
		1,019–1,971	0.64	2.04	3.20	39
2	Slope (°)	0–8.29	33.00	5.61	0.17	3
		8.29–17.50	23.50	26.02	1.11	20
		17.50–26.76	23.16	42.86	1.85	33
		26.76–38.71	15.57	19.90	1.28	23
		38.71–82.02	4.77	5.61	1.18	21
3	Aspect	Flat (–1)	4.14	0.51	0.12	1
		North (0–22.5; 337.5–360)	13.08	14.80	1.13	14
		Northeast (22.5–67.5)	12.84	17.86	1.39	17
		East (67.5–112.5)	11.81	18.88	1.60	19
		Southeast (112.5–157.5)	12.30	7.65	0.62	7
		South (157.5–202.5)	11.94	13.78	1.15	14
		Southwest (202.5–247.5)	12.05	10.20	0.85	10
		West (247.5–292.5)	10.32	7.14	0.69	8
		Northwest (292.5–337.5)	11.52	9.18	0.80	10
4	Plan curvature	Concave (<–0.05)	36.37	34.69	0.95	32
		Flat (–0.05–0.05)	25.41	20.92	0.82	28
		Convex (>0.05)	38.22	44.39	1.16	40
5	Distance to river (m)	<100	21.44	21.94	1.02	16
		100–200	15.64	16.84	1.08	17
		200–300	11.64	17.35	1.49	24
		300–400	8.59	8.67	1.01	16
		400–500	6.34	5.61	0.89	14
		>500	36.35	29.59	0.81	13
6	Drainage density (km ² /km)	0–0.58	42.86	35.71	0.83	14
		0.58–1.58	20.41	23.47	1.15	20
		1.58–2.68	17.35	21.43	1.24	21
		2.68–3.89	11.58	13.27	1.15	20
		3.89–5.47	6.09	5.10	0.84	14
		5.47–13.48	1.71	1.02	0.60	10
7	TWI	0.64–4.68	25.22	32.65	1.29	29
		4.68–6.26	36.02	43.37	1.20	27
		6.26–8.37	17.45	18.37	1.05	24

(Continued on following page)

TABLE 2 (Continued) Results of the frequency ratio for subclass weighting for the 15 causative factors used in the model.

No.	Factor	Class	Pixel (%)	Landslide pixel (%)	FR	RF
		8.37–10.74	10.94	2.04	0.19	4
		10.74–13.90	9.08	3.06	0.34	8
		13.90–23.12	1.29	0.51	0.40	9
8	Distance to fault (m)	<100	6.83	6.12	0.90	14
		100–200	6.43	5.10	0.79	12
		200–300	6.25	9.18	1.47	23
		300–400	6.04	8.16	1.35	21
		400–500	5.76	5.10	0.89	14
		>500	68.69	66.33	0.97	15
9	Soil	Other	8.48	0.51	0.06	1
		Epi Lithi Humic Acrisols (ACu-I1)	1.21	3.57	2.95	27
		Calcisols (CLs)	21.54	9.18	0.43	4
		Epi Lithi Ferralic Acrisols (ACf-I1)	40.11	51.02	1.27	12
		Leptosols (LPs)	3.10	4.08	1.32	12
		Endolithi Ferralic Acrisols (ACf-d2)	9.81	22.96	2.34	21
		Hapli Ferralic Acrisols (ACf-h)	3.80	4.08	1.07	10
		Ferric Acrisols (ACfe)	2.66	1.02	0.38	3
		Other Acrisols (Arenic, Albic, and Plinthic) (ACs)	2.51	0.51	0.20	2
		Fluvisols (FLs)	5.04	2.04	0.41	4
		Epi Skeletic Ferralic (ACf-sk1)	1.74	1.02	0.59	5
10	Geomorphology	Slow gravity slope (I)	22.89	31.12	1.36	12
		Wash slope (II)	9.97	18.88	1.89	17
		Landform with origin of stream flow (III)	12.40	10.71	0.86	8
		Corroded slope (IV)	3.56	6.63	1.86	17
		Remaining surface of the pediment basin (V)	2.17	3.57	1.65	15
		Quick gravity slope (VI)	7.69	12.76	1.66	15
		Deluvi–coluvi agglomerating slope (VII)	2.79	2.04	0.73	7
		Remaining surface of the peneplain (VIII)	1.68	0.51	0.30	3
		Others (IX)	14.40	0.00	0.00	0
		Karst landform (X)	22.45	13.78	0.61	6
11	Land cover	Tree cover	84.63	93.88	1.11	33
		Grassland	3.54	3.06	0.87	25
		Cropland	6.22	0.51	0.08	2
		Built-up	1.83	0.51	0.28	8
		Bare/sparse vegetation	1.83	0.51	0.28	8
		Water bodies	1.95	1.53	0.78	23
12	Distance to road (m)	<100	14.63	9.18	0.63	11
		100–200	8.04	5.61	0.70	13

(Continued on following page)

TABLE 2 (Continued) Results of the frequency ratio for subclass weighting for the 15 causative factors used in the model.

No.	Factor	Class	Pixel (%)	Landslide pixel (%)	FR	RF
		200–300	5.47	3.06	0.56	10
		300–400	4.12	4.59	1.11	20
		400–500	3.34	4.59	1.38	25
		>500	64.40	72.96	1.13	21
13	NDVI	−0.83–0.05	1.47	1.02	0.70	16
		0.05–0.29	3.86	2.55	0.66	15
		0.29–0.44	5.45	3.57	0.65	15
		0.44–0.58	7.82	4.59	0.59	13
		0.58–0.73	13.09	9.18	0.70	16
		0.73–0.83	68.32	79.08	1.16	26
14	Precipitation (mm/day)	2.78–6.56	1.12	1.02	0.91	16
		6.56–11.12	14.84	4.59	0.31	5
		11.12–13.27	34.83	37.76	1.08	19
		13.27–15.30	25.97	28.06	1.08	19
		15.30–17.58	14.71	18.88	1.28	22
		17.58–23.27	8.53	9.69	1.14	20
15	Climate	IA1a	5.12	4.59	0.90	6
		IA1b	20.15	27.04	1.34	9
		IB0d	12.79	1.02	0.08	1
		IB1a	5.42	8.67	1.60	11
		IB1b	20.71	20.92	1.01	7
		IB1d	1.53	1.02	0.67	5
		IC0d	1.62	0.00	0.00	0
		IC1c	2.21	1.53	0.69	5
		IIA2a	13.70	21.94	1.60	11
		IIB2b	13.65	9.18	0.67	5
		IIIA2a	2.79	2.55	0.91	6
		IVA3a	0.32	1.53	4.77	33

most influential subclasses. In case of the group set by hydrological variables, distance to river spanning 200–300 m, drainage density between 1.6 and 2.7 km²/km, and the range of the TWI of 0.6–4.7 become more sensitive compared to other corresponding subcategories. The soil of Epi Lithi Humic Acrisols (ACu-I1), wash slope and corroded slope, and 400–500 m proximity to the fault gave the most pressure in the geological group. The group of land cover conditions and anthropogenic activities witnessed the most significant susceptibility in subclasses of tree cover, distance to road of 400–500 m, and a range value of the NDVI, approximately 0.7 – 0.8. Last, weather-based components estimated the rainfall amount on average of 15.6–23.3 mm/day, and two climate patterns (IB1a and IIA2a) are the most impact subcategories contributing to the landslide probability.

Table 3 represented the AHP order matrix for 15 conditioning factors, with a range of positive integer values from 1 to 7 applied for comparison among these aforementioned criteria. The achieved metrics λ_{max} , CI, and CR are equal to 15.64, 0.045, and 0.028, respectively, strongly confirmed for the consistency of the matrix. Relative weights for all factors in the method of the AHP, SE, and AHP–SE were determined and illustrated in Figure 4. From the charts, subjective judgment strictly obeys the AHP process, with the most important causative factors being precipitation and slope. In contrast, data-based statistics SE accounting for soil and climate affect much of the landslide susceptibility model. The final ranking, which incorporated both AHP and SE, identified slope and soil as the most crucial factors for detection of landslide-prone regions. When considering all three methods, soil, climate, slope, and

TABLE 3 Pairwise comparison matrix built on AHP method (λ_{max} is the maximum eigenvalue of the matrix, Consistency Index (CI), and Consistency Ratio (CR)).

No	Factors	1	2	3	4	5	6	7	8	9	10	11	12	13	14	15
1	Elevation	1	1/2	1	3	2	2	2	1/2	1	1	2	2	3	1/2	1
2	Slope		1	2	6	3	3	3	2	2	2	5	3	3	1	3
3	Aspect			1	3	2	1/3	2	1/2	1/3	1	3	2	5	1/2	1/2
4	Plan curvature				1	1/3	1/3	1/2	1/5	1/4	1/3	1	1/3	1	1/5	1/4
5	Distance to river					1	1	1	1/3	1/3	1/2	1	1	1	1/4	1/3
6	Drainage density						1	1	1/2	1/2	1	2	2	2	1/4	1/2
7	TWI							1	1/2	1/2	1/2	2	1	2	1/2	1/2
8	Distance to fault								1	1	2	3	2	3	1	1
9	Soil									1	1	3	3	3	1/3	1/2
10	Geomorphology										1	3	2	3	1/3	1/2
11	Landcover											1	1	1	1/6	1/3
12	Distance to road												1	1	1/4	1/3
13	NDVI													1	1/5	1/3
14	Precipitation														1	2
15	Climate															1
$\lambda_{max} = 15.64$, CI = 0.045, CR = 0.028																

precipitation were recognized as the top important factors, with significantly higher weights than those of the rest. For example, the lowest weight value for slope in SE was 0.138, while the highest weight value for climate in AHP–SE was 0.194. The plan curvature was found to contribute the least to the model, with the lowest weight assigned to it in all three methods (AHP: 0.009, SE: 0.021, and AHP–SE: 0.002). Notably, AHP–SE showed a significant difference between the most crucial factor, climate, and the least important one, plan curvature, with weight values ranging from 0.002 to 0.194.

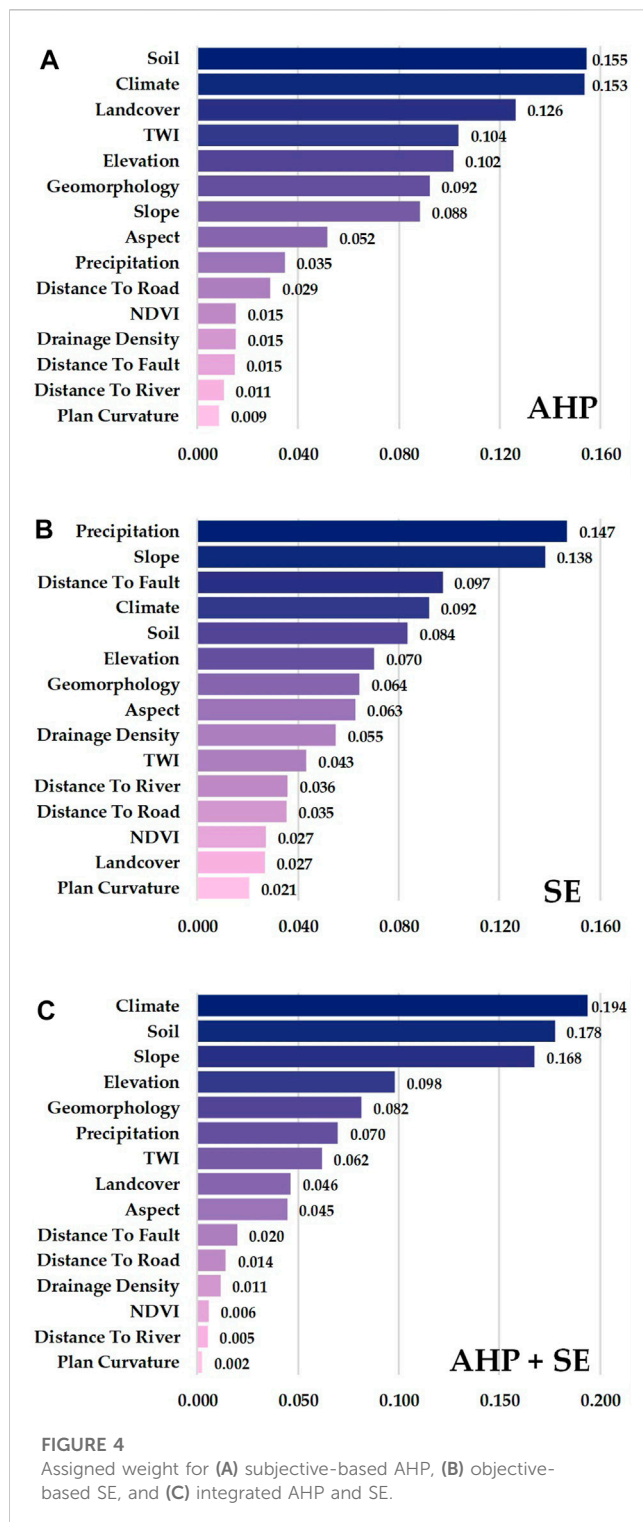
4.2 Landslide susceptibility mapping

Figure 5 illustrated the distribution of landslide sensitivity using the AHP, SE, and the synergy of these two methods. The maps clearly demonstrated that the most sensitive landslides are located along the Truong Son mountain range in Vietnam, stretching from the northwest to the southeast. In contrast, coastal areas showed a very low to low proportion of landslide occurrences. The polar chart (Figure 5D) summarized the statistics area of the five levels of landslide susceptibility based on AHP, SE, and the integrated approach. Overall, the major landslide-prone areas belong to the high level in all three methods, on average, accounting for nearly a quarter of the total study area. In particular, the AHP method showed the highest percentage (29.83%) of the high landslide-prone category, while the SE method exhibited slightly different proportions for high and very high levels, i.e., 28.76% and 26.05%, respectively. The combined approach AHP–SE resulted in 28.97% for high risk and 21.93% for very high risk zones. The figures for moderate risk of landslide trigger in the three methods appeared to be similar, with negligible differences in area percentage, ranging from the lowest 21.32% (AHP) to the highest 22.70% (SE).

Looking into the classes of low and very low susceptibility, it is evident that these classes resulted in the smallest percentage of the susceptibility area compared to the three remaining categories. In the SE, approximately 11% of the natural area was identified as having the least landslide probability, and the number remains unchanged for the level of low sensitivity. Using the AHP model, the proportions of very low and low levels were found to be 11.71% and 15.65% of the total area, respectively, whereas 14% and 13.30% of the area are shown in very low and low landslide susceptibility degrees according to the combined method AHP–SE. In comparison to categories of the high landslide sensitivity class, the statistical data for the level of very low susceptibility revealed significantly lower values, i.e., only one-third of the values obtained through the AHP and the SE method and half the number of the high landslide sensitivity class identified through the AHP–SE method. By comparing these three methods, the statistics strongly suggest that the examined area exhibited landslide predisposition mostly at high and very high levels.

4.3 Model performance

Figure 6 summarized the performance of the SE, AHP, and the AHP–SE method for landslide susceptibility mapping based on ROC curves with AUC values and R-index for landslide probability levels. Overall, all three models were reliable, with the AUC higher than the random guess (0.5) and classified as a very good prediction (AUC ranging from 0.8–0.9). Interestingly, the integrated AHP–SE method outperformed both the two individual methods, with the AUC reaching the highest score of well over 0.87. Objective-based SE



was better than subjective-based AHP, i.e., AUC values are nearly 0.85 and 0.81, respectively. Compared to the lowest AUC derived from the AHP, the synergy of the objective and subjective weighting method, AHP-SE, led to a notable improvement in the landslide susceptibility model by approximately 7%. The R-index derived for very high landslide sensitivity levels in AHP, SE, and AHP-SE maps is 63.35%, 71.09%, and 78.41%, respectively, indicating the best prediction of AHP-SE models.

5 Discussion

5.1 Sensitivity analysis of causative factors and subclasses

Out of the 15 selected factors, the weighting approach subjectively and objectively resulted in different relative importance levels. For knowledge-based weighting using AHP, confirmation for the most important factor, slope, was also found in different case studies (Kayastha et al., 2013; Mondal and Maiti, 2013; Moragues et al., 2021; Agrawal and Dixit, 2022; Khalil et al., 2022). Slope is a widely used variable in the field of landslide hazard zonation (Pourghasemi et al., 2018; Reichenbach et al., 2018). Notwithstanding, its importance in relation to landslide sensitivity may vary depending on the specific circumstance. Recent research settings on different characteristics of the area found other factors to be more influential, such as land use (Guo et al., 2023) and lithology (Yalcin, 2008; Pourghasemi et al., 2013). Particularly in the tropical climate region, precipitation was recognized as the most significant component related to landslide sensitivity (Shahabi and Hashim, 2015). Related to the data-driven methods, the results indicated that calculation based on SE gave the most important factors of soil. It was also confirmed by the same method (Devkota et al., 2013; Agrawal and Dixit, 2022). For the integrated model, climate was the most influential factor in the landslide susceptibility model, especially in tropical monsoon areas. The factor was rarely used due to data availability and it is unnecessary in some general case studies. Here, we aimed to highlight the impact of the typical climate form under tropical monsoon areas as one of the key variables leading to the high degree of landslide triggers. An updated global map of landslide sensitivity strongly suggested that Southeast Asia, with its classical tropical environment, has one of the most frequent landslide occurrences (Stanley et al., 2021).

We also have a deep insight into the contribution of different landslide conditioning factors, which allows us to suggest the necessary datasets in regions with the same environmental conditions. Based on the AHP method, our subjective knowledge indicated that the top five important factors are soil, climate, land cover, TWI, and elevation. The AHP-based results suggested that each fundamental group contains at least one factor with a significant contribution to the landslide hazard predictive model. However, approaching data-based statistics, the SE method has shown that precipitation, slope, distance to fault, climate, and soil were estimated as the highest weight factors. For the combined AHP-SE, climate, soil, slope, elevation, and geomorphology become the highest weight factors of the landslide-prone predictive model. Considering both individual and integrated methods, two groups of land cover conditions and anthropogenic activities and hydrology contributed the least to the landslide susceptibility model. This is a confirmation for the most essential group of weather, topography, and geology compared to the two remaining groups of hydrology and natural-artificial conditions. The topography group also contained the most significant factor, slope, and the least important factor, plan curvature, in all the three methods.

It should be noted that subclasses in conditioning factors significantly affect the results of landslide susceptibility

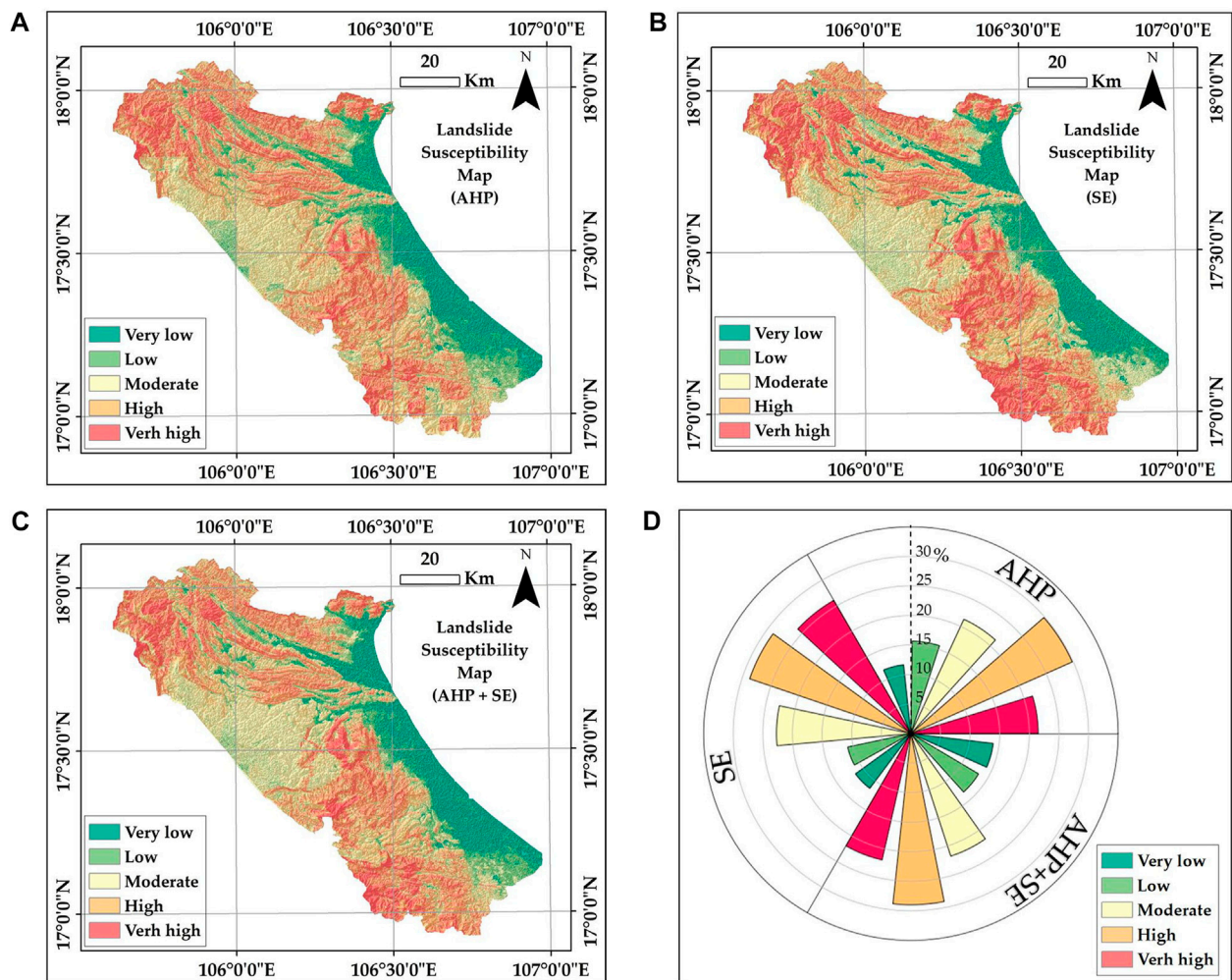


FIGURE 5 Maps of landslide susceptibility obtained by the methods of (A) AHP, (B) SE, (C) integration of SE and AHP, and (D) percentage area representing landslide sensitivity levels following corresponding methods.

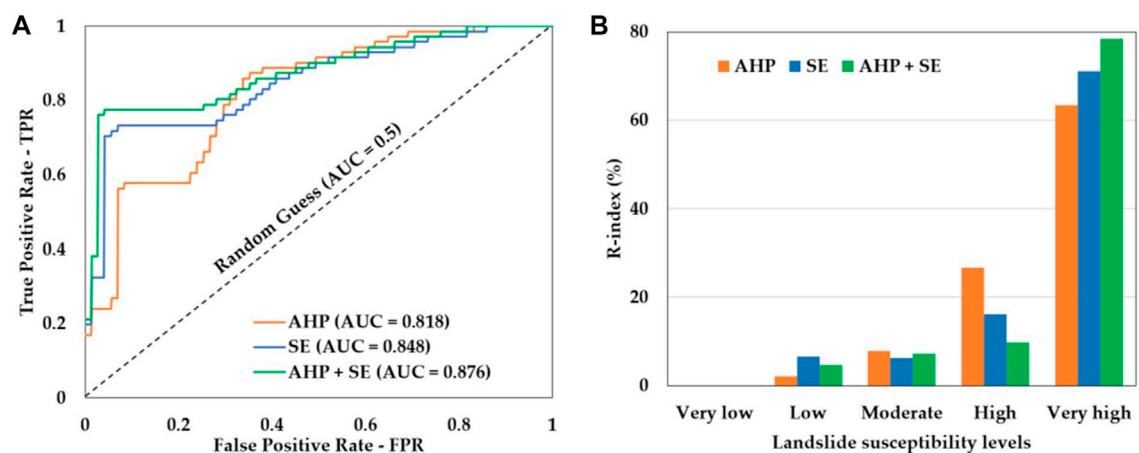


FIGURE 6 Performance of SE, AHP, and the integrated approach AHP–SE for landslide susceptibility mapping through (A) ROC curves with AUC values and (B) R-index of five landslide sensitivity categories.

modeling, especially for high-weight factors. Figure 7 represented the percentage of landslide inventory validation recorded in each specific subclass, which analyzed the relationship between landslide occurrence and different subclasses in causal factors. In summary, the sensitivity of landslide over the case study area was observed mostly in hilly areas (98–268 m), steep slopes (18–27°), slope aspects of east and northeast, both concave and convex of planform curvature, distance to river under 100 m, drainage density below 0.58 km²/km, TWI ranging from 0.64 to 6.26, distance to fault higher than 500 m, soil class of Epi Lithi Ferralic Acrisols, geomorphology landform of slow gravity slope, land cover of tree cover, distance to road higher than 500 m, high NDVI values, daily rainfall spanning between 11.1 and 13.3 mm/day, and the

climate form of tropical monsoon climate Ia1b separated by dry seasons (high temperature and moderator drought) and rainy seasons (from May to November with the total amount of precipitation 2,500–2,800 mm).

5.2 Effectiveness of modeling strategies

Among the followed methods, AHP is one of the most common techniques due to its easy approach and implementation (Tyagi et al., 2022). Even with the subjective limitation, AHP was still conducted in many applications of case studies (Pourghasemi et al., 2018; Yong et al., 2022). The method applied in our study was less accurate than the SE, with no significant difference, however.

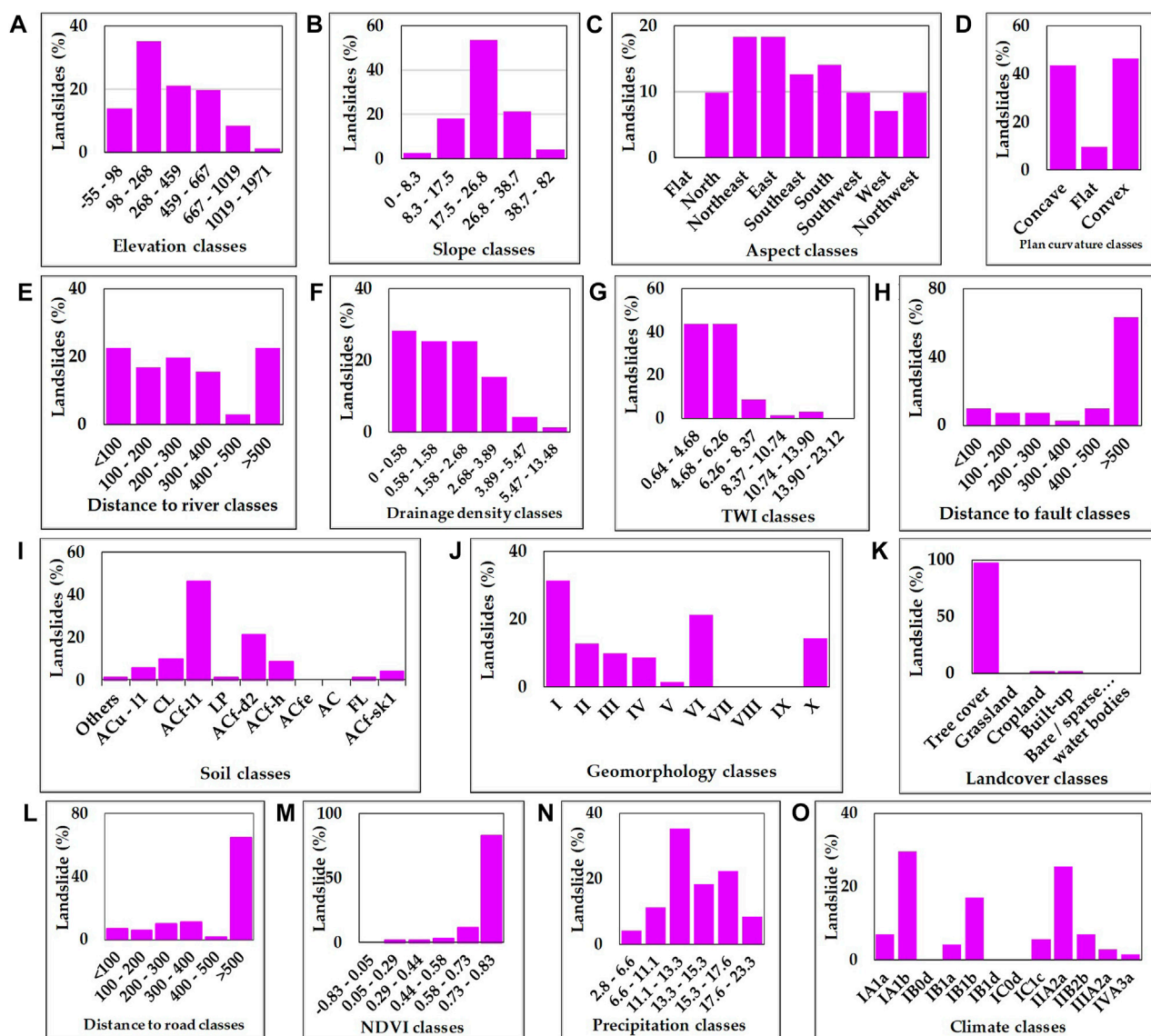


FIGURE 7

Percentage of landslide validation data based on each subclass of fifteen considered factors: (A) elevation; (B) slope; (C) aspect; (D) plan curvature; (E) distance to river; (F) drainage density; (G) TWI; (H) distance to fault; (I) soil; (J) geomorphology; (K) landcover; (L) distance to road; (M) NDVI, (N) precipitation; and (O) climate.

Previous experiences also confirmed the slightly lower performance than that of data-driven methods such as statistical analysis (Panchal and Shrivastava, 2021) and machine learning models (Khalil et al., 2022). Nonetheless questions about the requirement of expert knowledge contributing to the landslide susceptibility model still remained, with the continuous proposal for different combined approaches. Various studies demonstrated a better performance by integration of AHP with different strategies, i.e., WLC (Hung et al., 2016), FR (Mondal and Maiti, 2013), fuzzy (Agrawal and Dixit, 2022), and evidential belief function (EBF) (Althuwaynee et al., 2014). Furthermore, incalculable fluctuation of changing climate leads to ill-posed problems, while depending individually on data-driven methods (Gariano and Guzzetti, 2016; Zêzere et al., 2017), thus emphasizing the necessity of knowledge-based contribution in diverse landslide susceptibility models.

On the other hand, the objective-based weighting approach, SE, predicted better landslide sensitivity than the AHP with the confirmation of all the mentioned accuracy metrics. The method was applied in numerous works as demonstrated for the best model while being compared to LR (Devkota et al., 2013), Bayesian conditional probability model (Pourghasemi et al., 2012), AHP (Panchal and Shrivastava, 2021), statistical information value (Singh et al., 2021), and FR (Jaafari et al., 2014). These techniques employ mathematical models to determine criteria weights without incorporating the subjective preferences of decision-makers, thereby avoiding the potential influence of personal bias on the final decision outcome. Despite the fact that weights assigned by the relationship of history landslide records and thematic layers are explicit and objective, the method is affected by the resolution of spatial explanatory factors and both the quality and quantity of landslide inventory data (Zêzere et al., 2017).

In the light of various combined methods, we deployed the synergy of AHP and SE, as noticed for the lack of a combination in the field of landslide susceptibility assessment. Generally, both of the proposal weighting approaches have self-advantages and disadvantages. The SE is based on objective data, while the field dataset of landslide occurrences and the detail or resolution of the thematic layers affect the performance of the predictive process. The AHP is based on subjective decisions that may have the tendency of following rigid perspectives or epistemic uncertainty. To overcome the disadvantages and yield advantages in both the methods, we integrated subjective and objective approaches to deliver an optimal weight for each corresponding landslide-controlling factor. Statistical metrics of the AHP–SE method were revealed in this research. The performance of the combined approach was demonstrated to be more accurate compared to that of AHP and SE, thus increasing the reliability of the predictive model.

5.3 Future implementation

In the present study, we involved 15 factors in an effort to consider the entire prevalent landslide-predisposing aspects of topography, geology, hydrology, land cover environment and anthropogenic activities, and weather. However, it is hard to confirm the best selection of conditioning factors as the task is a major challenge in hazard prediction modeling. Among hundreds of factors (with their original name) used in the landslide susceptibility, more than 23 factors were mostly used (Reichenbach et al., 2018). Analysis of studies during

2005–2016 also indicated the same number of factors used more than 30 times (Pourghasemi et al., 2018). Due to the unavailability of standard guidelines to select the most effective factors, the optimal factors are mainly based on landslide type, examined area conditions, methods applied in available data, and scale requirements (Pourghasemi et al., 2018). The accuracy of models by adopting different factors was demonstrated by Gaidzik and Ramírez-Herrera (2021). Therefore, future implementation should involve quantitative analysis to suggest the most significant factors and to improve our profound understanding of how predisposing factors affected landslide susceptibility.

The geospatial data DEM is the main source used to generate different landslide-related spatial products such as slope, aspect, and curvature. Although various studies confirmed the unimpacted topographic product resolution on the performance of landslide susceptibility models (Tian et al., 2008; Chen et al., 2020), suggestions for the most congruous raster pixel size of the DEM were also discussed in detail. Gaidzik and Ramírez-Herrera (2021) indicated that a finer resolution of topographic data leads to better prediction; however, the quantity and quality of input data seem to be important with lower resolution. Lee et al. (2004) concluded that the proper resolution of 30 m, while constructing the map with scales ranging from 1:5,000 to 1:50,000 (Tian et al., 2008), implied that for a changed study area, the size decided the meaningful spatial resolution, while also mentioning that flat, ridge, and slope foot terrain shape is more difficult to predict than landslide probability in the case of lower DEM resolution. In addition, the choice of suitable methods is also mentioned, for instance, the FR applied in low-resolution products seemed to be better than the entropy-based method and WoE (Chen et al., 2020), or the AHP is appropriate in the medium-resolution scale (1:250,000–1:25,000) (Yong et al., 2022). Therefore, further analysis needs to be considered for calculating the spatial resolution of topographic products in specific conditions of the area and for selecting the most suitable input data, methodologies, and map scale results.

Apart from the proposed methods already applied in this study, further experiments should attempt to continue accessing different methods including statistics, expert-based methods, artificial intelligence solutions, and a synergy of these methods to choose the most suitable approach (Chakraborty et al., 2022). Big data also leads to the uncertainty of traditional methods due to the complex analysis process. Combining advanced high-performance machine learning and deep learning models with big geospatial data may help in resolving complicated issues and significantly improving the performance of the landslide model. This could be a potential solution for the transferability of accurate landslide susceptibility models over different areas and for temporal analysis.

6 Conclusion

Our study demonstrated the successful prediction of landslide sensitivity over a Vietnamese coastal mountainous area through the subclass weighting FR and factor weighting of AHP and SE on 15 independent landslide-causative factors. By combining subjective and objective approaches, we improved the performance of the predictive model and provided statistical evidence to support our findings. Under the perspective of integrating expert-based knowledge and data-driven methods, we also emphasized the importance of

considering climate patterns in tropical monsoon areas when assessing landslide susceptibility. Sensitivity analysis indicated the most impacted subclass for individual landslide causative variables, providing valuable insights for the considered area. Notwithstanding the proposed methods, it showed a promising solution; further research is needed to improve our understanding related to the influences of different conditioning factors, input spatial factors, data sampling methods, advanced techniques, and model transferability for large-scale spatiotemporal analysis. The research contributed to the field of GIS-based landslide sensitivity zonation in Vietnam, enabling the potential for early warning of disastrous hazards and mitigation efforts based on not only knowledge but also statistical evidence, especially in the context of uncertain future climate changes.

Data availability statement

The raw data supporting the conclusion of this article will be made available by the authors, without undue reservation.

Author contributions

Conceptualization: NB and PHa; methodology: PHa, NB, and GT; software: PHg and GT; data curation: NB, GT, and PHg; investigation: PHa, NT, and NB; formal analysis: GT and PHg; writing—original draft preparation: PHa, NT, PHg, GT, and NB; writing—review and editing: PHa and NB. All authors contributed to the article and approved the submitted version.

References

- Agrawal, N., and Dixit, J. (2022). Assessment of landslide susceptibility for Meghalaya (India) using bivariate (frequency ratio and Shannon entropy) and multi-criteria decision analysis (AHP and fuzzy-AHP) models. *All Earth* 34, 179–201. doi:10.1080/27669645.2022.2101256
- Althuwaynee, O. F., Pradhan, B., Park, H. J., and Lee, J. H. (2014). A novel ensemble bivariate statistical evidential belief function with knowledge-based analytical hierarchy process and multivariate statistical logistic regression for landslide susceptibility mapping. *Catena (Amst)* 114, 21–36. doi:10.1016/j.catena.2013.10.011
- Beven, K. J., and Kirkby, M. J. (1979). A physically based, variable contributing area model of basin hydrology/Un modèle à base physique de zone d'appel variable de l'hydrologie du bassin versant. *Hydrol. Sci. Bull.* 24, 43–69. doi:10.1080/02626667909491834
- Budimir, M. E. A., Atkinson, P. M., and Lewis, H. G. (2015). A systematic review of landslide probability mapping using logistic regression. *Landslides* 12, 419–436. doi:10.1007/s10346-014-0550-5
- Bui, D. T., Pradhan, B., Revhaug, I., Nguyen, D. B., Pham, H. V., and Bui, Q. N. (2015). A novel hybrid evidential belief function-based fuzzy logic model in spatial prediction of rainfall-induced shallow landslides in the Lang Son city area (Vietnam). *Geomatics, Nat. Hazards Risk* 6, 243–271. doi:10.1080/19475705.2013.843206
- Bui, D. T., Tsangaratos, P., Nguyen, V. T., Liem, N. V., and Trinh, P. T. (2020). Comparing the prediction performance of a Deep Learning Neural Network model with conventional machine learning models in landslide susceptibility assessment. *Catena (Amst)* 188, 104426. doi:10.1016/j.catena.2019.104426
- Cellek, S. (2021). "The effect of aspect on landslide and its relationship with other parameters," in *Landslides. Rijeka: IntechOpen*. Editors Y. Zhang and Q. Cheng Ch. 2. doi:10.5772/intechopen.99389
- Chakraborty, R., Pal, S. C., Roy, P., Saha, A., and Chowdhuri, I. (2022). Novel ensemble approach for landslide susceptibility index assessment in a mountainous environment of India. *Geocarto Int.* 37, 13311–13336. doi:10.1080/10106049.2022.2076924
- Chapter VIII Stream and Drainage Densities (1985). Chapter VIII stream and drainage densities. *Dev. Water Sci.* 101, 135–153. doi:10.1016/s0167-5648(08)70420-9
- Chen, Z., Ye, F., Fu, W., Ke, Y., and Hong, H. (2020). The influence of DEM spatial resolution on landslide susceptibility mapping in the Baxie River basin, NW China. *Nat. Hazards* 101, 853–877. doi:10.1007/s11069-020-03899-9
- Cong, N. C., Binh, N. Q., and Phuoc, V. N. D. (2020). "Landslide susceptibility mapping by combining the analytical hierarchy process and regional frequency analysis methods: A case study for quangngai province (vietnam)," in *Apac 2019 - proceedings of the 10th international conference on asian and pacific coasts*. doi:10.1007/978-981-15-0291-0_180
- Dao, D. V., Jaafari, A., Bayat, M., Mafi-Gholami, D., Qi, C., Moayedi, H., et al. (2020). A spatially explicit deep learning neural network model for the prediction of landslide susceptibility. *Catena (Amst)* 188, 104451. doi:10.1016/j.catena.2019.104451
- Devkota, K. C., Regmi, A. D., Pourghasemi, H. R., Yoshida, K., Pradhan, B., Ryu, I. C., et al. (2013). Landslide susceptibility mapping using certainty factor, index of entropy and logistic regression models in GIS and their comparison at Mugling-Narayanghat road section in Nepal Himalaya. *Nat. Hazards* 65, 135–165. doi:10.1007/s11069-012-0347-6
- Froude, M. J., and Petley, D. N. (2018). Global fatal landslide occurrence from 2004 to 2016. *Nat. Hazards Earth Syst. Sci.* 18, 2161–2181. doi:10.5194/nhess-18-2161-2018
- Funk, C., Peterson, P., Landsfeld, M., Pedreros, D., Verdin, J., Shukla, S., et al. (2015). The climate hazards infrared precipitation with stations - a new environmental record for monitoring extremes. *Sci. Data* 2, 150066. doi:10.1038/sdata.2015.66
- Gaidzik, K., and Ramirez-Herrera, M. T. (2021). The importance of input data on landslide susceptibility mapping. *Sci. Rep.* 11, 19334. doi:10.1038/s41598-021-98830-y
- Gariano, S. L., and Guzzetti, F. (2016). Landslides in a changing climate. *Earth Sci. Rev.* 162, 227–252. doi:10.1016/j.earscirev.2016.08.011
- Guo, Z., Tian, B., Li, G., Huang, D., Zeng, T., He, J., et al. (2023). Landslide susceptibility mapping in the Loess Plateau of northwest China using three data-driven techniques-a case study from middle Yellow River catchment. *Front. Earth Sci. (Lausanne)* 10. doi:10.3389/feart.2022.1033085
- Guzzetti, F., Reichenbach, P., Ardizzone, F., Cardinali, M., and Galli, M. (2006). Estimating the quality of landslide susceptibility models. *Geomorphology* 81, 166–184. doi:10.1016/j.geomorph.2006.04.007
- Highland, L. M., and Bobrowsky, P. (2008). *The landslide Handbook - a guide to understanding landslides*. Reston, VA: US Geological Survey Circular.

Funding

This research was funded by the grant number CT0000.10/21-23.

Acknowledgments

This research was supported by the project CT0000.10/21-23. The authors thank the Vietnam Academy of Science and Technology (VAST) for funding the research project, grant number CT0000.10/21-23.

Conflict of interest

The authors declare that the research was conducted in the absence of any commercial or financial relationships that could be construed as a potential conflict of interest.

Publisher's note

All claims expressed in this article are solely those of the authors and do not necessarily represent those of their affiliated organizations, or those of the publisher, the editors, and the reviewers. Any product that may be evaluated in this article, or claim that may be made by its manufacturer, is not guaranteed or endorsed by the publisher.

- Hodasová, K., and Bednarik, M. (2021). Effect of using various weighting methods in a process of landslide susceptibility assessment. *Nat. Hazards* 105, 481–499. doi:10.1007/s11069-020-04320-1
- Hung, L. Q., Van, N. T. H., Duc, D. M., Ha, L. T. C., Van Son, P., Khanh, N. H., et al. (2016). Landslide susceptibility mapping by combining the analytical hierarchy process and weighted linear combination methods: A case study in the upper lo river catchment (vietnam). *Landslides* 13, 1285–1301. doi:10.1007/s10346-015-0657-3
- Jaafari, A., Najafi, A., Pourghasemi, H. R., Rezaeian, J., and Sattarian, A. (2014). GIS-based frequency ratio and index of entropy models for landslide susceptibility assessment in the Caspian forest, northern Iran. *Int. J. Environ. Sci. Technol.* 11, 909–926. doi:10.1007/s13762-013-0464-0
- Kayastha, P., Dhital, M. R., and De Smedt, F. (2013). Application of the analytical hierarchy process (AHP) for landslide susceptibility mapping: A case study from the tinau watershed, west Nepal. *Comput. Geosci.* 52, 398–408. doi:10.1016/j.cageo.2012.11.003
- Khalil, U., Imtiaz, I., Aslam, B., Ullah, I., Tariq, A., and Qin, S. (2022). Comparative analysis of machine learning and multi-criteria decision making techniques for landslide susceptibility mapping of Muzaffarabad district. *Front. Environ. Sci.* 10. doi:10.3389/fenvs.2022.1028373
- Kieu, L. Q., and Ngo, G. V. (2022). Landslide susceptibility assessment for warning of dangerous areas in Tan Uyen district, Lai Chau province, Vietnam. *Geogr. Ann. Ser. A, Phys. Geogr.* 104, 183–200. doi:10.1080/04353676.2022.2091915
- Lee, S., Choi, J., and Woo, I. (2004). The effect of spatial resolution on the accuracy of landslide susceptibility mapping: A case study in boun, korea. *Geosciences J.* 8, 51–60. doi:10.1007/BF02910278
- Lee, S., and Talib, J. A. (2005). Probabilistic landslide susceptibility and factor effect analysis. *Environ. Geol.* 47, 982–990. doi:10.1007/s00254-005-1228-z
- Li, H., Mao, Z., Sun, J., Zhong, J., and Shi, S. (2022). Landslide susceptibility mapping using weighted linear combination: A case of gucheng town in ningxia, China. *Geotechnical Geol. Eng.* 41, 1247–1273. doi:10.1007/s10706-022-02333-0
- Liao, M., Wen, H., and Yang, L. (2022). Identifying the essential conditioning factors of landslide susceptibility models under different grid resolutions using hybrid machine learning: A case of wushan and wuxi counties, China. *Catena (Amst)* 217, 106428. doi:10.1016/j.catena.2022.106428
- Limbirt, H., Limbert, D., Hieu, N., Phái, V. V., Kinh Bac, D., Phuong, T. H., et al. (2016). The discovery and exploration of hang Son Doong. *Bol. Geol. Min.* 127.
- Ling, S., Zhao, S., Huang, J., and Zhang, X. (2022). Landslide susceptibility assessment using statistical and machine learning techniques: A case study in the upper reaches of the minjiang river, southwestern China. *Front. Earth Sci. (Lausanne)* 10. doi:10.3389/feart.2022.986172
- Lombardo, L., Tanyas, H., and Nicu, I. C. (2020). Spatial modeling of multi-hazard threat to cultural heritage sites. *Eng. Geol.* 277, 105776. doi:10.1016/j.enggeo.2020.105776
- Long, D. V., Cong, N. C., Cuong, N. T., Binh, N. Q., and Phuoc, V. N. D. (2022). “An assessment of terrain quality and selection model in developing landslide susceptibility map – a case study in mountainous areas of Quang Ngai province, vietnam,” in *Lecture notes in mechanical engineering*. doi:10.1007/978-981-16-3239-6_75
- Long, N. T., and De Smedt, F. (2018). Analysis and mapping of rainfall-induced landslide susceptibility in A luoi district, thua thien Hue province, vietnam. *WaterSwitzerl.* 11, 51. doi:10.3390/w11010051
- Ma, W., Dong, J., Wei, Z., Peng, L., Wu, Q., Wang, X., et al. (2023). Landslide susceptibility assessment using the certainty factor and deep neural network. *Front. Earth Sci. (Lausanne)* 10. doi:10.3389/feart.2022.1091560
- Mirda, H. A., Bera, S., and Chatterjee, R. (2022). Vulnerability assessment of mountainous households to landslides: A multidimensional study in the rural himalayas. *Int. J. Disaster Risk Reduct.* 71, 102809. doi:10.1016/j.ijdr.2022.102809
- Mondal, S., and Maiti, R. (2013). Integrating the Analytical Hierarchy Process (AHP) and the frequency ratio (FR) model in landslide susceptibility mapping of Shiv-khola watershed, Darjeeling Himalaya. *Int. J. Disaster Risk Sci.* 4, 200–212. doi:10.1007/s13753-013-0021-y
- Moragues, S., Lenzano, M. G., Lanfri, M., Moreiras, S., Lannutti, E., and Lenzano, L. (2021). Analytic hierarchy process applied to landslide susceptibility mapping of the North Branch of Argentino Lake, Argentina. *Nat. Hazards* 105, 915–941. doi:10.1007/s11069-020-04343-8
- Nhu, V. H., Hoang, N. D., Nguyen, H., Ngo, P. T. T., Thanh Bui, T., Hoa, P. V., et al. (2020). Effectiveness assessment of Keras based deep learning with different robust optimization algorithms for shallow landslide susceptibility mapping at tropical area. *Catena (Amst)* 188, 104458. doi:10.1016/j.catena.2020.104458
- Nicu, I. C., and Asăndulesei, A. (2018). GIS-based evaluation of diagnostic areas in landslide susceptibility analysis of Bahluiet River Basin (Moldavian Plateau, NE Romania). Are Neolithic sites in danger? *Geomorphology* 314, 27–41. doi:10.1016/j.geomorph.2018.04.010
- Nicu, I. C. (2017). Frequency ratio and GIS-based evaluation of landslide susceptibility applied to cultural heritage assessment. *J. Cult. Herit.* 28, 172–176. doi:10.1016/j.culher.2017.06.002
- Pal, S. C., Chakraborty, R., Saha, A., Bozchaloei, S. K., Pham, Q. B., Linh, N. T. T., et al. (2022). Evaluation of debris flow and landslide hazards using ensemble framework of Bayesian- and tree-based models. *Bull. Eng. Geol. Environ.* 81, 55. doi:10.1007/s10064-021-02546-2
- Panchal, S., and Shrivastava, A. K. (2021). A comparative study of frequency ratio, shannon's entropy and analytic hierarchy process (Ahp) models for landslide susceptibility assessment. *ISPRS Int. J. Geoinf* 10, 603. doi:10.3390/ijgi10090603
- Pham, B. T., Vu, V. D., Costache, R., Phong, T. V., Ngo, T. Q., Tran, T. H., et al. (2022). Landslide susceptibility mapping using state-of-the-art machine learning ensembles. *Geocarto Int.* 37, 5175–5200. doi:10.1080/10106049.2021.1914746
- Phong, T. V., Phan, T. T., Prakash, I., Singh, S. K., Shirzadi, A., Chapi, K., et al. (2021). Landslide susceptibility modeling using different artificial intelligence methods: A case study at muong lay district, vietnam. *Geocarto Int.* 36, 1685–1708. doi:10.1080/10106049.2019.1665715
- Pourghasemi, H. R., Mohammady, M., and Pradhan, B. (2012). Landslide susceptibility mapping using index of entropy and conditional probability models in GIS: Safarood Basin, Iran. *Catena (Amst)* 97, 71–84. doi:10.1016/j.catena.2012.05.005
- Pourghasemi, H. R., Moradi, H. R., and Fatemi Aghda, S. M. (2013). Landslide susceptibility mapping by binary logistic regression, analytical hierarchy process, and statistical index models and assessment of their performances. *Nat. Hazards* 69, 749–779. doi:10.1007/s11069-013-0728-5
- Pourghasemi, H. R., Teimoori Yansari, Z., Panagos, P., and Pradhan, B. (2018). Analysis and evaluation of landslide susceptibility: A review on articles published during 2005–2016 (periods of 2005–2012 and 2013–2016). *Arabian J. Geosciences* 11, 193. doi:10.1007/s12517-018-3531-5
- Ramli, M. F., Yusof, N., Yusoff, M. K., Juahir, H., and Shafri, H. Z. M. (2010). Lineament mapping and its application in landslide hazard assessment: A review. *Bull. Eng. Geol. Environ.* 69, 215–233. doi:10.1007/s10064-009-0255-5
- Razavizadeh, S., Solaimani, K., Massironi, M., and Kavian, A. (2017). Mapping landslide susceptibility with frequency ratio, statistical index, and weights of evidence models: A case study in northern Iran. *Environ. Earth Sci.* 76, 499. doi:10.1007/s12665-017-6839-7
- Reichenbach, P., Rossi, M., Malamud, B. D., Mihir, M., and Guzzetti, F. (2018). A review of statistically-based landslide susceptibility models. *Earth Sci. Rev.* 180, 60–91. doi:10.1016/j.earscirev.2018.03.001
- Roodposhti, M. S., Aryal, J., Shahabi, H., and Safarrad, T. (2016). Fuzzy shannon entropy: A hybrid GIS-based landslide susceptibility mapping method. *Entropy* 18, 343. doi:10.3390/e18100343
- Saaty, T. L. (1977). A scaling method for priorities in hierarchical structures. *J. Math. Psychol.* 15, 234–281. doi:10.1016/0022-2496(77)90033-5
- Saaty, T. (1980). *The analytical hierarchy process, planning, priority, resource allocation*. McGraw-Hill International Book Company.
- Sbroglia, R. M., Reginatto, G. M. P., Higashi, R. A. R., and Guimarães, R. F. (2018). Mapping susceptible landslide areas using geotechnical homogeneous zones with different DEM resolutions in Ribeirão Baú basin, Ilhota/SC/Brazil. *Landslides* 15, 2093–2106. doi:10.1007/s10346-018-1052-7
- Scaioni, M., Longoni, L., Melillo, V., and Papini, M. (2014). Remote sensing for landslide investigations: An overview of recent achievements and perspectives. *Remote Sens. (Basel)* 6, 9600–9652. doi:10.3390/rs6109600
- Shahabi, H., and Hashim, M. (2015). Landslide susceptibility mapping using GIS-based statistical models and Remote sensing data in tropical environment. *Sci. Rep.* 5, 9899. doi:10.1038/srep09899
- Shannon, C. E. (1948). A mathematical theory of communication. *Bell Syst. Tech. J.* 27, 379–423. doi:10.1002/j.1538-7305.1948.tb01338.x
- Singh, P., Sharma, A., Sur, U., and Rai, P. K. (2021). Comparative landslide susceptibility assessment using statistical information value and index of entropy model in Bhanupali-Beri region, Himachal Pradesh, India. *Environ. Dev. Sustain* 23, 5233–5250. doi:10.1007/s10668-020-00811-0
- Sørensen, R., Zinko, U., and Seibert, J. (2006). On the calculation of the topographic wetness index: Evaluation of different methods based on field observations. *Hydrol. Earth Syst. Sci.* 10, 101–112. doi:10.5194/hess-10-101-2006
- Stanley, T. A., Kirschbaum, D. B., Benz, G., Emberson, R. A., Amatya, P. M., Medwedeff, W., et al. (2021). Data-driven landslide nowcasting at the global scale. *Front. Earth Sci. (Lausanne)* 9. doi:10.3389/feart.2021.640043
- Thanh, L. N., Fang, Y.-M., Chou, T.-Y., Hoang, T.-V., Nguyen, Q. D., Lee, C.-Y., et al. (2022). Using landslide statistical index technique for landslide susceptibility mapping: Case study: Ban khoeang commune, Lao cai province, vietnam. *Water (Basel)* 14, 2814. doi:10.3390/w14182814
- Tian, Y., Xiao, C., Liu, Y., and Wu, L. (2008). Effects of raster resolution on landslide susceptibility mapping: A case study of shenzhen. *Sci. China, Ser. E Technol. Sci.* 51, 188–198. doi:10.1007/s11431-008-6009-y
- Titti, G., van Westen, C., Borgatti, L., Pasuto, A., and Lombardo, L. (2021). When enough is really enough? On the minimum number of landslides to build reliable susceptibility models. *Geosci. Switz.* 11, 469. doi:10.3390/geosciences11110469
- Tyagi, A., Kamal Tiwari, R., and James, N. (2022). A review on spatial, temporal and magnitude prediction of landslide hazard. *J. Asian Earth Sci. X* 7, 100099. doi:10.1016/j.jaesx.2022.100099

- Van Den Eeckhaut, M., and Hervás, J. (2012). State of the art of national landslide databases in Europe and their potential for assessing landslide susceptibility, hazard and risk. *Geomorphology* 139–140, 545–558. doi:10.1016/j.geomorph.2011.12.006
- Wang, B., and Zhang, S. (2018). A subjective and objective integration approach of determining weights for trustworthy measurement. *IEEE Access* 6, 25829–25835. doi:10.1109/ACCESS.2018.2829622
- Wang, S., Lin, X., Qi, X., Li, H., and Yang, J. (2022). Landslide susceptibility analysis based on a PSO-DBN prediction model in an earthquake-stricken area. *Front. Environ. Sci.* 10. doi:10.3389/fenvs.2022.912523
- Wang, W. D., Guo, J., Fang, L. G., and Chang, X. S. (2012). A subjective and objective integrated weighting method for landslides susceptibility mapping based on GIS. *Environ. Earth Sci.* 65, 1705–1714. doi:10.1007/s12665-011-1148-z
- Wang, Y., Feng, L., Li, S., Ren, F., and Du, Q. (2020). A hybrid model considering spatial heterogeneity for landslide susceptibility mapping in Zhejiang Province, China. *Catena (Amst)* 188, 104425. doi:10.1016/j.catena.2019.104425
- Yalcin, A. (2008). GIS-based landslide susceptibility mapping using analytical hierarchy process and bivariate statistics in Ardesen (Turkey): Comparisons of results and confirmations. *Catena (Amst)* 72, 1–12. doi:10.1016/j.catena.2007.01.003
- Yong, C., Jinlong, D., Fei, G., Bin, T., Tao, Z., Hao, F., et al. (2022). Review of landslide susceptibility assessment based on knowledge mapping. *Stoch. Environ. Res. Risk Assess.* 36, 2399–2417. doi:10.1007/s00477-021-02165-z
- Zanaga, D., Van De Kerchove, R., Daems, D., De Keersmaecker, W., Brockmann, C., Kirches, G., et al. (2022). ESA WorldCover 10 m 2021 v200. doi:10.5281/ZENODO.7254221
- Zêzere, J. L., Pereira, S., Melo, R., Oliveira, S. C., and Garcia, R. A. C. (2017). Mapping landslide susceptibility using data-driven methods. *Sci. Total Environ.* 589, 250–267. doi:10.1016/j.scitotenv.2017.02.188
- Zhang, S., Bai, L., Li, Y., Li, W., and Xie, M. (2022). Comparing convolutional neural network and machine learning models in landslide susceptibility mapping: A case study in wenchuan county. *Front. Environ. Sci.* 10. doi:10.3389/fenvs.2022.886841
- Zhou, S., Chen, G., Fang, L., and Nie, Y. (2016). GIS-based integration of subjective and objective weighting methods for regional landslides susceptibility mapping. *Sustain. Switz.* 8, 334. doi:10.3390/su8040334
- Zhu, A. X., Miao, Y., Wang, R., Zhu, T., Deng, Y., Liu, J., et al. (2018). A comparative study of an expert knowledge-based model and two data-driven models for landslide susceptibility mapping. *Catena (Amst)* 166, 317–327. doi:10.1016/j.catena.2018.04.003



OPEN ACCESS

EDITED BY

Sandipan Das,
Symbiosis International University, India

REVIEWED BY

Zerouali Bilel,
University of Chlef, Algeria
Sajjad Hussain,
COMSATS Institute of Information
Technology, Pakistan

*CORRESPONDENCE

Waheed Ullah,
✉ wullah@ra.ac.ae,
Shibiao Bai,
✉ shibiaobai@njnu.edu.cn

RECEIVED 02 March 2023

ACCEPTED 27 June 2023

PUBLISHED 06 July 2023

CITATION

Rahman ZU, Ullah W, Bai S, Ullah S,
Jan MA, Khan M and Tayyab M (2023),
GIS-based flood susceptibility mapping
using bivariate statistical model in Swat
River Basin, Eastern Hindukush
region, Pakistan.
Front. Environ. Sci. 11:1178540.
doi: 10.3389/fenvs.2023.1178540

COPYRIGHT

© 2023 Rahman, Ullah, Bai, Ullah, Jan,
Khan and Tayyab. This is an open-access
article distributed under the terms of the
[Creative Commons Attribution License](#)
(CC BY). The use, distribution or
reproduction in other forums is
permitted, provided the original author(s)
and the copyright owner(s) are credited
and that the original publication in this
journal is cited, in accordance with
accepted academic practice. No use,
distribution or reproduction is permitted
which does not comply with these terms.

GIS-based flood susceptibility mapping using bivariate statistical model in Swat River Basin, Eastern Hindukush region, Pakistan

Zahid Ur Rahman^{1,2}, Waheed Ullah^{3*}, Shibiao Bai^{4*}, Safi Ullah^{5,6},
Mushtaq Ahmad Jan⁷, Mohsin Khan⁸ and Muhammad Tayyab⁹

¹Key Laboratory of Digital Earth Science, Aerospace Information Research Institute, Chinese Academy of Sciences, Beijing, China, ²University of Chinese Academy of Sciences, Beijing, China, ³Defense and Security, Rabdan Academy, Abu Dhabi, United Arab Emirates, ⁴College of Marine Science and Engineering, Jiangsu Center for Collaborative Innovation in Geographical Information Resource Development and Application, Nanjing Normal University, Nanjing, China, ⁵Environmental Science and Engineering Program, Biological and Environmental Science and Engineering Division, King Abdullah University of Science and Technology (KAUST), Thuwal, Saudi Arabia, ⁶Climate and Livability Initiative (CLI), King Abdullah University of Science and Technology (KAUST), Thuwal, Saudi Arabia, ⁷Centre for Disaster Preparedness and Management (CDPM), University of Peshawar, Peshawar, Pakistan, ⁸Department of Biological Sciences, Ohio University, Athens, OH, United States, ⁹Institute of Natural Disaster Research, School of Environment, Northeast Normal University, Changchun, China

Frequent flooding can greatly jeopardize local people's lives, properties, agriculture, economy, etc. The Swat River Basin (SRB), in the eastern Hindukush region of Pakistan, is a major flood-prone basin with a long history of devastating floods and substantial socioeconomic and physical damages. Here we produced a flood susceptibility map of the SRB, using the frequency ratio (FR) bivariate statistical model. A database was created that comprised flood inventory as a dependent variable and causative factors of the flood (slope, elevation, curvature, drainage density, topographic wetness index, stream power index, land use land cover, normalized difference vegetation index, and rainfall) as independent variables and the association between them were quantified. Data were collected using remote sensing sources, field surveys, and available literature, and all the studied variables were resampled to 30 m resolution and spatially distributed. The results show that about 26% of areas are very high and highly susceptible to flooding, 19% are moderate, whereas 55% are low and very low susceptible to flood in the SRB. Overall, the southern areas of the SRB were highly susceptible compared to their northern counterparts, while slope, elevation, and curvature were vital factors in flood susceptibility. Our model's success and prediction rates were 91.6% and 90.3%, respectively, based on the ROC (receiver operating characteristic) curve. The findings of this study will lead to better management and control of flood risk in the SRB region. The study's findings can assist the decision-makers to make appropriate sustainable management strategies for the mitigation of future damage in the study region.

KEYWORDS

flood susceptibility map, frequency ratio (FR) model, Swat River Basin (SRB), eastern Hindu Kush region, Pakistan

1 Introduction

Floods are considered the major natural disasters globally, posing significant threats to human lives, livelihoods, properties as well as socio-cultural heritage (Billa et al., 2006; Samanta S. et al., 2018b; Rentschler et al., 2022; Shen et al., 2022; Liu et al., 2023). The number of major flood disasters in the last three decades was more pronounced indicating climate change (Sarkar and Mondal, 2020; Tariq et al., 2023). Flooding causes more than 2,000 deaths annually and affects over 75 million people worldwide in different ways (Zou et al., 2013; Rentschler et al., 2022; Abbas et al., 2023).

Pakistan is among the worst climate change-affected countries, experiencing extreme hydrometeorological events (Bhatti et al., 2020; Abbas et al., 2022; Baqa et al., 2022). The recent catastrophic flooding events are the eye-witness of climate change in Pakistan (Khan I. et al., 2022a; Shah et al., 2023). The country has witnessed approximately 25 devastating floods between 1950 and 2020 that killed more than 9,088 people with a total estimated loss of 20 billion USD (Khan et al., 2021; Ahmed et al., 2023). Pakistan was struck by one of the most devastating floods in its history in 2010 due to brutal monsoon precipitation that caused substantial damages across the country (Gaurav et al., 2011; Khan et al., 2016; Farooq et al., 2019), affecting around 20 million people in 78 districts, and killed 1,985 people causing an estimated 9.7 billion USD loss to Pakistan's economy (F. Ullah et al., 2021; Ahmed et al., 2023).

In 2012, heavy monsoon rains triggered floods in major parts of the country, including the Khyber Pakhtunkhwa, Upper Sindh, Southern Punjab, and Balochistan provinces (Saeed et al., 2021; Shah et al., 2023). Following these devastating flooding events, the country was struck by catastrophic flash flooding in August 2013 (Butt et al., 2020). In the recent monsoon floods of 28 August 2022, Pakistan suffered 1,033 deaths, 949,858 people were affected, over 450,000 residential structures were damaged, 149 bridges were destroyed, and 110 districts were affected (Crisis24, 2022; NDMA, 2022; PMD, 2022; ReliefWeb, 2022). Overall, Pakistan faced about 6 major floods in the last 12 years, i.e., 2010, 2011, 2012, 2013, 2020, and 2022, highlighting Pakistan's vulnerability to climate extremes (Ahmed et al., 2023; Majeed et al., 2023).

Although flooding is inevitable and hard to avoid, appropriate analysis and susceptibility mapping techniques can assess and manage future floods (Hussain et al., 2021; Henao and Nájera, 2022). Depending upon the flood's nature, different information and techniques are required for its assessment and management. These include information from hydrological, meteorological, geomorphological, and socioeconomic sectors. Consequently, flood susceptibility maps are drawn that greatly assist in flood mitigation and planning by providing regional planners and decision-makers with a better understanding of flood attributes thus, ensuring a sustainable and safe future (Youssef et al., 2016; Mahmood and Rahman, 2019; Hussain et al., 2021). Identifying flood-prone locations and mapping the flood hazard areas is key to its management and/or timely prevention (Hussain et al., 2023b). Alternatively, selecting areas that have less exposure to flooding may be an indication of ideal regions for residency and operation development (Hizbaron et al., 2021).

A plethora of research has been done, which indicates that accurate flood risk assessment and modeling can help decision-

makers in the development of sustainable risk reduction strategies (Arnell and Gosling, 2016; Dawood et al., 2021; Malik et al., 2021) and used both qualitative and quantitative techniques for flood susceptibility assessment and mapping. Likewise, Saeed et al. (2021) used Artificial Neural Network (ANN) algorithm to effectively determine flood-inundated areas in Peshawar Vale with nine geospatial flood causative factors. A study conducted by Khoirunisa et al. (2021) used a GIS-based artificial neural network (GANN) model based on a Back-Propagation Neural Network (BPNN) to provide flood susceptibility; the proposed method provided good accuracy in predicting flood susceptibility of Keelung City, Taiwan. To model and simulate flood-prone regions of the Johor River Basin, Malaysia, Kia et al. (2012) also attempted to construct a flood model considering seven flood causative factors utilizing ANN approaches and geographic information systems (GIS). Similarly, Ahmadlou et al. (2019) utilized an adaptive neuro-fuzzy interface system (ANFIS) for flood susceptibility assessment in contrast with biogeography-based optimization (BBO) and BAT algorithms. McGrath and Gohl, (2022) also stressed the impact of meteorological variables on flood vulnerability mapping using machine learning approaches. Moreover, Liu et al. (2021) proposed a hybrid model by integrating fuzzy membership value (FMV) and three machine learning models of convolutional neural network (CNN), classification and regression trees (CART), and support vector machine (SVM) for flood assessment. In another study, Ha et al. (2022) combined machine learning (ML) and analytical hierarchy process (AHP) techniques to analyze and map flood hazards, vulnerabilities, and risks in Quang Binh province, Vietnam. Recently, Liu et al. (2023) utilized a hybrid approach, combining ResNet-18 and a hydrological model based on remote sensing data, to create a map of global flood susceptibility; Majeed et al. (2023) applied an integrated algorithm, combining the AHP technique and frequency ratio (FR) model to predict susceptibility to flash floods. The AHP, relative frequency ratio (RFR), ANFIS, fuzzy variable theory, logistic regression, ANN, Shannon's entropy, and others are notable among them. Irrespective of their inherent pros and cons, the performance of each technique is dependent on the selected variables as well as the case study (Tehrany et al., 2014; Hong et al., 2018; Kadam et al., 2018; Ahmed et al., 2023). In addition, advanced GIS and remote sensing (RS) techniques are prominently used for flood hazard calculation and risk analysis modeling (Ali et al., 2016; Khoirunisa et al., 2021; Tayyab et al., 2021).

GIS and RS are emerging tools that provide various types of advanced data access and manipulation tools for flood susceptibility mapping and its forecast with proper justification (Vojtek and Vojteková, 2019; Rehman et al., 2022). Both GIS and RS images can assist in assessing flood regions and are effective tools for creating land use/land cover (LULC) maps and detecting their changes (Feloni et al., 2020). This technology makes an incredibly wonderful environment in which various models can run and modify data to assess the impacts of flooding with coherent and logical outcomes (Khosravi et al., 2016a). Moreover, these techniques provide an authentic and simple way to prepare flood susceptibility maps using the FR model (Sarkar and Mondal, 2020; Islam et al., 2022). The FR model is a profoundly satisfactory method for highly precise hazard evaluation (Althuwaynee et al., 2014; Ullah and Zhang, 2020; Majeed et al., 2023). Rehman et al. (2022) and Shu

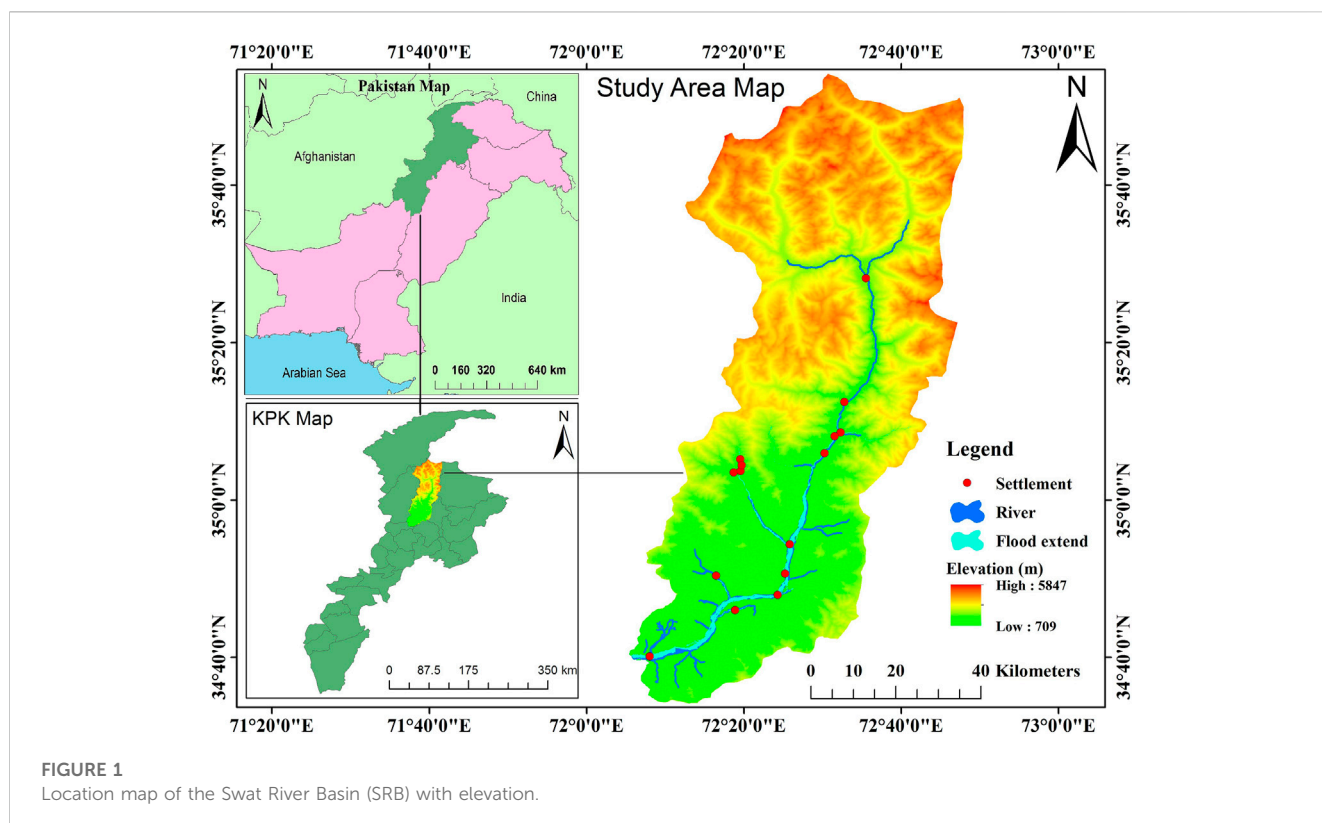


FIGURE 1
Location map of the Swat River Basin (SRB) with elevation.

et al. (2021) define FR as the probability of occurrence of a phenomenon concerning the absence of a phenomenon. The FR model is a bivariate statistical model that gives weightage to every factor class of each variable and assesses its effects on flood occurrence (Jebur et al., 2014; Ullah and Zhang, 2020; Shah et al., 2023). It is a foremost well-known bivariate statistical approach to determine the flood hazard zones (Ullah and Zhang, 2020; Rehman et al., 2022) and potential landslide zones (Wang et al., 2020; Islam et al., 2022) based on the relationship between their inventory (dependent) and causative factors (independent). As a simple and widespread bivariate statistical method, the FR model is commonly used in many research fields, including geosciences, hazards and disaster management, physical sciences, environmental sciences, etc., (Althuwaynee et al., 2014; Arabameri et al., 2019; Rehman et al., 2022; Majeed et al., 2023). Therefore, it is imperative to assess the degree of vulnerability to flood hazards and develop a flood susceptibility map to reduce the potential risks of floods in the future. It is worth mentioning that flood susceptibility maps are also useful for policymakers and planners to formulate flood risk management plans (Kia et al., 2012; Esteves, 2013; Haghizadeh et al., 2017).

Swat River Basin (SRB) is experiencing frequent and intense floods due to climatic variations and diverse topography. Over the past few decades, this region has witnessed several catastrophic flooding events, including the historic 2010 and 2022 floods (Figure 1). However, it is worth stating that a very limited number of studies on flood susceptibility assessment and/or flood management have been conducted in the SRB. Considering the SRB's vulnerability and exposure to flood hazards, there is an urgent need for flood susceptibility mapping using advanced techniques and models.

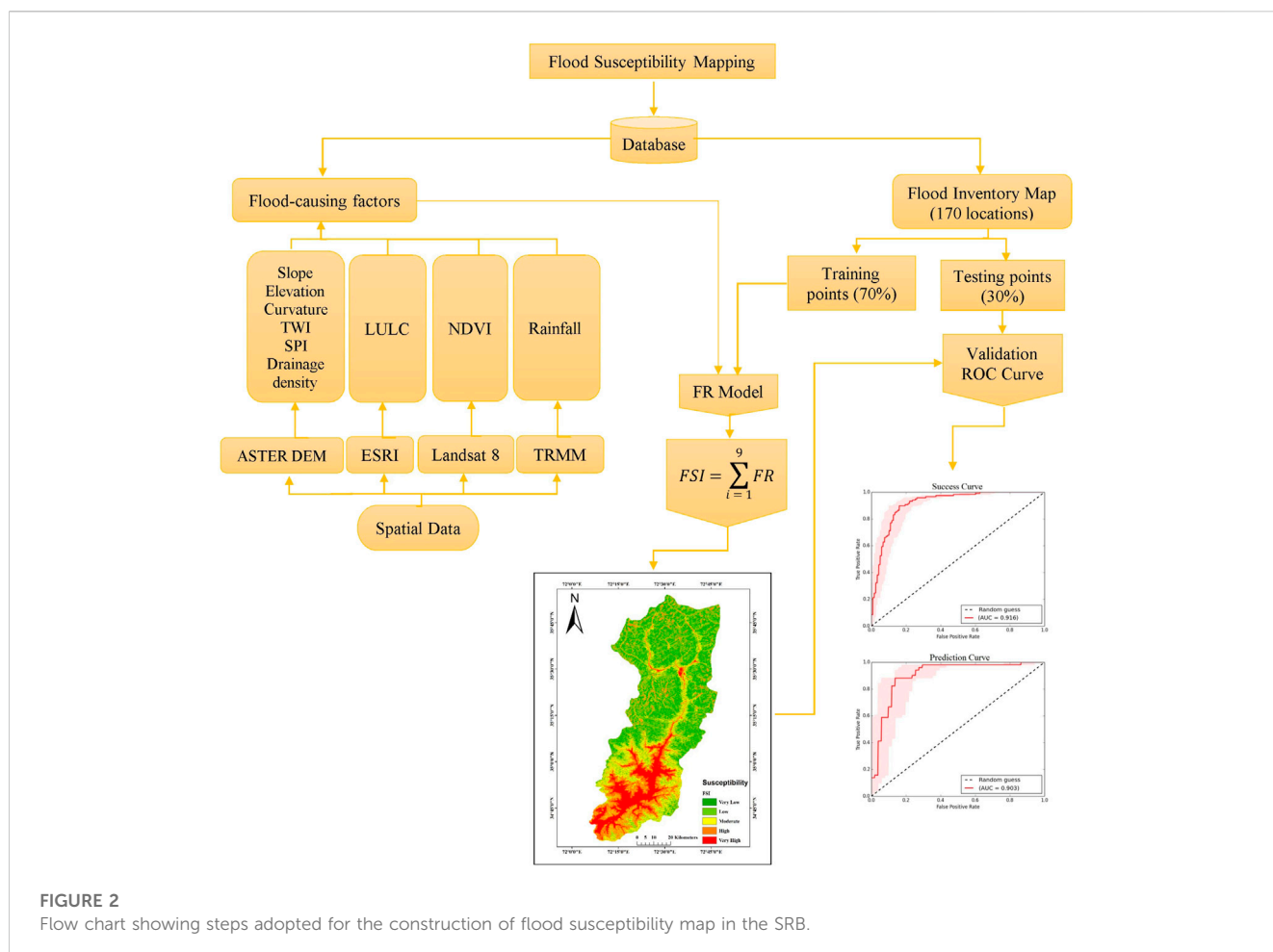
Here we aimed to construct the first-ever flood susceptibility mapping of the SRB, in the eastern Hindu Kush region of Pakistan through a GIS-based FR model. Moreover, the study determined the relative contributions of the selected flood-causing factors in exacerbating the susceptibility of the region to flooding. The study also evaluated the efficiency of the FR bivariate statistical model in mapping the flood susceptibility of the SRB. We believe that our study could provide valuable information to the relevant stakeholders for effective flood risk management and sustainable development.

2 Materials and methods

An integrated approach is adopted to construct a flood susceptibility map for the SRB, eastern Hindu Kush region, Pakistan. The flood susceptibility map was developed by integrating remote sensing and field data on flood causal factors. The overall methodology consists of seven main steps (Figure 2). These include; 1) study area, 2) data collection and analysis, 3) flood inventory map, 4) flood-causing factors, 5) frequency ratio (FR) model, 6) flood susceptibility mapping, and 7) receiver operating characteristic (ROC) technique. All these steps are discussed in detail in the following sections.

2.1 Study area

This study covers the SRB, located in the eastern Hindu Kush region of Pakistan, with geographical coordinates of 34° 35' 60" and



35° 43'52" north latitudes and 72° 08'53" and 72° 30'50" east longitudes (Khan W. et al., 2022; Islam et al., 2022). The region covers a total area of 5,065.28 km² (Nasir et al., 2020; Islam et al., 2022). Across the basin, the northern parts contain high snow-covered mountains featuring rough territory, while the southern parts are rather plain having farmland along the riverbank. The precipitation pattern in the high-altitude northern region is influenced by winter precipitation received from the Mediterranean Sea mainly in the form of snow (Ullah et al., 2018; Rebi et al., 2023), whereas, the lower southern region is dominated by summer monsoon rainfall (Khan et al., 2020; W; Ullah et al., 2021). Extremely low winter temperatures facilitate snow and glacier accumulation while the melting of snow and glaciers is triggered by high summer temperatures (Hussain et al., 2023a; Rahman et al., 2019; S; Ullah et al., 2019a; b, 2023).

River Swat originates from the Hindu Kush Mountains and generally flows from the northern high-elevated areas to the southern plains (Ahmad et al., 2018; Farooq et al., 2019; Dawood et al., 2021; Islam et al., 2022). At Kalam, the river Ushu and river Gabral converge into river Swat, which flows down through the entire Swat District, joining River Panjkora in District Dir Lower, and finally outflows into the River Kabul at Nisatta, District Charsadda. Geomorphologically, the river channel is steep in the northern area and gentle in the southern part. Due to the physical terrain, flash floods dominate the upstream areas, and river floods in

the gently sloping low-lying areas of the basin (Mahmood and Rahman, 2019; Rahman et al., 2019; Nasir et al., 2020) such as (Figure 1).

The approximate altitude of the basin in the northern area is 5800 m which gradually decreases up to 710 m downstream at Shamoza valley. Swat River is a natural living space for fish and birds and a wellspring of irrigation and electric power generation. Currently, three hydroelectric power plants with a total 123 MW capacity are operational on water from the river Swat and one more hydroelectric power plant with a capacity of 740 MW of electricity is under construction (Dawood et al., 2021). The region experiences disastrous floods almost yearly, especially in the monsoon season between June and September. Climate change, complex topography, and socioeconomic vulnerability in the region intensify the risk of flooding in the study area (Rahman et al., 2019; Dawood et al., 2021).

SRB is one of the major flood-prone basins in Pakistan (Ahmad et al., 2015; Nasir et al., 2020). The diverse climatic conditions, complex topography, and fragile socioeconomic conditions have exacerbated the risk of flooding in the region (Mahmood and Rahman, 2019). The region has a long history of devastating floods, which caused substantial socioeconomic and physical damages (Khan et al., 2021). In 2010, the monsoon system caused heavy rainfalls, leading to disastrous floods in various tributaries of the Swat, ultimately destroying whatever stood in its path (Butt et al., 2020; Hussain et al., 2021). The deadly water surge started in the mountainous region, while the peculiar terrain of the

TABLE 1 Types of data and their sources.

S. No	Type of data	Source of extracted data	Extracted data
I	Flood historical data	NDMA, PDMA, and Irrigation Department	Literature
II	ASTER DEM (Grid) 30 m × 30 m resolution	NASA's official website https://search.earthdata.nasa.gov	Hillshade, Slope, Elevation, Curvature, Drainage Density, and TWI
III	LULC data (Grid) 10 m × 10 m resolution	ESRI 2020 data, https://livingatlas.arcgis.com/landcover/	Land use/land cover map
IV	Landsat8 Imagery (band5, band4)	USGS official website https://earthexplorer.usgs.gov	NDVI map
V	Precipitation (TRMM data)	NASA's official website https://giovanni.gsfc.nasa.gov/giovanni/	Rainfall map

valley gave this surge an enormous force that destroyed infrastructure, human settlements, buildings, cropped lands, irrigation networks highways, and bridges, and made communication inaccessible (Tehrany et al., 2014; Farooq et al., 2019). It has been reported that in the 2010 floods, a total of 2,751 families were displaced, 988 houses and 26 water channels were completely or partially damaged in the region (Butt et al., 2020). Similarly, on 29 August 2020, a heavy rainfall-induced flash flood in the Shagram torrent of the SRB, resulted in the deaths of at least 14 people coupled with complete or partial damages to 45 houses, and over 3 bridges (Nasir et al., 2020). Despite the frequent and intense occurrence of flooding in the SRB, no suitable measures have been taken in the region so far to hinder or reduce the losses from flood hazards.

2.2 Data collection and analysis

To develop a flood susceptibility map of the SRB, various types of data were collected from several government agencies and official web sources, as outlined in Table 1. Literature and historical flood data were collected from the National Disaster Management Authority (NDMA), Pakistan, Provincial Disaster Management Authority (PDMA), Khyber Pakhtunkhwa, and Regional Irrigation Department Swat. The Advanced Spaceborne Thermal Emission and Reflection Radiometer Digital Elevation Model (ASTER DEM) with a 30 m spatial resolution was obtained from the official website of the National Aeronautics and Space Administration (NASA) (www.search.earthdata.nasa.gov). Land use/land cover (LULC) imagery was downloaded from the Environmental Systems Research Institute (ESRI) 2020 LULC data. Landsat 8 (OLI) imagery was obtained from the official website of the United States Geological Survey (USGS) (<https://earthexplorer.usgs.gov>), and the average annual rainfall of the case study was obtained using the Tropical Rainfall Measuring Mission (TRMM) data, which were retrieved from the NASA official website (<https://gpm.nasa.gov/data>) (S. Ullah et al., 2018; W; Ullah et al., 2019; Arshad et al., 2021). The amalgamation and analysis of these multiple data sources facilitated the creation of the flood susceptibility map of the SRB.

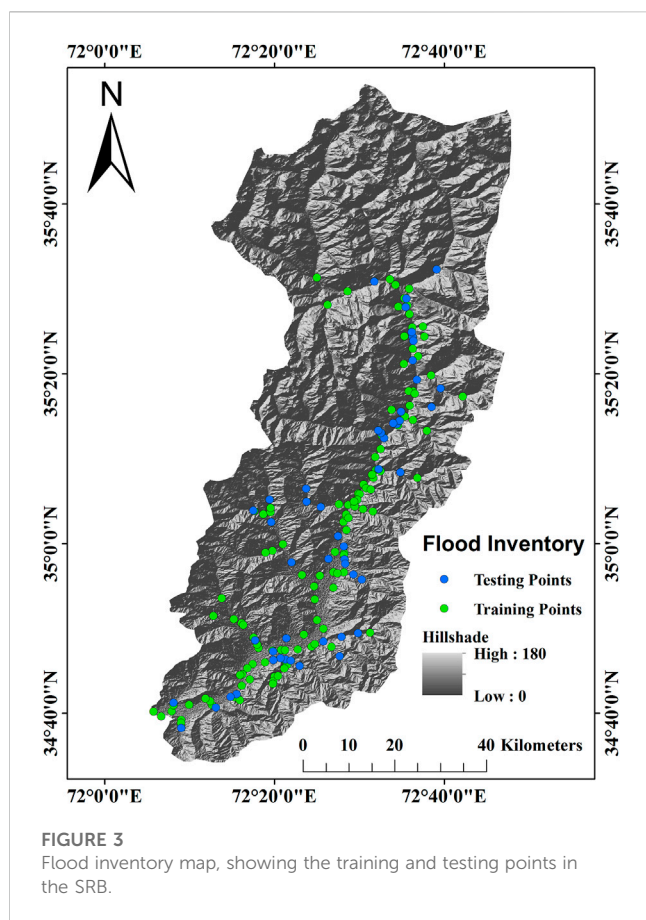
2.3 Flood inventory map

To study the correlation between flood-causing factors and flood occurrence, a database of historical floods and their damages is very

important (Kia et al., 2012; Liu et al., 2021). Appropriate data with high accuracy are vital to constructing the flood inventory mapping (Tehrany et al., 2015; Ullah and Zhang, 2020). In the current study, a flood inventory map was prepared with a total of 170 flood-affected locations identified in the whole SRB through a field survey using handheld GPS and satellite imagery. The points of inundation were validated with historical flood data and previous reports of NDMA Pakistan, PDMA Khyber Pakhtunkhwa, and Regional Irrigation Department Swat, Pakistan. The flood-affected locations were divided into 51 (30%) testing points and 119 (70%) training points using the geo-statistical tool in ArcGIS 10.2.2 (Figure 3). The training points were randomly used for the development of the model whereas; the efficiency of the model was validated with the testing points.

2.4 Flood-causing factors

To build a comprehensive strategy for assessing flood susceptibility, it is critical to determine the impact and linkage between flood-causing factors and flood occurrence (Wang et al., 2018; El-Magd, 2019; Khoirunisa et al., 2021; Ha et al., 2022). It should be noted that various natural and anthropogenic factors, which cause floods in a specific region and the same factors may not be effective for another region. Therefore, to get reliable results, the selection of relevant factors is extremely important (Tehrany et al., 2015; Zhao et al., 2022). A total of nine flood-causing factors were selected due to their critical roles in causing flooding in the study region (Ullah and Zhang, 2020; Saeed et al., 2021). These factors include; slope, elevation, curvature, drainage density, topographic wetness index (TWI), stream power index (SPI), LULC, normalized difference vegetation index (NDVI), and rainfall. These selected factors have been used by various studies to assess the relationship between flood-causing factors and flood occurrence in the study area and other regions (Samanta S. et al., 2018; Sarkar and Mondal, 2020; Thongley and Vansarochana, 2021). All flood-causing variables were changed into raster maps and resampled with 30 m × 30 m resolution (pixel) (Jensen, 2005; Sabatakakis et al., 2013). The selected factors were reclassified for FR analysis using the popular natural breaks (Jenks) method by reclassifying (spatial analyst) tools in ArcGIS 10.2 (Ullah and Zhang, 2020; Majeed et al., 2023). The selected flood-causing factors are discussed one by one below.



2.4.1 Slope

The slope is one of the most important factors in hydrological studies because it controls surface runoff and water flow intensity that incites soil erosion and vertical infiltration process (Tehrany et al., 2015; Khosravi et al., 2016b). The area with a higher slope gradient has low exposure to flooding while the area with a low slope gradient is highly exposed to flooding (Liuzzo et al., 2019). We derived a slope map from the ASTER DEM of 30 m resolution utilizing the slope tool in ArcGIS and categorized it into five sub-classes ranging from 0°–75.74° (Figure 4A).

2.4.2 Elevation

The elevation is a prime factor in flood vulnerability assessment (Rahmati et al., 2016; Das, 2019; Shen et al., 2021). Usually, water flow is from high-altitude areas towards low-altitude areas, so low-lying areas may get flooded rapidly. The probability of flooding is higher in low-elevated areas as compared to the areas of high elevation (Das, 2018; Liuzzo et al., 2019; Elkhachy, 2022). The elevation map of the SRB was prepared from the ASTER DEM using spatial analyst tools in the ArcGIS environment and split into five categories. As shown in Figure 4B, the altitude of the study area ranges from 709 to 5,847 m above mean sea level.

2.4.3 Curvature

Curvature is another extremely necessary factor for flood mapping. Curvature is the rate at which gradients change in a specific direction, and the values indicate the morphological feature

of topography (Wang et al., 2015; M Amen et al., 2023). The curvature map of the SRB was prepared from the ASTER DEM and divided into three classes; concave, flat, and convex (Figure 4C). A negative value is allocated to upward concave curvature, a zero value is allocated to the flat surface whereas, a positive value indicates a convex curvature (Charlton et al., 2006; Ullah and Zhang, 2020). Areas of zero values (flat surface) are most exposed to flooding as compared to the convex and concave curvature (Nachappa et al., 2020).

2.4.4 Drainage density

Drainage density is characterized as the entire length of the waterways and streams in a river basin divided by the whole area of the basin (Rahmati et al., 2016). Areas of higher drainage density have greater chances of flooding whereas; areas of lower drainage density have fewer chances of flooding (Paul et al., 2019). Drainage density measures how well and how poorly the basin is drained by streams. To calculate the drainage density of the SRB, the stream order was taken from the ASTER DEM through the line density tool in the ArcGIS environment and classified into five classes utilizing the natural break (Jenks) tool (Figure 4D). The following equation (Eq. (1)) was used to calculate the drainage of the SRB.

$$Dd = \frac{\sum L}{A} \quad (1)$$

Where drainage density is denoted by Dd , the length of waterways is signified by L , and the total area of the basin is signified with symbol A .

2.4.5 Topographic wetness index (TWI)

The topographic wetness index (TWI) is another important factor for flood susceptibility mapping. TWI has a direct relationship with flood vulnerability (Chapi et al., 2017; Costache, 2019). The region with high TWI is more vulnerable to flooding whereas, the region with low TWI is less vulnerable to flooding (Paul et al., 2019). The TWI was calculated from the ASTER DEM with the following formula (Eq. 2).

$$TWI = \ln \left(\frac{AS}{\tan(\beta)} \right) \quad (2)$$

Where the upstream contributing area is denoted by AS and the gradient of the slope is denoted by β . The final TWI map was divided into five classes ranging from 1.96 to 19.73 (Figure 4E).

2.4.6 Stream power index (SPI)

The stream power index (SPI) refers to an estimate of the erosional power of water flows in a catchment area (Jebur et al., 2014; Wang et al., 2023). A greater distance to the stream and a lower SPI increases the chances of flood occurrence (Tehrany et al., 2014; Wang et al., 2023). The SPI map was constructed with the given equation (Eq. 3).

$$SPI = AS \tan \beta \quad (3)$$

Similar to TWI, the upstream drainage area is denoted by AS , and the slope gradient (in degrees) is denoted with β . The SPI map of the case study was prepared in the ArcGIS environment and split into five classes ranging from –13.82 to 14.54 (Figure 4F).

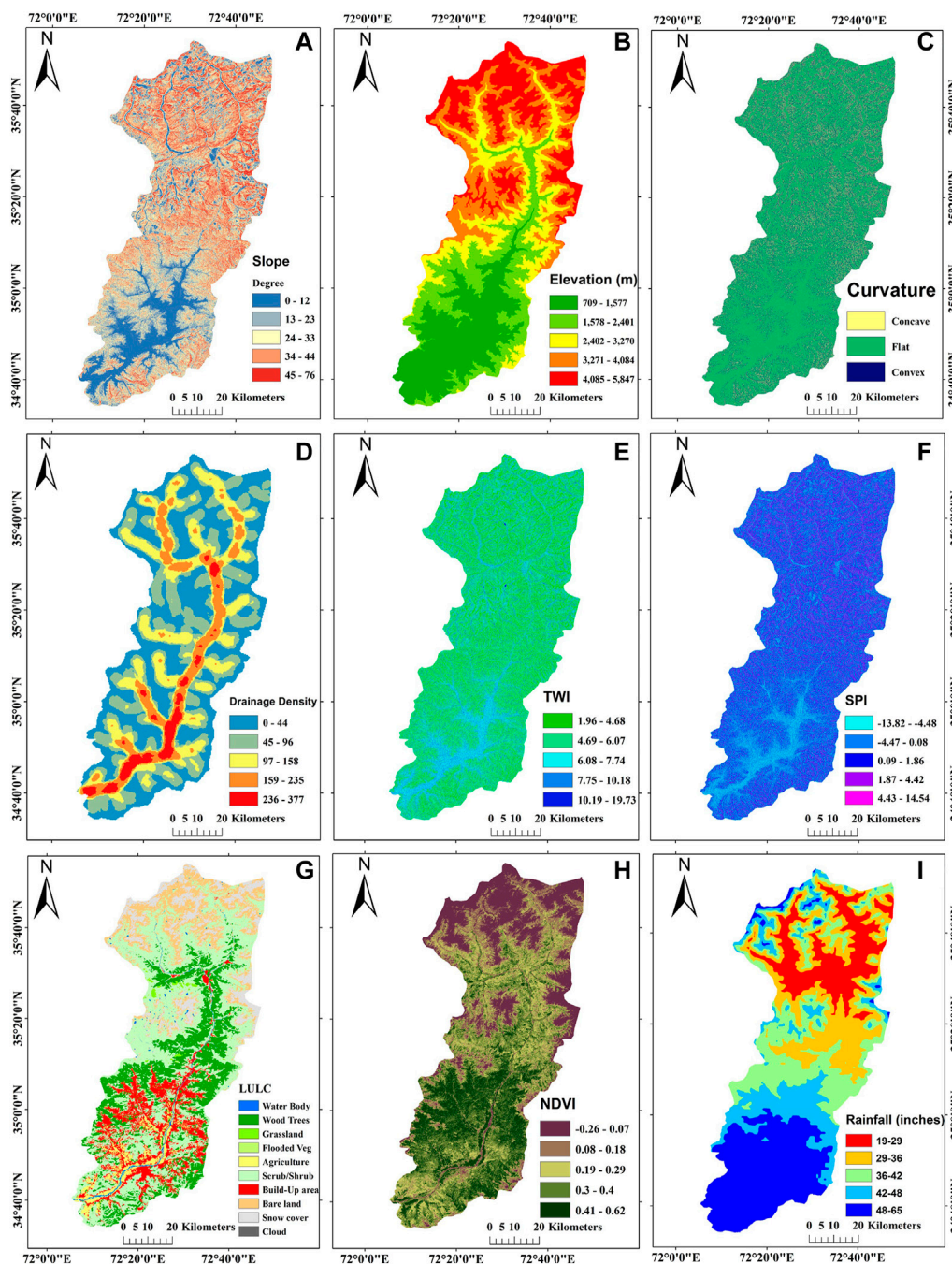


FIGURE 4

Spatial distributions of the flood-causing factors in the SRB; (A) Slope, (B) Elevation, (C) Curvature, (D) Drainage density, (E) TWI, (F) SPI, (G) LULC, (H) NDVI, and (I) Rainfall.

2.4.7 Land use/land cover (LULC)

Land use/land cover (LULC) is vital in producing water runoff and causing floods in a catchment area (Khosravi et al., 2016b; Das, 2019; Riazi et al., 2023). The strong nexus between LULC and flooding is unquestionable since land use and land cover have their influence on increasing or reducing the flow of water (Samanta S. et al., 2018; Hussain et al., 2021). The LULC data were collected from the ESRI 2020 data source of global land use and land cover published in July 2021 (Arenu-Rangel et al., 2019; Karra et al.,

2021; Tariq and Mumtaz, 2022). The LULC data were classified into ten classes, namely, water bodies, wood trees, grassland, flooded vegetation, agriculture, scrub/shrub, built-up area, barren land, snow cover, and clouds (Figure 4G).

2.4.8 Normalized difference vegetation index (NDVI)

Normalized difference vegetation index (NDVI) is another main ecological flood-causing factor. The normal value of the NDVI is

ranging from -1 to $+1$ (Khosravi et al., 2016b; Riazi et al., 2023). The positive NDVI value is considered active vegetation coverage like dense forest, the value close to zero represents barren areas, while the negative values are referred to the water body (Wang et al., 2020; Ziwei et al., 2023). For the preparation of the NDVI map, satellite data were collected from the Landsat 8 collection 1, of the USGS department, and the value was calculated with the following formula (Eq. 4).

$$NDVI = \frac{NIR - Red}{NIR + Red} \quad (4)$$

Where the *NIR* represents near-infrared light and the *Red* is the visible light. The NDVI map of the SRB was categorized into five sub-categories ranging from -0.26 to 0.62 using the natural break tool (Figure 4H).

2.4.9 Rainfall

Heavy rainfall is a common flood-triggering factor. According to Liuzzo et al. (2019) and Paul et al. (2019), rainfall has a direct relationship with flood hazards. For rainfall map preparation, the TRMM data were downloaded for the period 2000–2020 (Arshad et al., 2021; W; Ullah et al., 2021). The rainfall map of the SRB was classified into five sub-classes (Figure 4I). Since the TRMM data have performed well over different climatic regions of Pakistan, including the study region (Arshad et al., 2021); therefore, we preferred the use of this dataset over other gridded precipitation products.

2.5 Frequency ratio (FR) model

Flood susceptibility mapping is the foremost important method to identify the high-risk zone and the factors-affecting floods in a river basin. Flood is triggered by natural and socioeconomic factors and it is usual to assume that future floods will be caused by the same causative factors as the previous floods (Tehrany et al., 2013; Kadam et al., 2018; Moazzam et al., 2018). The FR model is a quantitative bivariate statistical analysis technique commonly used for flood and landslide susceptibility mapping (Tehrany et al., 2015; Islam et al., 2022). The FR model shows the spatial relationship between flood inventory (dependent factors) and flood-causing factors (independent factors). In the current study, the FR bivariate statistical model was used to prepare the flood susceptibility map of the SRB. The FR value of each factor was calculated by determining the quantitative relationship of independent factors with respect to flood occurrence (Pradhan and Lee, 2010; Khosravi et al., 2016a; Ahmadi et al., 2019). When the FR weightage is more than 1, it indicates a strong correlation whereas, when the weightage is below 1, it shows a weak correlation between dependent and independent factors (Pradhan and Lee, 2010; Akgun et al., 2012; Rehman et al., 2022). The FR is characterized as the percent of the flood locations within the factor class divided by the percentage of individual class areas. The FR model was calculated with the following Eq. 5.

$$FR = \frac{FP/P}{FA/A} \quad (5)$$

Where *FP* is the flood point in factor class, *P* is the total flood Points, *FA* is the factor class area, and *A* is the total area.

After that, the RF was calculated to normalize the FR in probability ranges (0, 1) using the following Eq. 6.

$$RF = \frac{FR \text{ of factor class}}{\sum FR \text{ of factor classes}} \quad (6)$$

After the calculation of RF, the prediction rate (PR) was also calculated to find the interrelationship between flood-causing factors and the training data set using the given Eq. 7.

$$PR = \frac{(RF_{max} - RF_{min})}{(RF_{max} - RF_{min}) Min} \quad (7)$$

2.6 Flood susceptibility mapping

The flood susceptibility map of the SRB was developed by calculating and classifying the flood susceptibility index (FSI). The FSI indicates the degree of susceptibility of the area to flood occurrences. Areas with greater FSI indicate high susceptibility to flooding occurrence and *vice versa*. The FSI was calculated based on the RF values and PR values, which were determined in the above Eqs 6, 7, respectively. The calculation of FSI is shown in Eq. 8.

$$FSI = \sum_{i=1}^9 PR_i \times RF_i \quad (8)$$

In the above equation, 9 indicates flood-causing factors (slope, elevation, curvature, drainage density, TWI, SPI, LULC, NDVI, and rainfall). The final flood susceptibility map was categorized into five categories: very high, high, moderate, low, and very low (Figure 5).

2.7 Receiver operating characteristic (ROC) technique

The performance and efficiency of the flood susceptibility map were validated with the ROC technique. The ROC curve is one of the most effective techniques used for susceptibility map validation (Chung and Fabbri, 2003; Tehrany et al., 2013; Liuzzo et al., 2019). The ROC curve was developed with the ArcSDM tool in ArcGIS 10.2. The training points were used to check the success rate whereas, the testing points were used for the prediction rate of the flood (Zhao et al., 2019; Tayyab et al., 2021). The area under the curve (AUC) for the success and the prediction rates were 0.916 and 0.903, respectively, which are significant and greatly acceptable in hydrometeorological studies (Sharif et al., 2016; Wang et al., 2023).

3 Results

3.1 Relationship of flood-causing factors and flood occurrence

We developed a flood susceptibility map of the SRB by employing FR bivariate statistical model. As shown in Table 2, the relationship between flood-causing factors and flood occurrence was assessed using FR values. The slope was classified into five classes: 0° – 12° , 13° – 23° , 24° – 33° , 34° – 44° , and 45° – 76° . Overall, FR weightage had a negative relationship with slope. For example, the

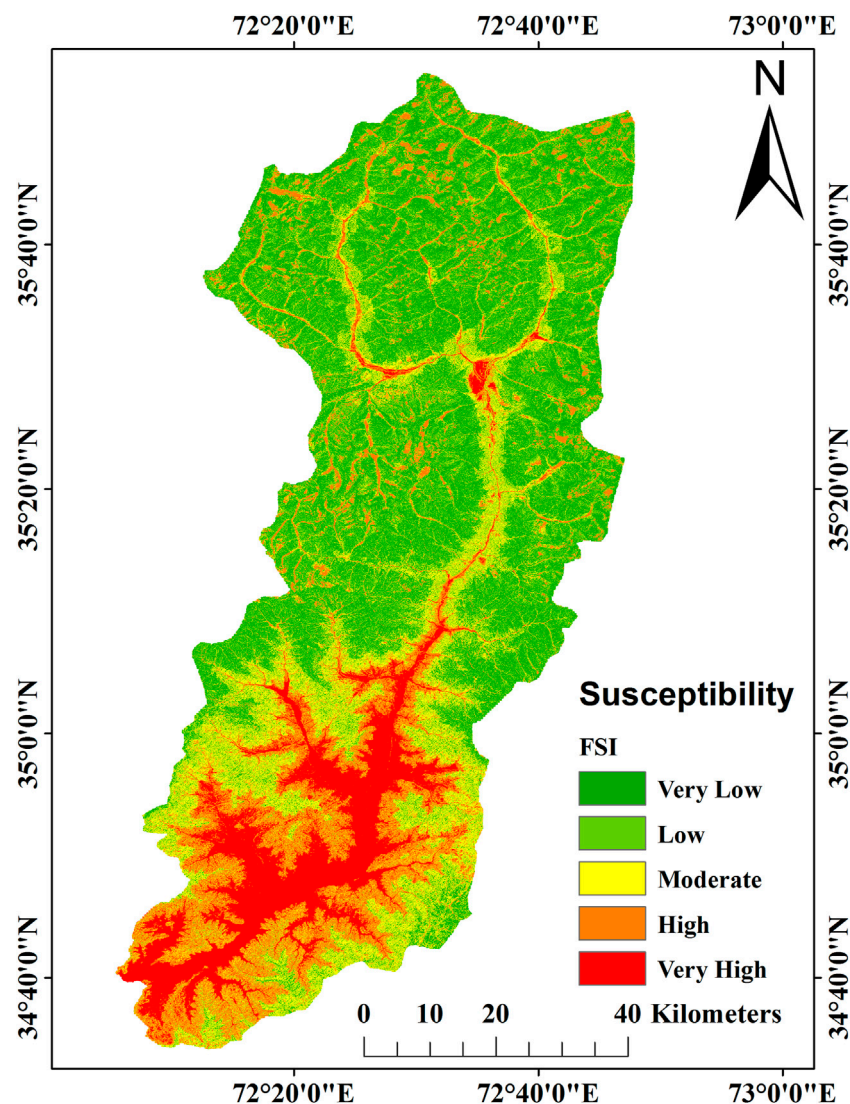


FIGURE 5
Flood susceptibility map, showing susceptible areas in the SRB.

lower slope class (0° – 12°) has a greater FR weightage (4.64). In contrast, as the slope increased, the FR weightage decreased gradually until the highest degree slope class (45° – 76°) had a zero FR value. This means that locations with a steep slope are less likely to flood, and *vice versa*. In terms of slope spatial pattern, the northern part of the SRB has a higher slope than the southern part (Figure 4A). In a nutshell, the northern areas of the SRB are less prone to flooding than the southern parts.

Furthermore, when the elevation of the area increased, the FR value declined steadily, resulting in a negative relationship between the two variables. The first two classes of lowest elevated places (709–1,577 m and 1,578–2,401 m) have greater FR values (3.42 and 1.07) than the next three higher elevation classes, according to Table 2. Recent studies show that areas with the highest elevations are less prone to flooding than those with lower elevations (Yu et al., 2022; Majeed et al., 2023; Wang et al., 2023). The regional elevation pattern of the SRB (Figure 4B)

verifies the findings that the high-altitude areas are less susceptible to flooding. In addition, the curvature map has been divided into three categories: concave, flat, and convex. Concave, flat, and convex surfaces had FR values of 0.43, 1.34, and 0.11, respectively. Floods are more likely to occur in flat areas than in concave or convex areas, as shown by the FR values and consistent with the curvature map (Figure 4C).

We further analyzed our data based on drainage density values and have classified SRB into five major categories (i.e., 0–44, 45–96, 97–158, 159–235, and 236–377). Our analysis indicated a positive correlation between drainage density and FR values. As an example, the highest FR value was assigned to class 5 (8.26) followed by class 4 (4.32), class 3 (0.81), class 2 (0.34), and class 1 (0.00). These results can be confirmed by the spatial distribution of the drainage density in the study area (Figure 4D). On the other hand, data on the TWI were obtained and then divided into five classes for analysis. Class 1 had the lowest FR value (0.09) and class 5 had the highest (6.23),

TABLE 2 Details of the flood-causing factors and their FR values.

Factor	Class	Points	% points	Class area	% class area	FR value	RF
Slope	1	81,900	77.12	994,742	16.64	4.64	0.82
	2	19,800	18.64	1,292,383	21.62	0.86	0.15
	3	2,700	2.54	1,614,896	27.01	0.09	0.02
	4	1800	1.69	1,452,839	24.30	0.07	0.01
	5	0	0.00	624,220	10.44	0.00	0.00
Elevation	1	81,900	77.12	1,347,456	22.54	3.42	0.74
	2	21,600	20.34	1,138,231	19.04	1.07	0.23
	3	2,700	2.54	1,021,585	17.09	0.15	0.03
	4	0	0.00	1,298,419	21.72	0.00	0.00
	5	0	0.00	1,173,389	19.62	0.00	0.00
curvature	1	7,200	6.78	936,437	15.66	0.43	0.23
	2	97,200	91.53	4,090,702	68.42	1.34	0.71
	3	1800	1.69	951,941	15.92	0.11	0.06
Drainage density	1	0	0.00	2,240,618	37.48	0.00	0.00
	2	10,800	10.08	1,786,244	29.88	0.34	0.02
	3	16,200	15.13	1,121,793	18.76	0.81	0.06
	4	46,800	43.70	605,173	10.12	4.32	0.31
	5	33,300	31.09	225,106	3.76	8.26	0.60
TWI	1	2,700	2.54	1,760,650	29.45	0.09	0.01
	2	28,800	27.12	2,172,288	36.33	0.75	0.07
	3	36,000	33.90	1,306,215	21.85	1.55	0.15
	4	17,100	16.10	544,893	9.11	1.77	0.17
	5	21,600	20.34	195,076	3.26	6.23	0.60
SPI	1	37,800	35.59	1,612,021	26.96	1.32	0.17
	2	26,100	24.58	1,290,763	21.59	1.14	0.15
	3	18,900	17.80	1,810,364	30.28	0.59	0.08
	4	6,300	5.93	1,038,671	17.37	0.34	0.04
	5	17,100	16.10	227,212	3.80	4.24	0.56
LULC	1	7,200	6.78	45,772	0.77	8.86	0.49
	2	4,500	4.24	1,198,919	20.05	0.21	0.01
	3	0	0.00	36,961	0.62	0.00	0.00
	4	0	0.00	9	0.00	0.00	0.00
	5	10,800	10.17	219,664	3.67	2.77	0.15
	6	16,200	15.25	2,599,766	43.48	0.35	0.02
	7	63,000	59.32	638,677	10.68	5.55	0.31
	8	4,500	4.24	728,735	12.19	0.35	0.02
	9	0	0.00	510,691	8.54	0.00	0.00
	10	0	0.00	10	0.00	0.00	0.00

(Continued on following page)

TABLE 2 (Continued) Details of the flood-causing factors and their FR values.

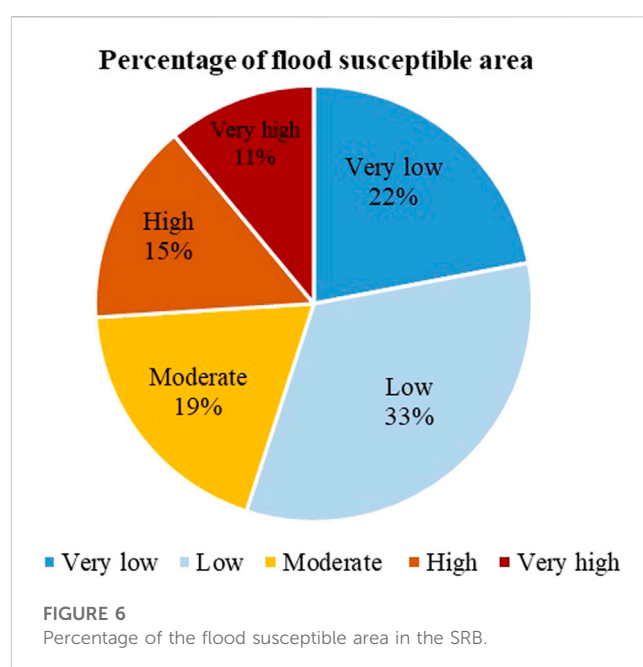
Factor	Class	Points	% points	Class area	% class area	FR value	RF
NDVI	1	3,600	3.39	1,225,636	20.50	0.17	0.03
	2	37,800	35.59	907,311	15.17	2.35	0.44
	3	26,100	24.58	1,232,992	20.62	1.19	0.22
	4	26,100	24.58	1,470,790	24.60	1.00	0.19
	5	12,600	11.86	1,142,460	19.11	0.62	0.12
Rainfall	1	57,600	53.78	1,978,334	33.23	1.62	0.29
	2	18,000	16.81	545,959	9.17	1.83	0.33
	3	9,900	9.24	540,975	9.09	1.02	0.18
	4	8,100	7.56	624,725	10.49	0.72	0.13
	5	13,500	12.61	2,264,041	38.03	0.33	0.06

showing that class 5 is very susceptible to flooding and *vice versa* (Figure 4E). In the case of SPI, the map was divided into five classes: Class 1 (−13.82 to −4.48), class 2 (−4.47 to −0.08), class 3 (0.09–1.86), class 4 (1.87–4.42), and class 5 (4.43–14.54). The highest FR value (4.24) was allocated to class 5, thus indicating a direct relationship between the SPI value and the FR weightage. Interestingly, lower flat areas situated on the southern belt of the SRB have the lowest SPI, whereas the mountainous and steep slope areas situated on the northern side of the SRB have higher SPI (Figure 4F).

Similarly, the data obtained on land use/land cover (LULC) was classified into ten distinct classes: water bodies, wood trees, grassland, flooded vegetation, agriculture, scrub/shrub, build-up area, bare land, snow cover, and cloud (Figure 4E). According to our findings, the highest FR value was assigned to water bodies (8.86), followed by build-up areas (5.55) and agriculture areas (2.77). We further retrieved and analyzed data regarding the normalized difference vegetation index (NDVI) of the SRB. Of the total 5 NDVI classes, excluding the first class, the FR value was positive for the remaining four classes. The highest FR values were allocated to class 2, and class 3 (2.35, and 1.19, respectively). Besides, the rainfall data were divided into five classes, the highest FR values were calculated to be 1.62, 1.83, and 1.02, for classes 1, 2, and 3, respectively (Figure 4I).

3.2 Flood susceptibility index (FSI)

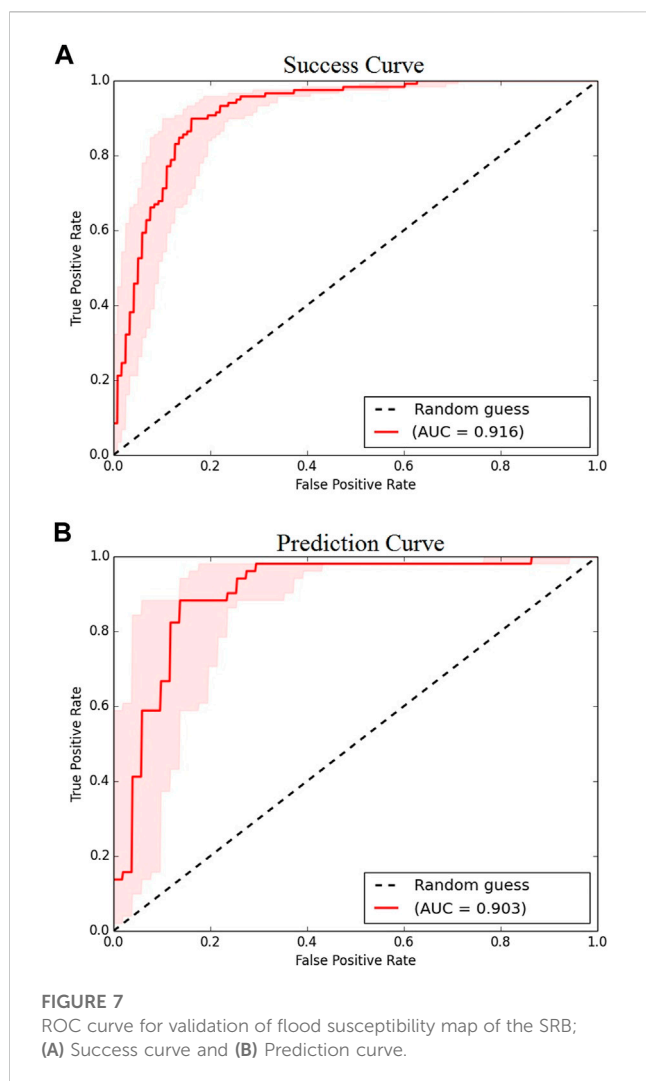
Overall, the FSI values in our study revealed a broad range, ranging from 2,896 to 97,44. The map was categorized into five classes based on the natural break technique, namely, very low (2,896 to 16,996), low (16,997 to 27,581), moderate (27,582 to 39,280), high (39,281 to 59,142), and very high (59,143 to 97,440) (Figure 5). Our findings generally indicate that very high and high flood-susceptible areas are those situated in the southern plain areas along the river banks. In contrast, the northern parts of the SRB have a relatively steep slope, high elevation, convex curvature, high SPI and NDVI, vegetation land cover, low drainage density, and TWI with a minimum tendency of rainfall,



which can be attributed to their lower susceptibility to flood hazards. Furthermore, our findings indicate that approximately 26% of the study area is characterized as being at a very high or high susceptibility to flooding, 19% as moderate, while the remaining 55% is classified as having low or very low susceptibility to flooding in the SRB. (Figure 6).

3.3 Validation of flood susceptibility map

The validity of the flood susceptibility model was assessed through a rigorous process of comparing the flood inventory data, which represents past flood occurrences, with the newly developed flood susceptibility map. In the validation process, flood testing points (30%) that have not been used for the preparation of the FR model are generally considered as the



future flood location. It is noteworthy that the AUC value of the success rate was 91.6% and the prediction rate was 90.3%, respectively (Figure 7). These results demonstrate the effectiveness of the flood susceptibility model in predicting the likelihood of future floods and provide valuable insights for flood risk management and mitigation.

3.4 Contributions of flood-causing factors in flood susceptibility

Overall, the study provides valuable insights into the factors that contribute to flood susceptibility in the SRB. As shown in Table 3, the slope with the highest PR value (3.01) has emerged as the foremost contributor to flood susceptibility in the study area. Moreover, elevation and curvature have the second and third highest PR values at the rate of 2.71 and 2.41, respectively, suggesting their prominent roles in flood susceptibility. In contrast, rainfall is considered the least flood-contributing factor bearing 1 PR value. The overall results infer that the susceptibility of the SRB in general, and low-lying southern flat areas in particular, are more dependent on the topographic and meteorological conditions in northern mountainous regions. The spatial pattern

of flood susceptibility indicates that the areas located in the southern plain along the river banks are highly susceptible to floods.

4 Discussion

In this work, we created a flood susceptibility map of the SRB in the Eastern Hindukush region of Pakistan by applying a GIS-based bivariate statistical model, and further leveraged the correlation between various flood-causing variables and the occurrence of floods in the area. To achieve our desired goals, data were obtained and analyzed on a total of nine independent variables (slope, elevation, curvature, drainage density, TWI, SPI, LULC, NDVI, and rainfall).

Consistent with several previous reports by Sarkar and Mondal, (2020) and Ullah and Zhang, (2020), our analysis showed a negative correlation between slope and flood occurrence, highlighting the fact that low-lying areas in the southern parts of the SRB are highly susceptible to floods. Similarly, elevation was found inversely proportional to flood susceptibility, indicating that elevated areas with steep slopes are relatively less susceptible to flood hazards compared to their counterparts. These findings are largely concordant with similar previous reports (Samanta R. K. et al., 2018; Majeed et al., 2023). Based on our curvature map, we have found that floods are more likely to hit flat areas in contrast to concave or convex areas. For example, we have seen maximum areas in the SRB are flat surfaces, especially the areas nearby the river and tributaries, thus making them highly susceptible to flooding. This is understandable as topography or curvature of the area plays an important role in flood susceptibility. Our analysis together with a set of literature (Khosravi et al., 2016b; Das, 2019; M Amen et al., 2023) has confirmed that flat areas are relatively more susceptible to floods than convex or concave areas. Our results also support earlier studies, reporting about 83% of floods on flat and/or convex surfaces (Ullah and Zhang, 2020; Amen et al., 2023).

Drainage density is an important flood-causing factor and has a direct relationship with flooding as it depends on surface runoff (Tehrany et al., 2015; Kadam et al., 2018). The likelihood of flooding is increasing as the drainage density increases and the likelihood of flood is decreasing with decreasing drainage density (Ullah and Zhang, 2020; Ha et al., 2022). Consistent with these findings and as confirmed by our spatial distribution of the drainage density data, we uncovered a direct relationship between floods and drainage density, substantiating previous reports. TWI represents the soil moisture status of an area and the saturated source of topography. It is a very important factor for the prediction of future floods because there is a direct relationship between TWI and flood occurrence (Sarkar and Mondal, 2020). Our analysis found that TWI was positively associated with floods in the SRB, thus supporting all previous assertions (Khoirunisa et al., 2021). The designated relationship between the SPI value and the FR weightage shows that lower flat areas situated in the southern belt of SRB have low SPI whereas, the mountainous and steep slope areas have high SPI. This is in line with a previous study warranting that flooding is more likely to occur in an area with a lower SPI (Arnell and Gosling, 2016; Wang et al., 2023).

TABLE 3 PR values of flood-causing factors, and their contributions to flood Susceptibility.

Factors	Min RF	Max RF	Max-min RF	(Max-min) Min RF	PR value
Slope	0.00	0.82	0.82	0.27	3.01
Elevation	0.00	0.74	0.74	0.27	2.71
Curvature	0.06	0.71	0.66	0.27	2.41
Drainage Density	0.00	0.60	0.60	0.27	2.21
TWI	0.01	0.60	0.59	0.27	2.18
SPI	0.04	0.56	0.51	0.27	1.88
LULC	0.00	0.49	0.49	0.27	1.80
NDVI	0.03	0.44	0.41	0.27	1.51
Rainfall	0.06	0.33	0.27	0.27	1.00

There is a solid relationship between LULC and flood since land use strongly influences decreasing and increasing surface runoff (Ahmad et al., 2018; Ziwei et al., 2023). A LULC pattern determines the type of land use by individuals and natural processes (Ullah et al., 2019b). The area where there is no vegetation covers bear more probability of flooding and soil erosion, and the areas are considered highly vulnerable to floods. Consistently, we have found that areas, such as agricultural land, and built-up areas were highly likely to face flooding. This suggests that rapid urbanization in the southern flat areas is greatly responsible for changes in hydrological processes and disturbing drainage networks, ultimately resulting in flooding (Butt et al., 2020). Likewise, ever-growing croplands along the river banks are highly susceptible to flooding (Youssef et al., 2016).

The NDVI is another key flood-causing factor in the way that lower NDVI weights indicate high flood susceptibility while higher NDVI weights represent a lower risk of flooding (Ullah et al., 2019b; Rehman et al., 2022). Alternatively, the lowest NDVI values represent unhealthy vegetation, mostly occupying the elevated snowcapped northern areas (Shrestha et al., 2020; Ziwei et al., 2023). Based on the NDVI measurements, our analysis revealed that all, except one, classes are highly flood susceptible. Rainfall is undoubtedly the most common cause of floods in any area where sudden and heavy rainfall can exceed the capability of an area and thus lead to floods (Samanta R. K. et al., 2018). Using rainfall data from NASA, we found that southern parts of the SRB were comparatively more susceptible to floods than its northern territories. This is because SRB has semi-arid climatic conditions where the rainfall pattern in lower southern parts is influenced by the summer monsoon, while in upper northern parts, the rainfall pattern is dominated by the winter rainfall, occurring due to the western disturbance of the Mediterranean Sea (Khan et al., 2020; Wang et al., 2020; Hussain et al., 2021; Xu et al., 2022).

Furthermore, we calculated FSI by translating FR and PR values for all variables under our investigation. Overall, the FSI value ranged from 2,896 to 97,440. The resulting flood susceptibility map showed that very high and high flood susceptible areas were mostly situated in the southern plain areas and along the river banks. Thus, people living in the low-lying southern parts and along the river banks are more exposed to both riverine and flash floods. It should be noted that the southern parts of the SRB have lower slope

angles, less elevation, flat curvature, lower SPI, and NDVI, improper land use, high drainage density, and TWI with maximum rainfall intensity, which could be the possible reasons for their higher susceptibility to floods. On the other hand, the northern parts of the SRB have a relatively steep slope, high elevation, convex curvature, high SPI and NDVI, vegetation land cover, low drainage density, and TWI with a minimum tendency of rainfall, which can be attributed to their lower susceptibility to flooding hazards. The results further show that about 26% of areas are very high and highly susceptible to flooding, 19% are moderate whereas 55% are low and very low susceptible to flood in the SRB. The AUC value of the prediction rate was 90.3% and that of the success rate was 91.6%, which is highly acceptable and important in hydrometeorological studies (Sharif et al., 2016; Tayyab et al., 2021; Wang et al., 2023).

The prediction rate (PR) of every flood-causing factor was calculated in order to find out the maximum and minimum contribution of an individual factor in exacerbating flood susceptibility in the SRB (Ullah and Zhang, 2020; Wang et al., 2020; Hussain et al., 2021). Collectively, the slope has the highest PR values (3.01), showing that the slope is the prime contributor to exacerbating the susceptibility of the study area to flooding. Moreover, elevation and curvature have the second and third-highest PR values at the rate of 2.71 and 2.41, respectively. This suggests that both elevation and curvature also significantly contributed to flood susceptibility in the SRB. Rainfall, however, emerged as the least flood-contributing factor bearing 1 PR value. This is not surprising as a similar study by (Ullah and Zhang, 2020) identified rainfall as the least contributor to flooding in the Panjkora river basin.

5 Conclusion

The present work generated a GIS-based flood susceptibility mapping of the SRB using the FR bivariate statistical model. The results indicate that flood susceptibility of the SRB in general, and low-lying southern flat areas in particular, are more dependent on the topographic and meteorological conditions of the northern mountainous regions. The spatial pattern of flood

susceptibility shows that highly susceptible areas were primarily located along the river banks and in the southern plain of the SRB. Based on the ROC curve, the efficiency of the model was found to be high with a success rate of 91.6% and a prediction rate of 90.3%. Of the nine independent variables; slope, elevation, and curvature played an intensifying role in increasing flood susceptibility in the SRB. The findings of this study provide useful information for land-use planners, engineers, decision-makers, and relevant authorities to effectively manage flood hazards in the SRB. The findings of this study could be used as leverage for developing flood risk assessment plans, devising mitigation measures, establishing early warning systems, etc., in the study region. Based on the study findings, we recommend the adaptation of a comprehensive approach that integrates multiple flood management and mitigation strategies, including risk assessment, evacuation plans, early warning systems, resilient infrastructures, and construction of dams and levees, to minimize flood risks in the study SRB. Although this study provides a comprehensive and diligent assessment of flood susceptibility in the SRB, future research should use high-resolution satellite imagery and other cutting-edge analytical techniques like ML, CNN, and ANN algorithms to enhance the effectiveness, accuracy, and reliability of the model outputs.

Data availability statement

Publicly available datasets were analyzed in this study. This data can be found here: The data that support the findings of this study are openly accessible. The following publicly available sources were used to derive these data. NASA (www.search.earthdata.nasa.gov), ESRI 2020 (<https://livingatlas.arcgis.com/landcover/>), and USGS (<https://earthexplorer.usgs.gov>). The field data that support the findings of this study are available on request from the corresponding authors.

Author contributions

Conceptualization: ZR and SB; Methodology: ZR, SB, WU, and SU; Formal analysis and investigation: ZR, SB, and MJ;

Writing—original draft preparation: ZR; Writing—review and editing: ZR, SB, MK, and MT; Funding acquisition: WU; Resources: SB and ZR; Supervision: SB. All authors contributed to the article and approved the submitted version.

Funding

This work was supported by the National Natural Science Foundation of China (Grant Nos 41941017 and 41877522).

Acknowledgments

The authors acknowledge the National Disaster Management Authority (NDMA), Pakistan, and Provincial Disaster Management Authority (PDMA), Khyber Pakhtunkhwa, Pakistan for providing historical and spatial data on flood damages. The authors acknowledge Rabdan Academy, UAE for supporting Article Processing Charges (APC). The authors are thankful to the National Aeronautics and Space Administration (NASA) for TRMM data, Environmental Systems Research Institute (ESRI) for land use land/cover data, and the United States Geological Survey (USGS) for Landsat 8 images, and DEM.

Conflict of interest

The authors declare that the research was conducted in the absence of any commercial or financial relationships that could be construed as a potential conflict of interest.

Publisher's note

All claims expressed in this article are solely those of the authors and do not necessarily represent those of their affiliated organizations, or those of the publisher, the editors and the reviewers. Any product that may be evaluated in this article, or claim that may be made by its manufacturer, is not guaranteed or endorsed by the publisher.

References

- Abbas, A., Bhatti, A. S., Ullah, S., Ullah, W., Waseem, M., Zhao, C., et al. (2023). Projection of precipitation extremes over south asia from CMIP6 GCMs. *J. Arid. Land* 15, 274–296. doi:10.1007/s40333-023-0050-3
- Abbas, A., Ullah, S., Ullah, W., Waseem, M., Dou, X., Zhao, C., et al. (2022). Evaluation and projection of precipitation in Pakistan using the coupled model intercomparison project phase 6 model simulations. *Int. J. Climatol.* 42, 6665–6684. doi:10.1002/joc.7602
- Ahmad, I., Tang, D., Wang, T., Wang, M., and Wagan, B. (2015). Precipitation trends over time using mann-kendall and spearman's rho tests in swat River Basin, Pakistan. *Adv. Meteorology* 2015, 1–15. doi:10.1155/2015/431860
- Ahmad, I., Zhang, F., Liu, J., Anjum, M. N., Zaman, M., Tayyab, M., et al. (2018). A linear bi-level multi-objective program for optimal allocation of water resources. *PLoS One* 13, e0192294. doi:10.1371/journal.pone.0192294
- Ahmadlou, M., Karimi, M., Alizadeh, S., Shirzadi, A., Parvinnejhad, D., Shahabi, H., et al. (2019). Flood susceptibility assessment using integration of adaptive network-based fuzzy inference system (ANFIS) and biogeography-based optimization (BBO) and BAT algorithms (BA). *Geocarto Int.* 34, 1252–1272. doi:10.1080/10106049.2018.1474276
- Ahmed, E., Saddique, N., Al Janabi, F., Barfus, K., Asghar, M. R., Sarwar, A., et al. (2023). Flood predictability of one-way and two-way WRF nesting coupled hydrometeorological flow simulations in a transboundary chenab River Basin, Pakistan. *Remote Sens. (Basel)* 15, 457. doi:10.3390/rs15020457
- Akgun, A., Sezer, E. A., Nefeslioglu, H. A., Gokceoglu, C., and Pradhan, B. (2012). An easy-to-use MATLAB program (MamLand) for the assessment of landslide susceptibility using a Mamdani fuzzy algorithm. *Comput. Geosci.* 38, 23–34. doi:10.1016/j.cageo.2011.04.012
- Ali, K., Bajracharya, R. M., and KoiralaLal, H. (2016). A review of flood risk assessment. *Int. J. Environ. Agric. Biotechnol.* 1, 1065–1077. doi:10.22161/ijeab/1.4.62
- Althuwaynee, O. F., Pradhan, B., Park, H.-J., and Lee, J. H. (2014). A novel ensemble bivariate statistical evidential belief function with knowledge-based analytical hierarchy process and multivariate statistical logistic regression for landslide susceptibility mapping. *Catena (Amst)* 114, 21–36. doi:10.1016/j.catena.2013.10.011

- Arabameri, A., Pradhan, B., Rezaei, K., and Lee, C.-W. (2019). Assessment of landslide susceptibility using statistical- and artificial intelligence-based FR-RF integrated model and multiresolution DEMs. *Remote Sens.* 11 (9), 999.
- Areu-Rangel, O., Cea, L., Bonasia, R., and Espinosa-Echavarria, V. (2019). Impact of urban growth and changes in land use on river flood hazard in villahermosa, tabasco (Mexico). *Water (Basel)* 11, 304. doi:10.3390/w11020304
- Arnell, N. W., and Gosling, S. N. (2016). The impacts of climate change on river flood risk at the global scale. *Clim. Change* 134, 387–401. doi:10.1007/s10584-014-1084-5
- Arshad, M., Ma, X., Yin, J., Ullah, W., Ali, G., Ullah, S., et al. (2021). Evaluation of GPM-IMERG and TRMM-3B42 precipitation products over Pakistan. *Atmos. Res.* 249, 105341. doi:10.1016/j.atmosres.2020.105341
- Baqa, M. F., Lu, L., Chen, F., Nawaz-ul-Huda, S., Pan, L., Tariq, A., et al. (2022). Characterizing spatiotemporal variations in the urban thermal environment related to land cover changes in karachi, Pakistan, from 2000 to 2020. *Remote Sens. (Basel)* 14, 2164. doi:10.3390/rs14092164
- Bhatti, A. S., Wang, G., Ullah, W., Ullah, S., Fiifi Tawia Hagan, D., Kwesi Nooni, I., et al. (2020). Trend in extreme precipitation indices based on long term *in situ* precipitation records over Pakistan. *Water (Basel)* 12, 797. doi:10.3390/w12030797
- Billa, L., Shattri, M., Rodzi Mahmud, A., and Halim Ghazali, A. (2006). Comprehensive planning and the role of SDSS in flood disaster management in Malaysia. *Disaster Prev. Manag. Int. J.* 15, 233–240. doi:10.1108/09653560610659775
- Butt, A. A., Aslam, H. M. U., Shabir, H., Javed, M., Hussain, S., Nadeem, S., et al. (2020). Climatic events and natural disasters of 21st century: A perspective of Pakistan. *Int. J. Econ. Environ. Geol.* 11, 46–54. doi:10.46660/ijeeg.Vol11.Iss2.2020.445
- Chapi, K., Singh, V. P., Shirzadi, A., Shahabi, H., Bui, D. T., Pham, B. T., et al. (2017). A novel hybrid artificial intelligence approach for flood susceptibility assessment. *Environ. Model. Softw.* 95, 229–245. doi:10.1016/j.envsoft.2017.06.012
- Charlton, R., Fealy, R., Moore, S., Sweeney, J., and Murphy, C. (2006). Assessing the impact of climate change on water supply and flood hazard in Ireland using statistical downscaling and hydrological modelling techniques. *Clim. Change* 74, 475–491. doi:10.1007/s10584-006-0472-x
- Chung, C.-J. F., and Fabbri, A. G. (2003). Validation of spatial prediction models for landslide hazard mapping. *Nat. Hazards* 30, 451–472. doi:10.1023/B:NHAZ.0000007172.62651.2b
- Costache, R. (2019). Flash-flood Potential Index mapping using weights of evidence, decision Trees models and their novel hybrid integration. *Stoch. Environ. Res. Risk Assess.* 33, 1375–1402. doi:10.1007/s00477-019-01689-9
- Crisis24 (2022). A Gardaworld Company. *Disruptions due to flooding are ongoing across many parts of Pakistan as of Aug 28*. Available at: <https://crisis24.garda.com/alerts/2022/08/pakistan-disruptions-due-to-flooding-are-ongoing-across-many-parts-of-the-country-as-of-aug-28-update-1#:~:text=Event,the%20past%2024%2D36%20hours> (Accessed October 21, 2022).
- Das, S. (2018). Geographic information system and AHP-based flood hazard zonation of Vaitarna basin, Maharashtra, India. *Arabian J. Geosciences* 11, 576. doi:10.1007/s12517-018-3933-4
- Das, S. (2019). Geospatial mapping of flood susceptibility and hydro-geomorphic response to the floods in Ulhas basin, India. *Remote Sens. Appl.* 14, 60–74. doi:10.1016/j.rse.2019.02.006
- Dawood, M., Rahman, A., Mahmood, S., Rahman, G., and Nazir, S. (2021). Assessing the impact of climatic change on discharge in Swat river basin using fuzzy logic model. *Arabian J. Geosciences* 14, 1850. doi:10.1007/s12517-021-08219-4
- El-Magd, Sh. A. A. (2019). Flash flood hazard mapping using GIS and bivariate statistical method at wadi bada'a, gulf of suuez, Egypt. *J. Geoscience Environ. Prot.* 07, 372–385. doi:10.4236/gep.2019.78025
- Elkhachy, I. (2022). Flash flood water depth estimation using SAR images, digital elevation models, and machine learning algorithms. *Remote Sens. (Basel)* 14, 440. doi:10.3390/rs14030440
- Esteves, L. S. (2013). Consequences to flood management of using different probability distributions to estimate extreme rainfall. *J. Environ. Manage* 115, 98–105. doi:10.1016/j.jenvman.2012.11.013
- Farooq, M., Shafique, M., and Khattak, M. S. (2019). Flood hazard assessment and mapping of River Swat using HEC-RAS 2D model and high-resolution 12-m TanDEM-X DEM (WorldDEM). *Nat. Hazards* 97:2 97, 477–492. doi:10.1007/S11069-019-03638-9
- Gaurav, K., Sinha, R., and Panda, P. K. (2011). The indus flood of 2010 in Pakistan: A perspective analysis using remote sensing data. *Nat. Hazards* 59, 1815–1826. doi:10.1007/s11069-011-9869-6
- Gudiyangada Nachappa, T., Tavakkoli Piralilou, S., Gholamnia, K., Ghorbanzadeh, O., Rahmati, O., and Blaschke, T. (2020). Flood susceptibility mapping with machine learning, multi-criteria decision analysis and ensemble using Dempster Shafer Theory. *J. Hydrol. (Amst)* 590, 125275. doi:10.1016/j.jhydrol.2020.125275
- Ha, H., Bui, Q. D., Nguyen, H. D., Pham, B. T., Lai, T. D., and Luu, C. (2022). A practical approach to flood hazard, vulnerability, and risk assessing and mapping for Quang Binh province. Vietnam: Environment, Development and Sustainability 2021, 1–30. doi:10.1007/S10668-021-02041-4
- Haghizadeh, A., Siahkamari, S., Haghiabi, A. H., and Rahmati, O. (2017). Forecasting flood-prone areas using Shannon's entropy model. *J. Earth Syst. Sci.* 126, 39. doi:10.1007/s12040-017-0819-x
- Henao Salgado, M. J., and Zambrano Nájera, J. (2022). Assessing flood early warning systems for flash floods. *Front. Clim.* 4. doi:10.3389/fclim.2022.787042
- Hizbaron, D. R., Ismayani, N., Ernawan, F. N., Puspitasari, N. N. A., Yulianda, Y., and Jati, R. (2021). Comparative urban capacity analysis for flood-prone areas: Method and a case study of sidoarjo, Indonesia. *Environ. Dev. Sustain.* 23(9 23), 14027–14045. doi:10.1007/S10668-021-01249-8
- Hong, H., Panahi, M., Shirzadi, A., Ma, T., Liu, J., Zhu, A.-X., et al. (2018). Flood susceptibility assessment in Hengfeng area coupling adaptive neuro-fuzzy inference system with genetic algorithm and differential evolution. *Sci. Total Environ.* 621, 1124–1141. doi:10.1016/j.scitotenv.2017.10.114
- Hussain, M., Tayyab, M., Zhang, J., Shah, A. A., Ullah, K., Mehmood, U., et al. (2021). GIS-based multi-criteria approach for flood vulnerability assessment and mapping in district shangla: Khyber Pakhtunkhwa, Pakistan. *Sustainability* 13, 3126. doi:10.3390/su13063126
- Hussain, A., Hussain, I., Ali, S., Ullah, W., Khan, K., Ullah, S., et al. (2023a). Spatiotemporal temperature trends over homogenous climatic regions of Pakistan during 1961–2017. *Theor. Appl. Climatol.*, 1–19. doi:10.3390/su13063126
- Hussain, M., Tayyab, M., Ullah, K., Ullah, S., Rahman, Z. U., Zhang, J., et al. (2023b). Development of a new integrated flood resilience model using machine learning with GIS-based multi-criteria decision analysis. *Urban Cli.* 50, 101589. doi:10.1016/j.uclim.2023.101589
- Islam, F., Riaz, S., Ghaffar, B., Tariq, A., Shah, S. U., Nawaz, M., et al. (2022). Landslide susceptibility mapping (LSM) of Swat District, Hindu Kush Himalayan region of Pakistan, using GIS-based bivariate modeling. *Front. Environ. Sci.* 10. doi:10.3389/fenvs.2022.1027423
- Jebur, M. N., Pradhan, B., and Tehrany, M. S. (2014). Optimization of landslide conditioning factors using very high-resolution airborne laser scanning (LiDAR) data at catchment scale. *Remote Sens. Environ.* 152, 150–165. doi:10.1016/j.rse.2014.05.013
- Jensen, J. R. (2005). *Introductory digital image processing: A remote sensing perspective*. 3rd ed. Prentice-Hall Inc.
- Kadam, A., Karnewar, A. S., Umrikar, B., and Sankhua, R. N. (2018). Hydrological response-based watershed prioritization in semiarid, basaltic region of Western India using frequency ratio, fuzzy logic and AHP method. *Environ. Dev. Sustain.* 21, 1809–1833. doi:10.1007/S10668-018-0104-4
- Karra, K., Kontgis, C., Statman-Weil, Z., Mazzariello, J. C., Mathis, M., and Brumby, S. P. (2021). "Global land use/land cover with Sentinel 2 and deep learning," in *2021 IEEE international geoscience and remote sensing symposium IGARSS (IEEE)*, 4704–4707. doi:10.1109/IGARSS47720.2021.9553499
- Khan, A. N., Khan, S. N., Ullah, S., Aqil, M., et al. (2016). Flood vulnerability assessment in union council, jahangira, district nowshera, Pakistan. *J. Sci. Technol.* 40, 21–30.
- Khan, I., Ali, A., Waqas, T., Ullah, S., Ullah, S., Shah, A. A., et al. (2022a). Investing in disaster relief and recovery: A reactive approach of disaster management in Pakistan. *Int. J. Disaster Risk Reduct.* 75, 102975. doi:10.1016/j.ijdr.2022.102975
- Khan, I., Lei, H., Shah, A. A., Khan, I., and Muhammad, I. (2021). Climate change impact assessment, flood management, and mitigation strategies in Pakistan for sustainable future. *Environ. Sci. Pollut. Res.* 28, 29720–29731. doi:10.1007/s11356-021-12801-4
- Khan, I., Waqas, T., Samiullah, and Ullah, S. (2020). Precipitation variability and its trend detection for monitoring of drought hazard in northern mountainous region of Pakistan. *Arab. J. Geosci.* 13, 1–18.
- Khan, W., Naqvi, S. M. H. M., Ahmad, N., Kamal, M., Hassan, H., Noor, A., et al. (2022b). Prevalence of rabdochioniasis in snow trout of river Swat and river Panjkora, Khyber Pakhtunkhwa province, Pakistan. *Braz. J. Biol.* 82, e238874. doi:10.1590/1519-6984.238874
- Khoirunisa, N., Ku, C.-Y., and Liu, C.-Y. (2021). A GIS-based artificial neural network model for flood susceptibility assessment. *Int. J. Environ. Res. Public Health* 18, 1072. doi:10.3390/ijerph18031072
- Khosravi, K., Nohani, E., Maroufinia, E., and Pourghasemi, H. R. (2016a). A GIS-based flood susceptibility assessment and its mapping in Iran: A comparison between frequency ratio and weights-of-evidence bivariate statistical models with multi-criteria decision-making technique. *Nat. Hazards* 83, 947–987. doi:10.1007/s11069-016-2357-2
- Khosravi, K., Pourghasemi, H. R., Chapi, K., and Bahri, M. (2016b). Flash flood susceptibility analysis and its mapping using different bivariate models in Iran: A comparison between Shannon's entropy, statistical index, and weighting factor models. *Environ. Monit. Assess.* 188, 656. doi:10.1007/s10661-016-5665-9
- Kia, M. B., Pirasteh, S., Pradhan, B., Mahmud, A. R., Sulaiman, W. N. A., and Moradi, A. (2012). An artificial neural network model for flood simulation using GIS: Johor River Basin, Malaysia. *Environ. Earth Sci.* 67, 251–264. doi:10.1007/s12665-011-1504-z
- Liu, J., Liu, K., and Wang, M. (2023). *Residual neural network integrated with a hydrological model for global flood susceptibility mapping based A residual neural network integrated with a hydrological model for global flood susceptibility mapping based on remote sensing datasets*. doi:10.3390/rs15092447

- Liu, J., Wang, J., Xiong, J., Cheng, W., Sun, H., Yong, Z., et al. (2021). Hybrid models incorporating bivariate statistics and machine learning methods for flash flood susceptibility assessment based on remote sensing datasets. *Remote Sens. (Basel)* 13, 4945. doi:10.3390/rs13234945
- Liuzzo, L., Sammartano, V., and Freni, G. (2019). Comparison between different distributed methods for flood susceptibility mapping. *Water Resour. Manag.* 33, 3155–3173. doi:10.1007/s11269-019-02293-w
- M Amen, A. R., Mustafa, A., Kareem, D. A., Hameed, H. M., Mirza, A. A., Szydlowski, M., et al. (2023). Mapping of flood-prone areas utilizing GIS techniques and remote sensing: A case study of duhok, kurdistan region of Iraq. *Remote Sens. (Basel)* 15, 1102. doi:10.3390/rs15041102
- Mahmood, S., and Rahman, A. (2019). Flash flood susceptibility modeling using geomorphometric and hydrological approaches in Panjkora Basin, Eastern Hindu Kush, Pakistan. *Environ. Earth Sci.* 78, 43. doi:10.1007/s12665-018-8041-y
- Majeed, M., Lu, L., Anwar, M. M., Tariq, A., Qin, S., El-Hefnawy, M. E., et al. (2023). Prediction of flash flood susceptibility using integrating analytic hierarchy process (AHP) and frequency ratio (FR) algorithms. *Front. Environ. Sci.* 10. doi:10.3389/fenvs.2022.1037547
- Malik, S., Pal, S. C., Arabameri, A., Chowdhuri, I., Saha, A., Chakraborty, R., et al. (2021). GIS-based statistical model for the prediction of flood hazard susceptibility. *Environ. Dev. Sustain.* 23(11 23), 16713–16743. doi:10.1007/S10668-021-01377-1
- McGrath, H., and Gohl, P. N. (2022). Accessing the impact of meteorological variables on machine learning flood susceptibility mapping. *Remote Sens. (Basel)* 14, 1656. doi:10.3390/rs14071656
- Moazzam, M. F. U., Vansarochana, A., and Rahman, A. (2018). Analysis of flood susceptibility and zonation for risk management using frequency ratio model in District Charsadda, Pakistan. *Int. J. Environ. Geoinformatics* 5, 140–153. doi:10.30897/ijegeo.407260
- Nasir, M. J., Iqbal, J., and Ahmad, W. (2020). Flash flood risk modeling of Swat River sub-watershed: A comparative analysis of morphometric ranking approach and el-shamy approach. *Arabian J. Geosciences* 13, 1082. doi:10.1007/s12517-020-06064-5
- NDMA (2022). National disaster management authority, Pakistan. Available at: <http://cms.ndma.gov.pk/news> (Accessed October 21, 2022).
- Paul, G. C., Saha, S., and Hembram, T. K. (2019). Application of the GIS-based probabilistic models for mapping the flood susceptibility in bansloi sub-basin of ganga-bhagirathi river and their comparison. *Remote Sens. Earth Syst. Sci.* 2, 120–146. doi:10.1007/s41976-019-00018-6
- PMD (2022). Pakistan meteorological department. Available at: <https://www.pmd.gov.pk/en/> (Accessed October 21, 2022).
- Pradhan, B., and Lee, S. (2010). Delineation of landslide hazard areas on Penang Island, Malaysia, by using frequency ratio, logistic regression, and artificial neural network models. *Environ. Earth Sci.* 60, 1037–1054. doi:10.1007/s12665-009-0245-8
- Rahman, A., Mahmood, S., Dawood, M., Rahman, G., and Chen, F. (2019). "Impact of climate change on flood factors and extent of damages in the Hindu Kush region," in *Oxford research encyclopedia of natural hazard science* (Oxford University Press). doi:10.1093/acrefore/9780199389407.013.316
- Rahmati, O., Haghizadeh, A., Pourghasemi, H. R., and NoorMohamadi, F. (2016). Gully erosion susceptibility mapping: The role of GIS-based bivariate statistical models and their comparison. *Nat. Hazards* 82, 1231–1258. doi:10.1007/s11069-016-2239-7
- Rebi, A., Hussain, A., Hussain, I., Cao, J., Ullah, W., Abbas, H., et al. (2023). Spatiotemporal precipitation trends and associated large-scale teleconnections in northern Pakistan. *Atmos. (Basel)* 14, 871. doi:10.3390/atmos14050871
- Rehman, A., Song, J., Haq, F., Mahmood, S., Ahamad, M. I., Basharat, M., et al. (2022). Multi-hazard susceptibility assessment using the analytical hierarchy process and frequency ratio techniques in the northwest himalayas, Pakistan. *Remote Sens. (Basel)* 14, 554. doi:10.3390/rs14030554
- ReliefWeb (2022). Rapid need assessment flood emergency - balochistan & sind (28th aug 2022) - Pakistan. Available at: <https://reliefweb.int/report/pakistan/rapid-need-assessment-flood-emergency-balochistan-sind-28th-aug-2022> (Accessed October 21, 2022).
- Rentschler, J., Salhab, M., and Jafino, B. A. (2022). Flood exposure and poverty in 188 countries. *Nat. Commun.* 13, 3527. doi:10.1038/s41467-022-30727-4
- Riazi, M., Khosravi, K., Shahedi, K., Ahmad, S., Jun, C., Bateni, S. M., et al. (2023). Enhancing flood susceptibility modeling using multi-temporal SAR images, CHIRPS data, and hybrid machine learning algorithms. *Sci. Total Environ.* 871, 162066. doi:10.1016/j.scitotenv.2023.162066
- Sabatidakis, N., Koukis, G., Vassiliades, E., and Lainas, S. (2013). Landslide susceptibility zonation in Greece. *Nat. Hazards* 65, 523–543. doi:10.1007/s11069-012-0381-4
- Saeed, M., Li, H., Ullah, S., Rahman, A., Ali, A., Khan, R., et al. (2021). Flood hazard zonation using an artificial neural network model: A case study of Kabul River Basin, Pakistan. *Sustainability* 13, 13953. doi:10.3390/su132413953
- Samanta, R. K., Bhunia, G. S., Shit, P. K., and Pourghasemi, H. R. (2018a). Flood susceptibility mapping using geospatial frequency ratio technique: A case study of subarnarekha River Basin, India. *Model. Earth Syst. Environ.* 4, 395–408. doi:10.1007/s40808-018-0427-z
- Samanta, S., Pal, D. K., and Palsamanta, B. (2018b). Flood susceptibility analysis through remote sensing, GIS and frequency ratio model. *Appl. Water Sci.* 8, 66. doi:10.1007/s13201-018-0710-1
- Sarkar, D., and Mondal, P. (2020). Flood vulnerability mapping using frequency ratio (FR) model: A case study on kulik river basin, indo-Bangladesh barind region. *Appl. Water Sci.* 10, 17. doi:10.1007/s13201-019-1102-x
- Shah, A. A., Ullah, A., Khan, N. A., Shah, M. H., Ahmed, R., Hassan, S. T., et al. (2023). Identifying obstacles encountered at different stages of the disaster management cycle (DMC) and its implications for rural flooding in Pakistan. *Front. Environ. Sci.* 11. doi:10.3389/fenvs.2023.1088126
- Sharif, H. O., Al-Juaidi, F. H., Al-Othman, A., Al-Dousary, I., Fadda, E., Jamal-Uddeen, S., et al. (2016). Flood hazards in an urbanizing watershed in Riyadh, Saudi Arabia. *Geomatics, Nat. Hazards Risk* 7, 702–720. doi:10.1080/19475705.2014.945101
- Shen, L., Wen, J., Zhang, Y., Ullah, S., Cheng, J., and Meng, X. (2022). Changes in population exposure to extreme precipitation in the Yangtze River Delta, China. *Clim. Serv.* 27, 100317.
- Shen, L., Zhang, Y., Ullah, S., Pepin, N., and Ma, Q. (2021). Changes in snow depth under elevation-dependent warming over the Tibetan Plateau. *Atmos. Sci. Lett.* 22. doi:10.1002/asl.1041
- Shrestha, S., Sattar, H., Khattak, M. S., Wang, G., and Babur, M. (2020). Evaluation of adaptation options for reducing soil erosion due to climate change in the Swat River Basin of Pakistan. *Ecol. Eng.* 158, 106017. doi:10.1016/j.ecoleng.2020.106017
- Shu, H., Guo, Z., Qi, S., Song, D., Pourghasemi, H. R., and Ma, J. (2021). Integrating landslide typology with weighted frequency ratio model for landslide susceptibility mapping: A case study from lanzhou city of northwestern China. *Remote Sens. (Basel)* 13, 3623. doi:10.3390/rs13183623
- Tariq, A., Mumtaz, F., Majeed, M., and Zeng, X. (2023). Spatio-temporal assessment of land use land cover based on trajectories and cellular automata Markov modelling and its impact on land surface temperature of Lahore district Pakistan. *Environ. Monit. Assess.* 195, 114. doi:10.1007/s10661-022-10738-w
- Tariq, A., and Mumtaz, F. (2022). Modeling spatio-temporal assessment of land use land cover of Lahore and its impact on land surface temperature using multi-spectral remote sensing data. *Environ. Sci. Pollut. Res.* 30, 23908–23924. doi:10.1007/s11356-022-23928-3
- Tayyab, M., Zhang, J., Hussain, M., Ullah, S., Liu, X., Khan, S. N., et al. (2021). GIS-based urban flood resilience assessment using urban flood resilience model: A case study of peshawar city, khyber Pakhtunkhwa, Pakistan. *Remote Sens. (Basel)* 13, 1864. doi:10.3390/rs13101864
- Tehrany, M. S., Lee, M.-J., Pradhan, B., Jebur, M. N., and Lee, S. (2014). Flood susceptibility mapping using integrated bivariate and multivariate statistical models. *Environ. Earth Sci.* 72, 4001–4015. doi:10.1007/s12665-014-3289-3
- Tehrany, M. S., Pradhan, B., and Jebur, M. N. (2015). Flood susceptibility analysis and its verification using a novel ensemble support vector machine and frequency ratio method. *Stoch. Environ. Res. Risk Assess.* 29, 1149–1165. doi:10.1007/s00477-015-1021-9
- Tehrany, M. S., Pradhan, B., and Jebur, M. N. (2013). Spatial prediction of flood susceptible areas using rule based decision tree (DT) and a novel ensemble bivariate and multivariate statistical models in GIS. *J. Hydrol. (Amst)* 504, 69–79. doi:10.1016/j.jhydrol.2013.09.034
- Thongley, T., and Vansarochana, C. (2021). Landslide susceptibility assessment using frequency ratio model at ossey watershed area in Bhutan. *Eng. Appl. Sci. Res.* 48, 56–64. doi:10.14456/easr.2021.7
- Ullah, F., Ali Shah, S. A., Saqib, S. E., Yaseen, M., and Haider, M. S. (2021). Households' flood vulnerability and adaptation: Empirical evidence from mountainous regions of Pakistan. *Int. J. Disaster Risk Reduct.* 52, 101967. doi:10.1016/j.ijdrr.2020.101967
- Ullah, K., and Zhang, J. (2020). GIS-based flood hazard mapping using relative frequency ratio method: A case study of Panjkora River Basin, eastern Hindu Kush, Pakistan. *PLoS One* 15, e0229153. doi:10.1371/journal.pone.0229153
- Ullah, S., You, Q., Ali, A., Ullah, W., Jan, M. A., Zhang, Y., et al. (2019b). Observed changes in maximum and minimum temperatures over China-Pakistan economic corridor during 1980–2016. *Atmos. Res.* 216, 37–51. doi:10.1016/j.atmosres.2018.09.020
- Ullah, S., You, Q., Ullah, W., and Ali, A. (2018). Observed changes in precipitation in China-Pakistan economic corridor during 1980–2016. *Atmos. Res.* 210, 1–14. doi:10.1016/j.atmosres.2018.04.007
- Ullah, S., You, Q., Ullah, W., Ali, A., Xie, W., and Xie, X. (2019a). Observed changes in temperature extremes over China-Pakistan Economic Corridor during 1980–2016. *Int. J. Climatol.* 39, 1457–1475. doi:10.1002/joc.5894
- Ullah, S., You, Q., Ullah, W., Sachindra, D. A., Ali, A., Bhatti, A. S., et al. (2023). Climate change will exacerbate population exposure to future heat waves in the China-Pakistan economic corridor. *Weather Clim. Extrem.* 40, 100570. doi:10.1016/j.wace.2023.100570

- Ullah, W., Wang, G., Ali, G., Tawia Hagan, D., Bhatti, A., and Lou, D. (2019). Comparing multiple precipitation products against in-situ observations over different climate regions of Pakistan. *Remote Sens. (Basel)* 11, 628. doi:10.3390/rs11060628
- Ullah, W., Wang, G., Lou, D., Ullah, S., Bhatti, A. S., Ullah, S., et al. (2021). Large-scale atmospheric circulation patterns associated with extreme monsoon precipitation in Pakistan during 1981–2018. *Atmos. Res.* 253, 105489. doi:10.1016/j.atmosres.2021.105489
- Vojtek, M., and Vojteková, J. (2019). Flood susceptibility mapping on a national scale in Slovakia using the analytical hierarchy process. *Water (Basel)* 11, 364. doi:10.3390/w11020364
- Wang, Y., Hong, H., Chen, W., Li, S., Pamučar, D., Gigović, L., et al. (2018). A hybrid GIS multi-criteria decision-making method for flood susceptibility mapping at shangyou, China. *Remote Sens. (Basel)* 11, 62. doi:10.3390/rs11010062
- Wang, Y., Sun, D., Wen, H., Zhang, H., and Zhang, F. (2020). Comparison of random forest model and frequency ratio model for landslide susceptibility mapping (LSM) in yunyang county (chongqing, China). *Int. J. Environ. Res. Public Health* 17, 4206. doi:10.3390/ijerph17124206
- Wang, Z., Chen, X., Qi, Z., and Cui, C. (2023). Flood sensitivity assessment of super cities. *Sci. Rep.* 13(1), 5582.
- Wang, Z., Lai, C., Chen, X., Yang, B., Zhao, S., and Bai, X. (2015). Flood hazard risk assessment model based on random forest. *J. Hydrol. (Amst)* 527, 1130–1141. doi:10.1016/j.jhydrol.2015.06.008
- Xu, H., Xu, K., Wang, T., and Xue, W. (2022). Investigating flood risks of rainfall and storm tides affected by the parameter estimation coupling bivariate statistics and hydrodynamic models in the coastal city. *Int. J. Environ. Res. Public Health* 19, 12592. doi:10.3390/ijerph191912592
- Youssef, A. M., Pradhan, B., and Sefry, S. A. (2016). Flash flood susceptibility assessment in Jeddah city (Kingdom of Saudi Arabia) using bivariate and multivariate statistical models. *Environ. Earth Sci.* 75, 12. doi:10.1007/s12665-015-4830-8
- Yu, P., Ma, H., Qiu, L., Zhang, T., and Li, S. (2022). Optimization of a flood diversion gate scheme in flood storage and detention areas based on flood numerical simulation. *Front. Environ. Sci.* 10. doi:10.3389/fenvs.2022.978385
- Zhao, G., Pang, B., Xu, Z., Peng, D., and Xu, L. (2019). Assessment of urban flood susceptibility using semi-supervised machine learning model. *Sci. Total Environ.* 659, 940–949. doi:10.1016/j.scitotenv.2018.12.217
- Zhao, P., Masoumi, Z., Kalantari, M., Aflaki, M., and Mansourian, A. (2022). A GIS-based landslide susceptibility mapping and variable importance analysis using artificial intelligent training-based methods. *Remote Sens. (Basel)* 14, 211. doi:10.3390/rs14010211
- Ziwei, L., Xiangling, T., Liju, L., Yanqi, C., Xingming, W., and Dishan, Y. (2023). GIS-based risk assessment of flood disaster in the Lijiang River Basin. *Sci. Rep.* 13, 6160. doi:10.1038/s41598-023-32829-5
- Zou, Q., Zhou, J., Zhou, C., Song, L., and Guo, J. (2013). Comprehensive flood risk assessment based on set pair analysis-variable fuzzy sets model and fuzzy AHP. *Stoch. Environ. Res. Risk Assess.* 27, 525–546. doi:10.1007/s00477-012-0598-5



OPEN ACCESS

EDITED BY

Sandipan Das,
Symbiosis International University, India

REVIEWED BY

Andrea Tertulliani,
National Institute of Geophysics and
Volcanology (INGV), Italy
Voltaire Alvarado Peterson,
University of Concepcion, Chile

*CORRESPONDENCE

Edris Alam,
✉ ealam@ra.ac.ae

RECEIVED 15 March 2023

ACCEPTED 03 July 2023

PUBLISHED 27 July 2023

CITATION

Alam E (2023), A Modified Mercalli
Intensity map of Bangladesh: a proposal
for zoning of earthquake hazard.
Front. Earth Sci. 11:1187176.
doi: 10.3389/feart.2023.1187176

COPYRIGHT

© 2023 Alam. This is an open-access
article distributed under the terms of the
[Creative Commons Attribution License
\(CC BY\)](https://creativecommons.org/licenses/by/4.0/). The use, distribution or
reproduction in other forums is
permitted, provided the original author(s)
and the copyright owner(s) are credited
and that the original publication in this
journal is cited, in accordance with
accepted academic practice. No use,
distribution or reproduction is permitted
which does not comply with these terms.

A Modified Mercalli Intensity map of Bangladesh: a proposal for zoning of earthquake hazard

Edris Alam^{1,2*}

¹Department of Geography and Environmental Studies, University of Chittagong, Chittagong, Bangladesh,

²Faculty of Resilience, Rabdan Academy, Abu Dhabi, United Arab Emirates

Bangladesh is vulnerable to a variety of natural hazards including frequent tropical cyclones, floods and, less commonly, earthquakes and tsunamis. The country has developed an effective response mechanism for frequently experiencing hazards. However, at the same time, the nation has not developed an effective response mechanism for earthquake as a result of limited experiences with this type of hazard in the recent past. This research constructs a new catalogue consisting of 144 earthquakes (between 810BC and 2015) occurring within Bangladesh and the adjacent region. From this new catalogue, the effects of earthquakes are available for 80 events which are used in order to construct the geography of hazard in Bangladesh. The construction of a detailed Modified Mercalli Intensity (MMI) map using the new earthquake data suggests that this will be useful for supporting future risk reduction efforts in Bangladesh. Specifically, the findings support the revision of the current seismic zoning map of Bangladesh to include Chittagong and Dhaka in the high-risk zone for effective earthquake risk reduction. Finally, this research concludes that analyses of long-term data helps to identify new hazard exposure and develop knowledge that is useful to formulate new disaster risk reduction policies and rectify existing know zones in Bangladesh.

KEYWORDS

earthquake, hazard, intensity, risk, data, Bangladesh

1 Introduction

Bangladesh has developed a well-planned disaster responses and mitigation mechanisms for tropical cyclones and floods, however, the mitigation programme for earthquake risk reduction is still in progress. Bangladesh is susceptible to earthquakes due to its location between active seismic zones within and adjacent to the nation. Earthquakes occurring from the adjacent region of Bangladesh has significantly affected this country (Alam and Dominey-Howes, 2014; Alam and Dominey-Howes, 2016). The present seismic zoning map and policies to mitigate the effects of the earthquake hazard in Bangladesh have been developed based on those earthquakes occurring only after 1885, neglecting the potential for large earthquakes from adjacent active faults, particularly the detachment thrust (Choudhury, 2005). Bangladesh is a heavily densely populated country having over 1,000 people per km² and fragile infrastructure in major city areas. There is no Modified Mercalli Intensity map to identify areas of social risk based on long-term hazard data. Therefore, more detailed archival research is required to identify high risk areas based upon available earthquake hazards in Bangladesh and adjacent regions.

In order to construct geographies of the earthquake hazard, it is necessary to understand the sources of hazards that originate in the region of Bangladesh. The Himalayan Mountains are located

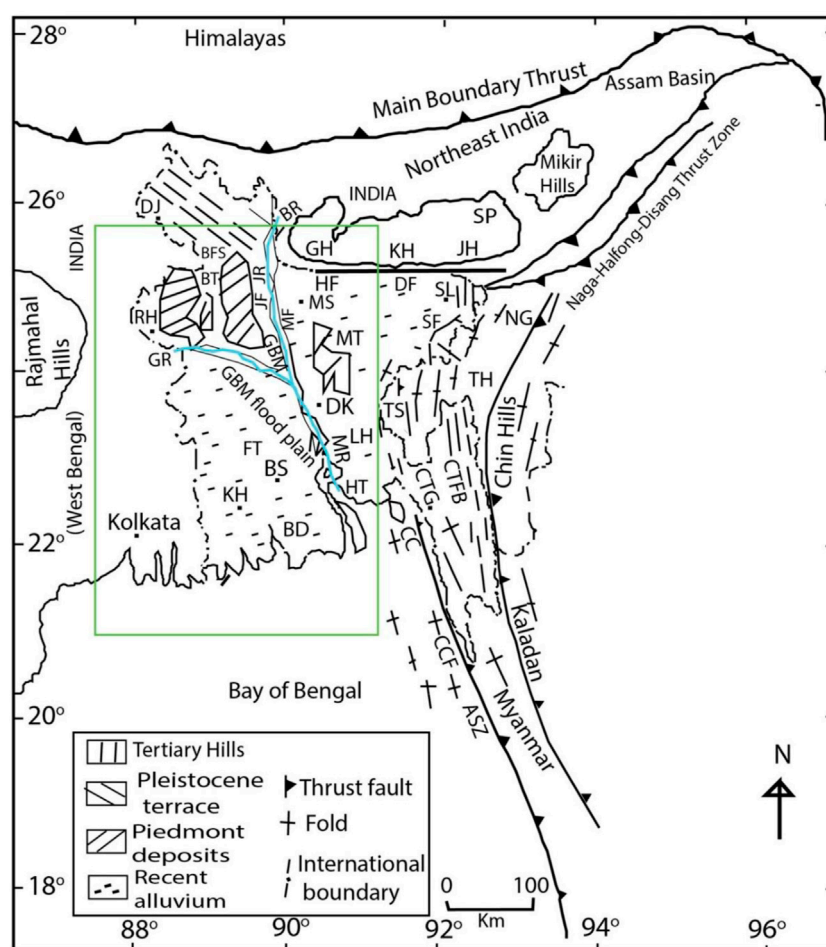


FIGURE 1

Location of Bangladesh in relation to regional active fault sources and the primary physiographic units: Tertiary Hills, Pleistocene uplands (the Barind and Madhupur terrace) and Recent sediments. The red solid contour lines show the demarcation of different zones from the mean sea level. The green box shows the location of the Bengal Basin. Key features include ASZ, Arakan Subduction Zone; BD, Bengal Delta; BFS, Bogra Fault System; BR, Brahmaputra River; BT, Barind Tract; BS, Barisal; CC, Chittagong coast; CTFB, Chittagong-Tripura fold belt; DF, Dauki Fault; DK, Dhaka; FT, Faridpur Through; GH, Garo Hills; GR, Ganges River; HF, Haluaghat Fault; HT, Hatiya Through; JF, Jamuna Fault; JH, Jaintia Hills; KH, Khasi Hills; LH, Lalmai Hills; MF, Madhupur Fault; MT, Madhupur Tract; MR, Meghna River; MS, Mymensingh; RH, Rajshahi; SF, Sylhet Fault; SL, Sylhet Hills and SP, Shillong Plateau (Source: map prepared adapting tectonic elements from Alam et al., 2003; Ali and Choudhury, 2001; Khan, 2012; Mukherjee et al., 2009).

200 km from the northern border of Bangladesh. Between the Himalayan Mountains and Bangladesh, the Dauki Fault and the Assam Seismic Fault are located (Figure 1). Additionally, the Bogra Fault System (BGF), the Jamuna Fault (JF), the Madhupur Fault (MF) and the Sylhet Fault (SF) are located within Bangladesh (Figure 1). To the south, the country is bordered by the Bay of Bengal. The Arakan Subduction Zone (ASZ) along the northern end of the Bay of Bengal extends up to the SE Bangladesh. It is a tropical low-lying country having a long funnel shaped coast (Figure 1). Bangladesh has experienced earthquakes those originated from within and adjacent seismic sources in recent and distant past.

The country is affected by earthquakes originating in India and Myanmar. In order to construct a complete geography of the hazard, it is necessary to consider active seismic sources from the adjacent countries particularly adjoining Bangladesh (Figure 1). The research proposes a new Modified Mercalli Intensity map which has been

developed based upon the average effects of 80 earthquakes in Bangladesh occurring between BC810 and 2015 in Bangladesh and adjacent regions.

This paper begins with discussing earthquake hazard zoning and preparation activities. This is followed by a review of data sources used for this research. The methods of the new MMI map construction are detailed and illustrated followed by a presentation of the results. The last sections discuss the significance of the findings and detail the conclusions.

2 Earthquake hazard zoning and preparation activities in Bangladesh

In the late 1970s and early 1980s, was a period where many bridges, buildings and industrial structures constructed

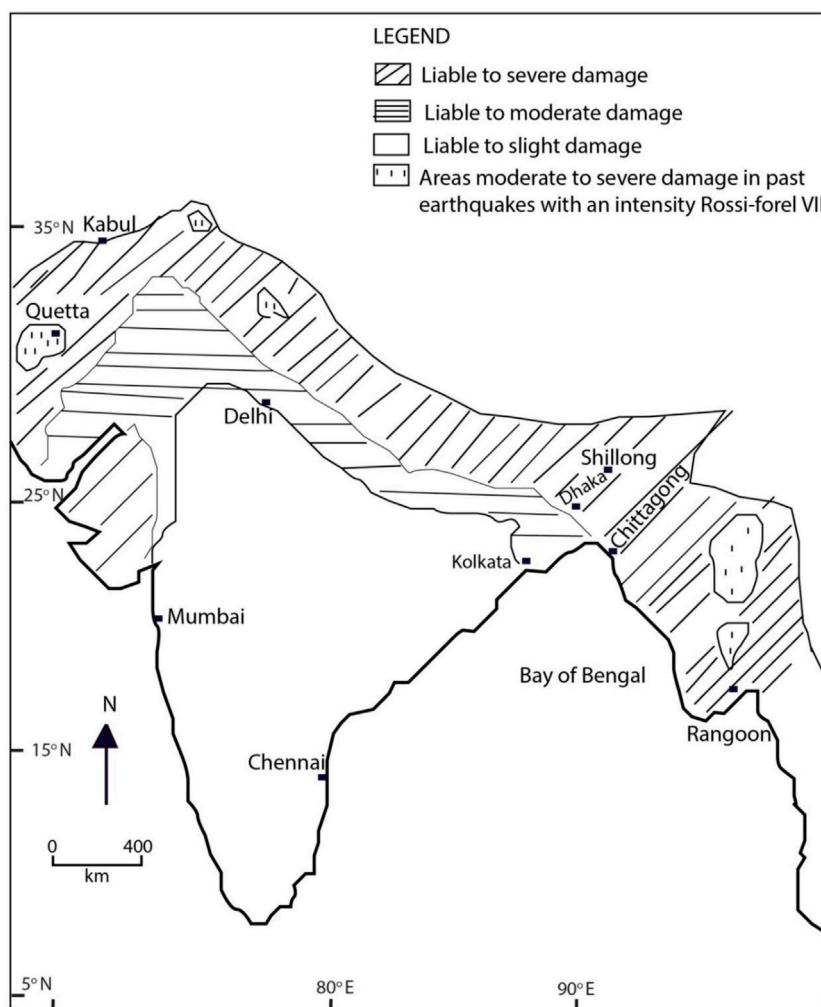


FIGURE 2

Indian sub-continent seismic zone map which was prepared by the Geological Survey of India in 1935 (Source: redrawn from [Ali and Choudhury, 2001](#)).

throughout Bangladesh. Following this, the assessment of seismic risk in different regions in the country was a great concern of engineers and scientists ([Ali and Choudhury, 2001](#)). Research was undertaken to identify areas liable to severe seismic effects in Bangladesh ([Kamal, 2008](#); [Sarker et al., 2010](#)). The seismic zoning maps of Bangladesh have been revised continuously with the revised standing orders on disasters which was published in 2010, emphasised the need for mapping areas liable to earthquake damage. To understand the effectiveness of program and policies in relation to earthquake risk reduction, it is necessary to review relevant policies and how they align. Earthquake hazard management includes three key initiatives a) seismic zoning and introduction of building codes, b) seismic and geomagnetic observatories and c) public education and awareness. The first two initiatives are much relevant to the background of this study have been detailed in the following sections.

2.1 Seismic zoning and introduction of building codes

The Geological Survey of India developed the first seismic zoning map for the sub-continent in 1935. North, north-east and south-east regions of Bangladesh had been included in the severe seismic risk zone of the Geological Survey of India map ([Figure 2](#)). After Bangladesh became an independent country in 1971, separating from Pakistan the mid 1970s, saw large industrial complexes (e.g., fertilizer factories et al.) built and designed which demanded a sophisticated investigation of seismic risk ([Ali and Choudhury, 2001](#)). The 12 May 1977 earthquake (M_s 5.7) along Bangladesh-India border further reaffirmed this requirement to be incorporated in their design. Consequently, in June 1977, the Government of Bangladesh formed a committee of experts to undertake seismic zoning of Bangladesh and formulate policy options. The committee reviewed all the available information,

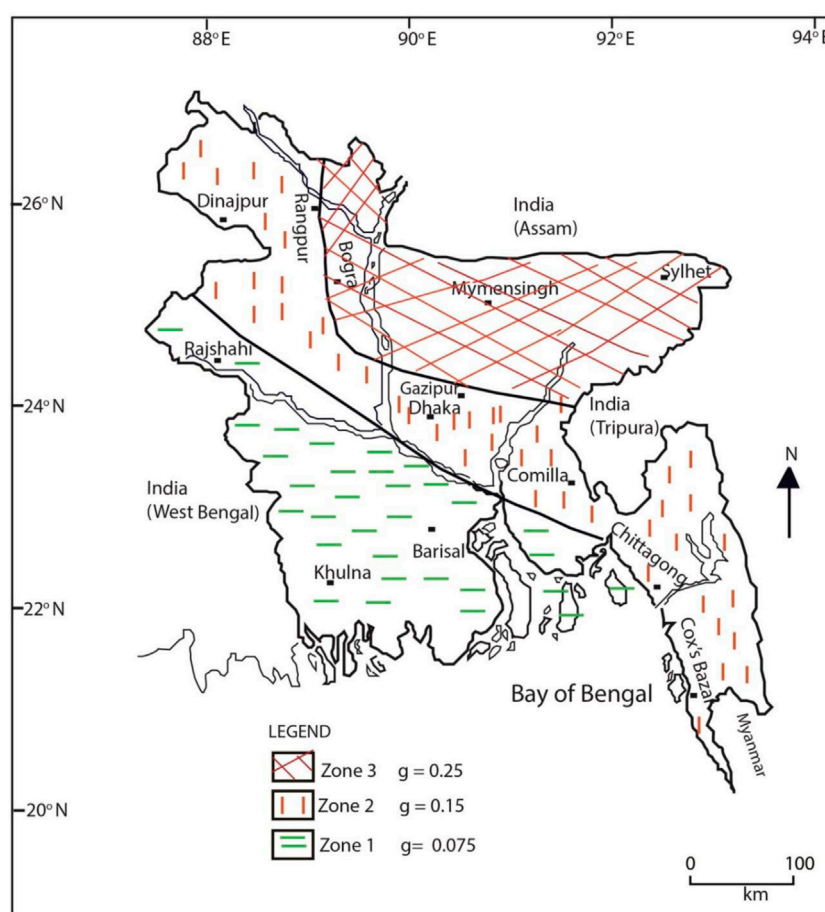


FIGURE 3

The current seismic zoning map of Bangladesh indicating probable earthquake zone coefficients. The g value equals maximum ground acceleration that can be expected based upon historic earthquakes over the last 200 years. Zone 1 includes NE of Bangladesh and Sylhet City lies within this zone. Zone 2 includes Dhaka and Chittagong cities. Zone 3 includes SW Bangladesh (Source: redrawn from Ali and Choudhury, 2001).

revised seismic risk maps and outlined the newly established building codes for earthquake resistant designs. In 1992, this exercise was repeated, with policies, rules and laws embracing new research and knowledge in earthquake zones and engineer and construction practices. Furthermore, seismic risk maps and building codes were revised to provide improved guidelines for earthquake resistant design. For this mapping exercise, Bangladesh was divided into three zones (Figure 3): Zone 3 (liable to severe damage); Zone 2 (liable to moderate damage); and Zone 1 (liable to slight damage).

2.2 Seismic and geomagnetic observatories

The Bangladesh Meteorological Department established an observatory in Chittagong in 1954, with facilities for seismic and geomagnetic observations (Ali and Choudhury, 2001). Until 2007, this was the only seismic observatory in Bangladesh. Although in 1977 the committee of experts recommended the establishment of a minimum of three observatories throughout the country, it has taken over 30 years to establish such observatories which are located

in Sylhet, Rangpur and Gazipur (Figure 3) including the modernisation of the Chittagong centre in 2007. Currently in Bangladesh, different institutions such as Dhaka University Earth Observatory (DUEO), Bangladesh University of Engineering and Technology (BUET), Geological Survey of Bangladesh (GSB) and Bangladesh Meteorological Department (BMD) operate seismic monitoring networks separately of each other.

Efforts to identify areas of high seismic risk in Bangladesh have been in progress for some time (Kamal, 2008; Sarker et al., 2010). A number of UN funded projects have worked and been continued to work retrofitting in Dhaka, Sylhet and Mymensingh. There is also still an outstanding need to identify and retrofit fragile buildings in Dhaka and other major cities of Bangladesh (Paul and Bhuiyan, 2010). The pre 2012, policies and practices, which are based on tropical cyclones and floods, may not be adequate to mitigate the consequences of earthquake and tsunamis. However, the drafted disaster management policies of 2012, have initiated several effective measures for earthquake risk reduction. These include:

- enhancing institutional capacity to mitigate earthquake risk, updating building codes, purchasing equipment for the fire

service and civil defense department to effectively respond in the post disaster period;

- generating awareness among people about earthquake hazard and risk and arranging training for volunteers;
- developing seismic hazard risk maps for urban areas (for example, Dhaka, Chittagong, Sylhet and Rangpur);
- retrofitting fragile buildings in the above urban areas and developing guidelines for people about the retrofitting;
- developing a program of actions to mitigate consequences of earthquake occurrence in local level urban administration. For example, forming disaster management committee and volunteer teams for awareness generation and operating search, rescue operations with highest participation of local people;
- enhancing earthquake hazard response mechanisms in institutions (Hospital, school and garments);
- conducting research about earthquake hazard and risk; and
- enhancing efficient and professional management team in post disaster rehabilitation.

The review of the work of the Ministry of Disaster Management and Relief, and Disaster Management Department suggests that the Government of Bangladesh is still working towards identifying earthquake prone areas and improving DRR for earthquake related hazards. In order to develop an effective earthquake risk reduction program, it is necessary to review past hazard events and their geographical distribution and impacts in Bangladesh. This research will show how reviewing long-term earthquake data can help accurately identify appropriate seismic risk mapping in Bangladesh.

3 Data sources and methods

The records of Bangladesh earthquakes can be classified according to four types of data sources: geological, archaeological, historical and instrumental data. Each type of record has been collected from existing recognised and published sources. In order to develop a comprehensive earthquake catalogue, data sources were obtained from online global earthquake databases e.g., the National Geophysical Data Center (NGDC, 2012) and Geoscience Australia (GA), (Geoscience Australia, 2011a), International Seismological Centre (ISC, 2023), Incorporated Research Institutions for Seismology (IRIS, 2023), the Novosibirsk Tsunami Laboratory, Russia (NTL), regional catalogue (i.e., Oldham, 1883), annals, chronicles, diaries, letters, travellers, published earthquake catalogues, articles in the peer reviewed literature, books, reports, newspaper articles, local historical books, institutional and administrative memoirs and the historical archive from the India Office Records of the British Library and Royal Society, London. Whilst this research focuses on identifying events that have affected Bangladesh, it has broadened the study to include the area located between Latitude 18.5°S to 28.15°N and Longitude 87° E to 95.5° E to ensure the comprehensive coverage of the study area and adjacent seismically active regions (Figure 1).

3.1 Recording and conversion of earthquake magnitudes

While collecting and collating earthquake magnitudes from secondary sources listed below Table 1, it has been noted several challenges relating to the use of different magnitude scales and the lack of any magnitude scale for some events. On occasion, a source provides Modified Mercalli Intensity (MMI) values for the effects of an earthquake. However, when neither an MMI or magnitude scale was provided, it has been attempted to collect and review the effects of the earthquakes if available. After careful analysis of the effects, this has been converted to the MMI scale and a new MMI value has been provided in Table 1. In this study, when a source material item has been consulted, it is considered to be a secondary source. For example, for the 1764 event, this study has consulted several sources (Anon., 1897; Chandra, 1977; Nandy, 1994), which are considered as secondary sources. Nandy (1994) referred to Campbell (1809) from where information was collected for this particular event. At this stage, this study is not able to consult Campbell (1809) and consider this reference as a primary source for that event. Hence, primary sources are those that this study has not yet consulted for a particular event and secondary sources are those that this has consulted.

For quantification and graphical presentation of the earthquakes, the size of earthquakes should be classified based on their magnitude or intensity scales. For the new earthquake catalogue presented in Table 1, the size of earthquakes was provided in magnitude scales by most source materials. The conversion of earthquake scales from either “magnitude” to “intensity” or *vice versa*, could distort the actual values of the size of each earthquake. In some cases, intensity values were recorded from secondary sources (Table 1). For example, for the 1676 earthquake (Even #13 in Table 1), an intensity value of 7 was provided by the source document; this intensity value has been converted to 5.7 on the magnitude scale. This conversion of the intensity values of earthquakes to magnitude measured on the Richter scale were performed using the magnitude and intensity relationship (see supplementary material Table 1) provided by the Missouri Department of Environmental Resources (Gere and Shah, 1984). It should be borne in mind that MMI values are often skewed to higher values by locations with higher shaking susceptibility, certain types of soil texture, or locations with buildings that respond to a particular ground shaking frequency in disastrous ways (Ambraseys and Douglas, 2004). As such, converted magnitude from the MMI that has been provided in Table 1 should be treated with caution for the purpose of reuse and further research to more accurately refine these MMIs is required but was beyond the scope of this research.

3.2 Cross checking and validation of data

A total of 99 source documents were consulted to assist with development of the new earthquake catalogue (Table 1). However, inconsistencies in citations, differences in the date of events, differences in magnitude and intensity were identified. Accordingly, it was necessary to employ a rigorous system for cross-checking and validating data. This has been achieved by cross-checking multiple sources and performing a content

TABLE 1 A catalogue of historical and palaeoseismic evidence of earthquake in Bangladesh and adjacent regions between BC810 and AD2015.

Event number	Year	Month	Day	Earthquake locations			Earthquake parameters			Earthquake effects				Primary	Secondary	Comments
				Location names	Lat	Long	Magnitude	Intensity	Focal depth	Deaths	Injuries	Damage (in m US \$)	House destroyed/damaged			
1*	810BC-400	*	*	India: Assam	26.1	92.56	*	*	*	*	*	*	*	-	99	Radiocarbon dating of sediments calibrated age 810BC-400
2	535BC-530	*	*	India: Assam	26.1	92.56	*	*	*	*	*	*	*	-	99	Radiocarbon dating of sediments calibrated age 535BC-530
3	645–980	*	*	India: Assam	26.1	92.56	*	*	*	*	*	*	*	-	99	Radiocarbon dating of sediments calibrated age 645BC-980
4	825–835	*	*	India: Assam	26.1	92.56	8	*	*	*	*	*	*	-	5, 15, 99	The earthquake destroy temples and palaces in Assam
5	1440–1470	*	*	Bangladesh	25.15	90.3	*	*	*	*	*	*	*	-	30	The radiocarbon age of charcoals shows date as 1440–1470
6	1548	*	*	India and Bangladesh	26	94	7	9	*	*	*	*	*	45	30, 42, 52, 98	The first recorded earthquake in Bangladesh. Sylhet and Chittagong were violently shaken
7	1596	*	*	India: Assam	26.1	92.56	7	9	*	*	*	*	*	-	92	
8	1601	*	*	India: Assam	26.1	92.56			*	*	*	*	*	-	92	
9	1642	*	*	India: Assam	26.1	92.56	6	*	*	*	*	*	*	-	22, 42, 46, 92	Most severe damage occurred in Bangladesh

(Continued on following page)

TABLE 1 (Continued) A catalogue of historical and palaeoseismic evidence of earthquake in Bangladesh and adjacent regions between BC810 and AD2015.

Event number	Year	Month	Day	Earthquake locations			Earthquake parameters			Earthquake effects				Primary	Secondary	Comments
				Location names	Lat	Long	Magnitude	Intensity	Focal depth	Deaths	Injuries	Damage (in m US \$)	House destroyed/damaged			
10	1649	*	*	India: Assam	26.1	92.56	3	3	*	*	*	*	*	-	46	
11	1663	2	19	India: Assam	26.1	92.56	8		*	*	*	*	*	-	42, 92, 96, 97, 98	The earthquake was so devastating that Mir Jumla is believed to have fled Assam
12	1664	*	*	Bangladesh	25	90	M _w 7.79		*	*	*	*	*	-	30, 51	The earthquake may be relevant to the activity of the Dauki Fault
13	1676	9/10	*	Bangladesh	22.22	91.48	5.7	7	*	*	*	*	*	-	46	Chittagong was destroyed by an earthquake and severe tropical cyclone
14	1679	1	28	Myanmar	19.42	93.57	7	9	*	*	*	*	*	-	46	The earthquake was very severe and affected a wide area of Arakan, Bengal and India
15	1696	*	*	India: Assam	26.1	92.56		*	*	*	*	*	*	-	92	The reign of King Rudra Singha experienced earthquakes twice in 1696 and 1749
16	1749	*	*	India: Assam	26.1	92.56			*	*	*	*	*	-	92	-
17	1750	*	*	Myanmar coast	18.5	93.4	5.7	7	*	*	*	*	*	1	1, 16	The earthquake may have caused eruptions of mud volcanoes

(Continued on following page)

TABLE 1 (Continued) A catalogue of historical and palaeoseismic evidence of earthquake in Bangladesh and adjacent regions between BC810 and AD2015.

Event number	Year	Month	Day	Earthquake locations			Earthquake parameters			Earthquake effects				Primary	Secondary	Comments
				Location names	Lat	Long	Magnitude	Intensity	Focal depth	Deaths	Injuries	Damage (in m US \$)	House destroyed/damaged			
18	1762	4	2	Bangladesh: Chittagong	22	92	8	11	*	200	*	*	*	6, 8,9,11,16, 17, 18, 19, 20	1, 2, 3, 4, 7, 34, 40,43, 50, 52, 77, 79,80, 91, 93	Alam et al. (2012) concluded the earthquake caused local tsunamis and huge effects on social infrastructures
19	1762	7	13	India: Kolkata	22.3	88.2	4.3	5 ⁽⁷¹⁾	*	*	*	*	*	-	10, 20, 71	-
20	1764	6	4	Bangladesh-India: on the bank of the Ganga River	24	88	6	8 ^(10,71)	*	*	*	*	*	70	10, 21, 71	Many houses destroyed and large number of people and cattle were killed ⁽²¹⁾
21	1772	*	*	India: Assam	26.1	92.56	M _s 6.5	*	*	*	*	*	*	-	93	The earthquakes damaged the part of Assam
22	1775	4	10	Bangladesh: Dhaka	23.38	90.25	4.3	5	*	*	*	*	*	-	42, 98	Severe earthquake felt in Dhaka
23	1787	*	*	Bangladesh	24.26	89.43	7	10	*	*	*	*	*	-	46, 54, 98	The earthquake caused shifting of river courses
24	1808	4	13	India: Kolkata	22.6	88.4	4.3	5 ⁽¹⁰⁾	*	*	*	*	*	-	10, 20, 71	Cracks in house walls were observed
25	1810	4	1	India: Kolkata	22.3	88.2	3.7	4 ⁽¹⁰⁾	*	*	*	*	*	-	10, 20, 71	The earthquake felt very severely in Kolkata
26	1810	5	13	India: Kolkata	22.3	88.2	4.3	5 ⁽¹⁰⁾	*	*	*	*	*	-	10, 20, 71	-

(Continued on following page)

TABLE 1 (Continued) A catalogue of historical and palaeoseismic evidence of earthquake in Bangladesh and adjacent regions between BC810 and AD2015.

Event number	Year	Month	Day	Earthquake locations			Earthquake parameters			Earthquake effects				Primary	Secondary	Comments
				Location names	Lat	Long	Magnitude	Intensity	Focal depth	Deaths	Injuries	Damage (in m US \$)	House destroyed/damaged			
27	1811	2	1	India: Kolkata	22.3	88.2	5	6 ⁽¹⁰⁾	*	*	*	*	*	-	10, 20, 71	-
28	1812	5	11	Bangladesh		Dhaka	6	8	*	*	*	*	*	-	42, 98	The earthquake felt violently in Sylhet
29	1816	7	11	India: Kolkata	22.3	88.2	3.7	4 ⁽¹⁰⁾	*	*	*	*	*	-	10, 20, 71	-
30	1822	4	3	Bangladesh	24.3	90.5	7.1 ⁽⁹⁹⁾	8 ⁽¹⁰⁾	*	*	*	*	*	55	20, 71, 98	Several shocks felt in Bengal
31	1822	8	16	India: Kolkata	22.3	88.2	5	6 ⁽¹⁰⁾	*	*	*	*	*	56	10, 20, 71	Walls of houses were moved from north to south
32	1823	4	3	Kolkata	22.3	88.2	4.3	5 ⁽¹⁰⁾	*	*	*	*	*		10, 20, 71	-
33	1823	11	26	Kolkata	22.3	88.2	4.3	5 ⁽¹⁰⁾	*	*	*	*	*	57	10, 20, 71	Accompanied by subterranean noises
34	1825	1	8	Bangladesh	24.4	90.33	4.3	5	*	*	*	*	*	57, 58	20	-
35	1827	1		India: Kolkata	22.3	88.2	4.3	5 ⁽¹⁰⁾	*	*	*	*	*		10, 20, 71	-
36	1827	1	19	India: Kolkata	22.3	88.2	4.3	5 ⁽¹⁰⁾	*	*	*	*	*	60	10, 20, 71	-
37	1828	7	8	India: Kolkata	22.32	88.23	5.7	7 ⁽¹⁰⁾	*	*	*	*	*	61	10, 20	-
38	1828	9	18	India: Kolkata	22.3	88.2	4.3	5 ⁽¹⁰⁾	*	*	*	*	*	62	10, 20, 71	-
39	1828	10	8	Bangladesh: Dhaka	23.42	90.24	5		*	*	*	*	*	62	20	Four distinct shocks in successions
40	1829	9	18	India: Kolkata	22.3	88.2	5	6 ⁽¹⁰⁾	*	*	*	*	*	63	10, 20, 71	-

(Continued on following page)

TABLE 1 (Continued) A catalogue of historical and palaeoseismic evidence of earthquake in Bangladesh and adjacent regions between BC810 and AD2015.

Event number	Year	Month	Day	Earthquake locations			Earthquake parameters			Earthquake effects				Primary	Secondary	Comments
				Location names	Lat	Long	Magnitude	Intensity	Focal depth	Deaths	Injuries	Damage (in m US \$)	House destroyed/damaged			
41	1830	12	31	Bangladesh: Chittagong	22.47	91.59	6.5	*	*	*	*	*	*	64	20, 48	Very violent earthquake and all houses were seriously cracked
42	1832			India: Assam	26.1	92.56	6.5	*	*	*	*	*	*	-	93	The earthquakes damaged the part of Assam
43	1834	7	8	Bangladesh: Rangpur	25.33	89.1	6	8 ⁽¹⁰⁾	*	*	*	*	*	74	10, 20, 71	-
44	1834	7	21	Bangladesh: Rangpur	25.33	89.1	6	8 ⁽¹⁰⁾	*	*	*	*	*	74	10, 20, 71	-
45	1842	5	21	India: Bengal	25	87	5.7	7 ⁽¹⁰⁾	*	*	*	*	*	73	10, 20, 71	-
46	1842	5	23	India: Bengal	25	87	4.3	5 ⁽¹⁰⁾	*	*	*	*	*	73	10, 20, 71	-
47	1842	10	23	Bangladesh: Chittagong	22.47	91.59	4.3	5	*	*	*	*	*	73	20	Motion east to west
48	1842	11	11	Bangladesh	24	89.2	M _w 7.3	9 ⁽¹⁰⁾	*	*	*	*	*	44	10, 20, 71, 73, 98	Felt also sharply at sea
49	1843	10	30	Myanmar: Ramree and Cheduba	18.5	94.1	6	8	*	*	*	*	*	67	20	Very sharp at Gukiong, on sea, 145 miles to south
50	1845	7	24	India: Serampore, Kolkata	22.7	88.4	4.3	5	*	*	*	*	*	-	10, 20, 71	-
51	1945	7	26	India: Serampore	22.7	88.4	4.3	5	*	*	*	*	*	-	10, 20, 98	-
52	1845	8	6	India: Guwahati, Sylhet	22.7	88.4	M _w 7.1 ⁽⁹⁹⁾	7 ⁽¹⁰⁾	*	*	*	*	*	-	7, 10, 20, 71	-
53	1846	10	18	Bangladesh	23.52	90.23	M _s 6.2	*	*	*	*	*	*	Friend of India	7, 20	Masonry buildings were cracked in every direction in Dhaka

(Continued on following page)

TABLE 1 (Continued) A catalogue of historical and palaeoseismic evidence of earthquake in Bangladesh and adjacent regions between BC810 and AD2015.

Event number	Year	Month	Day	Earthquake locations			Earthquake parameters			Earthquake effects				Primary	Secondary	Comments
				Location names	Lat	Long	Magnitude	Intensity	Focal depth	Deaths	Injuries	Damage (in m US \$)	House destroyed/damaged			
54	1848			India: Assam	26.1	92.56	5.7	7	*	*	*	*	*	-	93	The earthquake damaged the part of Assam
55	1848	2	20	India: Kolkata	22.3	88.2	4.3	5 ⁽¹⁰⁾	*	*	*	*	*	Friend of India	20, 71	-
56	1848	11	30	India: Kolkata	22.3	88.2	3.7	4 ⁽¹⁰⁾	*	*	*	*	*	Friend of India	10, 20, 71	-
57	1849	1	22	India: Kolkata	22.3	88.2	3.7	4 ⁽¹⁰⁾	*	*	*	*	*	105	10, 20, 71	-
58	1851	1	8	Bangladesh: Chittagong	22.47	91.59	5.7	7	*	*	*	*	*	Hooker's Journal vol. 2	20	Motion apparently from south
59	1851	2	9	India: Kolkata	22.3	88.2	5.7 ⁽⁷¹⁾	7 ⁽¹⁰⁾	*	*	*	*	*	Friend of India	10, 20	-
60	1852	2	9	India: Kolkata	22.3	88.2	3.7	4 ⁽¹⁰⁾	*	*	*	*	*	-	10, 20	-
61	1852	8	9	Bangladesh: Dhaka	23.43	90.24	4.3	5	*	*	*	*	*	Perry	20	Oscillation lasted 15 seconds
62	1861	2	16	India: Kolkata	22.3	88.2	5.7	7 ⁽¹⁰⁾	*	*	*	*	*	Friend of India	10, 20	Water in tanks rose about 0.3 m above its level
63	1861	4	18	India: Kolkata	22.3	88.2	3.7	4 ⁽¹⁰⁾	*	*	*	*	*	-	10, 20, 71	-
64	1864	1	5	Bangladesh: Dhaka	23.42	90.24	4	*	*	*	*	*	*	Friend of India	10, 20	Houses much shaken
65	1864 or 1865	*	*	Bangladesh: Chittagong	22.22	91.50	5.7	7	*	*	*	*	*	-	41	A violent shock of an earthquake in the year 1764 or 1765, triggered mud volcanoes

(Continued on following page)

TABLE 1 (Continued) A catalogue of historical and palaeoseismic evidence of earthquake in Bangladesh and adjacent regions between BC810 and AD2015.

Event number	Year	Month	Day	Earthquake locations			Earthquake parameters			Earthquake effects				Primary	Secondary	Comments
				Location names	Lat	Long	Magnitude	Intensity	Focal depth	Deaths	Injuries	Damage (in m US \$)	House destroyed/damaged			
66	1865	11	17	Bangladesh: Jessore	23.2	89.2	4.3	5 ⁽¹⁰⁾	*	*	*	*	*	Official Record	10, 20, 71	-
67	1865	12	19	Bangladesh	23.23	91.13	5.5		*	*	*	*	*	-	7, 20, 37, 91	Many buildings were cracked in Chittagong
68	1866	1	6	Bangladesh: Chittagong	22.22	91.48	3.7	4	*	*	*	*	*	Friend of India	10, 20	Light shock
69	1866	5	23	India: Bengal	25	87	5.6 ⁽⁷¹⁾	8 ⁽¹⁰⁾	*	*	*	*	*	Friend of India	7, 10, 20, 71	Some houses fell down
70	1869	1	10	India: Assam	24.75	93.25	M _w 7.3		*	*	*	*	*	-	51, 93,97,98	-
71	1869	6	9	India: Kolkata	22.3	88.2	4.3 ⁽⁷¹⁾	5 ⁽¹⁰⁾	*	*	*	*	*	-	10, 20, 71	-
72	1870	4	22	Bangladesh: Dhaka	23.42	90.24	5.5		*	*	*	*	*	Times	7	-
73	1874	5		Bangladesh: Bhola	22	89	*	*	*	*	*	*	*	-	82, 83	-
74	1876	12	13	Bangladesh	23.42	90.25	4.3	5	*	*	*	*	*	-	85, 98	It was felt in Dhaka
75	1885	7	14	Bangladesh	24.8	89.5	M _w 6.9	7 ⁽¹⁰⁾	*	75	*	*	*	-	1, 7, 10, 28, 47, 51, 71, 85, 86	The felt areas extended in the entire northeast India and Myanmar
76	1891	6	17	Bangladesh: Sirajganj	20.5	86.55	5	5 ⁽¹⁰⁾	*	*	*	*	*	-	7, 10	-
77	1897	6	12	India: Assam	26	91	M _s 8.7	*	60	1626	*	*	*	9, 11, 12, 13, 14, 18, 23	1, 7, 21, 24, 25, 33, 40, 49, 68, 73, 87, 91, 92	A great tidal wave swept up the Brahmaputra River over 250 miles from sea

(Continued on following page)

TABLE 1 (Continued) A catalogue of historical and palaeoseismic evidence of earthquake in Bangladesh and adjacent regions between BC810 and AD2015.

Event number	Year	Month	Day	Earthquake locations			Earthquake parameters			Earthquake effects				Primary	Secondary	Comments
				Location names	Lat	Long	Magnitude	Intensity	Focal depth	Deaths	Injuries	Damage (in m US \$)	House destroyed/damaged			
78	1906	9	29	India: Kolkata	22.3	88.2	5 ⁽⁷¹⁾	6 ⁽¹⁰⁾	*	*	*	*	*	78	10, 71	-
79	1906	12	6	India: Kolkata	22.3	88.2	5 ⁽⁷¹⁾	6 ⁽¹⁰⁾	*	*	*	*	*	78	10, 71	-
80	1918	7	8	Bangladesh	24.5	91.7	M _s 7.6	*	14	9	50	*	*	-	1, 25, 81, 76, 92, 98	Severe damage in Srimangal, but minor effects in Dhaka
81	1923	9	9	Bangladesh	25.18	91	M _s 7.1	*	*	50	*	*	*	-	40, 88, 92, 95, 98	The earthquake caused heavy damage in Mymensingh
82	1930	7	2	India: Assam	25.8	90.2	M _s 7.1	*	*	1	*	*	*	-	1, 28, 92, 94	The earthquake caused major damage in the eastern Rangpur district
83	1930	9	24	Bangladesh	24.9	93.86	M _w 6.18	*	*	*	*	*	*	-	89	-
84	1932	3	24	Bangladesh: North	25	90	M _s 5.7	*	*	*	*	*	*	-	10, 38, 40, 71	-
85	1932	3	27	Bangladesh	24.3	92	M _w 5.7	*	*	*	*	*	*	-	40, 89	-
86	1932	9	11	India	26.3	92	M _w 5.8	*	*	*	*	*	*	-	40, 89	-
87	1933	3	6	Bangladesh	26	90.3	M _w 5.9	*	*	*	*	*	*	-	89	-
88	1934	1	15	Bihar-Nepal	26.5	86.5	M _s 8.4	*	*	*	*	*	*	-	76, 88	The earthquake caused damage in Rangpur
89	1935	3	21	Bangladesh: Pabna	24	89.14	M _w 5.8	*	*	*	*	*	*	27	10, 71, 89, 98	-
90	1941	1	21	Bhutan	27	92	M _w 6.43	*	*	*	*	*	*	-	40, 89	-

(Continued on following page)

TABLE 1 (Continued) A catalogue of historical and palaeoseismic evidence of earthquake in Bangladesh and adjacent regions between BC810 and AD2015.

Event number	Year	Month	Day	Earthquake locations			Earthquake parameters			Earthquake effects				Primary	Secondary	Comments
				Location names	Lat	Long	Magnitude	Intensity	Focal depth	Deaths	Injuries	Damage (in m US \$)	House destroyed/damaged			
91	1950	8	15	India: Assam	28.12	94.05	M _w 6	*	*	*	*	*	*	-	29, 31, 32, 42, 89	Water bodies in Dhaka remained in a state of agitation for an hour
92	1954	3	22	Myanmar	24.5	95.3	M _s 7.4	*	*	*	*	*	*	-	1, 26, 98	In Dhaka residents wake up and ran outdoor
93	1957	7	1	India-Myanmar border	25	94	M _s 7	*	*	*	*	*	*	-	92	-
94	1957	12	6	Bangladesh: Dhaka	24	90		*	*	*	*	*	*	10	11	-
95	1964	2	27	Myanmar	21.7	94.4	M _w 6.1	*				*	*	-	89, 90	-
96	1965	6	11	Bhutan	27.12	91.36	M _b 5.1	*	*	*	*	*	*	-	40, 38	-
97	1967	9	6	Bangladesh	24.6	91.42	M _w 5.1	*	*	*	*	*	*	-	40, 89	-
98	1967	9	15	Bhutan	27.24	91.48	M _w 5.8	*	*	*	*	*	*	-	40, 89	-
99	1967	11	14	Bangladesh	25	91.3	M _w 5.3	*	*	*	*	*	*	-	40, 89	-
100	1968	12	27	Bangladesh	24.06	91.36	M _w 5.4	*	*	*	*	*	*	-	40, 89	-
101	1969	5	11	Bhutan	27.42	90.12	5	*	*	*	*	*	*	-	40	-
102	1970	7	25	Bangladesh	25.42	88.3	M _w 5.4	*	*	*	*	*	*	-	40, 89	-
103	1970	8	28	Bangladesh	24.42	91.42	M _w 5.3	*	*	*	*	*	*	-	40, 89	-
104	1971	2	2	Bangladesh	23.48	91.48	M _w 5.4	*	*	*	*	*	*		40, 89	-
105	1972	11	6	India: Assam	27	88.42	M _b 4.8	*	*	*	*	*	*	-	40, 38	-
106	1974	9	21	India: Assam	25.42	90.54	M _b 4.8	*	*	*	*	*	*	-	40, 89	-
107	1976	6	23	Bangladesh	21.24	88.42	M _b 5.3	*	*	*	*	*	*	-	40, 89	Water movement in sea adjacent to the Chittagong coast was observed by local people

(Continued on following page)

TABLE 1 (Continued) A catalogue of historical and palaeoseismic evidence of earthquake in Bangladesh and adjacent regions between BC810 and AD2015.

Event number	Year	Month	Day	Earthquake locations			Earthquake parameters			Earthquake effects				Primary	Secondary	Comments
				Location names	Lat	Long	Magnitude	Intensity	Focal depth	Deaths	Injuries	Damage (in m US \$)	House destroyed/damaged			
108	1977	5	8	Bangladesh	24.89	92.25	M _b 5.6	*	*	*	*	*	*	-		The earthquake had led to cracking of at least 5 buildings in Sylhet
109	1977	5	12	Bangladesh-Myanmar border	21.75	92.99	M _s 5.7	*	*	*	200	*	*	-	89, 98	Cracks were developed in buildings in Chittagong and numerous people were injured
110	1979	4	11	Bangladesh	25.9	88.8	M _b 4.8	*	*	*	*	*	*	72	71, 89	-
111	1984	5	21	Bangladesh	23.42	91.3	M _b 5.3	*		*	*	*	*		40, 89	-
112	1984	9	30	Bangladesh	23.42	91.3	M _b 5.1	*	*	*	*	*	*	-	40, 89	-
113	1984	12	31	India: Assam	24.64	92.89	M _w 6	*	*	*	*	*	*	-	89, 93	-
114	1988	2	6	Bangladesh: Sylhet	24.68	91.57	M _s 5.8	*		2	100	*	*	-	1	-
115	1988	8	6	Myanmar	25.14	95.12	M _s 7.3	*		2	12	*	*	-	93	-
116	1988	8	21	India-Nepal border	26.7	86.8	M _s 7.8	*	998	*	*	*	*	-	36,98	Seismic seiches observed in many rivers including capsizing boats in the Jamuna River killing 2 people and missing almost 30 people
117	1989	6	12	Bangladesh: Banaripara	21.86	89.76	M _s 5.1	*	6	1		*	*	38, 39	1	-
118	1993	6	12	Bangladesh: South	21.83	89.7	5.7 ⁽⁷¹⁾	*	*	*	*	*	*	-	71	-

(Continued on following page)

TABLE 1 (Continued) A catalogue of historical and palaeoseismic evidence of earthquake in Bangladesh and adjacent regions between BC810 and AD2015.

Event number	Year	Month	Day	Earthquake locations			Earthquake parameters			Earthquake effects				Primary	Secondary	Comments
				Location names	Lat	Long	Magnitude	Intensity	Focal depth	Deaths	Injuries	Damage (in m US \$)	House destroyed/damaged			
119	1997	5	8	Bangladesh	24.89	92.25	M_w 6.0 ⁽⁸⁹⁾ M_b 5.6	*	34	*	*	*	*	-	75, 84	The earthquake had led to cracking in at least 5 buildings in Sylhet
120	1997	11	21	India-Bangladesh border: Chittagong	22.21	92.7	M_w 6.1	*	54	23	200	*	1	39	1, 20, 42, 48, 65, 89, 95	The collapse of buildings and deaths occurred in Chittagong
121	1999	7	22	Bangladesh: Mohekhali Island	21.54	91.89	M_b 5.2 ⁽⁸⁹⁾ M_s 4.2 ⁽³⁵⁾	*	10	6	200	*	700	39	1, 35, 48, 75, 93	Houses cracked and in some cases collapsed
122	2000	1	3	India-Bangladesh border	22.13	92.77	M_b 4.6	*	33	*	*	*	*	39	1	-
123	2000	1	19	Bangladesh			M_s 4.5	*	*	*	100		*	-	98	Few buildings in areas of old Dhaka city were damaged
124	2003	7	26	Bangladesh: Borkal	22.85	92.31	M_w 5.7	*	10	3	25	*	500	39	1, 48, 53, 89, 98	Transformer of power supply exploded in Chittagong
125	2007	5	20	India	27.15	88.44	M_w 4.9	*	*	*	*	*	*	-	40, 89	-
126	2007	8	11	India: Assam	26.27	89.24	M_b 5	*	*	*	*	*	*	-	40, 89	-
127	2007	9	19	India	25.18	90.59	M_b 5.1	*	*	*	*	*	*	-	40, 89	-
128	2007	11	7	Bangladesh: Bandarban, Chittagong, Rangamati	22.15	92.38	M_s 5.1	*	29	*	10	*	*	39	1	-
129	2008	1	12	Bangladesh: Rangamati	22.76	92.33	M_b 5	*	34	*	*	*	*	39	1, 89	-
130	2008	3	13	Bhutan	27.46	91	4.5	*	*	*	*	*	*	-	58	-
131	2008	5	29	India	26.24	91.46	M_b 4.5	*	*	*	*	*	*	-	40, 89	-

(Continued on following page)

TABLE 1 (Continued) A catalogue of historical and palaeoseismic evidence of earthquake in Bangladesh and adjacent regions between BC810 and AD2015.

Event number	Year	Month	Day	Earthquake locations			Earthquake parameters			Earthquake effects				Primary	Secondary	Comments
				Location names	Lat	Long	Magnitude	Intensity	Focal depth	Deaths	Injuries	Damage (in m US \$)	House destroyed/damaged			
132	2008	7	5	India	26.07	91.39	Ms 5.1	*	*	*	*	*	*	-	40, 38	-
133	2008	9	20	Bangladesh: Sylhet	23.5	91.07	M _b 4.5	*	*	*	*	*	*	-	40, 89	-
134	2009	1	6	Bangladesh	24.11	89.25	M _b 4.7	*	*	*	*	*	*	-	40, 89	-
135	2009	2	27	Bangladesh	20.29	89.31	M _b 4.8	*	*	*	*	*	*	-	40, 89	-
136	2009	7	13	India	26.09	89.39	Ms 4.5	*	*	*	*	*	*	-	40, 38	-
137	2009	9	21	Bhutan	27.4	91.36	M _w 6.1	*	*	*	*	*	*	-	1, 40, 89	-
138	2009	10	30	Bhutan	27.29	91.46	M _w 5.1	*		*	*	*	*	-	40, 89	-
139	2009	12	31	Bhutan	27.31	91.15	M _b 5.3	*		*	*	*	*	-	1, 40	-
140	2010	9	11	India	25.52	90.39	M _b 5.2	*	*	*	*	*	*	-	1, 40	-
141	2011	9	18	India: Sikkim	27.73	88.15	M _w 6.9	*	*	97	*	*	*	-	1, 89	-
142	2012	3	18	Bangladesh	23.66	90.26	M _b 4.5	*	*	44	*	*	*	-	89	People in Dhaka and adjacent district got panic
143	2015	4	25	Nepal: Gorkha	28.15	84.70	M _w 7.8		15	8200	17,866				1	-
144	2015	5	12	Nepal: Dolakha	27.83	86.07	M _w 7.3		15	117	2800				1	-

Note: Asterisk (*) indicates no information available.

Reference # and detail of primary and secondary sources for each earthquake event referred to in columns 15 and 16.

1. National Geophysical Data Center (NGDC), (2012), 2. Gulston, (1763), 3. Verelst, (1763), 4. Hirst, (1763), 5. Banerji, (1923), 6. Nutalaya, et al. (1985), 7. Milne, (1911), 8. Bapat, et al. (1983), 9. Chaudbury, (1965), 10. Chandra, (1977), 11. Singh, (1966), 12. Davidson, (1936), 13. Lomnitz, C., (1974), 14. Bath, (1973), 15. Chaudhury, (1964), 16. Berninghausen, (1966), 17. Benerji, (1957), 18. Wei, and Zhuoli, (1987), 19. Lyell, (1875), 20. Oldham, (1883), 21. Anon., (1897a), 22. Rizvi, (1970), 23. Richter, (1958), 24. Anon., (1897b), 25. Pervez and Ram, (1997), 26. Duda, (1965), 27. Gutenberg and Richter (1965), 28. Khan and Chouan, (1996), 29. Murty and Rafiq (1991), 30. Morino, (2011), 31. Tandon, (1950), 32. Tillotson, (1951), 33. Curray, (1982), 34. Rennell and Banks, (1781), 35. Ansary, et al. (2000), 36. Anon., (1988), 37. Islamabadi, (1987), 38. ISC, (2023) 39. NEIC (2023), 40. BMD (2011), 41. Hunter, (1876), 42. Islam, (2004), 43. Fergusson, (1863), 44. Mandal, et al. (2000), 45. United Nations Office for the Coordination of Humanitarian Affairs (1993), 46. Iyengar, et al. (1999), 47. Middlemiss, (1885), 48. Alam, et al. (2006), 49. Hough, et al. (2005), 50. Alam, et al. (2012), 51. Ambraseys and Douglas (2004), 52. Steckler, et al. (2008), 53. Khan (2010), 54. Kamaluddin and Rahman, (1985), 63. Anon., (1843b), 65. Khan, (2004), 66. Anon., (1843a), 67. Anon., (1844), 68. Ambraseys, (2000), 69. Anon., (1849), 70. Campbell (1809), 71. Nandy, (1994), 72. Singh and Shankar, (1992), 73. Anon., (2023), 75. Paul and Bhuiyan, (2010), 76. Gupta, (1993), 77. Gupta and Gahalaut, (2009), 78. Mithal and Srivastava (1962), 79. Webster, (1911), 80. Smith, (1844), 81. Ali and Choudhury, (2001), 82. Rastogi and Jaiswal (2006), 83. Jaiswal, et al. (2008), 84. Sharfuddin, (2010), 85. Rizvi, (1969), 86. Khan and Hossain, (2005), 87. Bilham and England, (2001), 88. Geoscience Australia, (2011b), 89. USGS (2023), 90. IRIS (2023), 91. Rizvi, (1970), 92. Chakrabarti and Gosh, (2011), 93. Martin, and Szeliga, (2010), 94. Choudhury, (2005), 95. Dasgupta, (2011), 97. Gait (1906), 98. Akhter, (2010), 99. Rajendran, et al. (2004).

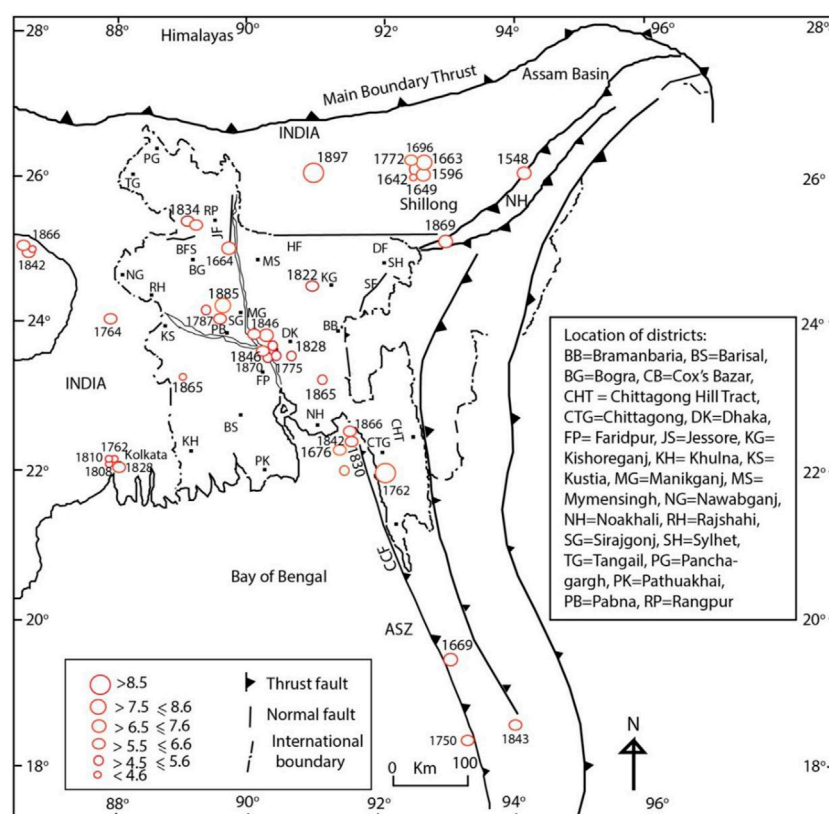


FIGURE 4

Earthquake distribution in Bangladesh and adjacent regions from BC810 to AD1900. The dates of all of the major events are labelled in map. High magnitude earthquakes are located in the active seismic areas in Bangladesh and adjacent India and Myanmar. ASZ, Arakan Subduction Zone; BFS, Bogra Fault System; CCF, Chittagong Cox's Bazar Fault; DF, Dauki Fault; HF, Haluaghat Fault; JF, Jamuna Fault and SF, Sylhet Fault (Source: base map adapted from Mukherjee et al., 2009).

analysis. This process verifies the date of occurrence of an event, explores inconsistencies in citations and identifies problems relating to magnitudes of earthquakes and evaluates likely effects. The new catalogue Table 1 is the output of this process.

3.3 Data analysis

To construct a geography of earthquake hazards in Bangladesh, the locations of earthquake epicenters are presented in a series of maps to reveal hazards and risks in Bangladesh. A new MMI map is constructed by using the content analysis of 47 source documents for 80 earthquake events occurring in Bangladesh and adjacent regions. Arc GIS was used to construct this map. The presentation and analysis of these earthquakes provides much better earthquake hazard geographies and associated risks in Bangladesh than has previously been available.

4 Results and discussion

In the following sections, it has been introduced key aspects of data, and discussed spatial-temporal distributions of earthquake events in the entire study region and analysed earthquake hazard geographies in Bangladesh.

A total of 144 earthquakes have been identified in the study region between 810BC and AD 2015. Of these events (Table 1) one earthquake (event # 5) was identified from archaeological sources, four earthquakes (event # 1, 2, 4, and 8) were identified from geological sources, the remaining 94 events were identified from historical and instrumental sources. The catalogue comprises the event number, the event date, earthquake locations (including coordinates and geographical location names), earthquake parameters (magnitude, intensity and focal depth), earthquake effects (deaths, injuries, damage in million US \$ and house destroyed) information about primary and secondary sources for the event and key comments about earthquakes.

4.1 Earthquakes in and adjacent to Bangladesh

A total of 144 earthquakes are reported to have affected Bangladesh and the adjacent region (Table 1). The locations of these earthquakes are shown in Figures 4, 5. Evidence for three paleoseismic events in 810-400BC, 535-530BC and AD645-980 became available through the geological investigation of the great AD1897 earthquake in Assam (Rajendran et al., 2004). Banerji (1923) and Chaudhury (1964) found the evidence of the AD825-

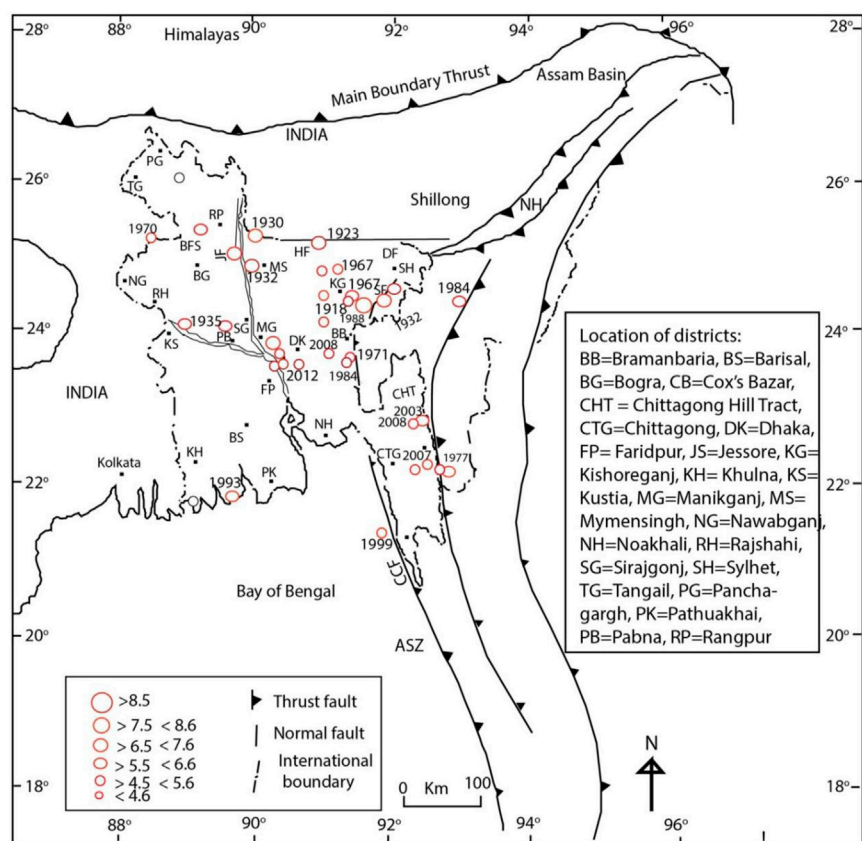


FIGURE 5 Earthquake distribution in Bangladesh and adjacent regions areas from 1900 to 2015. The dates of all of the major events are labelled in map. High magnitude earthquakes are located in the active seismic areas in Bangladesh and adjacent India and Myanmar. ASZ, Arakan Subduction Zone; BFS, Bogra Fault System; CCF, Chittagong Cox's Bazar Fault; DF, Dauki Fault; HF, Haluaghat Fault; JF, Jamuna Fault and SF, Sylhet Fault (Source: base map adapted from Mukherjee et al., 2009).

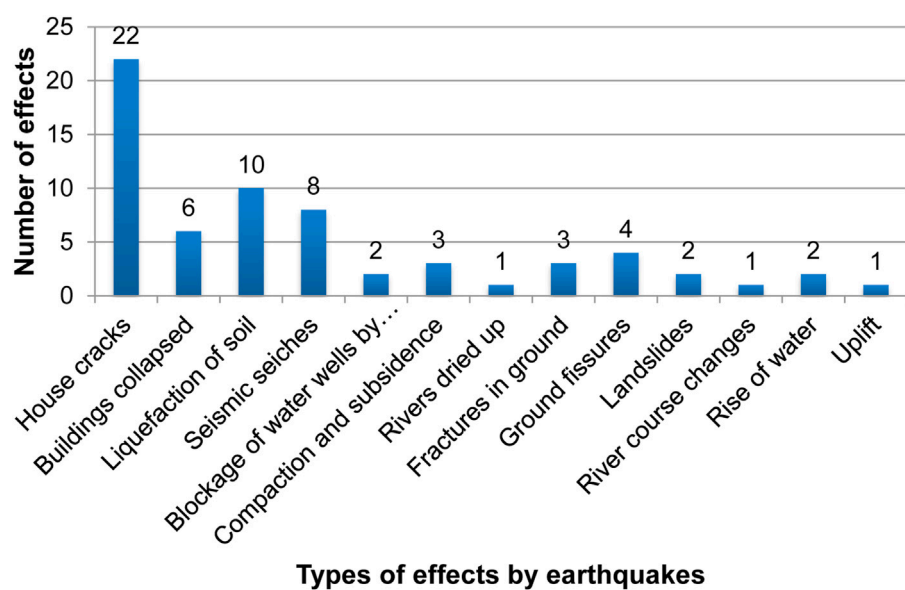


FIGURE 6 The types of impacts caused by earthquakes in Bangladesh (Source: reports numbers at the bottom of Table 1 #s 2, 3, 4, 5, 10, 11, 15, 21, 22, 23, 26, 47, 48, 50, 51, 52, 53, 54, 55, 56, 61, 62, 64, 65, 69, 70, 71, 75, 77, 80, 81, 83, 86, 99, 104, 111, 112, 114, 116, 127, 140, 143, 150, 151, 152, 153, 159, 161, 162, 163, 164, 165, 166, 167, 168).

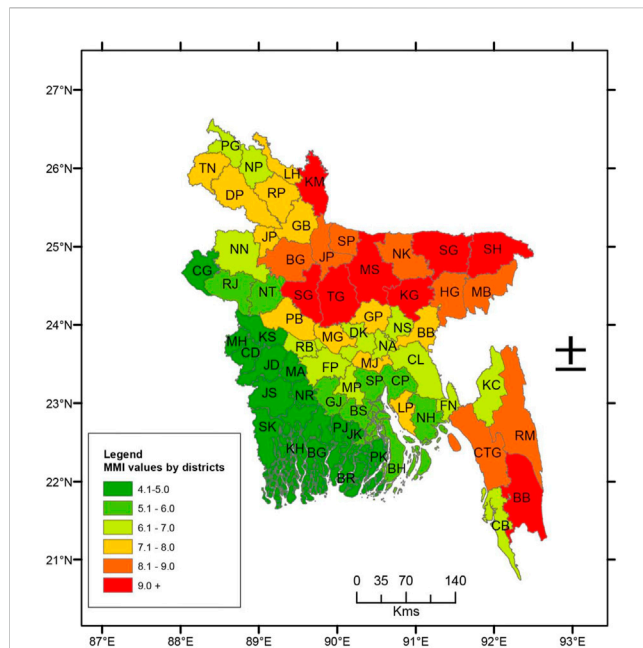


FIGURE 7

An MMI map of the average effects of 80 earthquakes in Bangladesh occurring between BC810 and AD2015 in Bangladesh and adjacent regions. BB, Bandarban; BE, Bagerhat; BG, Bogra; BH, Bhola; BR, Barguna; BS, Barisal; CB, Cox's Bazar; CD, Chuadanga; CG, Chapai Nawabganj; CL, Comilla; CP, Chandpur; CTG, Chittagong; DK, Dhaka; DP, Dinajpur; FN, Feni; FP, Faridpur; GB, Gaibandha; GJ, Gopalganj; GP, Gazipur; HG, Habiganj; JD, Jhenidah; JP, Jaipurhat; JL, Jamalpur; JS, Jessore; JK, Jhalakati; KC, Khagrachari; KG, Kishoreganj; LP, Lakshmipur; LH, Lalmonirhat; KH, Khulna; KM, Kurigram; KS, Kustia; MA, Magura; MB, Moulvibazar; MG, Munshiganj; MP, Madaripur; MS, Mymensingh; MH, Meherpur; NA, Narayanganj; NH, Noakhali; NK, Netrokona; NN, Noaganj; NT, Nattore; NP, Nilphamari; NR, Narail; NS, Narshingdi; PB, Pabna; PG, Panchgarh; PJ, Pirojpur; PK, Patuakhali; RB, Rajbari; RJ, Rajshahi; RM, Rangamati; RP, Rangpur; SG, Sunamganj; SJ, Sunamganj; SH, Sylhet; SK, Satkhira; SP, Shariatpur; TG, Tangail; TN, Thakurgaon (Source: reports numbers at the bottom of Table 1 #s 2, 3, 4, 5, 10, 11, 15, 20, 21, 22, 24, 32, 33, 34, 35, 36, 37, 40, 41, 42, 43, 44, 46, 47, 48, 49, 51, 52, 53, 54, 56, 68, 71, 72, 79, 84, 85, 86, 87, 91, 93, 94, 95, 96, 97, 98, 99).

835 earthquake by conducting archaeological investigation in Assam. The geological records of the AD1440-1470 earthquake emerged from the work of Morino et al. (2011) at Mymensingh. Analysis of earthquakes generated in Bangladesh and adjacent areas indicate that the 1762, 1885 and 1897 earthquakes in Bangladesh caused widespread damage. A repeat of similar earthquakes from any of the active seismic sources could cause damage, destruction and death within major population centres in Bangladesh. The effects of recent earthquakes occurring in 1977, 1997, 1999, 2003, and 2007 suggest that lesser magnitude earthquakes could cause significant damage to urban centres that are home to large highly exposed and huge vulnerable communities.

4.2 The construction of a new MMI map for Bangladesh

Analysis of the 47 reports (see list of reports below Figure 6) that contain information relating to the effects of 80 earthquakes suggest that

severe damage occurred to bamboo houses and masonry buildings in Bangladesh. Disturbances of inland water bodies were also observed in Bangladesh. Co-seismic subsidence, uplift, landslides and compaction were associated with the 1762 earthquake (Alam and Dominey-Howes, 2014). Subsidence and uplift are evidence of neotectonic activity in Bangladesh and adjacent areas (Khan and Chouan, 1996; Hoque and Alam, 1997; Das et al., 2010). The existing flow of the Jamuna River came into its present course only after the 1787 earthquake (Kamaluddin and Rahman, 1985; Bandyopadhyay et al., 2021; Richards et al., 2021). Before the shift of its course, it flowed further east by its original name 'Old Brahmaputra' before meeting the Meghna River (Rennell and Banks, 1781; Richards et al., 2021). Additionally, the uplift of the Madhupur surface was possibly associated with the occurrence of the 1762 earthquake (Fergusson, 1863).

The effects of earthquakes reports are obtained for 80 events (Table 1 events # 8, 9, 14, 16, 17, 21, 23, 37, 38, 39, 42, 43, 44, 55, 64, 69, 74, 76, 79, 84, 85, 95, 97, 98, 107, 108, 161, 119, 153, 165, 168, 170, 178, 190, 191, 196, 204, 209, 217, 236, 245, 260, 262, 268, 269, 274, 278, 282, 322, 333, 341, 363, 378, 382, 396, 401, 407, 408, 411, 426, 428, 429, 430, 439, 441, 442, 445, 446, 447, 452, 457, 459, 460, 475, 503, 512, 536, 561, 562). An analysis of 47 reports on 80 earthquakes suggests that in eight (i.e., Bandarban, Kurigram, Kishoreganj, Mymensingh, Sunamganj, Sirajganj, Sylhet, and Tangail) of 64 districts, the effects were over IX on the MMI scale (Figure 7). These districts are located in the northern region of Bangladesh and are close to the Bogra Fault System, Dauki Fault, Haluaghat Fault, Jamuna Fault, Madhupur Fault, Sylhet Fault, and Himalayan seismic sources. The results of the highest risk districts based on the effects of earthquakes measured on the MMI scale coincide with the current seismic zoning map of Bangladesh (Figure 2).

The damage intensity caused by earthquakes in Chittagong was rated VIII on the MMI scale. The high MMI value for Chittagong is due to the effects of historical and recent earthquakes that occurred in 1762, 1842, 1851, 1997, 1999, 2003, 2007, and 2008. Chittagong is located along the Arakan Subduction Zone and is close to seismic sources in Myanmar. The damage intensity reached VI on the MMI scale in Dhaka. Although, Dhaka city is comparatively far from seismic sources, the fragile infrastructure and fluvial delta experienced a multitude of different types of effects from earthquakes occurring from adjacent sources. The MMI in the SW districts were 5 or below indicating that they were prone to less damage.

5 Conclusion

This research documented and analysed geological, archaeological and documentary records of earthquakes in Bangladesh to better understand and quantify the hazard—a first step towards improved earthquake risk reduction. The key finding from this research reveals that using long-term hazard data in conjunction with spatial analysis could provide an opportunity to detect areas of high earthquake occurrences. However, records are only available for greater magnitude (7 and above) earthquakes of 1762, 1885, and 1997. No detailed records are available for lesser magnitude earthquakes. This research also supports the revision of current seismic zoning map of Bangladesh to include Chittagong and Dhaka in the high-risk zone for effective earthquake risk reduction. Finally, this research concludes that analyses of long-

term data help identify new hazard exposure and develop knowledge that can be useful to formulate new disaster risk reduction policies and rectify existing ones in Bangladesh.

Data availability statement

The raw data supporting the conclusion of this article will be made available by the authors, without undue reservation.

Author contributions

The author confirms being the sole contributor of this work and has approved it for publication.

References

- Akhter, S. H. (2010). "Earthquakes of Dhaka," in *Environment of capital Dhaka - plants wildlife gardens parks air water and earthquake*. Editors M. A. Islam, S. U. Ahmed, and A. K. M. Rabbani (Ramna, Dhaka, Bangladesh: Asiatic Society of Bangladesh), 401–426.
- Alam, E., and Dominey-Howes, D. (2016). A catalogue of earthquakes between 810BC and 2012 for the Bay of Bengal. *Nat. Hazards* 81 (3), 2031–2102. doi:10.1007/s11069-016-2174-7
- Alam, E., and Dominey-Howes, D. (2014). An analysis of the AD1762 earthquake and tsunami in SE Bangladesh. *Nat. Hazards* 70 (1), 903–933. doi:10.1007/s11069-013-0841-5
- Alam, E., Dominey-Howes, D., Goff, J., and Chagué-Goff, C. (2012). Tsunamis of the northeast Indian ocean with a particular focus on the Bay of Bengal region—a synthesis and review Indian ocean with a particular focus on the Bay of Bengal region—a synthesis and review. *Earth-Science Rev.* 114 (1–2), 175–193. doi:10.1016/j.earscirev.2012.05.002
- Alam, M., Alam, M. M., Curray, J. R., Chowdhury, M. L. R., and Gani, M. R. (2003). An overview of the sedimentary geology of the Bengal Basin in relation to the regional tectonic framework and basin-fill history. *Sediment. Geol.* 155, 179–208. doi:10.1016/s0037-0738(02)00180-x
- Alam, M. J., Bhuiyan, M. A. R., and Islam, M. R. "Seismic structural assessment of damaged Chittagong public library building during 27 July 2003 earthquake," in Proceedings of the 4th International Conference on Earthquake Engineering, Taipei, Taiwan, October 2006.
- Ali, M. H., and Choudhury, J. R. (2001). "Assessment of seismic hazard in Bangladesh," in *Disaster in Bangladesh: Selected readings. Disaster research training and management centre*. Editor K. Nizamuddin (Dhaka, Bangladesh: University of Dhaka), 197.
- Ambraseys, N., and Douglas, J. (2004). Magnitude calibration of north Indian earthquakes. *Geophys. J. Int.* 159, 165–206. doi:10.1111/j.1365-246x.2004.02323.x
- Ambraseys, N. (2000). Reappraisal of north-Indian earthquakes at the turn of the 20th century. *Curr. Sci.* 79 (9), 1237–1250.
- Anon (1897b). *Cablegraphic news. KalgoorieWestern argus*. Parkes, Australia: National Library of Australia, 19.
- Anon (1988). *Earthquake in Bihar-Nepal: Felt in entire country*. Bangladesh: Bangladesh Observer.
- Anon (1897a). *Earthquakes in India*. Lawrence, New Zealand: Tuapeka Times, 1.
- Anon (1843b). *Journal of the asiatic society of bengal*. Calcutta, India: Bishop's College Press.
- Anon (1844). *Journal of the asiatic society of bengal*. Calcutta, India: Bishop's College Press.
- Anon (1849). *Journal of the asiatic society of bengal*. Calcutta, India: Baptist Mission Press.
- Anon (1843a). *The asiatic journal and monthly register for British and foreign India, China and australasia*. Leadenhall Street, London: Parbury, Allen, and Company, 25.
- Anon (2023). *The journal of asiatic society of bengal*. Huay Ya, Chonburi Province, Thailand: White Lotus Press, 1053.
- Ansary, M. A., Al-Hussaini, T. M., and Sharfuiddin, M. (2000). "Damage assessment of July 22, 1999 moheshkhali earthquake, Bangladesh," in Proceedings of the 8th ASCE specialty conference on probabilistic mechanics and structural reliability, Indiana, USA, July 2000, 22–26.
- Bandyopadhyay, S., Das, S., and Kar, N. S. (2021). Avulsion of the Brahmaputra in Bangladesh during the 18th–19th century: A review based on cartographic and literary evidence. *Geomorphology* 384, 107696. doi:10.1016/j.geomorph.2021.107696
- Banerji, R. D. (1923). *Annual report. Archaeological society of India*. Calcutta, India: Central Publication Branch, 80–81.
- Bapat, A., Kulkarni, R. C., and Guha, S. K. (1983). *Catalogue of earthquake in India and Neighborhood from historical period up to 1979*. Roorkee, India: Indian Society of Earthquake Technology, 211.
- Bath, M. (1973). *Introduction to Seismology*. New York, NY, USA: Halsted Press, 395.
- Benerji, S. K. (1957). *Earthquakes in the himalayan region*. Jadavpur, Calcutta, India: Indian Association for the Cultivation of Science, 64.
- Berninghausen, W. H. (1966). Tsunamis and seismic seiches reported from regions adjacent to the Indian Ocean. *Bull. Seismol. Soc. Am.* 56, 69–74. doi:10.1785/bssa0560010069
- Bilham, R., and England, P. (2001). Plateau 'pop-up' in the great 1897 Assam earthquake. *Nature* 40, 806–809. doi:10.1038/35071057
- Bmd (2011). Earthquake data in and around Bangladesh from 1918 to 2010. Bangladesh meteorological department (BMD), meteorological complex, agargaon, Dhaka, government of the people's republic of Bangladesh. Web access at <http://www.bmd.gov.bd/Earthquake.php>.
- Campbell, L. D. (1809). *A view of the history of hindustan and of the politics, commerce and literature of asia*. London, UK: The Asiatic Society.
- Chakrabarti, P. G. D., and Gosh, C. (2011). *National workshop on earthquake risk management in the north east region* Guwahati, Assam, India: National Institute of Disaster Management, 24–25.
- Chandra, U. (1977). Earthquakes of Peninsular India-A seismotectonic study. *Bull. Seismol. Soc. Am.* 67 (5), 387–1413.
- Chaudbury, M. H. (1965). "Seismology in India," in *Individual studies by participants to the international Institute of Seismology and earthquake engineering* (Tokyo, Japan: International Institute of Seismology and Earthquake Engineering), 14–33.
- Chaudhury, P. D. (1964). *Archaeology in Assam*. Gauhati, India: Dept. of Archaeology, 77.
- Choudhury, J. R. (2005). *Earthquake-tsunami: The threat looms. Independent weekend*. Dhaka, Bangladesh: Free Press Ltd.
- Curry, J. R., Emmel, F. J., Moore, D. G., and Raitt, E. W. (1982). "Structure, tectonics and geological history of the north-eastern Indian Ocean," in *The Ocean basin and margin*. Editors A. E. M. Nairn, and F. G. Stchli (New York, NY, USA: Plenum Press), 399–450.
- Das, J. D., Saraf, A. K., and Shujat, Y. (2010). A remote sensing technique for identifying geometry and geomorphological features of the Indo-Burman frontal fold belt. *Int. J. Remote Sens.* 31 (61), 4481–4503. doi:10.1080/01431160903154366
- Dasgupta, S. "Earthquake geology, geomorphology and hazard scenario in northeast India: An appraisal," in Proceedings of the National workshop on earthquake mitigation strategy in northeast, Guwahati, Assam, February 2011, 24–29.
- Davidson, C. (1936). *Great earthquakes*. London, United Kingdom: Thomas Murty and Co., 286.
- Duda, S. J. (1965). Secular seismic energy release in the circum-Pacific belt. *Tectonophysics* 2 (5), 409–452. doi:10.1016/0040-1951(65)90035-1
- Fergusson, J. (1863). On recent changes in the delta of the Ganges. *Q. J. Geol. Soc. Lond.* 19, 321–354. doi:10.1144/gsl.jgs.1863.019.01-02.35
- Gait, E. A. (1906). *A history of Assam*. Darjeeling, India: Thacker, Spink and Co., 383.
- Geoscience Australia (2011a). *Earthquake@Geoscience Australia*. Symonston, Canberra, Australian: Geoscience Australia.
- Geoscience Australia (2011b). *Earthquake@Geoscience Australia*. Available: <http://www.ga.gov.au/earthquakes/searchQuake.do> (Accessed 28th June, 2011).
- Gere, J. M., and Shah, H. C. (1984). *Terra non firma: Understanding and preparing for earthquakes*. New York, NY, USA: W. H. Freeman, 204.

Conflict of interest

The author declares that the research was conducted in the absence of any commercial or financial relationships that could be construed as a potential conflict of interest.

Publisher's note

All claims expressed in this article are solely those of the authors and do not necessarily represent those of their affiliated organizations, or those of the publisher, the editors and the reviewers. Any product that may be evaluated in this article, or claim that may be made by its manufacturer, is not guaranteed or endorsed by the publisher.

- Gulston, E. (1763). An account of an earthquake at chattigaon: Translated from the Persian by mr. Edward gulston, in the service of the honourable east India company, and communicated by him to the reverend mr. Hirst. *Philos. Trans.* 53, 1683–1775.
- Gupta, H., and Gahalaut, V. (2009). Is the northern Bay of bengal tsunamigenic? *Bull. Seismol. Soc. Am.* 99 (6), 3496–3501. doi:10.1785/0120080379
- Gupta, H. K. (1993). Seismic hazard assessment in the Alpine belt from Iran to Burma. *Ann. Di Geofis.* 36 (3–4), 61–82.
- Gutenberg, B., and Richter, C. F. (1965). *Seismicity of the earth and associated phenomena*. New York, NY, USA: Princeton University Press, Hafner Publishing Company, 310.
- Hirst, W. (1763). An account of an earthquake in the east indies, of two eclipses of the sun and moon, observed at Calcutta. *Philosophical Trans.* 53, 1683–1775.
- Hoque, M., and Alam, M. (1997). Subsidence in the lower deltaic areas of Bangladesh. *Mar. Geol.* 20 (1), 105–120. doi:10.1080/01490419709388098
- Hough, S. E., Bilham, R., Ambraseys, N., and Feldl, N. (2005). Revisiting the 1897 shilong and 1905 kangra earthquake in the northern India: Site response, moho reflections and a triggered earthquake. *Curr. Sci.* 88 (10), 1632–1638.
- Hunter, W. W. (1876). “A statistical account of bengal,” in *Chittagong hill tracts, and districts of Chittagong, noakhali, tripperah, hill tripperah* (London, UK: Trübner and Co.), 444.
- Iris (2023). Seismic event data. Seismological facility for the advancement of geoscience. access on 14 May 2023 at <https://ds.iris.edu/ds/nodes/dmc/data/types/events/>.
- Isc (2023). ISC bulletin: Event catalogue search. International seismological centre (ISC). accessed on 19 May 2023 at <http://www.isc.ac.uk/iscbulletin/search/catalogue/>.
- Islam, S. I. (2004). *Banglapedia: National encyclopedia of Bangladesh*. Dhaka, Bangladesh: Asiatic Society of Bangladesh.
- Islamabadi, A. (1987). *Chattragram smwarani (A memorial in Chittagong) (in Bengali)*. Chittagong, Bangladesh: Azadi Printers Limited, 159.
- Iyengar, R. N., Sharma, D., and Siddiqi, J. M. (1999). Earthquake history of India in medieval times. *Indian J. Hist. Sci.* 34 (3), 181–237.
- Jaiswal, R., Rastogi, B. K., and Murty, T. S. (2008). Tsunamigenic sources in the Indian ocean. *Sci. Tsunami Hazards* 27 (2), 32–53.
- Kamal, A. S. M. M. (2008). Seismic hazard assessment for Chittagong city corporation area, Bangladesh. *Int. Geol. Congr. Oslo*, 6–14. doi:10.4172/2167-0587.1000154
- Kamaluddin, A. F. M., and Rahman, K. M. (1985). “The pattern of the structures of rural employment in Bangladesh – a study of the thanas in Sirajganj,” in *Geographical essays* (New Delhi, India: Inter India Publications).
- Khan, A. A., and Chouan, R. K. S. (1996). The crustal dynamics and the tectonic trends in the Bengal Basin. *J. Geodyn.* 22 (3–4), 267–286. doi:10.1016/0264-3707(96)00022-1
- Khan, A. A. (2004). *Earthquake vulnerability and hazard assessment in the active collision margin of Bangladesh with special reference to Dhaka, Chittagong, and Sylhet triangular region*. Bangladesh: Research Report Ministry of Science and Information and Communication Technology Government of Bangladesh, 96.
- Khan, A. A. (2010). *Earthquake, tsunami and geology of Bangladesh*. Dhaka, Bangladesh: University Grant Commission of Bangladesh, 331.
- Khan, A. A., and Hossain, M. M. (2005). Recurrence of 1885 bengal earthquake and hazard vulnerability status of Dhaka metropolitan city, Bangladesh. *Orient. Geogr.* 49 (2), 205–216.
- Khan, A. A. (2012). Seismogenic sources in the Bay of Bengal vis-à-vis potential for tsunami generation and its impact in the northern Bay of Bengal coast. *Nat. Hazards* 61, 1127–1141. doi:10.1007/s11069-011-9970-x
- Lomnitz, C. (1974). *Global tectonics and earthquake risk*. Amsterdam, Netherlands: Elsevier.
- Lyell, S. C. (1875). *Principles of geology* London, UK: Murray, 1–179.
- Mandal, P., Rastogi, B. K., and Gupta, H. K. (2000). Recent Indian earthquakes. *Curr. Sci.* 79 (9), 368–379.
- Martin, S., and Szeliga, W. (2010). A catalog of felt intensity data for 570 earthquakes in India from 1636 to 2009. *Bull. Seismol. Soc. Am.* 100 (2), 562–569. doi:10.1785/0120080328
- Middlemiss, C. S. (1885). Reports on the bengal earthquake of july 14th, 1885. *Rec. Geol. Surv. India* 18, 200–221.
- Milne, J. “Catalogue of destructive earthquakes,” in Proceedings of the 81st meeting of the British Association for the Advancement of Science, Portsmouth, London, 1911, 649–740.
- Mithal, R. S., and Srivastava, L. S. (1962). “Seismicity of the area around Baraundi, Bihar,” in *Proc. Symp. Earthquake eng* (Roorkee, India: University of Roorkee), 527–538.
- Morino, M., Kamal, A. S. M. M., Muslim, D., Ali, R. M. E., Kamal, M. A., Rahman, M. Z., et al. (2011). Seismic event of the Dauki Fault in 16th century confirmed by trench investigation at gabrakhari village, Haluaghat, Mymensingh, Bangladesh. *J. Asian Earth Sci.* 42, 492–498. doi:10.1016/j.jseas.2011.05.002
- Mukherjee, M., Fryar, A. E., and Thomas, W. A. (2009). Geologic, geomorphic and hydrologic framework and evolution of the Bengal basin, India and Bangladesh. *J. Asian Earth Sci.* 34, 227–244. doi:10.1016/j.jseas.2008.05.011
- Murty, T. S., and Rafiq, R. (1991). A tentative list of tsunamis in the marginal seas of the north Indian Ocean. *Nat. Hazards* 4 (1), 81–83. doi:10.1007/bf00126560
- Nandy, D. R. (1994). Earthquake hazard potential of central and south Bengal Basin. *Indian J. Earth Sci.* 21 (2), 59–64.
- Neic (2023). Earthquake events. NOAA national centres for environmental information (NEIC). access on 21 May 2023 at <https://www.ngdc.noaa.gov/hazel/view/hazards/earthquake/search>.
- Ngdc (2012). Global significant earthquake database from 2000 B.C. to present. Available: <http://www.ngdc.noaa.gov/hazard/earthqk.shtml> (Accessed June 1, 2012).
- Nutalaya, S., Sodsri, S., and Arnold, E. P. (1985). *Series on Seismology*. Thailand: Southeast Asia Association of Seismology and Earthquake Engineering and U. S. Geological Survey.
- Oldham, R. D. (1883). A catalogue of Indian earthquakes from the earliest time to the end of A.D 1869. *Memoirs Geol. Surv. India* 19 (3), 163–215.
- Paul, B. K., and Bhuiyan, R. H. (2010). Urban earthquake hazard: Perceived seismic risk and preparedness in Dhaka city, Bangladesh. *Disasters* 34 (2), 337–359. doi:10.1111/j.1467-7717.2009.01132.x
- Pervez, I. A., and Ram, A. (1997). Probabilistic assessment of earthquake hazards in the North-East Indian peninsula and Hindukush regions. *Pure Appl. Geophys.* 149 (4), 731–746. doi:10.1007/s000240050049
- Rajendran, C. P., Rajendran, K., Duarah, B. P., Baruah, S., and Earnest, A. (2004). Interpreting the style of faulting and paleoseismicity associated with the 1897 Shillong, northeast India, earthquake: Implications for regional tectonism. *Tectonics* 23 (TC4009), 419–429. doi:10.1029/2003tc001605
- Rastogi, B. K., and Jaiswal, R. K. (2006). A catalogue of tsunamis in the Indian Ocean. *Sci. Tsunami Hazards* 25 (3), 128–143.
- Rennell, J., and Banks, J. (1781). An account of the Ganges and burrampooter rivers. *Philosophical Trans. R. Soc. Lond.* 71, 87–114.
- Richards, K., Brammer, H., and Saunders, L. P. (2021). The historical avulsion of the Tista River, and its relationship to the Brahmaputra: Map and archive evidence from 1750 to 1835. *Geogr. J.* 187 (3), 253–268. doi:10.1111/geoj.12391
- Richter, C. F. (1958). *Elementary Seismology*. San Francisco, CA, USA: W. H. Freeman, 768.
- Rizvi, S. N. H. (1970). *Bangladesh district gazetteers, Sylhet*. Dhaka, Bangladesh: Government of the People's Republic of Bangladesh.
- Rizvi, S. N. H. (1969). *East Pakistan district gazetteers: Dacca*. Dhaka, Bangladesh: East Pakistan Government Press, 353.
- Sarker, J. K., Ansary, M. A., Rahman, M. S., and Safiullah, A. M. M. (2010). Seismic hazard assessment for Mymensingh, Bangladesh. *Environ. Earth Sci.* 60 (3), 643–653. doi:10.1007/s12665-009-0204-4
- Sharfuddin, M. (2010). “Earthquake hazard analysis for Bangladesh,”. MSc Thesis (Dhaka, Bangladesh: Department of Civil Engineering, Bangladesh University of Engineering and Technology).
- Singh, K. (1966). Earthquakes in India and neighbourhood. *Indian J. Meteorology Geophys.* 4 (17), 521–528. doi:10.54302/mausam.v17i4.5753
- Singh, V. P., and Shankar, D. (1992). On the seismicity and tectonic activity of the Bengal Basin. *Mausam* 43, 371–378. doi:10.54302/mausam.v43i4.3504
- Smith, R. B. (1844). Memoir on Indian earthquakes, Part III. *J. Asiatic Soc. Bengal* 156, 964–983.
- Steckler, M. S., Akhter, S. H., and Seeber, L. (2008). Collision of the ganges–brahmaputra delta with the Burma arc: Implications for earthquake hazard. *Earth Planet. Sci. Lett.* 273, 367–378. doi:10.1016/j.epsl.2008.07.009
- Tandon, A. N. (1950). The very great earthquake of August 15, 1950. *Sci. Cult.* 16 (4), 14.
- Tillotson, E. (1951). The great Assam earthquake of august 15, 1950. *Nature* 167, 128–130. doi:10.1038/167128a0
- United Nations Office for the Coordination of Humanitarian Affairs (1993). *India earthquake september 1993, UN DHA situation reports*. New York, United States: United Nations Office for the Coordination of Humanitarian Affairs, 1–8.
- Usgs (2023). Earthquake hazard program. United states geological Survey (USGS). accessed on 17 May 2023 at <https://earthquake.usgs.gov/data/comcat/>.
- Verelst (1763). An account of the earthquakes that have been felt in the province of islamabad, with the damages attending them, from 2nd to the 19th of april, 1762: Translated from the Persian, and communicated to henry vantsittart, esq; president and governor of fort william in bengal, by mr. Verelst, chief of the hon. East India company's Affairs at islamabad. *Philos. Trans.* 53, 1683–1775.
- Webster, J. E. (1911). *Eastern bengal and Assam district gazetteer: Noakhali*. Allahabad, India: The Pioneer Press, 107.
- Wei, L., Nengqian, J., and Zhuoli, L. (1987). Deformation and displacement fields of the Himalayan arc, seismicity and large earthquake hazards in its eastern segment and vicinity. *Tectonophysics* 138 (1), 93–107. doi:10.1016/0040-1951(87)90068-0



OPEN ACCESS

EDITED BY

Sandipan Das,
Symbiosis International University, India

REVIEWED BY

Subham Roy,
University of North Bengal, India
Parama Baanerji,
West Bengal State University, India

*CORRESPONDENCE

Giha Lee,
✉ leegiha@knu.ac.kr

RECEIVED 28 July 2023

ACCEPTED 08 September 2023

PUBLISHED 20 September 2023

CITATION

Le X-H, Eu S, Choi C, Nguyen DH, Yeon M
and Lee G (2023), Machine learning for
high-resolution landslide susceptibility
mapping: case study in Inje County,
South Korea.
Front. Earth Sci. 11:1268501.
doi: 10.3389/feart.2023.1268501

COPYRIGHT

© 2023 Le, Eu, Choi, Nguyen, Yeon and
Lee. This is an open-access article
distributed under the terms of the
[Creative Commons Attribution License
\(CC BY\)](#). The use, distribution or
reproduction in other forums is
permitted, provided the original author(s)
and the copyright owner(s) are credited
and that the original publication in this
journal is cited, in accordance with
accepted academic practice. No use,
distribution or reproduction is permitted
which does not comply with these terms.

Machine learning for high-resolution landslide susceptibility mapping: case study in Inje County, South Korea

Xuan-Hien Le^{1,2}, Song Eu³, Chanul Choi¹, Duc Hai Nguyen²,
Minho Yeon¹ and Giha Lee^{1*}

¹Department of Advanced Science and Technology Convergence, Kyungpook National University, Sangju, Republic of Korea, ²Faculty of Water Resources Engineering, Thuyloi University, Hanoi, Vietnam, ³Department of Forest Environment and Conservation, National Institute of Forest Science, Seoul, Republic of Korea

Landslides are a major natural hazard that can significantly damage infrastructure and cause loss of life. In South Korea, the current landslide susceptibility mapping (LSM) approach is mainly based on statistical techniques (logistic regression (LR) analysis). According to previous studies, this method has achieved an accuracy of approximately 75.2%. In this paper, we expand upon this traditional approach by comparing the performance of six machine learning (ML) algorithms for LSM in Inje County, South Korea. The study employed a combination of geographical data gathered from 2005 to 2019 to train and evaluate six algorithms, including LR, Gaussian Naive Bayes (GNB), Support Vector Machine (SVM), K-Nearest Neighbors (KNN), Random Forest (RF), and Extreme Gradient Boosting (XGB). The effectiveness of these models was measured by various criteria, such as the percentage of correct classification (PCC) score, F1 score, and Kappa score. The results demonstrated that the PCC and F₁ scores of the six models fell between [0.869–0.941] and [0.857–0.940], respectively. RF and XGB had the highest PCC and F₁ scores of 0.939 and 0.941, respectively. This study indicates that ML can be a valuable technique for high-resolution LSM in South Korea instead of the current approach.

KEYWORDS

disaster management, extreme gradient boosting (XGB), feature importance, landslide, landslide probability, landslide susceptibility mapping (LSM), random forest (RF), risk map

1 Introduction

Landslides are a typical natural disaster that can occur anywhere on the earth and have devastating consequences, including loss of lives and harm to society and the economy (Highland and Bobrowsky, 2008; Biswas et al., 2022). The Republic of Korea, hereafter referred to as South Korea, is particularly susceptible to landslide-induced catastrophes. In South Korea, landslides are primarily concentrated in the summer, when approximately 60% of the annual rainfall occurs due to the Asian Monsoon. Climate change has intensified this pattern, evidenced by the nearly doubled mean annual landslide-damaged area, from 276.6 ha/year in 1981–2000 to about 527.6 ha/year in 2001–2020 (Korea Forest Service, 2021). Despite the great efforts, including installing check dams to prevent fatalities and property loss since 1986, several landslide disasters have often inflicted severe damage. One of the fatal landslides in 2011 killed 43 people due to landslide-induced debris flows in Seoul

and Chuncheon, with an estimated damage of 824 ha (Kim et al., 2011). Moreover, 2020 experienced a prolonged monsoon period of 54 days, the third-longest in the recorded weather history of South Korea, which resulted in 1,343 ha of damaged area and nine fatalities (Lee et al., 2021).

Identifying landslide-prone areas and implementing measures to prevent or mitigate their impacts necessitates a practical landslide susceptibility assessment (Huabin et al., 2005; Chikalomo et al., 2020). This evaluation includes an examination of numerous elements that might contribute to landslides, such as land use, rainfall, slope, rainfall, and geology (Pourghasemi et al., 2018). The involvement of fluvial processes and the hydro-geomorphic characteristics they generate is one crucial component that might contribute to the danger of landslides (Tran et al., 2022). These water-moving activities can change the terrain in ways that raise the danger of landslides. LSM is central to understanding the risk associated with landslides in various regions. By conducting an LSM, we can better understand the frequency and location of landslides and take steps to lessen the danger of these disasters (Eker et al., 2015; Maes et al., 2017).

Over the past decades, researchers have developed a myriad of techniques to gauge the potential for landslides. However, constructing an effective LSM presents several challenges, primarily related to the completeness and quality of the incoming data (Pardeshi et al., 2013; Chae et al., 2017). The effectiveness of an LSM significantly depends on the data quality it is based upon. Yet, such data might be marred by incompleteness, inaccuracies, or spatial inconsistencies, resulting in reduced map accuracy (Thirugnanam et al., 2020; Caleca et al., 2022). Historically, diverse methods ranging from geomorphological assessments to statistical models have been employed to predict landslide-prone zones (Cardinali et al., 2002). While pivotal, these methods have challenges, ranging from extensive ground truthing to dependency on consistent spatial data (Lombardo et al., 2020; Shano et al., 2020). Due to their inherently dynamic nature, landslide-causing conditions can differ dramatically across temporal and spatial scales, making it arduous to pinpoint the likelihood of landslides in a given location (Atkinson and Massari, 2011). There may also be a lack of resources and technology available to monitor areas continuously for potential landslides, particularly in remote or inaccessible regions (Zêzere et al., 2017; Piciullo et al., 2018). This can make identifying the circumstances that could lead to a landslide on time challenging. Furthermore, the traditional statistical models used to construct LSMs are based on statistical relationships and assumptions that may not always hold in reality, resulting in uncertainty in the predictions made by the model (Lee and Min, 2001; Huang et al., 2020).

LSM utilizes a variety of strategies, such as statistical methods and ML algorithms, to predict potential landslide zones (Stanley et al., 2021; Rahman et al., 2022). One such statistical technique is LR analysis, which assesses the association between a dependent variable (e.g., occurrence or absence of landslides) and several independent elements (e.g., land use, slope, and geology) (Lee, 2005; Woo et al., 2014). This technique is attractive due to its ability to handle multiple independent variables and its probabilistic outcome, offering a likelihood of occurrence for landslides in specific areas (Reichenbach et al., 2018). Another frequently applied statistical method in LSM is bivariate statistical analysis (Mersha

and Meten, 2020). Bivariate analysis examines the relationship between two variables—landslides and slope inclination—to uncover patterns and trends. This analysis's simplicity and ability to identify statistically significant associations between landslide occurrence and influencing factors make it a valuable tool in LSM (Yalcin, 2008; Hong et al., 2019). These statistical techniques have garnered popularity due to their simplicity and capability to handle multiple variables, as they often operate under assumptions of linearity and independence among predictors. Such assumptions can restrict their predictive power in complex natural terrains (Yalcin et al., 2011).

Recently, ML techniques have emerged as powerful tools in LSM due to their ability to analyze large volumes of data, identify hidden patterns and relationships that may not be evident to human analysts (Lv et al., 2022; Wang et al., 2023). Common models employed for LSM include decision trees (DTs), RF, SVM, and neural networks (Azarafza et al., 2021; Wang et al., 2021). DTs are a form of ML technique that includes building a tree-like model of decisions based on various variables or attributes. This model is designed to forecast the chance of landslides occurring across multiple territory regions (Kadavi et al., 2019). RFs include ensembling a group of DTs and utilizing their aggregate forecasts to produce more accurate predictions about the risk of landslides happening (Dou et al., 2019; Sahin et al., 2020). SVMs estimate the likelihood of landslides occurring in various parts of the region by locating the hyperplane in a high-dimensional space that maximum separates distinct classes (Pham et al., 2016; Ye et al., 2023). These ML algorithms can be beneficial for detecting locations at high risk of landslides and developing strategies to mitigate this risk (Youssef and Pourghasemi, 2021). Despite its efficacy, each algorithm presents its strengths and challenges. The success of these algorithms largely depends on the nature of the data and the research context (Merghadi et al., 2020; Ado et al., 2022). Therefore, it is essential to compare the performance of several ML algorithms to identify the most effective approach for a given study area.

In South Korea, LSM relies on the statistical technique of LR analysis, which has an accuracy rate of approximately 75.2% (Lee et al., 2015). Although LR has been helpful, it has certain limitations, mainly when modeling non-linear interactions. This has motivated the exploration of alternative ML techniques, each presenting unique strengths: GNB's probabilistic approach, KNN's adaptability to non-linear data boundaries, SVM's prowess in high-dimensional spaces, and the ensemble capabilities of RF and XGB that efficiently capture complex data relationships. However, comprehensive comparative studies on these ML algorithms, especially in the South Korean setting, are limited due to past restrictions in accessing high-resolution data.

This study aims to fill this gap by investigating the performance of 6 ML algorithms for high-resolution LSM in Inje County, Gangwon, South Korea, an area characterized by steep terrain and a high frequency of landslides (Lee et al., 2016). The novelty of this study lies in its comprehensive comparison of the performance of 6 ML algorithms, providing a more extensive analysis than previous research in the South Korean context. This study also leverages high-resolution data to provide a detailed evaluation of each algorithm's performance, addressing previous limitations in data availability.

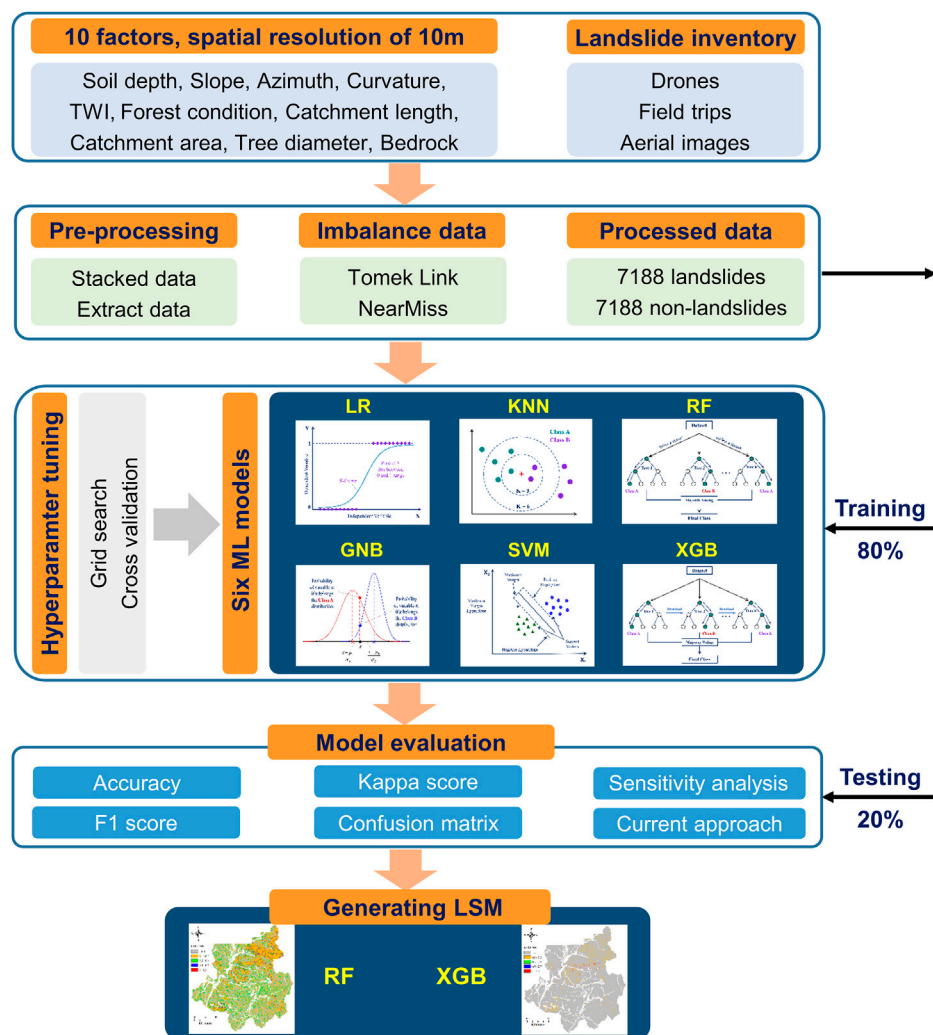


FIGURE 1
Flowchart of this study.

This article discusses the following important research questions: 1) What is the overall accuracy of the ML algorithms for predicting landslide susceptibility? 2) How do the ML algorithms perform for specific assessment criteria like recall, precision, and F_1 score? 3) How do the ML algorithms perform across different landslide susceptibility classes? 4) How does the effectiveness of the ML algorithms compare to that of other methods, such as the traditional statistic method? 5) What are the critical factors influencing the performance of the ML techniques in the research area?

By identifying the most effective ML algorithms for LSM in South Korea, this study aims to contribute to developing more accurate and reliable landslide risk assessment models. These can underpin informed decision-making in disaster management, ultimately mitigating the impacts of landslide disasters. The remainder of the article is structured as follows: The Material and Methods section presents the data sources, the selection and implementation of the ML algorithms, and the evaluation of algorithm performance. The Results section describes the research results, and the Discussion section discusses the

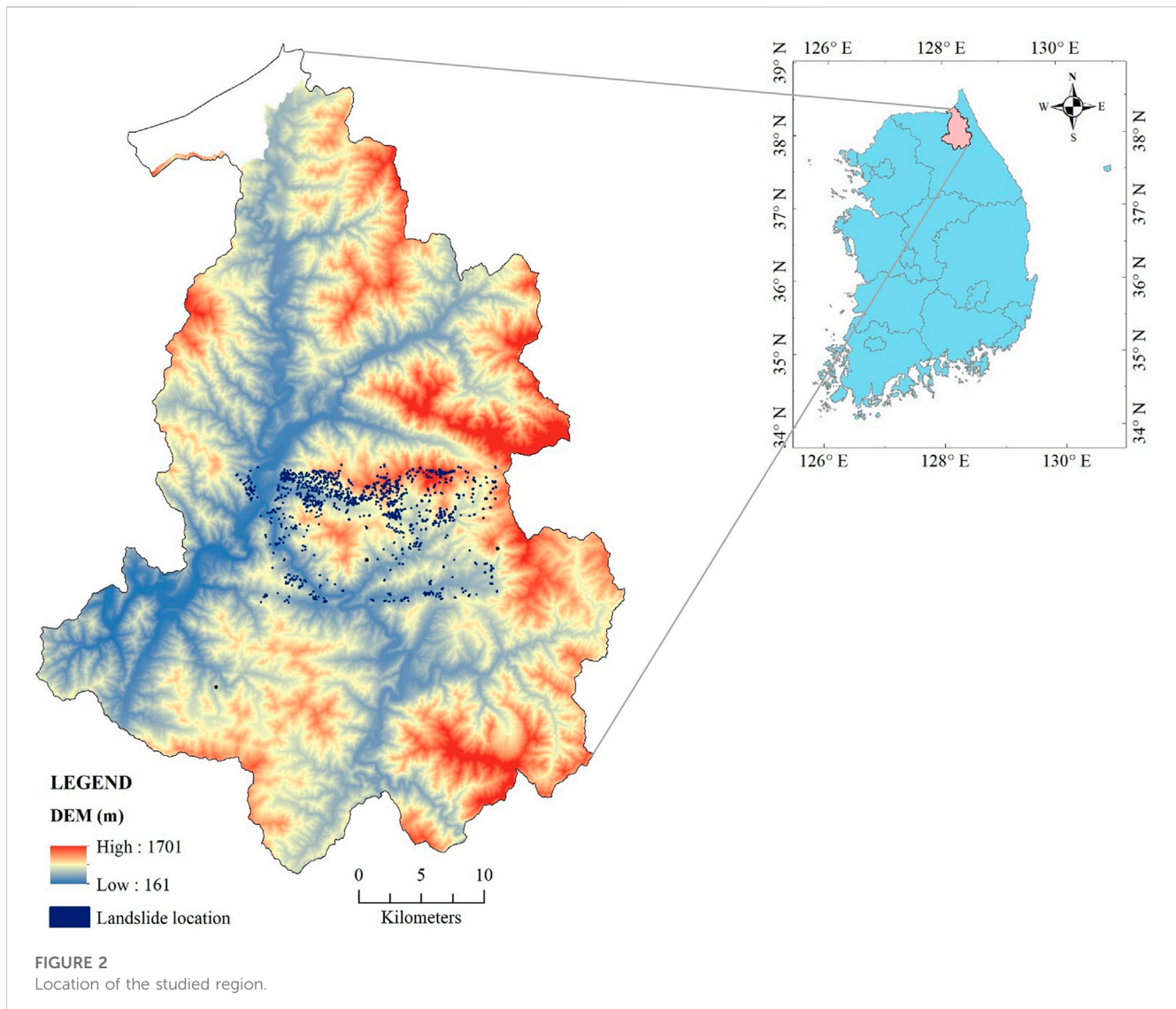
implications of the findings. The Conclusion section summarizes the key findings and provides recommendations for further study. The schematic diagram of this study is illustrated in Figure 1.

2 Materials and methods

2.1 Study area

Landslides are ground movements caused by the movement of slope-forming elements comprising rock, soil, vegetation, and water downward and outward. These movements can range from slow creep to rapid and destructive slides, often activated by factors like precipitation, geological attributes, human activity, or a combination of these triggers.

This investigation is centered in Inje County, Gangwon Province, South Korea. Situated in the eastern segment of the Korean Peninsula, Inje County is distinctly characterized by its steep terrains, predisposing it to a heightened risk of landslides (Yoo et al., 2009). These geophysical phenomena not only carry the

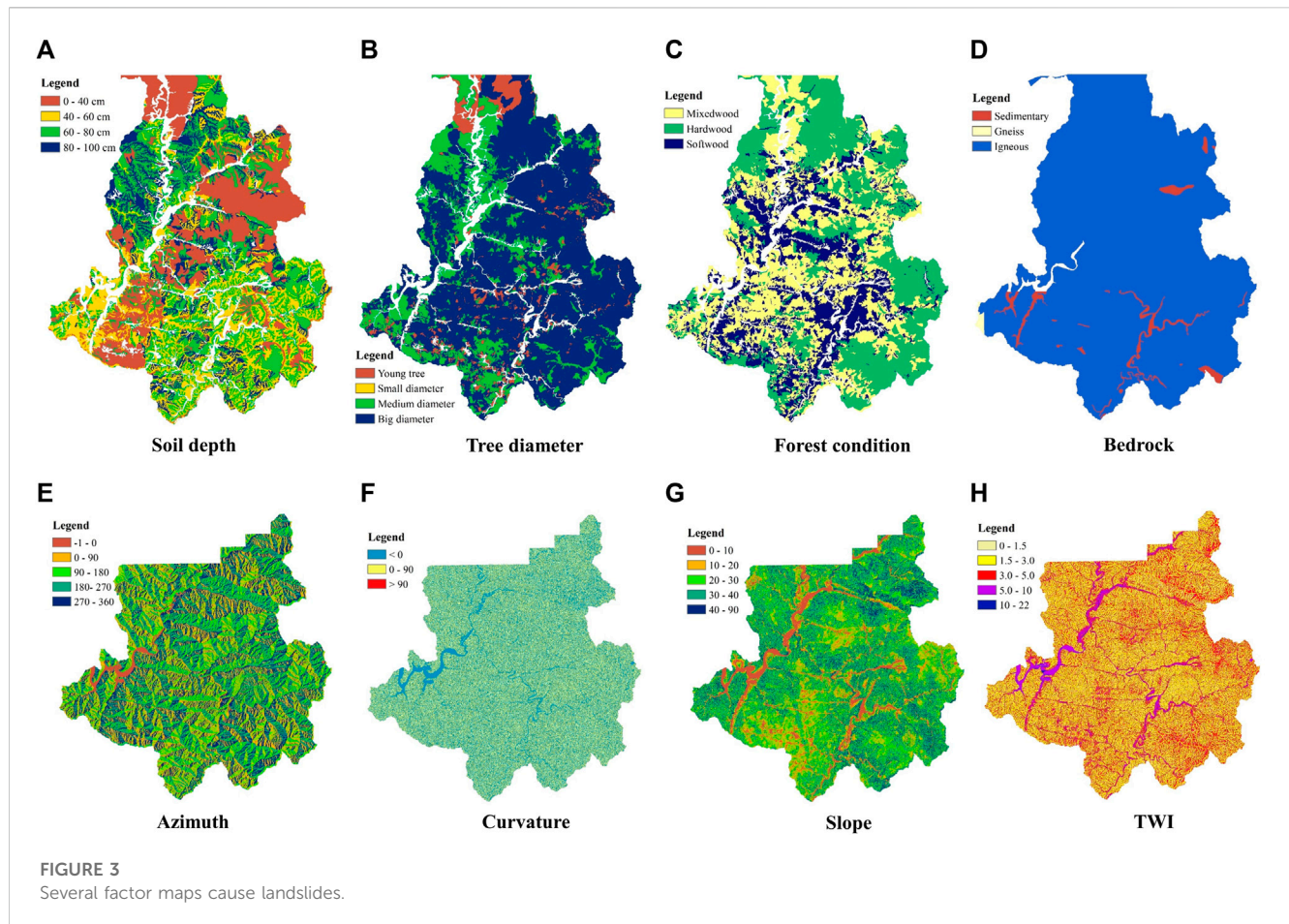


potential to damage infrastructure severely but also to impede transportation networks and critically impact local community livelihoods (Kadavi et al., 2019). Recently, Inje County has witnessed an uptick in the frequency and magnitude of landslide events, a pattern emerging from an intricate interplay of natural and anthropogenic influences. Intense meteorological events like heavy monsoons and shifts in land use patterns have amplified these landslide occurrences (Lee et al., 2015). Notably, the county is especially susceptible to landslides triggered by heavy rainfall events, typical during the monsoon phase (Lee et al., 2015). Figure 2 presents the study area.

For LSM, the input data quality and the selection of the appropriate modeling approach are among the components that have the most significant impact on the accuracy of the map (Yalcin, 2008). Because landslides are the slope's movement or the slope's instability and their control parameters, the fundamental causes of landslides are typically connected to geology, hydrology, morphology, and anthropogenic activities (Ayalew and Yamagishi, 2005). As a result, it is crucial to identify the

causative conditions for landslides in prone areas. Despite this, there is no universally accepted technique or approach for identifying effectiveness variables in LSM (Pourghasemi et al., 2018), and identifying these elements differs from one research to the next.

For this study, guided by recommendations from the National Institute of Forest Science, South Korea, we gathered data spanning ten distinct types selected as input attributes for the modeling process. These data sources included soil depth (SD), tree diameter (TD), forest condition (FC), bedrock (BR), curvature (CU), azimuth (AZ), topographic wetness index (TWI), catchment length (CL), catchment area (CA), and slope (SL). All variables have been compiled into a high-resolution raster grid format corresponding to a grid cell size of 10 m × 10 m. In addition, information on past landslide occurrences was also collected from the Korean Meteorological Administration database. All data were processed and analyzed using geographic information systems software. Figure 3 depicts a map of several conditions contributing to landslide occurrence in the region.



2.2 Data pre-processing

As previously highlighted, the ten factors collected in this research are rasterized with an impressive 10 m resolution. In addition to these datasets, we collected and processed data on landslide inventory for 2005–2019. It can be said that this is the most important dataset for studies on building LSM based on ML algorithms. This entire dataset was measured and analyzed by surveys at locations immediately after a landslide from aerial images, drones, and field trips. The pre-processing of this dataset for the ML models is marked by several integral phases. The landslide inventory dataset is first rasterized to match the grid cell size of the ten factors mentioned in this study, which is 10 m×10 m. This high resolution indicates that a single landslide event can be identified across multiple neighboring cells and the number of landslide-affected cells depending on the scale and size of the respective landslide event. Following rasterization, cell locations affected by landslides are carefully identified, inventoried, and labeled. Ten different data types are then stacked on the digitized landslide data. Once layered, data from all the superimposed layers is extracted for each grid cell. Based on their data attributes, these cells are systematically classified as landslides or non-landslides.

After processing and analyzing the data, it was found that approximately 7,188 grid cells recorded landslides, significantly lower than the number of grid cells that did not. The imbalance between these data classes is a typical problem in practice and can result in biased algorithms that perform poorly on the minority class

(Fernández et al., 2018). This occurs because ML models may learn to classify the majority class correctly while ignoring or incorrectly classifying the minority class (Ma and He, 2013). To solve this problem and boost the effectiveness of the ML models, this study applied several solutions, such as the Tomek Links technique and the Near Miss algorithm, to resample the data. The following subsections go into further depth about these approaches. After processing, the final dataset had 14,376 samples, comprising 7,188 landslide samples and 7,188 non-landslide samples.

2.2.1 Tomek Links technique

The Tomek Links technique is a data pre-processing technique frequently utilized to improve the efficiency of ML algorithms. It is based on the idea that a pair of samples near one other and belonging to distinct classes are termed Tomek Links (Tomek, 1976). This technique removes samples from the majority class for each pairing while expanding the gap between the two categories. This can be useful as noise and outliers often negatively affect the model's accuracy and reliability. This approach could be applied to any ML issue, including classification, regression, and clustering. Figure 4 depicts the resampling procedure of the Tomek Links techniques.

2.2.2 NearMiss algorithm

The NearMiss algorithm is commonly employed to boost the effectiveness of ML algorithms, especially for imbalanced datasets.

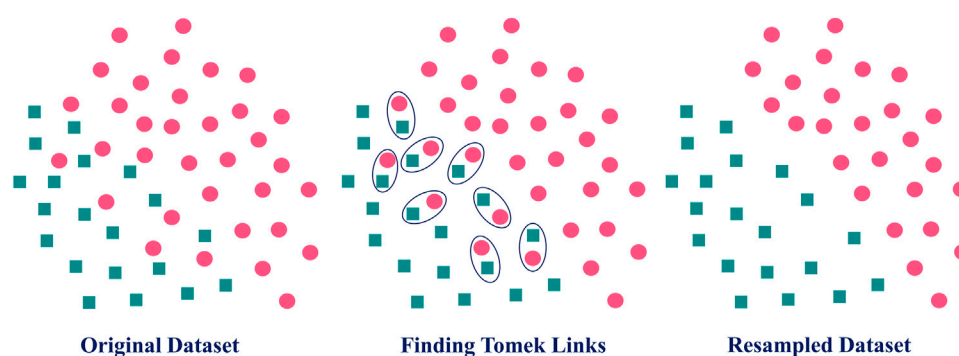


FIGURE 4
Illustration of Tomek Links technique.



FIGURE 5
Illustration of NearMiss algorithm.

An imbalanced dataset is one in which the number of samples in one category differs considerably from the number of samples in the other. This frequently results in poor performance of ML algorithms, as the minority class is often underrepresented and may not be adequately learned by the model.

The NearMiss algorithm tackles this issue by selecting a subset of samples from the majority group that is similar to samples from the minority group based on a distance measure like Euclidean distance (Zhang and Mani, 2003). The NearMiss algorithm has three variants: NearMiss1, NearMiss2, and NearMiss3. NearMiss1 chooses samples from the majority group nearest to the minority group. NearMiss-2 and NearMiss-3 select samples from the majority group that are furthest from the majority group and closest to the minority group, respectively. Figure 5 depicts the resampling procedure of the Near Miss algorithms.

2.3 ML algorithms

This study used 6 ML algorithms to classify areas as prone to landslides or not prone to landslides based on a set of input features. Each algorithm has its assumptions, strengths, and limits, and we chose various algorithms to provide robust and reliable results. In

addition, the cross-validation technique was utilized to analyze the performance of each algorithm and select the best-performing algorithm based on a range of evaluation criteria, for instance, PCC, recall, precision, and F_1 score. Before using ML algorithms to LSM, it is necessary first to gather a collection of labeled data, in which both the input characteristics and the landslide susceptibility (either “1” or “0”) are already established. ML models are then trained using the aforementioned labeled data via appropriate optimization algorithms.

2.3.1 LR

LR is a simple and popular classification method using linear regression and the logistic function as its primary building blocks (Cramer, 2002). In the context of LSM, LR is utilized to classify areas as either prone or not prone to landslides based on a collection of input features that are known to be associated with landslides. These elements may include geological and topographic characteristics, land use, land cover, and environmental factors like precipitation and slope angle. The LR objective is to find the line that best matches the data points and demarcates the two distinct groups of “landslide” and “non-landslide”. The output is a probability that ranges between 0 and 1, which is utilized to categorize the data into one of the two options. For instance, if the likelihood is higher than 0.5, the data is

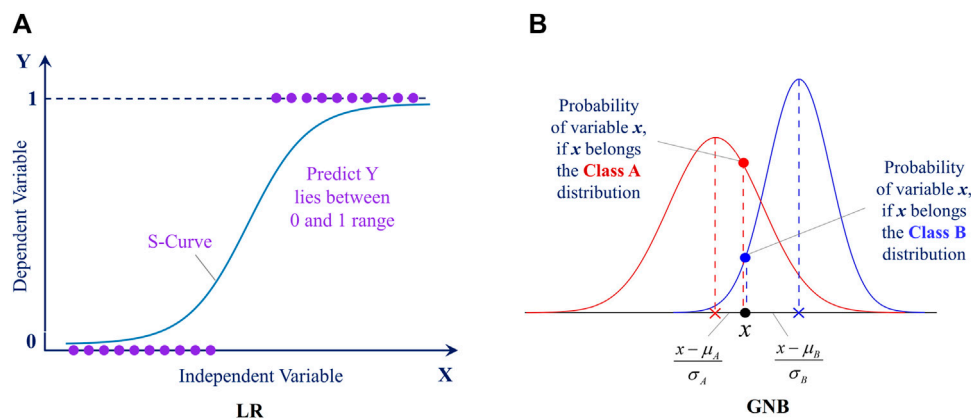


FIGURE 6
Illustration for (A) LR algorithm and (B) GNB algorithm.

classified as potentially affected by landslides. Still, if the probability is lower than 0.5, the data is categorized as not having the potential to be affected by landslides. Figure 6A briefly illustrates the LR algorithm. The probability of the event occurring is expressed as:

$$p(x) = \frac{1}{1 + e^{-(\beta_0 + \beta_1 x_1 + \beta_2 x_2 + \dots + \beta_n x_n)}} \quad (1)$$

Where β_0, β_1, \dots are the coefficients and x_1, x_2, \dots are the predictor variables

2.3.2 GNB

GNB classification algorithm is based on Bayesian probability theory and follows a Gaussian normal distribution, making it suitable for continuous data classification tasks. It is a straightforward and commonly adopted approach, mainly when the dataset is large. The method assumes that the input characteristics are independent of one other, called the “naive” assumption. This indicates that the probability of each factor is computed independently without considering the probabilities of the other characteristics. Through the use of the maximum likelihood estimate, it is possible to learn the possibility of the input characteristics given the various classes. The output is the likelihood that the data belong to each category, and the prediction is taken from the type with the highest probability. GNB can be sensitive to the assumptions of independence and normalcy of the features, even though it is a straightforward and efficient classification method that performs well on a wide range of datasets. Figure 6B briefly illustrates the GNB algorithm. Given a feature vector $X = (x_1, x_2, \dots, x_n)$, the probability that a sample belongs to class C_k is given by:

$$P(C_k | X) = \frac{P(X | C_k)P(C_k)}{P(X)} \quad (2)$$

2.3.3 KNN

KNN is an ML algorithm used for classification tasks. The core of this technique is rooted in the principle of instance-based learning, wherein the categorization of a new data point is established based on its similarity to prior data points within the

training dataset (Cover and Hart, 1967). The technique uses a distance metric, for instance, Euclidean or Manhattan distance, to estimate the distance from the new data point to all points. The K closest points to the latest data are then selected, where K is a value determined by the user. The new data point is assigned to the category with the highest frequency among the K nearest points. KNN is a prevalent choice for classification jobs because of its simplicity and performance on various input formats. Figure 7A briefly illustrates the KNN algorithm. The distance between two points x and y in the Euclidean space is:

$$d(x, y) = \sqrt{(x_1 - y_1)^2 + (x_2 - y_2)^2 + \dots + (x_n - y_n)^2} \quad (3)$$

2.3.4 SVM

SVM is a powerful and versatile classification algorithm that works by finding the hyperplane that maximally separates various classes in the feature space (Cortes and Vapnik, 1995). The fundamental of SVM is finding a decision margin that maximally divides the data points into multiple classifications. A set of support vectors defines the decision boundary, the data points in the training dataset nearest to the hyperplane. The relative position of the support vectors determines the hyperplane position. The SVM output is a score that indicates the likelihood of the data belonging to one class or the other. SVM is a powerful and effective classification technique suited for a wide range of datasets, although it can be computationally expensive when the training set is large. Figure 7B briefly illustrates the SVM algorithm. The decision function is:

$$f(x) = \langle \omega, x \rangle + b \quad (4)$$

Where ω is the normal vector to the hyperplane and b is the offset.

2.3.5 RF

RF is a classification algorithm incorporating numerous DT predictions to make more accurate and robust predictions (Tin Kam, 1998; Breiman, 2001). A DT is a tree-shaped model in which each node represents an individual characteristic, each branch a

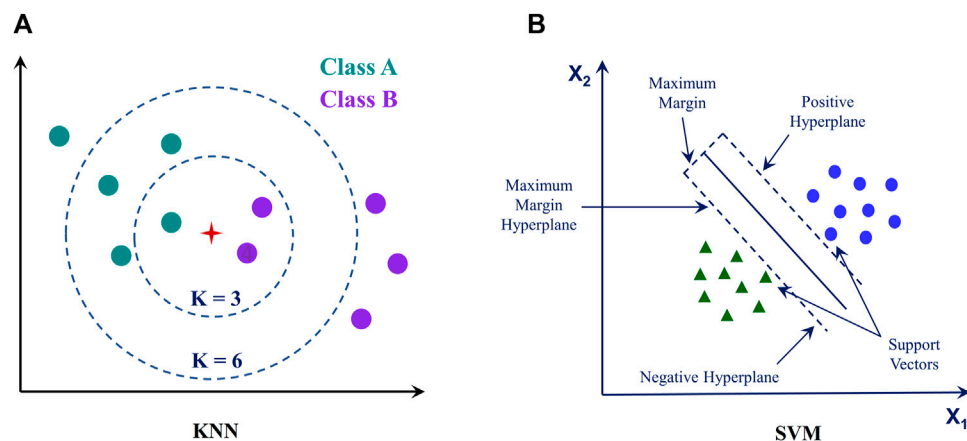


FIGURE 7
Illustration for (A) KNN algorithm and (B) SVM algorithm.

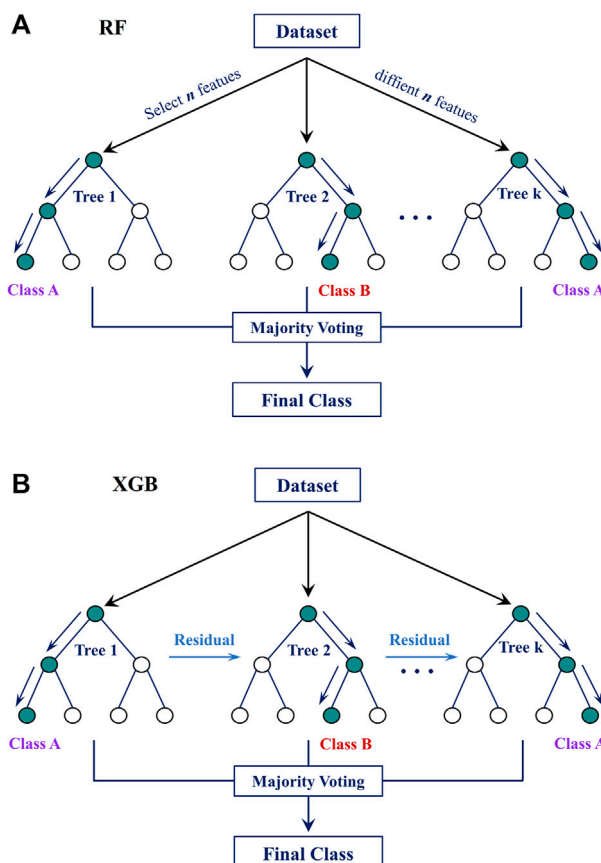


FIGURE 8
Illustration for (A) RF algorithm and (B) XGB algorithm.

particular choice, and each leaf node a distinct category or value. RF generates a collection of DT by bootstrapping a sample of the data and randomly picking a sample of the input data for every split. This means that each DT is constructed by drawing from a distinct sample of the data and a unique subset of the input variables. In

classification tasks, RF determines the final classification by taking the unweighted average of the predictions made by individual DTs and selecting the most commonly predicted category. RF is a robust and efficient method resistant to overfitting and can be used on various datasets. Figure 8A briefly illustrates the RF algorithm. The classification decision is made by majority voting:

$$Y_{RF} = f(Y_{T1}, Y_{T2}, \dots, Y_{Tn}) \quad (5)$$

Where Y_{Ti} is the prediction of the i th tree.

2.3.6 XGB

XGB is a well-known gradient-boosting technique that may be applied to classification and regression applications (Chen and Guestrin, 2016). It is based on DT and is meant to form an ensemble of DTs to make predictions based on data that has not been seen before. An optimization approach that minimizes the loss function generates a set of decision trees in XGB. This means the DTs are formed to reduce the gap between the observed and estimated values. XGB is a robust and efficient technique for classification and regression work. It is a popular algorithm because of its strong performance on a diverse range of data formats and its capacity to deal with categorical and numerical characteristics. Figure 8B briefly illustrates the XGB algorithm. Given a differentiable loss function $L(y, F(x))$, where y is the actual value and $F(x)$ is the prediction, the prediction model is updated iteratively:

$$F_t(x) = F_{t-1}(x) + \eta \sum_{i=1}^n f_i(x) \quad (6)$$

Where $f_i(x)$ is the prediction of the i th base learner (typically a DT), and η is the learning rate.

2.4 Hyperparameter tuning and model validation

This study employed the grid search strategy for hyperparameter tuning, a widely used approach that can effectively enhance the

TABLE 1 Parameter settings of each ML model used in the grid search.

Algorithm	Parameter	Value range	Optimal value
LR	C	0.01, 0.1, 1, 10, 100	10
	max_iter	100, 1,000, 10000	100
KNN	n_neighbors	[2, 30]	6
	weights	uniform, distance	distance
GNB	var_smoothing	[0, 1]	0.0029
SVM	C	0.1, 1, 10, 100	100
	kernel	linear, poly, rbf, sigmoid	rbf
	gamma	scale, auto	scale
RF	n_estimators	50, 100, 200	100
	max_depth	10, 50, 100	50
	max_features	auto, sqrt	auto
XGB	n_estimators	50, 100, 200	100
	max_depth	10, 50	10
	max_features	auto, sqrt, log2	sqrt

accuracy and reliability of the resulting LSMs. As its applicability to small to medium-sized datasets, this method trains and evaluates an ML algorithm for each set of hyperparameters defined within a specified grid. For each model, the Python scikit-learn library facilitates the implementation of the grid search method.

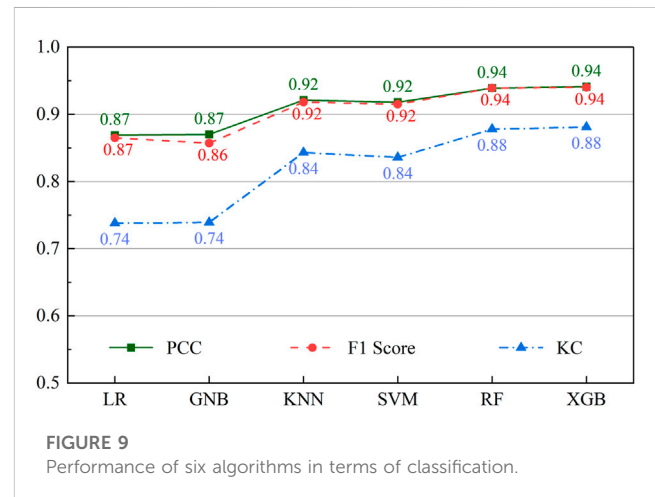
The final processed dataset for this study contained 14,376 samples, with a balanced distribution of landslide and non-landslide instances (7,188 each). By maintaining a balanced dataset, potential model bias is mitigated, and the generalizability of prediction tasks is improved. The dataset is separated into training and testing subsets, representing 80% and 20% of the total dataset. Thus, the training set includes 11,500 samples (5,750 landslides and 5,750 non-landslides), while the testing set consists of 2,876 samples (1,438 landslides and 1,438 non-landslides). A 5-fold cross-validation is performed throughout the grid search procedure to fine-tune the models. This ensures that the findings are not overly optimistic and can be generalized to unseen data. The selected parameters for each ML model used in the grid search are detailed in [Table 1](#).

2.5 Performance measures

Assessing algorithm performance is a crucial stage in using ML algorithms for LSM. It helps to identify the most accurate and reliable algorithm for a given study and can provide valuable insights into the strengths and limitations of the algorithms. This study used various evaluation criteria, including PCC, precision, recall, and F_1 score. PCC measures how well the model correctly classifies the data, whereas recall estimates the proportion of true positive (TP) predictions over total observed positive events. Precision measures how well the model avoids false positives (FP), and the F_1 score is the harmonic average of precision and recall. We estimated these evaluation metrics using a confusion matrix,

TABLE 2 Performance statistics of six models.

Metrics	LR	GNB	KNN	SVM	RF	XGB
PCC	0.869	0.870	0.921	0.918	0.939	0.941
F_1 Score	0.865	0.857	0.918	0.915	0.939	0.940
KC	0.738	0.739	0.843	0.836	0.878	0.881



which compares each case's predicted and actual values. A confusion matrix comprises four main components: TP, FP, true negatives (TN), and false negatives (FN). In this case, TP and RN stand for the number of samples rightly categorized as positive and negative. In contrast, FP and FN refer to the number of samples wrongly classified as positive and negative. The following is a description of these criteria.

$$\text{Precision} = \frac{TP}{TP + FP} \quad (7)$$

$$\text{Recall} = \frac{TP}{TP + FN} \quad (8)$$

$$F_1 \text{ score} = \frac{2 * \text{Precision} * \text{Recall}}{\text{Precision} + \text{Recall}} \quad (9)$$

$$PCC = \frac{TP + TN}{TP + FP + TN + FN} \quad (10)$$

$$PV = \frac{(TP + FP) * (TP + FN) + (FN + TN) * (FP + TN)}{(TP + FP + TN + FN)^2} \quad (11)$$

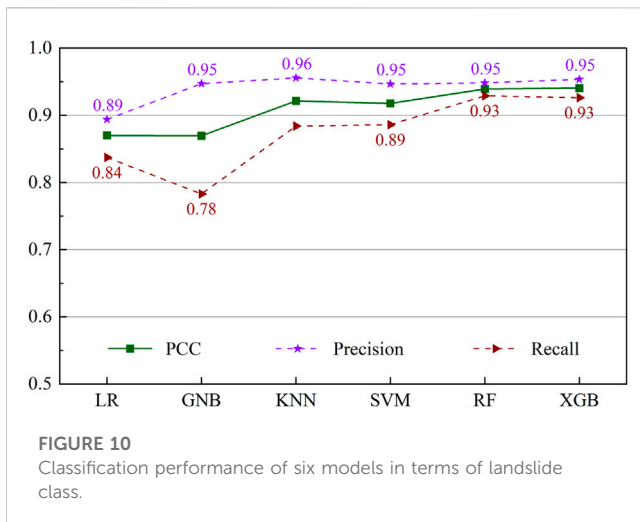
$$KC = \frac{PCC - PV}{1 - PV} \quad (12)$$

Where PCC means the percentage of correct classification (or accuracy), PV implies the probability of random agreement, and KC represents the Kappa coefficient.

3 Results

3.1 Comparison of six ML algorithms

To compare the performance of 6 ML algorithms for LSM in Inje County, South Korea, we use several evaluation metrics,



including PCC, F_1 score, and KC. The results of these evaluations are presented in Table 2 and Figures 9, 10 below.

All algorithms generally have relatively high PCC, F_1 score, and KC values, indicating that they all perform well overall. However, the performance of the various models differs slightly. RF and XGB algorithms had the highest PCC values, with 0.939 and 0.941, respectively. These models can correctly classify landslide-prone areas with a high percentage, indicating that they can detect zones with an increased susceptibility to landslides. Regarding the F_1 score metric, these models can balance the precision and recall well, as the corresponding values for RF and XGB were 0.939 and 0.940, respectively. This is important as it will reduce the number of FNs and FPs. The KC metric also revealed a strong agreement between the predictions of these models and actual observations, and the models are not just labeling all areas as landslide-prone. The best values for this metric were 0.878 and 0.881, belonging to RF and XGB algorithms.

In contrast, the PCC and F_1 score values of the LR and GNB were lower than those of the other algorithms (0.869 and 0.87, respectively), and their KC values were also lower (0.738 and 0.739, respectively), which indicated that they might not perform as well as the other models. This might be because these models are simple, and they may be incapable of capturing the complex relationships between the input variables and the landslide sensitivity, as well as other models such as RF or XGB. It is worth noting that the KNN and SVM algorithms also performed pretty well, with PCC, F_1 score, and KC values of 0.921, 0.918, and 0.843 for the KNN, and 0.918, 0.915, and 0.836 for the SVM, respectively. These models were capable of recognizing regions with a high risk of landslides. However, they are not as good as RF and XGB regarding balancing the precision, recall, and agreement between the model predictions and the observations.

Figure 10 illustrates the classification performance for the landslide class of the ML models corresponding to the PCC, precision, and recall criteria. Similar to the previous evaluation, the LR and GNB models had lower accuracy and recall values, with the earlier having scores of 0.894 and 0.947, while the latter had numbers of 0.837 and 0.783, respectively. The KNN and SVM algorithms depicted a similar pattern, with precision and recall scores of 0.956 and 0.884 for KNN and corresponding numbers

for SVM of 0.947 and 0.886, respectively. XGB had the highest precision value of 0.953 compared to other models, indicating its proficiency in identifying TPs and having a low FP rate. On the other hand, RF had the highest recall value of 0.929, demonstrating its ability to identify TP and low FN rates.

3.2 Robustness and sensitivity analysis

To offer a more thorough assessment of the robustness of RF and XGB models, an analysis of the confusion matrix and feature importance was performed and shown in Figure 11, Figure 12.

Figure 11 illustrates the confusion matrix details for both models. Out of 2,876 samples, the RF model yielded 1,365 TNs, 1,336 TPs, 73 FPs, and 102 FNs. In contrast, the XGB model resulted in 1,373 TNs, 1,332 TPs, 65 FPs, and 106 FNs. Regarding PCC, both the RF and XGB exhibited remarkable performance, registering classification accuracies of 93.9% and 94.1%, respectively. The precision and recall metrics underscore their efficacy, with RF showing 94.8% and 92.9%, respectively, whereas XGB showcased 95.3% and 92.6%.

Feature importance is a metric of how much each factor contributes to the predictions made by the model. According to the data presented in Figure 12, the variable considered to be of the utmost significance in both the RF and the XGB models was SD (soil depth), which had a value of 0.246 and 0.285, respectively. This means that soil depth was the most influencing variable when determining landslide susceptibility in the research region. The second most significant variable in the RF algorithm was CU, with a value of 0.133, followed by TWI, with 0.144. In the case of the XGB model, the CA variable was the second most important variable, followed by the TWI variable, which had values of 0.144 and 0.125. BR was the component with the lowest importance score in both models, with a value of 0.032 in RF and 0.038 in XGB models.

3.3 LSM of Inje area

The LSM generated by the RF and XGB algorithms were displayed in Figure 13, Figure 14, respectively. These maps were based on the likelihood of landslides occurring for each grid cell, which ranges from 0 to 1. As seen in these Figures, the LSM is segmented into five levels following the categorization used by the National Institute of Forest Science in South Korea. Among them, level 4, with a range of probability [0.5–0.7], and level 5, with a range of probability [0.7–1.0], are considered the most dangerous warning levels. The visualized results of the two algorithms revealed a slight difference in the landslide probability estimation for grid cells. This distinction was particularly noticeable when comparing level 1 (0–0.1) and level 3. In contrast, there was not much difference between the other levels, notably levels 4 and 5, each with a significant possibility of landslides.

3.4 Current approach for LSM in South Korea

The current approach for LSM in South Korea focuses primarily on using statistical techniques, particularly logistic regression

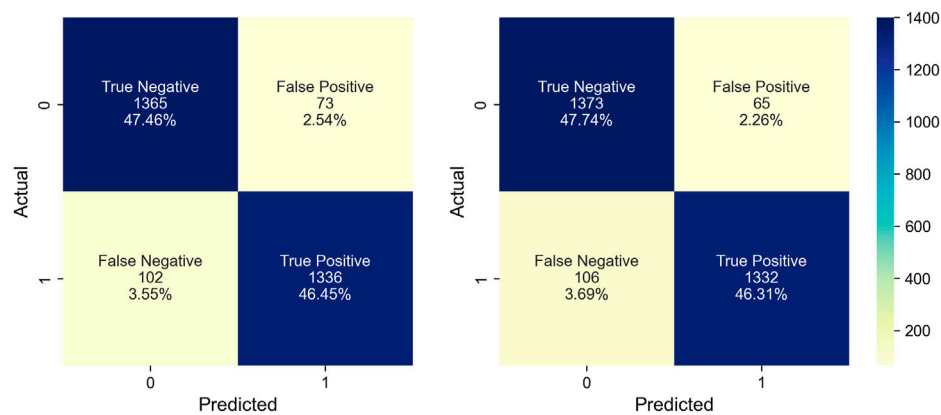


FIGURE 11
Confusion matrix for RF and XGB.

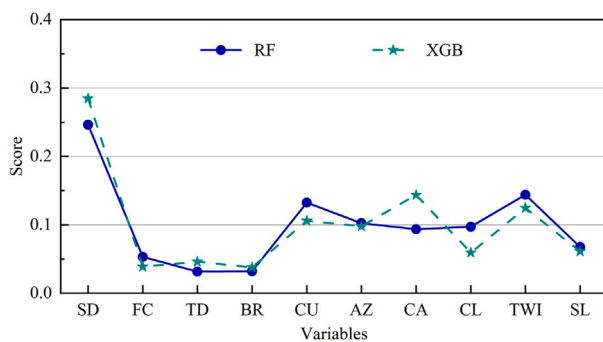


FIGURE 12
Variable importance of RF and XGB.

analysis, to identify the association between input factors (Woo et al., 2014). The following equations are used to calculate the probability of a landslide hazard at a specific site. The LSM for the Inje area was developed from these equations, as shown in Figure 15.

$$X = -2.596 + 0.069*SL - 0.022*CL + 0.011*CU + 0.734*TWI - 0.594*TD + 0.006*SD + AZ + BR + FC \quad (13)$$

$$P = \frac{e^X}{1 + e^X} \quad (14)$$

According to Lee et al. (2015), this methodology achieved an average accuracy of approximately 75.2%. When comparing this method to the ML approach presented in Section 3.1, the accuracy of ML models was about 92% on average, which was a significant improvement over the process that is currently being used. The PCC and F_1 scores of the 6 ML models range from 0.869 to 0.941 and 0.857 to 0.940, respectively. Among the six algorithms, RF and XGB performed best, with accuracy and F_1 values of [0.939–0.941]. The results of this study indicated that using ML algorithms for LSM can lead to more accurate and higher-resolution LSMs. It is essential to point out that one of the benefits of adopting an ML technique is that

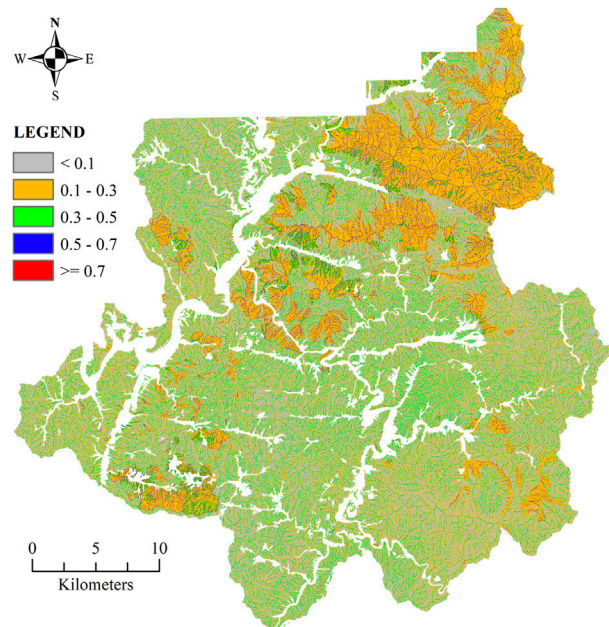
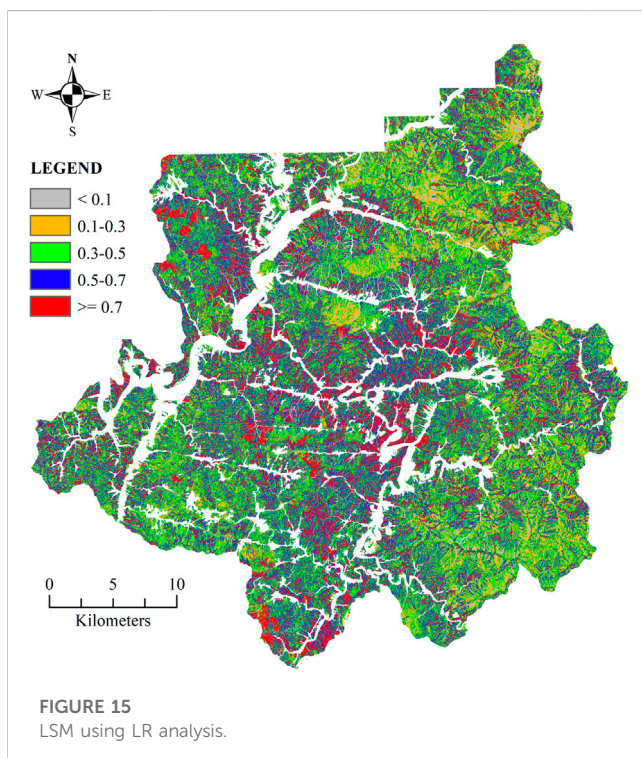
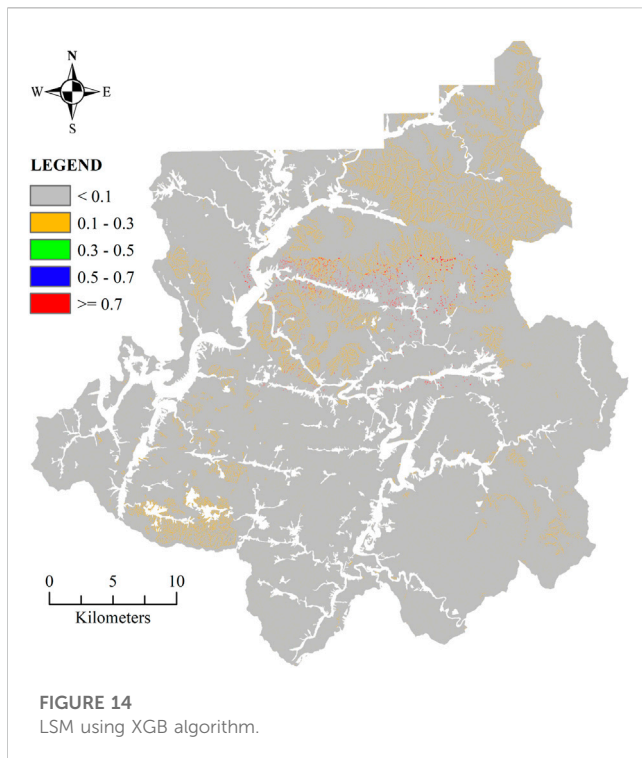


FIGURE 13
LSM using RF algorithm.

it is capable of handling complicated interactions between input variables and landslide susceptibility. These types of relationships may be difficult to capture using statistical methods. Additionally, the use of ML algorithms provides a valuable alternative to the current statistical approach in South Korea.

4 Discussion

The ability of ML algorithms to enhance LSM in contexts such as Inje County, South Korea, has been substantiated in this study. The RF and XGB models performed particularly well in correctly identifying landslide-prone areas, while KNN and SVM



performed well. Nonetheless, algorithm selection for such applications should be based on performance metrics and factors like ease of implementation, model interpretability, and inherent limitations (Zhou et al., 2021; Liu et al., 2023).

The poorer performance exhibited by LR and GNB resonates with prior literature on their inherent limitations. For instance, LR

assumes a linear relation between predictor and response variables, which often is not true in complex natural phenomena like landslides (Pham et al., 2016). Additionally, its sensitivity to outliers and imbalanced datasets hampers its ability to capture intricate non-linear associations (Akinci and Zeybek, 2021). Similarly, while GNB's simplicity and computational efficiency are well acknowledged, its assumption of input independence often leads to its suboptimal performance, consistent with our findings and those of Azarafza et al. (2021).

The comparable performance of KNN and SVM echoes prior works. KNN, though simple in its construct and devoid of data distribution assumptions, suffers when processing power is limited, given its requirement to compute distances between every training and new data point. The sensitivity of KNN to the choice of 'K' has been reported by studies such as Sameen et al. (2020). SVM's strength lies in its ability to grapple with high-dimensional data and intricate non-linear predictor-response relationships (Yao et al., 2008). However, SVM's sensitivity to kernel function choices and the regularization value, as corroborated in our study, is a limitation noted by Huang and Zhao (2018).

According to the findings of this research, the 2 ML algorithms most useful for LSM are RF and XGB. Both algorithms have the advantage of being capable of handling high-dimensional data and non-linear correlations between input characteristics and output. RF's resilience to data noise and outliers has been highlighted by Dou et al. (2019), whereas XGB's speed and robustness to missing data are mentioned in Biswas et al. (2022). However, the potential computational intensiveness of RF and the sometimes opaque results of XGB, as observed in our study, are consistent with the findings of Merghadi et al. (2020). Despite these limitations, both these models hold promise for LSM, and the choice between them should be reasonable, considering data characteristics and the study's objectives.

Adopting the ML-based approach for LSM holds substantial practical implications for regions like South Korea. Enhanced predictive accuracy not only aids in more effective resource allocation for disaster prevention but also offers a robust foundation for policymaking at both local and national scales. Proactively identifying high-risk zones, authorities can prioritize infrastructure development, design better evacuation strategies, and optimize disaster response protocols. This research thus paves the way for an integrated, data-driven approach to landslide management, potentially safeguarding communities and infrastructures against the devastating impacts of unforeseen landslides.

Despite the promising outcomes of this research, it is crucial to recognize its limitations. Data availability restricted our study to a specific timeframe and region, potentially affecting broader generalizations. Moreover, while the chosen ML algorithms offer advanced predictions, their complexity could pose challenges in real-time applications or when adapting to other regions with distinct geological characteristics. Future research could explore integrating diverse datasets for better model training and investigating simpler yet efficient algorithms. Additionally, cross-regional studies would be invaluable in assessing the universal applicability of the ML-based LSM approach.

5 Conclusion

The application of 6 ML algorithms for LSM in Inje County, South Korea, has revealed distinct efficiencies among the algorithms. RF and XG perform particularly well in accurately classifying landslide-prone areas, balancing precision and recall, and having PCC values up to about 94%. The KNN and SVM models with a PCC score of roughly 92% also performed well in correctly classifying landslide-prone areas. The two models, LR and GNB, have the lowest efficiency, corresponding to a PCC value of only about 87%. Despite this, the results demonstrate that the ML approach is superior to the existing statistical approach with logistic regression, which has an accuracy of about 75.2%.

This study provides a valuable starting point for further research into using ML techniques for LSM in South Korea and other regions. The RF and XGB models are highly recommended for LSM usage in South Korea. However, it is essential to consider the trade-offs between the performance and simplicity of implementation and interoperability. The efficiency of algorithms differs from location to region for various reasons, including geomorphology, land uses, and other factors.

The broader implications of this finding can potentially reshape disaster management policies in South Korea. A shift from traditional models to ML-based LSMs can facilitate more accurate predictions, allowing authorities to pre-emptively address and mitigate landslide risks in vulnerable zones. This study will substantially impact the understanding of landslide risk in Inje County. It will be valuable in developing effective mitigation techniques for landslides in the place.

Data availability statement

The raw data supporting the conclusion of this article will be made available by the authors, without undue reservation.

References

- Ado, M., Amitab, K., Maji, A. K., Jasińska, E., Gono, R., Leonowicz, Z., et al. (2022). Landslide susceptibility mapping using machine learning: A literature survey. *Remote Sens.* 14 (13), 3029. doi:10.3390/rs14133029
- Akinci, H., and Zeybek, M. (2021). Comparing classical statistic and machine learning models in landslide susceptibility mapping in Ardanuc (Artvin), Turkey. *Nat. Hazards* 108 (2), 1515–1543. doi:10.1007/s11069-021-04743-4
- Atkinson, P. M., and Massari, R. (2011). Autologistic modelling of susceptibility to landsliding in the Central Apennines, Italy. *Geomorphology* 130 (1), 55–64. doi:10.1016/j.geomorph.2011.02.001
- Ayalew, L., and Yamagishi, H. (2005). The application of GIS-based logistic regression for landslide susceptibility mapping in the Kakuda-Yahiko Mountains, Central Japan. *Geomorphology* 65 (1), 15–31. doi:10.1016/j.geomorph.2004.06.010
- Azarafza, M., Azarafza, M., Akgün, H., Atkinson, P. M., and Derakhshani, R. (2021). Deep learning-based landslide susceptibility mapping. *Sci. Rep.* 11 (1), 24112. doi:10.1038/s41598-021-03585-1
- Biswas, N. K., Stanley, T. A., Kirschbaum, D. B., Amatya, P. M., Meechaiya, C., Poortinga, A., et al. (2022). A dynamic landslide hazard monitoring framework for the Lower Mekong Region. *Front. Earth Sci.* 10, 1057796. doi:10.3389/feart.2022.1057796
- Breiman, L. (2001). Random forests. *Mach. Learn.* 45 (1), 5–32. doi:10.1023/A:1010933404324
- Caleca, F., Tofani, V., Segoni, S., Raspini, F., Franceschini, R., and Rosi, A. (2022). How can landslide risk maps be validated? Potential solutions with open-source databases. *Front. Earth Sci.* 10, 998885. doi:10.3389/feart.2022.998885
- Cardinali, M., Reichenbach, P., Guzzetti, F., Ardizzone, F., Antonini, G., Galli, M., et al. (2002). A geomorphological approach to the estimation of landslide hazards and risks in Umbria, Central Italy. *Nat. Hazards Earth Syst. Sci.* 2 (1/2), 57–72. doi:10.5194/nhess-2-57-2002
- Chae, B. G., Park, H. J., Catani, F., Simoni, A., and Berti, M. (2017). Landslide prediction, monitoring and early warning: A concise review of state-of-the-art. *Geosciences* 7 (6), 1033–1070. doi:10.1007/s12303-017-0034-4
- Chen, T., and Guestrin, C. (2016). "XGBoost: A scalable tree boosting system," in *Proceedings of the 22nd ACM SIGKDD international conference on knowledge discovery and data mining* (San Francisco, California, USA: Association for Computing Machinery).
- Chikalama, E. E., Mavrouli, O. C., Ettema, J., van Westen, C. J., Muntohar, A. S., and Mustofa, A. (2020). Satellite-derived rainfall thresholds for landslide early warning in Bogowonto Catchment, Central Java, Indonesia. *Int. J. Appl. Earth Observation Geoinformation* 89, 102093. doi:10.1016/j.jag.2020.102093
- Cortes, C., and Vapnik, V. (1995). Support-vector networks. *Mach. Learn.* 20 (3), 273–297. doi:10.1007/BF00994018
- Cover, T., and Hart, P. (1967). Nearest neighbor pattern classification. *IEEE Trans. Inf. Theory* 13 (1), 21–27. doi:10.1109/TIT.1967.1053964
- Cramer, J. S. (2002). *The origins of logistic regression*. Rotterdam, Netherlands: Tinbergen Institute Working Paper No. 2002-119/4. doi:10.2139/ssrn.360300
- Dou, J., Yunus, A. P., Tien Bui, D., Merghadi, A., Sahana, M., Zhu, Z., et al. (2019). Assessment of advanced random forest and decision tree algorithms for modeling rainfall-induced landslide susceptibility in the Izu-Oshima Volcanic Island, Japan. *Sci. Total Environ.* 662, 332–346. doi:10.1016/j.scitotenv.2019.01.221

Author contributions

X-HL: Formal Analysis, Visualization, Writing—original draft. SE: Formal Analysis, Investigation, Writing—review and editing. CC: Data curation, Investigation, Visualization, Writing—original draft. DN: Methodology, Writing—review and editing. MY: Data curation, Investigation, Writing—review and editing. GL: Supervision, Writing—review and editing.

Funding

The author(s) declare financial support was received for the research, authorship, and/or publication of this article. This research was supported by the Disaster-Safety Platform Technology Development Program of the National Research Foundation of Korea (NRF), funded by the Ministry of Science and ICT. (No. 2022M3D7A1090338).

Conflict of interest

The authors declare that the research was conducted in the absence of any commercial or financial relationships that could be construed as a potential conflict of interest.

Publisher's note

All claims expressed in this article are solely those of the authors and do not necessarily represent those of their affiliated organizations, or those of the publisher, the editors and the reviewers. Any product that may be evaluated in this article, or claim that may be made by its manufacturer, is not guaranteed or endorsed by the publisher.

- Eker, A. M., Dikmen, M., Cambazoglu, S., Düzgün, Ş. H. B., and Akgün, H. (2015). Evaluation and comparison of landslide susceptibility mapping methods: A case study for the ulus district, bartın, northern Turkey. *Int. J. Geogr. Inf. Sci.* 29 (1), 132–158. doi:10.1080/13658816.2014.953164
- Fernández, A., García, S., Galar, M., Prati, R. C., Krawczyk, B., and Herrera, F. (2018). *Learning from imbalanced data sets*. Springer Cham. doi:10.1007/978-3-319-98074-4
- Highland, L. M., and Bobrowsky, P. (2008). *The landslide handbook—a guide to understanding landslides*. Reston, Virginia: U.S. Geological Survey Circular.
- Hong, H., Shahabi, H., Shirzadi, A., Chen, W., Chapi, K., Ahmad, B. B., et al. (2019). Landslide susceptibility assessment at the wuning area, China: A comparison between multi-criteria decision making, bivariate statistical and machine learning methods. *Nat. Hazards* 96 (1), 173–212. doi:10.1007/s11069-018-3536-0
- Huabin, W., Gangjun, L., Weiya, X., and Gonghui, W. (2005). GIS-Based landslide hazard assessment: an overview. *Prog. Phys. Geogr. Earth Environ.* 29 (4), 548–567. doi:10.1191/0309133305pp462ra
- Huang, F., Cao, Z., Guo, J., Jiang, S. H., Li, S., and Guo, Z. (2020). Comparisons of heuristic, general statistical and machine learning models for landslide susceptibility prediction and mapping. *CATENA* 191, 104580. doi:10.1016/j.catena.2020.104580
- Huang, Y., and Zhao, L. (2018). Review on landslide susceptibility mapping using support vector machines. *CATENA* 165, 520–529. doi:10.1016/j.catena.2018.03.003
- Kadavi, P. R., Lee, C. W., and Lee, S. (2019). Landslide-susceptibility mapping in Gangwon-do, South Korea, using logistic regression and decision tree models. *Environ. Earth Sci.* 78 (4), 116. doi:10.1007/s12665-019-8119-1
- Kim, K., Koo, K., Yoon, H., Lee, C., Won, M., Woo, C., et al. (2011). *Forest disasters 2011*. Seoul: Korea Forest Research Institute.
- Korea Forest Service (2021). Landslide information system. Available At: <https://samsatai.forest.go.kr/gis/main.do> (Accessed February 22, 2023).
- Lee, B., An, H., Lee, C., Seo, K., Woo, C., Kwon, C., et al. (2021). *Forest disaster white paper*. Seoul: National Institute of Forest Science, 2020.
- Lee, C., Woo, C., Kim, D., Seo, J., Kwon, H., and Yun, H. (2015a). *Development of landslide disaster prevention system in urban living area*. South Korea: National Institute of Forest Science.
- Lee, M. J., Park, I., Won, J. S., and Lee, S. (2016). Landslide hazard mapping considering rainfall probability in Inje, Korea. *Geomatics, Nat. Hazards Risk* 7 (1), 424–446. doi:10.1080/19475705.2014.931307
- Lee, S. (2005). Application of logistic regression model and its validation for landslide susceptibility mapping using GIS and remote sensing data. *Int. J. Remote Sens.* 26 (7), 1477–1491. doi:10.1080/01431160412331331012
- Lee, S., and Min, K. (2001). Statistical analysis of landslide susceptibility at Yongin, Korea. *Environ. Geol.* 40 (9), 1095–1113. doi:10.1007/s002540100310
- Lee, S., Won, J. S., Jeon, S. W., Park, I., and Lee, M. J. (2015b). Spatial landslide hazard prediction using rainfall probability and a logistic regression model. *Math. Geosci.* 47 (5), 565–589. doi:10.1007/s11004-014-9560-z
- Liu, S., Wang, L., Zhang, W., He, Y., and Pijush, S. (2023). A comprehensive review of machine learning-based methods in landslide susceptibility mapping. *Geol. J.* 58 (6), 2283–2301. doi:10.1002/gj.4666
- Lombardo, L., Opitz, T., Ardizzone, F., Guzzetti, F., and Huser, R. (2020). Space-time landslide predictive modelling. *Earth-Science Rev.* 209, 103318. doi:10.1016/j.earscirev.2020.103318
- Lv, L., Chen, T., Dou, J., and Plaza, A. (2022). A hybrid ensemble-based deep-learning framework for landslide susceptibility mapping. *Int. J. Appl. Earth Observation Geoinformation* 108, 102713. doi:10.1016/j.jag.2022.102713
- Ma, Y., and He, H. (2013). *Imbalanced learning: foundations, algorithms, and applications*. Wiley-IEEE Press. doi:10.1002/9781118646106
- Maes, J., Kervyn, M., de Hontheim, A., Dewitte, O., Jacobs, L., Mertens, K., et al. (2017). Landslide risk reduction measures: A review of practices and challenges for the tropics. *Prog. Phys. Geogr. Earth Environ.* 41 (2), 191–221. doi:10.1177/0309133316689344
- Merghadi, A., Yunus, A. P., Dou, J., Whiteley, J., ThaiPham, B., Bui, D. T., et al. (2020). Machine learning methods for landslide susceptibility studies: A comparative overview of algorithm performance. *Earth-Science Rev.* 207, 103225. doi:10.1016/j.earscirev.2020.103225
- Mersha, T., and Meten, M. (2020). GIS-based landslide susceptibility mapping and assessment using bivariate statistical methods in Simada area, northwestern Ethiopia. *Geoenvironmental Disasters* 7 (1), 20. doi:10.1186/s40677-020-00155-x
- Pardeshi, S. D., Autade, S. E., and Pardeshi, S. S. (2013). Landslide hazard assessment: recent trends and techniques. *SpringerPlus* 2 (1), 523. doi:10.1186/2193-1801-2-523
- Pham, B. T., Pradhan, B., Tien Bui, D., Prakash, I., and Dholakia, M. B. (2016). A comparative study of different machine learning methods for landslide susceptibility assessment: A case study of uttarakhand area (India). *Environ. Model. Softw.* 84, 240–250. doi:10.1016/j.envsoft.2016.07.005
- Picciullo, L., Calvello, M., and Cepeda, J. M. (2018). Territorial early warning systems for rainfall-induced landslides. *Earth-Science Rev.* 179, 228–247. doi:10.1016/j.earscirev.2018.02.013
- Pourghasemi, H. R., Teimoori Yansari, Z., Panagos, P., and Pradhan, B. (2018). Analysis and evaluation of landslide susceptibility: A review on articles published during 2005–2016 (periods of 2005–2012 and 2013–2016). *Arabian J. Geosciences* 11 (9), 193. doi:10.1007/s12517-018-3531-5
- Rahman, G., Bacha, A. S., Ul Moazzam, M. F., Rahman, A. U., Mahmood, S., Almohamad, H., et al. (2022). Assessment of landslide susceptibility, exposure, vulnerability, and risk in shahpur valley, eastern hindu kush. *Front. Earth Sci.* 10, 953627. doi:10.3389/feart.2022.953627
- Reichenbach, P., Rossi, M., Malamud, B. D., Mihir, M., and Guzzetti, F. (2018). A review of statistically-based landslide susceptibility models. *Earth-Science Rev.* 180, 60–91. doi:10.1016/j.earscirev.2018.03.001
- Sahin, E. K., Colkesen, I., and Kavzoglu, T. (2020). A comparative assessment of canonical correlation forest, random forest, rotation forest and logistic regression methods for landslide susceptibility mapping. *Geocarto Int.* 35 (4), 341–363. doi:10.1080/10106049.2018.1516248
- Sameen, M. I., Pradhan, B., Bui, D. T., and Alamri, A. M. (2020). Systematic sample subdividing strategy for training landslide susceptibility models. *CATENA* 187, 104358. doi:10.1016/j.catena.2019.104358
- Shano, L., Raghuvanshi, T. K., and Meten, M. (2020). Landslide susceptibility evaluation and hazard zonation techniques – A review. *Geoenvironmental Disasters* 7 (1), 18. doi:10.1186/s40677-020-00152-0
- Stanley, T. A., Kirschbaum, D. B., Benz, G., Emberson, R. A., Amatya, P. M., Medwedeff, W., et al. (2021). Data-driven landslide nowcasting at the global scale. *Front. Earth Sci.* 9, 640043. doi:10.3389/feart.2021.640043
- Thirugnanam, H., Ramesh, M. V., and Rangan, V. P. (2020). Enhancing the reliability of landslide early warning systems by machine learning. *Landslides* 17 (9), 2231–2246. doi:10.1007/s10346-020-01453-z
- Tin Kam, H. (1998). The random subspace method for constructing decision forests. *IEEE Trans. Pattern Analysis Mach. Intell.* 20 (8), 832–844. doi:10.1109/34.709601
- Tomek, I. (1976). Two modifications of CNN. *IEEE Trans. Syst.* 6 (11), 769–772. doi:10.1109/TSMC.1976.4309452
- Tran, T. V., Alvioli, M., and Hoang, V. H. (2022). Description of a complex, rainfall-induced landslide within a multi-stage three-dimensional model. *Nat. Hazards* 110 (3), 1953–1968. doi:10.1007/s11069-021-05020-0
- Wang, H., Zhang, L., Yin, K., Luo, H., and Li, J. (2021). Landslide identification using machine learning. *Geosci. Front.* 12 (1), 351–364. doi:10.1016/j.gsf.2020.02.012
- Wang, X., Du, A., Hu, F., Liu, Z., Zhang, X., Wang, L., et al. (2023). Landslide susceptibility evaluation based on active deformation and graph convolutional network algorithm. *Front. Earth Sci.* 11, 1132722. doi:10.3389/feart.2023.1132722
- Woo, C., Kwon, H., Lee, C., and Kim, K. (2014). Landslide hazard prediction map based on logistic regression model for applying in the whole country of South Korea. *J. Korean Soc. Hazard Mitig.* 14 (6), 117–123. doi:10.9798/KOSHAM.2014.14.6.117
- Yalcin, A. (2008). GIS-Based landslide susceptibility mapping using analytical hierarchy process and bivariate statistics in ardesen (Turkey): comparisons of results and confirmations. *CATENA* 72 (1), 1–12. doi:10.1016/j.catena.2007.01.003
- Yalcin, A., Reis, S., Aydinoglu, A. C., and Yomralioglu, T. (2011). A GIS-based comparative study of frequency ratio, analytical hierarchy process, bivariate statistics and logistics regression methods for landslide susceptibility mapping in Trabzon, NE Turkey. *CATENA* 85 (3), 274–287. doi:10.1016/j.catena.2011.01.014
- Yao, X., Tham, L. G., and Dai, F. C. (2008). Landslide susceptibility mapping based on support vector machine: A case study on natural slopes of Hong Kong, China. *Geomorphology* 101 (4), 572–582. doi:10.1016/j.geomorph.2008.02.011
- Ye, C., Tang, R., Wei, R., Guo, Z., and Zhang, H. (2023). Generating accurate negative samples for landslide susceptibility mapping: A combined self-organizing-map and one-class SVM method. *Front. Earth Sci.* 10, 1054027. doi:10.3389/feart.2022.1054027
- Yoo, N. J., Lee, C. J., Choi, Y. J., and Lee, H. S. (2009). “A study on disaster and restoration of debris flow landslides at Inje, Kangwon Province, Korea,” in *17th international conference on soil mechanics and geotechnical engineering (ICSMGE)* (Alexandria, Egypt: IOS Press).
- Youssef, A. M., and Pourghasemi, H. R. (2021). Landslide susceptibility mapping using machine learning algorithms and comparison of their performance at Abha Basin, Asir Region, Saudi Arabia. *Geosci. Front.* 12 (2), 639–655. doi:10.1016/j.gsf.2020.05.010
- Zezere, J. L., Pereira, S., Melo, R., Oliveira, S. C., and Garcia, R. A. C. (2017). Mapping landslide susceptibility using data-driven methods. *Sci. Total Environ.* 589, 250–267. doi:10.1016/j.scitotenv.2017.02.188
- Zhang, J., and Mani, I. (2003). “KNN approach to unbalanced data distributions: A case study involving information extraction,” in *ICML’2003 workshop on learning from imbalanced data sets II* (Washington, DC: ICML).
- Zhou, X., Wu, W., Qin, Y., and Fu, X. (2021). Geoinformation-based landslide susceptibility mapping in subtropical area. *Sci. Rep.* 11 (1), 24325. doi:10.1038/s41598-021-03743-5



OPEN ACCESS

EDITED BY

Suresh Kumar,
Indian Institute of Remote Sensing, India

REVIEWED BY

Subodh Chandra Pal,
University of Burdwan, India
Uday Chatterjee,
Bhatter College, Dantan, India

*CORRESPONDENCE

Sk. Mustak,
✉ mustak.sk5@gmail.com

RECEIVED 28 February 2023

ACCEPTED 01 September 2023

PUBLISHED 28 September 2023

CITATION

Mohanty S, Mustak S, Singh D,
Van Hoang T, Mondal M and Wang C-T
(2023), Vulnerability and risk assessment
mapping of Bhitarkanika national park,
Odisha, India using machine-based
embedded decision support system.
Front. Environ. Sci. 11:1176547.
doi: 10.3389/fenvs.2023.1176547

COPYRIGHT

© 2023 Mohanty, Mustak, Singh, Van
Hoang, Mondal and Wang. This is an
open-access article distributed under the
terms of the [Creative Commons
Attribution License \(CC BY\)](https://creativecommons.org/licenses/by/4.0/). The use,
distribution or reproduction in other
forums is permitted, provided the original
author(s) and the copyright owner(s) are
credited and that the original publication
in this journal is cited, in accordance with
accepted academic practice. No use,
distribution or reproduction is permitted
which does not comply with these terms.

Vulnerability and risk assessment mapping of Bhitarkanika national park, Odisha, India using machine-based embedded decision support system

Shantakar Mohanty¹, Sk. Mustak^{1*}, Dharmaveer Singh²,
Thanh Van Hoang³, Manishree Mondal⁴ and Chun-Tse Wang⁵

¹Department of Geography, Central University of Punjab, Bathinda, Punjab, India, ²Symbiosis Institute of Geo-informatics, Symbiosis International University, Pune, Maharashtra, ³College of Construction and Development, Feng Chia University, Taichung, Taiwan, ⁴Department of Geography, Midnapore College (Autonomous), Midnapore, West Bengal, ⁵Ph.D program of Infrastructure Planning and Engineering, College of Construction and Development, Feng Chia University, Taichung, Taiwan

The vulnerability and flood risk assessment of Bhitarkanika National Park in Odisha, India, was conducted using a data-driven approach and a machine-based embedded decision support system. The park, located in the estuaries of the Brahmani, Baitarani, Dharma, and Mahanadi river systems, is home to India's second-largest mangrove environment and the world's most active and diverse saline wetland. To evaluate its vulnerability and risk, various threats were considered, with a focus on floods. Satellite imageries, such as Landsat 8 OLI, SRTM digital elevation model, open street map, Google pro image, reference map, field survey, and other ancillary data, were utilized to develop vulnerability and risk indicators. These indicators were then reclassified into 'Cost' and 'Benefit' categories for better understanding. The factors were standardized using the max-min standardization method before being fed into the vulnerability and risk model. Initially, an analytical hierarchy approach was used to develop the model, which was later compared with machine learning algorithms (e.g., SVM) and uncertainty analysis indices (e.g., overall accuracy, kappa, map quality, etc.). The results showed that the SVM-RBF machine learning algorithm outperformed the traditional geostatistical model (AHP), with an overall accuracy of 99.54% for flood risk mapping compared to AHP's 91.12%. The final output reveals that a large area of Bhitarkanika National park falls under high flood risk zone. The Eastern coastal regions of Govindapur, Kanhupur, Chinchri, Gobardhanpur and Barunei fall under high risk zone of tidal floods, The Northern and western regions of Ramachandrapur, Jaganathpur, Kamalpur, Subarnapur, Paramanandapur, etc., Fall under high risk region of riverine floods. The study also revealed that the areas covered with mangroves have a higher elevation and hence are repellent to any kind of flood. In the event of a flood high priority conservation measures should be taken along all high flood risk areas. This study is helpful for decision-making and carrying out programs for the conservation of natural resources and flood management in the national park and reserve forest for ecological sustainability to support sustainable development goals (e.g., SDGs-14, 15).

KEYWORDS

vulnerability, flood risk, national park, mangrove, decision-support system, machine learning

1 Introduction

In countries with subtropical climates like India, flash floods are a common occurrence, especially during the monsoon season. This particular sort of flood happens quickly, setting it apart from other natural disasters that result in significant economic loss and human casualties (Ruidas et al., 2022). National Parks play a vital role in conserving the world's biodiversity, food security, and human health (Fernández and Lutz, 2010; Li et al., 2012; Heidari, 2014; Wang et al., 2019). The values of National Parks range from protecting natural habitats and associated flora and fauna to maintaining the environmental stability of its surrounding regions (Taylor et al., 2011; Dawod et al., 2012; Schumann et al., 2018; Yadollahie, 2019; Ullah and Zhang, 2020). The vulnerability assessment has been one of the most discussed topics in recent eras for the physical, biological, and social systems (Ouma and Tateishi, 2014; Pourali et al., 2016; Bandi et al., 2019; Langlentombi and Kumar, 2021). The vulnerability of a system can be defined as the susceptibility to disturbances determined by exposure to perturbations, sensitivity to concerns, and the capacity to adapt (Nelson et al., 2010). Bhitarkanika National Park is a Ramsar site with India's second-largest mangrove forest. It is known for its mangroves, migratory birds, turtles, estuarine crocodiles, and innumerable creeks and is one of Odisha's best biodiversity hotspots. This unique habitat consists of 62 mangrove species, 28 species of mammals, 280 species of birds, and 47 species of amphibians and reptiles. It also includes the largest population of saltwater crocodiles in India (Khan et al., 2020).

Excess water allocation for industries has become a significant cause of concern for Bhitarkanika national park. This extra allocation reduces freshwater discharge to the sea (Hallegatte et al., 2013). The lack of normal freshwater flow in the area has led to increased saline ingression upstream, negatively impacting the local flora, fauna, and the livelihoods of fishermen and farmers who depend on the Brahmani river. Additionally, the region faces recurring challenges such as floods, forest fires, and overfishing. Overfishing, in particular, creates a food shortage for estuarine crocodiles and other species in the area. The reduction in water discharge also has a direct impact on the mangroves, which in turn affects the Gahirmatha marine sanctuary within the national park. The increased water salinity may prompt saltwater crocodiles to migrate from the core sanctuary area to upstream regions, leading to conflicts between humans and animals and causing disruptions for local residents.

According to the Census data, in 1991, there were 311 villages with a population of 118,951 inhabitants in the area. However, by 2011, the number of villages had increased to 312, with a population of 145,320. The total area covered by these villages was 672 square kilometers, resulting in a population density of 216 people per square kilometre. This level of population density is relatively high for a National Park. The flood hazards not only impact the ecosystem and natural landscape of the area but also have adverse effects on human

settlements and their occupations (Dewan et al., 2007; Hallegatte et al., 2013; Stefanidis and Stathis, 2013; Rahmati et al., 2016; Farhadi and Najafzadeh, 2021; Parsian et al., 2021; SAMI et al., 2021). The delicate ecosystem is under extreme pressure because of the population increase.

Bhitarkanika National Park is situated between the Brahmani and Baitarani rivers, which experience annual flooding due to heavy rainfall in the area and the discharge of floodwater from the Rengali Dam. Being located on the east coast of Odisha, the park is highly susceptible to cyclones, which result in storm surges and subsequent flooding of the shorelines. During Cyclone Yaas in 2021, coastal fishing villages in BNP were severely affected by tidal floods caused by storm surges, resulting in significant damage to houses. The majority of the population in the area relies on fishing, agriculture, and apiculture for their livelihoods. Fishing communities have settled near riverbanks and congregated in fishing villages along the coast, putting themselves at immediate risk during flooding events.

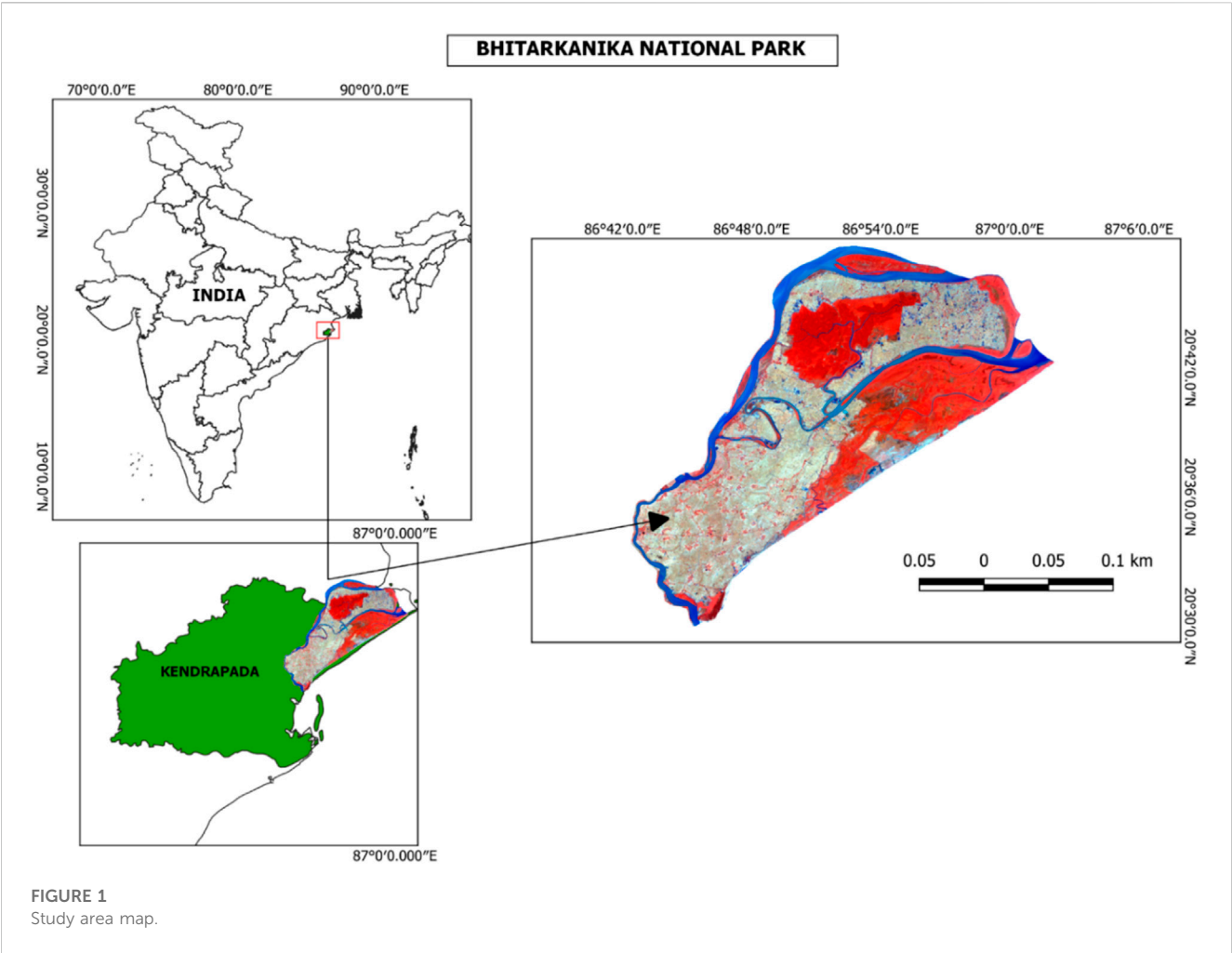
It is not only the human population that is affected by these calamities; the wildlife in the area is also impacted. The estuaries in the main mangrove area of BNP are home to approximately 1,700 estuarine crocodiles. During floods, their feeding grounds become submerged, leading them to migrate outside the estuaries and into river channels that pass through nearby villages. This migration poses a significant risk to both the crocodiles and the villagers.

Given the exponential increase in the number of flash flood events, identifying flood-prone areas has become a top priority. Mapping flash flood susceptibility can help mitigate the worst impacts of such risk phenomena. Therefore, there is an urgent need to develop accurate models for predicting flood susceptibility, which can aid in the creation of more effective flood management measures (Ruidas et al., 2022).

The main objective of this study is to compare traditional decision support models like AHP with machine learning algorithms for flood vulnerability and risk assessment in the Bhitarkanika National park. This study studied data-driven approaches (e.g., Sentinel 2A Multispectral, SRTM digital elevation model, open street map, Google Pro image, reference map, field survey, and other ancillary data and machine-based data approaches). The study is divided into seven sections, e.g., introduction, study area, datasets and software, methods, results and discussion, conclusion and recommendation, and references.

2 Selection of the study area

The Bhitarkanika National Park is situated between 86°46'to 87°01'East longitude and 20° 30'to 20° 48'North latitude in Brahmani and Baitarani deltaic region of the district of Kendrapara, Odisha, in the east coast of India (Figure 1). This area has been declared a proposed sanctuary since 1975 because of its ecological, faunal, floral, geomorphologic and biological association and importance. On its eastern side lies the Bay



of Bengal; to its north is the river Dhamara; to its west is the land mass of Kendrapada District and to its south lies the Mahanadi river.

The rich alluvial deposits and gently sloping topography of Bhitarkanika support rich flora and fauna and are well known for their ecological and biological diversity. Mangroves cover a core area of 145 sq. km. This core area was declared a National Park in 1998 (Kumar et al., 2015). In 2002, Bhitarkanika was designated as a “Ramsar site,” recognizing its status as a Wetland of International Importance due to its abundant biodiversity and ecological significance. The park can be accessed *via* two entry points: Rajnagar and Chandbali. Rajnagar is approximately 130 km away from the state capital, Bhubaneswar, while Chandbali is about 150 km away.

Bhubaneswar is well-connected by rail and air to other cities in India, making it convenient for visitors to reach Bhitarkanika National Park.

3 Methodology

3.1 Datasets and software

In this study, Landsat TM5 and Landsat8 OLI satellite data were obtained from Google Earth Engine using JavaScript codes. The Shuttle Radar Topography Mission (SRTM) Void filled Digital Elevation Model was obtained from the USGS Earth Explorer portal (Table 1). Digital Elevation Model (DEM) is the

TABLE 1 Datasets used.

S. No.	Satellite/Digital elevation model	Resolution (meter)	Spectral bands	Date of acquisition
1	Landsat 8 OLI	30	9	2021-05-18
2	Landsat TM	30	7	2000-01-10
3	SRTM DEM	30	1	2000-02-11

This study used QGIS, 3.16, ArcGIS, 10.8, google earth engine, Google Earth Pro, Open Street map, android-based GPS, microsoft office, etc.

digital representation of the land surface elevation and hydrogeomorphic parameters with respect to any reference datum widely used in flood disaster and risk modeling (Li et al., 2012; Stefanidis and Stathis, 2013; Balasubramanian, 2017; Ullah and Zhang, 2020). The SRTM DEM of the year 2000 was used for generating various flood vulnerability and risk indicators like elevation, slope, and water depth, *etc.*, and further processing these to form the vulnerability and risk map (Ouma and Tateishi, 2014; Pourali et al., 2016; Rahmati et al., 2016; Schumann et al., 2018; Bandi et al., 2019; Zhang et al., 2019). In addition, google earth image, open street map, and field survey (2022) were used to assess the models accurately.

3.2 Methods

The following methods were employed to achieve the main objective of this study (Figure 2). The main objective of this study is to compare traditional decision support models like AHP with the machine learning algorithm for flood vulnerability and risk assessment in the Bhitarkanika National Park (BNP). The methods are explained below as follows.

3.2.1 Background of machine learning algorithms

Machine Learning Algorithms like SVM, RF, Decision Tree, *etc.*, have turned out to be efficient methods for research in today's date due to their impeccable accuracy and reliability. Support Vector Machine (SVM) is a type of supervised machine learning that can effectively identify intricate patterns in noisy and complex datasets, and due to their simplicity and adaptability, they can achieve balanced predictive accuracy even in situations where there are limited samples (Hongmao, 2016). Random Forests (RF) improve prediction accuracy and efficiency by randomly selecting features for each decision split, reducing correlation between trees, and increasing the diversity of the model (Breiman, 2001). Decision Tree (DT) is an inductive algorithm used for classification and prediction, where classification rules are represented as decision trees derived from a set of disorderly and irregular instances, and the tree is constructed in a top-down recursive manner by comparing attributes between internal nodes and making decisions based on different attributes, ultimately leading to a conclusion at the leaf nodes (Dai et al., 2016). The significant advancements in machine learning and artificial intelligence, including logistic regression,

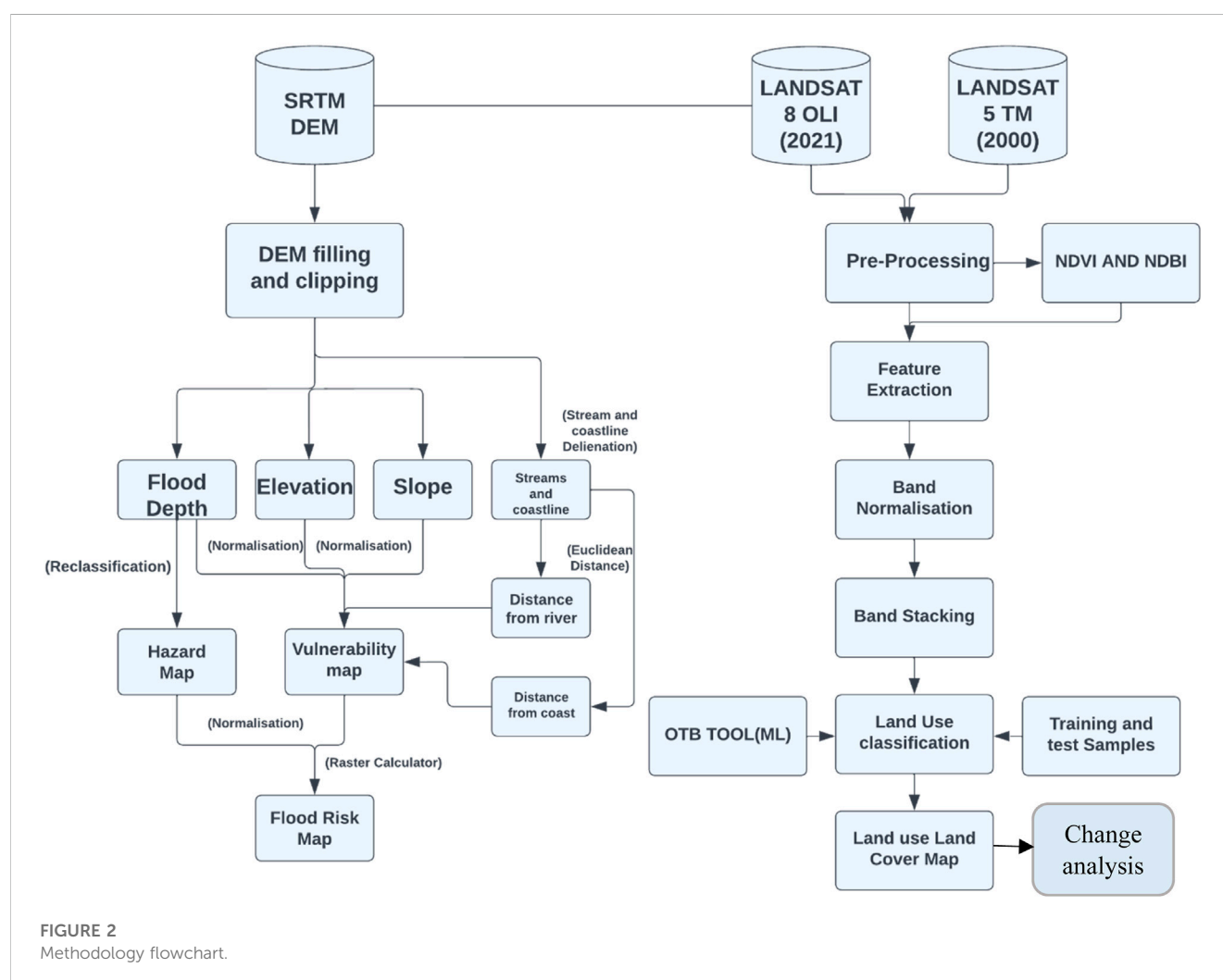


FIGURE 2
Methodology flowchart.

decision trees, artificial neural networks, random forests, and support vector machines, have gained immense importance due to their ability to handle large datasets and deliver high levels of accuracy (Ruidas et al., 2021).

Several researchers have used ML algorithms to create remarkable research projects in variety of sectors such as (Ruidas et al., 2022) in Hydrogeochemical Evaluation of Groundwater Aquifers (Ruidas et al., 2022), in water resources vulnerability assessment (Ruidas et al., 2022), in flood-susceptibility assessment (Ruidas et al., 2021), in Characterization of groundwater potential zones (Jaydhar et al., 2022), in Hydrogeochemical evaluation and health risk from arsenic and fluoride, *etc.*

The use of ML algorithms in disaster prediction, Vulnerability and risk assessment, mitigation has become a sought-after procedure in the current scenario and this research has used the same to generate comprehensive risk and vulnerability zones of the fragile Bhitarkanika National Park region. Pham et al. (2019) in their research used hybrid machine learning models, including bagging (BA), random subspace (RS), and rotation forest (RF), with alternating decision tree (ADTree) as base classifier for the spatial prediction of Landslides (Parvin et al., 2022). in their study used 3 ML models, namely, Bayesian logistic regression (BLR), the artificial neural networks (ANN), and the deep learning neural networks (DLNNs) for flood vulnerability assessment in a densely urbanized city. Opella and Hernandez (2019) in their study generated flood susceptibility and probability map using SVM and obtained a robust flood map that clearly outperforms the traditional methods. Xiong et al. (2019) in their study adopted SVM model for flash flood vulnerability assessment and mapping in China. This study uses the SVM-RBF model to generate a robust vulnerability and risk Map of the Bhitarkanika National Park region taking in view previous studies, which have used the same model for its impeccable accuracy. The map generated using SVM-RBF exhibits an accuracy of 99.54% with a complementing Kappa Index of 99.18% compared to the 91.12% accuracy using traditional AHP, thus solidifying the SVM-RBF model as a formidable classification ML classification.

3.2.2 Pre-processing

Pre-processing of data, such as satellite imagery and digital elevation models (DEM), is crucial for the processing, analysis, and modeling in this study. In order to map the land use and land cover (LULC) of Bhitarkanika National Park, satellite imagery underwent pre-processing steps including band stacking, clipping, mosaicking, and normalization using the min-max scaler. These pre-processing tasks were performed using QGIS. Similarly, the SRTM DEM was pre-processed using both ArcGIS and QGIS. The DEM was initially clipped to the study area by applying a mask. Auto co-registration and filling techniques were then employed using the hydrology toolbox in ArcGIS and QGIS to ensure alignment with the LULC data and to address sinkholes, which are often not captured by satellites. The DEM was further reclassified to generate an elevation map, and the slope was calculated using the Arc Toolbox.

These pre-processing steps were undertaken to ensure the data was appropriately prepared for subsequent analysis and modeling in the study.

3.2.3 Land use/land cover classification

Land use and land cover change have become central to current strategies for managing natural resources and monitoring environmental changes (Kaul and Sopan, 2012). The standard land use and land cover (LULC) classes (Table 2) were selected based on the literature review and local LULC classification scheme. Based on the previous literature it was observed that uniform LULC classification scheme is missing in disaster study (Hao et al., 2022). Landsat 8 Operational Land Imager (OLI) and Landsat 5 Thematic Mapper (TM) images of 2021 and 2000, respectively, with cloud cover of less than 2%, were obtained from the google earth engine using JavaScript codes. Further processing was done in QGIS, including feature extraction (e.g., NDVI, NDBI, *etc.*), classification, post-processing, accuracy assessment, and change analysis.

The Normalized difference Vegetation Index (NDVI) is widely used in classifying land use/cover which was calculated using following formula (Ruidas et al., 2021):

$$NDVI = \frac{NIR - RED}{NIR + RED} \quad (1)$$

The value of the NDVI varies in between +1 and −1. NDVI is equal to +1 shows healthy vegetation while −1 shows waterbodies. In addition, Normalized Difference Built-up Index provide vivid information of the built-up which was calculated using following formula (He et al., 2010).

$$NDBI = \frac{Band5 - Band4}{Band5 + Band4} \quad (2)$$

Higher the value of NDVI shows more the built-up information which lower values shows vegetation and other land use classes.

Table 2 shows the training and test samples used for the training and validation of the classification model.

There are various types of classifiers in machine learning (ML). This study uses the SVM classifier with Radial Basis Function (SVM-RBF) via the OTB toolbox to generate LULC maps and the flood risk map (Deroliya et al., 2022). This is because machine learning algorithms outperform any complex decision-making compared to other traditional algorithms (Farhadi and

TABLE 2 Training and test samples.

LULC_ID	LULC_CLASS	Training samples	Test samples
1	Built-up	50	50
2	Mangroves	50	50
3	Agriculture	50	50
4	Water Bodies	50	50
5	Barren Land	50	50

Najafzadeh, 2021; Deroliya et al., 2022). This study selected SVM-RBF because this algorithm is robust for complex problems compared to the other machine learning algorithms such as Random Forest, Decision Tree, etc (Ruidas et al., 2021; Ruidas et al., 2022). Two LULC maps (e.g., 2021 and 2000) were generated using the image classifier function in the OTB tool. The accuracy assessment of all the maps generated using ML was done by computing their confusion matrix using the OTB tool. Change detection analysis, one of the import approaches, is incorporated with the flood risk analysis (Gharagozlou et al., 2011; Lawal et al., 2014) carried out between the 2000 and 2021 LULC maps using the post-processing algorithm and Raster Unique Values Report function in QGIS.

3.2.4 Flood depth calculation

When floods hit inhabited areas, significant losses are usually registered in terms of both impacts on people (i.e., fatalities and injuries) and economic impacts on urban areas, commercial and productive sites, infrastructures, and agriculture. To properly assess these, several parameters are needed, among which flood depth is one of the most important as it governs the models used to compute damages in economic terms (Cian et al., 2018). In this study, the Raster calculator was used in ArcGIS to analyze flood/water depth manually. The inundation depth is estimated to be 2.5 m through multiple literature reviews and field surveys. Based on the last 20 years' flood inundation information, the binary mask was created as one and none flooded area as zero.

$$\text{Output Raster} = \text{DEM} \times \text{Binary Mask} \quad (3)$$

The result gave the elevation values of DEM for areas, which are flooded, and zeros for non-flooded areas. Consequently, the highest elevation value represents the water table.

$$\text{Water Depth} = \text{Value_water_table} \times \text{Binary Mask} \quad (4)$$

$$\text{Where, value_water_table} = 2.5\text{m}$$

The resultant raster thus obtained represents the Water/Flood depth of the study area.

3.2.5 Euclidean distance from the coast and river

The shortest straight-line distance connects all sites or the Euclidean distance (Zhang, 2019). Geoprocessing analysis is performed to fill sinks (pits) and to generate data on flow direction, flow accumulation, catchments, streams, stream segments, and watersheds. These data are then used to develop a vector representation of catchments and drainage lines from selected points that can then be used in network analysis (Soni, 2012). To calculate the Euclidean distance from the river, the process begins with stream delineation using the hydrology toolbox in ArcGIS. This involves using the fill tool followed by the flow direction tool, which determines the downslope direction of each cell and helps identify the flow paths of the streams. The flow accumulation tool is then applied to estimate cumulative flow, representing the total weight of cells flowing into each downslope cell. By setting a threshold value, the number of streams included in the final layer can be controlled. Lower threshold values result in more streams, while higher values reduce the number of streams.

TABLE 3 Indicators.

Cost indicator	Benefit indicators
Water Depth	Elevation, Slope, Distance from Coast, Distance from River

Once the streams are delineated, the Euclidean distance tool is used to calculate the distance from the stream. Similarly, the coastline of BNP is manually digitized, and the Euclidean distance tool is applied to determine the distance from the coast. These steps enable the calculation of the Euclidean distance from both the river and the coastline, providing valuable information for further analysis and modeling in the study.

3.2.6 Flood hazard mapping

The goal of flood hazard assessment is to understand the probability that a flood of a particular intensity will occur over an extended period of time. Hazard assessment aims to estimate this probability over periods of years to decades to support risk management activities (Wright, 2015). Intensity is typically defined as the sum of flood depth and horizontal flood extent. However, depending on the circumstance, other intensity parameters like flow velocity and flood duration may also be significant (Stefanidis and Stathis, 2013; Farhadi and Najafzadeh, 2021; Deroliya et al., 2022). Hydrological models like water depth and other factors like frequency and area of Impact were used to estimate the flood hazard.

$$\text{Where,} \quad HS = FS \times AIS \times IS \quad (5)$$

HS = Hazard Score

FS = Frequency Score

AIS = Area of Impact Score

IS = Intensity Score

3.2.7 Vulnerability mapping

Aside from flood danger, another critical factor in flood risk is flood vulnerability. Understanding a system's vulnerability will help you predict how floods may damage it. Examples of potential systems include physical structures like homes or bridges that might sustain damage or destruction, a company or service whose supply chain might be disrupted, or a community that might experience fatalities, property losses, and detrimental health effects following a flood (Wright, 2015).

TABLE 4 Normalised weight.

Indicators	Normalized weight
Elevation (F1)	0.30
Distance from River (F2)	0.30
Distance from coast(F3)	0.15
Water Depth(F4)	0.15
Slope (F5)	0.10
Total	1.00

Various indicators are used to estimate the vulnerability of BNP. The indicators used are elevation, slope, water depth, distance from the coast, and distance from the river (Stefanidis and Stathis, 2013; Farhadi and Najafzadeh, 2021). The indicators have been reclassified into 'Cost' and 'Benefit' to better understand the assessment (Table 3).

Further, all the cost and benefits indicators are normalised, and the AHP model was applied to achieve flood vulnerability of BNP using formula 6-7 in the raster calculator tool in ArcGIS.

1. Normalisation

The practice of making specific data that are separated by time periods identical, such as atmospheric correction or pixel resampling, so that an acceptable change may be observed without being impacted by other factors is referred to as normalisation.

Cost indicator:

$$Normalisation = 1 - \frac{Indicator - indicator_min}{indicator_max - indicator_min} \quad (6)$$

Benefit Indicator:

$$Normalisation = \frac{Indicator - indicator_min}{indicator_max - indicator_min} \quad (7)$$

2. Analytic Hierarchy Process- Weight Overlay Analysis

Analytic Hierarchy Process (AHP) is a robust multi-criteria decision-making (MCDM) was used to achieve the weight of the factors for the overall decision-making (Ouma and Tateishi, 2014; Rahmati et al., 2016; Kumar et al., 2021; Parsian et al., 2021). This model is widely used in raster-based GIS overlay analysis in several applications such as land suitability analysis, flood risk and vulnerability analysis, zoning, and site suitability analysis (Mustak et al., 2018). In AHP, the following sub-processes were employed to derive the weight of the indicators (Stefanidis and

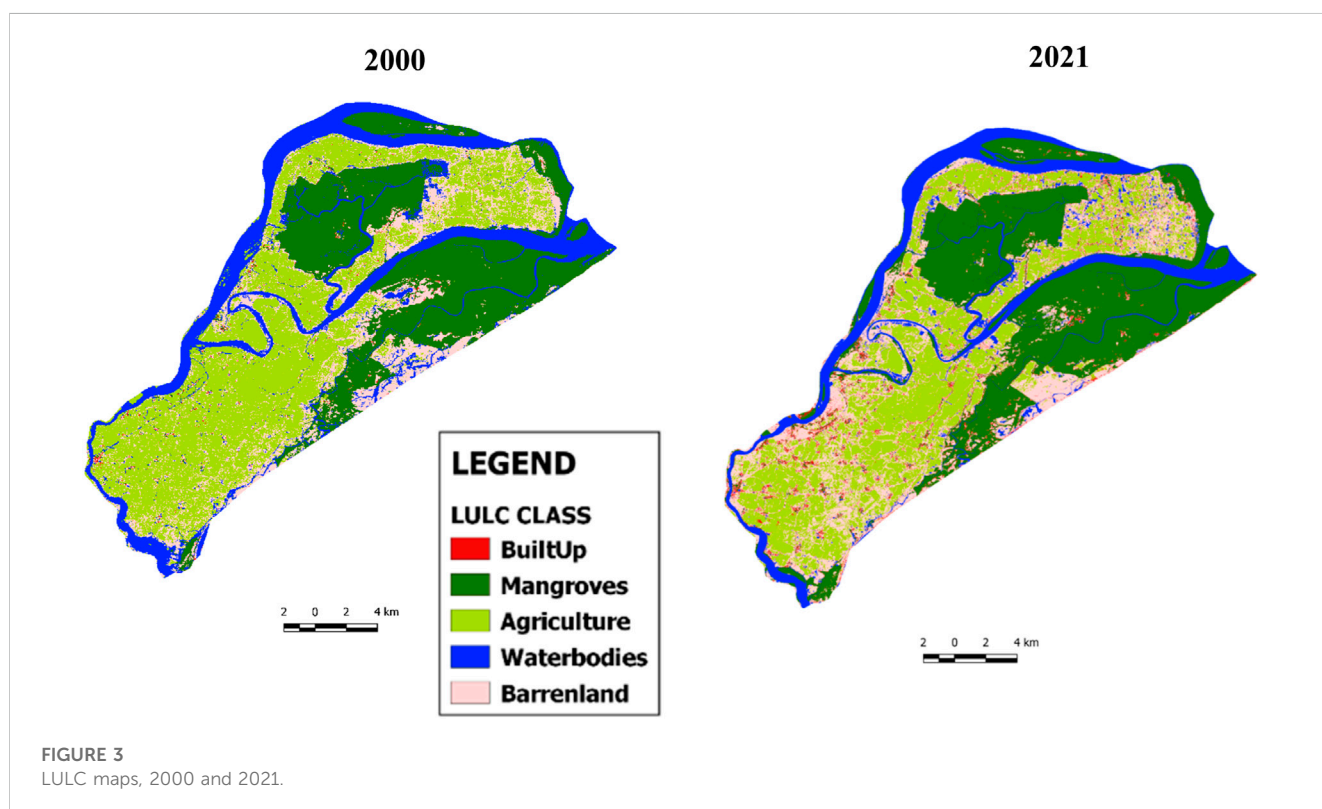


TABLE 5 LULC statistics.

LULC ID	LULC class	Area in sq. Km (2000)	Percentage of area (2000) (%)	Area in sq. Km (2021)	Percentage of area (2021) (%)	Change in (%)
1	Built-Up	1.94	0.3	13.84	2.8	2.5
2	Mangroves	139.49	28.40	165.74	33.75	5.3
3	Agriculture	183.60	37.39	136.00	27.69	9.7
4	Waterbodies	88.31	17.9	67.50	13.74	4.2
5	Barren land	77.89	15.86	108.22	22.04	6.1

Stathis, 2013), e.g., 1) selection of indicators and arrange in the square-matrix, 2) indicators were compared, and relative importance given based on the Saaty's nine-point scale of absolute number, 3) normalized weight of the individual indicator was derived using the geometric mean method (Table 4). The weighted overlay analysis is one of the most used methods to address multi-criteria issues like site selection, land suitability analysis, and assessing model appropriateness (Kumar et al., 2021).

The sum of the normalized weight is 1. After the calculation of weights, raster calculator was used to derive the final vulnerability index VI, which varies from 0 to 1 using the following Formula 6. The VI, equal to 0, shows low vulnerability, while 1 shows high vulnerability.

$$Vulnerability = ((F1 \times 0.3) + (F2 \times 0.3) + (F3 \times 0.15) + (F4 \times 0.15) + (F5 \times 0.1)) \quad (8)$$

The final output raster is symbolised using the quartile method, and the resultant raster is the vulnerability map.

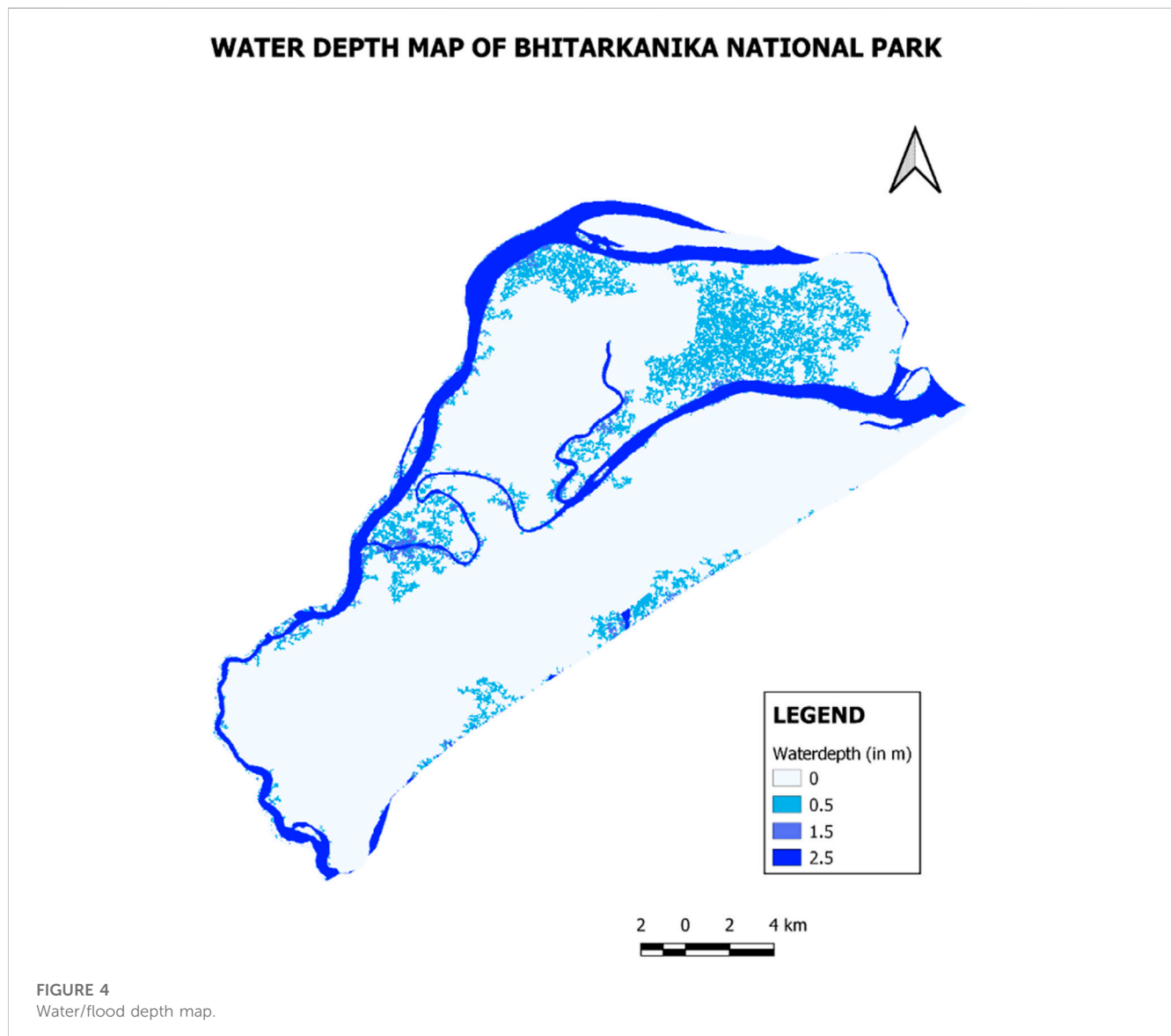
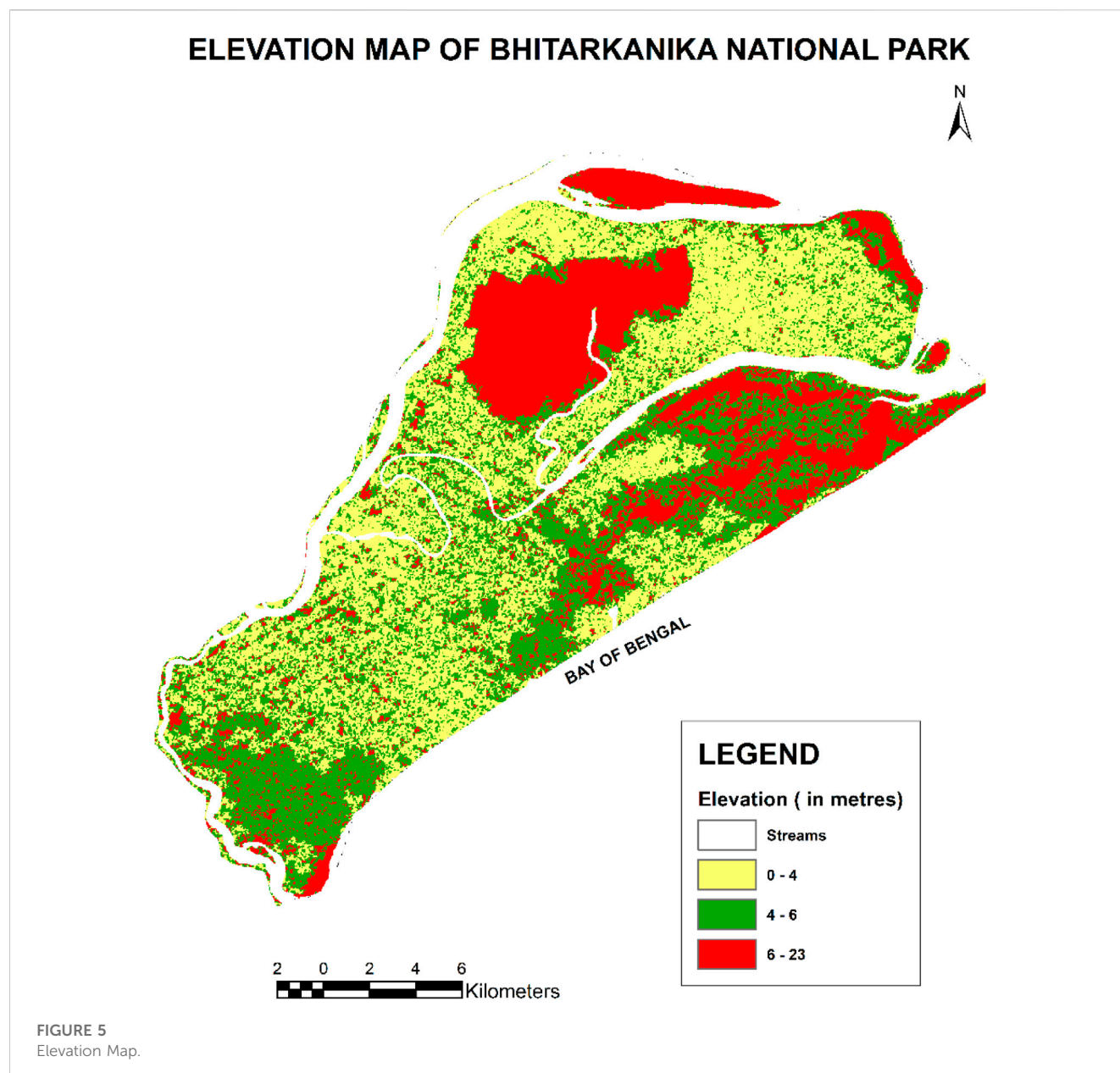


TABLE 6 Water depth statistics.

ID	Class (m)	Flood hazard	Area in sq. km	Percentage (%)
1	0	No Hazard	383.92	78.00
2	0.5	Low	47.00	9.5
3	1.5	Medium	5.18	1.05
4	2.5	High	55.14	11.23

**TABLE 7** Elevation statistics.

Elevation in meter	Flood hazard	Area sq. km	Percentage (%)
0-4	High	233.37	47.5
4-6	Medium	148.58	30.14
6-23	Low	109.27	22.36

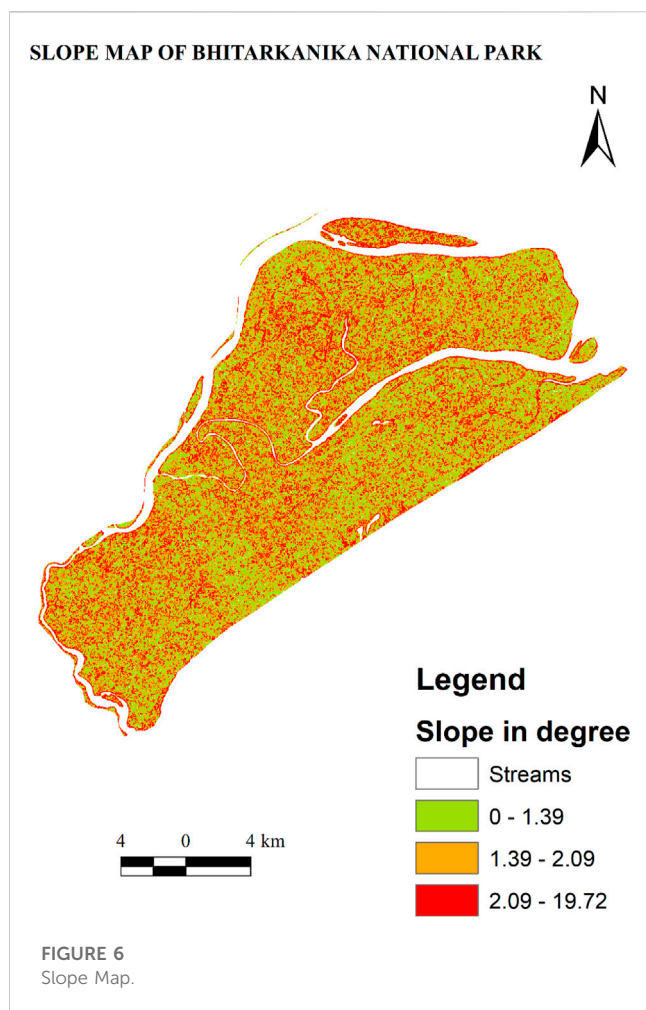
3.2.8 Flood risk mapping

The most common approach to define flood risk is that it is the product of hazard, i.e., the physical and statistical aspects of the actual flooding (e.g., the return period of the flood, extent, and depth of inundation, and flow velocity), and the vulnerability, i.e., the exposure of people and assets to floods and the susceptibility of the elements at risk to suffer from flood damage (Serda et al., 2002). After

calculating the Flood Hazard and flood vulnerability, it becomes relatively simpler to calculate the Flood Risk.

$$\text{Flood Risk} = \text{Flood Hazard} \times \text{Flood Vulnerability} \quad (9)$$

The hazard and vulnerability maps produced before are normalised first and then multiplied using the raster calculator tool. The resultant raster gives us the flood risk



map of BNP, which is further classified into High, Medium, and low based on the corresponding intensity value.

4 Results and discussions

4.1 Land use land cover

The below figures show the Land Use Land Cover of BNP in 2000 and 2021, respectively. A stark difference can be seen in the LULC maps of 2000 and 2021. The difference is explained in detail in Figure 3 and Table 5.

Over the years, significant changes have been observed in the areal extent of various classes. The built-up area has experienced exponential growth, expanding from 1.94 Sq. km in 2000 to nearly 14 Sq. km in 2021. This alarming trend highlights the

encroachment of human settlements and related activities into this biosphere reserve. The increase in built-up areas not only signifies a rise in population but also amplifies the vulnerability to floods by intensifying the hazard factor. However, it is worth noting that the area covered by mangroves has seen a positive development, expanding by 26.25 Sq. km. This growth can be attributed to the conservation efforts of the Government of Odisha, as well as the active involvement of local forest dwellers and naturalists.

The area under agriculture has significantly decreased due to salinity ingress, leading to an increase in barren land. This decline in agricultural activities is a result of the rapid growth of aquaculture activities in BNP and salinity ingress. The number of aquaculture ponds in BNP has been increasing at an alarming rate. The maps above illustrate the significant expansion of aquaculture ponds in just 20 years, primarily concentrated in the north-eastern areas of the national park. Interestingly, as the number of artificial aquaculture ponds has risen, the area covered by water bodies has decreased by approximately 20 sq. km. This reduction is attributed to the drying up of estuaries on the eastern coast near the Gahirmatha Marine Sanctuary, which can be attributed to anthropogenic activities and climate change.

4.2 Cost indicators

4.2.1 Flood/water depth

As observed from the resultant map, a substantial area of BNP has a water depth of 0 m constituting to 383.92 sq. km and 78% of the total area (Figure 4). This area represents minimal flood hazard. An area of 47 sq. km or 9.5% of the total area has a water depth of 1 m representing low flood hazard. A water depth of 1.5 m is observed across 5.18 sq. km or 1.05% of the area representing a medium flood hazard. The Brahmani and Dharma river systems, as well as the areas of Ramchandrapur, Jagannathpur, Padmanavpur, Narayanpur, Saradaprasad, Paramanandpur, and Mohanpur, exhibit a water depth of more than 2.5 m covering an area of 55.14 sq. km or 11.23% of the total area (Table 6). These areas are most prone to flooding and have a high flood hazard.

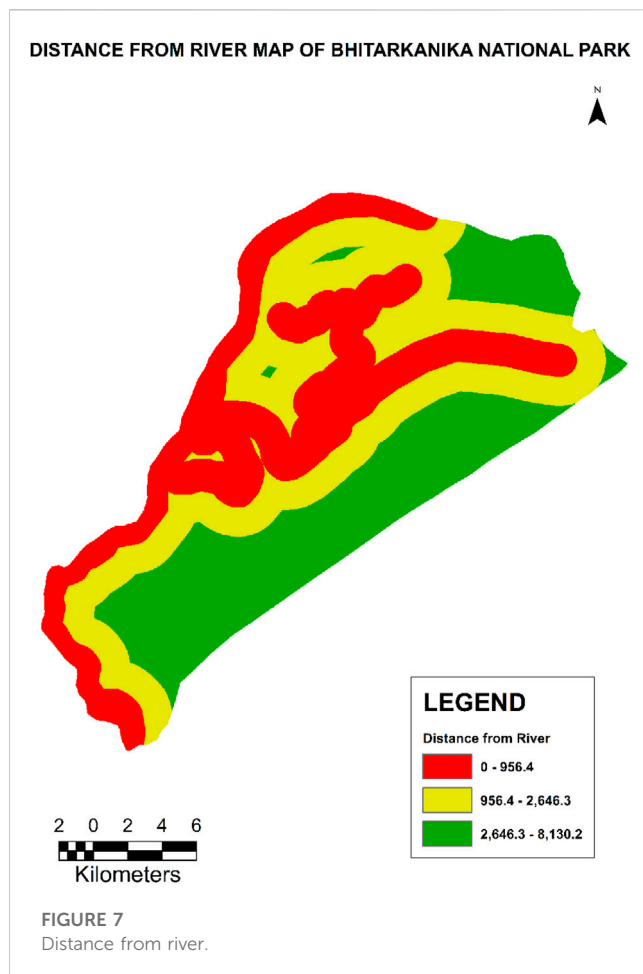
4.3 Benefit indicators

4.3.1 Elevation

BNP has a maximum elevation of 23 m. The lower the elevation higher is the risk of getting affected by flood and

TABLE 8 Slope statistics.

Slope class (degree)	Flood hazard	Area sq. km	Percentage (%)
0-1.39	High	131.15	26.71
1.39-2.09	Medium	188.14	38.31
2.09-19.72	Low	171.71	34.97



vice versa. As observed in the elevation map, all the areas under mangrove vegetation have a medium to high elevation, which makes these areas resilient to flooding (Figure 5; Table 7). The areas surrounding the mangroves and the riverbanks subsequently have lower elevations. The areas near the coast also have a lower elevation, excluding those covered by mangroves.

4.3.2 Slope

The slope is the most crucial aspect of hydrology since it directly affects surface runoff and floods. Since low-elevation locations often have a gentle or low-level slope (0–1.39 m), they are more susceptible to flooding and waterlogging because steep slopes generate more incredible velocity than flat or gentle slopes and may dispose of runoff more quickly. Runoff from a level or gently sloping land is collected and released gradually. In contrast to high-gradient slopes, low-gradient slopes

at lower reaches are more susceptible to flooding (Ramesh and Iqbal, 2022).

The BNP area has varied slope values and is unevenly distributed (Figure 6; Table 8). A large area of the national park appears to have low-medium slope values (1.39–2.09°). High slope values (2.09–19.72 m) appear to be scarce and scattered.

4.3.3 Distance from the river

The result was obtained using the Euclidean distance tool in ArcGIS. The BNP area is bordered by three rivers: Brahmani, Baitarani, and Dharma. The Dharma River is formed at the confluence of the Brahmani and Baitarani Rivers. The Brahmani River covers a significant portion of the riverine area within BNP. It both surrounds and cuts through the national park, eventually flowing into the Bay of Bengal. As a result, many areas in BNP are located near the riverbanks and are susceptible to flooding. The geography of BNP is characterized by its surrounded by rivers and the ocean on all sides.

The map produced is classified into three classes: High Proximity (<956.4 m), Medium Proximity (956.40–2646.30 m), and Low Proximity (>2646.30 m) (Figure 7; Table 9). The map displays the surrounding areas of Praharajpur, Gobardhanpur, Raj Nagar, Ramchandrapur, Govindpur, Subarnapur, as well as the central villages of Balabhadrapur, Purushottampur, Gupti, Padmanavpur, Jaganaathpur, and others. These areas are situated along the riverbanks of the Brahmani and Dharma rivers, making them highly proximate to these water bodies.

4.3.4 Distance from the coast

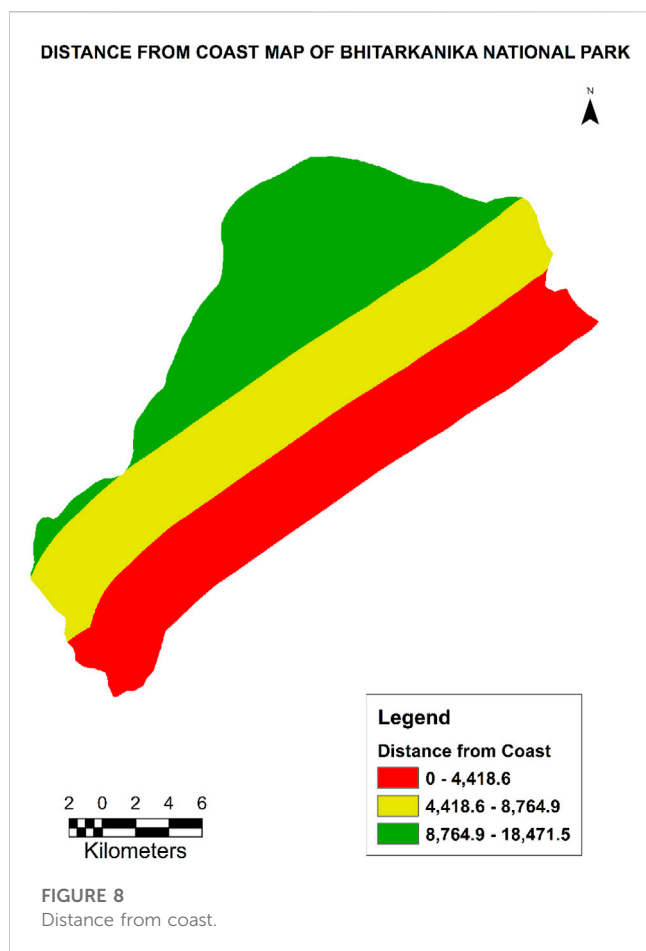
The Bay of Bengal lines the whole eastern area of BNP. This Proximity to the sea makes the coastal areas of BNP extremely vulnerable to tidal floods, especially during storm surges and tsunamis. Added to that, the Bay of Bengal is very prone to cyclones. The Gahirmatha Marine Sanctuary is shielded from such degradation due to the presence of mangroves. The map produced is classified into three classes: High Proximity (<4418.60 m), Medium Proximity (4418.60–8764.90 m), and Low Proximity (>8764.90 m). The coastal areas of Paramanandapur, Karanjia, Kanhupur, Gupti, Barunei, Satabhaya, Pentha, Jamboo, Batighar, Suniti, Kansarbadadandua, Ramanagar, and Baulakani all fall under the high proximity class and are highly vulnerable to tidal floods (Figure 8; Table 10).

4.4 Flood hazard

This map indicates all areas with a high flood hazard and those with a low flood hazard. The higher the flood hazard greater the probability of flood and *vice versa*. This map is classified into five classes—Streams,

TABLE 9 Distance from the river statistics.

Distance class (metre)	Flood hazard	Area in sq. km	Percentage (%)
High Proximity	High	159.85	32.4
Medium Proximity	Medium	164.95	33.4
Low Proximity	Low	166.24	34.2



High, Medium, Low, and no hazard. As can be seen from the resulting image, an area of 55.18 sq. km (11.23% of the total area) is covered by the Brahmani and Dharma river systems, as well as the localities of Ramchandrapur, Jagannathpur, Padmanavpur, Narayanpur, Saradaprasad, Paramanandapur, and Mohanpur, these regions have a high flood hazard hence are the most flood-prone regions (Figure 9; Table 11). An area of 4.11 sq. km or 0.8% of the total area falls under the medium hazard region and exhibits a moderate threat of floods. Low flood hazard areas include the localities of Sailendra Nagar, Baghamari, Birabhanjapur, Govindapur, Kanhupur, *etc.*, covering an area of 34.08 sq. km and 6.9% of the total area. A sizeable portion of the BNP is 383.39 Sq. km or 78% of the entire area has no flood hazard.

4.5 Flood vulnerability

The above map represents the area of BNP classified in terms of vulnerability to flooding. It is classified into four

classes: waterbodies, high, medium, and low, represented by blue, Red, Yellow, and Green, respectively. As the map indicates, a substantial part of BNP is under a high vulnerability zone. The eastern coast along the Bay of Bengal and the northern and eastern regions of BNP is the most vulnerable zones of BNP.

The High vulnerability areas include the villages of Karanjia, Praharajpur, Pentha Beach, Jaudia Teisi Mauza, Nuagan, Paramanandapur, Kanhupur, Satavaya, Bagapatia, Balunga Patia, Gupti, Rajrajeshwaripur, Jagannathpur, Padmanavpur, Balarampur, Junus Nagar, Sila pokhari, Purusottampur, Narayanapur, Sir Rajendrapur, Banipal, Pravati, Ahirajpur, Sailendra Sarai and Trilochanpur (Figure 10; Table 12). This zone covers an area of 118.68 Sq. Km and 24.28% of the total area. The medium vulnerability zone covers an area of 165.94 Sq. km and 33.9% of the entire area. This zone includes villages like Subarnpur, Birabhanjapur, Badapal, Bimisnagar, Chakradharpur, Balarampur, *etc.* The low vulnerability region covers an area of 137.43 Sq. Km and 28.12% of the total area and mainly includes the mangrove forests of BNP.

4.6 Flood risk

The study findings reveal that a significant portion of the BNP area falls within a high flood-risk zone. The map provided in Figure 13 classifies the area into four categories: Waterbodies, High, Medium, and Low, represented by the colours Blue, Red, Yellow, and Green, respectively. The Bhitarkanika National Park region has a low elevation and a gentle slope, with the Brahmani River and the Bay of Bengal surrounding it on all sides. This geographical configuration puts BNP at a heightened risk of floods and coastal areas being submerged due to future sea-level rise. The study indicates that the eastern regions of BNP, particularly those near the riverbanks or the coast, are classified as high flood-risk zones. The coastal villages of Govindapur, Kanhupur, Mohanpur, Paramanandapur, Satavaya, Bankua, Nuagan, Baghadiya, Jaudiya, Joginatha, and Sailendra Sarai are located within these high-risk regions, susceptible to tidal floods and sea-level rise. This is further proven in other studies that coastal region of BNP are projected to be submerged due to sea-level rise by the year 2050 (Mishra et al., 2021).

These villages, such as Saradaprasad, Trilochanpur, Kamalpur, Badhadia, Subarnpur, Sailendra Nagar, Talchua, Sourendrapur, Baghamari, Narayanpur, Sir Rajendrapur, Pravati, Gopaljew Patana, Ajar Patia, Purusottampur, Junus Nagar, Panchu Palli, Ramachandrapur, Ghadiamal, Padmanavpur, Jagannathpur, Balarampur, Jharpada,

TABLE 10 Distance from the coast statistics.

Class	Flood hazard	Area in sq. km	Percentage (%)
High Proximity	High	164.42	33.5
Medium Proximity	Medium	161.44	32.94
Low Proximity	Low	165.47	33.7

FLOOD HAZARD MAP OF BHITARKANINKA NATIONAL PARK

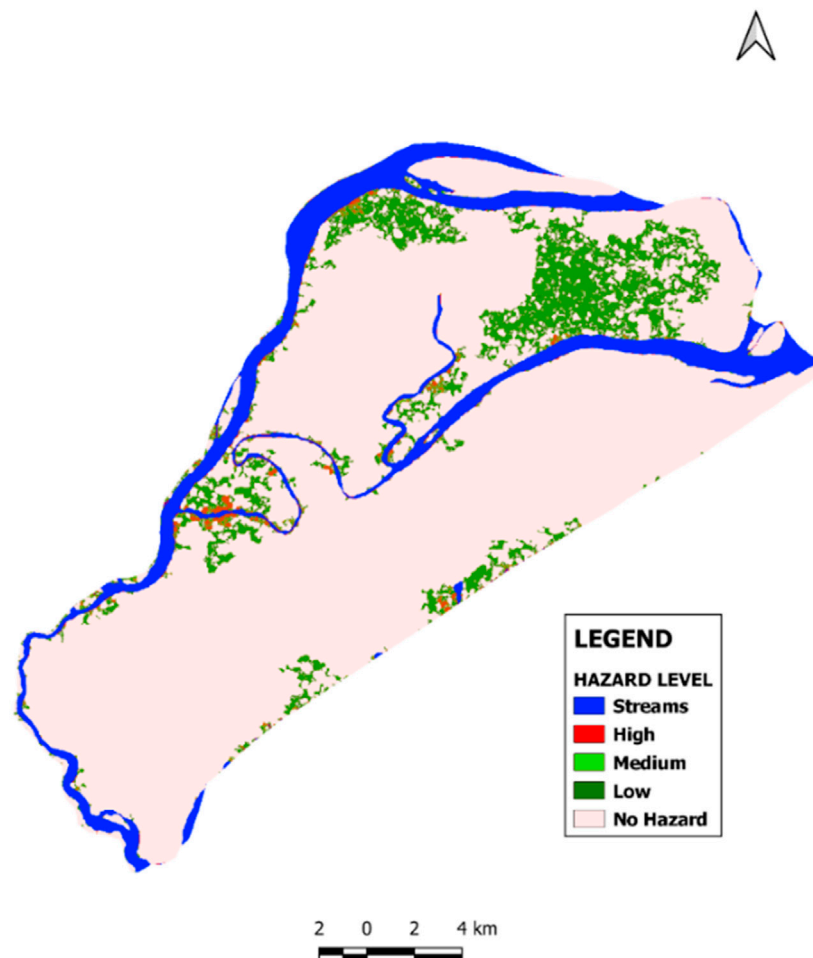


FIGURE 9
Flood hazard map.

TABLE 11 Flood hazard statistics.

Hazard level	Area in sq. Km	Percentage (%)
Streams	55.18	11.23
High	14.24	2.9
Medium	4.11	0.8
Low	34.08	6.9
No Hazard	383.39	78.08

Rajagarh, parts of Rajnagar, Praharajpur, and Kadalichua, are all located along the banks of the Brahmani and Dharma Rivers. These villages are situated within the high-risk zone for riverine floods. Additionally, villages like Balarampur, Gajrajpur, Mahinsasur, Gobindapur, Amanapari, Bhitargarh, Sribantapur, Tikayat Nagar, Rabindrapur, and others fall within the medium

flood risk zone. This zone covers an area of 171.51 sq. km, accounting for 35.10% of the total area. These areas have a moderate risk of flooding, but they also have the potential to transition into high-risk zones in the coming years.

The mangrove forests in BNP, located primarily along the estuaries, have the highest elevation. These areas experience daily fluctuations in water levels during high and low tides, making them naturally resistant to floods. Instead, these mangrove areas serve as a protective barrier, shielding the nearby regions from storms and floods. As a result, the majority of the low flood risk zone comprises mangrove forests along BNP and Gahirmatha WLS. Other villages in the area, such as Barunei, Kantia Khai, Rajendranarayanpur, Krishnanagar, Kanaknagar, Baghua, Dighi, Madhupur, and others, also fall within this low-risk zone and are not immediately susceptible to floods. This low-risk zone covers an area of 132.39 Sq. km and constitute 27.09% of the total area (Figure 11; Table 13).

VULNERABILITY MAP OF BHITARKANIKA NATIONAL PARK

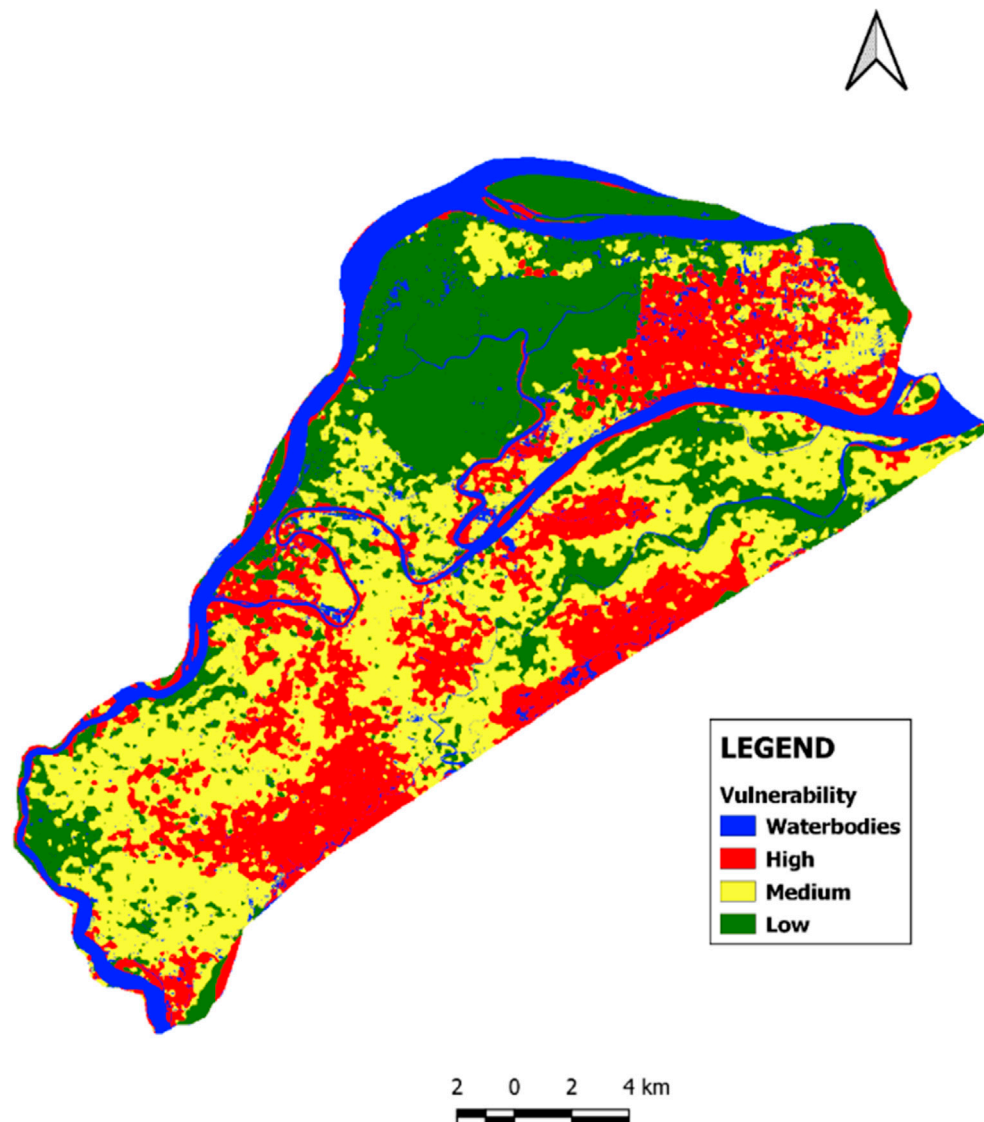
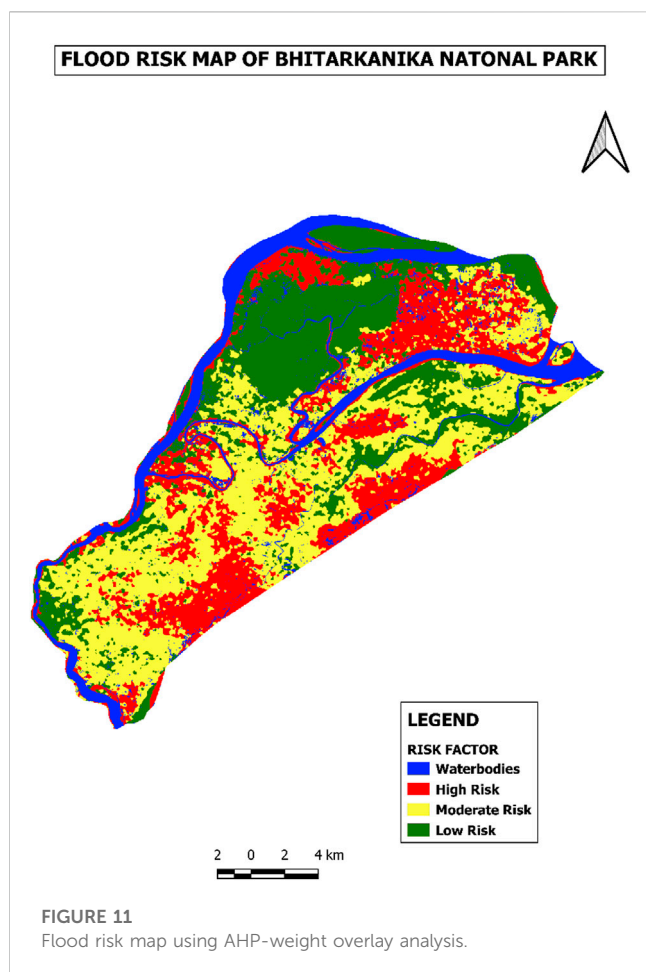


FIGURE 10
Vulnerability map using AHP-weight overlay analysis.

TABLE 12 Vulnerability statistics.

Vulnerability classes	Flood risk	Area in sq. km	Percentage (%)
Waterbodies	N/A	66.48	13.60
High	High	118.68	24.28
Medium	Medium	165.94	33.90
Low	Low	137.43	28.12



4.7 Flood risk mapping using machine learning

Figure 12 has been generated using machine learning algorithms (SVM-RBF). This output provides better results than the results obtained using conventional methods. The risk zones created using this method are more distinctive and easier to interpret. The flood risk map developed by machine learning algorithms provides accurate in terms of overall accuracy and kappa value (Table 14). In addition, the machine learning-based flood risk map shows better visual quality regarding zoning, smoothness and aerial extent as compared to conventional methods (Figure 11; Figure 12; Figure 13; Table 13).

TABLE 13 Flood risk statistics.

Flood risk classes	Flood risk	Flood risk using AHP		Flood risk using machine learning	
		Area in sq. km	Percentage (%)	Area in sq. km	Percentage (%)
Waterbodies	N/A	66.30	13.50%	62.01	12.60%
High	High	118.40	24.23%	188.33	38.35%
Medium	Medium	171.51	35.10%	107.41	21.87%
Low	Low	132.39	27.09%	133.54	27.19%

The below figure shows a side-by-side comparison of both maps.

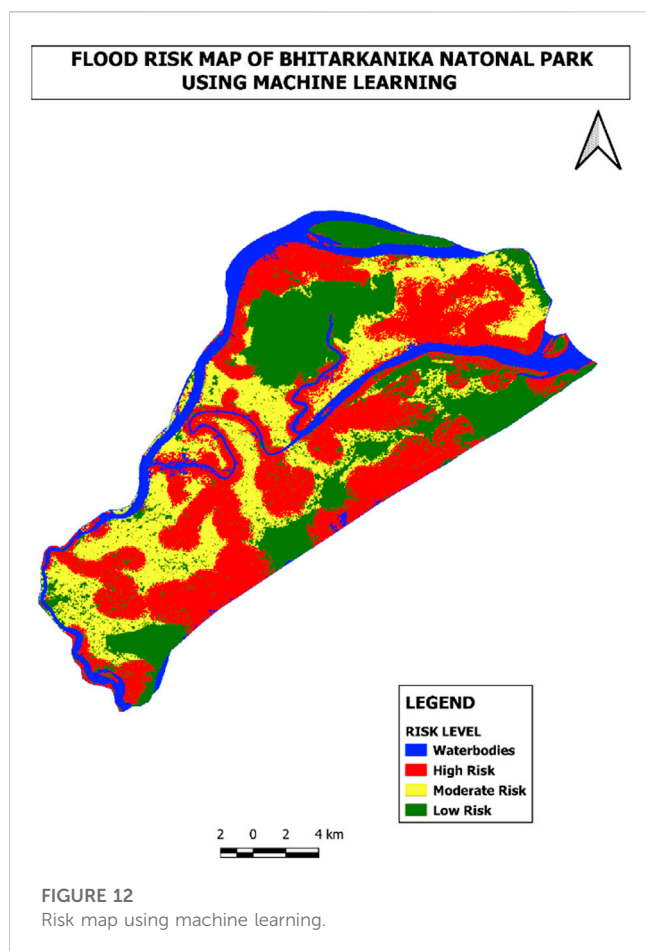
In today's time machine-learning algorithms due to their association with Artificial Intelligence (AI) are widely used for vulnerability mapping as seen in a number of studies (Avand et al., 2021; Liu et al., 2021; Ghosh et al., 2022). The result of the present study shows that machine-learning algorithms outperform Weight Overlay Analysis methods based on the map's precision, kappa index, and overall quality. This is clearly showcased in the accuracy assessment conducted using the OTB tool. It has been proved repeatedly in other studies too that SVM is the most reliable ML algorithm for flood zonation (Wu et al., 2019; Xiong et al., 2019).

5 Mitigation strategies and conclusion

5.1 Mitigation for human settlement

Given the significant economic investment needed for flood mitigation measures globally, as well as the unique nature of floods requiring targeted strategies, it is crucial to pay considerable attention to the performance of these strategies and their optimal design under diverse and complex environmental conditions. This emphasis on performance evaluation and optimal design is of utmost importance to ensure effective and efficient flood mitigation efforts (Binns, 2020). It is fundamental to determine which measures are the most effective in optimising the response to floods in local communities (Genovese and Thaler, 2020).

This study provides a comprehensive understanding of the vulnerable and risk-prone regions within Bhitarkanika National Park (BNP). It reveals that a significant portion of BNP is classified as a high flood risk zone, necessitating immediate actions and mitigation measures. Coastal villages such as Govindapur, Kanhupur, Mohanpur, Paramanandapur, Satavaya, Bankua, Nuagan, Baghadiya, Jaudiya, Joginatha, Sailendra Sarai, Purusottampur, Junus Nagar, Panchu Palli, Ramachandrapur, Ghadiamal, Padmanavpur, Jagannathpur, Balarampur, Jharpada, Rajagarh, and Raj Nagar are located in high-risk areas prone to tidal and riverine floods. These areas have high population densities and require the establishment of proper flood and storm centres. It is essential to educate the residents about first aid and provide them with training in disaster resilience. Additionally, these



villages should have well-connected road networks to nearby regional centres to ensure the timely arrival of emergency supplies during floods. Considering the potential submergence of coastal fishing villages due to rising sea levels in the coming decades, proper resettlement planning must be carried out in advance. Adequate relief and compensation should be provided to the residents of these fishing villages and nearby agricultural villages in the event of flood damage.

5.2 Conservation of ecology

The mangrove forest area in Bhitarkanika National Park has been steadily increasing thanks to the effective mitigation measures implemented by the Odisha Forest Department. Despite challenges such as illegal apiculture activities leading to forest fires, the mangrove area has expanded from 139.49 sq. km in 2000 to nearly 166 sq. km in 2021.

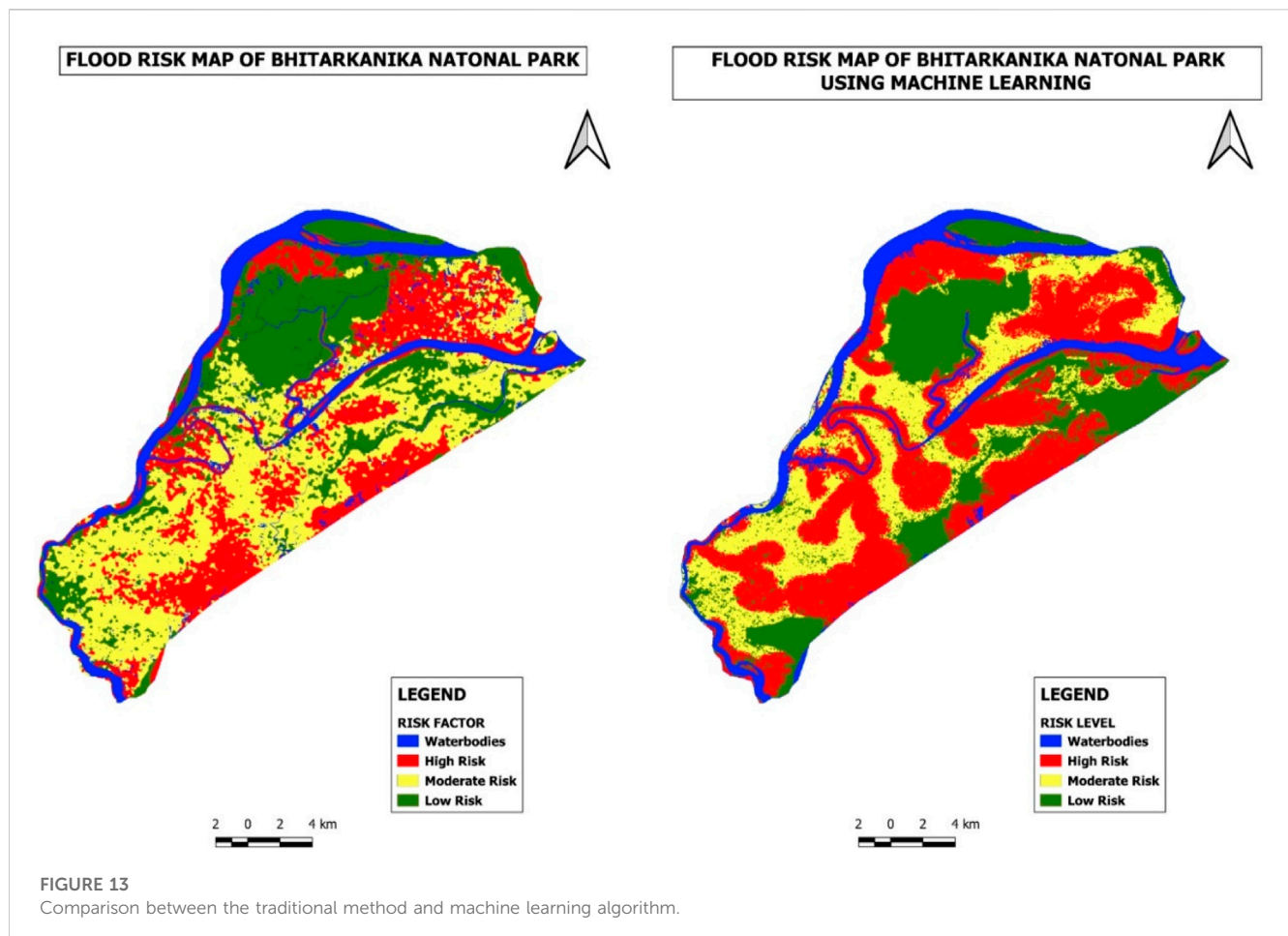
The forest department has been successful in addressing threats such as overfishing, poaching, and shifting cultivation, thereby stabilizing the mangrove ecosystem. On the other hand, the area under agriculture has experienced a significant decrease due to the expansion of aquaculture activities and salinity ingress in agricultural areas. Aquaculture has seen exponential growth in the past 2 decades due to its profitability. Numerous aquaculture ponds are being established along the national park area, posing a potential threat in the future. Salinity ingress from nearby estuaries is also a major factor contributing to the decline in agricultural activities as it negatively affects soil fertility.

The saltwater crocodile population in the BNP area is thriving, which is a positive sign for the biosphere reserve. However, this has also resulted in an increase in human-animal conflicts. During floods, crocodiles often venture out of the main estuary area and into nearby rivers, posing a risk to local villagers. It is crucial to implement measures to mitigate these conflicts and ensure the safety of both humans and crocodiles. Additionally, the study highlights the need to declare the Gahirmatha WLS area as a no-fishing zone with strict enforcement to protect the turtles. This will help preserve the biodiversity and maintain the ecological balance in the region. Furthermore, the study demonstrates that machine learning techniques outperform Weight Overlay Analysis techniques in terms of accuracy. The Weight Overlay Analysis map achieved an accuracy of 91.12%, while the machine learning map achieved an accuracy of 99.54%. This indicates that the machine learning approach provides a clearer and more accurate representation of the flood risk zones in BNP.

The Bhitarkanika National Park area experiences annual floods, yet there has been a lack of comprehensive studies that intricately delineate the flood risk zones in this ecologically important region. This study fills that gap by clearly identifying the flood-prone areas within the fragile BNP region and proposing potential mitigation measures aligned with the Sustainable Development Goals (SDGs). Implementing proper mitigation strategies in the high-risk zones identified in the study can help minimize damage to both human lives and wildlife. The National Disaster Management Authority (NDMA) and the Government of Odisha can utilize this study to make Bhitarkanika National Park more resilient to flood-related damages and to promote harmonious coexistence between humans and animals. Additionally, the study demonstrates that the SVM-RBF algorithm is a superior method for flood risk zoning, surpassing the traditional AHP method. This finding encourages the widespread adoption of the SVM-RBF algorithm in future studies, further enhancing flood risk assessment and management efforts.

TABLE 14 Flood risk comparison.

Methods used	Kappa index (%)	Overall accuracy (%)
Risk map using AHP-Weight Overlay Analysis	87.41	91.12
Risk Map using Machine Learning-SVM-RBF	99.19	99.54



Data availability statement

The original contributions presented in the study are included in the article/supplementary material, further inquiries can be directed to the corresponding author.

Author contributions

SM: drafting, processing, analysis of land use/cover mapping and change analysis, vulnerability, hazards, and risk mapping. SkM: Assisted in remote sensing data processing, GIS, and machine learning application. DS: assisted in developing different indicators for flood vulnerability and risk assessment. TV: editing, rewriting and reviewing of the article. MM: Assisted in conceptualizing research article. C-TW: editing and rewriting of the article. All authors contributed to the article and approved the submitted version.

References

- Avand, M., Moradi, H., and lasboyee, M. R. (2021). Spatial modeling of flood probability using geo-environmental variables and machine learning models, case study: Tajan watershed, Iran. *Adv. Space Res.* 67 (10), 3169–3186. doi:10.1016/j.asr.2021.02.011
- Balasubramanian, A. (2017). *Digital elevation model (dem) in gis*. doi:10.13140/RG.2.2.23976.47369
- Bandi, A. S., Meshapam, S., and Deva, P. (2019). A geospatial approach to flash flood hazard mapping in the city of Warangal, Telangana, India. *Environ. Socio-Economic Stud.* 7 (3), 1–13. doi:10.2478/ENVIRON-2019-0013
- Binns, A. D. (2020). Flood mitigation measures in an era of evolving flood risk. *J. Flood Risk Manag.* 13, e12659. doi:10.1111/jfr3.12659

Conflict of interest

The authors declare that the research was conducted in the absence of any commercial or financial relationships that could be construed as a potential conflict of interest.

Publisher's note

All claims expressed in this article are solely those of the authors and do not necessarily represent those of their affiliated organizations, or those of the publisher, the editors and the reviewers. Any product that may be evaluated in this article, or claim that may be made by its manufacturer, is not guaranteed or endorsed by the publisher.

- Breiman, L. (2001). Random forests. *Mach. Learn.* 45 (1), 5–32. doi:10.1023/A:1010933404324
- Cian, F., Marconcini, M., Ceccato, P., and Giupponi, C. (2018). Flood depth estimation by means of high-resolution SAR images and lidar data. *Nat. Hazards Earth Syst. Sci.* 18 (11), 3063–3084. doi:10.5194/nhess-18-3063-2018
- Dai, Q.-Y., Zhang, C.-P., and Wu, H. (2016). Research of decision tree classification algorithm in data mining. *Int. J. Database Theory Appl.* 9 (5), 1–8. doi:10.14257/ijtda.2016.9.5.01
- Dawod, G. M., Mirza, M. N., and Al-Ghamdi, K. A. (2012). GIS-based estimation of flood hazard impacts on road network in Makkah city, Saudi Arabia. *Environ. Earth Sci.* 67 (8), 2205–2215. doi:10.1007/S12665-012-1660-9
- Deroliya, P., Ghosh, M., Mohanty, M. P., Ghosh, S., Rao, K. H. V. D., and Karmakar, S. (2022). A novel flood risk mapping approach with machine learning considering geomorphic and socio-economic vulnerability dimensions. *Sci. Total Environ.* 851, 158002. doi:10.1016/J.SCITOTENV.2022.158002
- Dewan, A. M., Islam, M. M., Kumamoto, T., and Nishigaki, M. (2007). Evaluating flood hazard for land-use planning in greater Dhaka of Bangladesh using remote sensing and GIS techniques. *Water Resour. Manag.* 21 (9), 1601–1612. doi:10.1007/S11269-006-9116-1
- Farhadi, H., and Najafzadeh, M. (2021). Flood risk mapping by remote sensing data and random forest technique. *Water* 13 (21), 3115. doi:10.3390/W13213115
- Fernández, D. S., and Lutz, M. A. (2010). Urban flood hazard zoning in Tucumán Province, Argentina, using GIS and multicriteria decision analysis. *Eng. Geol.* 111 (1–4), 90–98. doi:10.1016/J.ENGEO.2009.12.006
- Genovese, E., and Thaler, T. (2020). The benefits of flood mitigation strategies: effectiveness of integrated protection measures. *AIMS Geosci.* 6 (4), 459–472. doi:10.3934/geosci.2020025
- Gharagozlou, A., Nazari, H., and Seddighi, M. (2011). Spatial analysis for flood control by using environmental modeling. *J. Geogr. Inf. Syst.* 03 (04), 367–372. doi:10.4236/JGIS.2011.34035
- Ghosh, S., Saha, S., and Bera, B. (2022). Flood susceptibility zonation using advanced ensemble machine learning models within Himalayan foreland basin. *Nat. Hazards Res.* 2 (4), 363–374. doi:10.1016/J.NHRES.2022.06.003
- Hallegatte, S., Green, C., Nicholls, R. J., and Corfee-Morlot, J. (2013). Future flood losses in major coastal cities. *Nat. Clim. Change* 3 (9), 802–806. doi:10.1038/NCLIMATE1979
- Hao, L., van Westen, C., Rajaneesh, A., Sajinkumar, K. S., Martha, T. R., and Jaiswal, P. (2022). Evaluating the relation between land use changes and the 2018 landslide disaster in Kerala, India. *Catena* 216, 106363. doi:10.1016/j.catena.2022.106363
- He, C., Shi, P., Xie, D., and Zhao, Y. (2010). Improving the normalized difference built-up index to map urban built-up areas using a semiautomatic segmentation approach. *Remote Sens. Lett.* 4, 213–221. doi:10.1080/01431161.2010.481681
- Heidari, A. (2014). Flood vulnerability of the Karun River System and short-term mitigation measures. *J. Flood Risk Manag.* 7 (1), 65–80. doi:10.1111/JFR3.12032
- Hongmao, S. (2016). Quantitative structure–activity relationships. *A Pract. Guide Ration. Drug Des.* 2016, 163–192. doi:10.1016/B978-0-08-100098-4.00005-3
- Jaydhar, A. K., Chandra Pal, S., Saha, A., Islam, A. R. M. T., and Ruidas, D. (2022). Hydrogeochemical evaluation and corresponding health risk from elevated arsenic and fluoride contamination in recurrent coastal multi-aquifers of eastern India. *J. Clean. Prod.* 369, 133150. doi:10.1016/J.JCLEPRO.2022.133150
- Kaul, H. A., and Sopan, I. (2012). Land use land cover classification and change detection using high resolution temporal satellite data. *J. Environ.* 01, 146–152.
- Khan, W., Hore, U., Mukherjee, S., and Mallapur, G. (2020). Human-crocodile conflict and attitude of local communities toward crocodile conservation in Bhitarkanika Wildlife Sanctuary, Odisha, India. *Mar. Policy* 121, 104135. doi:10.1016/J.MARPOL.2020.104135
- Kumar, A., Lakshmanan, G., Selvam, V., Ramasubramanian, R., and Kar, C. (2015). Developing a spectral library of mangrove species of Indian East Coast using field spectroscopy. *Geocarto Int.* 2015. doi:10.1080/10106049.2014.985743
- Kumar, M., Kalra, N., Singh, H., Sharma, S., Singh Rawat, P., Kumar Singh, R., et al. (2021). Indicator-based vulnerability assessment of forest ecosystem in the Indian Western Himalayas: An analytical hierarchy process integrated approach. *Ecol. Indic.* 125, 107568. doi:10.1016/J.ECOLIND.2021.107568
- Langlentombi, L. C., and Kumar, M. (2021). Inherent vulnerability of forests: A case study from Jharkhand in India. *J. Trop. For. Sci.* 33 (4), 455–460. doi:10.26525/jtfs2021.33.4.455
- Lawal, D. U., Matori, A. N., Yusuf, K. W., Hashim, A. M., and Balogun, A. L. (2014). Analysis of the flood extent extraction model and the natural flood influencing factors: A GIS-based and remote sensing analysis. *IOP Conf. Ser. Earth Environ. Sci.* 18 (1), 012059. doi:10.1088/1755-1315/18/1/012059
- Li, K., Wu, S., Dai, E., and Xu, Z. (2012). Flood loss analysis and quantitative risk assessment in China. *Nat. Hazards* 63 (2), 737–760. doi:10.1007/S11069-012-0180-Y
- Liu, Y., Lu, X., Yao, Y., Wang, N., Guo, Y., Ji, C., et al. (2021). Mapping the risk zoning of storm flood disaster based on heterogeneous data and a machine learning algorithm in Xinjiang, China. *J. Flood Risk Manag.* 14 (1), e12671. doi:10.1111/JFR3.12671
- Mishra, S. P., Kumar Barik, K., and Patnaik, S. K. (2021). The vulnerability and management to the blue carbon ecosystem: Coastal Odisha. *Int. j. lakes rivers* 14 (1), 43–70.
- Mustak, S., Baghmar, N. K., Srivastava, P. K., Singh, S. K., and Binolakar, R. (2018). Delineation and classification of rural–urban fringe using geospatial technique and onboard DMSP–Operational Linescan System. *Geocarto Int.* 33 (4), 375–396. doi:10.1080/10106049.2016.1265594
- Nelson, R., Kocic, P., Crimp, S., Martin, P., Meinke, H., Howden, S. M., et al. (2010). The vulnerability of Australian rural communities to climate variability and change: Part II—integrating impacts with adaptive capacity. *Environ. Sci. Policy* 13 (1), 18–27. doi:10.1016/J.ENVSCI.2009.09.007
- Opella, J. M. A., and Hernandez, A. A. (2019). “Developing a flood risk assessment using support vector machine and convolutional neural network: A conceptual framework,” in *Proceedings - 2019 IEEE 15th International Colloquium on Signal Processing and Its Applications*, Penang, Malaysia, 8–9 March 2019, 260. doi:10.1109/CSPA.2019.8695980
- Ouma, Y. O., and Tateishi, R. (2014). Urban flood vulnerability and risk mapping using integrated multi-parametric AHP and GIS: Methodological overview and case study assessment. *WaterSwitzerl.* 6 (6), 1515–1545. doi:10.3390/W6061515
- Parsian, S., Amani, M., Moghimi, A., Ghorbanian, A., and Mahdavi, S. (2021). Flood hazard mapping using fuzzy logic, analytical hierarchy process, and multi-source geospatial datasets. *Remote Sens.* 13 (23), 4761. doi:10.3390/RS13234761
- Parvin, F., Ali, S. A., Calka, B., Bielecka, E., Linh, N. T. T., and Pham, Q. B. (2022). Urban flood vulnerability assessment in a densely urbanized city using multi-factor analysis and machine learning algorithms. *Theor. Appl. Climatol.* 149 (1–2), 639–659. doi:10.1007/S00704-022-04068-7
- Pham, B. T., Shirzadi, A., Shahabi, H., Omidvar, E., Singh, S. K., Sahana, M., et al. (2019). Landslide susceptibility assessment by novel hybrid machine learning algorithms. *Sustain. Switz.* 11 (16), 4386. doi:10.3390/su11164386
- Pourali, S. H., Arrowsmith, C., Chrisman, N., Matkan, A. A., and Mitchell, D. (2016). Topography wetness index application in flood-risk-based land use planning. *Appl. Spatial Analysis Policy* 9 (1), 39–54. doi:10.1007/S12061-014-9130-2
- Rahmati, O., Zeinivand, H., and Besharat, M. (2016). Flood hazard zoning in Yasooj region, Iran, using GIS and multi-criteria decision analysis. *Geomatics, Nat. Hazards Risk* 7 (3), 1000–1017. doi:10.1080/19475705.2015.1045043
- Ramesh, V., and Iqbal, S. S. (2022). Urban flood susceptibility zonation mapping using evidential belief function, frequency ratio and fuzzy gamma operator models in GIS: a case study of greater Mumbai, Maharashtra, India. *Geocarto Int.* 37 (2), 581–606. doi:10.1080/10106049.2020.1730448
- Ruidas, D., Chakraborty, R., Islam, A. R. Md. T., Saha, A., and Pal, S. C. (2022a). A novel hybrid of meta-optimization approach for flash flood-susceptibility assessment in a monsoon-dominated watershed, Eastern India. *Environ. Earth Sci.* 81 (5), 145. doi:10.1007/s12665-022-10269-0
- Ruidas, D., Pal, S. C., Islam, A. R. M. T., and Saha, A. (2021). Characterization of groundwater potential zones in water-scarce hardrock regions using data driven model. *Environ. Earth Sci.* 80 (24), 809–818. doi:10.1007/s12665-021-10116-8
- Ruidas, D., Pal, S. C., Towfiqul Islam, A. R. M., and Saha, A. (2022b). Hydrogeochemical evaluation of groundwater aquifers and associated health hazard risk mapping using ensemble data driven model in a water scarce plateau region of eastern India. *Expo. Health* 15 (1), 113–131. doi:10.1007/s12403-022-00480-6
- Ruidas, D., Saha, A., Islam, A. R. Md. T., Costache, R.-D., and Pal, S. (2022c). Development of geo-environmental factors controlled flash flood hazard map for emergency relief operation in complex hydro-geomorphic environment of tropical river, India. *Environ. Sci. Pollut. Res.* 2022. doi:10.1007/s11356-022-23441-7
- Sami, G., Abdelwahhab, F., Yahyaoui, H., and Abdelghani, F. (2021). Flood hazard in the city of chemora (Algeria). *Analele Univ. Din. Oradea, Ser. Geogr.* 31 (1), 22–27. doi:10.30892/AUOG.311103-835
- Schumann, G. J. P., Brakenridge, G. R., Kettner, A. J., Kashif, R., and Niebuhr, E. (2018). Assessing flood disaster response with earth observation data and products: A critical assessment. *Remote Sens.* 10 (8), 1230. doi:10.3390/RS10081230
- Serda, M., Becker, F. G., Cleary, M., Team, R. M., Holtermann, H., The, D., et al. (2002). Risk, performance and uncertainty in flood and coastal defence - a review. *Univ. Slaski* 7 (1), 343–354.
- Soni, B. (2012). *Exercise 4-watershed and stream network delineation from DEMs prepared by ayse kilic and. In CIVE 835-GIS in water resources fall.* Available at: <http://maps.waterdata.usgs.gov/mapper/index.html>.
- Stefanidis, S., and Stathis, D. (2013). Assessment of flood hazard based on natural and anthropogenic factors using analytic hierarchy process (AHP). *Nat. Hazards* 68 (2), 569–585. doi:10.1007/S11069-013-0639-5
- Taylor, J., Lai, K., Davies, M., Clifton, D., Ridley, I., and Biddulph, P. (2011). Flood management: Prediction of microbial contamination in large-scale floods in urban environments. *Environ. Int.* 37 (5), 1019–1029. doi:10.1016/J.ENVINT.2011.03.015

- Ullah, K., and Zhang, J. (2020). GIS-based flood hazard mapping using relative frequency ratio method: A case study of panjkora river basin, eastern hindu kush, Pakistan. *PLoS ONE* 15 (3), e0229153. doi:10.1371/JOURNAL.PONE.0229153
- Wang, Y., Hong, H., Chen, W., Li, S., Panahi, M., Khosravi, K., et al. (2019). Flood susceptibility mapping in Dingnan County (China) using adaptive neuro-fuzzy inference system with biogeography based optimization and imperialistic competitive algorithm. *J. Environ. Manag.* 247, 712–729. doi:10.1016/j.jenvman.2019.06.102
- Wright, D. B. (2015). *Methods in flood hazard and risk assessment*. Available at: <https://openknowledge.worldbank.org/handle/10986/22982>.
- Wu, J., Liu, H., Wei, G., Song, T., Zhang, C., and Zhou, H. (2019). Flash flood forecasting using support vector regression model in a small mountainous catchment. *WaterSwitzerl.* 11 (7), 1327. doi:10.3390/w11071327
- Xiong, J., Li, J., Cheng, W., Wang, N., and Guo, L. (2019). A GIS-based support vector machine model for flash flood vulnerability assessment and mapping in China. *ISPRS Int. J. Geo-Information* 8 (7), 297. doi:10.3390/ijgi8070297
- Yadollahie, M. (2019). The flood in Iran: A consequence of the global warming? *Int. J. Occup. Environ. Med.* 10 (2), 54–56. doi:10.15171/IJOEM.2019.1681
- Zhang, K., Gann, D., Ross, M., Robertson, Q., Sarmiento, J., Santana, S., et al. (2019). Accuracy assessment of ASTER, SRTM, ALOS, and TDX DEMs for Hispaniola and implications for mapping vulnerability to coastal flooding. *Remote Sens. Environ.* 225, 290–306. doi:10.1016/j.rse.2019.02.028
- Zhang, Z., Gao, J., and Cai, Y. (2019). The effects of environmental factors and geographic distance on species turnover in an agriculturally dominated river network. *Environ. Monit. Assess.* 191, 201–217. doi:10.1007/s10661-019-7309-3



OPEN ACCESS

EDITED BY

Sandipan Das,
Symbiosis International University, India

REVIEWED BY

Rebeka Sultana,
University of Rajshahi, Bangladesh
Biraj Kanti Mondal,
Netaji Subhas Open University, India

*CORRESPONDENCE

Uday Chatterjee,
✉ raj.chatterjee459@gmail.com
Subodh Chandra Pal,
✉ geo.subodh@gmail.com
Abu Reza Md. Towfiqul Islam,
✉ towfiq_dm@brur.ac.bd

RECEIVED 19 August 2023

ACCEPTED 30 October 2023

PUBLISHED 16 November 2023

CITATION

Setiawati MD, Chatterjee U, Djamil YS, Alifatri LO, Nandika MR, Rachman HA, Supriyadi IH, Hanifa NR, Muslim AM, Eguchi T, Prayudha B, Oktaviani A, Adi NS, Renyaan J, Sulha S, Wouthuyzen S, Pal SC, Islam ARMT, Alam E and Islam MK (2023), Seribu islands in the megacities of Jakarta on the frontlines of the climate crisis. *Front. Environ. Sci.* 11:1280268. doi: 10.3389/fenvs.2023.1280268

COPYRIGHT

© 2023 Setiawati, Chatterjee, Djamil, Alifatri, Nandika, Rachman, Supriyadi, Hanifa, Muslim, Eguchi, Prayudha, Oktaviani, Adi, Renyaan, Sulha, Wouthuyzen, Pal, Islam, Alam and Islam. This is an open-access article distributed under the terms of the [Creative Commons Attribution License \(CC BY\)](https://creativecommons.org/licenses/by/4.0/). The use, distribution or reproduction in other forums is permitted, provided the original author(s) and the copyright owner(s) are credited and that the original publication in this journal is cited, in accordance with accepted academic practice. No use, distribution or reproduction is permitted which does not comply with these terms.

Seribu islands in the megacities of Jakarta on the frontlines of the climate crisis

Martiwi Diah Setiawati¹, Uday Chatterjee^{2*},
Yudha Setiawan Djamil³, La Ode Alifatri¹,
Muhammad Rizki Nandika¹, Herlambang Aulia Rachman⁴,
Indarto Happy Supriyadi¹, Nuraini Rahma Hanifa⁵,
Aidy M. Muslim⁶, Tsuyoshi Eguchi⁷, Bayu Prayudha¹,
Aulia Oktaviani⁵, Novi Susetyo Adi⁸, Jeverson Renyaan¹,
Siti Sulha^{1,9}, Sam Wouthuyzen¹, Subodh Chandra Pal^{10*},
Abu Reza Md. Towfiqul Islam^{11,12*}, Edris Alam^{13,14} and
Md Kamrul Islam¹⁵

¹Research Center for Oceanography, National Research and Innovation Agency (BRIN), Jakarta, Indonesia, ²Department of Geography, Bhatler College, Vidyasagar University, Dantan, West Bengal, India, ³Research Center for Climate and Atmosphere, National Research and Innovation Agency (BRIN), Bandung, Indonesia, ⁴Department of Marine Sciences, University of Trunojoyo Madura, Bangkalan, Indonesia, ⁵Research Center for Geological Disaster, National Research and Innovation Agency (BRIN), Bandung, Indonesia, ⁶Institute of Oceanography and Environment (INOS), Universiti Malaysia Terengganu (UMT), Kuala Terengganu, Malaysia, ⁷Center for Research and Application of Satellite Remote Sensing (YUCARS), Yamaguchi University, Ube city, Japan, ⁸Directorate of Small Islands and Coastal Area Utilization, Ministry of Marine Affairs and Fisheries (MMAF), Jakarta, Indonesia, ⁹Bureau for Public Communication, General Affairs, and Secretariat, National Research and Innovation Agency (BRIN), Jakarta, Indonesia, ¹⁰Department of Geography, The University of Burdwan, Purba Bardhaman, India, ¹¹Department of Disaster Management, Begum Rokeya University, Rangpur, Bangladesh, ¹²Department of Development Studies, Daffodil International University, Dhaka, Bangladesh, ¹³Faculty of Resilience, Rabdan Academy, Abu Dhabi, United Arab Emirates, ¹⁴Department of Geography and Environmental Studies, University of Chittagong, Chittagong, Bangladesh, ¹⁵Department of Civil and Environmental Engineering College of Engineering, King Faisal University, Al-Ahsa, Saudi Arabia

Jakarta, the biggest city in Indonesia, has one district that consists of hundreds of islands that face severe climate hazards called the Seribu Islands complex. This study explores the evidence of local climate trends, the potential impact, and its policy intervention on Seribu Islands, which are classified as small island states and widely recognized as being especially at risk from climate change, threatening their economic and social growth. Long-term in-situ climate data, satellite data, interviews with local stakeholders, and literature reviews were utilized to conduct an exploratory descriptive analysis. The result revealed that Seribu Island experienced a 2.2°C increase in minimum temperature from 1980 until 2021, 3.5-fold of the frequency of extreme temperature and precipitation, 4.17 mm/year of sea level rise, and 10.8 ha land expansion in the densest island. Moreover, about 67% of the inhabitant's islands were occupied by built-up areas that cover more than 50% of the region. Further, under the worst-case SLR scenario, about 58.4% of the area will be affected, and about 29 islands will disappear. This evidence was also reinforced by every single local respondent's viewpoint who felt that climate change is occurring in the region. Even though the region faces a severe threat of climate change, the issue of climate change adaptation has not been mainstreamed yet into their local policy. Therefore, the urgency of a real-time climate ground station, a real-time early warning system, and establishing a

Regional Disaster Management Agency (BPBD) at the district level have yet to be addressed. Furthermore, the knowledge gained from such case studies is outlined, along with some scientific evidence that may assist small island states in better fostering the opportunities provided by climate change adaptation.

KEYWORDS

Seribu islands, climate change, longterm climate data, anthropogenic pressure, climate change adaptation, land expansion

1 Introduction

Climate change has been recognized as a severe concern, threatening people's lives by generated hazards and environmental deterioration (Fujimori et al., 2019). Policies regarding climate change are widely acknowledged as a viable approach to address global warming, which includes a set of rules or tactics developed by a nation or state/province (Meckling and Allan, 2020). In the past few years, more nations have developed applicable climate policies focused on their local or international needs, aiming to create a resilient society for future generations. Thus, various policy measures can be utilized to combat climate change, including legislation, monetary interventions such as taxes and levies, financial aid in subsidies, volunteerism strategies, and educational initiatives (Zheng et al., 2023).

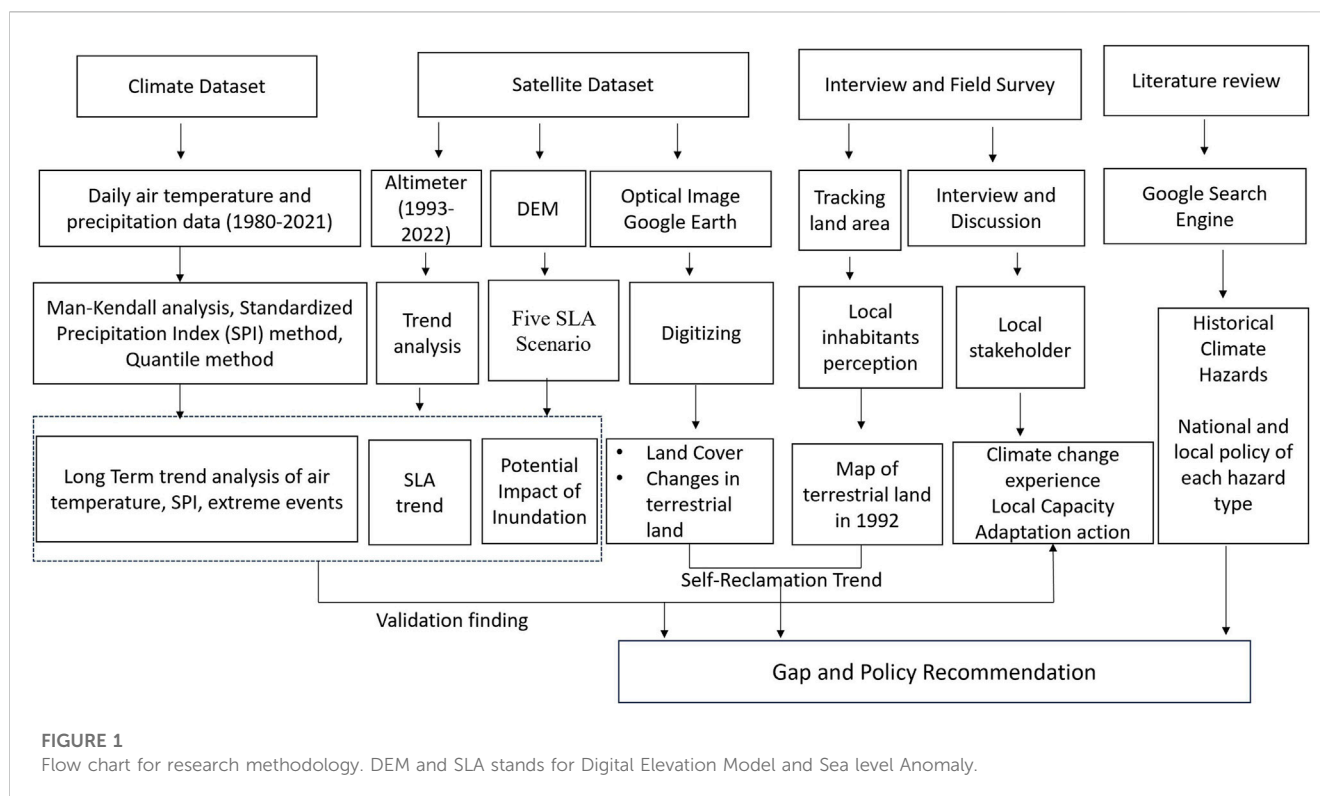
Various policy measures have multiple functions in addressing the effects of climate change. Economic tools, for example, primarily manage financial difficulties by providing funds, subsidies, tax breaks, credits, and direct investment. Legislative instruments, on the other hand, are focused on improving energy use efficiency and increasing renewable energy generation by obligatory criteria like norms, standards, and obligation schemes (Liu et al., 2019). While the threat of climate change grows, policies have been reinforced and improved. Yet, some nations are constrained by the present policy combination. For example, Brazil employed mixed policies for climate change adaptation, but instead of promoting sustainable production and climate risk management, it frequently encourages the accomplishment of societal vulnerability targets (Milhorance et al., 2020). Another study revealed that most adaptation strategies demonstrated "one-size-fits-all governance arrangements," which were mostly voluntary activities, lacked a coordination hub and relied on sectoral self-interest, and those policies are insufficient to tackle complex issues such as climate change (Clar and Steurer, 2019). Local conditions, a limited choice of policy tools, a lack of robust supervisory procedures, poor awareness of environmental protection, and a missing political will can all lead to policy setbacks (Sokolowski and Heffron, 2022).

Indonesia is listed as one of the most vulnerable countries regarding climate risk, with a high vulnerability to flooding and extreme temperatures (Neumann et al., 2015). Moreover, recent studies revealed that nine growing cities in Indonesia are exposed to serious sea level rise (SLR) and floods (Nagu et al., 2016); for instance, the SLR in Ternate City leads to sea salt intrusion of groundwater and a decline in the supply of clean water (Gaborit, 2022). Another study also revealed that there is a 1.37% decline in the number of foreign visitors to Indonesia for every 1% increase in temperature and relative humidity (Susanto et al., 2020), which is a significant loss for the country since six percent of Indonesia's GDP

came from tourism (World Travel and Tourism Council, 2019). Moreover, climate change also affects public health in the country, whereas Sumatra has experienced an increase in respiratory illnesses during the past 20 years due to the complex linkages of soil degradation, deforestation, and climatic change (Gan et al., 2021). Also, the severity of these threats is projected to increase in the future (The World Bank Group and Asian Development Bank, 2021). In addition, by 2050, Indonesia is projected to experience a loss of 8.6 billion USD, or 1.3% of the current Indonesian GDP (USAID, 2016). Besides, without effective adaptation, this country will face permanent flooding by 2070, impacting millions of people (The World Bank Group and Asian Development Bank, 2021). Therefore, addressing the climate change impact becomes a severe issue.

Seribu Islands district is a group of small islands located in the capital city of Indonesia, Jakarta. The territory consists of 116 islands which are located 30 km away from the northern part of Jakarta. This district has about 28 thousand inhabitants by 2021 who shared a total land area of 8.7 km² (BPS Seribu Islands, 2022). Its nominal Gross Regional Domestic Product (GRDP) at Current Market Prices in 2021 was 0.5 billion USD which equals 0.28% of Jakarta's GRDP. Moreover, in the past 5 years, mining and quarrying (i.e., 77%) remain the highest contributor to the GRDP in the region, followed by agriculture, forestry, and fishing (5.4%) (BPS Seribu Islands, 2022). Mining and quarrying mainly involved oil, gas, and geothermal in the islands. In recent years, the hospitality industry has been developed, with a total number of visitors in 2021 of 159 thousand people (BPS Seribu Islands, 2022), but still, it is not the region's primary revenue.

Even though the region is within the territory of Jakarta Province, all of the population lived in the rural, remote islands. Also, among five districts in Jakarta city, Seribu Islands has the highest poverty rate (i.e., 15%) and the lowest human development index (BPS DKI Jakarta, 2021). Therefore, like other small island developing States, Seribu Islands are very vulnerable to the adverse impact of climate change due to its geographic conditions and socio-economic aspects (Enssle and Kabisch, 2020). Extreme weather events such as drought, heat stress, ocean acidification, tropical cyclones and related storm surge, shifting patterns of precipitation, sea level rise, and coastal flooding endanger inhabitants' livelihoods and impact all economic sectors (Change, 2014). In other words, climate change is an obstacle to economic and social development in a region. Moreover, research conducted by ICCR (2010) stated that Indonesia experienced SLR with an average rate of 6 mm/year, and it is almost threefold than the global SLR rate (2.2 mm/year). Also, six islands (i.e., Ubi Besar Island, Ubi Kecil Island, Salak Island, Nyamuk Besar Island, Dakun Island, and Anyer Kecil) were reported disappeared in the region due to the abrasion (Kompas, 2015). Consequently, appropriate mitigation and adaptation plans are critical to human resilience and survival against climate change.



Most of the studies in Seribu Islands focused on benthic habitat and mangrove biodiversity (Johan et al., 2015; Cahyarini et al., 2016; Draisma et al., 2018), marine pollution and particular natural disasters (Lestari et al., 2022) in this region and those topics were explored in separate issues. However, almost no paper conducted integrated studies on the local evidence of climate change and its related impact on the communities in this area. Therefore, this research explores the local realities of climate change evidence, potential impact, and local preparedness in the Seribu Islands by utilizing climate dataset, satellite imageries, literature review on policy documents and deep interview with local stakeholders. This type of research will assist policymakers in developing development plans by incorporating scientific assessment through a multidisciplinary approach.

2 Materials and methods

This study is an exploratory analysis that integrated four main data sets; the time series climate data, satellite data, interview and field survey and literature review (Figure 1). The climate data set was used to determine the trend of temperature and rainfall patterns over the 41 years period in the study area. We utilized the climate dataset in Kemayoran Station (i.e., the longest and closest climate data station near Jakarta Bay), Jakarta (Figure 2) because there is no available long term *in-situ* climate dataset within the Seribu Islands complex (i.e., the government just installed the Automatic Weather System within the islands in June 2020) (DKI Jakarta Government, 2023). The satellite data set was used to analyze the possible impact of climate change and

anthropogenic pressure in the region. The literature review was utilized to record the historical trend of climate-related hazard in the area, to determine the potential impact on society, and to identify the national and local policies of each hazard type in the small islands. While interview with local stakeholders were used as a validation for the finding and to explore more on their personal experience on climate change along with their capacity and adaptation effort. Moreover, field survey was conducted to map the native land of the densest island by considering local resident perception. Table 1 shows the list of the data set used in this study.

2.1 Study area

Figure 2 shows the area coverage of the study area of the Seribu Islands. This administrative map was obtained from Indonesian Geospatial Agency in 2010. Based on the figure, Seribu Islands consists of 106 islands with names and 8 islands without names. The area of the islands ranged from 0.04 ha to 59.9 ha with an average area of 8.7 ha. Therefore, there are no rivers or springs on the Seribu Islands, which are sources of surface hydrology. Despite the size of the island being relatively small, most of this region was categorized as a low-lying area where the elevation ranged from 0 to 31.88 m with an average of 3.9 m above sea level (DEMNAS, 2018). Since it is located in the tropical region the temperature is almost similar throughout the year. The annual average rainfall and wind speed were 1888.74 mm and 4–10 m/s, respectively (BPS Seribu Islands, 2022). The highest precipitation rate and wind speed mainly occurred during the West monsoon (November to April), while dry condition occurs in the East Monsoon (June to September). The monsoon condition affects the daily life of local

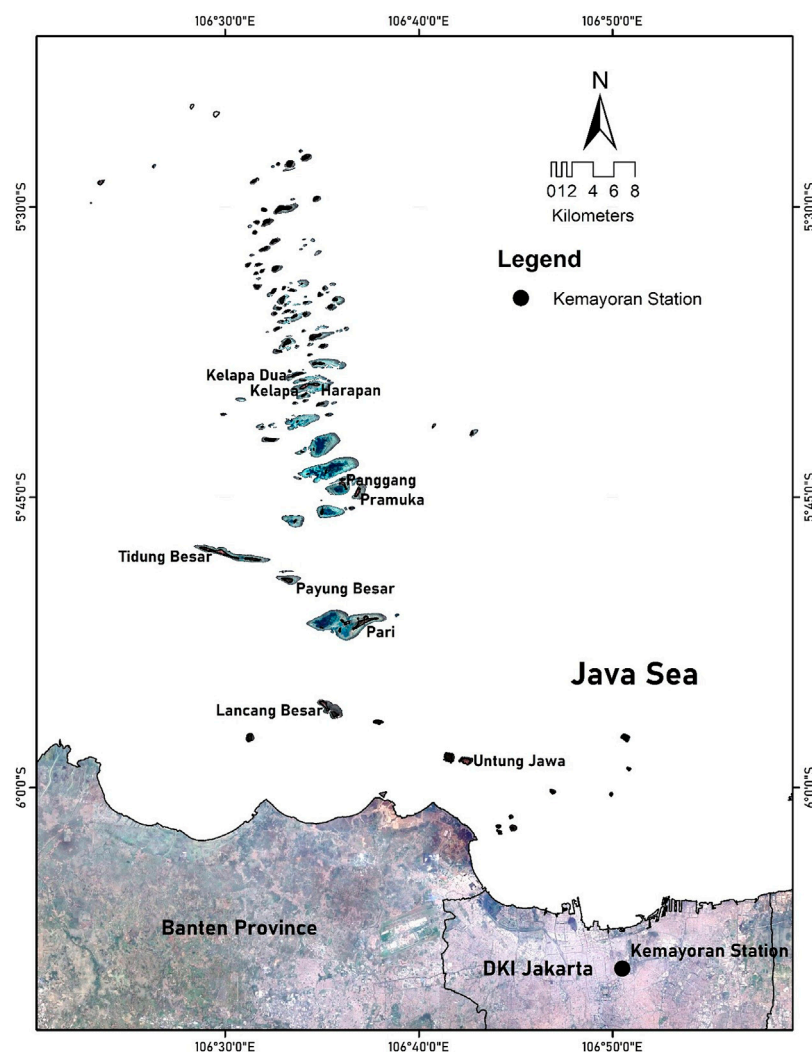


FIGURE 2

Map of the study area at Seribu Islands Complex, Jakarta. Basemap of Seribu Islands Complex: Sentinel 2A- 24 April 2021 and Sentinel 2B-28 July 2021.

communities in the regions that mostly relies their job on natural resources.

Seribu Islands has two main sub-districts: The North Seribu Islands and The South Seribu Islands. The population in the North is higher than in the South, but the population density in the South is higher than in the North (BPS Seribu Islands, 2022). Moreover, the population has increased by 30% from 2009 until 2021 (BPS DKI Jakarta, 2022), which means the population will double by 2045. This condition put heavy anthropogenic pressure on these small islands, affecting the coastal ecosystem and local communities.

2.2 Climate analysis

This paper utilized long-term daily climate data sets such as minimum temperature, average temperature, and maximum temperature from the Kemayoran climate station in Jakarta (Table 1). To visualize the trend of the air temperature in the study area, we conducted a moving average analysis with three

types of time scales (i.e., monthly, 12-month scale, and 60-month scales) and calculated the frequency of extreme temperature (i.e., percentile 90 and percentile 99). Moreover, in order to know the significant of the temperature trend, we utilized Mann-Kendal (MK) Test. Detailed on how to calculate the MK test can refer the equation from Kandya et al., 2021. This MK test is non-parametric test that has been suggested by the world meteorological organization (World Meteorological Organization, 2012b) due to its data distribution and outlier consideration (Nashwan and Shahid, 2018).

Since the precipitation amount and pattern have seasonal variation, we conducted the standardized precipitation Index (SPI) under the WMO 2012a methodology (WMO, 2012a) and the frequency of extreme precipitation (i.e., percentile 99) to determine the wet and dry levels and the possible impact. Moreover, we estimated the trend of sea level anomaly (SLA), as an impact of the anthropogenic global warming, around Seribu Islands by using satellite multi-mission altimeter data from the E. U. Copernicus Marine and

TABLE 1 The detailed dataset used in this study.

No	Category	Parameter	Time range	Source
1	Climate data set at Kemayoran station	Daily minimum temperature	1980–2021	Data online BMKG https://dataonline.bmkg.go.id/home
		Daily average temperature		
		Daily maximum temperature		
		Daily precipitation		
2	Satellite data set	Digital elevation model (DEM): 8 m of spatial resolution	2018	DEM nasional (DEMNAS) https://tanahair.indonesia.go.id/demnas/#/demnas
		Sea Level Rise: 0.25 degree of spatial resolution, with the specific area of (6S to 5S, 106E to 107E)	1993–2022	Copernicus marine environment monitoring service (CMEMS) https://marine.copernicus.eu/
		Land use: Google Earth time slider	2015–2022	Google Earth pro https://www.google.com/earth/versions/ Detail in Supplementary Table A6
		Land Expansion in Panggang Island: Google Earth yime slider	Dec 11, 2009 and Mar 10, 2022	Google Earth pro https://www.google.com/earth/versions/
		Base map study area sentinel 2B: 10 meters of spatial resolution	July 28, 2021	Copernicus open access hub https://scihub.copernicus.eu/dhus/#/home
		Base map study area sentinel 2A: 10 meters of spatial resolution	April 24, 2021	
3	Original land area	GPS data point of land area based on local community knowledge	25–29 July 2023	Field survey using Handheld GPSMAP 86i-Garmin
4	Literature review	Climate-related hazards	2015–2022	Supplementary Table A2 S1
		National and local policy	2010–2023	Google search engine with the following keywords: <i>RPJMD DKI Jakarta, RPJMD Kepulauan Seribu, Reinstra DKI Jakarta, Reinstra Kepulauan Seribu, Kebijakan Banjir rob, Kebijakan Kebakaran Hutan, Kebijakan angin putting beliung, Kebijakan abrasi, KLHK, Taman nasional, mangrove, ekosistem pesisir</i> (Table 3)
5	Interview	-Discussion with the national and local authorities in the Islands -Interview with 21 local communities in four islands (Pramuka Islands, Panggang Islands, Kelapa Island and Pari Island)	July 23–29, 2023	Supplementary Table A5

Environment Monitoring Service (CMEMS) (Table 1). This CMEMS dataset was recommended by Fenoglio-Marc et al. (2012) following the validity of the SLA trend from the dataset with the *in-situ* data from deep-water tide gauges around western Maritime Continent. For the shallow-water area, such as Seribu Islands, despite the overestimation of the SLA trend by the satellite data over the tide-gauges's, their range of uncertainties remain overlapped (Nurmaulia et al., 2010).

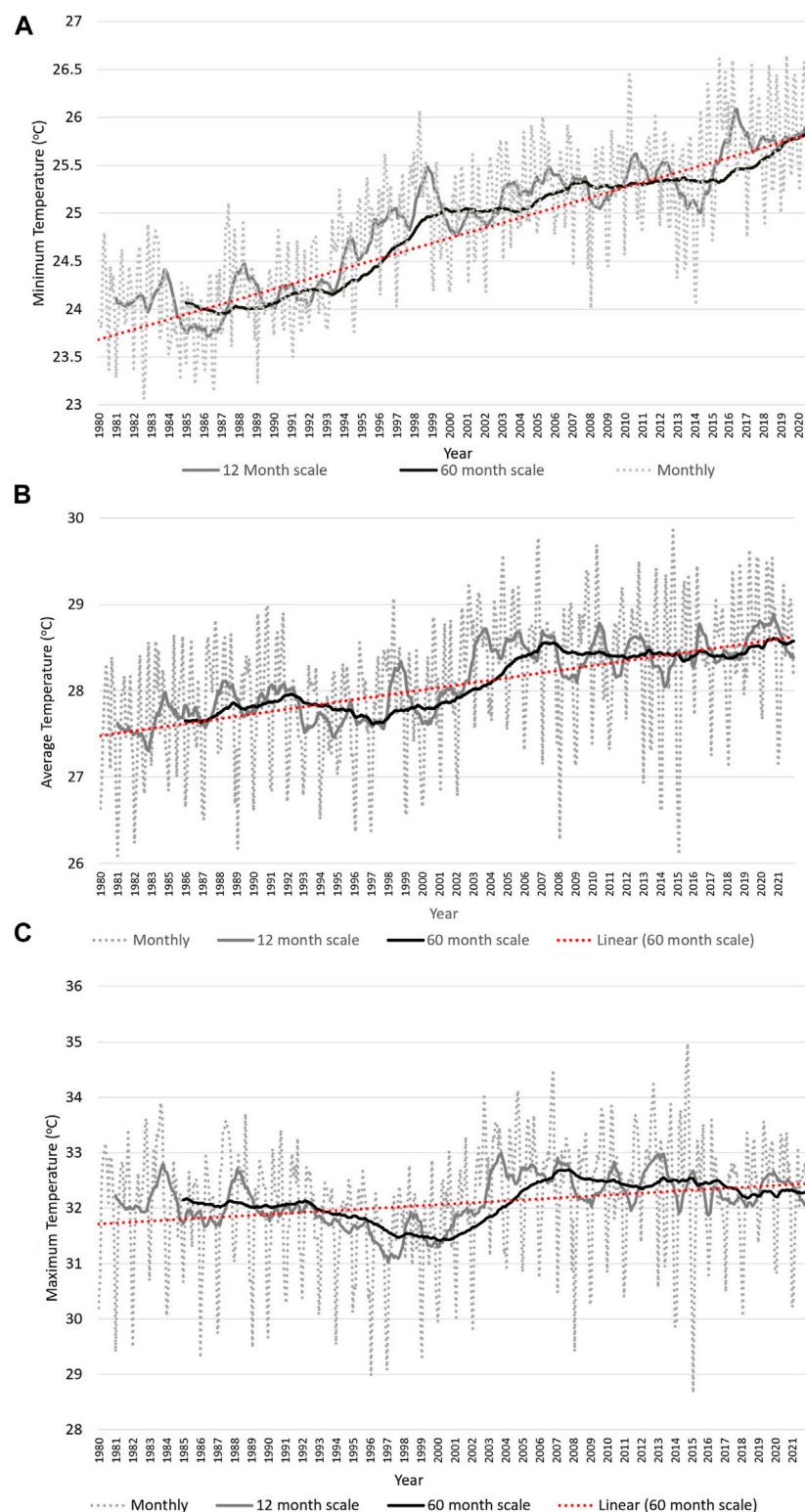
2.3 Potentially affected area

In this paper, we used five SLR scenarios; 1 m, 2 m, 3 m, 4 m, and 5 m, and utilized geographic information system (GIS) software (ArcGIS 10.8.2) to extract the inundation zone based on the DEM data set. We utilized this scenario because it was previously applied by the world bank for a global impact assessment report (Dasgupta et al., 2009; Pickering et al., 2017), and it also was due to the variation of the elevation of the region of interest. The dimension of the potentially affected area will be

the percentage of the affected area, number of populations, and number of missing islands.

2.4 Land cover and land expansion analysis

In this paper land cover analysis and land expansion analysis was conducted by digitizing the feature using Google Earth Pro. We utilized the latest recorded image of Google earth time slider in order to digitize the land cover (Detailed in Supplementary Table A6). The land cover analysis was only conducted in the inhabitant islands (ten islands), while land expansion analysis only was conducted in the most-dense island in the region (Panggang Island). Meanwhile for land expansion we did field survey for mapping the original land area based on local communities' perception (i.e., people who live more than 30 years within the region) and we digitized in the Google Earth Pro of the oldest very high-resolution image (2009) and the newest high - resolution image in the targeted areas (2022) (Table 1). Finally, all the dataset then converted to shapefile and proceed for land calculation in the Arc. GIS 10.8.2.

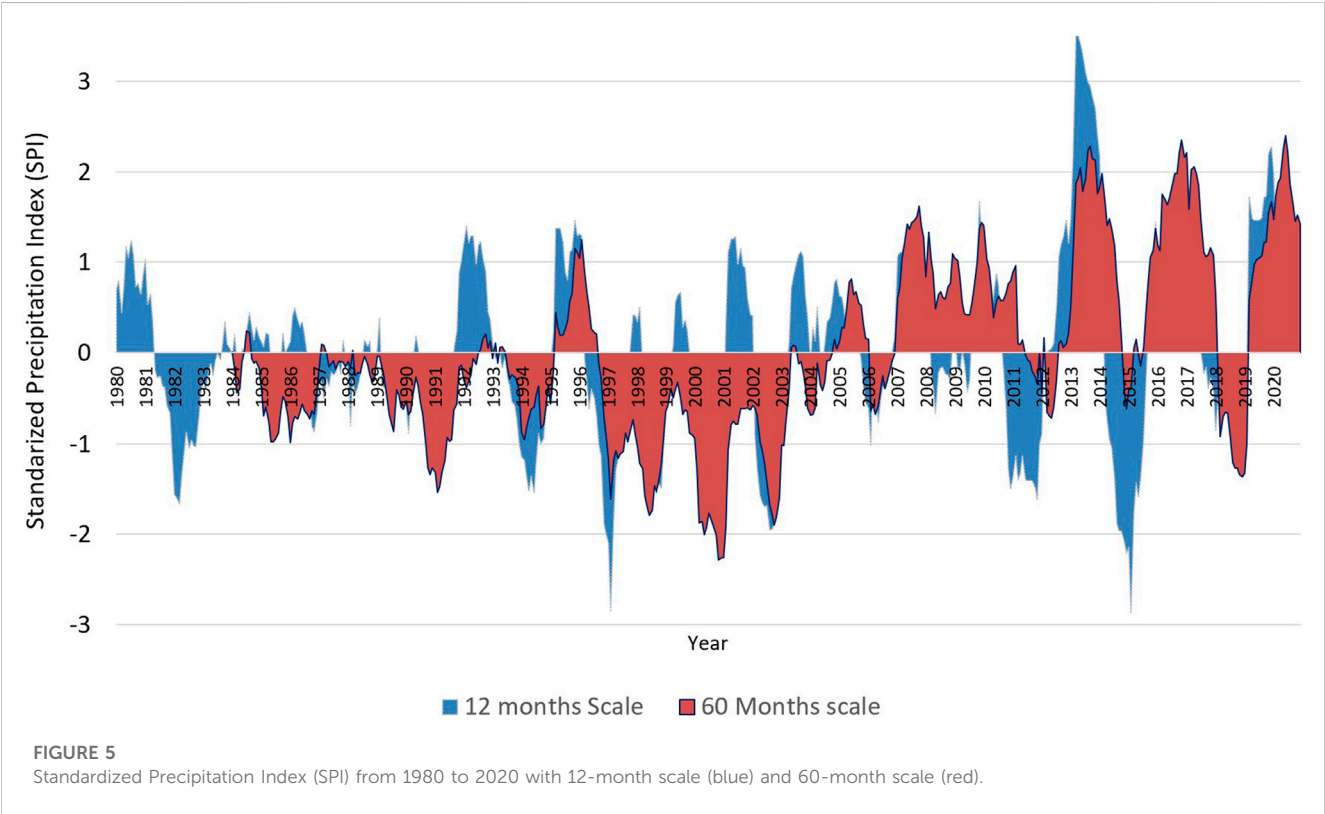
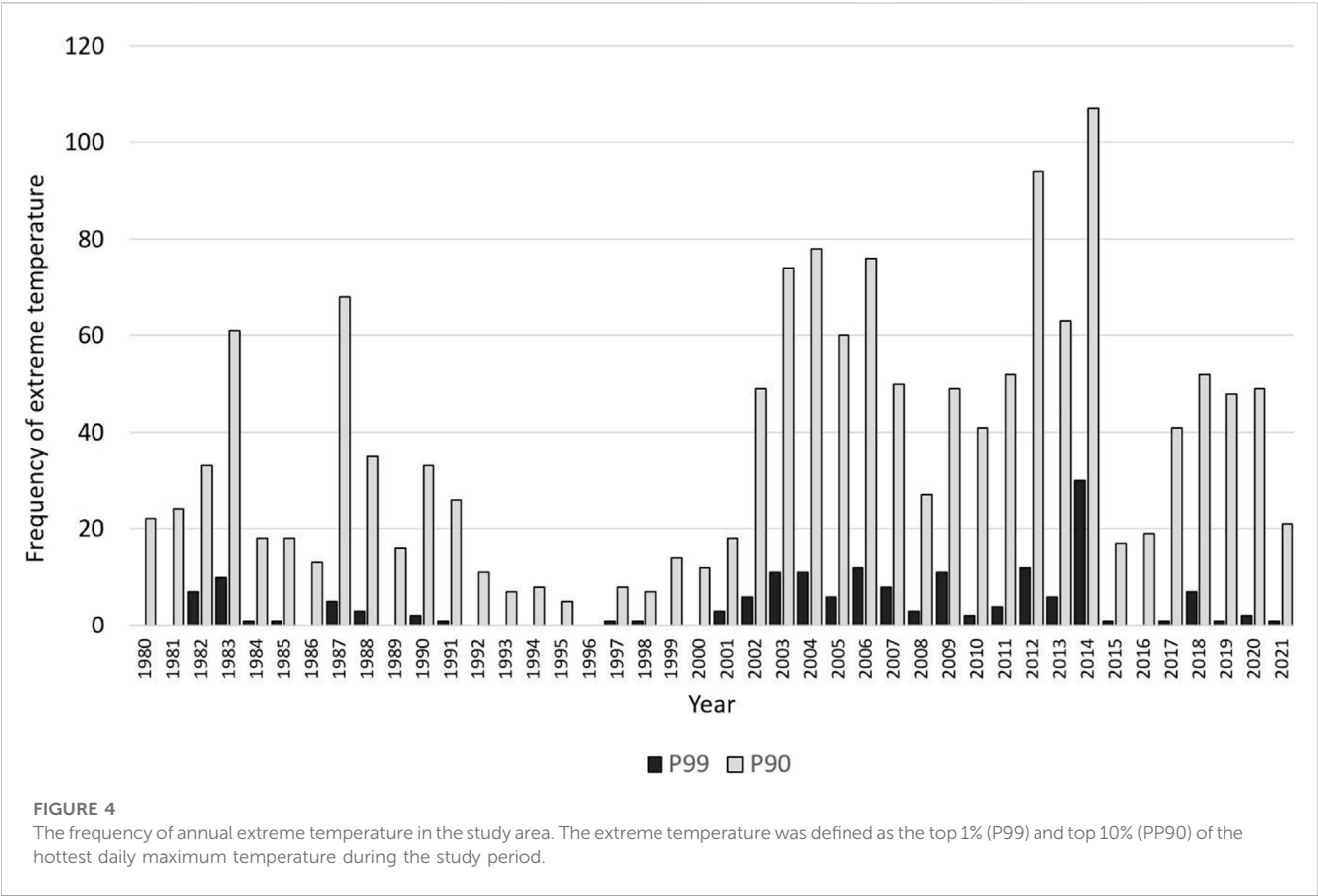
**FIGURE 3**

The minimum temperature (A), average temperature (B), and maximum temperature (C) trend from 1980 to 2021 in the study area.

2.5 Policy analysis

For the policy study, an assessment of the literature was carried out using the Google search engine. In this study, we didn't use a

scientific internet search engine to find the grey literature since most action plans usually exist in governmental development plan documents, governmental regulations, or project reports. Additionally, we limited our keyword searches to Bahasa



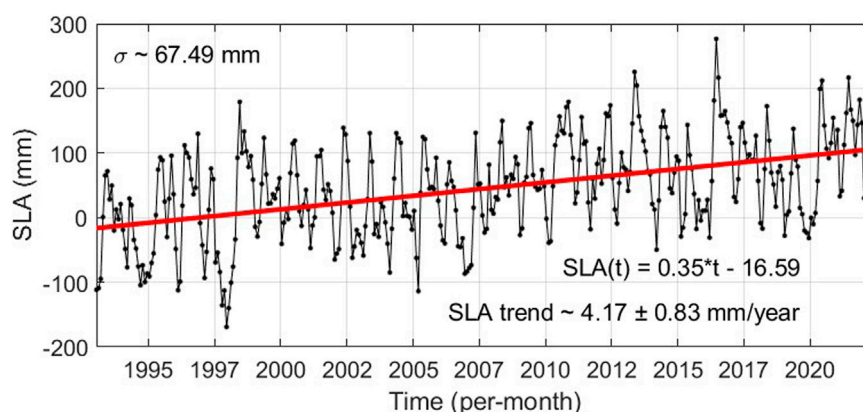


FIGURE 6

Monthly sea level anomaly (SLA) for the period of 1993–2022 from the CMEMS satellite altimeter dataset averaged around Seribu Islands area (6S to 5S, 106E to 107E). Red line is the long-term trend of the monthly SLA based on linear regression with its equation below it. The yearly trend is also presented with its range of uncertainty at 95% confidence level. Sigma is the standard deviation of the detrended SLA.

TABLE 2 Impact of sea level rise (SLR) in the study area. The calculation based on DEMNAS dataset.

SLR scenario	The affected area (%)	Number of islands that 100% inundated	People affected
Scenario 1 m	25.8	20	7285.92
Scenario 2 m	32.7	21	9234.48
Scenario 3 m	41.3	24	11663.12
Scenario 4 m	49.6	24	14007.04
Scenario 5 m	58.4	29	16492.16

Indonesia as the primary language since we focused on national and local policy intervention in disaster risk reduction. The following keywords were used in this study: RPJMD DKI Jakarta, RPJMD Kepulauan Seribu, Reinstra DKI Jakarta, Reinstra Kepulauan Seribu, Kebijakan Banjir rob, Kebijakan Kebakaran Hutan, Kebijakan angin putting beliung, Kebijakan abrasi, KLHK, Taman nasional, mangrove, ekosistem pesisir. Moreover, we also did a research dissemination and discussion to three representative of Kepulauan Seribu local authorities and one representative of the national park and deep interviews with 21 local communities in four islands (Panggang, Pramuka, Pari, and Kelapa Islands) from 23–29 July 2023 to qualitatively validate our climate hazard analysis and to know what kind of local authorities/communities action had been taken to tackle those disasters.

3 Results

3.1 Trends in temperature

Figure 3 shows the air temperature trend over 41 years period within the study area. As shown in the figure, the annual minimum, average, and maximum air temperature ranged from 23.9°C to 25.8°C, 26.1°C–29.9°C and 29°C–34.5°C, respectively. Moreover, based on the Man Kendall test, it can be inferred that the minimum, average and maximum temperature over the study

period has statistically significant of increasing trend at 99% confidence level [Supplementary Table A3](#). Moreover, Based on the linear regression of the 60-month scale of moving average analysis, the minimum temperature (Figure 3A) and average temperature (Figure 2B) have a strong tendency of an increasing trend with a correlation coefficient of 0.97 and 0.84, respectively. Meanwhile, the maximum temperature (Figure 3C) depicts a low tendency of warming trend with a coefficient correlation of 0.53, respectively. Also, the study area's minimum and average temperatures experienced an increasing trend of 0.05°C/year and 0.03°C/year. It means, from the initial year (1980) until 2021, the study area experienced a 1.4°C increase in average temperature and 2.2°C in minimum temperature, respectively.

Figure 4 depicts the annual frequency of extreme temperatures that occurred in Seribu Islands. The P99 and P90 define as the frequency of the top one percent (i.e., $\geq 35.2^{\circ}\text{C}$) and 10% ($\geq 34^{\circ}\text{C}$) hottest temperature during the study period. Based on Figure 4, almost every year, the study area experienced an extreme temperature of P90 and P99 with an average of 36 times/year and four times/year. However, the frequency of extreme temperatures (P90 and P99) is more frequent after the year 2002, with the peak occurrences in 2014 (i.e., P90 ~ 107 times/year and P99 ~ 30 times/year). Moreover, compared with the period of 1980–2001, the millennium period shows 150% and 324% of P90 and P99 more frequently, which means the frequency of potential natural disasters might double/triple. Also, based on the

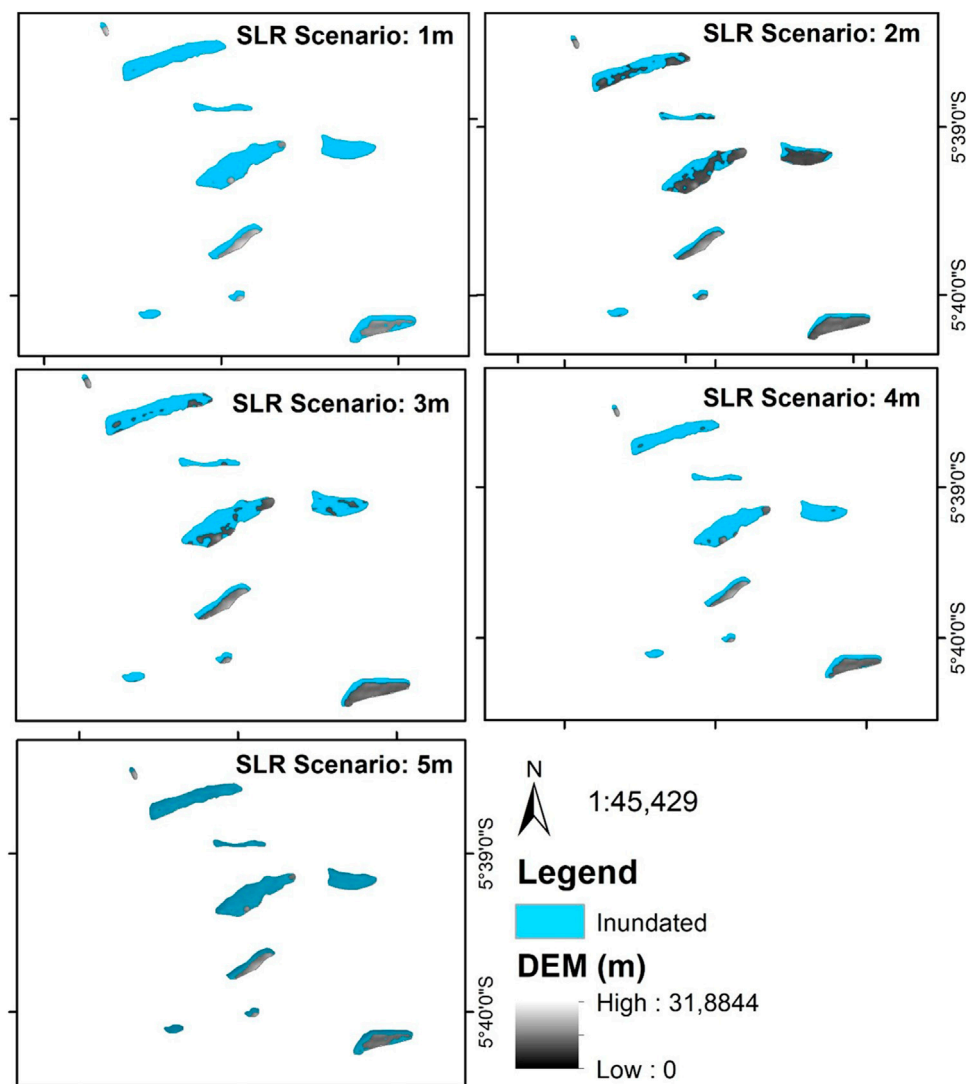


FIGURE 7
Simulation of inundation area from various SLR scenarios in Harapan dan Kelapa Islands. Basemap: DEMNAS 2018 with spatial resolution of 8 m

MK test depicted that the extreme temperature has statistically increasing trend over 41 years in the study area at confidence level of 95% (Supplementary Table A3).

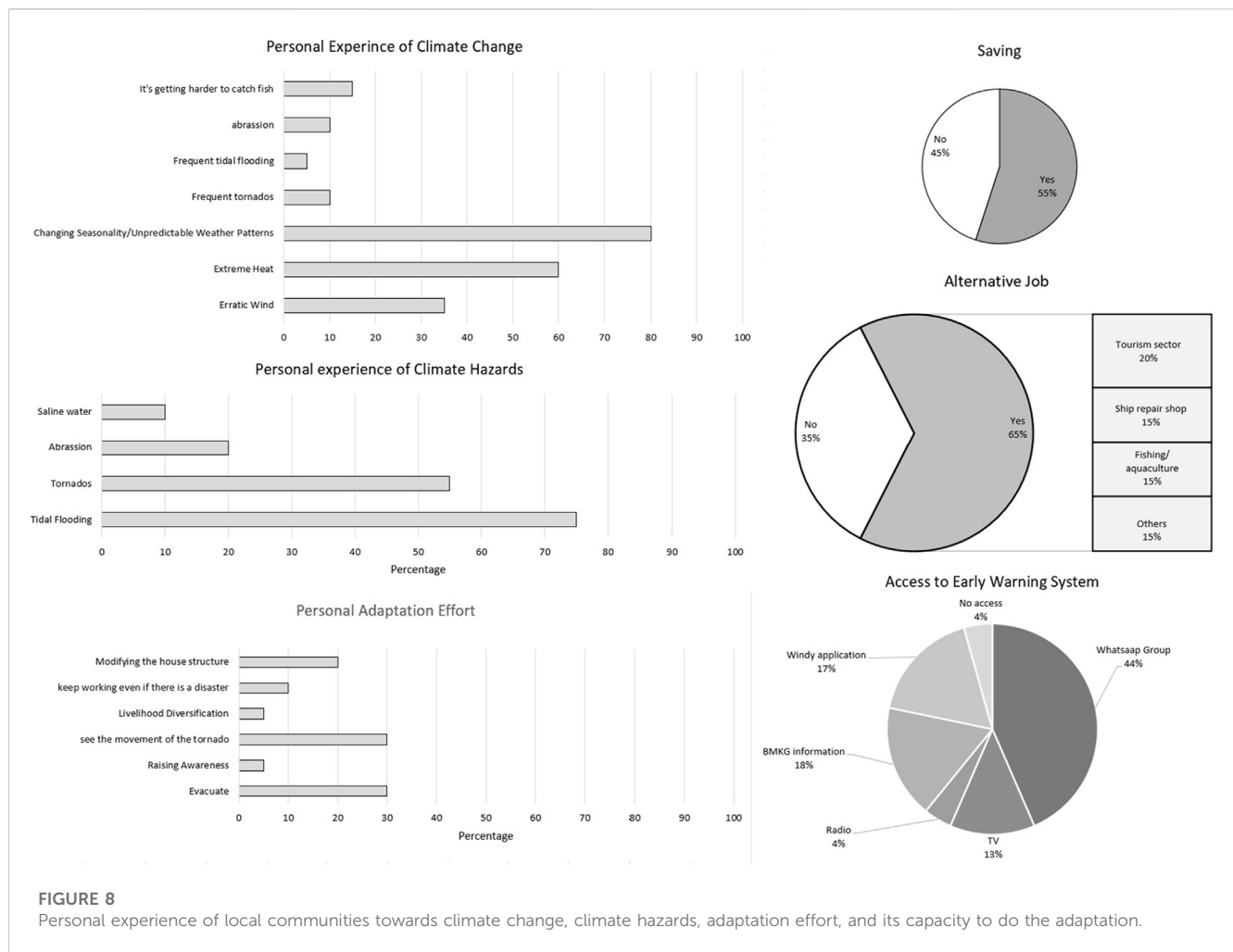
3.2 Trends in Standardized Precipitation Index

Figure 5 describes the wetness and the drought level in a certain period in Seribu Islands. The range of 12-month scale of the SPI index ranged from -3 to +3.5, which defined that the study area experienced extreme dryness (≤ -2) and extreme wetness ($\geq +2$). The annual extreme dry occurred in 1997/1998 and 2015/2016, while the extreme wetness occurred in 2013/2014 and 2020/2021. Moreover, the study area experienced a long-term wetness period (red color) from 2007 to 2021, where from 2013 to 2021 experienced three periods of extreme wetness. Meanwhile, from 1997 until 2013, the region continuously experienced moderate to extreme dryness levels

(red color). Moreover, in the period between 1980 and 1996, the study area depicts a normal condition (i.e., $-1 \leq \text{SPI} \leq 1$).

3.3 Sea level anomaly

Figure 6 shows SLA trend within the study area for 29 years based on CMEMS dataset. The figure shows that the study area experienced an increase of SLA of 4.17 ± 0.83 mm/year from 1993 to 2022 (Figure 6). The result generally indicated future SLA increases and showed a slow-rising trend. Furthermore, this research area has seen a rise in sea level of almost 150.8 mm since 1993. This number looks very small, but when it occurs during the spring tide or during the storm surge, the impact is adverse for the local communities (i.e., it exceeds 250 mm). Moreover, since the turn of the century, the global sea level has risen by around 178 mm, and by the end of the century, SLR may have risen by 0.3–1.8 m (Jevrejeva et al., 2016).



3.4 Impact of sea level rise

Therefore, we simulated the potential impact using some worst-case scenarios as introduced by Dasgupta et al., 2009; Pickering et al., 2017. Table 2 depicts the summary of SLR impact in Seribu Islands, and Figure 7 shows the simulations in three inhabitants islands (i.e., Harapan, Kelapa, and Kelapa Dua Island) under five SLR scenario. The result revealed that under a 1 m SLR scenario, 25.8% of the Seribu Islands area would be inundated, affecting about seven thousand people. Moreover, under this scenario, about 20 islands will disappear within the study area. Additionally, under a 5 m SLR scenario, about 29 islands will disappear, with about 16.5 thousand people will be affected.

Figure 7 depicts a simulation of nine islands in the study area; three have inhabitants. The blue color indicates the inundated area, while the grey gradation color presents the basemap of DEM. Among the three islands, Kelapa Islands has the highest population, followed by Harapan Island and Kelapa Dua Islands. In Kelapa Islands, under a 1 m SLR scenario, around 16.7% area will be inundated. Meanwhile, under a 2 m SLR scenario, nearly 43% of the site will be permanently inundated, which means about 2703 people would be severely affected. Moreover, in Harapan Island and Kelapa Dua Island, nearly 83% and 93% of the areas would be permanently inundated under the 3 m SLR scenario.

Kelapa, Kelapa Dua, and Harapan Islands were known as one of the main tourist destinations, especially for domestic visitors around Jakarta Capital City. For instance, in 2021, even during the pandemic, domestic visitors reached 22,251 people in those islands (BPS Seribu Islands 2022). Therefore, having permanent inundation on that island would create a massive economic loss for the coastal communities (i.e., major job losses, loss of properties, and massive migration to the mainland). Moreover, under the worst-case scenario (5 m), those three inhabitants' islands would disappear, and the condition would create the mainland of Jakarta city severely affected by sea level rise, storm surge, and salt intrusion due to no natural protection anymore.

3.5 Experience of local communities toward climate change

Figure 8 shows the descriptive statistics on how local communities experience the climate change along its capacity to cope the problem within the Seribu Island Complex. Based on the interview from 21 respondent from four different islands, all the respondent experienced the change of climate whereas most of them experience changing seasonality/unpredictable weathers followed by extreme heat, erratic winds and

TABLE 3 Summary of the national and local policy of each hazard type in the Seribu Islands.

Scale	Policy document	Notes/Action program	Type of climate hazard	Source
National	Government Regulation (PP) Number 64 of 2010	Disaster Mitigation in Coastal Areas and Small Islands	Tidal flooding, tornados, landslides, flooding, storm surge, abrasion, forest fire	Government Regulation (2010)
National	Perka BNPB No. 1 of 2012	General guidelines for disaster-resilient villages	Tidal flooding, tornados, landslides, flooding, storm surge, abrasion, forest fire	BNPB (2012)
National	Ministry of Public Works And People's Housing Strategic Plan For 2020–2024	Mainly focused on the main island of the northern part of Java. The small island has not yet become a national target	Tidal Flooding	PUPR (2020)
National	Regulation of The Minister of Environment and Forestry No. p.7/Menlhk/Setjen/Otl.0/1/2016	The Seribu Islands National Park Management Section is in charge of controlling forest fires	Forest Fire	KLHK (2016)
National	Perka BMKG (Meteorological, Climatological, and Geophysical Agency of Republic of Indonesia) No. Kep. 009 of 2010	Standard operational procedures for implementing early warning, reporting, and dissemination of extreme weather information	Tornados, cyclone, flash flood	BMKG Regulation No.9 (2010)
Province	Mid-term Development Plan (RPJMD) of DKI Jakarta 2017–2022	Tidal flooding has become one of the strategic issues for DKI Jakarta Province	Tidal Flooding	Jakarta (2018a)
		Extended the conservation of marine ecosystem area by 2.5 Ha in Seribu Islands	Tidal Flooding, Tornados, abrasion, storm surge	
Province	Mid-Term Development Plan (RPJMD) of DKI Jakarta Province 2023–2028	Disaster resilience has become the top strategic issue within DKI Jakarta Province	Tidal flooding, tornados, landslides, flooding, storm surge, abrasion, forest fire	Jakarta (2018b)
		In 2020, 31 Automatic Weather System (AWS) was installed in DKI Jakarta, including in the Seribu Islands	Tidal flooding, tornados, landslides, flooding, storm surge	
		As of June 2021, Mangrove planting has reached 54.28% or around 38,000 trees in Seribu Islands	Tidal Flooding, Tornados, abrasion, storm surge	
		The Seribu Islands serve as a center for ecological conservation	Tidal Flooding, Tornados, abrasion, storm surge	
		Biodiversity Management Program (Kehati) in Seribu Islands Indicator: Percentage of Green Open Space Managed by District Administration)	Tidal Flooding, Tornados, abrasion, storm surge	
		Preventing Coastal Abrasion in Seribu Islands	Abrasion	
		Disaster mitigation program	Tidal flooding, tornados, landslides, flooding, storm surge, abrasion, forest fire	
Regency	Mid-term Strategic Plan (Reinstra) of Seribu Islands Regency 2017–2022	Mitigation efforts in natural disaster	Tidal flooding, tornados, landslides, flooding, storm surge, abrasion, forest fire	Seribu Island Government (2018)
Regency	Mid-term Strategic Plan (Reinstra) of Seribu Islands Regency 2023–2026	Mitigation efforts in natural disaster	Tidal flooding, tornados, landslides, flooding, storm surge, abrasion, forest fire	Seribu Island Government (2023)

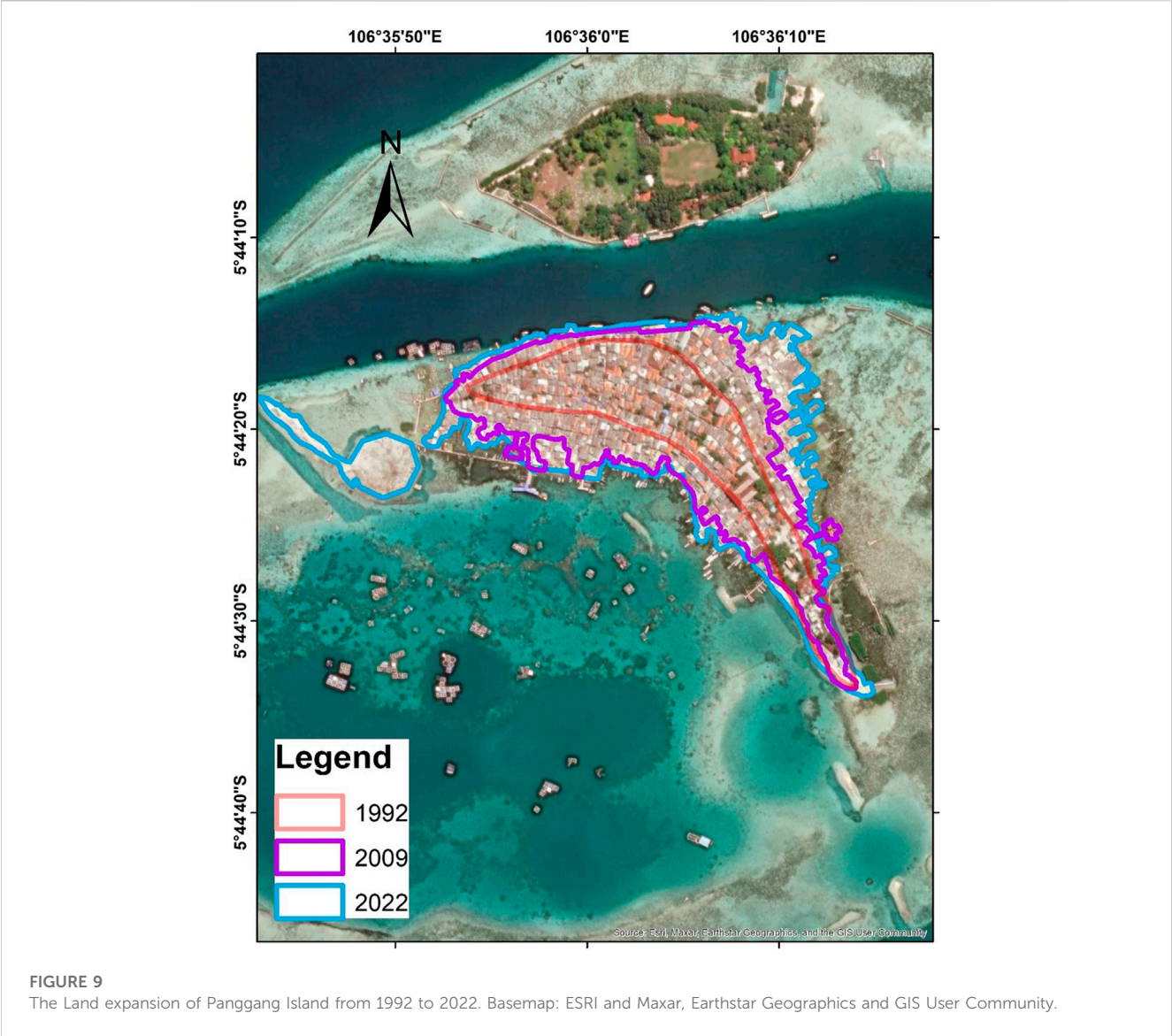
frequent climate hazards. Moreover, tidal flooding and tornados were the most common severe climate hazards faced by the local inhabitants. Since the climate hazards were frequent hit the islands, the local communities did the adaptation effort as follows: pay attention with the movement of tornados, evacuate in the safer place and modifying the house structure. However, not all local communities are resilient of climate severe climate hazards since 45% and 35% of the respondent does not have saving and job alternative and 4% responded did not have access to early warning system. Furthermore, nearly half of respondent received the early warning system from Whatsapp group followed by BMKG information and Windy application.

3.6 National and local regulations on minimizing the impact of climate hazards

Table 3 depicts the national and local policy/commitment on mitigating the climate hazards within the study area. In this study, the climate hazards was referred to threats posed by the climate and weather condition such as tidal flooding, cyclone, tornados, flooding, forest fires etc. (Setiawati et al., 2023a). According to the Table 3, the regulation regarding specified climate hazard preventing and mitigating program mostly issued by the national government such as forest fire, tidal flooding and extreme weather. In case of abrasion and tidal flooding, the provincial government put an extra effort to

TABLE 4 The built-up area coverage in the inhabitants (local communities and oil company) islands.

Island name	Green space (Ha)	Build up area (Ha)	Built-up (%)
Pari	44.14	9.20	17.65
Lancang Besar	15.24	16.58	56.88
Untung Jawa	23.77	13.1	35.68
Tidung Besar	28.787	30.38	47.67
Pramuka	9.01	19.03	67.87
Kelapa and Harapan	13.53	36.93	73.19
Panggang	0.70	16.63	95.96
Payung Besar	27.59	1.33	4.6
Kelapa Dua	2.76	2.71	49.54
Pabelokan (oil company)	7.31	6.18	45.81



tackle the problem within Seribu Islands complex; whereas they put tidal flooding as the top priority issues and various provincial government program to reduce the risk of those hazards. However, at the district level development program, they mainly worked on the general disaster management such as providing the basic needs after the disaster, raising awareness, cross-sectoral coordination during/after the disaster, and conducting data collection. According to Mid-term Strategic Plan (Reinstra) of Seribu Islands Regency 2023–2026, there is two main climate hazards that pose severe impacts within the region; tornados and tidal flooding. However, the specific national regulation or provincial mid-term development program have not addressed this issue yet.

4 Discussion

4.1 Increasing trend of air temperature

The primary objective of this study was to reveal the local evidence of climate change and its potential impact on the Seribu Islands. The study shows that these islands were exposed to a significant increase in air temperatures and the frequency of extreme temperatures during the study period (Figures 3, 4). The IPCC, 2022 suggests limiting the warming temperature to below 2°C by 2030. However, the study area experienced a warming temperature of 2.2°C by 2021 (Figure 3A) and without any significant policy change, the temperature will continue to increase. This warming temperature also exist in other small islands region in the tropical region, such as Bintan Island (Setiawati et al., 2023b); Mauritius Island (Doorga, 2022); Carribean SIDS (Taylor et al., 2018) and other small Island states (Nurse et al., 2001). The study also revealed that the frequency of extreme temperatures of P99 since 2002 was almost 3.5-fold more often than in the year between 1980 and 2001 (Figure 4). This condition implies that the pilot study will face more frequent and severe climate-related hazards.

We also interviewed local communities in four islands within the region, and 60% of the respondents said that it is tough to live within the islands without air conditioner (AC) (Figure 8). Also, the weather is getting hotter, even at night. Moreover, 80% of Panggang and Kelapa Islands respondents confirmed that the weather is getting hotter and uncomfortable both day and night, which caused increasing electricity bills. The increase in the minimum and the extreme temperatures significantly contribute to heat stress. Obradovich et al. (2017) stated that the increasing minimum temperature causes insufficient sleep to the 765 thousand respondents of US citizens. This sleep deprivation has an implication for lower productivity at work (McKibben et al., 2010), increasing Posttraumatic Stress Disorder (PTSD) severity (Brown et al., 2011), and the mortality rate (Cappuccio, 2010). Moreover, a recent study by Samaniego-Rascón et al. (2019) revealed that compared to typical days, the extreme heat stress level could accelerate the risk of death by 43%, where the elderly population, people without education, and outdoor workers are among the most vulnerable inhabitants. Considering the

socio-economic condition of the islands where 82.7% of inappropriate roof types that were worsening the indoor temperature environment (BPS Seribu Islands 2022), 94.7% of outdoor workers (BPS Seribu Islands 2022), and 17% of the vulnerable age group (BPS Seribu Islands., 2022), the region has big exposure and sensitive demographic condition toward thermal stress (Setiawati et al., 2023a).

4.2 Change in precipitation and mean sea level

Despite the extreme heat stress, the study area is also vulnerable to frequent coastal flooding, drought and tornados, as shown in Supplementary Tables A2, A5. According to the SPI index of 60-month scales, the study area experience long-term moderate to extreme wetness from 2007 until 2021 and moderate to extreme dryness from 1997 to 2004 (Figure 5). Previous study also revealed that extreme precipitation significantly influences island countries and is frequently linked to flooding and tropical storms (Khouaki et al., 2017; IPCC 2018). This condition is also supported by the Supplementary Table A1, which states that extreme precipitation is more frequent from 2013 until 2021. Moreover, the study area also faced a slow onset phenomenon called an increasing trend sea level anomaly (Figure 6).

These conditions imply that the study area also faced frequent climate-related hazards during recent years, particularly coastal flooding and tornados (Supplementary Table A2). Moreover, all respondents in the Pari Islands stated that they experienced frequent coastal flooding (5–8 times a year) recently, with the worst flooding in 2022, where the inundation depth ranged from 10 cm to 130 cm (Supplementary Table A2). Also, nearly 80% respondents in Pari Islands confirmed that there is massive abrasion of terrestrial land in Pari Island due to the sea level rise (Supplementary Table A5). The local respondent also stated that the sea level rise, abrasion and coastal flooding in this island decreased the water quality for freshwater supply, increased the cost for having the water (i.e., purchasing reverse osmosis water and bottle water), and killed the terrestrial plant. This condition also reported by previous studies which states that the ratio of fresh water availability and water demand decreased by 67%, while water quality decreased significantly (Wulan et al., 2023).

On the other hand, in Kelapa Island, all the respondents experienced tornados in recent years, whereas last year, they experienced three times a year. Most of the respondents said that in the past, there was no such frequent coastal flooding and tornados on Pari Island and Kelapa Island, and they could predict the west and east monsoon seasons. However, after 2000, they could not expect the season anymore (Figure 8), so it is hard for them to plan proper fishing activities, do home business for women, have more risk to go to the sea for the fisherman, and increase fishing capital costs. Increasing extreme condition, unpredictable season and slow onset phenomenon (i.e., abrasion and sea level rise) also faced others small island region such as Bintan Islands (Setiawati et al., 2023b), Solomon Islands (Albert et al., 2016), Micronesia (Nunn et al., 2017), Carribean Islands (Oberle et al., 2017).

Seribu Islands consist of 116 islands, but in this paper, we only analyze 114 islands (Figure 2) due to data limitations of DEM

dataset. The land area ranged from 0.05 ha to 59.9 ha, and among 114 islands, only two islands have a land area larger than 50 ha, and only 10 islands have inhabitants. The small island states are the most vulnerable to climate change considering their size, elevation, and climate variability. As the SLR scenario of 2 m (Table 2), the islands with inhabitants will mostly be inundated since the average elevation of those islands is 2.4 m above the sea level, and under the 3 m SLR scenario, all inhabitant's islands will be fully inundated (Figure 7). Since those islands have low-land areas with mostly dense built-up areas (Table 4), the area will face an economic loss due to frequent coastal flooding or other related climate hazards. Particularly, Panggang Island, Harapan Island, Kelapa Island, Pramuka Island, Pabelokan Island, Tidung Besar, Lancang Besar and Kelapa Dua face a serious impact of climate change because the built-up area occupancy was over 45%, respectively (Table 4). Those local communities not only have an economic loss due to the direct impact but will also face cascading effects such as waterborne diseases, respiratory diseases, etc. (Setiawati et al., 2023a).

4.3 Adaptation measures by local authorities and communities

As stated above, the Seribu Islands face a severe risk of climate change (Figures 3–8; Tables 2, 4). Moreover, the mid-term strategic plan document (Reinstra) for 2017–2022 and Reinstra for 2023–2026 stated that climate-related hazards are the primary challenge of the mid-term development plan within the region (Seribu Island Government, 2018; Seribu Island Government, 2023). Therefore, tackling climate-related hazards was one of the main strategic issues in this area. However, the association between the issue, policy direction, and action to reduce natural disaster risk was not coherent. That incoherency was clearly stated in the performance indicators for each stated program/action (Seribu Island Government, 2018; Seribu Island Government, 2023). For instance, the index of public satisfaction with public services and the number of disaster victims who received fast food are the main indicators for the disaster mitigation program (Seribu Islands Government 2020), which is only short-term problem-solving. Mainstreaming the issue of natural disaster mitigation in the Reinstra is a good start, but achieving resilient communities toward climate change through those actions was not enough.

As a small island district with high exposure to climate change hazards, this region should have its own Regional Disaster Management Agency (BPBD) and not only rely on BPBD Jakarta main island since Seribu Islands has different geographic features and challenges. So, having its own BPBD is necessary so that the region has its own local assessment of potential risk due to the disaster and has good planning both for prevention and mitigation of climate hazards as other small island districts did in Indonesia (e.g., Bintan, Natuna, East Flores, etc.). Moreover, in the Jakarta Midterm Development Planning Agenda of 2017–2022 (RPJMD), the issue of climate-related hazards only focused on the main island of Jakarta

Province, and the issue of climate change only focused on mitigation (reducing greenhouse gases emissions) without considering the adaptation action (Jakarta., 2018a; Jakarta, 2018b). The neglect of adaptation issues can be seen from the unavailability the long-term of *in situ* climate data measurement stations within the island complex which can record daily temperature, precipitation, wind speed, tide, and humidity. This *in-situ* climate data is crucial since the area is an archipelagic district that the communities have to commute on a daily basis by vessel where accurate weather prediction is necessary for safety reasons. Moreover, having local climate data is also essential for developing an early warning system for climatic hazards, which benefits local communities, commercial entities, and tourists. Developing a proper early warning system is highly suggested by the IPCC Working Group 1 and II (Lal et al., 2012).

Despite the unavailability of the District level of BPBD, the provincial government put a lot of effort into tackling the climate change impact on the Seribu Islands in the current RPJMD (Table 3), which includes hard infrastructure (i.e., installed Automatic Weather System, coastal abrasion program, tidal flood mitigation program), ecosystem-based approach (i.e., mangrove planting, deciding the region as center for ecological conservation) and soft technique (i.e., rising awareness, strengthening the adaptive capacity for local authorities). Seribu Islands have two main climate hazards: tidal flooding and tornados (Seribu Island Government. 2023). However, most of the effort from the local authorities was to tackle tidal flooding and abrasion; this commitment was reflected by the construction of concrete sea walls along the inhabitant islands (Table 3), building a breakwater, constructing infiltration wells, constructing water canals, constructing rainwater tanks, creating portable pumps for tidal flood defences, creating vertical drainage to handle local rainfall, and creating floodgates to regulate tides (Supplementary Table A5). However, national and local governments did not pay serious attention to tornados that frequently hit the Seribu Utara sub-district, even though this disaster caused severe damage in 2008, 2012, 2014, 2016, 2017, and 2018 (Supplementary Table A2).

As mentioned above, the study area also experienced the abrasion which indicated by the shoreline changes. For example, in Tidung Island, the abrasion caused a 6.4 ha land mass loss from 1913 to 2007 (Farhan and Lim, 2011). Moreover, in the Western and Eastern land area of Pari Island was lost about 4.1 ha from 1999 to 2017 (Farhan and Lim, 2011). Therefore, to overcome the problem the local authorities built the concrete seawall and breakwater and national and local authorities as well as local communities did massive mangrove planting in Pramuka island, Rambut Island and Pari Island. Even the mangrove planting was targeted by the local government in the RPJMD 2023–2026 and this is part of ecosystem-based approach (EBA) to climate change adaptation. This EBA is a sustainable way to minimize the risk of climate change and increase the resilience of the local communities (Colls et al., 2009). A proper mangrove planting is one of the ideal adaptation strategies since it does not have no-regret strategies, a flexible approach (one program can achieve multiple targets), involve local communities, multi-partner strategy development, and apply an adaptive management approach (Colls et al., 2009).

4.4 Challenges on local adaptation

The Seribu Islands experienced abrasion and did land expansion, particularly in the densely populated island (i.e., Panggang Island). No residents want to migrate outside the island, while population growth in these locations is high with very dense area (Table 4). So, the local communities did self-reclamation using organic rubbish and reef stone, which has been taking place for over 30 years (Figure 9, Supplementary Tables A4, A5). Therefore, the land area was expanded nearly 165% from 1992 to 2022, as shown in Figure 9. Before 2009, land reclamation was conducted on both sides (West and East). Still, since 2009, they reclaimed the land toward the east since the eastern side has yet to be built by the seawall, and the depth of the beach is relatively shallow. When the local government does not act decisively to stop the reclamation, most of the benthic habitat around the area (i.e., seagrass and coral reef) will disappear in the future and be replaced by the built-up areas.

Moreover, the under-control self-reclamation sacrifices the ideal marine ecosystem health in the region, which also influences the surrounding island communities for their economic income. For instance, the sand area (underwater) on Panggang Island was reduced significantly and transformed into seagrass, followed by deep sea water, and disappeared (Ningsih et al., 2021). Moreover, since 2000, the seaweed cultivation business in Panggang and Pramuka Island has entirely stopped because the yield has decreased due to the poor quality of the environment (Bahri et al., 2017) (Supplementary Table A5).

Due to the island's small size, the high exposure to climate hazards, and the locals' unwillingness to leave the area, Seribu Island residents have had to adapt intensively by maintaining or expanding their islands to prevent them from being eroded by sea waves. Pramuka Island and Pari Island are two islands that decided to grow mangroves since 2004 to prevent abrasion and retain silt (Supplementary Table A5). In contrast, Panggang Island takes particularly active measures to complete its reclamation (Figure 9, Supplementary Table A4). Also, locals attempt to diversify their employment in the previously dominated fishing industry service sector (Figure 8). Without considering any consequences, the local community's adaptation is categorized as a reaction to incidental activity (Shahid et al., 2021).

Local authorities put climate change as the severe challenge for Seribu Islands in their mid-term development planning agenda. However, there needed to be more consistency between the effort taken and the severe climate hazard the local communities faced. For instance, tornadoes in the Northern part of Seribu Island are crucial hazards that need to be addressed to reduce the risk; however, local authorities did not mention specific efforts in their development planning agenda. Moreover, massive mangrove planting that has been carried out since 2004 needs to be evaluated. Some local communities complained they could not see the sea scenery and enjoy the cool weather because dense mangrove forests blocked it. Moreover, law enforcement on illegal self-reclamation by reef stone must be realized since fringing reefs, coral reefs, and seagrass are vital to reducing the force of waves and currents around the coastal region.

5 Conclusion

This paper highlights the importance of understanding the effects of climate change on small islands and identifying appropriate local solutions. Based on the long-term climate data and spatial analysis results, Seribu Island faces a severe threat of climate change, such as accelerating air temperature, frequent extreme events, increasing SLR, massive land expansion in Panggang Island and under the worst-case scenarios one-quarter of the islands complex will be fully inundated in the future. The analysis of the significant threat of climate change within the study area helps us to 1) identify the main climate hazards faced by the local inhabitants in different islands and 2) urge the need for real-time weather station within the islands complex along with the real-time early warning system 3) urge the need of having district-level BPBD 4) align local populations' needs for additional land with those of natural capital, protect natural ecosystems, and use their ecosystem services to face climate change. A limitation of the present study was the unavailability of a long-term climate data ground station within the islands complex; therefore, we utilized the closest station to the study area. Moreover, we only involved twenty-one local communities who were spread over four islands, one national authorities and three local authorities as our objective was to obtain a thorough understanding of their individual experiences of climate change and its capacity to cope with the problem rather than to reach statistical significance. For future research, it is necessary to have more quantitative analysis for future projections of climate data sets and combine it with the socio-economic vulnerability analysis. Then, an integrated risk assessment that considers the role of natural capital, climate change scenarios, and local communities within the study area could be built for future studies.

Data availability statement

The original contributions presented in the study are included in the article/Supplementary Material, further inquiries can be directed to the corresponding author.

Author contributions

MS: Conceptualization, Data curation, Formal analysis, Funding acquisition, Investigation, Methodology, Supervision, Validation, Visualisation, Writing-original draft, Writing-review and editing. UC: Conceptualization, Methodology, Writing-review and editing. YD: Formal analysis, Investigation, Visualisation, Writing-review and editing. LA: Investigation, Formal analysis, Visualisation. MN: Investigation. HR: Investigation. IS: Investigation, Writing-review and editing. NH: Investigation, Validation, Visualisation. AM: Conceptualization, Funding acquisition, Writing-review and editing. TE: Writing-review and editing. BP: Investigation, Supervision. AO: Investigation. NA: Writing-review and editing. JR: Investigation. SS: Investigation, Project administration. SW: Investigation,

Writing–review and editing. SCP: Writing–review and editing. AI: writing–review and editing. EA: writing–review and editing. MI: writing–review and editing.

Funding

The author(s) declare financial support was received for the research, authorship, and/or publication of this article. Research Funding: Asia Pacific Network for Global Change Research-CRRP2022-06MY-Muslim project. This work was financially supported by the Deanship of Scientific Research at the King Faisal University, Saudi Arabia (grant: 4,060).

Acknowledgments

We would like to thank Asia Pacific Network for Global Change Research for funding this research under the CRRP 2022-06MY-Muslim project. We also thank to Wanda Andella Putri for digitizing the land area of Panggang Island.

References

- Albert, S., Leon, J. X., Grinham, A. R., Church, J. A., Gibbs, B. R., and Woodroffe, C. D. (2016). Interactions between sea-level rise and wave exposure on reef island dynamics in the Solomon Islands. *Environ. Res. Lett.* 11 (5), 054011. doi:10.1088/1748-9326/11/5/054011
- Bahri, A. D., Hamdani, A., and Wibowo, A. (2017). Di balik krisis agraria dan ekosistem kepulauan Seribu: apakah wisata bahari adalah jawabannya. https://terbitan.sajogyo-institute.org/wp-content/uploads/2017/08/Laporan-Final-Seribu_Draft-0_2017-April-28.pdf.
- BMKG Regulation No.9 (2010). Peraturan kepala badan meteorologi, klimatologi, dan geofisika tentang prosedur standar operasional pelaksanaan peringatan dini, pelaporan, dan diseminasi informasi cuaca ekstrim [regulation of the head of the meteorology, climatology and geophysics agency concerning standard operational procedures for implementing early warning, reporting and dissemination of extreme weather information]. <https://peraturan.bpk.go.id/Home/Details/191418/perka-bmkg-no-kep9-tahun-2010>.
- Bnpb. (2012). PEDOMAN UMUM DESA/KELURAHAN TANGGUH BENCANA (General guidelines for disaster-resilient villages). <https://bnpb.go.id/storage/app/media/uploads/24/peraturan-kepala/2012/perka-1-tahun-2012.pdf>.
- BPS DKI Jakarta (2021). Tabel dinamis subjek indeks pembangunan manusia (table on human development index). <https://jakarta.bps.go.id/subject/26/indeks-pembangunan-manusia.html#subjekViewTab5>.
- BPS DKI Jakarta (2022). Persentase penduduk miskin menurut kabupaten/kota di Provinsi DKI Jakarta (persen), 2020–2022. <https://jakarta.bps.go.id/indicator/23/1125/1/persentase-penduduk-miskin-menurut-kabupaten-kota-di-provinsi-dki-jakarta.html>.
- BPS Seribu Islands (2022). Seribu islands regency in figures. <https://kepulauanseribukab.bps.go.id/publication/2022/02/25/6565bcc5c12b74dbfcbcf17/kabupaten-kepulauan-seribu-dalam-angka-2022.html>.
- Brown, T. H., Mellman, T. A., Alfano, C. A., and Weems, C. F. (2011). Sleep fears, sleep disturbance, and PTSD symptoms in minority youth exposed to Hurricane Katrina. *J. Trauma. stress* 24, 575–580. doi:10.1002/jts.20680
- Cahyarini, S. Y., Zinke, J., Troelstra, S., Aldrian, E., and Hoeksema, B. W. (2016). Coral Sr/Ca-based sea surface temperature and air temperature variability from the inshore and offshore corals in the Seribu Islands, Indonesia. *Mar. Pollut. Bull.* 110, 694–700. doi:10.1016/j.marpolbul.2016.04.052
- Cappuccio, F. P., and D'Elia, L. (2010). Sleep duration and all-cause mortality: a systematic review and meta-analysis of prospective studies. *Sleep Durat. all-cause Mortal. a Syst. Rev. meta-analysis Prospect. Stud.* 33, 585–592. doi:10.1093/sleep/33.5.585
- Change, I. C. (2014). Impacts, adaptation and vulnerability. Part A: global and sectoral aspects. Contribution of working group II to the fifth assessment report of the intergovernmental Panel on Climate Change 1132. <https://www.ipcc.ch/report/ar5/wg2/>.
- Clar, C., and Steurer, R. (2019). “Climate change adaptation at different levels of government: characteristics and conditions of policy change,” in *Natural resources forum* (Hoboken, New Jersey, United States: Online Library), 121–131.
- Colls, A., Ash, N., and Ikkala, N. (2009). *Ecosystem-based Adaptation: a natural response to climate change*. Switzerland: Iucn Gland.
- Dasgupta, S., Laplante, B., Meisner, C., Wheeler, D., and Yan, J. (2009). The impact of sea level rise on developing countries: a comparative analysis. *Clim. Change* 93, 379–388. doi:10.1007/s10584-008-9499-5
- DKI Jakarta Government (2018). Mid-term development plan of DKI Jakarta 2017–2022. Access on [https://bappeda.jakarta.go.id/rpjmd/September 6, 2023](https://bappeda.jakarta.go.id/rpjmd/September%206,%202023).
- DKI Jakarta Government (2023). Mid-term development plan of DKI Jakarta province 2023–2028. Access on [https://bappeda.jakarta.go.id/dokumen-rencana-pembangunan-daerah-tahun-2023-2026/September 6, 2023](https://bappeda.jakarta.go.id/dokumen-rencana-pembangunan-daerah-tahun-2023-2026/September%206,%202023).
- Doorga, J. R. (2022). Climate change and the fate of small islands: the case of Mauritius. *Environ. Sci. Policy* 136, 282–290. doi:10.1016/j.envsci.2022.06.012
- Draisma, S. G., Prud'homme van Reine, W. F., Herandarudewi, S. M., and Hoeksema, B. W. (2018). Macroalgal diversity along an inshore-offshore environmental gradient in the Jakarta Bay–Thousand Islands reef complex, Indonesia. *Estuar. Coast. Shelf Sci.* 200, 258–269. doi:10.1016/j.ecss.2017.11.010
- Enssle, F., and Kabisch, N. (2020). Urban green spaces for the social interaction, health and well-being of older people—an integrated view of urban ecosystem services and socio-environmental justice. *Environ. Sci. policy* 109, 36–44. doi:10.1016/j.envsci.2020.04.008
- Farhan, A. R., and Lim, S. (2011). Resilience assessment on coastline changes and urban settlements: a case study in Seribu Islands, Indonesia. *Ocean Coast. Manag.* 54, 391–400. doi:10.1016/j.ocecoaman.2010.12.003
- Fenoglio-Marc, L., Schöne, T., Illigier, J., Becker, M., Manurung, P., and Khafid, (2012). Sea level change and vertical motion from satellite altimetry, tide gauges and GPS in the Indonesian region. *Mar. Geod.* 35 (Suppl. 1), 137–150. doi:10.1080/01490419.2012.718682
- Fujimori, S., Hasegawa, T., Krey, V., Riahi, K., Bertram, C., Bodirsky, B. L., et al. (2019). A multi-model assessment of food security implications of climate change mitigation. *Nat. Sustain.* 2, 386–396. doi:10.1038/s41893-019-0286-2

Conflict of interest

The authors declare that the research was conducted in the absence of any commercial or financial relationships that could be construed as a potential conflict of interest.

Publisher's note

All claims expressed in this article are solely those of the authors and do not necessarily represent those of their affiliated organizations, or those of the publisher, the editors and the reviewers. Any product that may be evaluated in this article, or claim that may be made by its manufacturer, is not guaranteed or endorsed by the publisher.

Supplementary material

The Supplementary Material for this article can be found online at: <https://www.frontiersin.org/articles/10.3389/fenvs.2023.1280268/full#supplementary-material>

- Gaborit, P. (2022). Climate adaptation to multi-hazard climate related risks in ten Indonesian cities: ambitions and challenges. *Clim. Risk Manag.* 37, 100453. doi:10.1016/j.crm.2022.100453
- Gan, C. C., Oktari, R. S., Nguyen, H. X., Yuan, L., Yu, X., Kc, A., et al. (2021). A scoping review of climate-related disasters in China, Indonesia and Vietnam: disasters, health impacts, vulnerable populations and adaptation measures. *Int. J. Disaster Risk Reduct.* 66, 102608. doi:10.1016/j.ijdrr.2021.102608
- Government Regulation, (2010). Mitigasi bencana di wilayah pesisir dan pulau pulau Kecil (disaster mitigation in coastal areas and small islands). Access on <https://peraturan.bpk.go.id/Details/5088> September 6, 2023).
- Intergovernmental Panel on Climate Change (2018). "Global warming of 1.5°C. An IPCC special report on the impacts of global warming of 1.5°C above pre-industrial levels and related global greenhouse gas emission pathways," in *The context of strengthening the global response to the threat of climate change, sustainable development, and efforts to eradicate poverty*. Editors V. Masson-Delmotte, P. Zhai, H.-O. Pörtner, D. Roberts, J. Skea, et al. (Geneva, Switzerland: Intergovernmental Panel on Climate Change).
- Jakarta, D. L. H. (2018a). Rencana strategis 2017-2022 dinas lingkungan hidup Jakarta. <https://lingkunganhidup.jakarta.go.id/program/rencanastrategis>.
- Jakarta, DSDA (2018b). Rencana strategis dinas sumberdaya air provinsi jakara. https://dsda.jakarta.go.id/dokumen/Restra-DSDA-20172022_1668138187.pdf.
- Johan, O., Bengen, D. G., Zamani, N. P., and Sweet, M. J. (2015). The distribution and abundance of black band disease and white syndrome in Kepulauan Seribu, Indonesia. *HAYATI J. Biosci.* 22, 105–112. doi:10.1016/j.hjb.2015.09.001
- Khouakhi, A., Villarini, G., and Vecchi, G. A. (2017). Contribution of tropical cyclones to rainfall at the global scale. *J. Clim.* 30 (1), 359–372. doi:10.1175/jcli-d-16-0298.1
- KLHK (2016). Regulation of the minister of environment and forestry No. P.7/Menlhk/Setjen/Otl.0/1/2016. Access on https://ksdae.menlhk.go.id/assets/news/peraturan/P.7_ORGANISASI_DAN_TATA_KERJA_UPT_TN.pdf September 6, 2023).
- Kompas, (2015). DKI terancam kehilangan 23 pulau di Seribu islands. <https://megapolitan.kompas.com/read/2015/09/14/15311201/DKI.Terancam.Kehilangan.23.Pulau.di.Kepulauan.Seribu#:~:text=Adapun%20enam%20pulau%20yang%20telah,Kecil%20seluas%200%2C55%20hektar.AksesFebruary%209,%202023>.
- Lal, P. N., Mitchell, T., Aldunce, P., Auld, H., Mechler, R., Miyan, A., et al. (2012). "National systems for managing the risks from climate extremes and disasters," in *Managing the risks of extreme events and disasters to advance climate change adaptation field*. Editors V. Barros, T. F. Stocker, D. Qin, D. J. Dokken, K. L. Ebi, M. D. Mastrandrea, et al. (Cambridge, UK: Cambridge University Press), 339–392.
- Lestari, F., Adiwibowo, A., Kadir, A., and Ramadhan, N. A. (2022). Validating the 6 year (2016–2021) anthropogenic induced small island wildfire hazards in Pulau Seribu archipelago, Indonesia. *Prog. Disaster Sci.* 14, 100236. doi:10.1016/j.pdisas.2022.100236
- Liu, W., Zhang, X., and Feng, S. (2019). Does renewable energy policy work? Evidence from a panel data analysis. *Renew. energy* 135, 635–642. doi:10.1016/j.renene.2018.12.037
- McKibben, J. B., Fullerton, C. S., Ursano, R. J., Reissman, D. B., Kowalski-Trakofler, K., Shultz, J. M., et al. (2010). Sleep and arousal as risk factors for adverse health and work performance in public health workers involved in the 2004 Florida hurricane season. *Disaster Med. public health Prep.* 4, S55–S62. doi:10.1001/dmp.2010.9
- Meckling, J., and Allan, B. B. (2020). The evolution of ideas in global climate policy. *Nat. Clim. Change* 10, 434–438. doi:10.1038/s41558-020-0739-7
- Milhorance, C., Sabourin, E., Le Coq, J.-F., and Mendes, P. (2020). Unpacking the policy mix of adaptation to climate change in Brazil's semiarid region: enabling instruments and coordination mechanisms. *Clim. Policy* 20, 593–608. doi:10.1080/14693062.2020.1753640
- Nagu, N., Lessy, M. R., and Achmad, R. T. (2018). Adaptation strategy of climate change impact on water resources in small island coastal areas: case study on ternate island-north maluku. *KnE Soc. Sci.* 3, 424–441. doi:10.18502/kss.v3i5.2347
- Nashwan, M. S., and Shahid, S. (2018). Spatial distribution of unidirectional trends in climate and weather extremes in Nile river basin. *Theor. Appl. Climatol.* 137, 1181–1199. doi:10.1007/s00704-018-2664-5
- Neumann, B., Vafeidis, A. T., Zimmermann, J., and Nicholls, R. J. (2015). Future coastal population growth and exposure to sea-level rise and coastal flooding: a global assessment. *PloS one* 10, e0118571. doi:10.1371/journal.pone.0118571
- Ningsih, E. N., Setiawan, A., Hartoni, H., and Fauziah, F. (2021). Perubahan luasan pulau Pramuka, pulau Panggang dan pulau karya kepulauan Seribu DKI Jakarta menggunakan data citra satelit penginderaan jauh. *J. Penelit. Sains* 23, 84–90. doi:10.56064/jps.v23i2.628
- Nunn, P. D., Kohler, A., and Kumar, R. (2017). Identifying and assessing evidence for recent shoreline change attributable to uncommonly rapid sea-level rise in Pohnpei, Federated States Of Micronesia, Northwest Pacific Ocean. *J. Coast. Conserv.* 21 (6), 719–730. doi:10.1007/s11852-017-0531-7
- Nurmaulia, S., Fenoglio-Marc, L., and Becker, M. (2010). Long-term sea level change from satellite altimetry and tide gauges in the Indonesian region. *Proc. ESA Living Planet Symp.*
- Nurse, L. A., Sem, G., Hay, J. E., Suarez, A. G., Wong, P. P., Briguglio, L., et al. (2001). "Small island states," in *Climate change 2001. Impacts, adaptation and vulnerability. Contribution of working group II to the third assessment report of the intergovernmental panel on climate change*. Editors J. J. McCarthy, O. F. Canziani, N. A. Leary, D. J. Dokken, and K. S. White (Cambridge, UK: Cambridge University Press), 844–875.
- Obradovich, N., Migliorini, R., Mednick, S. C., and Fowler, J. H. (2017). Nighttime temperature and human sleep loss in a changing climate. *Sci. Adv.* 3, e1601555. doi:10.1126/sciadv.1601555
- Pickering, M. D., Horsburgh, K. J., Blundell, J. R., Hirschi, J.-M., Nicholls, R. J., Verlaan, M., et al. (2017). The impact of future sea-level rise on the global tides. *Cont. Shelf Res.* 142, 50–68. doi:10.1016/j.csr.2017.02.004
- Presidential Regulation 73 (2012). STRATEGI NASIONAL PENGELOLAAN EKOSISTEM MANGROVE (National strategy for managing mangrove ecosystems). Access on <https://peraturan.go.id/id/perpres-no-73-tahun-2012> September 6, 2023).
- PUPR (2020). Peraturan menteri pekerjaan umum dan perumahan rakyat tentang peraturan menteri pekerjaan umum dan perumahan rakyat tentang perubahan atas peraturan menteri pekerjaan umum dan pekerjaan rakyat nomor 27/PRT/M/2015 tentang bendungan [regulation of the minister of public works and public housing concerning regulation of the minister of public works and public housing concerning amendments to the PUPR regulation (27) year 2015 concerning dams]. Access on <https://peraturan.bpk.go.id/Home/Details/144523/permen-pupr-no-6-tahun-2020> September 6, 2023).
- Samaniego-Rascón, D., Gameiro da Silva, M. C., Ferreira, A. D., and Cabanillas-Lopez, R. E. (2019). Solar energy industry workers under climate change: a risk assessment of the level of heat stress experienced by a worker based on measured data. *Saf. Sci.* 118, 33–47. doi:10.1016/j.ssci.2019.04.042
- Seribu Island Government, (2017). Rencana strategis kabupaten administrative kepulauan Seribu 2017-2022 (mid term strategic plan of Seribu islands regency 2017-2022). Access on <https://pulauseribu.jakarta.go.id/file/1.%20RENSTRA%20Kabupaten%20Tahun%202017-2022.pdf> September 6, 2023).
- Seribu Island Government, (2023). Mid-term strategic plan (Reinstra) of Seribu islands regency 2023-2026. Access on <https://pulauseribu.jakarta.go.id/file/20230619141944.pdf> September 6, 2023).
- Setiawati, M. D., Jarzebski, M. P., Miura, F., Mishra, B. K., and Fukushima, K. (2023a). "The public health risks of waterborne pathogen exposure under a climate change scenario in Indonesia," in *Ecological footprints of climate change: adaptive approaches and sustainability* (Berlin, Germany: Springer), 607–624.
- Setiawati, M. D., Nandika, M. R., Supriyadi, I. H., Iswari, M. Y., Prayudha, B., Wouthuyzen, S., et al. (2023b). Climate change and anthropogenic pressure on Bintan Islands, Indonesia: an assessment of the policies proposed by local authorities. *Regional Stud. Mar. Sci.* 66, 103123. doi:10.1016/j.rsm.2023.103123
- Shahid, R., Shijie, L., Shahid, S., Altaf, M. A., and Shahid, H. (2021). Determinants of reactive adaptations to climate change in semi-arid region of Pakistan. *J. Arid Environ.* 193, 104580. doi:10.1016/j.jaridenv.2021.104580
- Sokolowski, M. M., and Heffron, R. J. (2022). Defining and conceptualising energy policy failure: the when, where, why, and how. *Energy Policy* 161, 112745. doi:10.1016/j.enpol.2021.112745
- Susanto, J., Zheng, X., Liu, Y., and Wang, C. (2020). The impacts of climate variables and climate-related extreme events on island country's tourism: evidence from Indonesia. *J. Clean. Prod.* 276, 124204. doi:10.1016/j.jclepro.2020.124204
- Taylor, M. A., Clarke, L. A., Centella, A., Bezanilla, A., Stephenson, T. S., Jones, J. J., et al. (2018). Future caribbean climates in a world of rising temperatures: the 1.5 vs 2.0 dilemma. *Am. Meteorol. Soc.* 31 (7), 2907–2926. doi:10.1175/JCLI-D-17-0074.1
- USAID (2016). Indonesia: costs of climate change 2050 policy brief. access on <https://www.climate-links.org/sites/default/files/asset/document/Indonesia%20Costs%20of%20CC%202050%20Policy%20Brief.pdf> September 11, 2023).
- WMO (World Meteorological Organization) (2012a). Standardized precipitation index user guide. https://library.wmo.int/doc_num.php?explnum_id=7768.
- World Travel, and Tourism Council, (2019). Travel and tourism: world economic impact 2019. *Curr. Issues Tour.*, doi:10.2167/cit/mp004.0
- World Meteorological Organization (WMO), 2012b: Standardized precipitation index user. Guide. Access on September 6, 2023 at https://www.droughtmanagement.info/literature/WMO_standardized_precipitation_index_user_guide_en_2012.pdf
- Wulan, D. R., Sintawardani, N., Marganingrum, D., Triyono, T., Bararah, V., Santoso, H. B., et al. (2023). Water sources, consumption, and water-related sanitation on Pari Island, Indonesia: a mixed-focus group discussion and survey study. *AQUA – Water Infrastructure, Ecosyst. Soc.* 72 (8), 1359–1372. doi:10.2166/aqua.2023.137
- Zheng, S., Pu, Y., Lu, H., Zhang, J. J., Wang, D., and Ma, X. (2023). Global climate policy effectiveness: a panel data analysis. *J. Clean. Prod.* 412, 137321. doi:10.1016/j.jclepro.2023.137321



OPEN ACCESS

EDITED BY

Sandipan Das,
Symbiosis International University, India

REVIEWED BY

Subham Roy,
University of North Bengal, India
Sanu Dolui,
University of Kalyani, India

*CORRESPONDENCE

Moonkyung Chung,
✉ mkchung@kict.re.kr

RECEIVED 20 July 2023

ACCEPTED 23 November 2023

PUBLISHED 06 December 2023

CITATION

Seo S, Park J, Ko Y, Kim G and Chung M (2023), Geotechnical factors influencing earth retaining wall deformation during excavations.
Front. Earth Sci. 11:1263997.
doi: 10.3389/feart.2023.1263997

COPYRIGHT

© 2023 Seo, Park, Ko, Kim and Chung.
This is an open-access article distributed under the terms of the [Creative Commons Attribution License \(CC BY\)](https://creativecommons.org/licenses/by/4.0/).
The use, distribution or reproduction in other forums is permitted, provided the original author(s) and the copyright owner(s) are credited and that the original publication in this journal is cited, in accordance with accepted academic practice. No use, distribution or reproduction is permitted which does not comply with these terms.

Geotechnical factors influencing earth retaining wall deformation during excavations

Seunghwan Seo¹, Jongjeon Park², Younghun Ko¹,
Gunwoong Kim¹ and Moonkyung Chung^{1*}

¹Department of Geotechnical Engineering Research, Korea Institute of Civil Engineering and Building Technology, Goyang, Gyeonggi, Republic of Korea, ²Department of Civil and Environmental Engineering, Yonsei University, Seoul, Republic of Korea

This study aims to identify and evaluate the significance of the key design factors that impact the stability of Earth retaining wall anchor-supported structures during excavations in urban areas. Although there are many previous studies on the deformation of Earth retaining walls during excavation, there is a lack of verification studies that quantitatively examine the stability of various influencing factors such as wall, ground characteristics, and external influencing factors. To this end, finite-element analyses were conducted, and their results were compared and validated with field measurements. These comparisons demonstrated that the numerical modeling technique employed in this study effectively simulates the wall's behavior under excavation conditions. Subsequently, the impact of the main design factors, including ground properties, external conditions, and structural stiffness, on the behavior of the wall was quantitatively assessed by applying variation ratios. The findings indicate that the horizontal displacement of the wall, induced by excavation, is significantly dependent on the unit weight and shear strength of the soil. Conversely, the groundwater level location, surcharge load, and structural stiffness exhibit a relatively minor effect. Finally, the variability of the main design parameters was investigated, considering the specific ground layer where the wall is installed, revealing distinct influences of these variables across different ground layers. Consequently, it is expected that the importance of the influencing geotechnical factors will be selected and used for predicting the behavior of Earth retaining walls and actual design, which will help to efficient wall design.

KEYWORDS

Earth retaining wall, excavation, deformation, parametric study, finite-element method

1 Introduction

Although the advance in civil engineering technologies has led to a decrease in the number of work accidents at construction sites, collapse-type accidents during Earth retaining wall excavations continue to occur with some frequency. This can be attributed to various factors, including the inherent uncertainty in the properties of the ground compared to those of other structures and the scale of the excavation.

In the design of Earth retaining wall, prediction methods for lateral displacement have been applied by conventional researches. It is essential to accurately predict the behavior of the ground and wall according to the excavation for the efficient design of the Earth retaining wall, and the change of the ground and the wall displacement during the step-by-step excavation should also be accurately predicted in advance and considered in the design

(Hsiung, 2009; Khoiri and Ou, 2013; Bhatkar et al., 2017; Dong et al., 2018). The methods used for design are studied for clay or sandy ground, so it is difficult to predict wall displacement under various ground conditions. During construction, the stability of the Earth retaining wall is evaluated by the wall displacement measured by instrumentation (Ran et al., 2011; Fearnhead et al., 2014; Wu et al., 2015). However, there is a difference between the predicted displacement and the actual displacement during construction due to the fundamental problem that the methods proposed by conventional researches cannot properly describe the site conditions with various characteristics (Dmochowski and szolomicki 2021). The factors affecting the wall displacement during excavation are influenced by several parameters such as ground material properties, external influences such as groundwater level (GL) and surcharge load at the back and structure stiffness (Do and Ou, 2020; Zhang et al., 2020).

Previous researchers have conducted numerous studies on the behavior of retaining walls during the excavation of the surrounding ground. Caspe (1966) investigated wall displacement and Poisson’s ratio in a viscous clay ground, Peck (1969) studied settlement characteristics based on actual measurements, Bowles (1996) proposed a simplified method, and Clough and O’Rourke (1990) used field measurements and the finite-element method to analyze settlement levels considering the separation between different ground layers. Yoo et al. (2000) conducted a study in Korea analyzing wall displacement and surrounding ground behavior at three stages of the excavation process: pre-excavation, excavation, and support beam removal. Other studies on the response of adjacent structures to ground displacement caused by excavation include Boscardin and Cording’s (1989) investigation of the effect of horizontal ground displacement on the deformation of adjacent structures, Son and Cording (2005, 2007) research on the

TABLE 1 Parametric numerical analyses.

Condition	Soil properties	Retaining wall	Support	Water level
Parametric	Unit weight	Types	Anchor	Steady state flow
	Cohesion			
	Friction angle	Stiffness	Strut	
	Poisson's ratio		Raker	
	Young's modulus	Embedded depth	Empty	

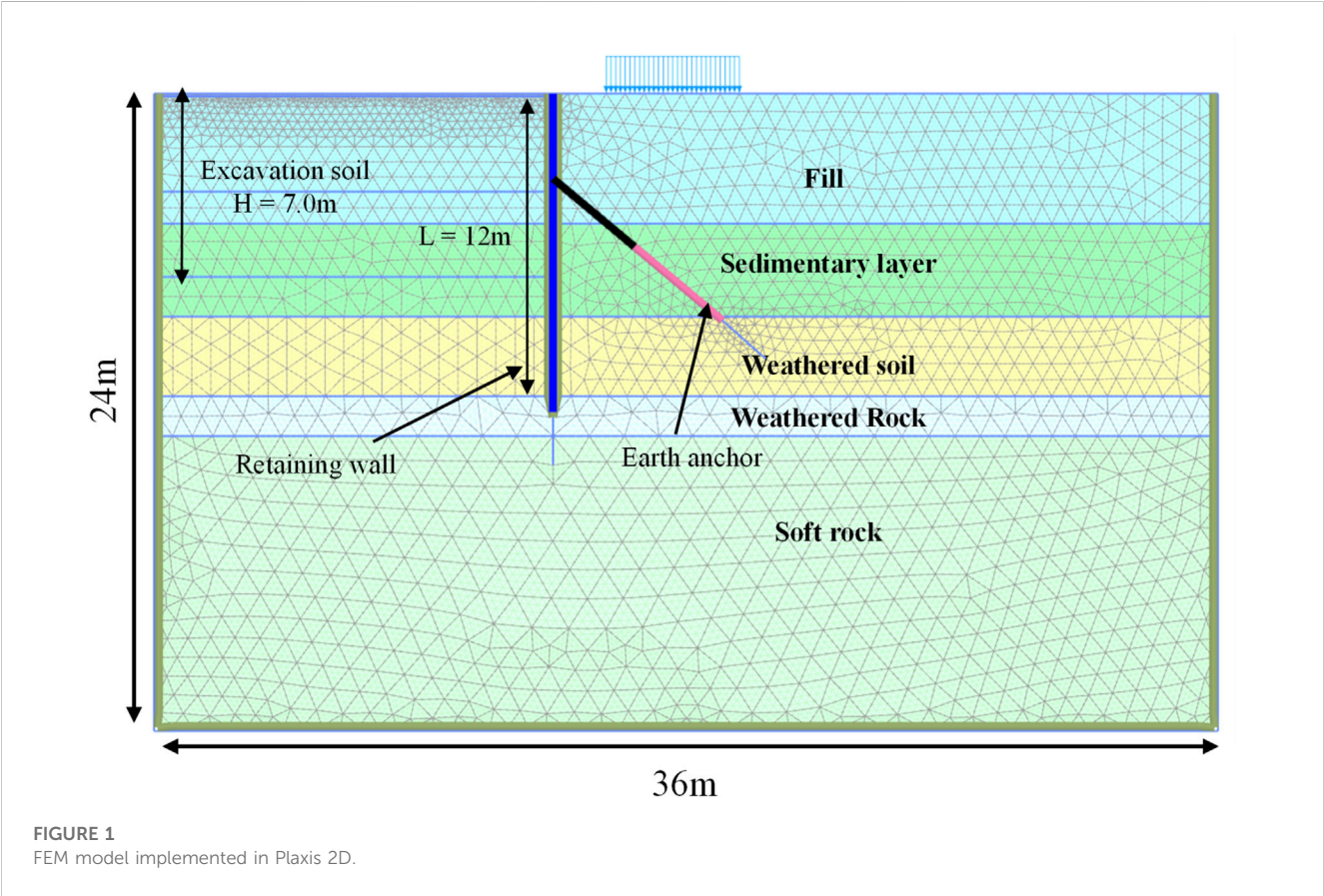


TABLE 2 Soil properties.

Soil type	γ (kN/m ³)	E (MPa)	c (kPa)	Φ (°)	ν	R_{inter}
Fill layer	17	16.8	0	26	0.3	0.67
Sedimentary layer	18	19.2	0	28		
Weathered soil	18	24.0	10	28		
Weathered rock	20	100.0	30	33		
Soft rock	23	500.0	40	35		1.0

TABLE 3 Material properties.

Type	Properties
Cast-in-place (CIP) wall	Diameter, $D = 0.5$ m
	Young's modulus, $E = 2.8 \times 10^5$ kPa
H-pile	Dimensions ^a , H-300 mm x 305 mm x 15 mm x 15 mm
	Horizontal spacing, $S_H = 1.8$ m
	Young's modulus, $E = 2.1 \times 10^4$ kPa

^aH-pile size description: H-height x flange widthxweb thicknessxflange thickness.

relationship between ground settlement, deformation rate, and damage level in adjacent structures, and [Lee et al. \(2007\)](#) assessment of damage risk to adjacent buildings during excavation by combining the Peck and Bowles methods.

[Peck \(1969\)](#) demonstrated that ground settlement depends on the stiffness of the soil, showing that stiffer soils, such as sandy soil and hard clay, exhibit lower settlement compared to softer soils like soft to medium clay. [Clough and Tsui \(1974\)](#) and [Mana and Clough \(1981\)](#) found that the overall behavior of the ground depends on soil stiffness, with lateral displacement rates and magnitudes increasing as the risk of uplift augments or the excavation failure safety factor approaches one. [Song and Yoo \(2018\)](#) conducted an indoor model experiment to analyze the impact of groundwater levels (GLs) on retaining walls during excavation. Their findings revealed that as the GL increased, wall displacement increased while wall stiffness decreased. [Park and Joung \(2020\)](#) conducted a numerical study on the excavation width and deformation characteristics of retaining walls, identifying the extent of mutual interference caused by Earth pressure using two-dimensional numerical analyses. [St John \(1975\)](#) determined that compared to three-dimensional simulations, two-dimensional analyses tend to overestimate the deformation of retaining walls in stiff clay excavations. [Naylor and Pande \(1981\)](#) compared three- and two-dimensional analyses and found that, while ground settlement did not differ significantly between the two analyses, the horizontal wall displacement was approximately twice as large in the three-dimensional analysis. [Jeong and Kim \(2009\)](#) confirmed the suitability of the three-dimensional numerical methods for considering the characteristics of retaining walls and support materials. They suggested that the depth to consider in the analysis should be set at more than twice the excavation depth to achieve more accurate results in three-dimensional numerical analysis. [Yoo and Kim \(2000\)](#)

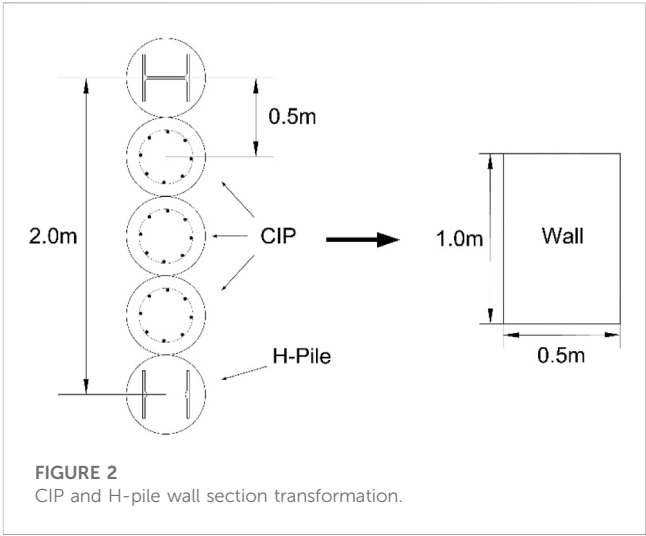


TABLE 4 Interface reduction factor.

Soil/Material	R_{inter}
Sandy soil/Steel material	2/3
Cohesive soil/Steel material	0.5
Sandy soil/Concrete	0.8–1.0
Cohesive soil/Concrete	0.7–1.0
Soil/Geogrid	1.0
Soil/Geotextile	0.5–0.9

examined the influence of factors such as ground stiffness, wall bending stiffness, and over-excavation on the behavior of retaining walls using indoor model experiments and finite-element analysis. The results revealed that the behavior of retaining walls is highly affected by the construction process, the stiffness of wall components, and whether over-excavation occurs. Reducing the installation gap proved more effective in suppressing wall displacement than increasing the stiffness of the support structure. The influence area of settlement expanded as the degree of over-excavation increased, with the maximum settlement reaching approximately 70% of the maximum horizontal wall displacement.

[Chen et al. \(2014\)](#) conducted a three-dimensional numerical analysis to study changes in effective horizontal stress and interstitial water pressure during the installation of a diaphragm wall. The installation of diaphragm walls in soft ground resulted in significant ground settlement, reduced ground stress, and changes in interstitial water pressure ([Ng, 1992](#); [Symons and Carder, 1993](#); [Powrie and Kantartzi, 1996](#); [Poh and Wong, 1998](#)). These changes in ground conditions depend on factors such as the thickness and length of the basement continuation wall, soil type, and construction techniques. [Schäfer and Triantafylidis \(2004, 2006\)](#) analyzed the effects of deep excavation on the behavior and stress evolution of basement continuation walls in normally consolidated clay (NC) and found significant stress evolution in the ground prior to construction.

The behavior of Earth retaining walls is influenced by various factors, including soil type, excavation shape, wall type, support system,

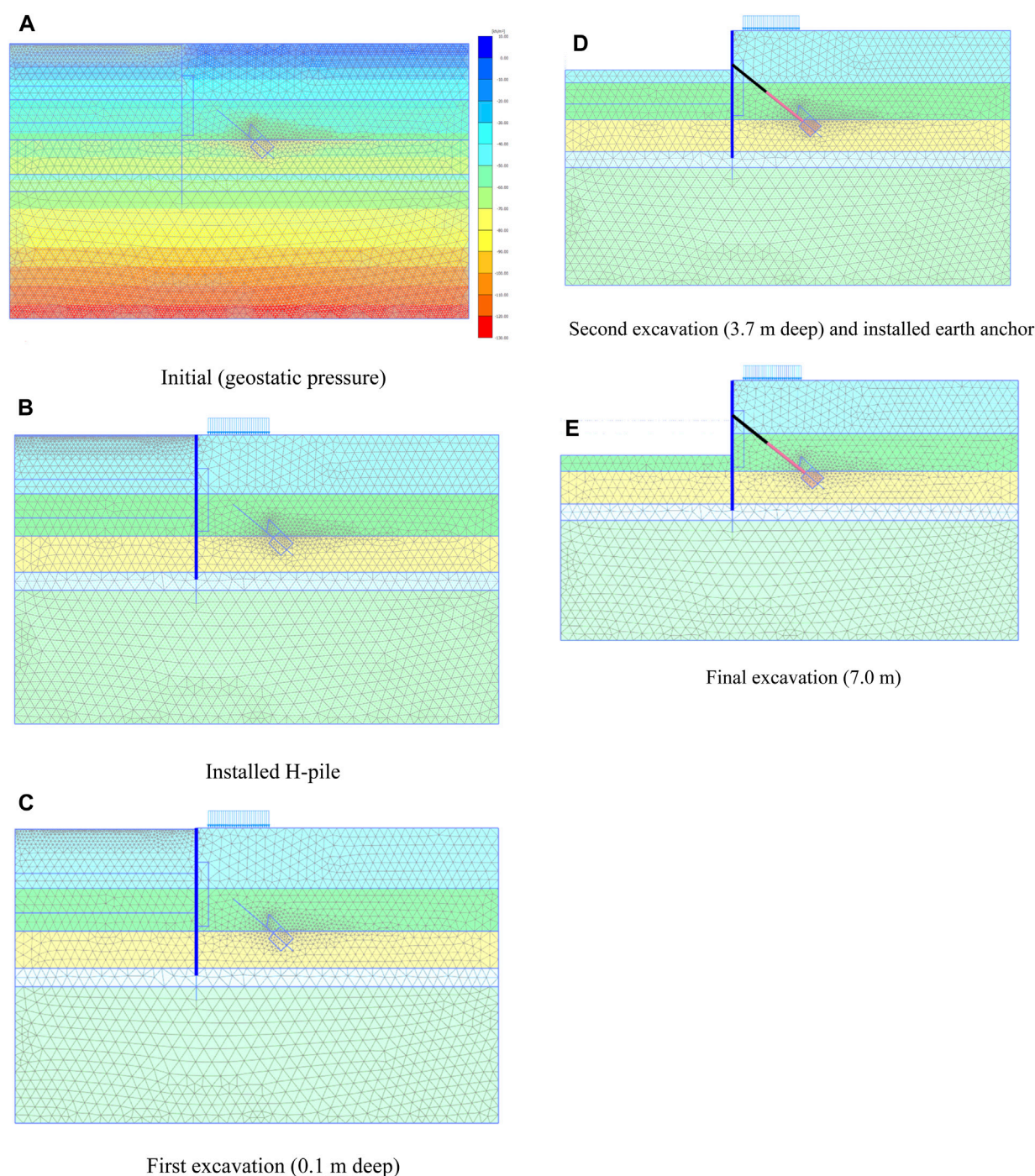


FIGURE 3

Numerical simulation procedure: (A) Initial, (B) Installed H-pile, (C) First excavation, (D) Second excavation, (E) Final excavation.

and construction technique (Ou et al., 1993; Poh and Wong, 1998; Wong and Poh, 2000; Zhang et al., 2015, 2018). Additionally, the impact of deep excavation on ground behavior is contingent upon the length and depth of the wall, the depth of the support layer, and the stiffness of the support material (Ou et al., 1993; Goh et al., 2020). Recent studies have focused on corner joints of retaining walls, employing three-dimensional numerical analyses. Tanner Blackburn and Finno (2007) observed that horizontal deformation and ground settlement increase

from the corner to the center of the retaining walls. Hsieh and Ou (1998) reported a reduction of 20%–60% in horizontal wall displacement at the corner compared to the maximum settlement at the center. In addition, a recent study analyzed the factors affecting the behavior of embedded retaining wall through inverse analysis. Through inverse analysis of post-construction monitoring data, it was reported that the nonlinear soil stiffness has the largest impact on wall deformation in stiff clay condition (Foo et al., 2023).

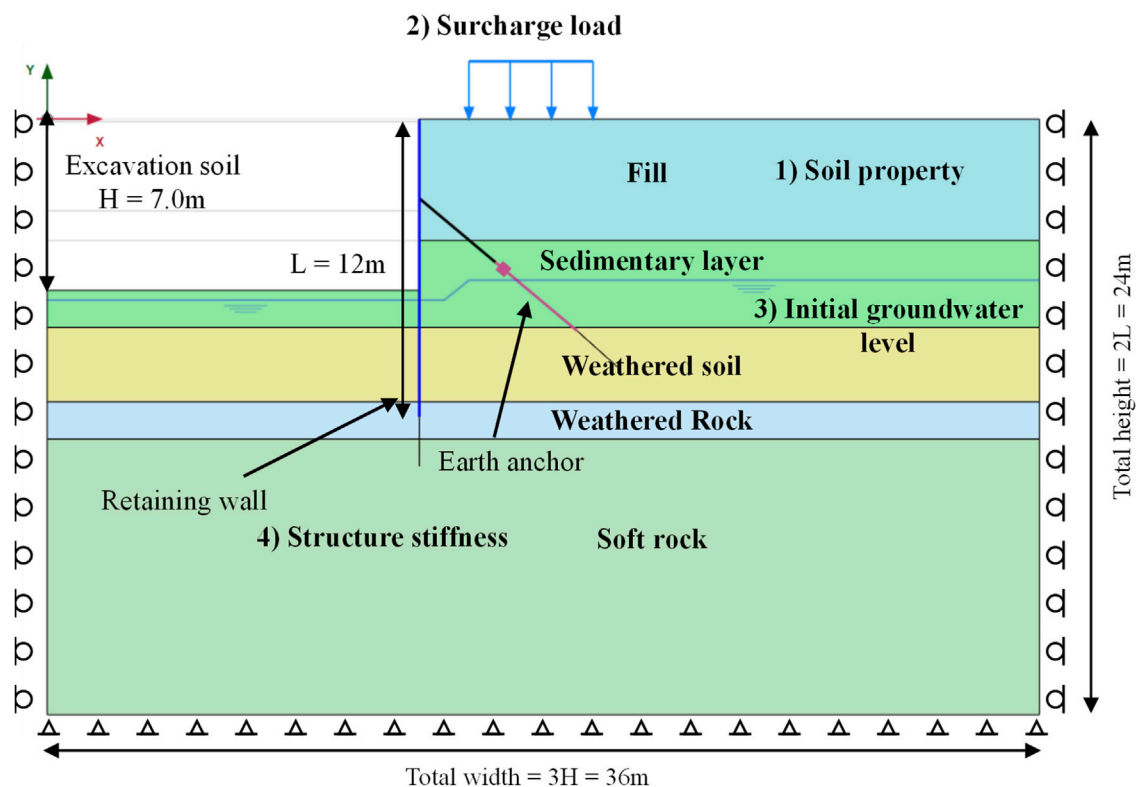


FIGURE 4
Influence factor for retaining wall and Earth anchor in 2D FE model.

As mentioned above, there are many previous studies on the deformation of Earth retaining walls during excavation, however there is lack of validation study that examines the stability of various influencing factors such as wall, soil properties, and external influencing factors. This study aims to thoroughly analyze the factors that influence the response of retaining walls during ground excavations based on the results obtained from numerical analyses of a single process at an earthwork excavation site. Prior to the numerical analyses, the results obtained from field applications and finite-element analysis were compared to validate the numerical modeling scheme used for analyzing the wall behavior. The finite-element analyses were conducted setting as parameters the factors that affect the horizontal displacement of the wall during excavation, including ground material properties, external influences (such as GL location and surcharge load at the back), and structural stiffness. Subsequently, the significance of these influencing factors was determined by analyzing the behavior characteristics of the wall and the magnitude of deformation due to excavation, and the results were utilized to predict the horizontal wall displacement during the design process.

2 Methodology

2.1 Elastic-plastic beam-on-foundation and finite-element analysis (FEA)

Among the analysis methods used for stability assessment of continuous underground walls, the elastic-plastic beam-on-

foundation analysis method is commonly employed in design due to the simplicity and minimal expertise requirements for the input data. However, this method combines the wall and ground after analyzing separately their structural failure points. Consequently, accurately calculating the active failure surface, while considering the effects of the wall, Earth anchors, and surrounding ground, becomes challenging, particularly in inverse analysis scenarios such as when determining the cause of retaining wall collapses. To address this limitation, this study adopts the finite-element method (FEM), which incorporates the shear strength reduction method to automatically consider changes in the active failure surface. This is achieved by performing a continuum analysis that accounts for the excavation and construction stages. Accordingly, the influencing factors for the elastic-plastic beam-on-foundation analysis method and the FEM model were selected differently. The input data required to characterize the geotechnical properties for the elastic-plastic beam-on-foundation analysis included the wet unit weight, underwater unit weight, adhesion, internal friction angle, and coefficient of transverse ground reaction force (K_s). On the other hand, the geotechnical properties utilized for the finite-element analysis included the wet unit weight, underwater unit weight, adhesion, internal friction angle, and elastic modulus (E). Previous research results [Jeong and Kim \(2009\)](#) have indicated that the elastic-plastic beam-on-foundation analysis method has the disadvantage of not being able to simultaneously consider the resistance of the structure and the ground at each analysis point. Consequently, it does not account for the continuity of the analysis or the soil-structure interaction.

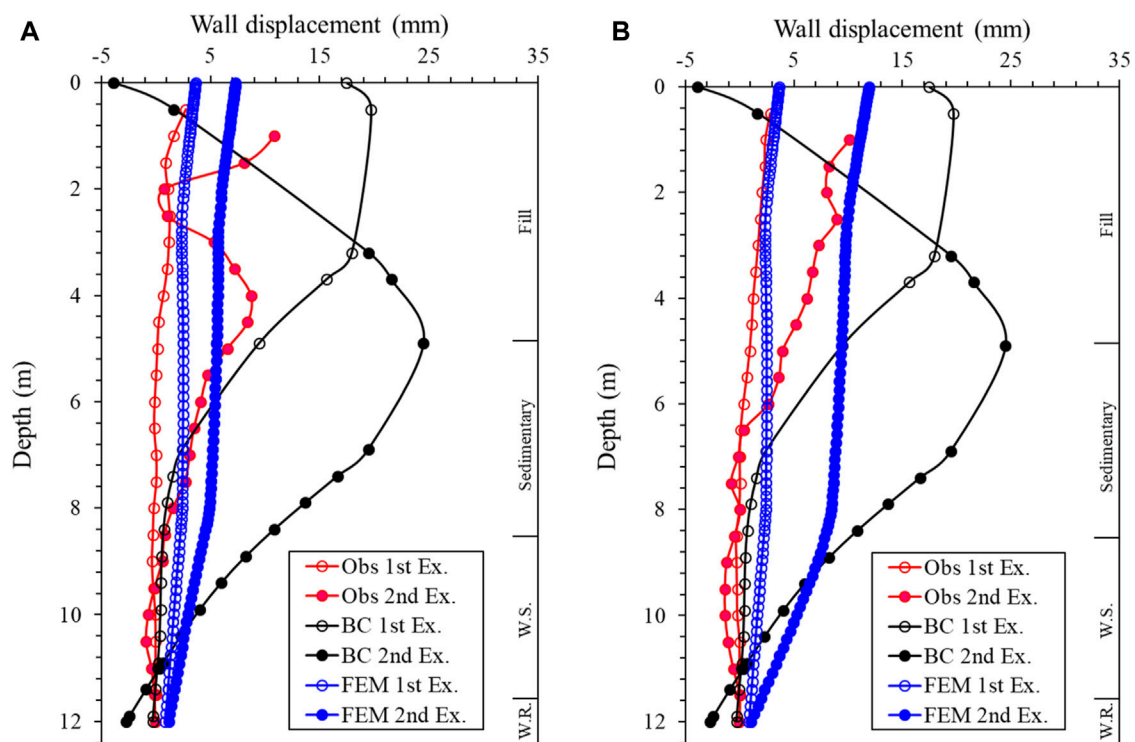


FIGURE 5
Horizontal displacement for Sections (A,B).

Notably, the difference between the transverse ground reaction force coefficient and elastic modulus represents a significant distinction between the two analysis methods.

2.2 Selection of influence factors

The excavation site data were based on field measurements, whereas the basic data were selected using the input values from SUNEX, a beam-column program widely used in practical applications. The ground properties considered were the type, wet unit weight, underwater unit weight, adhesion, internal friction angle, transverse ground reaction coefficient, depth, layer thickness, and average N-value. To account for water pressure on the wall during design, the initial GL was expressed from the ground surface.

The input properties, such as elastic modulus, cross-sectional area, and cross-sectional secondary moment, were based on the same values as those used for vertical walls. Regarding the anchors, the initial tensile force is known to impact the final behavior of the wall. The pouring of the building wall, which occurs after excavation is completed, has negligible contribution to the stability evaluation of the wall. Dependent on its location and size, the background load influences the horizontal displacement of the wall during excavation and can act as an external force along with the GL (Ou et al., 1993; Goh et al., 2020). Based on a literature review and field data, four major influencing factors were selected for this study. The types of wall and support materials were reviewed according to their axial and bending stiffnesses (EA and EI, respectively). It is important to

note that the nature of the analysis program used in the design led to variations from the actual site conditions. Therefore, the behavior of each type of wall and support material was analyzed by considering the quantitative variations, rather than analyzing each type separately using different methods. Table 1 lists the influencing factors considered in the analysis.

2.3 Numerical modeling

The numerical analysis utilizes the commercial FE software PLAXIS 2D (2022). The typical 2D FE model used in this study is shown in Figure 1. The soil and rock are composed of 15-node triangular elements, while the retaining wall is modeled using 5-node plate elements. The model employs fourth-order interpolation for displacements and twelve Gauss points for numerical integration (stress points). The interfaces consist of five pairs of 10-node interface elements that can connect with 15-node soil elements. The numerical model has a total height equal to the height of the retaining wall (L) plus an additional 1.0L below the retaining toe level, and extends three times the excavation width (H) from the retaining wall center. These dimensions were chosen to minimize boundary effects on the retaining wall's behavior. A finer mesh was used near the retaining wall and surrounding soil interface, while a coarser mesh was used further away. The typical retaining wall had a width of 0.3 m and a length of 12 m. The bearing end of the wall was on weathered rock and continued into a layer of sand. The mesh consisted of 40,110 nodes and 4,848 fifteen-node triangular elements. Assuming a rigid, unyielding strata, such as a rock

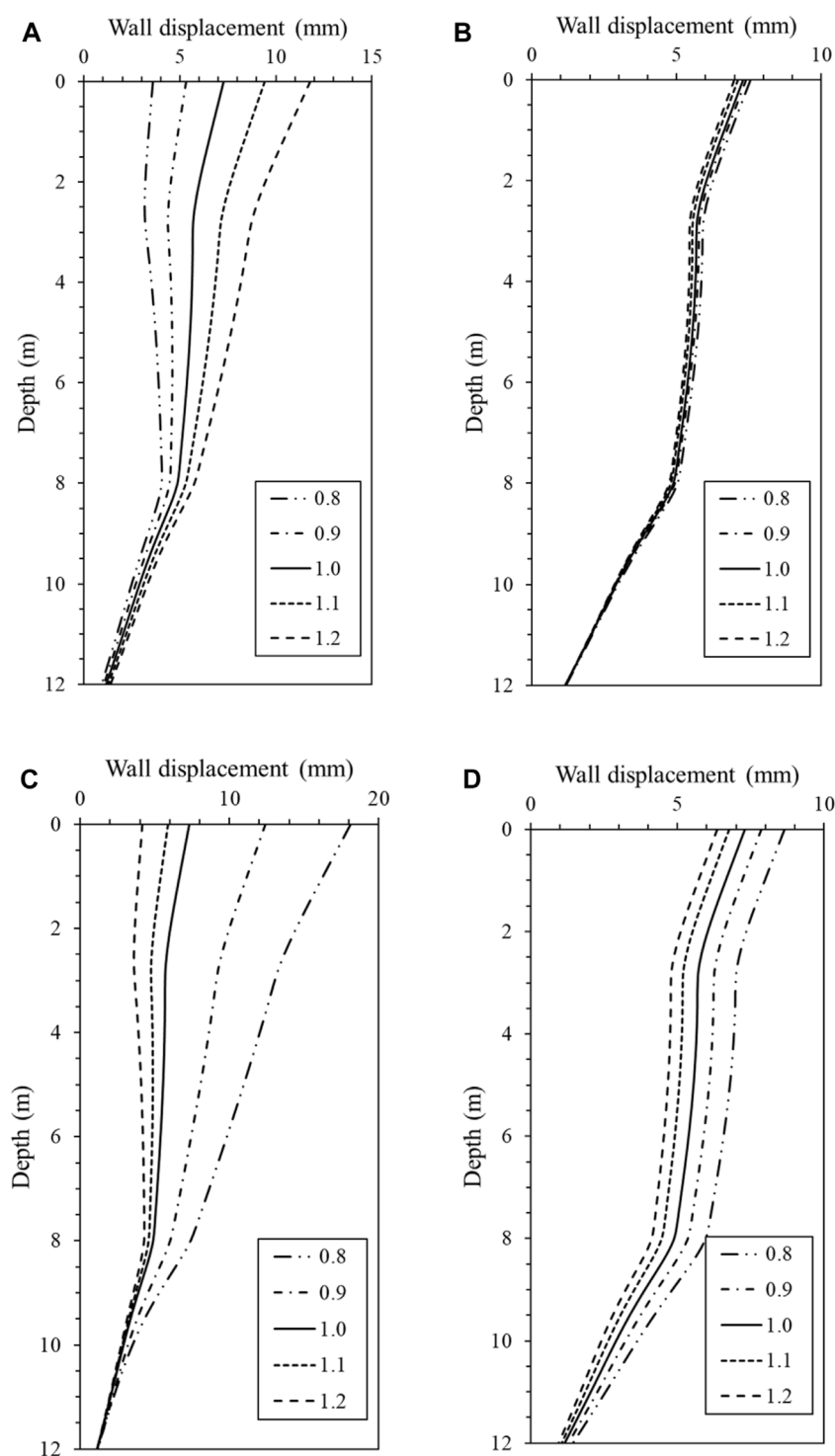


FIGURE 6

Results of numerical analysis of soil properties: (A) unit weight; (B) cohesion, (C) friction angle; and (D) elastic modulus.

layer, the vertical boundaries are allowed to move only in the vertical direction, while the bottom boundary is fixed in both the horizontal and vertical directions.

The conditions for the finite-element analysis were as follows. The Mohr–Coulomb (M–C) model, commonly used in practice, was applied to the ground model, while an elastic model was employed

for the retaining wall. Underground anchors were modeled using node-to-node anchor elements and embedded piles. The ground and structural properties used in the finite-element analysis are listed in Tables 2, 3.

Although the cast-in-place (CIP) wall consists of a continuous arrangement of concrete columns with rebars and H-piles, the

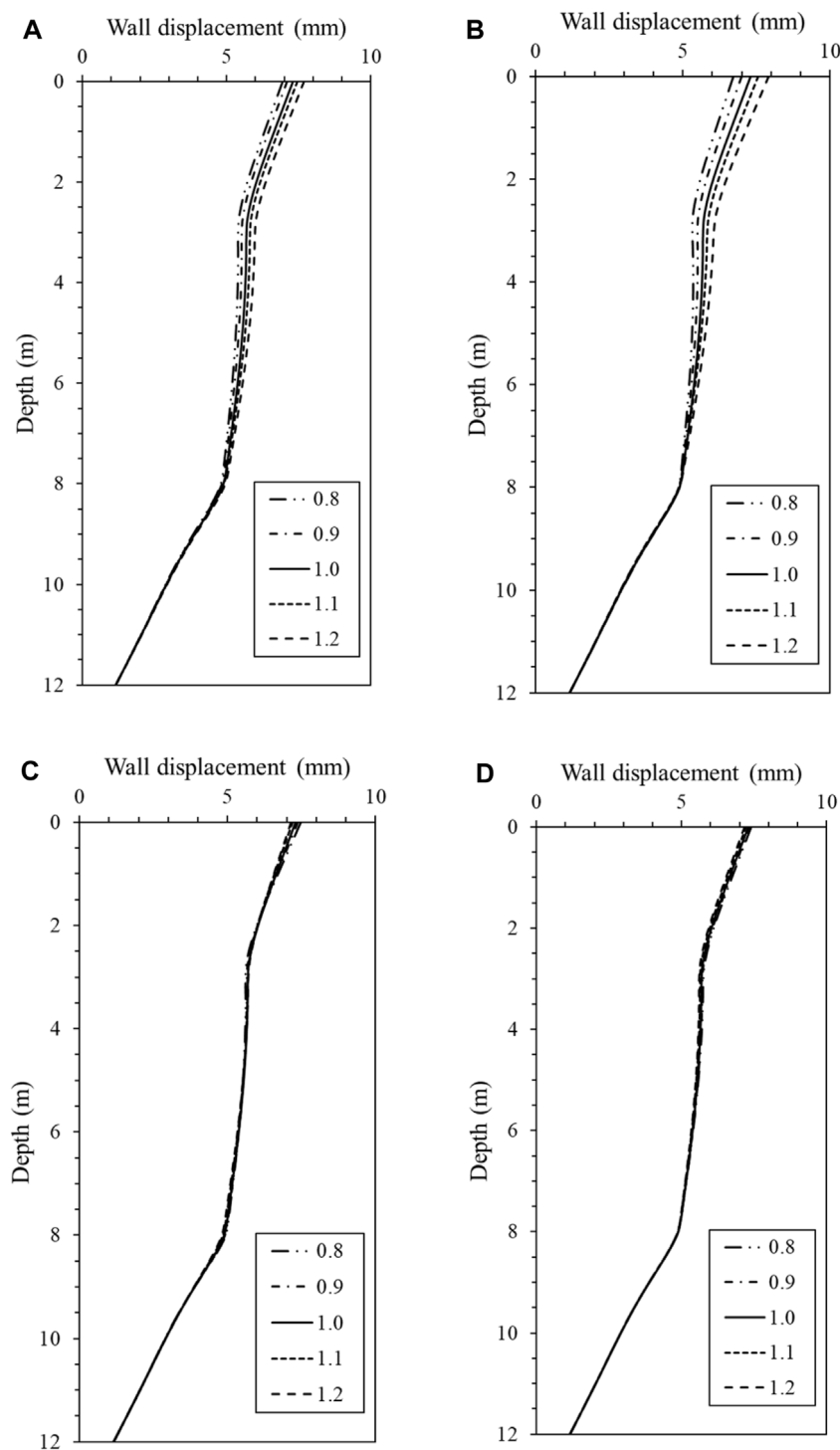


FIGURE 7

Results of numerical analysis of external force and structure stiffness: (A) surcharge loading, (B) initial GL, (C) wall stiffness, and (D) strut stiffness.

analysis was performed in two-dimensional plane strain due to the characteristics of a continuous wall where the differences in stiffness among the concrete columns are minimal. The equivalent physical properties were calculated using Equation (1) to replace the elastic modulus (E) and sectional secondary moment (I) of the continuous wall. In Figure 2, the earth-membrane wall represents a unit width of 1 m.

$$E_p I_p \times N_p \times E_c I_c \times N_c = E_a I_a$$

where,

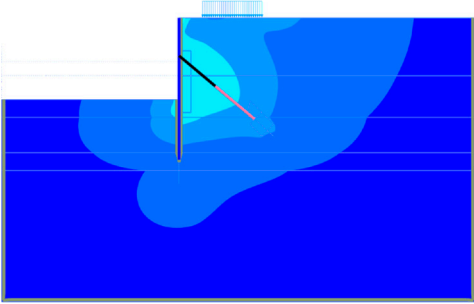
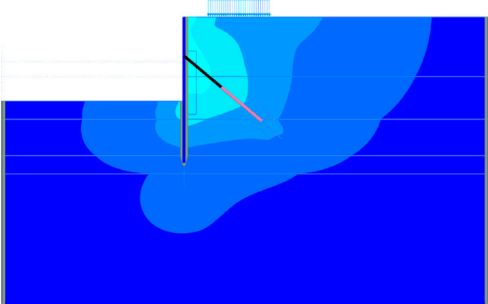
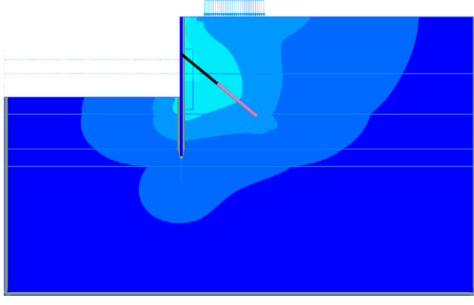
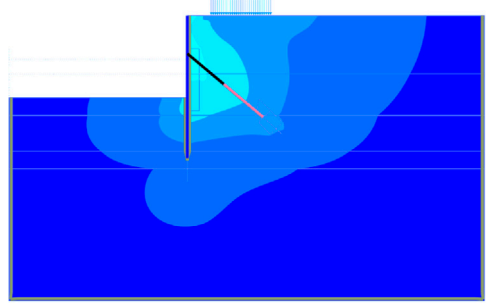
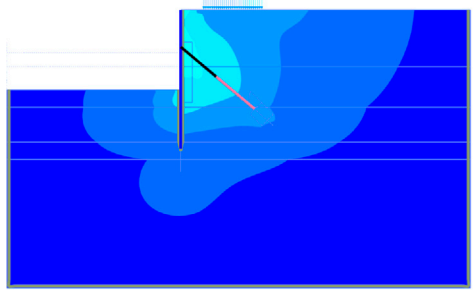
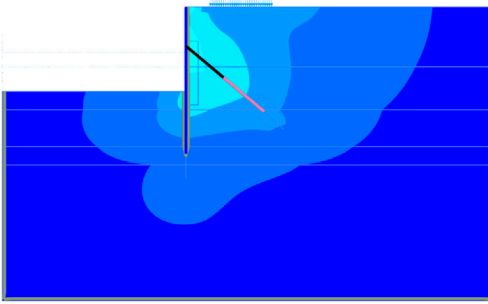
E_p = modulus of elasticity of H-pile (kPa);
 I_p = cross-sectional secondary moment of H-pile (m^4);
 N_p = number of H-piles per unit width;

TABLE 5 Comparison of the shear strain for Earth retaining wall with variation ratio changes (Shear strain for the minimum and maximum changes of variation rate by influencing factor under the geometric conditions shown in Figure 4).

Factors	Minimum variation ratio 0.8	Maximum variation ratio 1.2
Unit weight		
Cohesion		
Friction angle		
Elastic modulus		
Surcharge loading		

(Continued on following page)

TABLE 5 (Continued) Comparison of the shear strain for Earth retaining wall with variation ratio changes (Shear strain for the minimum and maximum changes of variation rate by influencing factor under the geometric conditions shown in Figure 4).

Factors	Minimum variation ratio 0.8	Maximum variation ratio 1.2
Initial GL		
wall stiffness		
strut stiffness		

E_c = modulus of elasticity of the concrete wall (kPa); and
 I_c = secondary moment of a concrete wall section (m^4).

For the analysis area, the boundary conditions were defined as vertical displacement constraints for the lower boundary, horizontal displacement constraints for the left and right boundaries, and a free surface for the upper boundary along the axial direction of the global coordinate system. After the construction of the earth-membrane wall, the ground area inside the wall entered a stress-relieved state due to excavation. To simulate the separation behavior between the ground and wall, an interface element was applied. The interface element allowed for modeling the relative displacement between the soil and wall. Without the use of the interface element, the ground near the wall did not settle due to the arching effect between the elements. Table 4 summarizes the strength reduction factors for each soil and structural material when employing the interface element.

A step-by-step analysis was conducted to examine the displacement and external stability of the retaining wall in accordance with the actual construction stages. The construction stages were simulated as follows: Step 1: H-pile construction, Step 2: step-by-step excavation, Step 3: anchor installation, Step 4: repetition of Steps 2 and 3, and final excavation, based on the construction system at the site, as shown in Figure 3.

2.4 Numerical analysis with influence factors

To analyze the influencing factors, specific influence factor selection and analysis cases were determined, as illustrated in Figure 4. Verification was previously conducted using field measurement data, and an additional analysis was carried out. When subdividing the influencing factors, the ground physical properties encompassed unit weight, adhesion, friction angle, and elastic modulus, with the analysis

performed considering the magnitude of the surcharge load at the back. Additionally, the GL required adjustment based on the step-by-step analysis. However, for this project, only the initial GL (−3.2 m) was selected and reviewed, and the influence factor analysis was conducted by varying the position of the GL accordingly. Lastly, the stiffness of the Earth wall was chosen as an influencing factor, and the EA and EI values were analyzed.

For the influence factor analysis method, a representative cross-section was selected based on validated field cases, and weights were assigned to each factor for assessment. To ensure the properties of the influencing factors remained within a reasonable range, the assigned weights were limited. In other words, the range is chosen to ensure that no exceptional properties are assigned. The analysis was conducted using the same properties as those used for validation. In this study, each influence factor was assigned a weight ranging from 80% to 120%, and a variation ratio of 0.8–1.2 was applied to examine the effect on the horizontal displacement of the retaining wall.

3 Test results

3.1 Validation of numerical analysis

This section presents the comparison and analysis of the behavioral characteristics of the Earth shield excavation method based on field application cases, along with the verification of the validity of the 2D finite-element analysis technique and beam-column analysis employed in this study. The parameters and properties of the retaining wall and ground structures used in the numerical analysis were consistent with those employed in the field. Verification was conducted for Sites A and B, and the results of the field measurement and numerical analysis are depicted in Figure 5, illustrating the horizontal displacement of the retaining wall caused by ground excavation. As observed in the figure, the horizontal displacement resulting from step-by-step excavation progressively increased. For the validation, specific representative cross-sections of Sites A and B were selected, and the field measurements were based on the inclinometer readings from those cross-sections. The inclinometers were measured on a bi-weekly basis and the measurement reports for these sites were utilized.

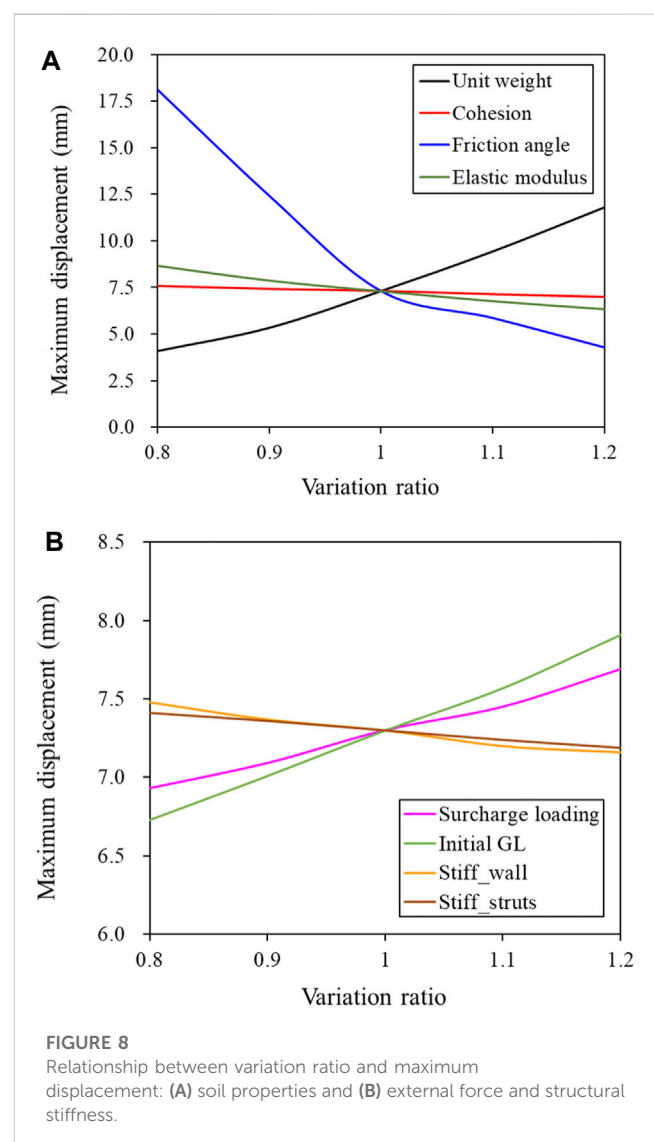
However, the maximum horizontal displacements for Sites A and B, at the final stage of excavation, were measured at 10.86 mm and 10.13 mm, respectively. These values fall within the allowable standard ($\delta h_{\max} < 0.2\%H$, where H represents the excavation depth). With increasing excavation depth, the finite-element analysis indicated a continuous increase in displacement, while the Elastic-Plastic Beam-on-Foundation analysis exhibited a tendency to decrease to approximately 0.0 mm. This disparity can be attributed to the fact that beam-column analysis is a one-dimensional approach, lacking the continuity analysis that considers the interaction between the ground and the structure. Consequently, it is inferred that as the excavation stage progressed, the combined force of the member force and Earth pressure on the upper analysis point of the wall became excessive in the beam-column analysis.

As a result, it was found that the finite-element analysis results were generally similar to the actual inclinometer measurements

compared to the results of beam-column analysis. In fact, even if the inverse analysis is performed, it is a very demanding task to perfectly match the numerical analysis results with the measured values, and it is difficult to consider all site conditions such as ground material properties. This numerical analysis is a conservative result of the 2D analysis, and Figure 5A shows that the measured values at the final excavation stage are in error at 2 m and 4 m. In addition, it is judged that the calculation of ground properties does not reflect 100% of the actual ground properties. However, the validity of the finite element analysis was confirmed by the maximum displacement and the shape of the deformation profile of the wall.

3.2 Results of influence factors analysis

The numerical analysis results were utilized to compare the horizontal displacement of the wall for each influencing factor, as depicted in Figure 6. In terms of unit weight, it was observed that the horizontal displacement tended to increase with an increase in



weight. This can be attributed to the larger load on the wall resulting from the higher unit weight. For adhesion and friction angle, factors indicating the shear strength of the ground, the horizontal displacement decreased with increasing values due to the improved ground stiffness. Notably, the friction angle had a more pronounced effect on the horizontal displacement of the wall compared to the adhesion force. This finding can be attributed to the presence of a fill layer in most excavation sites, where adhesion force is absent. As indicated in Table 2, the absence of adhesion in the fill and sedimentary layers confirms their minimal impact on the wall relative to the friction angle. In regard to the elastic modulus, its impact was smaller than that of unit weight and friction angle, but still greater than that of adhesion. Based on these results, the priority of the influencing factors in terms of subgrade properties was determined as follows: friction angle > unit weight > elastic modulus > adhesion. The effects of surcharge load and initial GL, which can be categorized as external influencing factors, were found to be smaller compared to those of the ground material. Specifically, the horizontal displacement of the wall exhibited similar behavior regardless of the size of the surcharge load. Concerning the initial GL, it was observed that a higher initial GL led to larger horizontal displacement of the wall, attributed to the water pressure exerted on the wall (Figure 7B).

The results related to the stiffness of the structure are presented in Figures 7C, D, indicating that the horizontal displacement of the wall was not significantly affected. While the stiffness of the members may have a substantial impact when considering member forces, the horizontal displacement of the wall is primarily influenced by the ground properties rather than the stiffness of the members. This is in line with the results of a research case analyzed through reverse analysis of an actual embedded retaining wall (Foo et al., 2023). In this study, each influencing factor was quantitatively analyzed and prioritized to provide information that can be used in actual design. Table 5 shows the shear strain results when the variation ratio for each influencing factor is set to the minimum (0.8) and maximum (1.2), and it is helpful to visually understand the effect of the change of each factor on the retaining walls.

4 Discussion

4.1 Sensitivity analysis of influencing factors

The sensitivity of the influencing factors was examined based on the displacement changes of the retaining wall as described in the

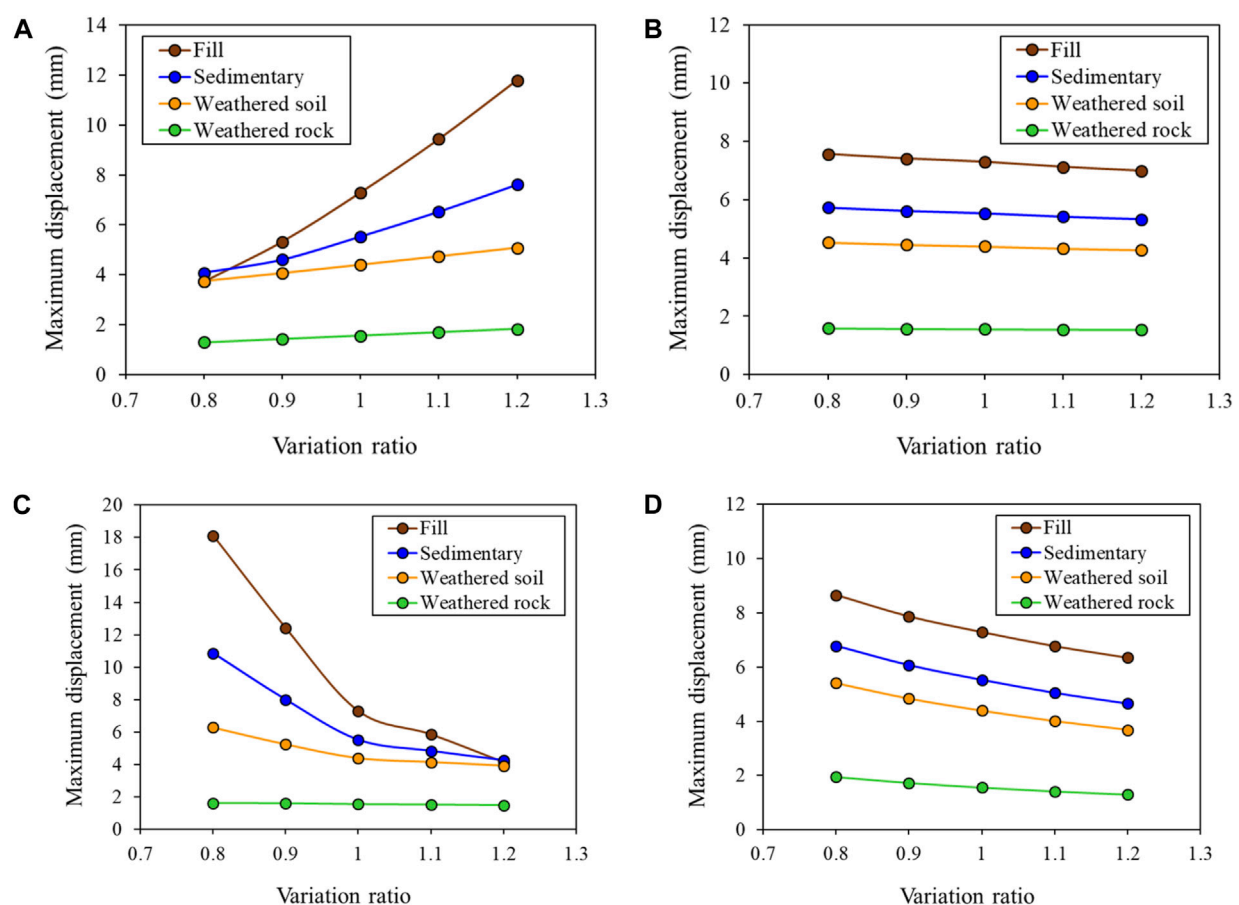


FIGURE 9

Relationship between variation ratio and maximum displacement by soil layer: (A) unit weight; (B) cohesion; (C) friction angle; and (D) elastic modulus.

previous section. Figure 8 illustrates the maximum displacement of the retaining wall in relation to the variation ratio of each influencing factor, including both increasing and decreasing ratios based on a reference ratio of one. As depicted in Figure 8A, the displacement demonstrated a substantial increase with an increase in unit weight. Conversely, as cohesion and elastic modulus values increased, the displacement exhibited a linear decrease. The friction angle displayed a significant impact on wall displacement, particularly when the value fell below the design constant. This finding is consistent with the results of the finite-element analysis conducted in this study, which demonstrated the direct influence of shear strength and friction angle on wall behavior, attributable to the M-C model. It should be noted that while this study focused on sandy soil and rocky ground, the impact of adhesion force is likely to be more pronounced in clay ground, unlike in the current investigation. Figure 8B reveals that an increase in the surcharge load and initial GL of the backfill ground corresponded to a decrease in the strength of the wall and support. This suggests that the influence of wall stiffness and support material

strength, which directly affect the design of the excavation for retaining walls, is considered insignificant due to the role of the temporary structure (support material). However, the initial GL and surcharge load, acting as external loads, exhibited a substantial effect on the wall behavior.

4.2 Analyzing influencing factors by ground type

This study revealed that the variations in influencing factors had different effects depending on the soil type. Figure 9 illustrates the maximum displacement generated by each ground type as the variation ratio of the influencing factors changes. It can be observed that the extent of maximum displacement differs for each subgrade layer as the subgrade properties vary. When the variation ratio of unit weight is set to 0.8, indicating a 20% reduction from the design constant, the sedimentary layer

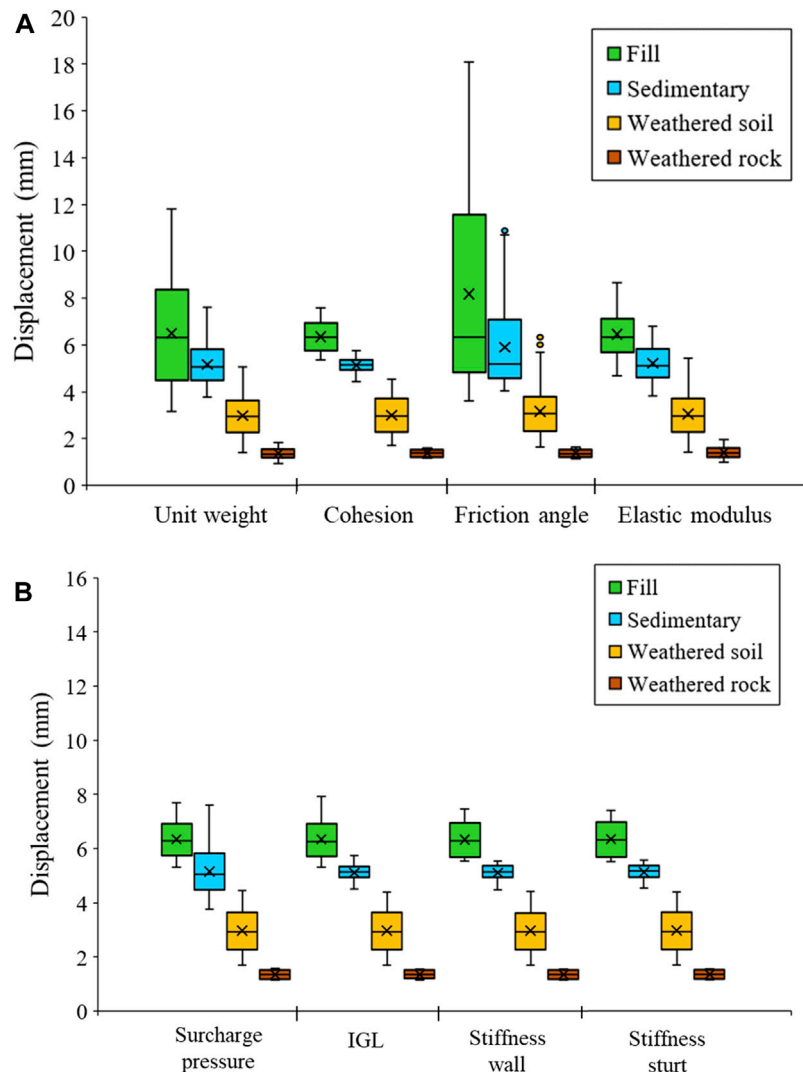


FIGURE 10

Variability of retaining wall displacement with soil type and influencing factors: (A) soil type and (B) external force and structural stiffness.

exhibits the highest maximum displacement. The unit weights of the fill layer and the sedimentary layer, which are significantly lower in magnitude, measure 13.6 kN/m^3 and 14.4 kN/m^3 , respectively. The lower degree of displacement change can be attributed to the presence of anchors constructed in the upper fill layer. Furthermore, it was observed that the maximum horizontal displacement occurs outside the range of anchor support during excavation with a maximum depth of 6.9 m. In terms of cohesion variability, no significant differences were observed among the various ground types, and the impact was negligible in weathered rock. Conversely, similar to unit weight, the friction angle exhibited a substantial effect on wall behavior as it increased or decreased compared to the design constant. Notably, in the fill layer, a significant change in maximum wall displacement occurs when the friction angle deviates more than 10% from the design constant. Furthermore, when the friction angle exceeds 1.2 times the design constant, the maximum displacement is observed in the sedimentary layer. This suggests that a decrease of more than 10% in the friction angle of the fill layer leads to a substantial displacement of 23° , exceeding the typical range of ground properties and resulting in displacements greater than 10 mm. In the sediment layer, with a 20% reduction in the design constant, the friction angle measures 22.4° , resulting in a wall displacement of approximately 12 mm. The relatively smaller displacement observed when the friction angle exceeds 1.2 times can be attributed to the influence of unit weight due to the presence of anchors in the upper fill layer. The effect of changes in elastic modulus value was found to be similar across the various ground types.

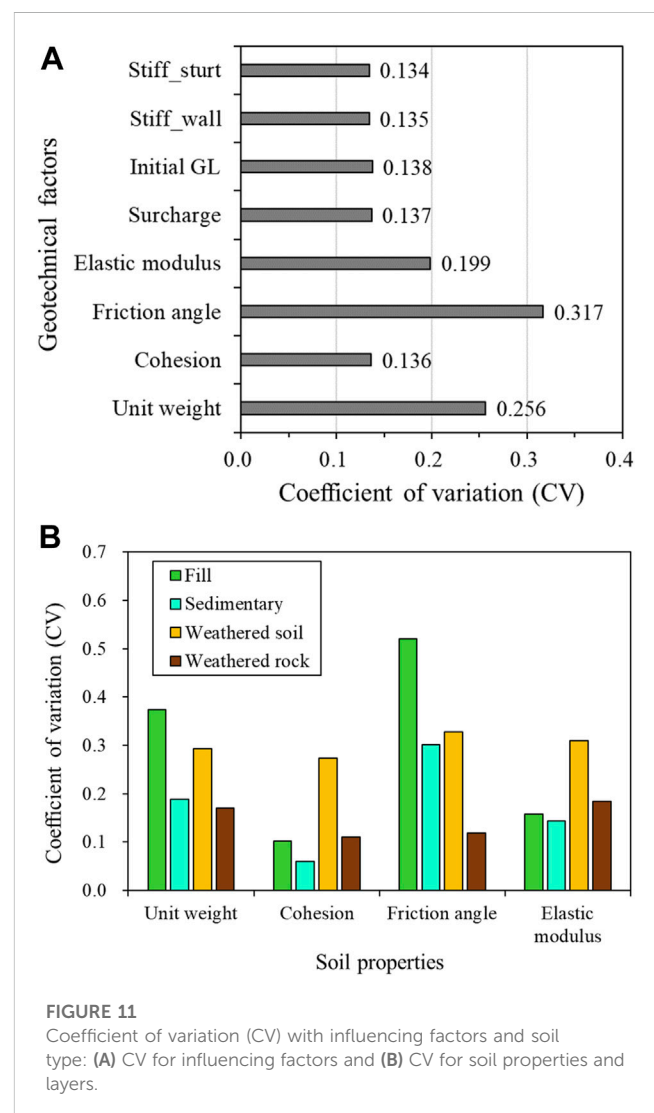
4.3 Coefficient of variation for influencing factors

Figure 10A displays the distribution of displacement data for the retaining wall based on the variation ratio of subgrade properties according to the subgrade type. The displacement values for each subgrade layer, as influenced by the variations in the four subgrade properties, follow the order of fill, sedimentary, weathered soil, and weathered rock. Regardless of the subgrade material, the average displacement value decreases from the fill layer to the weathered rock layer as the depth of excavation increases. The friction angle exerts the most significant influence among the subgrade properties, and outliers in displacement values can be observed in the sedimentary and weathered soil layers. In terms of the impact degree of subgrade type, the displacement value changes for unit weight and friction angle appear significant in the fill and sedimentary layers, while the overall subgrade material seems to be evenly affected in the weathered soil and weathered rock layers. Figure 10B presents the displacement data for the retaining wall according to ground type, considering external forces (surcharge pressure and initial GL) and structural stiffness. Unlike the results based on ground properties, it is challenging to discern specific variations in data distribution for influencing factors or ground types. However, the largest data distribution is observed in the weathered soil layer.

To assess the variability of data, we calculated the coefficient of variation (CV), a unitless measure widely used in various research

fields to demonstrate data variation. The CV is obtained by dividing the standard deviation of the sample by the arithmetic mean. When units differ or data exhibit significant scale differences, the CV provides a means to compare variation equality. Figure 11 illustrates the CV for various influencing factors and subgrade types. Figure 11A displays the CV for all influencing factors, revealing similar variations except for the ground physical properties. The CV for subgrade material is greater compared to other influencing factors. The fill layer and sedimentary layer exhibit high variability in unit weight and friction angle, suggesting that these two properties significantly influence wall displacement in these ground types. In the weathered soil layer, the variability of all four geotechnical properties is similar, indicating that each property influences wall displacement. The weathered rock layer, located at the deepest level, demonstrates overall low variability. Unlike the other layers, the weathered rock layer exhibits a high CV for unit weight and elastic modulus.

The results proposed in this paper can be applied to the calculation of geotechnical properties in the design stage of masonry walls. In the actual masonry wall design stage, the



geotechnical properties are calculated based on the SPT N value for convenience, which is difficult to fully reflect the actual geotechnical properties. Therefore, it is believed that a more reliable wall design can be achieved if a minimum geotechnical investigation is performed for the influential factors as shown in Figure 11A.

5 Conclusion

This study aimed to analyze the key design factors influencing the stability of retaining wall-anchor-support structures during excavation in urban areas by considering field application results and conducting finite-element analysis. Based on the findings, the following conclusions can be drawn:

- 1) The finite-element analysis provided more accurate results compared to the conventional beam-column analysis in terms of considering soil pressure and displacement during ground excavation. The beam-column analysis, being one-dimensional, yielded a displacement of approximately 0 mm at the top of the wall, which does not correspond to the actual value. This discrepancy arises due to the excessive application of combined anchor force and Earth pressure as the excavation stage progressed. In contrast, the finite-element analysis accounted for the interaction between the ground and the structure, resulting in more realistic displacement values.
- 2) The selected influencing factors for the excavation of retaining walls included ground properties, external loads (such as GL and surcharge load), and structural stiffness. Variation ratios ranging from 0.8 to 1.2 were used to compare the quantitative results. The analysis revealed that an increase in unit weight and shear strength of the ground led to a decrease in the maximum horizontal displacement of the wall. On the other hand, the position of the GL, surcharge load, and structural stiffness had a negligible effect on wall displacement.
- 3) Sensitivity analysis of the influencing factors demonstrated that unit weight exhibited a positive correlation with ground properties, while cohesion, friction angle, and elastic modulus showed a negative correlation. Furthermore, the surcharge load and initial GL exhibited a positive correlation, whereas the stiffness exhibited a negative correlation. Of particular note is the friction angle, which proved to be a critical design variable as even small changes in its value resulted in significant variations in wall displacement.
- 4) The CV analysis highlighted the significance of the friction angle, unit weight, and elastic modulus as influential variables impacting the behavior of earth-membrane walls due to their substantial variability. The analysis also revealed that the fill layer exhibited variability in both friction angle and unit weight, while the weathered soil layer demonstrated uniform variability across all ground properties. Therefore, accurate property calculations for the corresponding ground layer are essential for the precise design of retaining walls.
- 5) A quantitative analysis of geotechnical factors affecting wall displacement during excavation was conducted to determine the ranking of factors with large influence. The calculation of

ground physical parameters during the design phase of an actual Earth retaining wall is thought to be possible using this conclusion. Currently, there are limitations in considering the actual ground physical properties by calculating the ground physical properties based on SPT N-values in the design. Based on the findings of this study, it is determined that if a minimal ground survey is carried out for highly influential ground features, a more dependable wall design may be feasible. In conclusion, it is determined that by carrying out a design based on the accurate calculation of parameters, it is possible to design economically while providing stability by changing the cross section of the wall and the type of support material (anchor, strut etc.).

- 6) Although there are many previous studies on the deformation of Earth retaining walls during excavation, there is lack of validation study that examines the stability of various influencing factors such as wall, soil properties, and external influencing factors. Furthermore, there is no study that prioritizes these factors and presents them as a basis for Earth retaining wall design. Based on the results obtained at a specific site, this study conducted an examination of the influence for geotechnical parameters. In addition, based on an actual field case, this study conducted an influence factor analysis on one typical site for Earth retaining walls using a variety of combinations of wall types, ground conditions, and support material types. In order to execute the analysis properly, different wall types and ground conditions should be taken into consideration. However, because there are limitless combinations of these circumstances, this study concentrated on site characteristics and wall construction techniques that are primarily employed in South Korea. Further study is expected to be able to offer data that may be used to enhance the actual design effectiveness of various Earth retaining wall construction techniques.

Data availability statement

The original contributions presented in the study are included in the article/supplementary material, further inquiries can be directed to the corresponding author.

Author contributions

SS: Data curation, Formal Analysis, Methodology, Visualization, Writing-original draft. JP: Formal Analysis, Writing-review and editing. YK: Resources, Writing-review and editing. GK: Writing-review and editing. MC: Funding acquisition, Resources, Writing-review and editing.

Funding

The author(s) declare financial support was received for the research, authorship, and/or publication of this article. This research was supported by the Korea Institute of Civil Engineering and Building Technology through the project "Development of Smart

Complex Solution for Large-Deep Underground Space Using Artificial Intelligence” (grant No. 20230105-001).

Conflict of interest

The authors declare that the research was conducted in the absence of any commercial or financial relationships that could be construed as a potential conflict of interest.

References

- Bhatkar, T., Barman, D., Mandal, A., and Usmani, A. (2017). Prediction of behaviour of a deep excavation in soft soil: a case study. *Int. J. Geotechnical Eng.* 11 (1), 10–19. doi:10.1080/19386362.2016.1177309
- Boscardin, M. D., and Cording, E. J. (1989). Building response to excavation-induced settlement. *J. Geotechnical Eng.* 115 (1), 1–21. doi:10.1061/(asce)0733-9410(1989)115:1(1)
- Bowles, J. E. (1996). *Foundation analysis and design*. 5th Edn. New York: The McGraw-Hill Companies, Inc.
- Caspe, M. S. (1966). Surface settlement adjacent to braced open cuts. *J. Soil Mech. Found. Div. ASCE* 92 (SM4), 51–59. doi:10.1061/JSEFAQ.0000889
- Chen, S. L., Ho, C. T., and Gui, M. W. (2014). Diaphragm wall displacement due to creep of soft clay. *Proc. Institution Civ. Engineers-Geotechnical Eng.* 167 (3), 297–310. doi:10.1680/jgeot.11.00050
- Clough, G. W., and O'Rourke, T. D. (1990). “Constructed induced movements of in-situ walls,” in *In Proc. ASCE Specialty Conference (Cornell)*. doi:10.1061/(ASCE)0733-9410(1992)118:4(665)
- Clough, G. W., and Tsui, Y. (1974). Performance of tied-back walls in clay. *J. Geotechnical Eng. Div.* 100 (12), 1259–1273. doi:10.1061/AJGEB6.0000128
- Dmochowski, G., and Szolomicki, J. (2021). Technical and structural problems related to the interaction between a deep excavation and adjacent existing buildings. *Appl. Sci.* 11 (2), 481. doi:10.3390/app11020481
- Do, T. N., and Ou, C. Y. (2020). Factors affecting the stability of deep excavations in clay with consideration of a full elastoplastic support system. *Acta Geotech.* 15 (7), 1707–1722. doi:10.1007/s11440-019-00886-8
- Dong, Y. P., Burd, H. J., and Houlsby, G. T. (2018). Finite element parametric study of the performance of a deep excavation. *Soils Found.* 58 (3), 729–743. doi:10.1016/j.sandf.2018.03.006
- Fearnhead, N., Maniscalco, K., Standing, J. R., and Wan, M. S. (2014). Deep excavations: monitoring mechanisms of ground displacement. *Proc. Institution Civ. Engineers-Geotechnical Eng.* 167 (2), 117–129. doi:10.1680/jgeot.13.00047
- Foo, C. F., Le, T., Bailie, P., and Standing, J. R. (2023). “Back-analysis of an embedded retaining wall in stiff clay,” in *Proceedings of the Institute of Civil Engineers-Geotechnical Engineering*. doi:10.1680/jgeen.22.00072
- Goh, A. T. C., Zhang, R. H., Wang, W., Wang, L., Liu, H. L., and Zhang, W. G. (2020). Numerical study of the effects of groundwater drawdown on ground settlement for excavation in residual soils. *Acta Geotech.* 15, 1259–1272. doi:10.1007/s11440-019-00843-5
- Hsieh, P. G., and Ou, C. Y. (1998). Shape of ground surface settlement profiles caused by excavation. *Can. geotechnical J.* 35 (6), 1004–1017. doi:10.1139/t98-056
- Hsiung, B. C. B. (2009). A case study on the behaviour of a deep excavation in sand. *Comput. Geotechnics* 36 (4), 665–675. doi:10.1016/j.compgeo.2008.10.003
- Jeong, S. S., and Kim, Y. H. (2009). Characteristics of collapsed retaining walls using elastoplastic method and finite element method. *J. Korean Geotechnical Soc.* 25 (4), 19–29. doi:10.7843/kgs.2020.36.1.29
- Khoiri, M., and Ou, C. Y. (2013). Evaluation of deformation parameter for deep excavation in sand through case histories. *Comput. Geotechnics* 47, 57–67. doi:10.1016/j.compgeo.2012.06.009
- Lee, S. J., Song, T. W., Lee, Y. S., Song, Y. H., and Kim, H. K. (2007). A case study of building damage risk assessment due to the multi-propped deep excavation in deep soft soil. *4th Int. Conf. Soft Soil Eng.* Vancouver, London, Taylor Francis.
- Mana, A. I., and Clough, G. W. (1981). Prediction of movements for braced cuts in clay. *J. Geotechnical Eng. Div.* 107 (6), 759–777. doi:10.1061/AJGEB6.0001150
- Naylor, D. J., and Pande, G. N. (1981). *Finite elements in geotechnical engineering*. Swansea, UK: Pineridge Press.
- Ng, C. W. W. (1992). *An evaluation of soil-structure interaction associated with a multi-propped excavation*. PhD thesis. Bristol, England: Univ. of Bristol.
- Ou, C. Y., Hsieh, P. G., and Chiou, D. C. (1993). Characteristics of ground surface settlement during excavation. *Can. geotechnical J.* 30 (5), 758–767. doi:10.1139/t93-068
- Park, C. S., and Joung, S. M. (2020). Numerical investigations on the excavation width and property of deformation of earth retaining wall. *J. Korean Geotechnical Soc.* 36 (12), 57–68. doi:10.7843/kgs.2020.36.12.57
- Peck, R. B. (1969). “Deep excavations and tunneling in soft ground. State-of-the-Art report,” in *Proc. of the 7th International Conference on Soil Mechanics and Foundation Engineering (Mexico City: State-of-the-Art)*, 225–290. *Plaxis 2D ver 2022 manuals*, Bentley.
- Poh, T. Y., and Wong, I. H. (1998). Effects of construction of diaphragm wall panels on adjacent ground: field trial. *J. geotechnical geoenvironmental Eng.* 124 (8), 749–756. doi:10.1061/(asce)1090-0241(1998)124:8(749)
- Powrie, W., and Kantartzi, C. (1996). Ground response during diaphragm wall installation in clay: centrifuge model tests. *Geotechnique* 46 (4), 725–739. doi:10.1680/geot.1996.46.4.725
- Ran, L., Ye, X. W., and Zhu, H. H. (2011). Long-term monitoring and safety evaluation of a metro station during deep excavation. *Procedia Eng.* 14, 785–792. doi:10.1016/j.proeng.2011.07.099
- Schäfer, R., and Triantafyllidis, T. (2004). Modelling of earth and water pressure development during diaphragm wall construction in soft clay. *Int. J. Numer. Anal. Methods Geomechanics* 28 (13), 1305–1326. doi:10.1002/nag.388
- Schäfer, R., and Triantafyllidis, T. (2006). The influence of the construction process on the deformation behaviour of diaphragm walls in soft clayey ground. *Int. J. Numer. Anal. methods geomechanics* 30 (7), 563–576. doi:10.1002/nag.480
- Son, M., and Cording, E. J. (2005). Estimation of building damage due to excavation-induced ground movements. *Geotech. Geoenvironmental Eng.* 131 (2), 162–177. doi:10.1061/(ASCE)1090-0241(2005)131:2(162)
- Son, M., and Cording, E. J. (2007). Evaluation of building stiffness for building response analysis to excavation-induced ground movements. *Geotech. Geoenvironmental Eng.* 133 (8), 995–1002. doi:10.1061/(ASCE)1090-0241(2007)133:8(995)
- Song, J. S., and Yoo, C. S. (2018). Effect of ground water table on deep excavation performance. *J. Korean Geosynth. Soc.* 17 (3), 33–46. doi:10.12814/jkgss.2018.17.3.033
- St John, H. D. (1975). *Field and theoretical studies of the behaviour of ground around deep excavations in London clay*. PhD thesis. Cambridge, UK: Cambridge University.
- Symons, I. F., and Carder, D. R. (1993). “Stress changes in stiff clay caused by the installation of embedded retaining walls,” in *Retaining structures* (Thomas Telford Publishing), 227–236.
- Tanner Blackburn, J., and Finno, R. J. (2007). Three-dimensional responses observed in an internally braced excavation in soft clay. *J. Geotechnical Geoenvironmental Eng.* 133 (11), 1364–1373. doi:10.1061/(asce)1090-0241(2007)133:11(1364)
- Wong, I. H., and Poh, T. Y. (2000). Effects of jet grouting on adjacent ground and structures. *J. Geotechnical Geoenvironmental Eng.* 126 (3), 247–256. doi:10.1061/(asce)1090-0241(2000)126:3(247)
- Wu, I. C., Lu, S. R., and Hsiung, B. C. (2015). A BIM-based monitoring system for urban deep excavation projects. *Vis. Eng.* 3, 2–11. doi:10.1186/s40327-014-0015-x
- Yoo, C. S., and Kim, Y. J. (2000). Behavior of propped walls during deep excavation. *J. Korean Geosynth. Soc.* 20 (3), 195–204.
- Zhang, D. M., Xie, X. C., Li, Z. L., and Zhang, J. (2020). Simplified analysis method for predicting the influence of deep excavation on existing tunnels. *Comput. Geotechnics* 121, 103477. doi:10.1016/j.compgeo.2020.103477
- Zhang, W., Goh, A. T., and Xuan, F. (2015). A simple prediction model for wall deflection caused by braced excavation in clays. *Comput. Geotechnics* 63, 67–72. doi:10.1016/j.compgeo.2014.09.001
- Zhang, W., Wang, W., Zhou, D., Zhang, R., Goh, A. T. C., and Hou, Z. (2018). Influence of groundwater drawdown on excavation responses—A case history in Bukit Timah granitic residual soils. *J. Rock Mech. Geotechnical Eng.* 10 (5), 856–864. doi:10.1016/j.jrmge.2018.04.006

Publisher's note

All claims expressed in this article are solely those of the authors and do not necessarily represent those of their affiliated organizations, or those of the publisher, the editors and the reviewers. Any product that may be evaluated in this article, or claim that may be made by its manufacturer, is not guaranteed or endorsed by the publisher.

Frontiers in Environmental Science

Explores the anthropogenic impact on our
natural world

An innovative journal that advances knowledge of
the natural world and its intersections with human
society. It supports the formulation of policies that
lead to a more inhabitable and sustainable world.

Discover the latest Research Topics

[See more →](#)

Frontiers

Avenue du Tribunal-Fédéral 34
1005 Lausanne, Switzerland
frontiersin.org

Contact us

+41 (0)21 510 17 00
frontiersin.org/about/contact

